



*Preprint*

**AAS/GSFC 13th International Symposium on  
Space Flight Dynamics**

**Volume 2**

*Tom Stengle, Editor*

*Proceedings of a conference held at  
Goddard Space Flight Center, Greenbelt, Maryland  
May 11-15, 1998*

National Aeronautics and  
Space Administration

**Goddard Space Flight Center**  
Greenbelt, Maryland 20771



## The NASA STI Program Office ... in Profile

Since its founding, NASA has been dedicated to the advancement of aeronautics and space science. The NASA Scientific and Technical Information (STI) Program Office plays a key part in helping NASA maintain this important role.

The NASA STI Program Office is operated by Langley Research Center, the lead center for NASA's scientific and technical information. The NASA STI Program Office provides access to the NASA STI Database, the largest collection of aeronautical and space science STI in the world. The Program Office is also NASA's institutional mechanism for disseminating the results of its research and development activities. These results are published by NASA in the NASA STI Report Series, which includes the following report types:

- **TECHNICAL PUBLICATION.** Reports of completed research or a major significant phase of research that present the results of NASA programs and include extensive data or theoretical analysis. Includes compilations of significant scientific and technical data and information deemed to be of continuing reference value. NASA's counterpart of peer-reviewed formal professional papers but has less stringent limitations on manuscript length and extent of graphic presentations.
- **TECHNICAL MEMORANDUM.** Scientific and technical findings that are preliminary or of specialized interest, e.g., quick release reports, working papers, and bibliographies that contain minimal annotation. Does not contain extensive analysis.
- **CONTRACTOR REPORT.** Scientific and technical findings by NASA-sponsored contractors and grantees.
- **CONFERENCE PUBLICATION.** Collected papers from scientific and technical conferences, symposia, seminars, or other meetings sponsored or cosponsored by NASA.
- **SPECIAL PUBLICATION.** Scientific, technical, or historical information from NASA programs, projects, and mission, often concerned with subjects having substantial public interest.
- **TECHNICAL TRANSLATION.** English-language translations of foreign scientific and technical material pertinent to NASA's mission.

Specialized services that complement the STI Program Office's diverse offerings include creating custom thesauri, building customized databases, organizing and publishing research results . . . even providing videos.

For more information about the NASA STI Program Office, see the following:

- Access the NASA STI Program Home Page at <http://www.sti.nasa.gov/STI-homepage.html>
- E-mail your question via the Internet to [help@sti.nasa.gov](mailto:help@sti.nasa.gov)
- Fax your question to the NASA Access Help Desk at (301) 621-0134
- Telephone the NASA Access Help Desk at (301) 621-0390
- Write to:  
NASA Access Help Desk  
NASA Center for AeroSpace Information  
800 Elkridge Landing Road  
Linthicum Heights, MD 21090-2934



*Preprint*

**AAS/GSFC 13th International Symposium on  
Space Flight Dynamics**

**Volume 2**

*Tom Stengle, Editor  
Goddard Space Flight Center, Greenbelt, Maryland*

*Proceeding of a conference held at  
Goddard Space Flight Center, Greenbelt, Maryland  
May 11–15, 1998*

National Aeronautics and  
Space Administration

**Goddard Space Flight Center**  
Greenbelt, Maryland 20771

This is a preprint of a paper intended for presentation at a conference. Because changes may be made before formal publication, this is made available with the understanding that it will not be cited or reproduced without the permission of the author.

Available from:

NASA Center for AeroSpace Information  
7121 Standard Drive  
Hanover, MD 21076-1320  
Price Code: A17

National Technical Information Service  
5285 Port Royal Road  
Springfield, VA 22161  
Price Code: A10

## Contents – Volume II

<u>Paper No.</u>	<u>TITLE</u>	
AAS 98-346	"Near Comet Orbit Planning and Navigation," Mora, Muñoz (GMV SA), Rodriguez-Canabal (ESOC)	541
AAS 98-347	"The CONTOUR NASA Discovery Mission," Reynolds (JHU/APL)	561
AAS 98-348	"Using Solar Radiation Pressure to Control Libration Point Orbits," Tene	575
AAS 98-349	"Trajectory Design Strategies That Incorporate Invariant Manifolds and SWINGBY," Guzmán, Howell (Purdue University), Cooley, Folta (NASA/GSFC)	581
AAS 98-350	"Long-Term Evolution in the Vicinity of Geostationary Orbit," Deleuze (CNES)	597
AAS 98-351	"An Autonomous Navigator for LEO Satellites," Pascal, Marcille, Damilano (Natra Marconi Space)	607
AAS 98-352	"Autonomous Acquisition and Maintenance of a Satellite Constellation using LQG/LTR Optimal Controller with GPS Measurements," Xing, Parvez (Space Products and Applications)	621
AAS 98-353	"Relative Navigation for Spacecraft Formation Flying," Lee, Kelbel, Long (CSC), Hartman, Gramling (NASA/GSFC)	635
AAS 98-354	"OnBoard Orbit Determination Algorithm Based On Earth-Referenced Attitude Sensors," Iida (NEC Corporation), Hashimoto, Ninomiya (ISAS)	651
AAS 98-355	"A Low Cost Approach to Simultaneous Orbit, Attitude, and Rate Estimation Using an Extended Kalman Filter," Deutschmann, Harman (NASA/GSFC), Bar-Itzhack (Technion-Israel Institute of Technology)	667
AAS 98-356	"Effects of Orbit Eccentricity on TSS-1 Pendulum-Like Oscillations," Bergamaschi, Colombatti (Università di Padova), Merlina (Alenia Aerospazio), Sinopoli (Istituto Universitario di Architettura)	677
AAS 98-357	"Control of the XMM orbit using momentum dumping manoeuvres," Rosengren (ESOC)	693
AAS 98-358	"RADARSAT Time Rate of Mean Semi-Major Axis Due to Drag," Marandi (Canadian Space Agency)	709
AAS 98-360	"Reentry Algorithm For Rescue Reentry Vehicle," Sikharoulidze, Kaluzhskikh (Keldysh Institute of Applied Mathematics)	715
AAS 98-361	"Flight Dynamic Designing of Manned Return Space Vehicle for Hyperbolic Entry," Ivanov, Kazakov, Rumynskiy, Sobolevskiy, Udalo (Mission Control Center)	727
AAS 98-362	"Improved Instrumental Magnitude Prediction from Version 2 of the NASA SKY2000 Master Star Catalog," Sande, Brasoveanu, Miller, Home (CSC), Tracewell (NASA/GSFC), Warren (Raytheon STX)	741
AAS 98-363	"Autonomous Star Tracker," Landi, Procopio, Lucarini (Alenia)	755
AAS 98-364	"Autonomous Star Identification Using Fuzzy Neural Logic Networks," Hong, Dickerson (Iowa State University)	757
AAS 98-365	"Probability Analysis for Spacecraft Attitude Acquisition Using Star Pattern Match Algorithm," Didinsky, Wu (Hughes)	773
AAS 98-366	"Star Identification for Three-Axis Attitude Estimation of French-Brazilian Scientific Micro-Satellite," Lopes, Carvalho, Silva (INPE)	775
AAS 98-367	"A Robust Star Acquisition Algorithm for the Wide-field Infrared Explorer," Stoneking (Orbital Sciences Corporations)	791



AAS 98-368	"Performance of Least Squares and Kalman Filter Algorithms For Orbit Determination Using Single- and Multi-Station Tracking of Geostationary Satellites," Halain, Rochus (Université de Liège), Welter, Francken, Krier, Wauthier (Société Européenne des Satellites)	803
AAS 98-369	"SOHO and WIND Orbit Determination Using a Sequential Filter," Hujsak, Stein, Chuba, Rose (Logicon Geodynamics)	817
AAS 98-370	"Navigation and Muses-B Mission-HALCA," Ichikawa, Kato (ISAS)	833
AAS 98-371	"Navigation of the Space VLBI Mission – HALCA," You, Ellis, Mottinger (NASA/JPL)	841
AAS 98-372	"Reentry Prediction Method Using Plural Two Line Elements," Konno, Tajima, Hirota (NASDA)	857
AAS 98-373	"EUV Reaction Wheel Assembly Calibration for Improved Spacecraft Slews," Bauer (Bauer Engineering Enterprises), Smith, Nevitt (UC Berkeley)	871
AAS 98-374	"Solar Torque Compensation Determination System for the GOES I-M Series Weather Satellites," DeGumbia (Lockheed Martin), Tsui (NOAA)	887
AAS 98-375	"Use of Microgravity Sensors for Quantification of Space Shuttle Orbiter Vernier Reaction Control System Induced Environments," Friend (Boeing)	899
AAS 98-376	"Attitude Commands Avoiding Bright Objects and Maintaining Communication With Ground Stations," Hablani (Boeing North American)	913
AAS 98-377	"Magnetic Torque Attitude Control of an Experimental Microsatellite in Equatorial Orbit," Vera, Alexandrov, Rangel, Pedroza, Mocencahua, Fournier (BUAP)	933
AAS 98-378	"MAP Stability, Design and Analysis," Ericsson-Jackson, Andrews, O'Donnell, Markley (NASA/GSFC)	937
AAS 98-379	"TOPEX/Poseidon Orbit Maintenance for First Five Years," Bhat, Shapiro, Frauenholz (NASA/JPL), Leavitt (Sterling Software)	953
AAS 98-380	"BeppoSAX Ground Attitude Determination," Libero, Gennaro (Telespazio), Pastor, Stornelli (Datspazio)	969
AAS 98-381	"Attitude Determination and Control in INTERBALL Project," Eismont, Khrapchenkov (Russian Academy of Sciences), Triska, Truhlik, Chum (Academy of Sciences of Czech Republic)	983
AAS 98-382	"Flight Dynamics LEOP and Routine Operations for SCD2, the INPE's Second Environmental Data Collecting Satellite," Orlando, Kuga, Guedes (INPE)	997
AAS 98-383	"Analysis of Docking Operations Experience of the Progress Vehicles and the MIR Stations Using Teleoperator Control," Matveeva (Rocket Space Corporation Energia)	1009
AAS 98-384	"Mars Global Surveyor Navigation and Aerobraking at Mars," Esposito, Demcak, Graat, Hohnston, Mase (NASA/JPL)	1011
AAS 98-385	"Martian Elliptic Balanced Satellite Orbits," Kudielka	1025
AAS 98-386	"Solar Photonic Assist Trajectory Design for Solar Sail Missions to the Outer Solar System and Beyond," Leipold (German Aerospace Center), Wagner (Technical University of Munich)	1031
AAS 98-387	"Accuracy Of Orbit Determination For Low Thrust Trajectory to the Mars," Akim, Stepaniants, Tuchin (Keldysh Institute of Applied Mathematics)	1043

AAS 98-388	"The Comparative Analysis of the Optimal Interplanetary Transfers with Large and Low-Thrust at Using the Middle-Class Launch Vehicles," Kolyuka, Zyuzin (MCC)	1055
AAS 98-389	"Close Approach to Sun Using Gravity Assists of the Inner Planets," Sukhanov (Russian Academy of Sciences)	1057

## NEAR COMET ORBIT PLANNING AND NAVIGATION\*

Dr. Miguel Belló Mora<sup>†</sup>, Mr. José Prieto Muñoz<sup>‡</sup>, Dr. José Rodríguez-Canabal<sup>‡</sup>

This paper presents the near comet orbit planning and navigation results obtained during the mission analysis study for the ROSETTA project of the European Space Agency. The orbital strategy for near comet operations is designed in 9 different phases including the approximation trajectory, global mapping of the nucleus, close observation of candidate landing sites and the ejection and landing on the nucleus of a Surface Science Package (SSP) to perform the in situ analysis of the comet. The orbit determination in the vicinity of the cometary nucleus will be primarily based on the combination of natural landmarks observations (using on board camera) and Range and Doppler measurements from ground stations. The navigation process includes the simultaneous estimation of the spacecraft position and velocity relative to the comet, the comet position and velocity relative to the Sun, the SSP position and velocity relative to the comet, the nucleus Euler angles to define the body fixed frame orientation relative to the inertial coordinate system, the angular velocity of the nucleus in body fixed frame, the nucleus gravitational field parameters (up to order and degree four), the inertia matrix of the cometary nucleus (inertia matrix and second order gravitational parameters are related) and the location of the selected landmarks. A navigation tool based on a Square Root Information Filter (SRIF) has been designed and integrated in the Rosetta Near Comet Operations Simulator (RONCOS) program which performs end to end numerical simulations of all near comet operations considering orbit strategy and navigation aspects. The most important results for all the phases in the vicinity of the comet are summarised in this paper.

### INTRODUCTION

The European Space Agency considers ROSETTA to be the third cornerstone of the Horizon 2000 Program. The prime objective of the ROSETTA Comet Rendezvous Mission is the in-situ analysis of the chemical, mineralogical and isotopic composition of a cometary nucleus, in this case the comet Wirtanen. ROSETTA will be launched by Ariane 5 from Kourou in January 2003, it will perform one swingby of Mars and two swingbys of Earth. In addition, it will do flybys of the asteroids Mimistrobell and Rodari. The comet rendezvous will be in 2011. A period of 32 months is required from launch to Mars arrival. The spacecraft will be in hibernation until approximately three months before the swingby date. A powered gravity assist of Mars will be performed in August 2005. Daily tracking with two groundstations will be resumed three months before Mars arrival for retargeting and correction maneuvers before and after the swingby. The first Earth gravity assist will be performed in

\* This work has been carried out under ESA contract (COPNAV, ESOC 11250/94/D/IM)

<sup>†</sup> GMV SA, Isaac Newton 11, PTM 28760 Tres Cantos, Madrid, Spain

<sup>‡</sup> ESA/ESOC, Robert Bosch Strasse 5, Darmstadt (Germany)



November 2005 with a hyperbolic excess velocity of 9.6 km/s. Similar the Mars swingby, daily operations will be resumed 3 months before the swingby and continue up to 1 month after the swingby for targeting and correction maneuvers. The first Earth gravity assist will inject the spacecraft into an orbit, which crosses the orbit of the asteroid Mimistrobell. The flyby of Mimistrobell will be performed in September 2006. Detection of the asteroid by the spacecraft will occur about 8 days before the flyby. Science data will be stored onboard for later transmission to Earth. The second Earth gravity assist will be performed in November 2007. This swingby will inject the spacecraft into a high energy heliocentric orbit on route to the comet Wirtanen. This trajectory will cross the orbit of the asteroid Rodari. A flyby of Rodari will be performed in May 2008 at a relative velocity of 11.3 km/s. ROSETTA spacecraft will arrive at the comet Wirtanen in 2011 near the cometary aphelion at a Sun distance of 4.5 AU. The relative velocity of the encounter will be 1.24 km/s. ROSETTA will start near comet operations after the rendezvous in 2011 and finish after the comet perihelion in 2013.

### THE ROSETTA NEAR COMET OPERATIONS SIMULATOR PROGRAM (RONCOS)

A Rosetta Near Comet Operations Simulator Program (RONCOS) with 120,000 lines of code has been developed for the analysis of the orbital strategy and navigation in the vicinity of the nucleus. This simulator program performs

- **orbit planning,**
- **navigation,**
- **parameter estimation and,**
- **auxiliary calculations**

for all the phases in the vicinity of the comet nucleus from the orbit matching manoeuvre up to the extended monitoring. RONCOS may be run in three different modes:

- **Nominal mode:** only orbit planning and simulation of the nominal trajectory is performed.
- **Navigation mode:** parameter estimation is also performed for a single simulation with the corresponding Covariance Analysis.
- **Monte Carlo mode:** several simulations are computed to get statistics of the navigation and parameter estimation errors for cross checking with the Covariance Analysis results.

The Rosetta Near Comet Operations Simulator includes the following modules:

- **INITIALISATION:** Characterisation of the irregular shape comet nucleus and navigation statistics for initial phase.
- **ORBIT PLANNING:** Computation of orbital strategy for each phase according to the best estimation of spacecraft and comet nucleus parameters.
- **SIMULATION:** Real World and On Ground Computer Modelled World are simulated:
  - **DYNAMICS:** Spacecraft dynamics (comet high order gravity, solar radiation pressure, solar tidal force, nucleus gas, dust and jets model, manoeuvre execution) and comet nucleus kinematics (rigid body motion with nutation) are simulated.
  - **MEASUREMENTS:** On ground (range, Doppler, Diff. VLBI) and on board (imaging system) measurements are simulated.
- **NAVIGATION:** A Square Root Information Filter (SRIF) is used for orbit determination and nucleus parameter estimation.
- **RESULTS EXPLOITATION:** An independent plotting system is used to monitor the evolution of all near comet orbit and navigation parameters (more than 200 different plots).

### Comet Nucleus Model

An irregular shape nucleus is considered in RONCOS (example in Figure 1), the cometary parameters selected for numerical simulations (28 cases) are summarised in Table 1.



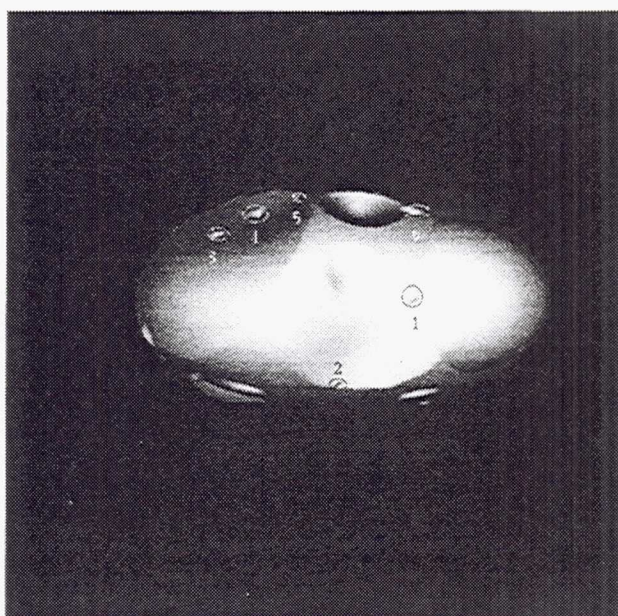


Figure 1. Typical Comet Nucleus Shape and Identified Landmarks.

Table 1  
COMET NUCLEUS REFERENCE CASES

Comet	Density	Rot. Period	Nutation	Spin	Shape Irre.	Activity	Case		
500 m Small	0.2 $\text{gr/cm}^3$	10 <i>hr</i>	5°	Perp.	Medium	Medium	<i>Small</i>		
		240 <i>hr</i>					12		
		10 <i>hr</i>					0°	13	
			10°				14		
			5°				Inclined	15	
		Perp.		High	16				
			Medium	High	17				
	1.5 $\text{gr/cm}^3$	Medium	18						
600 m Wirtanen	0.75 $\text{gr/cm}^3$	7 <i>hr</i>	5°	Perp.	Medium	Medium	<i>Wirtanen</i>		
		14 <i>hr</i>					22		
		240 <i>hr</i>					23		
		7 <i>hr</i>	0°				24		
			10°				25		
			5°	In Orbit			26		
				Inclined			27		
				To Sun			28		
				Perp.			Low	29	
							High	210	
		Medium	Low		211				
		High	212						
		2.5 Km Big	1.5 $\text{gr/cm}^3$	7 <i>hr</i>	5°	Perp.	Medium	Medium	<i>Big</i>
				240 <i>hr</i>	0°				32
7 <i>hr</i>	33								
	10°			34					
	5°			Inclined	35				
Perp.				High	36				
	Medium			High	37				
0.2 $\text{gr/cm}^3$	Medium		38						

The model of cometary activity has been developed by Prof. Ivashkin (Russian Academy of Sciences) under GMV contract. It is based on previous studies (J.F. Crifo, A.H. Delsemme, N. Divine, C. Froeschle, T.I. Gombosi, J.A.M. McDonnell, R.F. Probst, H. Rickman, Z. Sekanina, L.M. Shul'man, M.K. Wallis, F.L. Whipple, et al.) and it has been compared with more sophisticated models, astronomical observation and laboratory experimental data.

### **Near Nucleus Dynamics**

The motion of the S/C and the SSP in the vicinity of the comet is simulated taking into account:

- The gravitational field of the irregular nucleus up to order and degree four
- The solar tidal force
- The solar radiation pressure
- The effect of comet outgassing (background and jets, gas and dust)
- The kinematics equations of the nucleus which relates the Euler angles with the angular velocity
- The equations of the nucleus as rigid body which relates the angular velocity with the moments of inertia and external torque (due to jets)

### **Measurements Model**

The following measurements models have been implemented in this tool for cometary navigation:

#### **On ground radiometric measurements:**

- Two way range from up to 10 groundstations
- Two way range rate or Doppler from up to 10 groundstations
- Differential range from up to 10 baselines
- ΔDOR (Double Differential One Way Range) from up to 10 baselines

#### **On board measurements with Narrow (NAC) and Wide (WAC) Angle camera:**

- NAC and WAC optical tracking of comet direction as a point
- NAC and WAC optical tracking of comet direction as extended body
- NAC and WAC optical tracking of landmarks (up to 5) versus star background
- NAC and WAC optical tracking of landmarks (up to 5) without a fixed background
- Radar altimeter ranging to the comet surface

The results presented in this paper are based on the use of conventional range and Doppler (from Weilheim, Perth and Villafranca) combined with NAC ( $3.4^\circ \times 3.4^\circ$ ) and WAC ( $15^\circ \times 15^\circ$ ) images of the comet nucleus (differential VLBI and radar has not been used).

### **Near Comet Navigation**

The orbit determination in the vicinity of the cometary nucleus will be primarily based on the combination of natural landmarks observations (using the wide angle camera) and Range and Doppler measurements from ground stations. The navigation process includes the simultaneous estimation of the following dynamical state variables (53):

- Spacecraft position and velocity relative to the comet (6).
- Comet position and velocity relative to the Sun (6).
- SSP position and velocity relative to the comet (6).
- Euler angles (3) to define the body fixed frame orientation relative to the inertial system.
- Angular velocity of the nucleus in body fixed frame (3).
- Gravitational constant of the comet, gravitational field parameters and the inertia matrix of the cometary nucleus (inertia matrix and second order gravitational parameters are related).
- Coordinates of the selected landmarks in the body fixed frame (15 variables for 5 landmarks).



A navigation tool based on a Square Root Information Filter (SRIF) has been designed in the current Near Comet Orbit Planning and Navigation study. This tool has been integrated in the Rosetta Near Comet Operations Simulator (RONCOS).

## ROSETTA NEAR COMET OPERATIONS

The cometary environment will be largely unknown before the Rosetta spacecraft approaches the comet. Ground observations can possibly determine the size of the nucleus and the spin rate, but the shape, gravity and kinematics will be completely unknown. They will be determined by means of onboard observations during the near comet phase. A detailed analysis of all near comet operations has been performed within the Near Comet Orbit Planning and Navigation study. The near comet baseline is decomposed in 9 different phases, described in the subsequent paragraphs.

### NEAR COMET DRIFT PHASE

The comet rendezvous manoeuvres in 2011 will inject the spacecraft into a trajectory with a residual drift (about 25 m/s) with respect to the comet. Actual approach operations have to be delayed due to following technical constraints:

- Under the current design a maximum Sun distance of 4.2 AU is required for the solar array to provide the required power.
- In order to guarantee a high enough bit rate using the 15 m dish ESA antenna, a maximum distance to the Earth of 3.5 AU is imposed.

The drift phase is designed such that at the end of the required waiting period the spacecraft reaches a desired point relative to the comet at the time at which the actual approach operations can be started. The final point is selected such that cometary debris is avoided (normally near the comet flight path) and good comet illumination conditions are obtained. This is the **Comet Acquisition Point (CAP)**. A comet distance of 100,000 km has been proposed as baseline for the CAP. It is a compromise between safety, comet detection, time and initial target bias. A smaller value presents the problem of crossing the comet track at a short distance (a large dispersion is expected at CAP), in addition a complex scanning should be necessary to find the comet at a closer distance. A larger value presents the problem of very large distances for the beginning of the near comet drift (several millions of km). In addition, this distance ensures a very good acquisition even for the worst comet case. The CAP velocity is set to 25 m/s. Simulations with different values show that a smaller value imposes very large duration for the far approach while larger values imply very large distances for the beginning of the near comet drift.

The illumination angle at CAP has been set to 45°. A parametric analysis of the total required  $\Delta V$  as a function of the illumination angle has been performed. The total required  $\Delta V$  decreases for increasing values of the illumination angle. The maximum permissible angle is 70°. However, the very large dispersion at CAP (up to 20° in illumination angle) imposes a compromise of 45° with a corresponding  $\Delta V$  of 1235.6 m/s.

The bias target at CAP is 10,000 km. The orbit strategy is not very sensitive with respect to this parameter. The total number of manoeuvres has been set to 4. Simulations with 3 manoeuvres present a larger sensitivity with respect to manoeuvre execution errors while 5 manoeuvres strategies do not present important improvements.

The time before nominal rendezvous manoeuvre to start the near comet drift phase initialisation  $t_0$  has been set to 14 days. The total duration of the near comet drift phase is 98 days. The nominal size of manoeuvres is 710, 267, 108 and 53 m/s. The time between manoeuvres is 8.4 days (25 days for all manoeuvres). The total  $\Delta V$  budget for this phase is 1136 m/s. A final drift of 64 days at about 25 cm/s towards the CAP is done.

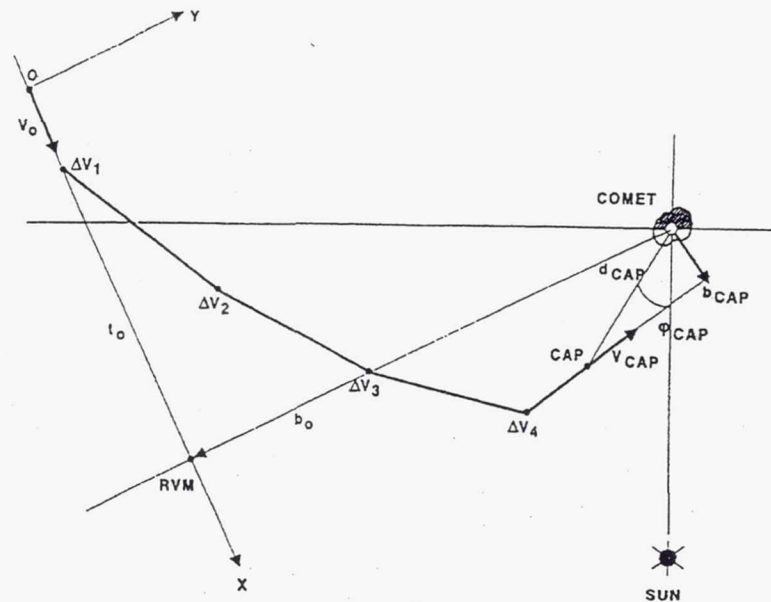


Figure 2: ROSETTA Near Comet Drift Phase

## FAR APPROACH TRAJECTORY PHASE

Far approach operations starts at CAP. Comet optical images are processed to improve the relative navigation. After detection, knowledge of the comet ephemeris will be drastically improved by the processing of the onboard observation. Image processing on ground will derive a coarse estimation of comet size, shape and kinematics. The approach manoeuvre sequence will sequentially reduce the relative velocity to finally 2.5 m/s after 77 days. The manoeuvre strategy will be design to:

- Progressively reduce the relative velocity.
- Retain an apparent motion of the comet with respect to the star background.
- Retain the illumination angle (Sun-comet-Spacecraft) below  $70^\circ$ .
- Avoid the danger of impact with the cometary nucleus in case of manoeuvre failure.

The Far Approach Trajectory ends at the **Approach Transition Point (ATP)**, which is the point where a first estimate of the comet Euler angles, angular velocity and location of landmarks is obtained from the analysis of the NAC images. The ATP is located on the Sun direction at about 300 comet radii from the nucleus. The far approach trajectory strategy is illustrated in Figure 3. The spacecraft moves from the Comet Acquisition Point CAP (defined by its distance  $d_{CAP} = 100,000$  km and illumination angle  $\phi_{CAP} = 45^\circ$ ) with a relative velocity  $V_{CAP} = 25$  m/s and target bias  $b_{CAP} = 10,000$  km, towards the Approach Transition Point ATP, which is also defined by a comet distance ( $d_{ATP}$ ) on the comet - Sun direction to optimise the illumination conditions with a given relative velocity  $V_{ATP}$  and target bias  $b_{ATP}$ . The duration of the far approach phase (77 days) is given by the Earth distance constraint imposed by the required transmission rate for operations.

The Approach Transition Point (ATP) is selected at a comet distance of 300 comet radii as baseline. The ATP point is characterised by the fact that at this moment, a first estimate of comet nucleus kinematics and landmarks location is derived. The ATP velocity is set to 2.5 m/s. Simulations with different values show that a smaller value imposes very large duration for the close approach while larger values imply very short duration for the same phase.

The illumination angle at ATP has been set to zero in order to optimise the nucleus illumination conditions in the subsequent phase which is critical for the characterisation of the comet nucleus



kinematics. The bias target at ATP is set to 50 comet radii. The total number of manoeuvres has been set to 5. The time between manoeuvres is 3.1, 37.7, 18.6, 9.4, 4.7 and 3.1 days respectively. The nominal size of manoeuvres is 6, 3.5, 3.7, 4.3 and 6.1 m/s. The total  $\Delta V$  budget is 23.7 m/s. The illumination angle during this phase is reduced from  $45^\circ$  to the final value of  $0^\circ$ .

**TABLE 2**  
**NAVIGATION ERRORS (1- $\sigma$ ) AT THE END OF THE FAR APPROACH PHASE**

Comet	S/C Pos. (Km)	S/C Vel. (mm/s)	Com. Pos. (Km)	Com. Vel. (mm/s)	Grav. Cte. (%)
Small	0.648	3.736	368.4	50.00	29.9
Wirtanen	0.766	4.354	368.6	50.15	30.0
Big	1.424	10.58	369.7	52.69	27.5

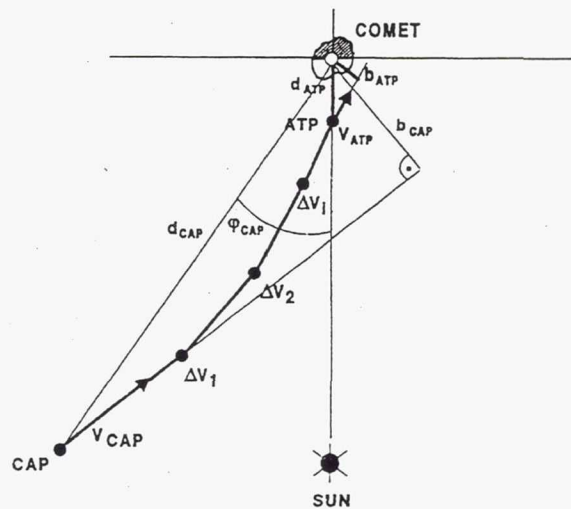


Figure 3: ROSETTA Far Approach Trajectory Phase

### CLOSE APPROACH TRAJECTORY PHASE

Close approach operations starts at ATP. Line of sight to comet nucleus landmarks are processed together with on ground radiometric measurements in order to estimate the s/c relative position and velocity, comet absolute position, comet Euler angles, nucleus angular velocity, gravitational field and location of landmarks. A very good estimate of the comet kinematics and gravitational constant is obtained at the end of this phase which is the Orbit Insertion Point (OIP). At this point the s/c is injected into a hyperbolic arc around the comet, at a typical distance of 60 comet radii and a velocity of some cm/s, depending on the comet size and density. The close approach trajectory strategy is illustrated in Figure 4. The spacecraft moves from the ATP (defined by its distance  $d_{ATP} = 300 R_C$  and illumination angle  $\phi_{ATP} = 0^\circ$ ) with a relative velocity  $V_{ATP} = 2.5$  m/s and target bias  $b_{ATP} = 50 R_C$  towards the Orbit Injection Point OIP which is also defined by a comet distance ( $d_{OIP}$ ) on the plane of the orbital mapping motion. The OIP is a point where the spacecraft is injected into a hyperbolic arc with impact vector  $b_{OIP}$  and pericenter radius  $R_P$ .

The OIP is located in the plane selected for global mapping. This is a plane which is defined by rotating an angle  $\alpha$  around the perpendicular to the comet - Sun line the plane determined by the angular momentum vector  $\mathbf{L}$  and the Sun direction. This rotation is introduced in order to avoid Sun eclipse and Earth occultation. Figure 4 illustrates the selection of the global mapping plane. The value

of the angle  $\alpha$  is computed from the following parameters: the safe distance to the eclipse condition ( $S_{DIS}$ , typically 1 comet radii), the minimum orbital radius at global mapping ( $R_{ORB}$ , about 10 comet radii) and the maximum comet radius  $R_{MAX}$

The angle  $\alpha$  is rotated in the direction to avoid Earth occultation constraints as it is illustrated in Figure 4. A comet distance of 60 comet radii has been proposed as baseline for the OIP. The pericenter of the hyperbolic arc is set to 25 comet radii (maximum mapping distance). The module of the impact vector is set to 35 comet radii. The total duration ranges between 3 (low density) and 13 days (dense). Total  $\Delta V$  for this phase ranges between 190 (big, dense) and 250 cm/s (small).

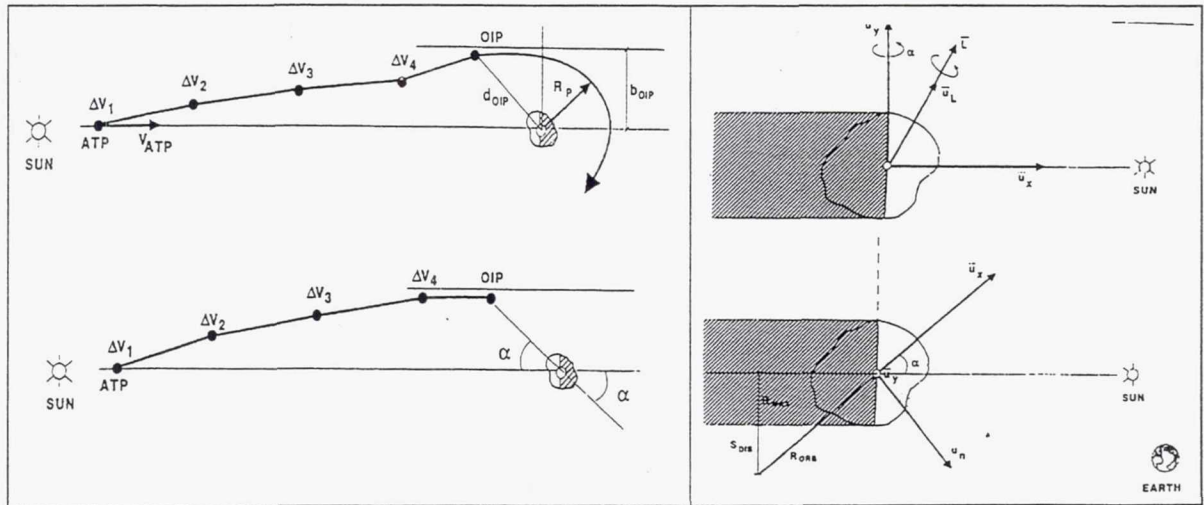


Figure 4: Close Approach Trajectory Phase

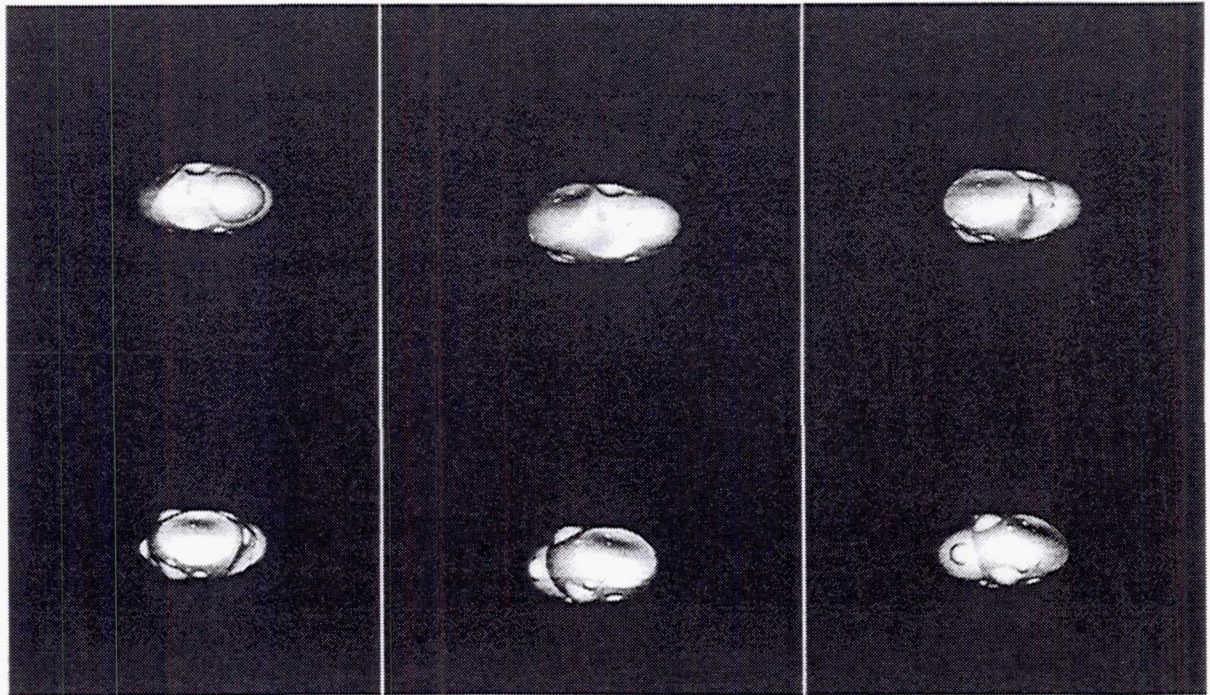


Figure 5. Typical Sequence of Nucleus Images at the Close Approach Phase.



TABLE 3

NAVIGATION ERRORS (1- $\sigma$ ) AT THE END OF THE CLOSE APPROACH PHASE

	Nom.	Long Per.	V.L. Per.	No Nut.	High Nut.	Spin In O.	Incl. Spin	Spin to Sun	Low Irreg.	High Irreg.	Low Act.	High Act.
SC Pos (m)	231.9	262.3	265.3	237.6	213.8	262.7	231.1	205.8	234.1	250.4	247.0	262.5
SC Vel. (mm/s)	1.38	1.48	1.47	1.41	1.33	1.49	1.40	1.28	1.38	1.49	1.45	1.50
Com. Pos. (Km)	341.9	341.8	341.8	341.9	333.6	343.6	242.3	343.1	341.9	341.5	333.9	343.6
Co. Vel. (mm/s)	47.1	47.1	47.1	47.1	46.5	47.2	47.2	47.2	47.1	47.1	46.5	47.2
Eul. Ang. (°)	1.04	1.20	3.14	0.885	1.35	0.85	0.96	1.39	0.96	0.828	0.864	0.849
Ang. Vel. (%)	0.058	0.080	2.21	0.028	0.081	0.053	0.049	0.050	0.055	0.059	0.053	0.054
Grav. Cte. (%)	28.3	28.4	28.3	28.4	28.2	28.6	28.5	28.40	28.41	28.72	28.50	28.68
$I_X$ (%)	10.0	10.0	10.0	10.0	10.0	10.0	10.0	10.0	10.0	10.0	10.0	10.0
$I_Y/I_X$	0.017	0.021	0.069	-	0.009	0.015	0.018	0.020	0.010	0.020	0.014	0.016
$I_Z/I_X$	0.022	0.025	0.057	-	0.011	0.020	0.024	0.023	0.025	0.023	0.018	0.020
X Land. (m)	10.2	10.4	20.8	10.4	7.7	8.7	13.3	16.7	9.8	9.3	7.9	8.7
YZ Land. (m)	6.3	9.9	32.0	6.2	5.0	7.3	9.8	3.2	6.6	8.5	5.9	8.4

## TRANSITION TO GLOBAL MAPPING PHASE

The transition to global mapping starts at the OIP. A hyperbolic arc is used down to a distance to the comet of about 25 comet radii where a capture manoeuvre circularize the orbit. Processing of on ground /on board measurements continue the estimation of all comet kinematics and gravitational parameters. This phase ends at the Global Mapping Injection Point (GMI) where the S/C is injected into a circular orbit to map the comet nucleus. The transition to global mapping strategy problem is illustrated in Figure 6. The spacecraft moves from the Orbit Insertion Point OIP (defined by its distance  $d_{OIP} = 60 R_C$ , impact vector modulus  $b_{OIP}$  and pericenter radius  $R_P$  of hyperbolic arc) towards the Global Mapping Injection Point GMI which is defined by a comet distance ( $R_{GM}$ , computed according to the mapping strategy) on the plane of the orbital mapping motion, in the opposite direction to the Sun projection on the orbit plane.

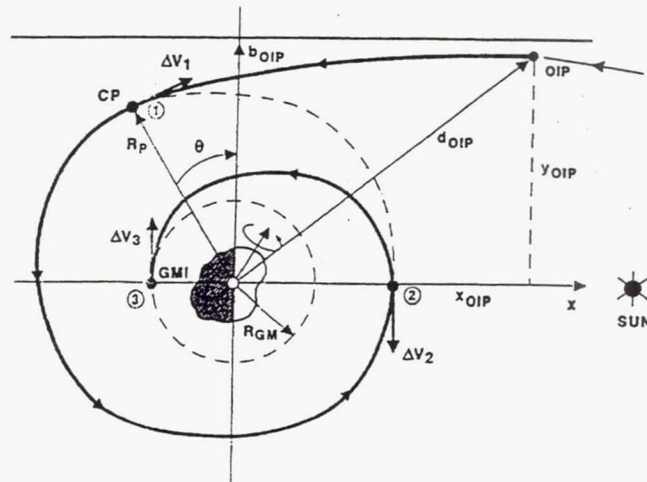


Figure 6: Transition to Global Mapping Phase

The total duration is 44, 24 and 5 days for small, Wirtanen and big comet respectively. The nominal size of manoeuvres ranges between 1 and 32 cm/s. Small trajectory correction manoeuvres (less than 1 cm/s) are introduced in large orbital arcs. The total  $\Delta V$  budget is 18, 23 and 72 cm/s for the small, Wirtanen and big comet respectively. The final relative velocity ranges between 4 and 46 cm/s. The final distance to the comet is 10-25 equivalent radii. The time between manoeuvres ranges between 40 hours (big) and 9 days (small comets).

**TABLE 4**  
**NAVIGATION ERRORS (1- $\sigma$ ) AT THE END OF THE TRANSITION TO GLOBAL MAPPING**

	Nom.	Long Per.	V. L. Per.	No Nut.	High Nut.	Spin In O.	Incl. Spin	Spin to Sun	Low Irreg.	High Irreg.	Low Act.	High Act.
SC Pos (m)	24.2	20.2	23.2	18.5	26.4	25.8	25.8	26.92	25.7	28.1	28.7	30.5
SC Vel. (mm/s)	0.380	0.379	0.321	0.380	0.387	0.374	0.363	0.390	0.436	0.425	0.394	0.411
Com. Pos. (Km)	166.4	166.5	165.9	166.1	164.7	167.0	165.9	167.4	165.9	165.5	163.3	166.5
Co. Vel. (mm/s)	27.8	27.8	27.7	27.8	27.3	27.9	27.6	28.1	27.6	27.5	27.2	27.8
Eul. Ang. (°)	0.151	0.162	0.583	0.129	0.208	0.169	0.229	0.134	0.208	0.171	0.138	0.267
Ang. Vel. (%)	0.007	0.008	0.122	0.002	0.014	0.011	0.009	0.008	0.007	0.009	0.010	0.012
Grav. Cte. (%)	0.577	0.561	0.599	0.557	0.601	0.527	0.600	0.559	0.579	0.604	0.596	0.774
$I_x$ (%)	9.9	9.9	9.9	10.0	10.0	10.0	10.0	10.0	9.9	9.5	10.0	9.9
$I_y/I_x$	0.003	0.003	0.016	-	0.001	0.004	0.003	0.003	0.001	0.004	0.004	0.004
$I_z/I_x$	0.003	0.004	0.019	-	0.002	0.004	0.004	0.004	0.003	0.005	0.005	0.005
X Land. (m)	2.3	2.4	5.6	3.3	1.5	8.7	3.0	16.7	2.5	9.3	7.9	8.7
YZ Land. (m)	0.9	0.9	6.2	0.86	0.83	8.4	1.4	2.3	0.8	8.5	7.7	8.4

## GLOBAL MAPPING PHASE

The preliminary survey of the surface of the comet is known as global mapping. At least 80 % of the illuminated surface is required to be mapped. Stable circular polar orbits around the comet at a distance between 10 and 25 nucleus radii will be used for the mapping of the surface. The semimajor axis of the mapping orbit will be chosen as a function of comet gravity and spin rate, taking into account the following constraints: coverage without gaps, safety considerations (no impact on comet nucleus), volume of data for real time transmission, maximum time to complete surface mapping, minimum resolution and viewing angle to surface normal and, continuous communications to Earth.

The following conclusions are derived from the analysis of the global mapping trajectory for the whole domain of comet nucleus density, rotation period, shape and kinematics conditions:

- The mapping distance ranges between 10 to 25 comet radii. Fast rotating comets require a smaller distance. The larger the shape irregularity or the nutation, the bigger the distance.
- Very slow comets requires 2 orbits, 3 orbits or two perpendicular (polar + equatorial) orbits.
- The mapping duration ranges between 4 days (full orbit) for fast and typical rotating comets up to 90 days for 3 orbits around an irregular and low dense comet.
- Orbit control manoeuvres are introduced at the crossing of the plane which contains the Sun direction and the perpendicular to the Sun direction (4 correction manoeuvres per orbit, targeting to the next crossing point). The total  $\Delta V$  for those correction manoeuvres is about 7 cm/s for the typical comet.

During this phase, the nucleus shape and surface properties (roughness, physiography) and kinematics and gravitational models will be derived using optical landmark observations. At the end of this phase, based on mapping and remote observation data, some five areas (500 x 500 m) will be selected for close observation.



**TABLE 5**  
**NAVIGATION ERRORS (1- $\sigma$ ) AT THE END OF THE GLOBAL MAPPING PHASE**

	Nom.	Long Per.	V. L. Per.	No Nut.	High Nut.	Spin In O.	Incl. Spin	Spin to Sun	Low Irreg.	High Irreg.	Low Act.	High Act.
SC Pos (m)	13.9	13.7	19.4	12.2	14.6	25.0	20.2	15.4	12.6	19.4	24.2	24.2
SC Vel. (mm/s)	0.274	0.298	0.327	0.286	0.276	0.427	0.357	0.296	0.270	0.356	0.425	0.514
Com. Pos. (Km)	140.8	133.2	130.9	144.2	126.7	141.8	140.8	141.3	140.9	130.4	139.0	142.7
Co. Vel. (mm/s)	23.51	22.58	22.17	23.90	21.77	23.66	23.51	23.64	23.50	22.18	23.3	23.87
Eul. Ang. (°)	0.13	0.12	0.32	0.11	0.91	0.15	0.17	0.125	0.151	0.137	0.122	0.226
Ang. Vel. (%)	0.006	0.006	0.101	0.002	0.012	0.007	0.009	0.007	0.004	0.009	0.009	0.012
Grav. Cte. (%)	0.28	0.19	0.180	0.259	0.216	0.279	0.295	0.298	0.286	0.199	0.259	0.507
I <sub>x</sub> (%)	9.9	9.8	9.5	9.9	7.78	10.0	10.0	9.9	6.7	8.7	10.0	9.9
I <sub>z</sub> /I <sub>x</sub>	0.002	0.002	0.008	-	0.001	0.003	0.003	0.003	0.001	0.003	0.002	0.003
I <sub>z</sub> /I <sub>x</sub>	0.003	0.003	0.009	-	0.001	0.004	0.003	0.003	0.003	0.004	0.003	0.004
X Land. (m)	1.8	1.7	3.67	2.55	1.13	2.3	2.53	2.6	2.0	2.2	2.3	2.3
YZ Land. (m)	0.62	0.59	3.59	0.61	0.51	1.4	1.1	1.5	0.6	1.2	1.2	1.4

### CLOSE OBSERVATION PHASE

A manoeuvre strategy has been design for sequences of **close observation** orbits to fly over the selected surface points at altitudes below 1 nucleus radius, taking into account: uninterrupted communications, continuous illumination of solar arrays, safety constraint (no nucleus encounter in case of manoeuvre failure), debris, dust and gas jets avoidance, observed area under illumination and viewing angle normal to the local surface below 30°.

The full close observation phase is performed in the same plane in order to avoid expensive change of plane manoeuvres. The orbital plane is selected to avoid eclipse and Earth occultation, to maximise the achievable comet surface and to provide a flyover close to the terminator for the analysis of the warming up. The flyover time corresponding to each candidate site is given by the time of crossing of this site with the selected orbital plane. The flyover altitude of each candidate site is selected according to the resolution, field of view and safety constraints. Only in-plane phasing manoeuvres are required in order to ensure the flyover of the spacecraft above the candidate site at the right time. Two phasing manoeuvres are required per flyover. In-plane phasing manoeuvres are very cheap (nearly Hohmann transfer type). Several options are feasible depending on the number of complete revolutions of the comet nucleus before flyover. If the number of revolutions increases, the phasing  $\Delta V$  decreases and the duration increases. The final result is obtained as a trade off between duration and propellant requirements. The selection of the close observation orbital plane is performed by taking into account that eclipse and occultation must be avoided, observation close to the terminator is desirable, the coverage of comet surface must be maximised, and the maximum illumination angle is 70°.

The best plane for eclipse and occultation avoidance and warming up observation is the terminator. However, the illumination angle at flyover of a candidate site in this plane is close to 90°, violating the constraint of maximum value (70°). The finally selected orbital plane for close observation is the one resulting from the rotation of the terminator an angle of 40° around the line perpendicular to the Sun and contained in the plane defined by the comet-Sun line and the comet spin axis (angular momentum vector if it is nutating). This plane provides a good comet surface coverage under the required illumination constraint while being close to the terminator for analysis of surface warming up and avoidance of eclipse and occultation constraint. In addition, the dynamics perturbation on the spacecraft due to the comet gas, dust and jets is minimised in this plane close to the terminator.

The total duration of this phase is 12, 11 and 6 days for small, Wirtanen and big comet respectively. Nominal manoeuvres ranges between 1 and 50 cm/s. Small trajectory correction manoeuvres are introduced (less than 1 cm/s) in large orbital arcs. The total  $\Delta V$  budget for this phase is about 18 cm/s for small comets and 3 m/s for big comets. The final relative velocity ranges between 5 and 150 cm/s. The final distance to the comet is 1 equivalent radii. The time between manoeuvres ranges between 12 hours and 1 day depending on the comet size.

**TABLE 6**  
**NAVIGATION ERRORS (1- $\sigma$ ) AT THE END OF THE CLOSE OBSERVATION**

	Nom.	Long Per.	V. L. Per.	No Nut.	High Nut.	Spin In O.	Incl. Spin	Spin to Sun	Low Irreg.	High Irreg.	Low Act.	High Act.
SC Pos (m)	7.1	8.7	7.2	15.0	8.5	7.1	6.6	7.8	7.5	7.5	6.8	11.8
SC Vel. (mm/s)	0.46	0.59	0.57	4.29	1.4	0.453	0.45	0.59	0.78	0.62	0.42	1.5
Com. Pos. (Km)	105.0	99.0	85.0	91.5	92.1	108.6	107.0	102.0	107.0	97.0	105.0	111.0
Co. Vel. (mm/s)	20.1	19.5	18.2	20.8	18.9	20.5	20.3	20.0	20.3	19.3	20.1	20.6
Eul. Ang. (°)	0.15	0.14	0.34	0.30	0.15	0.16	0.16	0.14	0.15	0.17	0.13	0.23
Ang. Vel. (%)	0.005	0.007	0.073	0.002	0.009	0.009	0.007	0.006	0.005	0.007	0.008	0.010
Grav. Cte. (%)	0.15	0.13	0.12	0.16	0.14	0.16	0.17	0.15	0.17	0.13	0.15	0.23
$I_x$ (%)	5.42	4.15	5.0	5.1	3.7	3.5	3.37	0.61	5.87	2.13	4.08	3.66
$I_y/I_x$	0.002	0.002	0.005	-	0.001	0.003	0.003	0.002	0.001	0.003	0.002	0.003
$I_z/I_x$	0.002	0.003	0.006	-	0.001	0.003	0.003	0.003	0.003	0.004	0.002	0.003
X Land. (m)	1.5	1.5	2.5	2.0	1.1	1.9	1.8	1.8	1.7	1.8	1.8	1.9
YZ Land. (m)	0.5	0.3	1.8	0.4	0.3	1.0	1.0	1.3	0.5	1.1	1.2	1.3

### **SURFACE SCIENCE PACKAGE (SSP) DELIVERY PHASE**

Three different options are considered for the SSP delivery system:

- ❑ **Passive System:** It is based on a passive SSP which is ejected from the main S/C with a given separation velocity (tunable up to 50 cm/s). The SSP flies down to the comet nucleus without manoeuvring capability. The orbiter aligns the Z-axis along the normal to the comet surface at landing before ejection of the SSP. A momentum wheel on the SSP guarantees the attitude stability down to the comet surface.
- ❑ **Pyro-Thruster System:** The SSP ejection is performed in a similar way to the passive system (tunable Delta-V up to 50 cm/s). After ejection, a pyro thruster (solid propellant) in the SSP provides a vertical (non tunable)  $\Delta V$  in the range 10 to 30 cm/s. This manoeuvre is done 5 minutes after ejection (150 m S/C distance for a separation manoeuvre of 50 cm/s) in the opposite direction to the vector normal to the nucleus surface point at impact.
- ❑ **Active Descent or Cold Gas System:** The SSP is equipped with an active cold gas system. This active system concept is similar to the previous options up to the ejection: the orbiter aligns the Z-axis along the normal to the comet surface at landing before ejection of the SSP and a separation mechanism ejects the SSP with a tunable Delta-V up to 50 cm/s. After ejection, the active descent system provides a lander slew manoeuvre to align X-axis if required. A thruster along the X-axis provides a tunable  $\Delta V_x$  if it is required. A second thruster along the Z-axis provides a tunable  $\Delta V_z$  along the opposite direction to the vector normal to the nucleus surface point at impact (Z-axis). The maximum total  $\Delta V$  is limited to 1 m/s.

The geometry of the Surface Science Package (SSP) delivery is illustrated in Figure 7. At the ejection point the orbiter Z-axis (in the same direction that the SSP axis) aligns the vector normal to the comet nucleus surface at landing point to provide the required probe attitude at impact. The X-axis aligns the SSP ejection direction vector. An ejection mechanism separates the SSP with a tunable ejection  $\Delta V$



(maximum of 50 cm/s). The angle  $\delta$  between the SSP axis and the ejection  $\Delta V$  is  $90^\circ$  (perpendicular ejection). The ejection velocity vector can be selected in any direction within the plane perpendicular to the surface normal vector. The reference direction in this plane is the intersection with the plane of the SSP orbital motion which is shown in Figure 7 ( $\bar{u}_x$ ). The angle between the reference direction and the ejection manoeuvre  $\psi$  completely defines the ejection  $\Delta V$  vector.

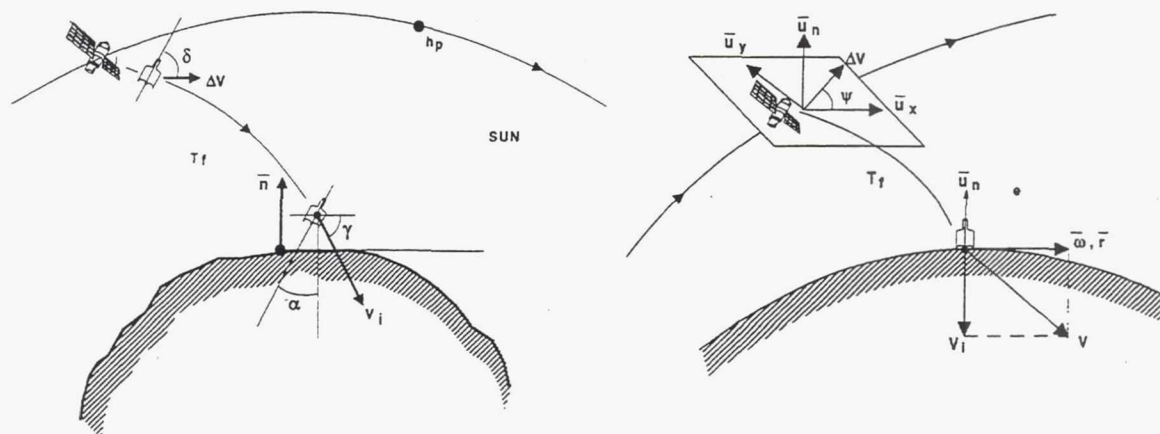


Figure 7: Geometry of Surface Package Delivery

SSP manoeuvres are performed depending on the above defined delivery system option. Five minutes after ejection, the orbiter performs a manoeuvre in order to provide optimum visibility conditions of the SSP at impact (overfly). The impact velocity  $V_i$  is the SSP velocity with respect to the landing site at the impact point. The maximum is actually set to 2 m/s. The impact angle  $\gamma$  is the angle between the impact velocity and the local surface. It must be maximised to ensure stabilisation at touch down, the optimum value is  $90^\circ$ . The angle of attack  $\alpha$  is the angle between the SSP axis and the normal vector to the local surface at touch down. It must be minimised to ensure the correct attitude at touch down, the optimum value is  $0^\circ$ . The SSP delivery strategy problem is formulated as a constrained parameter optimisation. The cost function is the SSP flight time duration. Minimum time delivery presents the best performances in term of impact dispersion errors which are critical for the feasibility of the mission (in addition, there is a larger duration of batteries for payload operations). The following constraints are imposed:

- **Safety Constraint:** The safety constraint is imposed by defining a safe volume around the irregular comet nucleus (minimum altitude of 1 km must be guaranteed). This volume should never be intersected by the spacecraft trajectory. The safe volume is an ellipsoid of rotation with the symmetry axis along the direction of the angular momentum of the comet nucleus.
- **Visibility Constraint:** One of the requirements of the SSP is the visibility of the probe from the spacecraft during the period 15 minutes before and after impact. There are two ways:
  - By including this constraint within the SSP delivery optimisation process.
  - By performing a manoeuvre in the spacecraft after ejection.
 Both solutions have been analysed, the conclusion of that analysis was that the best option is to provide SSP coverage at impact by performing a post-ejection manoeuvre to the orbiter.
- **Minimum time in delivery orbit before ejection:** The spacecraft shall remain within the vicinity of the comet (at a maximum distance between 15 and 20 comet radii depending on the size of the nucleus) a minimum period of time before (for good orbit determination after the last manoeuvre).

A period of 16 hours has been selected in this study as minimum time between the injection into the delivery orbit and the ejection point.

- **Impact Velocity Constraint:** A maximum value of 2 m/s is imposed to the impact velocity due to the limitation of the damping system.
- **Ejection  $\Delta V$  Constraint:** A maximum value of 50 cm/s is imposed to the ejection  $\Delta V$ .
- **Solar Aspect Angle Constraint:** The solar aspect angle of the orbiter at the ejection must be in the range  $60^\circ - 120^\circ$  in order to guarantee the required energy.
- **Solar Panel Articulation ( $180^\circ$  rotation) Constraint:** A limitation in the solar panel articulation (only  $180^\circ$  of freedom) is included as a technical constraint.
- **Eclipse Constraint:** The orbiter and SSP trajectories are design such that eclipse is avoided.
- **Illumination Constraint:** In order to ensure a good illumination of the SSP at landing, the maximum illumination angle at impact is constrained to  $60^\circ$  (minimum Sun elevation of  $30^\circ$ ).

The obtained SSP delivery results (about 6000 cases have been solved) are summarised in Table 8.

**TABLE 8**  
**SUMMARY OF SSP DELIVERY PARAMETERS**

SSP SYSTEM	COMET SIZE	$\Delta V$ EJECT. (cm/s)	FLIGHT TIME (minutes)	IMPACT VEL. (cm/s)	EJECT. ALT. (Km)	VERT. $\Delta V$ (cm/s)	LAT. $\Delta V$ (cm/s)
PASSIVE	SMALL	10 $\rightarrow$ 22	125 $\rightarrow$ 285	10 $\rightarrow$ 18	1.5 $\rightarrow$ 1.9	0	0
	TYPICAL	19 $\rightarrow$ 37	75 $\rightarrow$ 236	22 $\rightarrow$ 43	1.5 $\rightarrow$ 2.5	0	0
	BIG	50	60 $\rightarrow$ 350	142 $\rightarrow$ 271	6.9 $\rightarrow$ 23	0	0
PYRO -T	SMALL	13 $\rightarrow$ 25	54 $\rightarrow$ 66	33 $\rightarrow$ 41	1.4 $\rightarrow$ 1.8	30	0
	TYPICAL	21 $\rightarrow$ 42	42 $\rightarrow$ 54	41 $\rightarrow$ 54	1.4 $\rightarrow$ 2.0	30	0
	BIG	50	48 $\rightarrow$ 348	127 $\rightarrow$ 281	6 $\rightarrow$ 24	30	0
COLD GAS	SMALL	13 $\rightarrow$ 25	24 $\rightarrow$ 27	100 $\rightarrow$ 108	1.4 $\rightarrow$ 1.7	100	0
	TYPICAL	20 $\rightarrow$ 43	20 $\rightarrow$ 25	103 $\rightarrow$ 116	1.4 $\rightarrow$ 1.9	100	0
	BIG	50	21 $\rightarrow$ 66	120 $\rightarrow$ 235	3.0 $\rightarrow$ 5.9	0 $\rightarrow$ 83	17 $\rightarrow$ 100

Each cell of the table presents two values, they are the minimum and the maximum value found for all the simulated cases. A robust orbital strategy has been designed for the transfer between the final point of the close observation phase and the injection into the delivery orbit. The following approach is proposed (illustrated in Figure 8):

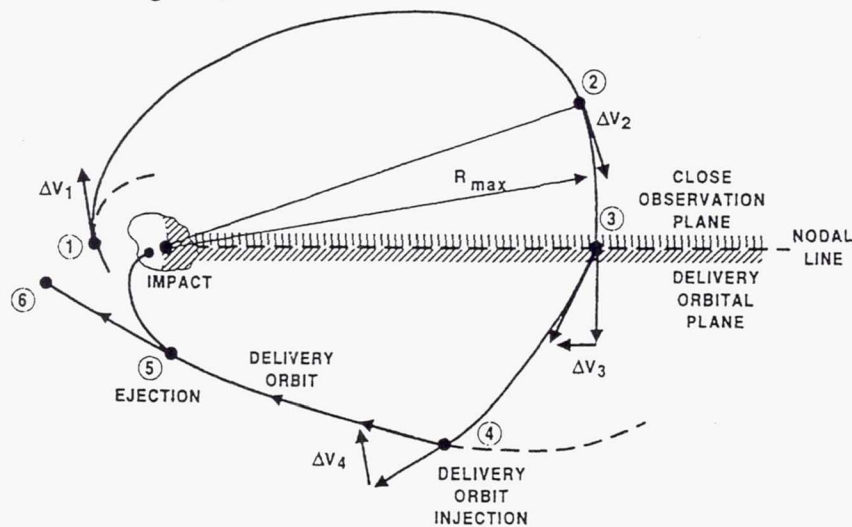


Figure 8: Orbital Strategy for SSP Delivery Preparation



The spacecraft is initially located in a close observation orbit with very low altitude (point 1). An apocenter raising manoeuvre  $\Delta V_1$  is performed at this initial point in order to reach a distance  $R_{\max}$ . This manoeuvre is done for safety considerations, to obtain a comet distance which reduces the required plane of change manoeuvre and to wait some time for the decision of the scientist on the selected landing point. At this stage, close observation of the last candidate site has been performed, some days are required for the analysis of results and the final decision on the impact point for the SSP. A very small variation of this maximum distance  $R_{\max}$  is used in the planning of the delivery strategy by the simulator in order to phase the impact point with the rotation of the comet nucleus. The size of this manoeuvre is about 3 cm/s, 5 cm/s and 35 cm/s for the small, Wirtanen and big comet respectively. At the subsequent apocenter (point 2) a circularization manoeuvre is performed ( $\Delta V_2$ ). The size of this manoeuvre is about 1 cm/s, 3 cm/s and 22 cm/s for the small, typical and big comet. The spacecraft circular orbit at  $R_{\max}$  is propagated up to the point 3 which is on the nodal line of intersection between the close observation plane and the delivery orbital plane. At this point, a change of plane manoeuvre  $\Delta V_3$  is performed in order to inject into the circular orbit at  $R_{\max}$  in the required orbital plane for the delivery. In the worst case the size of this manoeuvre is 6 cm/s, 14 cm/s and 0.75 m/s for the small, typical and big comet respectively. Two different cases (Figure 9) are presented for the final injection into the delivery orbit:

- **Case 1:** the apocenter of the delivery orbit is larger than the maximum distance  $R_{\max}$ . The orbit is propagated up to the intersection with the delivery orbit (4). At this point the spacecraft is injected into the delivery orbit by a manoeuvre  $\Delta V_4$ . Due to the imposed constraint, the spacecraft remains in this orbit for a period of at least 16 hours before the ejection of the SSP (5).
- **Case 2:** the apocenter of the delivery orbit is smaller than the maximum distance  $R_{\max}$ . The orbit is propagated in the circular orbit up to the crossing of the apsidal line (pericenter - apocenter) of the delivery orbit (4). At this point a braking manoeuvre injects the spacecraft into a transfer orbit to the apocenter of the delivery orbit (5). The delivery orbit injection manoeuvre  $\Delta V_5$  is performed at this point. This strategy is not optimal from the point of view of propellant (Hohmann transfer to pericenter is optimum), however safety considerations are overruling in this case.

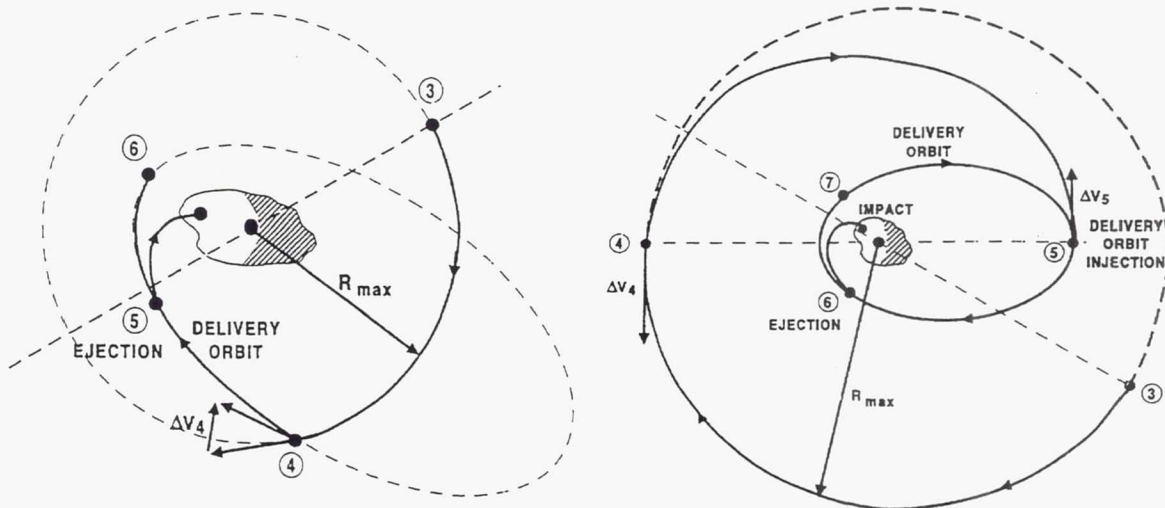


Figure 9: Orbital Strategy for SSP Delivery Preparation: Cases 1 and 2.

The dispersion errors at the impact point of the SSP landing ( $1 \sigma$  level) for the different delivery options and comet nucleus cases are illustrated in the following tables:

**TABLE 12**  
**PASSIVE DESCENT. WIRTANEN REFERENCE CASE: 1- $\sigma$  DISPERSION ERRORS**

CASE	Nom.	Long Per.	Very Long Per.	No Nut.	High Nut.	Spin In orbit	Incl. Spin	Spin to Sun	Low Irr.	High Irr.	Low Act.	High Act.
Longitude (m)	27	26	15	27	26	27	20	61	18	17	27	28
Latitude (m)	11	11	17	11	11	11	19	46	9	9	11	11
Longitude (°)	1.7	1.7	1.1	2.0	1.8	1.8	3.0	12.3	1.4	1.0	1.8	2.1
Latitude (°)	0.8	0.8	1.1	0.9	0.8	0.9	1.8	5.2	0.8	0.6	0.8	0.8
Altitude (m)	26	32	40	25	26	28	75	48	30	20	29	43
Impact time (s)	94	111	125	92	97	103	252	138	96	52	107	155
Impact Vel.(cm/s)	2.1	2.2	2.1	1.9	2.1	1.9	10.6	5.0	2.8	1.0	1.7	2.2
mean a.o.attack(°)	3.3	2.9	3.0	3.1	3.3	3.3	1.9	3.1	1.9	3.7	3.2	3.5
worst a.o.attack(°)	6.7	5.8	8.2	6.2	6.8	5.9	5.2	8.9	4.3	10.7	6.4	6.7
mean imp angle(°)	84	85	85	84	84	84	84	67	85	86	83	83
worst im. angle(°)	77	79	80	75	73	76	66	40	78	79	73	75

**TABLE 13**  
**PYRO-THRUSTER. WIRTANEN REFERENCE CASE: 1- $\sigma$  DISPERSION ERRORS**

CASE	Nom.	Long Per.	Very Long Per.	No Nut.	High Nut.	Spin In orbit	Incl. Spin	Spin to Sun	Low Irr.	High Irr.	Low Act.	High Act.
Longitude (m)	16	11	12	15	15	13	17	22	14	13	14	14
Latitude (m)	10	14	16	11	12	12	10	20	9	9	11	12
Longitude (°)	1.2	0.7	0.9	1.2	0.9	0.8	2.4	5.5	1.2	0.7	1.0	1.0
Latitude (°)	0.8	1.0	1.0	0.8	0.9	0.8	0.8	2.0	0.7	0.5	0.9	0.8
Altitude (m)	16	15	20	16	17	17	27	18	17	15	15	25
Impact time (s)	37	34	42	37	40	40	58	38	35	25	35	60
Impact Vel. cm/s)	1.3	1.0	1.0	1.2	1.2	1.2	6.3	3.4	1.7	0.7	1.2	1.3
mean a.o.attack(°)	2.6	2.7	2.7	2.7	2.5	2.4	1.1	1.3	1.6	3.0	2.5	2.6
worst a.o.attack(°)	5.6	5.9	6.2	5.6	5.9	5.3	2.5	3.2	3.3	10.6	5.4	5.3
mean imp angle(°)	86	86	87	86	87	87	88	79	88	87	86	86
worst im angle(°)	83	81	83	82	82	83	82	68	85	79	83	83

**TABLE 14**  
**COLD GAS. WIRTANEN REFERENCE CASE: 1- $\sigma$  DISPERSION ERRORS**

CASE	Nom.	Long Per.	Very Long Per.	No Nut.	High Nut.	Spin In orbit	Incl. Spin	Spin to Sun	Low Irr.	High Irr.	Low Act.	High Act.
Longitude (m)	16	12	19	10	9	10	9	11	16	14	10	10
Latitude (m)	9	15	17	16	16	12	14	13	11	10	12	16
Longitude (°)	0.7	0.8	0.5	0.6	0.7	0.7	1.4	2.7	1.1	0.8	0.7	0.8
Latitude (°)	1.0	1.1	0.3	1.0	1.2	0.9	1.1	1.4	0.9	0.6	0.8	1.1
Altitude (m)	15	17	19	14	15	15	15	13	18	16	13	19
Impact time (s)	14	16	17	13	14	14	14	12	16	14	13	18
Impact Vel.(cm/s)	1.2	1.1	1.0	1.1	1.1	1.1	2.4	1.9	1.2	1.1	1.0	1.1
mean a.o.attack(°)	2.5	2.7	3.5	2.5	2.9	2.3	0.9	0.8	1.8	3.8	2.2	2.9
worst a.o.attack(°)	7.9	8.3	8.9	7.8	7.7	5.3	1.9	2.0	3.5	10.8	5.2	8.1
mean imp angle(°)	87	87	86	87	87	87	89	88	88	86	87	87
Worst im angle(°)	78	81	80	81	81	84	87	85	85	78	84	81



There are some landing points which present larger dispersion errors due to the effect of outgassing and fourth order gravitational term errors when landing at high latitude close to large shape irregularities. The comparative analysis of the different SSP delivery options is presented in Table 15. The nominal small, Wirtanen and big comets are selected as test cases.

**TABLE 15**  
**COMPARATIVE ANALYSIS OF SSP DELIVERY ERRORS**

COMET	SSP DEL. SYSTEM	Eject. $\Delta V$ (cm/s)	Flight Time (hours)	Impact Vel. (cm/s)	long. error (m)	1 $\sigma$ lat. error (m)	1 $\sigma$ worst ang. att. (")	of worst impact ang. (")
Small	Passive	20	2.6	12	21.4	11.3	8.2	75.7
	pyro-thr.	21.5	1.0	33	12.3	11.1	5.9	81
	cold gas	16	0.43	100	10	13	5.5	83
Wirtanen	Passive	36	1.5	25	27	11	6.7	76.8
	pyro-thr.	37.5	0.85	42	15.1	10.9	5.6	82.8
	cold gas	28.5	0.39	104	9.5	16.1	7.9	79
Big	Passive	50	1.4	169	74.1	19.9	3.8	84
	pyro-thr.	50	0.9	158	31.6	13.1	3.4	85
	cold gas	50	0.4	162	39.5	15	3.5	85

### SSP Delivery Conclusions

A suitable SSP delivery strategy is found for landing at any illuminated point of all reference comets and descent options: passive, pyro-thruster and cold gas system. The impact dispersion errors associated to the passive descent system are very high for some comets and landing sites. The landing on high latitude regions of small and typical comets is not feasible (too large error in angle of attack and impact angle). The pyrothruster option reduces very much the impact dispersion errors allowing a feasible landing on any point of the reference comets. Only landing at high latitudes of a typical comet with spin axis close to the Sun direction presents a large value on the velocity impact angle (worst case 68°). The cold gas system descent further improves the two previous delivery options. Impact dispersion errors are in all simulations within a very good range of values.

The solar aspect angle constraint at ejection is satisfied without the need of a rotation mechanism and with a limited rotation capability of the solar panels (only 180°). Small and typical comets use the cold gas system manoeuvring capability in a single manoeuvre along the vertical component. Big comets perform two manoeuvres, a big one along the lateral direction and a second one with the remaining propellant (if any) along the vertical direction. For big comets and high solar declination, the maximum impact velocity must be increased up to 2.8 m/s for the passive and pyro-thruster systems and 2.35 m/s for the cold gas system in order to provide a feasible landing on a large nucleus region. The total duration of the SSP delivery phase ranges between 4 and 30 days. The total required  $\Delta V$  is about 0.5 m/s for the small comet, 1 m/s for Wirtanen and 3-5 m/s for the big comet.

Uncertainty in high order gravitational terms (fourth order expansion of gravitational field) provides a quick and sharp increase in the SSP velocity at impact, with important effect on the impact angle error. This is the most important contribution source to the final error in the SSP impact velocity. This effect is more important at high latitudes and close to shape irregularities. The uncertainty in the outgassing parameters generates a large dispersion error at the ejection point, with important influence on the final dispersion errors. Therefore very high activity provides much larger dispersion errors. If ejection is close to the comet zenith point, the dispersion is much larger due to the higher mass flow rate. The effect of the outgassing contribution to the impact dispersion error is more important for small and low dense comets. The flight of the S/C close to a gas jet during the preparation of the ejection produces a very large error on the impact point (several hundred of meters). Therefore jet overfly must be avoided during the SSP delivery phase. The above presented dispersion errors are very sensitive to the

outgassing error model: 3 ECRV's and 2 bias errors with a  $3\text{-}\sigma$  level of 60 % each. If larger errors are presented, larger dispersion errors are expected.

The final dispersion error is also very sensitive to the accuracy of the ejection mechanism. Above results are based on ejection errors of 1 % in size and  $0.5^\circ$  pointing ( $1\text{-}\sigma$  level). With this assumption, the impact dispersion error due to the ejection mechanism is similar to the error due to all other sources (about  $11 \times 7$  m). If a higher ejection error is considered, this is the dominant contribution to the impact dispersion. For ejection errors around 4 % in size and  $2^\circ$  pointing, the total dispersion error is multiplied by 3 ( $45 \times 27$  m).

### SURFACE PACKAGE RELAY PHASE

After SSP delivery, the spacecraft will be injected into an orbit which is best suited to receive the data transmitted from the surface package and to relay them to Earth. The surface package will have a nominal lifetime of 3.5 days. The following requirements have been defined: the SSP must be visible from the spacecraft during the period between 15 minutes before and after nucleus surface impact, communication is needed for three hours or more during the first 24 hours on the surface, and at least 15 minutes every 16 hours thereafter at a range of no more than 150 km, for the remaining 60 hours. The design of the relay orbit shall satisfy above set of requirements and in addition: the orbit shall be safe, in failure cases the predicted orbit shall not intersect the comet nucleus within a time of 10 days, continuous illumination of the solar arrays is required and, uninterrupted communications with Earth. The driving parameter for the selection of the relay orbit is to obtain a continuous link with the SSP along the whole duration of this phase (3.5 days). If continuous communications is not possible, the maximum gap shall be limited to 16 hours. The design of the relay orbit depends on the following parameters: comet nucleus shape, location of landing site (longitude and latitude), nucleus kinematics (rotation period and nutation), comet nucleus density, nucleus activity and comet gravitational field.

It is not possible to define a single relay orbit strategy which satisfy all the requirements for the full range of landing latitude ( $-90^\circ$  to  $90^\circ$ ), nucleus density ( $0.2$  to  $2 \text{ gr/cm}^3$ ) and comet rotation period (from 3 hours to infinity). Five different cases have been considered in order to provide the required SSP coverage for the full range of parameters:

- Case 1: Polar Elliptic Orbits (illustrated in Figure 10)
- Case 2: Synchronous Orbits
- Case 3: Equatorial Elliptic Orbits
- Case 4: Retrograde Elliptic Orbits
- Case 5: Retrograde Circular Equatorial Orbits

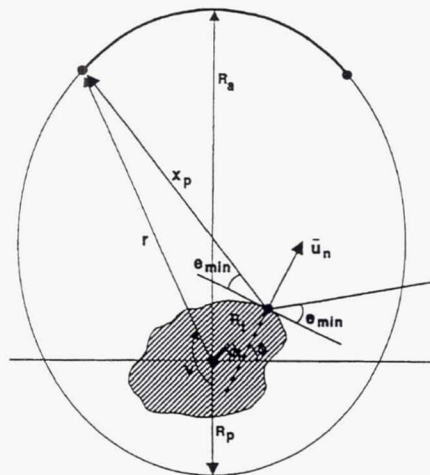


Figure 10: Polar Elliptic Relay Orbit (High Latitude Landing)



## EXTENDED MONITORING PHASE

After the end of the activities related to the surface package science, the spacecraft will spend at least 200 days in orbit in the vicinity of the comet until perihelion passage. The objective of this phase is to monitor the nucleus (active regions), dust and gas jets, and to analyse gas, dust and plasma in the inner coma from the onset to peak activity. The ground support activity will continue with two shifts of operations using two 15 m dish antenna ground stations.

Orbits design will depend on safety considerations and scientific goals taking into account that communication relay service has to be provided in case of long life surface packages. Mission planning will depend on the result of previous observations, such as the activity pattern of the comet. Extended monitoring of different regions in the vicinity of the nucleus will be performed by successive hyperbolic flybys configuring petals-like trajectories.

## CONCLUSIONS

A feasible orbit planning and navigation strategy for the complete end to end near comet operations of the ROSETTA mission has been proposed in this paper. Good navigation results have been obtained for the initial phases of the near comet operations and for the estimation of cometary parameters (ephemeris, Euler angles, angular velocity, nutation, gravitational field, moments of inertia, etc.). A feasible SSP delivery strategy is found for landing at any illuminated point of all reference comets and descent options: passive, pyro-thruster and cold gas system. The impact dispersion errors associated to the passive descent system are very high for some comets and landing sites. The landing on high latitude regions of small and typical comets is not feasible (too large error in angle of attack and impact angle). The pyrothruster option reduces very much the impact dispersion errors allowing a feasible landing on any point of the reference comets. Only landing at high latitudes of a typical comet with spin axis close to the Sun direction presents a large error on the velocity impact angle (worst case 68°). The cold gas system descent further improves the two previous delivery options. Impact dispersion errors are in all simulations within a very good range of values. The recommended option for the SSP delivery is the pyro-thruster option or the cold gas system. The pyro-thruster provides a feasible solution for all comets with less complexity. However, if redundancy for the ejection mechanism is required, the cold gas system is needed. In this case, with a lower total  $\Delta V$  it is possible to reduce the error in the impact parameters.

## REFERENCES

1. BAE, **Study of Orbit Strategies and Navigation Near a Comet**, ESA Contract 8947/90/D/MD, Final Report, Bristol, May 1992.
2. Belló Mora M., **On the ROSETTA Comet Approach Phase Orbit Strategies and Navigation**, MAS Working Paper No. 309, ESOC, April 1990.
3. Belló Mora M., Prieto Muñoz J., Rivero Jimenez E., **ROSETTA Near Comet Operations. SSP Relay Orbit Phase. Simulations Results**, Doc. No. GMVSA 2022/97, January 1997.
4. Belló Mora M., **ROSETTA Near Comet Operations. Extended Monitoring Phase**, Doc. No. GMVSA 2175/96, July 1996.
5. Belló Mora M., **ROSETTA Near Comet Operations. SSP Relay Orbit Planning**, Doc. No. GMVSA 2174/96, November 1996.
6. Belló Mora M., **ROSETTA Near Comet Operations. Upgrade of Surface Package Delivery Phase. Orbit Strategy and Navigation**, Doc. No. GMVSA 2139/96, July 1996.
7. Belló Mora M., **ROSETTA Near Comet Operations. Upgrade of Surface Package Delivery Results**, Doc. No. GMVSA 2008/97, January 1997.
8. Belló Mora M., Yañez Otero A., **ROSETTA Near Comet Operations. Close Approach Trajectory Phase. Orbit Strategy and Navigation**, Doc. No. GMVSA 2038/96, March 1996.
9. Belló Mora M., Yañez Otero A., **ROSETTA Near Comet Operations. Close Observation Phase. Orbit Strategy and Navigation**, Doc. No. GMVSA 2114/96, July 1996.

10. Belló Mora M., Yañez Otero A., **ROSETTA Near Comet Operations. Far Approach Trajectory Phase. Orbit Strategy and Navigation**, Doc. No. GMVSA 2037/96, March 1996.
11. Belló Mora M., Yañez Otero A., **ROSETTA Near Comet Operations. Global Mapping Phase. Orbit Strategy and Navigation**, Doc. No. GMVSA 2040/96, March 1996.
12. Belló Mora M., Yañez Otero A., **ROSETTA Near Comet Operations. Near Comet Drift Phase. Orbit Strategy and Navigation**, Doc. No. GMVSA 2036/96, February 1996.
13. Belló Mora M., Yañez Otero A., **ROSETTA Near Comet Operations. Reference Cases for Simulation**, Doc. No. GMVSA 2035/96, February 1996.
14. Belló Mora M., Yañez Otero A., **ROSETTA Near Comet Operations. Surface Package Delivery Phase. Orbit Strategy and Navigation**, Doc. No. GMVSA 2115/96, July 1996.
15. Belló Mora M., Yañez Otero A., **ROSETTA Near Comet Operations. Transition to Global Mapping Phase. Orbit Strategy and Navigation**, Doc. No. GMVSA 2039/96, March 1996.
16. Belló Mora M., Yañez Otero A., **Upgrade of ROSETTA Near Comet Operations Simulator (RONCOS)**, Doc. No. GMVSA 2034/96, February 1996.
17. Bierman, G. J., **Factorization Methods for Discrete Sequential Estimation** Academic Press, 1977.
18. Chaffaut F. X., **CHAMPOLLION Project: Landing Mission Analysis**, CNES, CT/ED/TU/EI 95-089, Toulouse, June 1995.
19. Fiat Avio S.P.A., **Rosetta Program Lander: Active Descent System Study**, Document No. NTE GEN 00079, May 1997
20. Fertig J., Morley T., **ROSETTA - A Pedestrian's Approach to the Flight Dynamics of Surface Science Package Delivery. Part 1**, Orbit Attitude Division OAD Working Paper No. 55, ESOC, November 16, 1995.
21. Gonzalez Laguna E., Hechler M., **ROSETTA Surface Science Station Delivery Dynamics**, Presentation at ROSETTA Surface Science Station Workshop, ESTEC, February 9, 1994.
22. Gonzalez Laguna E., **ROSETTA Navigation Near a Comet**, MAS Working Paper No. 344, ESOC, September 1993.
23. Gonzalez Laguna E., **ROSETTA Surface Science Station Delivery Dynamics and Navigation**, MAS Working Paper No. 351, ESOC, November 1994.
24. Hechler M., **ROSETTA Interplanetary and Near Comet Navigation - A Challenge for Ground Operations**, Sao José Dos Campos, February 1994.
25. Hechler M., **ROSETTA Mission Design**, Invited Paper, XXX COSPAR Scientific Assembly, Hamburg, Germany, 16 July 1994.
26. Ivashkin V.V., **ROSETTA Comet Surface Package Delivery Dynamics**, Final Report, GMV Madrid, June 1994.
27. Jones J.B., Yen C.L., Howell K.C., **Near-Comet trajectory Design**, Paper AIAA-80-0114, AIAA 18th Aerospace Sciences Meeting, Pasadena, California, January 1980.
28. Miller J. K., **Navigation of the Landing of a Spacecraft on a Comet Nucleus**, CNSR/JPL Technical Note 023, 17 January 1990.
29. Miller J. K., Weeks C.J., Wood L.J., **Orbit Determination of the Comet Rendezvous Asteroid Flyby Mission: Post-Rendezvous Phases**, Paper AIAA-89-0348, Reno Nevada, January 1989.
30. Miller J. K., Weeks C.J., Wood L.J., **Orbit Determination Strategy and Accuracy for a Comet Rendezvous Mission**, Journal of Guidance and Control, Vol. 13, No. 5, pp 775-784, Sep-Oct 1990.
31. Miller J. K., Wood L.J., **Navigation of the Mariner Tempel 2 Mission: Orbit Phase and Penetrator Deployment**, Paper AIAA-87-0092, Reno Nevada, January 1987.
32. Miller S.L., Sweetser T.H., **CRAF Mission Design**, Viewgraphs presented at CRAF PSG No. 6, February 1989.
33. Müller M., **ROSETTA - A Pedestrian's Approach to the Flight Dynamics of Surface Science Package Delivery. Part 2**, Orbit Attitude Division OAD Working Paper No. 558, ESOC, March 1996.
34. Noton M., **Orbit Strategies and Navigation Near a Comet**, ESA Journal Vol. 16, No. 3, 1992.
35. Richter L., **ROSETTA-SSP: RoLand, Mission Design, Analysis of the SSP Delivery Problem**, DLR, Presentation at the ROSETTA Project ESTEC Meeting, June 1995.
36. Schwehm G., Hechler M., **ROSETTA - ESA's Planetary Cornerstone Mission**, ESA Bulletin No. 77, February 1994.



## THE CONTOUR NASA DISCOVERY MISSION

Edward L. Reynolds<sup>†</sup>

The Comet Nucleus Tour (CONTOUR) mission has been selected by NASA as the sixth Discovery flight program. Over a period of six years, a single spacecraft will fly to within 100 kilometers of three major near-Earth comets – Comet Encke in 2003, Comet Schwassmann-Wachmann-3 in 2006, and Comet d'Arrest in 2008 – taking images, making spectral maps, and analyzing dust flowing from the bodies to dramatically improve our knowledge of comet nuclei and their diversity. The payload includes fixed and tracking imagers that will provide high resolution images and spectral maps of each comet nucleus on both approach and departure. In addition to the baseline three comet mission, CONTOUR's mission design allows spacecraft's trajectory to be retargeted to a "new" comet -- possibly another Hale-Bopp.

CONTOUR uses several innovative techniques for performing deep space flyby missions at very low cost. These techniques include its: 1) launch strategy, 2) unattended hibernation capability, and 3) an innovative mission design, and spacecraft design.

**Launch Strategy:** CONTOUR takes advantage of an innovative indirect launch mode that can potentially benefit many future high C3 deep space missions. The indirect launch mode uses phasing orbits around Earth, followed by a solid rocket motor injection to place CONTOUR on its initial mission trajectory. The indirect launch mode allows the use of a smaller launch vehicle, an unconstrained launch window, and the opportunity for checkout and calibration while the spacecraft orbits Earth prior to final injection.

**Cruise Hibernation:** While cruising, the spacecraft sleeps in a spin stabilized configuration with no contact from the ground for months at a time. This unattended cruise capability greatly reduces CONTOUR's mission operations staffing and costs.

**Mission and Spacecraft Design:** CONTOUR makes use of Earth gravitational assists as a tool to retarget from one comet encounter to the next. CONTOUR's baseline mission uses seven gravitational assists instead of relying on propellant. If a new comet is discovered while CONTOUR is on orbit, another gravitational assist will be used to intercept it. CONTOUR's spacecraft configuration is very simple and robust.

This paper provides an overview of the CONTOUR mission, the spacecraft, and its scientific payload.

## INTRODUCTION

The COMet Nucleus TOUR (CONTOUR) will investigate several comet nuclei and assess their similarity and diversity. Our aims are to extend knowledge of comet nuclei (structure, composition, processes) beyond the level realized by the Halley flybys and provide data which, in combination with those to be obtained by NASA's Stardust and the European Space

---

<sup>†</sup> CONTOUR Mission System Engineer. The Johns Hopkins University Applied Physics Laboratory, Laurel, Maryland USA 20723. Phone: USA 410-792-5101, FAX: USA 410-792-6556

Agency's (ESA's) Rosetta missions, will increase our understanding of comets. To achieve these aims, the CONTOUR mission will concentrate on improving knowledge of key comet characteristics and on assessing the diversity of comet nuclei. Table 1 lists CONTOUR's science objectives and Figure 1 shows an artists conception of CONTOUR approaching a comet.

The measurements will be obtained by a focused, four-instrument payload. The primary goal of the payload is to improve our knowledge of nucleus surface structure, composition, and processes. The payload consists of: a wide-angle imager (CFI), a high-resolution imager/spectral mapper (CRISP), a dust analyzer (CIDA), and a neutral gas/ion mass spectrometer (NGIMS). All four will allow, for the first time, a meaningful assessment of the diversity of the nuclei of short-period comets and a comparison of these properties with those of the Comet Halley nucleus, and eventually with Wild2 (Stardust) and Wirtanen (Rosetta).

Comets are widely believed to be the most pristine, primitive bodies remaining in our solar system. Due to their pristine nature, comets should preserve clues to the important chemical and physical processes that took place when the planets formed, clues which have been so strongly altered by subsequent processes in larger bodies as to be difficult to recognize. Therefore, comet nuclei may be the only accessible objects that still retain a clear memory of the key chemical and physical events that took place during the formation of the solar system, processes such as condensation, agglomeration, and mixing. They probably also contain clues to the chemistry that led to the formation of the complex organic molecules known to exist in comet nuclei and which may have been the original source of organics on Earth from which life arose. It is also very likely that comets contain a variety of presolar system, interstellar grains that can provide clues to which locales in the galaxy the solar nebula materials came from.

**Table 1.**  
**SCIENCE OBJECTIVES**

Image parts of the nucleus at effective resolutions of 4 meters per pixel to reveal details of morphology and processes that will show us how comets work.
Determine nucleus size, shape, rotation state, albedo/color heterogeneity, and activity through global imaging.
Map composition of nucleus surface and coma through spectroscopy.
Obtain detailed compositional measurements of gas and dust in the near-nucleus environment at precisions comparable to those of Giotto or better.
Assess level of outgassing through imaging and spectroscopy as well as gas and dust measurements.
Assess the diversity of comets.
If possible, investigate a new comet.

The spectacular results obtained by Giotto during its flyby of comet Halley provided the first essential measurements, but left much to be done. CONTOUR, by studying a diversity of comets and by studying each to a finer degree of detail, provides the next logical step in the exploration of comets. It is also a valuable precursor to more complex comet missions such as Rosetta and can serve to extend the knowledge gained for Wild 2 by Stardust to other comets.

It is becoming evident that not all comets are alike. Remote sensing data indicate that there are significant differences in terms of the composition of both the volatile and refractory components, as well as in the relative amounts of the two. CONTOUR is an important first



step in addressing these differences. First, the CONTOUR mission will obtain detailed comparative data on three diverse short-period comets, allowing us to address the similarity and diversity of the gas and dust compositions, as well as their surface processes as revealed by the high-resolution imaging and spectroscopy. Second, the data obtained will be easily comparable to Halley Giotto data, helping us to address the question of diversity among Halley-like comets and truly short-period comets such as Encke, Schwassmann-Wachmann 3 and d'Arrest. Third, our dust analysis data will be directly comparable with those of Stardust (same dust analyzer), making it easier to extend the knowledge eventually gained from the direct analysis of Wild 2 sample materials to the CONTOUR comets. Finally, the mission flexibility of CONTOUR ensures the capability of taking advantage of the apparition of a new comet during the CONTOUR mission to address the most important question of diversity between a short-period and a long-period comet.

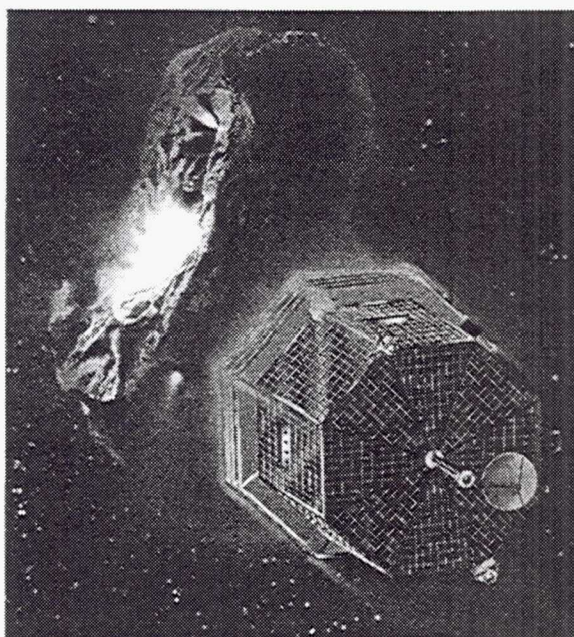


*Figure 1. Artist conception of CONTOUR approaching comet nucleus. Spacecraft is 3-axis stabilized during encounter. Dust shields protect spacecraft during closest approach.*

**Imaging Science.** The primary imaging objective is to characterize the physical, morphological, and geological nature of the cometary nucleus. These objectives will be addressed through observations at about 4-m resolution of surface structures, and of dynamic processes on the comet's surface and in its near-surface atmosphere (coma). In addition to these detailed studies, which will be accomplished using the highest resolution images, we will also determine important global properties for each comet nucleus, including data on its size, shape, and rotation characteristics, and produce a map showing major albedo, color, and geologic boundaries as well as the location of active jets. The CFI can be used to study the transition between the coma and tail structures.

There is abundant evidence that comet nuclei have highly irregular shapes and complex rotation states. Encounter imaging should establish an instantaneous rotation vector that satisfies the data. Coma images just before and after encounter will be compared to the high-resolution views and predicted positions of jet sources to test for a more complex rotation. Very little is known about the detailed surface configuration and surface processes on comets.



Of particular interest are the characteristics of surface mantles. The accumulation of non-volatile mantles is considered to play a primary role in the evolution of comets. Comets are believed to become inactive when their mantles grow too thick to be ejected during perihelion passages. CONTOUR images in conjunction with CRISP spectral mapping will make it possible to delineate the extent of mantling on each of the target nuclei. CONTOUR images will provide important new constraints on models of jet eruption and data on the crucial question of the degree to which jets are collimated. It may prove possible to determine ejection velocities from time-sequenced images.

**Gas Science.** The first objective for mass spectrometric observations is a chemical analysis of the gas to determine which molecular species are present. A second objective is the determination of the isotopic composition of the major volatile elements, of great interest for understanding the origin of cometary material and in identifying the contribution of this material to planetary volatile inventories.

Although the surfaces of short-period comets have been modified by both heat and cosmic and solar radiation, relatively unaltered materials should exist within meters of the surface and may in fact be exposed during venting events to which most comets are prone when close to the Sun. The mass spectrometer will determine the chemical composition of all gaseous species emitted from the comet nucleus within the range of the instrument sensitivity. Thermal ion composition measurements will also be made alternately with the neutral gas analysis to study the photochemical processes in the coma. CONTOUR provides the first opportunity to make such detailed compositional measurements for the comas of several short-period comets, and to compare these results to those obtained for Halley.

**Dust Science.** Dust analysis measurements on CONTOUR will allow a direct comparison of each comet with comet Halley as well as an intercomparison of our three comets. Given that CONTOUR will have a significantly upgraded version of the PIA instrument used so successfully at Halley, we expect to improve both the statistics and the quality of data available for the particulates. Furthermore, the lower encounter velocities on CONTOUR will facilitate detection of complex organic compounds. The extraordinarily high encounter velocities (70 km/sec) at Halley destroyed all but traces of these molecular signatures, and made calibration difficult. The lower velocities that obtain for CONTOUR can be readily duplicated by particle accelerators, making accurate instrument calibration possible. With comet Halley data in hand, the results expected from Wild 2 (Stardust), and the new data provided by CONTOUR, it will become possible to assess the diversity of dust in a comprehensive manner.

## THE CONTOUR COMETS

These targets were selected because of their different physical characteristics and their proximity to the Earth around the encounter dates. Encounter data regarding each comet is listed in Table 2.

**Encke:** Comet Encke has been observed at more apparitions (57) than any other comet including Halley. It is one of the most evolved comets that still remains active. Encke returns to perihelion (0.34 AU distance) every 3.3 years. Because Encke has been in this orbit for thousands of years, its continued high level of activity is puzzling.

**SW3:** First discovered in 1930, the activity pattern of SW3 is usually very predictable. However, in late 1995, SW3 split into three pieces. When CONTOUR arrives in 2006, it is likely that relatively unmantled materials will be visible in the cleaved areas, and that evidence of internal structures will remain exposed.

**d'Arrest:** Since its discovery in 1851, the observed light from apparition to apparition has been very repeatable. This suggests that the rotation state is stable, and that its surface outgassing vents change very little with time.

**Table 2**  
**Comet Encounter Data**

Encounter Date	Sun Distance (AU)	Earth Distance (AU)	Flyby Velocity (km/sec)
Encke, Nov 12, 2003	1.07	0.27	28.2
SW3, June 18, 2006	0.95	0.33	14.0
d'Arrest, Aug 16, 2008	1.35	0.36	11.8

## BASELINE MISSION PROFILE

The CONTOUR mission uses Earth-gravity assist maneuvers to accomplish the multiple encounters. The CONTOUR mission profile is extremely flexible and could be modified to include a first-ever study of a new comet.

A bipolar plot of the CONTOUR trajectory sequence is shown in Figure 2. The sequence begins with a 1-year Earth-return loop (segment 1) that positions the spacecraft for an encounter with Encke in November 2003. Two Earth-swingby maneuvers are then used to retarget the spacecraft for an encounter with Schwassmann Wachmann-3 in June 2006. Two more Earth swingbys enable CONTOUR to reach its final target, comet d'Arrest, in August 2008. Throughout the 6-year mission, the spacecraft-Earth distance is always less than 0.70 AU. The spacecraft-Sun distance varies between 0.83 and 1.35 AU. Especially noteworthy is the fact that all three encounters are extremely close to the Earth (0.27, 0.33, and 0.36 AU). All baseline comet encounters take place at times of excellent viewing from Earth, providing opportunities for cooperative worldwide supporting observations by ground-based and Earth-orbiting telescopes. In addition to professional astronomers, student and amateur observing teams are expected to play an important role in conducting these supporting observations.

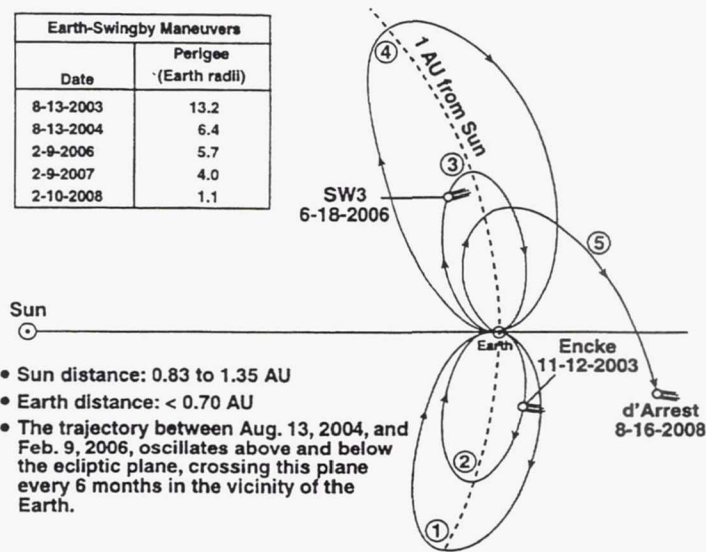


*Figure 2. Mission Trajectory Bi-Polar Plot*



The mission scenario requires injection at a fixed time on August 13, 2002, an innovative technique that employs "phasing orbits" is used to obtain an acceptable launch window. With phasing orbits, perigee heights and inclinations can be adjusted with small delta-V corrections to satisfy required conditions for the injection maneuver on August 13, 2002. The injection maneuver is performed with a STAR-30 solid rocket motor at a perigee altitude of approximately 300 kilometers. The delta-V cost is approximately 1745 m/s. The use of phasing orbits makes it possible to schedule a launch anytime before July 31, 2002. This flexibility allows considerable freedom in specifying a launch window for CONTOUR. Another advantage of using phasing orbits is the orbit checkout of the spacecraft while still close to Earth. By using phasing orbits, CONTOUR launches on a Medlite Delta 745.

## SPACECRAFT DESIGN

The spacecraft design is simple. Figures 3 and 4 show the spacecraft configuration in its flight configuration and with its outer shell removed, respectively. CONTOUR has few articulated mechanisms; the solar array is body mounted and does not require drive motors. The mission geometry allows CONTOUR to use fixed, passive, existing antenna designs. With the exception of along-track pointing of CRISP, all instrument pointing and antenna pointing is controlled by moving the spacecraft. A dust shield made of Nextel and Kelvar protects against impacts for the dust sizes and densities expected at the three encounters. The hydrazine thrusters mount in four pods located on the solar array shell. This arrangement provides maximum torque for efficient roll, pitch, and yaw maneuvers and keeps effluents well away from the science instruments.

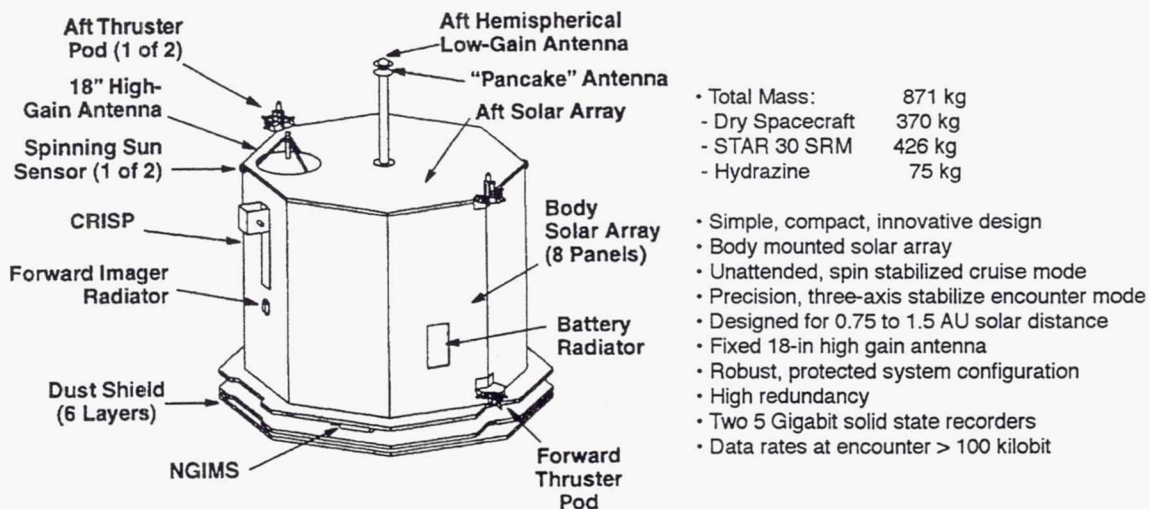


Figure 3. Flight Configuration.

The CONTOUR spacecraft has three operating modes: hibernation, rotisserie, and encounter mode. In both the hibernation and rotisserie modes the spacecraft spins about its main axis; in hibernation, the spin rate is 20 rpm and the spacecraft sleeps unattended for long periods of time. In rotisserie mode the spin rate is much slower and the spacecraft keeps the high-gain antenna pointed toward Earth for tracking and communication. Both spin modes keep the spacecraft temperatures even. Encounter mode is 3-axis stabilized, which is required for the imager operation. When the spacecraft stops rotating for an encounter, the



instruments cool to their optimum temperatures. The spacecraft attitude during an encounter is fixed with the dust shields and instruments aligned to the comet relative vector with only a small roll maneuver to keep the nucleus centered within CRISP. The spacecraft can stay 3-axis oriented for at least 6 hours.

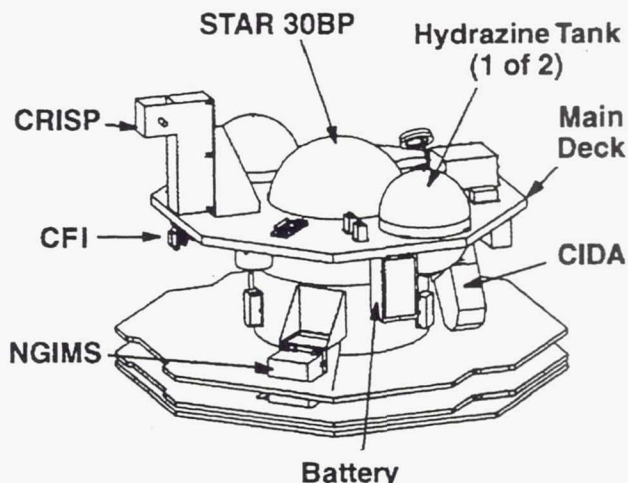


Figure 4. Internal Configuration.

During an encounter, the spacecraft is protected by its dust shield system mounted in the ram direction. The shield design is based on the Nextel Multishock Shield concept developed by NASA for Space Station. The basic concept of the shield is to use multiple layers of high-density fiber fabrics (Nextel) separated by space to break up an impacting dust particle and then to absorb the disbursed particle pieces using a Kevlar backstop.

## THE SCIENCE PAYLOAD

The CONTOUR payload consists of four instruments: a wide-angle imager (CONTOUR Forward imager, CFI), a high-resolution imager/spectral mapper (CONTOUR remote imager/spectrograph, CRISP), a dust analyzer (CONTOUR impact dust analyzer, CIDA), and a neutral gas/ion mass spectrometer (NGIMS).

### Imaging Instruments: CRISP and CFI

The core of the CONTOUR imaging and spectral mapping experiments is the CRISP. The imager/spectral mapper will have a target tracking capability to ensure that the key high-resolution frames are obtained. The imager is multispectral and has the capability to image in OH, CN, and C<sub>2</sub>. The spectral mapper will cover the spectral region 0.4 and 2.5  $\mu\text{m}$ . For reasons of economy, the spectral range of the spectral mapper does not extend into the 3-5  $\mu\text{m}$  region. Excellent supporting data of this type can be obtained from telescopic and Earth orbital facilities at the time of the encounters because all encounters occur at times of excellent viewing from Earth and near times of maximum comet activity. The instrument payload also includes a simple wide-angle camera to serve as backup and provide global views of the nucleus and coma. Key features of the CRISP and CFI are summarized in Tables 3 and 4. Figure 5 shows the physical layout of the two imaging instruments and Figure 6 shows the optics layout of the CRISP.

**Table 3**  
**CRISP Characteristics**

Mass	12 kilograms
Power	36 Watts
Telescope	Ritchey-Chretien reflecting
Focal Length	660 mm, f/6.6
Field of Regard	3° to 30° approach, 30° to 0° on departure
	<b>Imager</b>
Spatial Resolution	20 microrad/pixel (4 m @ 200 km)
Field of View	1.2° x 1.2°
Spectral Range	0.3 - 1.0 micrometer
Filter Wheel	8 positions ( 2 coma, 5 geology, 1 broadband )
Integration Time	10 ms to 100 seconds
Output	1 frame per second, 12 bits per pixel
Detector	1024 x 1024 square pixel CCD, 14 um pixels
	<b>Imaging Spectrograph</b>
Spatial Resolution	61 microrad per pixel (12 m @ 200 km )
Field of View	0.87° x 0.0035°
Spectral Range	0.4 - 2.5 um
Integration Time	10 ms to 1 second
Output	<10 frames per second, 12 bits per pixel
First Order	1.0 - 2.5 um, spec. res. 6.8 nm
Detector	256 x 256 square pixel HgCdTe array
Second Order	0.4 - 1.0 um, spec. res. 3.5 nm
Detector	14 um pitch

**Table 4**  
**CFI Characteristics**

Mass	3.9 kg, including mirror & dust protection
Power	1.9 Watts
Lense	Cooke triplet
Focal Length	85 mm, f/4
Detector	CCD with Lumogen, 1024x1024, 14um/pxl
Integration Time	10 ms to 100 seconds
Spatial Resolution	20 microrad/pixel (4 m @ 200 km)
Field of View	9.1° x 9.1°
Spectral Range	0.4 - 1.0 micrometer

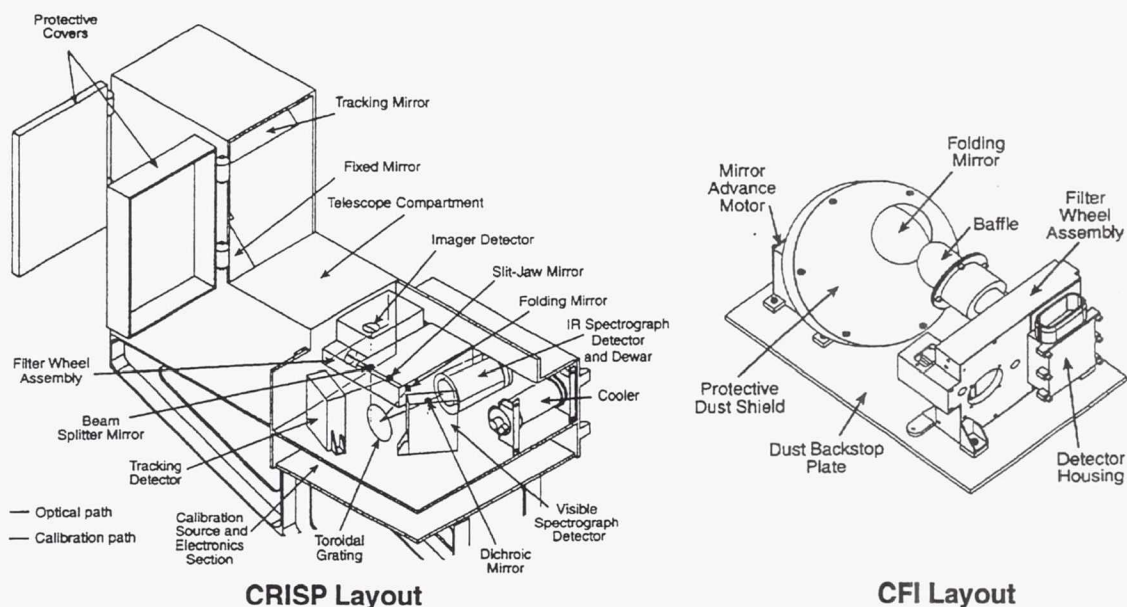


Figure 5. Layout Configuration of CONTOUR Imaging Instruments

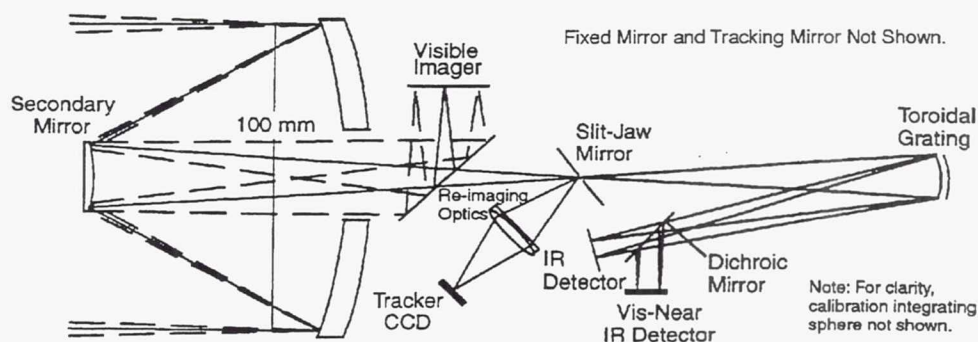


Figure 6. CRISP Optical Layout

### Gas and Dust: NGIMS and CIDA

The mass spectrometer, NGIMS, and dust analyzer, CIDA, will be mounted to look in the direction of flight at closest approach (CA). These two instruments have a very high degree of heritage and require no development. The dust analyzer is a significantly improved version of instruments that were flown successfully on Vega and Giotto during the Halley encounters, and is a copy of the instrument being supplied for the Stardust mission. It will be built and calibrated by vonHoerner and Sulger of Germany. CONTOUR's mass spectrometer (Neutral Gas Ion Mass Spectrometer, or NGIMS) will be provided by NASA GSFC. It is very similar to the INMS instrument on Cassini. The NGIMS instrument characteristics are detailed in Table 5 and the CIDA instrument characteristics are detailed in Table 6. NGIMS is placed on the spacecraft within the dust shield as far forward as possible to minimize contamination from spacecraft impact debris. It will be powered and collect data continuously during the 12 hours that surround closest approach. Figure 7 shows the schematic of the CIDA instrument sensor.



**Table 5**  
**NGIMS Characteristics**

Mass	8.8 kilograms
Power	22.6 Watts
Gas Sampling System	Open Source/molecular beaming; Closed source
Ion Sampling System	Thermal and suprathermal positive ions
Mass Analyzer	Quadrupole mass filter
Ion Source	Electron impact ionization
Mass Range	1 to 300 amu nominal
Viewing Angle	Open Source: 8°. Closed Source: 2 pi steradians
Scan Modes	Survey: mass scan over entire mass range in 1/8 or 1 amu steps; Adaptive Mode: selectable mass values
Detector	Dual-detector pulse-counting system; approximately $10^{11}$ for a signal to noise ratio of 1; background level 1 count/minute (0.017 seconds per period)

**Table 6**  
**CIDA Characteristics**

Mass	4.5 kg Electronics, 7.5 kg Sensor
Power	13 Watts
Target Size	100 cm <sup>2</sup>
Ion type	positive and negative ions
Mass range	1 to 330 Daltons
Resolution	m/dm=150 (goal of 300)
Dust grains	$2 \times 10^{-16}$ to $3 \times 10^{-9}$
Data Storage	60 kbits/spectrum, CIDA can store 15 to 25 spectra.

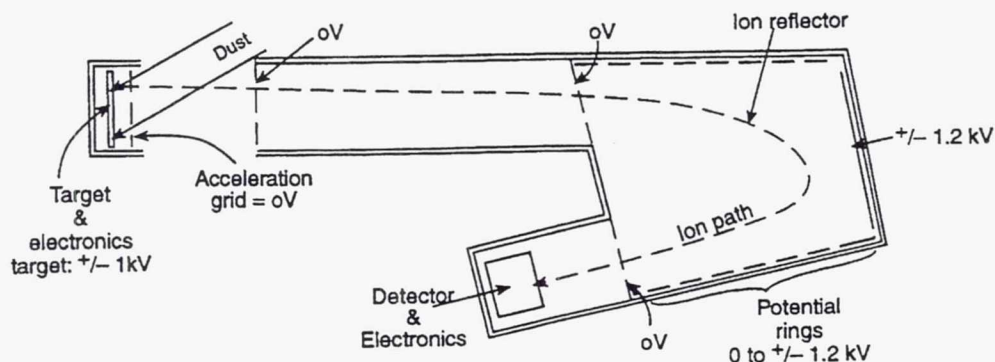


*Figure 7. Schematic of CIDA instrument sensor.*

## TYPICAL ENCOUNTER SCENARIO

During the Earth-swingby phase that precedes each of the comet encounters, the spacecraft and its instruments are awakened and thoroughly checked. Using tracking data, the spacecraft's trajectory is accurately determined, and a coarse targeting maneuver is executed at 25 days prior to the encounter. The science timeline begins at 10 days prior to an encounter. At this time, the spacecraft leaves its hibernation spin stabilized attitude and becomes



three-axis stabilized (with a slow 'rotisserie' rotation). Imaging and spectral observations begin when the imaging resolution is about 200 kilometers per pixel. OpNav and coma monitoring observations will be obtained each day. This phase will end one day prior to closest approach when the resolution becomes 20 kilometers per pixel.

The baseline 'miss' distance is 100 kilometers from the nucleus at closest approach. This distance is a trade-off between science value and spacecraft safety. For CONTOUR, at 100 kilometers there is less than a one percent probability of encountering a dust grain greater than 0.1 grams, while still capable of collecting 4 meter resolution images. Earth-based optical and radar observations of the comet's dust environment taken shortly before the encounter will be used to update the miss distance. The final targeting maneuver is executed one day prior to encounter. The encounter mode begins at E-0.5 days.

At this time, the range is about 500,000 kilometers and the resolution is close to the expected diameter of the comet nucleus. CRISP images can be obtained until 20,000 kilometers out (400 meters per pixel) after which the spacecraft will remain on a velocity vector orientation, allowing continuous coverage by NGIMS and CIDA for one-half hour on either side of closest approach. The last CFI image is obtained under 2 minutes before closest approach at 190 meters per pixel. High-resolution CRISP images start when the nucleus is  $6^\circ$  off the velocity vector with a resolution of 19 meters per pixel. Figure 8 shows the encounter of d'Arrest as viewed by the CRISP imager (the other two encounters are similar). CRISP images continue until a range of 200 kilometers (4 meters per pixel resolution), then resume at a similar range after closest approach. CRISP maintains a resolution of better than 200 m/pxl for nearly 15 min after encounter. The encounter phase ends at +0.5 days. Shortly after this time, the spacecraft's high-gain antenna is pointed at Earth and the high-rate downlink of encounter data begins.

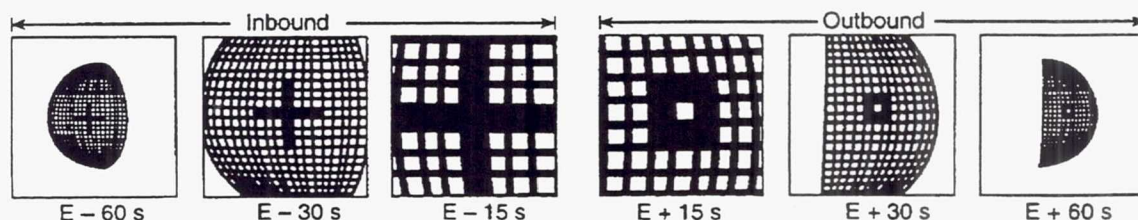


Figure 8. Encounter of Comet d'Arrest as viewed by CRISP. Using a tracking mirror system, images and spectra data are taken on both approach and departure.

## CRUISE STRATEGY

During the cruise intervals between comet encounters and Earth-swingby maneuvers, the CONTOUR spacecraft will be placed into a spin-stabilized 'hibernation' mode (similar to the Giotto spacecraft from 1986 to 1990). The spacecraft will be oriented with its major axis normal to the orbit plane and then spin stabilized at 20 rpm. Instruments and many subsystems will be powered off. Only the command receivers, thermo-statically controlled heaters, and critical components will be powered. It is assumed that there will be no ground contact with the spacecraft while it is in this hibernation state. Over CONTOUR's mission lifetime of roughly 6 years, DSN assets are required just 6% of the time.

## NEW COMET OPTION

A key aspect of CONTOUR is the flexibility to retarget to a new comet and extend the diversity study beyond the realm of the Jupiter family comets, allowing us to compare directly the characteristics of an Oort Cloud comet with those originating in the Kuiper Belt. By a new comet we mean one that is on its first pass through the inner solar system and experiencing its first, and possibly last, exposure to intense levels of sunlight. Almost half of these new comets are perturbed during their transit of the Sun's neighborhood onto hyperbolic orbits and escape from the solar system. As new comets approach the Sun, they often show unusually high levels of activity that gradually fade into normal behavior. This pattern is thought to reflect the removal of a surface layer of highly volatile materials. Mantle formation and the establishment of active regions may begin. A mantle may establish itself on the less active regions, while the more active areas remain mantle-free.

Newly discovered comets also include objects of long periods, such as the recently discovered Hale-Bopp and Hyakutake, that were perturbed into their present orbits many thousands of years ago. Such comets may have made several passes close to the Sun. The record preserved in the Jupiter family comets will reflect the characteristics of the nebular regions near the present-day Kuiper Belt, whereas the record in new long-period comets will be characteristic of nebular regions interior to Neptune's orbit, from where most of the comet nuclei now resident in the Oort Cloud are believed to have been scattered.

It is not possible to predict when a new or long-period comet will be discovered. However, on average about ten such comets are discovered each year. Most are discovered 1-3 months before their perihelion passage; a few, such as Kohoutek and Hale-Bopp, are discovered much earlier. Because of the relatively short time available to reach the average new comet and their generally near-parabolic eccentricities and high inclinations, newly discovered comets are challenging targets for space missions. The short planning, development, and flight times that must be accommodated and the ephemeris uncertainties intrinsic in initial orbit solutions, as well as large C3 requirements, demand an innovative approach if such comets are to be studied by spacecraft.

**What is the likelihood of retargeting CONTOUR to intercept a new comet ?** The answer is surprisingly good. CONTOUR's nominal mission uses Earth swingby events which can be used to retarget to a newly discovered long period comet. A series of Monte Carlo simulations combining comet discovery probabilities and optimal trajectory calculations (random sampling of intrinsic distribution of comet orbital elements and absolute magnitude). More than 50,000 sample trial results were obtained over CONTOUR's six Earth swingby events. The results show that the probability of at least one new comet flyby opportunity during the nominal CONTOUR mission profile is ninety-seven percent (Friedlander and German, 1996). Table 7 shows CONTOUR cumulative new comet encounter probabilities relative to brightness ( $H_{10} < 10$ ) and encounter phase angle (lighting conditions) constraints over the mission lifetime. If only large bright comets were acceptable ( $H_{10} < 6$ ) then the probability is reduced to 18%.

**Table 7**  
**Cumulative New Comet Encounter Probabilities**

Constraint of Phase Angle	Limiting absolute magnitude, $H_{10}$						
	10	9	8	7	6	5	4
< 140 degrees	0.969	0.863	0.636	0.386	0.180	0.064	0.017
< 110 degrees	0.933	0.786	0.544	0.315	0.143	0.050	0.013

Encounter constraints: Heliocentric distance between 0.8 and 1.4 AU; Earth distance < 2.4 AU.



## CONCLUSION

Using an innovative, flexible mission design, CONTOUR provides the major next step to understanding the diversity of comet nuclei. A simple, reliable spacecraft, a capable payload with high inheritance, and robust margins in all critical areas combine to make CONTOUR an excellent low-risk mission. CONTOUR's major asset is its dedicated Team, the core of which consists of highly experienced individuals with outstanding records on recent missions.

## ACKNOWLEDGMENT

This paper is the work of the entire CONTOUR team. The team is lead by Principal Investigator Joe Veverka of Cornell University. He is supported by a dedicated science team and implementation team. CONTOUR will be built integrated and tested at the Johns Hopkins University, Applied Physics Laboratory. Key individuals at APL include: Mary Chiu, Project Manager; Bob Farquhar, Mission Manager; David Dunham, Mission Designer; Jeff Warren, Imaging Instrument Lead Engineer; Kim Strohbahn, Image Tracking Lead Engineer; Mike Kreitz, Mechanical Engineer; Terry Betenbaugh, Stress Engineer; Doug Mehoke, Thermal Engineer; Mark Holdridge, Mission Operations Manager, Scott Murchie and Andrew Chang, Science.

**Page intentionally left blank**



## USING SOLAR RADIATION PRESSURE TO CONTROL L2 ORBITS

Noam Tene, Karen Richon, David Folta

The main perturbations at the Sun-Earth Lagrange points L1 and L2 are from solar radiation pressure (SRP), the Moon and the planets. Traditional approaches to trajectory design for Lagrange-point orbits use maneuvers every few months to correct for these perturbations. The gravitational effects of the Moon and the planets are small and periodic. However, they can not be neglected because small perturbations in the direction of the unstable eigenvector are enough to cause exponential growth within a few months.

The main effect of a constant SRP is to shift the center of the orbit by a small distance. For spacecraft with large sun-shields like the Microwave Anisotropy Probe (MAP) and the Next Generation Space Telescope (NGST), the SRP effect is larger than all other perturbations and depends mostly on spacecraft attitude. Small variations in the spacecraft attitude are large enough to excite or control the exponential eigenvector. A closed-loop linear controller based on the SRP variations would eliminate one of the largest errors to the orbit and provide a continuous acceleration for use in controlling other disturbances.

It is possible to design reference trajectories that account for the periodic lunar and planetary perturbations and still satisfy mission requirements. When such trajectories are used the acceleration required to control the unstable eigenvector is well within the capabilities of a continuous linear controller. Initial estimates show that by using attitude control it should be possible to minimize and even eliminate thruster maneuvers for station keeping.

### INTRODUCTION

Current numerical trajectory analysis does not take full advantage of optimization tools and analytical methods for designing transfer trajectories and gravity assists to the Sun-Earth L1 and L2 Lagrange points. The effects of perturbations due to the variation in solar radiation pressure and the periodic effects of the Moon should be used in selection of the nominal L2 orbit; . By redefining the nominal orbit instead of trying to control these perturbations later, we reduce deviations by several orders of magnitude. The authors are prototyping analytical tools in Mathematica and MATLAB to design and select nominal orbits of this type. The new tools are being designed so they can easily be incorporated into the next generation of operational flight dynamics tools.

These methods have applications for any Lagrange-point mission and implications for phasing loop and lunar gravity assist trajectories. The case studies used for this analysis focus on the MAP mission. The tolerance already available in the pointing of the MAP sun shield can be used to produce variations in the SRP. Although the resulting control force is small it is the same order of magnitude as the perturbations that remain after applying the new methods. This should allow for station keeping without requiring any propulsion maneuvers. This paper provides some of the mathematical background required for targeting to L2 and describes how it can be applied to identify the relationships between the targeting variables and goals for the MAP mission.

## MAP MISSION DESIGN CRITERIA

The mission requirements for the MAP trajectory design involve the fuel budget (110 m/s), launch vehicle dispersions (as large as 10 m/s) and the required launch window (any day of the month). In addition, constraints from the power, thermal and communication systems need to be taken into account.

The criteria for the L2 orbit design are defined using the Earth's shadow and the distance from the Earth-Sun vector. The spacecraft must stay out of the Earth's shadow to prevent loss of power from the solar arrays but still stay close enough to the Earth-Sun line to satisfy communication requirements and to keep thermal radiation from the Earth and Moon from bypassing the sun-shield. For MAP the angle between the Map-Earth vector and the sun-line must be between  $0.5^\circ$  and  $10^\circ$  which translates to a minimum distance of 13,000 Km and a maximum distance of 260,000 Km from the Earth-Sun line.

The minimum distance requirement rules out the option of going directly to the L2 point exactly and staying there. The types of orbits that can maintain this distance without escaping are halo orbits and Lissajous orbits. Lissajous orbits have different oscillation periods for the ecliptic-plane and out-of-plane motion. The resulting Lissajous pattern (Figure 1) inevitably passes through the shadow every 7.5 years. Halo orbits, on the other hand, are periodic and avoid the shadow problem by using non-linear effects of large amplitudes in the ecliptic plane. For MAP the maximum distance of 260,000 Km rules out halo orbits, leaving Lissajous patterns as the only choice. The eventual closing of the Lissajous pattern is not a major concern for MAP since the projected mission length is less than 3 years.

## TRANSFER TRAJECTORIES

Direct transfers to L2 are very sensitive to small launch vehicle (LV) dispersions. Figure 2 shows that a very small error in orbit determination or in  $\Delta V$  at perigee leads to very large errors in the approach to L2. Errors as small as 3 cm/sec are large enough to cause significant effects in the final orbit that must be corrected within a month or two of arrival. Dispersion errors can not be immediately corrected since it takes time to detect them. By the time the error has been detected, the spacecraft has climbed out of the Earth's gravity and the orbit is no longer as sensitive to the  $\Delta V$  of correction maneuvers. The magnification of the initial error becomes critical for realistic dispersion errors since an uncorrected injection error of 3 m/sec would miss the desired orbit at L2 and diverge from the desired trajectory in less than a month.

Direct insertion from parking orbit into large halo orbits can be achieved in special cases<sup>1</sup> (Figure 3). However, the final orbits have very large amplitudes that violate the 260,000 Km requirement. Achieving a tighter Lissajous pattern would require large insertion maneuvers at L2 even with no dispersion errors. For smaller Lissajous patterns with a reasonably short (6 months) flight time this option does not seem promising. The MAP trajectory design has opted to use a combination of phasing loops and a lunar flyby in order to save fuel, eliminate the need for an insertion maneuver at L2 and avoid the sensitivity of direct transfer<sup>2</sup>.

The lunar flyby provides a significant gravity assist that reduces the total launch energy ( $C_3$ ) and eliminates the need for an insertion maneuver to achieve a small Lissajous pattern near L2. Lunar flyby orbits of this type require precise targeting to achieve the correct timing and orientation. They are also very sensitive to LV dispersions and small variations in the orbital elements at perigee. These variations can cause the spacecraft to miss the Moon altogether or to fly by too close and achieve escape velocity from the Earth-Moon system. In addition to the sensitivity problems, direct injection into a lunar flyby trajectory would restrict the launch window to a few days each month.



## PHASING LOOPS

Phasing loops provide an elegant solution to both the launch window and LV dispersion problems. The injection burn into the phasing loop can be performed at almost any time of the month. The first loop is designed to purposely miss the Moon. The first apogee also provides an opportunity to raise perigee (if necessary) and adjust the orbit inclination at a very low  $\Delta V$  cost. Moreover, by the time of the next perigee, orbit determination (OD) should be good enough and the correction compensating for the initial dispersion would not require too much  $\Delta V$ .

The trajectory is still very sensitive to small variations in  $\Delta V$  and to the initial conditions on the launch date. However, this sensitivity is now an advantage, allowing us to use very small maneuvers to achieve our goals. We can wait for accurate OD data and use it to determine an optimal trajectory that is designed specifically for the known launch date and LV dispersion errors. The optimization goal for the phasing loop stage is to achieve the precise timing and orientation required for a successful lunar flyby.

To get an initial estimate of the timing, location and orientation of the flyby trajectories we can integrate the equations of motion backward from L2 and determine when, where and from which direction the spacecraft approaches lunar orbit. A rough initial approximation that does not include lunar gravity effects (Figure 4) shows that the spacecraft crosses the lunar orbit twice each month at a specific location and orientation. This rough approximation shows the location of the two lunar flyby opportunities within a few degrees. While the back-propagation results obtained by neglecting lunar gravity can not be used for approximating the actual flyby, they do provide us with some design information for the mission. The timing of the flyby is determined by the intersection of the spacecraft and lunar orbits since the Moon has to be close enough to provide a gravity assist. The asymptote for a B-plane analysis can also be determined with this method.

We can use the approximate flyby times to choose the number and periods of the phasing loops. The path followed by the spacecraft several days after the flyby is nearly independent of the lunar gravity. The arrival time at L2 is very sensitive to the exact timing of the flyby. The exact arrival time at L2 is not a major concern for most missions. We can therefore afford to make small adjustments in the timing of the flyby as long as the departing asymptote is adjusted to assure that the spacecraft arrives at the desired trajectory.

The final orbit parameters at L2 are extremely sensitive to the choice of departing asymptote from the lunar flyby. Numerical studies using Swingby\* show that small adjustments of the incoming asymptote (a day before the flyby) and at periselene are sufficient to determine the entry point on the Lissajous pattern or even to reverse its direction. However, the qualitative results of these numerical investigations are limited by the fact that very small numerical errors in the initial conditions grow exponentially with time so that numerical targeting schemes can not be used effectively for more than 5 months. Successive targeting with appropriate cost functions that measure the deviation from a nominal orbit at L2 can be used to achieve better results<sup>3</sup>. The definition of these cost functions relies on a linear approximation of the orbit at L2.

Meaningful definitions of the goals at L2 can be phrased in terms of the size of the unstable eigenvector, the size of the two oscillations ( $A_Y$  and  $A_Z$ ), the phase difference between the oscillations ( $\Delta\phi$ ), the common phase at insertion ( $\phi_{\text{bar}}$ ) and the arrival time. Controlling the unstable eigenvector is critical for maintaining an orbit at L2. However, the design of the phasing loops can not effectively perform this task. A station keeping method (periodic thrust maneuvers or induced SRP variations) must be used regardless of the phasing loop strategy. The size of the two oscillations  $A_Y$  and  $A_Z$  must satisfy the requirements for minimum and maximum angle from the sun line but are allowed to vary within that range. The phase

---

\* Swingby is the Mission Analysis tool developed and used by the Flight Dynamics Analysis Branch and Goddard Space Flight Center. Swingby was used for SOHO, WIND, Clementine and Lunar Prospector trajectory design and maneuver calibration.

difference  $\Delta\phi$  determines where the spacecraft is on the Lissajous pattern. Targeting to an opening Lissajous pattern (Figure 1b) assures that the spacecraft will not pass through the shadow for at least 3 years (as long as the unstable eigenvector is controlled).

The allowed variation in the three parameters  $A_y$ ,  $A_z$  and  $\Delta\phi$  is limited by mission requirements. However, the size of the stable eigenvector (related to the arrival time at L2) and  $\phi_{\text{bar}}$  (the position on the Lissajous orbit) do not affect any mission requirements and do not need to be controlled. In designing the phasing loops and lunar flyby,  $A_y$ ,  $A_z$  and  $\Delta\phi$  should be used as targeting goals instead of numerical estimates that rely on plane crossings available in tools like Swingby. This makes it possible to satisfy mission requirements without placing unnecessary restrictions on the targeter which make it converge on non-optimal solutions. This targeting method, when combined with accurate modeling of SRP and lunar perturbations can reduce errors to the point that intentional variations of the MAP sunshield attitude are sufficient to perform station keeping. Any deviations from desired performance can be controlled through the attitude control system and propulsive maneuvers are not required.

## LINEAR ANALYSIS AT L2

The formulation of the non-linear equations of motion is done in a rotating coordinate system centered at the Earth-Sun barycenter with the x-axis along the Sun-Earth line, the z-axis toward the ecliptic north and the y-axis chosen to complete an orthogonal right handed system. Normalized units for this system are 1 AU for length and Year/(2 $\pi$ ) for time. However, for practical calculations it is often convenient to express length as a fraction of the distance from L2 to Earth and time in a multiple of the time constant ( $\tau$ ) or periods ( $2\pi/\omega_{xy}$  and  $2\pi/\omega_z$ ) that correspond to the eigenvalues of the linear system.

Figure 5 shows a cross section along the XY plane (ecliptic) of the non-linear potential in the Rotating Libration Point (RLP) coordinate system centered at L2. We can see that a linear approximation about the Lagrange point is valid for a Lissajous pattern (the ellipse) with a maximum excursion of 5° from the Earth-Sun line. For larger orbits, the non-linear effects become more significant but the approximation still gives reasonable results even for a 10° excursion.

The linearized system has one unstable mode (eigenvector) that grows exponentially with an eigenvalue of  $1/\tau = 2.5 \cdot (2\pi/\text{year}) = 1/(23 \text{ days})$ . This means that small errors and the effects of perturbations in the direction of the unstable eigenvector will double every 16 days ( $\tau \ln 2$ ). The system also has a stable eigenvector that decays at the same rate. Initial displacements in the direction of the stable eigenvector will shrink to a half in 16 days as well.

In addition to the stable and unstable eigenvectors, the system also has two pairs of imaginary eigenvalues. One of the pairs ( $\omega_z = 1.99$  periods per year) corresponds to a pure oscillation in the z direction (the corresponding eigenvectors have no x and y components). The fact that all other eigenvectors have no z component indicates that as long as the linear approximation is valid, motion in the ecliptic plane and the out-of-plane oscillations are completely independent. The ellipse in Figure 5 traces the trajectory of a pure oscillation in the ecliptic plane which corresponds to the second pair of eigenvalues ( $\omega_{xy} = 2.07$  periods per year).

## SOLAR RADIATION PRESSURE (SRP) EFFECTS

As mentioned earlier, SRP is the main perturbation to spacecraft orbits in the near vicinity of the Earth-Sun L2 Lagrange point. Figure 6 shows the MAP spacecraft with its large, 5 meter diameter, sunshield. It is easy to compensate for the average MAP SRP value ( $0.2 \mu\text{N/s}^2$ )\* and for the first order effects of the Moon

---

\* Based on:

Mass = 850 Kg  
 Reflectivity = 1.9  
 Solar pressure =  $5 \mu\text{N/m}^2$



at L2 by moving the spacecraft a few hundred Kilometers closer to the Sun. However, very small variations in the orientation of large sun-shields can excite (or control) the unstable eigenvector and thereby cause (or prevent) escape from the vicinity of L2.

The effect of predicted errors in MAP attitude determination ( $0.02^\circ$ ) and attitude control ( $0.1^\circ$ ) on the x component of the SRP vector are expected to be negligible\*. However, a small bias in the spin axis of the spacecraft can generate a small constant acceleration in the y or z directions. The angle between the x-axis and the spacecraft-sun line depends on the size and phase of the orbit and introduces a known bias with a corresponding acceleration in the y or z direction. Known accelerations can be accounted for in the orbit design, however, with an attitude pointing tolerance of  $0.25^\circ$ , the variation in acceleration can be as high as:  $0.2 \mu\text{m/s}^2 * \sin(0.25^\circ) = 0.9 \text{ nm/s}^2$ .

An acceleration of  $0.9 \text{ nm/s}^2$  in the z direction is too small to have an effect on a periodic oscillation with magnitude measured in thousands of Kilometers. However, the same acceleration in the y direction contributes  $0.3 * \tau * 0.9 \text{ nm/s}^2 \approx 0.3 * (3.5 \text{ Km} / \tau) = 1.2 \text{ Km}/\tau^\dagger$  toward the derivative of the state component that grows exponentially in the direction of the unstable eigenvector. To compensate for this derivative the spacecraft would have to be 1.2 Km away from the nominal trajectory in the opposite direction. . If an unpredicted error of  $1.2 \text{ Km}/\tau$  is allowed to accumulate and we can not prepare for this displacement, we should expect the error to double every 16 days. If we assume eight maneuvers with a fuel budget of 8 m/s for stationkeeping, maneuvers are limited to  $1 \text{ m/s} \approx 2000 \text{ Km}/\tau$  and the time between maneuvers can not exceed 170 days ( $\tau \ln[2000/1.2] = 7.4\tau$ ).

On the other hand, a closed-loop onboard controller with access to the ACS-reference input can purposely generate a bias of up to  $0.2 \mu\text{m/s}^2 * \sin(0.25^\circ - 0.1^\circ) = 0.5 \text{ nm/s}^2$  to control deviations from the nominal trajectory. The controller would saturate for position errors larger than 2 Km (with no velocity error) or velocity errors of  $1 \text{ mm/s}$  ( $2 \text{ Km} / \tau$ , with no position error). Designing our nominal trajectories with sufficient detail to have deviations on the order of several hundred meters should allow us to maintain the orbit at L2 without saturating the onboard controller. This strategy would eliminate propulsion maneuvers for the duration of the mission.

## SYSTEM INTEGRATION

The results in this paper show a strong interaction between navigation, orbit determination and attitude control. In order to use a closed loop controller based on solar radiation pressure, the corresponding spacecraft systems would need to be integrated. The integrated system should communicate state parameters and use these parameters to improve the accuracy of the OD and control commands.

It is clear that both the OD and navigation need to have access to accurate and timely attitude data. In addition, the closed loop controller should be able to command the ACS to perform minor adjustments to the nominal direction of the spin axis.

---


$$\text{Sun shield area} \approx 20 \text{ m}^2$$

$$\text{Effective area} = 20 * \cos(22.5)$$

$$\text{Average acceleration} = 1.9 * 5 \mu\text{N/m}^2 * 20 \text{ m}^2 * \cos(22.5^\circ) / 850 \approx 0.2 \mu\text{m/s}^2$$

\* Since the MAP spacecraft makes a full rotation about an axis pointing away from the Sun every hour, the average SRP acceleration is directed away from the Sun. If the spin axis points exactly away from the Sun and the spin motion is symmetric, there would be no acceleration perpendicular to the spin axis. Any bias in the spin axis would cause a perpendicular force in the y or z direction (RLP coordinate system).

† The derivative was calculated in time units normalized so the time constant  $\tau$  of the unstable mode is 1.

## FUTURE ANALYSIS

The variation in SRP due to small changes in attitude should be included in the OD process. Most current OD tools assume a spherical spacecraft with constant cross-sectional area and do not model the forces as normal to the surfaces exposed to the SRP. In order to perform accurate control, the controller must have accurate data. Orbit determination methods need to be improved, to match the accuracy of the analysis. One way to do this is to design a Kalman filter that will perform OD in real time as part of an integrated onboard ACS and navigation system.

Future analysis should address the open questions regarding attitude control and the possibility of handling the windmill effect. The strategy of designing nominal momentum wheel states to match the expected perturbations created by the difference between the center of gravity and center of pressure can have similar results to those presented here. This option should be studied in more detail since the possibility of using small variation in attitude to control the remaining deviations may work in this case as well. The full advantage of eliminating station keeping maneuvers can not be realized if propulsion maneuvers are still required for momentum dumping. Solar radiation pressure also affects the total momentum of the spacecraft and it may be possible to use a similar strategy to eliminate the need for momentum dumping.

## CONCLUSIONS

The methods discussed in this paper can be applied to any Lagrange-point mission, with implications for phasing loop and lunar gravity assist trajectories. The importance of accurate SRP modeling in the design of the nominal trajectory has been demonstrated and a direct application for the MAP mission has been shown. Using attitude variations as small as  $0.25^\circ$  can affect the SRP enough to control the orbit at L2. This seems like a promising method for minimizing or eliminating propulsion stationkeeping maneuvers for MAP. If the onboard controller is successfully flown on MAP as a technology demonstration, NGST would be able to use it as proven technology.

## ACKNOWLEDGEMENTS

The authors would like to thank Kimberly Tene and Steve Cooley for their comments and assistance.

## REFERENCES

- 
- <sup>1</sup> K.C. Howell, D.L. Mains and B.T. Barden. Transfer Trajectories from Earth Parking Orbits to Sun-Earth Halo Orbits, August, 1997.
  - <sup>2</sup> K. Richon. An Overview of the MAP Trajectory Design, August, 1997.
  - <sup>3</sup> K. Richon, Noam Tene, 1998 paper, Boston.



# TRAJECTORY DESIGN STRATEGIES THAT INCORPORATE INVARIANT MANIFOLDS AND SWINGBY

J. J. Guzmán,\* D. S. Cooley,<sup>†</sup> K. C. Howell,<sup>‡</sup> and D. C. Folta<sup>§</sup>

Libration point orbits serve as excellent platforms for scientific investigations involving the Sun as well as planetary environments. Trajectory design in support of such missions is increasingly challenging as more complex missions are envisioned in the next few decades. Software tools for trajectory design in this regime must be further developed to incorporate better understanding of the solution space and, thus, improve the efficiency and expand the capabilities of current approaches. Only recently applied to trajectory design, dynamical systems theory now offers new insights into the natural dynamics associated with the multi-body problem. The goal of this effort is the blending of analysis from dynamical systems theory with the well established NASA Goddard software program SWINGBY to enhance and expand the capabilities for mission design. Basic knowledge concerning the solution space is improved as well.

## INTRODUCTION

The trajectory design software program SWINGBY, developed by the Guidance, Navigation and Control Center at NASA's Goddard Space Flight Center, is successfully used to design and support spacecraft missions. Of particular interest here are missions to the Sun-Earth collinear libration points. Orbits in the vicinity of libration points serve as excellent platforms for scientific investigations including solar effects on planetary environments. However, as mission concepts become more ambitious, increasing innovation is necessary in the design of the trajectory. Although SWINGBY has been extremely useful, creative and successful design for libration point missions still relies heavily on the experience of the user. In this work, invariant manifold theory and SWINGBY are combined in an effort to improve the efficiency of the trajectory design process. A wider range of trajectory options is also likely to be available in the future as a result.

Design capabilities for libration point missions have significantly improved in recent years. The success of SWINGBY for construction of trajectories in this regime is evidence of the improvement in computational capabilities. However, conventional tools, including SWINGBY, do not currently incorporate any theoretical understanding of the multi-body problem and do not exploit the dynamical relationships. Nonlinear dynamical systems theory (DST) offers new insights in multi-body regimes, where qualitative information is necessary concerning sets of solutions and their evolution. The goal of this effort is a blending of dynamical systems theory, that employs the dynamical relationships

---

\* Graduate Student, School of Aeronautics and Astronautics, Purdue University.

<sup>†</sup> Aerospace Engineer, Flight Dynamics Analysis Branch, Guidance, Navigation and Control Center, Goddard Space Flight Center.

<sup>‡</sup> Professor, School of Aeronautics and Astronautics, Purdue University.

<sup>§</sup> Aerospace Engineer, Systems Engineering Branch, Guidance, Navigation and Control Center, Goddard Space Flight Center.

to construct the solution arcs, and SWINGBY, with its strength in numerical analysis. Dynamical systems theory is, of course, a broad subject area. For application to spacecraft trajectory design, it is helpful to first consider special solutions and invariant manifolds, since this aspect of DST offers immediate insights. An understanding of the solution space then forms a basis for computation of a preliminary solution; the end-to-end approximation can then be transferred to SWINGBY for final adjustments. Accomplishing this objective requires an exchange of information between two software packages. At Purdue, various dynamical systems methodologies are included in an internal software tool called GENERATOR. GENERATOR includes several programs that *generate* different types of solution arcs, some based on dynamical systems theory; the user then collects all the arcs together and differentially corrects the trajectory segments to produce a complete path in a complex dynamical model. A two level iteration scheme is utilized whenever differential corrections are required; this approach produces position continuity (first level), then velocity continuity (second level).<sup>1-4</sup> SWINGBY, on the other hand, is an interactive *visual* tool that allows the user to model launches and parking orbits, as well as design transfer trajectories utilizing various targeting schemes.<sup>5</sup> SWINGBY is also an excellent tool for prelaunch analysis including trajectory design, error analysis, launch window calculations and ephemeris generation.<sup>6</sup> SWINGBY has proven to be an improvement over previous non-GUI (Graphical User Interface) programs. The goal here is a procedure to use the tools in combination for mutual benefit.

## INVARIANT MANIFOLDS

The geometrical theory of dynamical systems is based in phase space and begins with special solutions that include equilibrium points, periodic orbits, and quasi-periodic motions. Then, curved spaces (differential manifolds) are introduced as the geometrical model for the phase space of dependent variables. An invariant manifold is defined as an  $m$ -dimensional surface such that an orbit starting on the surface remains on the surface throughout its dynamical evolution. So, an invariant manifold is a set of orbits that form a surface. Invariant manifolds, in particular stable, unstable, and center manifolds, are key components in the analysis of the phase space. Bounded motions (including periodic orbits) exist in the center manifold, as well as transitions from one type of bounded motion to another. Sets of orbits that approach or depart an invariant manifold asymptotically are also invariant manifolds (under certain conditions) and these are the stable and unstable manifolds, respectively.

In the context of the three body problem, the libration points, halo orbits, and the tori on which Lissajous trajectories are confined are themselves invariant manifolds. First, consider a collinear libration point, that is, an equilibrium solution in terms of the rotating coordinates in the three-body problem. The libration point itself has a one-dimensional stable manifold, a one dimensional unstable manifold, and a four dimensional center manifold. As has been described in more detail in Ref. 7, there exist periodic and quasi-periodic motions in this center manifold. Two types of periodic motion are of interest here, i.e., the planar Lyapunov orbits as well as the nearly vertical (out of plane) orbits. The familiar periodic halo orbits result from a bifurcation along the planar family of Lyapunov orbits as the amplitude increases. Also in the center subspace are quasi-periodic solutions related to both the planar and the vertical periodic orbits. These three-dimensional, quasi-periodic solutions are those that have typically been denoted as Lissajous trajectories. Although not of interest here, a second type of quasi-periodic solution is the motion on tori that envelop the periodic halo orbits.

The periodic halo orbits, as defined in the circular restricted problem, are used as a reference solution for investigating the phase space in this analysis. It is possible to exploit the hyperbolic nature of these orbits by using the associated stable and unstable manifolds to generate transfer trajectories as well as general trajectory arcs in this region of space. (The results can also be extended to more complex dynamical models.<sup>4,8</sup>) Developing expressions for these nonlinear surfaces



is a formidable task, one that is unnecessary in the context of their role in this particular design process. Rather, the computation of the stable and unstable manifolds associated with a particular halo orbit is accomplished numerically in a straightforward manner. The procedure is based on the availability of the monodromy matrix (the variational or state transition matrix after one period of the motion) associated with the halo orbit. This matrix essentially serves to define a discrete linear map of a fixed point in some arbitrary Poincaré section. As with any discrete mapping of a fixed point, the characteristics of the local geometry of the phase space can be determined from the eigenvalues and eigenvectors of the monodromy matrix. These are characteristics not only of the fixed point, but of the halo orbit itself.

The local approximation of the stable (unstable) manifolds involves calculating the eigenvectors of the monodromy matrix that are associated with the stable (unstable) eigenvalues. This approximation can be propagated to any point along the halo orbit using the state transition matrix. Recall that the eigenvalues of a periodic halo orbit are known to be of the following form:<sup>9</sup>

$$\lambda_1 > 1, \quad \lambda_2 = (1/\lambda_1) < 1, \quad \lambda_3 = \lambda_4 = 1, \\ \lambda_5 = \lambda_6^*, \quad \text{and } |\lambda_5| = |\lambda_6| = 1,$$

where  $\lambda_5$  and  $\lambda_6$  are complex conjugates. Stable (and unstable) eigenspaces,  $E^S$  ( $E^U$ ) are spanned by the eigenvectors whose eigenvalues have modulus less than one (modulus greater than one). There exist local stable and unstable manifolds,  $W_{loc}^S$  and  $W_{loc}^U$ , tangent to the eigenspaces at the fixed point and of the same dimension.<sup>10,11</sup> Thus, for a fixed point  $\bar{X}^H$  defined along the halo orbit, the one-dimensional stable (unstable) manifold is approximated by the eigenvector associated with the eigenvalue  $\lambda_2$  ( $\lambda_1$ ). First, consider the stable manifold. Recall that a periodic orbit appears as one fixed point in a Poincaré map; thus, the halo orbit is identified as  $\bar{X}^H$  in the two dimensional representation in Figure 1. Let  $\bar{Y}^{W^S}$  denote a six-dimensional vector that is coincident with the stable eigenvector and is scaled such that the elements corresponding to position in the phase space have been normalized. This vector serves as the local approximation to the stable manifold ( $W^S$ ). Remove the fixed point  $\bar{X}^H$  from the stable manifold and there remain two half-manifolds,  $W^{S+}$  and  $W^{S-}$ . Each half-manifold is itself a manifold consisting of a single trajectory. Now, consider some point  $\bar{X}_o$  that lies exactly on  $W^{S+}$ . Integrating forward and backward in time from  $\bar{X}_o$  produces  $W^{S+}$ . Of course, the stable manifold approaches the fixed point asymptotically, so  $W^{S+}$  reaches  $\bar{X}^H$  only in infinite time. Nevertheless, conceptually, calculating a half manifold is composed of the following two steps: locating or approximating a point on  $W^{S+}$ , and numerically integrating from this point.

To numerically generate the stable manifold, an algorithm originally developed for second order systems has been employed.<sup>12</sup> The algorithm, however, does not possess any inherent limit to the

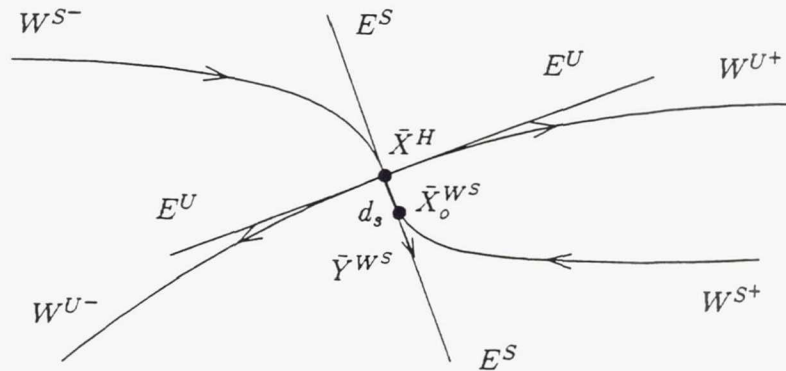


Figure 1 Stable and Unstable Manifolds Associated with a Fixed Point  $\bar{X}^H$

order of the system and has been used successfully here. Near the fixed point  $\bar{X}^H$ , the half-manifold  $W^{S+}$  is determined, to first order, by the stable eigenvector  $\bar{Y}^{W^*}$ . The next step is then to globalize the stable manifold. This can be accomplished by numerically integrating backwards in time. It also requires an initial state that is on  $W^{S+}$  but not on the halo orbit. To determine such an initial state, the position of the spacecraft is displaced from the halo in the direction of  $\bar{Y}^{W^*}$  by some distance  $d_s$  such that the new initial state, denoted as  $\bar{X}_o^{W^*}$ , is calculated as

$$\bar{X}_o^{W^*} = \bar{X}^H + d_s \bar{Y}^{W^*} \quad (1)$$

Higher order expressions for  $\bar{X}_o^{W^*}$  are available but not necessary. The magnitude of the scalar  $d_s$  should be small enough to avoid violating the linear estimate, yet not so small that the time of flight becomes too large due to the asymptotic nature of the stable manifold. This investigation is conducted with a nominal value of 200 km for  $d_s$  since this application is in the Sun-Earth system. A suitable value of  $d_s$  should be determined for each application. Note that a similar procedure can be used to approximate and generate the unstable manifold. One additional observation is notable. The stable and unstable manifolds for any fixed point along a halo orbit are one-dimensional and this fact implies that the stable/unstable manifolds for the entire halo orbit are two-dimensional. This is an important concept when considering design options.

## APPLICATION TO MISSION DESIGN

Trajectory design has traditionally been initiated with a baseline mission concept rooted in the two-body problem and conics. For libration point missions, however, a baseline concept derived from solutions to the three-body problem is required. Since no such general solution is available, the goal is to use dynamical systems theory to numerically explore the types of trajectory arcs that exist in the solution space. Then, various arcs can be "patched" together for preliminary design; the end-to-end solution is ultimately computed using a model that incorporates ephemeris data as well as other appropriate forces (e.g., solar radiation pressure).

### Force Models

The dynamical model that is adopted to represent the forces on the spacecraft includes the gravitational influences of the Sun, Moon and Earth. (Additional gravitational bodies can certainly be added. This subset, however, includes the dominant gravitational influences and is a convenient set for this discussion and demonstration.) All planetary, solar, and lunar states are obtained from the GSFC Solar Lunar and Planetary (SLP) files. The SLP files describe positions and velocities for nine solar system bodies (excluding Mercury) in the form of Chebyshev polynomial coefficients at 12 day intervals. These files are based on the Jet Propulsion Laboratory's Definitive Ephemeris (DE) 118 and 200 files.<sup>13</sup>

Solar radiation pressure is also included in the differential equations. It is modeled as follows:<sup>5,14</sup>

$$\bar{F} = \frac{F_s M}{r_{\text{sun-spacecraft}}^3} \bar{r}_{\text{sun-spacecraft}} = \left( \frac{kA}{M} \right) \cos^2(\beta) \left( \frac{S_o D_o^2}{c} \right) \frac{M}{r_{\text{sun-spacecraft}}^3} \bar{r}_{\text{sun-spacecraft}}, \quad (2)$$

where  $M$  is the spacecraft mass,  $\bar{r}_{\text{sun-spacecraft}}$  is the vector from the Sun to the spacecraft, and the scalar variable  $F_s$  is used to represent all other predetermined constants in the model. The scalar quantity  $F_s$  includes information regarding the characteristics of the spacecraft and certain physical constants. For instance, the parameter  $k$  represents the absorptivity of the spacecraft surface over the range  $0 \leq k \leq 2$ ;  $A$  is the effective cross sectional area;  $c$  is the speed of light;  $S_o$  is the solar light flux at 1 A.U. from the Sun;  $D_o$  is the nominal distance associated with  $S_o$ ; and  $\beta$  is the angle of incidence which can be calculated (for Sun radiating radially outward) as follows



$$\beta = \cos^{-1} \left( -\frac{\hat{n} \cdot \bar{r}_{\text{sun-spacecraft}}}{r_{\text{sun-spacecraft}}} \right), \quad (3)$$

where  $\hat{n}$  is the unit vector normal to the incident area. In this study, the solar radiation pressure model will be simplified by assuming that the force is always normal to the surface, i.e.,  $\beta = 0$ . In terms of the spacecraft engine, only impulsive maneuvers are considered. Of course, the analysis must be consistent across all analysis tools.

### Nominal Baseline Trajectory

Assume a mission concept that involves departure from a circular Earth parking orbit and transfer along a direct path to arrive in a halo or Lissajous trajectory associated with an  $L_1$  libration point, defined in terms of a Sun-Earth/Moon barycenter system. Thus, the baseline trajectory is composed of two segments: (a) the Earth-to-halo transfer, and (b) the Lissajous trajectory. The design strategy is based on computing the halo/Lissajous trajectory *first*, since this type of orbit enables the flow (the stable/unstable manifolds) in the region between the Earth and  $L_1$  to be represented relatively straightforwardly in configuration space using the invariant manifolds. An appropriate Lissajous orbit, i.e., one that meets the science and communications requirements, is computed using GENERATOR.<sup>1</sup> A Lissajous trajectory is quasi-periodic; however, two revolutions along the path can be assumed as a nearly periodic orbit for construction of a monodromy matrix. The transfer design process then consists of identifying the subspace (or surface) that flows from the vicinity of the Earth to the Lissajous trajectory by computation of the associated stable manifold. Using the stable manifold to construct the transfer trajectory from Earth implies an asymptotic approach to the "periodic" orbit and, even in actual practice, may result in no insertion maneuver. So, rather than a targeting problem to reach a specified insertion point on the halo orbit, the transfer design problem becomes one of insertion onto the stable manifold, directly from an Earth parking orbit, if possible. The flight time along such a path is actually very reasonable.

Unfortunately, not every halo/Lissajous orbit possesses stable manifolds that pass at the precise altitude of a specified Earth parking orbit. However, the stable/unstable manifolds control the behavior of all nearby solutions in this region of the phase space. Thus, the behavior of the manifolds provides insight into optimal transfers and serves as an excellent first approximation in a differential corrections scheme.<sup>3</sup> Of course, altitude is not the only launch constraint. Once an appropriate initial transfer path is available, a series of patch points ("control points") are automatically inserted. A two-level iteration scheme then shifts positions and times to satisfy constraints on launch altitude, launch date, and launch inclination as well as placement of the transfer trajectory insertion point as close to perigee as possible.<sup>15</sup> Note that this process for computation of the transfer leaves the Lissajous trajectory intact. This is extremely difficult to accomplish solely in SWINGBY (as it is currently structured).

After the transfer is produced, it is successfully transferred to SWINGBY. Note that, in this process, the transfer path emerges without a random search. Thus, this critical initial approximation is extremely important for the design of more complex missions (that might include phasing loops and/or gravity assists), since transferring to the nominal Lissajous orbit is, in general, a challenge for the trajectory analysts.<sup>16</sup> Once a suitable trajectory associated with a particular Lissajous trajectory is identified, SWINGBY can be further utilized for final adjustments, maneuver error analysis, and exploration of changes in the mission specifications. Understanding both the traditional design methodology and invariant manifold theory demonstrates that a tool that integrates manifold theory into the mission design process is very beneficial. Furthermore, like SWINGBY, this tool must possess an excellent graphical user interface.

## Implementation Issues

For comparison and data exchange between GENERATOR and SWINGBY, it is imperative that a consistent match exists in the following aspects: Coordinate Systems, Time Standards, and Integrators. To accomplish this task, SWINGBY is assumed as the reference and GENERATOR is modified to meet the conditions in the reference as closely as possible.

*Coordinate Systems.* To perform the integrations, the geocentric inertial (GCI) frame is used. This frame is defined with an origin at the Earth's center and an equatorial reference plane. For visualization, the Sun-Earth Rotating (SER) and the Rotating Libration Point (RLP) frames also prove to be invaluable. The SER frame uses an origin at the Earth and an ecliptic reference plane. The RLP frame also defines an origin at the moving libration point ( $L_1$  or  $L_2$ ) and, like the SER frame, uses an ecliptic reference plane.

*Time Standards.* Julian days, in atomic time standard, are assumed to advance the integration. The Julian Date system numbers days continuously, without division of years and months.<sup>17</sup> The atomic time standard is defined in terms of the oscillations of the cesium atom at mean sea level.<sup>5</sup>

*Integrators.* For the numerical integration scheme, a Runge-Kutta-Verner 8(9) integrator is incorporated. This Runge-Kutta integrator is, of course, based on the Verner methodology.<sup>18</sup> The Verner formulas provide an estimate of the local truncation errors that allow the development of an adaptive step size control scheme.<sup>5</sup> It is important to note that, when performing differential corrections, GENERATOR also integrates the 36 first order scalar differential equations from the state transition matrix that is associated with the equations of motion governing the position and velocity states. As a result, a total of 42 equations are simultaneously integrated. Therefore, for adequate error control, the scaling of the variables is very important.

## EXAMPLES

Given sets of mission specifications, two sample trajectories are computed below. The blended procedure is employed to demonstrate its implementation. The results can be compared to known solutions, if available. For the following examples, it is assumed that communication requirements impose minimum and maximum angles of 3 and 32 degrees, respectively, between the Sun/Earth line and the Earth-Vehicle vector (SEV angle) during the transfer from the Earth parking orbit to the vicinity of the libration point. The parking orbit is specified as circular with a 28.5 degree inclination (Earth equatorial) and an altitude of 185 km. (Deep Space Network coverage and shadowing/eclipse constraints will not be considered at this time.)

### SOHO Mission

On December 2, 1995, the Solar Heliospheric Observatory (SOHO) spacecraft was launched. Built by the European Space Agency to study the Sun, SOHO is part of the International Solar-Terrestrial Physics (ISTP) program.<sup>19</sup> To meet the science requirements, SOHO requires an uninterrupted view of the Sun and the minimization of the background noise due to particle flux. A halo/Lissajous orbit similar to the libration point ( $L_1$ ) orbit utilized for the ISEE-3 mission<sup>20</sup> is assumed. The science and communications requirements generate the following Lissajous amplitude constraints:  $A_x = 206,448$  km,  $A_y = 666,672$  km, and  $A_z = 120,000$  km. A Class I (northern) Lissajous, obtained<sup>1</sup> numerically with the appropriate amplitude characteristics, appears in Figure 2.

Given this Lissajous orbit, a transfer trajectory is sought. Initially, a limited set of points is selected along some specified part of the Lissajous trajectory; this specific region along the orbit in Figure 2 is identified as all the points in the shorter arc defined by the symbols "x". It is already known that the manifolds associated with these points will pass close to the Earth. This particular region along the nominal path is designated as the "Earth Access region".<sup>3,9</sup> Each point in the



Earth Access region can be defined as a fixed point  $\bar{X}^H$  and the corresponding one-dimensional stable manifold globalized. Together, these one-dimensional manifolds form a two-dimensional surface associated with this region of the nominal orbit. The projection of this surface onto configuration space appears in Figure 3. (Note that the manifolds in Figure 3 pass closest to the Earth as compared to those associated with any other region along the nominal orbit; altitude is the only characteristic used in determining this region.) From this invariant subspace, the one trajectory that passes closest to the Earth is selected as the initial guess for the transfer path. Some of the notable characteristics of this approximation are listed in Table 1 and a plot appears in Figure 4. Note in Figure 4 that the constraint on the SEV angle is met.

Given the initial guess and utilizing continuation, the transfer is differentially corrected to meet the requirements on the other constraints. This correction process can occur in GENERATOR or SWINGBY, although the methodology differs between the two algorithms; numerical data corresponding to the final solution that appears in Table 1 is from GENERATOR. (A plot of the final solution is indistinguishable from Figure 4.) Although there is no guarantee that this result represents an optimal solution, all constraints have been met and the solution process is automated. This transfer compares most favorably with the transfer solution actually used by SOHO. From this point, the solution is input directly into SWINGBY and appears in Figure 5. SWINGBY can now be used for further analysis including visualization, launch and maneuver error investigations, as well as midcourse corrections. Data can still be exchanged and new transfers computed as needed.

Table 1  
SOHO EXAMPLE: TRANSFER TRAJECTORY DESIGN

Initial Approximation	
Transfer Trajectory Insertion Date	12/03/95
Closest Approach (Altitude)	5,311 km
Inclination	15.58 degrees
Final Transfer Trajectory	
Transfer Trajectory Insertion Date	12/02/95
Closest Approach (Altitude)	185 km
Inclination	28.5 degrees
Ascending Node	292.63 degrees
Argument of Perigee	145.77 degrees
Transfer Insertion Cost	3193.9 m/s
Lissajous Insertion Cost	33.8 m/s
Time of Flight <sup>a</sup>	204.7 days

<sup>a</sup>The time of flight is calculated as follows: from transfer trajectory insertion until the point along the path such that the vehicle is within 200 km of the nominal Lissajous. This point is indicated in Figure 4 with a symbol '\*\*'.

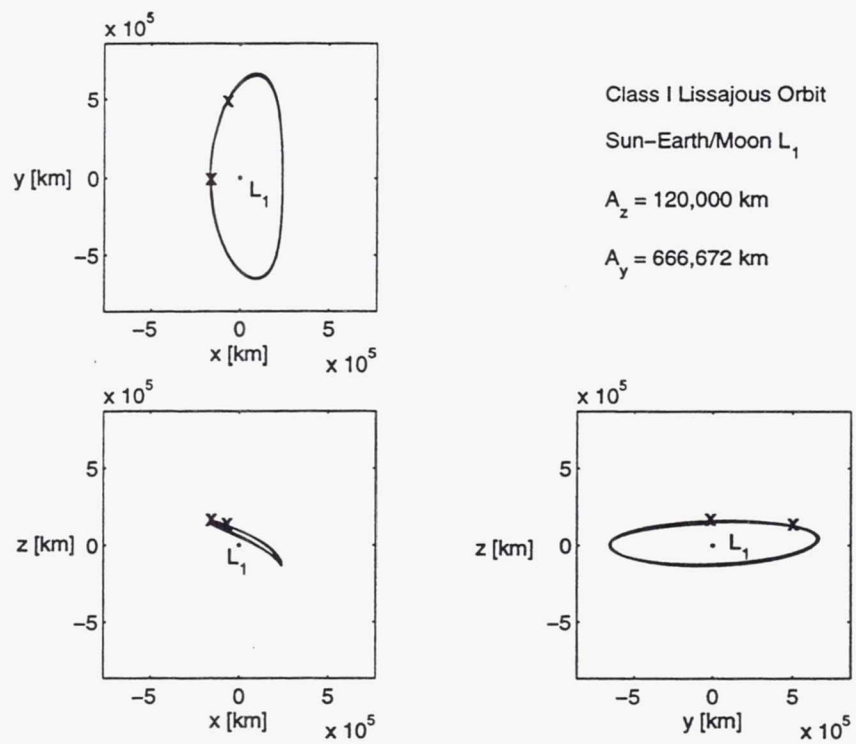


Figure 2 SOHO Example: Nominal Lissajous

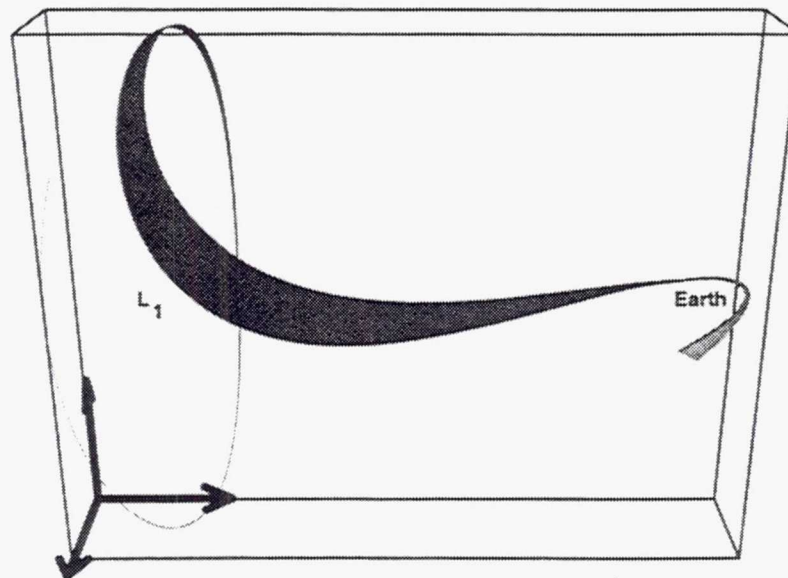


Figure 3 SOHO Example: Manifold Surface Section



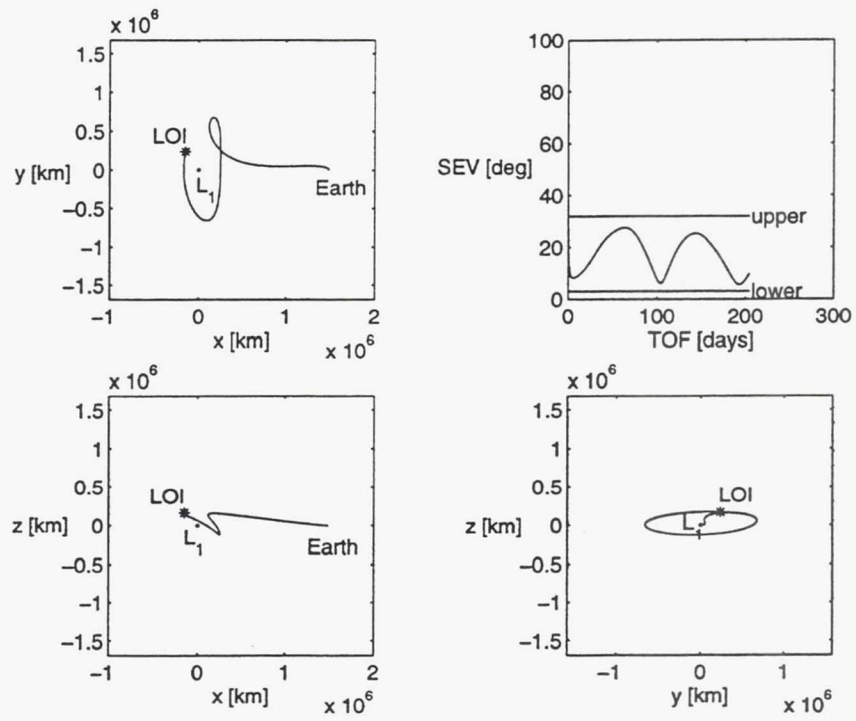


Figure 4 SOHO Example: Initial Approximation

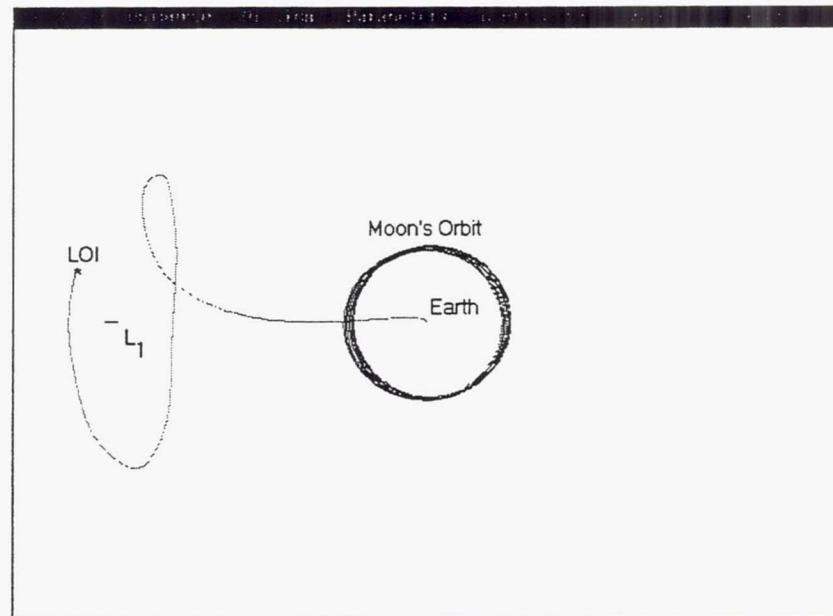


Figure 5 SOHO Example: SWINGBY

## NGST Mission

The Next Generation Space Telescope (NGST),<sup>21</sup> part of the NASA Origins Program, is designed to be the successor to the Hubble Space Telescope. Since for NGST the majority of the observations by the instruments aboard the spacecraft will be in the infrared part of the spectrum, it is important that the telescope be kept at low temperatures. To accomplish this, an orbit far from Earth and its reflected sunlight is desirable. There are several orbits that are satisfactory from a thermal point of view, and, in this study, an orbit in the vicinity of the  $L_2$  point is considered. Based on this information, the following Lissajous amplitudes<sup>21</sup> are incorporated:  $A_x = 294,224$  km,  $A_y = 800,000$  km, and  $A_z = 131,000$  km. A Class I (northern) Lissajous, obtained numerically, with the appropriate amplitude characteristics appears in Figure 6; note that the trajectory is 2.36 years in duration.

Again, given this Lissajous orbit, a transfer trajectory is sought. Using invariant manifold theory, several transfer paths can be computed; a surface is projected onto configuration space and the three-dimensional plot appears in Figure 7. Again, this particular section of the surface is associated with the "Earth Access region" along the  $L_2$  libration point orbit.<sup>4,9</sup> An interesting observation is apparent as motion proceeds along the center of the surface. The smoothness of the surface is interrupted because a few of the trajectories pass close to the Moon upon Earth departure. Lunar gravity was not incorporated into the approximation for the manifolds; but no special consideration was involved to avoid the Moon either. This information concerning the lunar influence can probably be exploited with further development of the methodology. From information available in Figure 7, the one trajectory that passes closest to the Earth is identified and used as the initial guess for the transfer path. Some of the notable characteristics of this approximation are listed in Table 2 and a plot appears in Figure 8.

**Table 2**  
**NGST EXAMPLE: TRANSFER TRAJECTORY DESIGN**

Initial Approximation	
Transfer Trajectory Insertion Date	09/30/2007
Closest Approach (altitude)	-2,520.6 km
Inclination	30.1 degrees
Final Transfer Trajectory	
Transfer Trajectory Insertion Date	10/01/2007
Closest Approach (altitude)	185 km
Inclination	28.5 degrees
Ascending Node	342.65 degrees
Argument of Perigee	210.74 degrees
Transfer Insertion Cost	3195.1 m/s
Lissajous Insertion Cost	15.4 m/s
Time of Flight <sup>b</sup>	210.8 days

<sup>b</sup>The time of flight is calculated as follows: from transfer trajectory insertion until the point along the path such that the vehicle is within 200 km of the nominal Lissajous. This point is indicated in Figure 8 with a symbol '\*'. \*



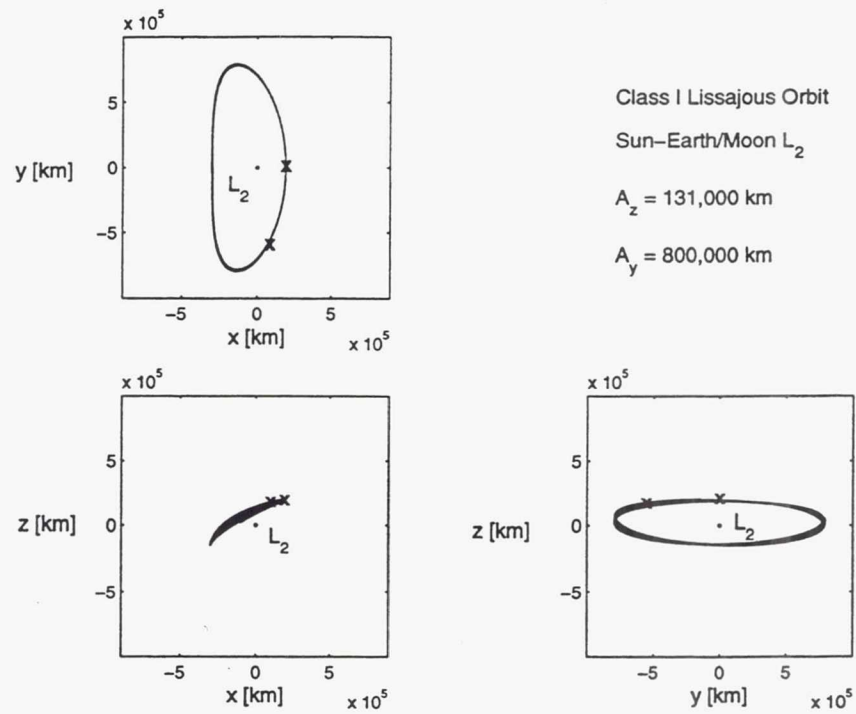


Figure 6 NGST Example: Nominal Lissajous

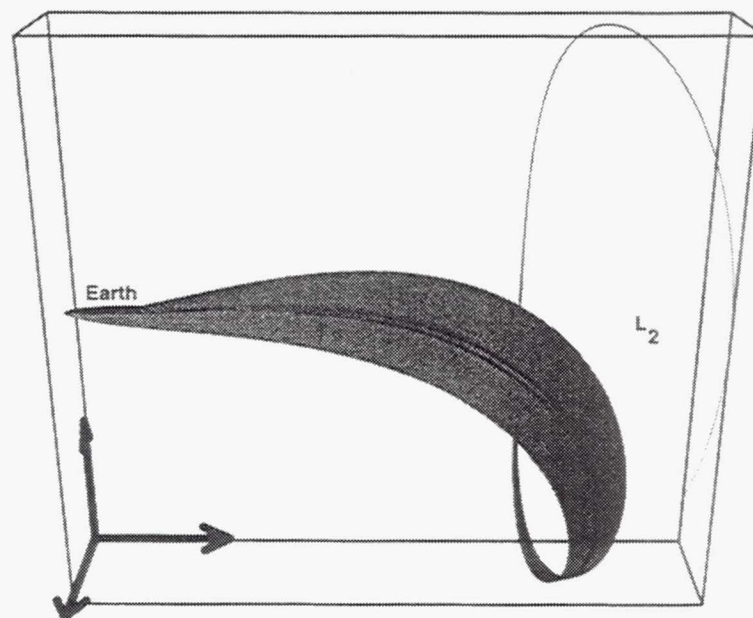


Figure 7 NGST Example: Manifold Surface Section

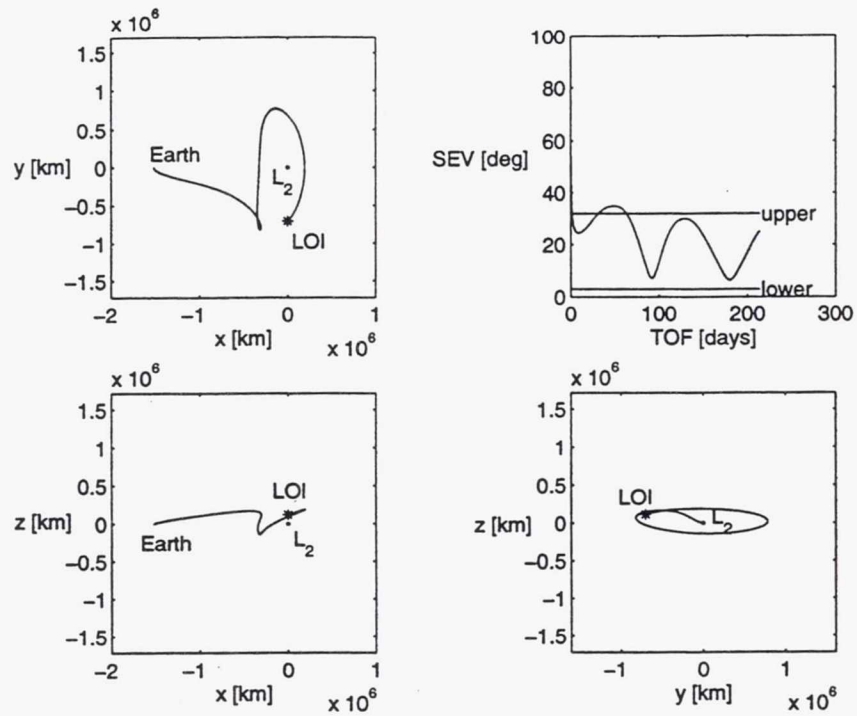


Figure 8 NGST Example: Initial Approximation

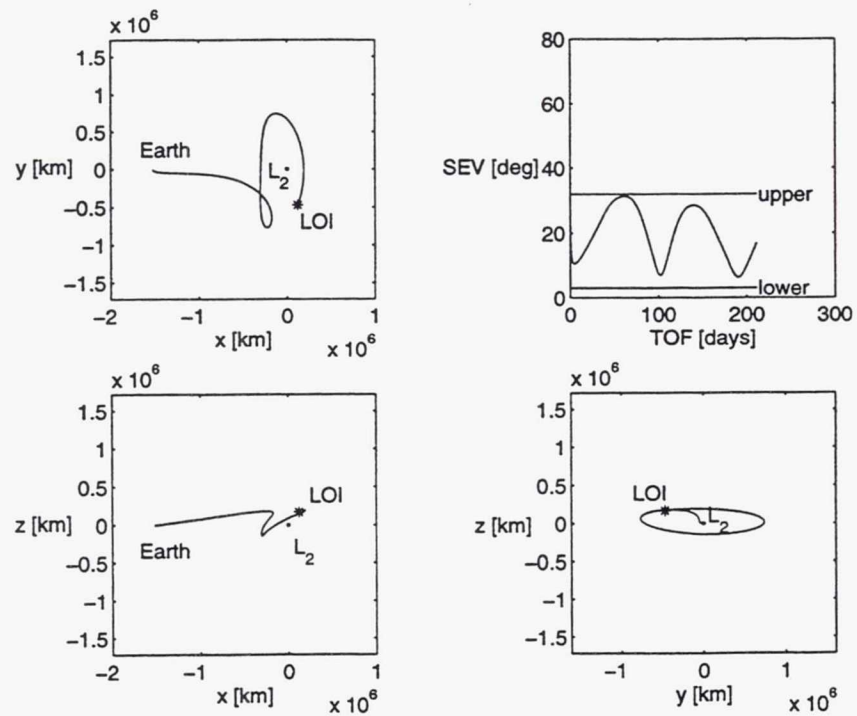
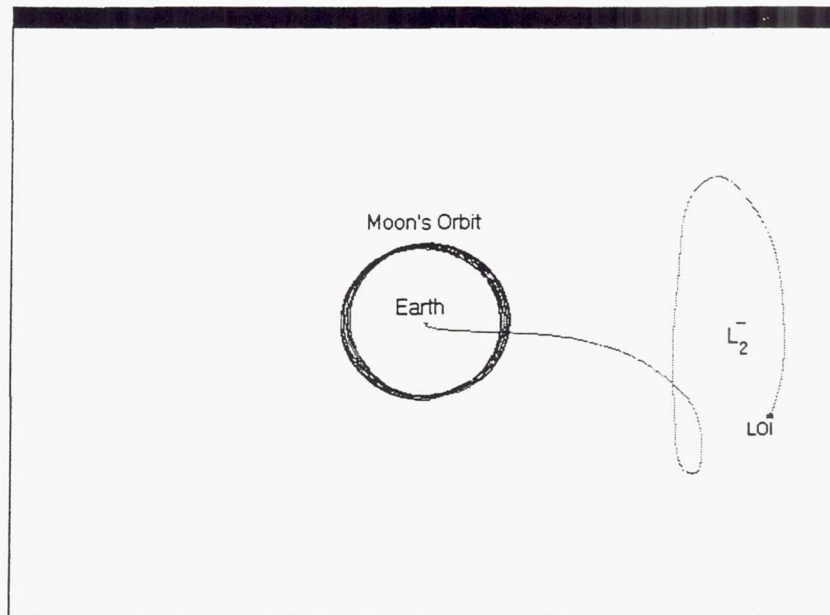


Figure 9 NGST Example: Final Trajectory





**Figure 10 NGST Example: SWINGBY**

Note from Table 2 that this particular approximation passes below the Earth's surface. The larger size of this Lissajous orbit, as compared to the SOHO example, reduces the Earth passage distance. Furthermore, note in Figure 8 that the constraint on the SEV angle is not met. Given the initial guess, the transfer is differentially corrected to meet the requirements on all the constraints except the SEV angle. In this case, after this process, the SEV constraint is met. The SEV constraint could certainly be added to the differential correction process, although it has not yet been incorporated. The final solution as seen in Figure 9 is from GENERATOR. From this point, the solution is input directly into SWINGBY and appears in Figure 10. Similar to the previous example, SWINGBY can now be used for further visualization, analysis of launch and maneuver errors, midcourse corrections, and other investigations.

## CONCLUDING REMARKS

The primary goal of this effort is the blending of analysis from dynamical systems theory with the well established NASA Goddard software program SWINGBY to enhance and expand the capabilities for mission design. Dynamical systems theory provides a qualitative and quantitative understanding of the phase space that facilitates the mission design. SWINGBY can then utilize this information to visualize and complete the end-to-end mission analysis. Combination of these two tools proves to be an important step towards the next generation of mission design software.

## ACKNOWLEDGMENTS

This work was supported by a NASA Goddard GSRP fellowship (NGT 528). Parts of the research were carried out at both Goddard Space Flight Center and Purdue University.

## REFERENCES

1. K. C. Howell and H. J. Pernicka, "Numerical Determination of Lissajous Trajectories in the Restricted Three Body Problem," *Celestial Mechanics*, Vol. 41, 1988, pp. 107-124.

2. G. Gómez, A. Jorba, J. Masdemont, and C. Simó, "Study of the Transfer from the Earth to a Halo Orbit Around the Equilibrium Point  $L_1$ ," *Celestial Mechanics and Dynamical Astronomy*, Vol. 56, No. 4, 1993, pp. 541-562.
3. K. C. Howell, D. L. Mains, and B. T. Barden, "Transfer Trajectories from Earth Parking Orbits to Sun-Earth Halo Orbits," *AAS/AIAA Spaceflight Mechanics Meeting*, Cocoa Beach, Florida, February 1994. AAS Paper 94-160.
4. K. C. Howell, B. T. Barden, and M. W. Lo, "Application of Dynamical Systems Theory to Trajectory Design for a Libration Point Mission," *Journal of the Astronautical Sciences*, Vol. 45, No. 2, 1997, pp. 161-178.
5. D. McGiffin and C. Roberts, *Mission Analysis and Design Tool (SWINGBY) Mathematical Principles*. Goddard Space Flight Center, Greenbelt, Maryland, September 1995. Revision 1.
6. J. Carrico, D. Conway, D. Ginn, D. Folta, and K. Richon, "Operational Use of SWINGBY-an Interactive Trajectory Design and Maneuver Planning Tool-for Missions to the Moon and Beyond," *AAS/AIAA Astrodynamics Specialists Conference*, Halifax, Nova Scotia, Canada, August 1995. AAS 95-323.
7. B. T. Barden and K. C. Howell, "Formation Flying in the Vicinity of Libration Point Orbits," *AAS/AIAA Spaceflight Mechanics Meeting*, Monterey, California, February 1998. AAS Paper 98-169.
8. K. C. Howell, B. T. Barden, R. S. Wilson, and M. W. Lo, "Trajectory Design Using a Dynamical Systems Approach with Application to GENESIS," *AAS/AIAA Astrodynamics Specialists Conference*, Sun Valley, Idaho, August 4-7 1997. AAS Paper 97-709.
9. B. T. Barden, "Using Stable Manifolds to Generate Transfers in the Circular Restricted Problem of Three Bodies," M.S. Thesis, Purdue University, West Lafayette, Indiana, December 1994.
10. J. Guckenheimer and P. Holmes, *NonLinear Oscillations, Dynamical Systems, and Bifurcations of Vector Fields*. New York: Springer-Verlag, 1983.
11. S. Wiggins, *Introduction to Applied Nonlinear Dynamical Systems and Chaos*. New York: Springer-Verlag, 1990.
12. T. S. Parker and L. O. Chua, *Practical Numerical Algorithms for Chaotic Systems*. New York: Springer-Verlag, 1989.
13. "Solar, Lunar and Planetary (SLP) Files," <http://fdd.gsfc.nasa.gov/SLP.html>. Goddard Space Flight Center.
14. K. C. Howell and J. L. Bell, "Solar Radiation Pressure and Sun-Earth  $L_1$  Libration Point Orbits," School of Aeronautics and Astronautics, Purdue University, Technical Report, West Lafayette, Indiana, 1992.
15. K. C. Howell and R. S. Wilson, "Trajectory Design in the Sun-Earth-Moon System Using Multiple Lunar Gravity Assists," *AAS/AIAA Astrodynamics Specialists Conference*, San Diego, California, pp. 630-640, July 1996. AIAA Paper 96-3642.
16. K. Richon and M. Mathews, "An Overview of the MAP Trajectory Design," *AAS/AIAA Astrodynamics Specialists Conference*, Sun Valley, Idaho, August 1997. AAS Paper 97-728.
17. *Cambridge Astronomy Dictionary*. New York, New York: Cambridge University Press, 1996.
18. J. H. Verner, "Explicit Runge-Kutta Methods with Estimates of the Local Truncation Error," *Society for Industrial and Applied Mathematics (SIAM) Journal of Numerical Analysis*, Vol. 15, August 1978, pp. 772-790.



19. S. Stalos, D. Folta, B. Short, J. Jen, and A. Seacord, "Optimum Transfer to a Large Amplitude Halo Orbit for the Solar and Heliospheric Observatory (SOHO) Spacecraft," *AAS/GSFC International Symposium on Space Flight Dynamics*, Greenbelt, Maryland, April 1993. AAS Paper 93-553.
20. R. W. Farquhar, D. P. Muhonen, C. R. Newman, and H. S. Heuberger, "Trajectories and Orbital Maneuvers for the First Libration-Point Satellite," *Journal of Guidance and Control*, Vol. 3, No. 6, 1980, pp. 549-554.
21. "NGST Homepage," <http://ngst.gsfc.nasa.gov/>. Goddard Space Flight Center.

**Page intentionally left blank**



## LONG-TERM EVOLUTION IN THE VICINITY OF GEOSTATIONARY ORBIT

M. Deleuze <sup>†</sup>

In the frame of the studies relative to end-of-life orbits of geostationary satellites, an analysis of the long-term perturbations in the vicinity of geostationary orbit has been performed.

The purpose of this paper is to present the long-term evolution of the semi-major axis and of the eccentricity for a classical end-of-life orbit in order to estimate the potential decreasing of the perigee altitude.

The final result of the study permits to have an idea on the minimal initial perigee altitude of end-of-life orbits insuring to remain above the geosynchronous region.

The study has been led using a prediction software based on a semi analytical theory for geosynchronous mean elements.

Each perturbation has been first analysed separately, and second all together in order to take into account the coupling between the periodic terms.

Thus, a long periodic term of 53 years (due to coupling between gravitational and non-gravitational forces) has been identified for the eccentricity.

### INTRODUCTION

Since the middle nineties, CNES (Centre National d'Etudes Spatiales), the french Space Agency, has been involved in the activities concerning the orbital debris in the framework of IADC (Inter Agencies Debris Committee). The mainly preoccupation of this committee is to make people aware of the probability of collision between space debris and satellites (geostationary as well as low earth orbits) and to elaborate some preventive recommendations.

Relative to geosynchronous satellites, two different collision types may happen :

- with low earth orbit debris during the first phases of launches,
- with non active geosynchronous satellites.

The present paper only deals with the second point. In this context, after a short consideration of geostationary orbit management, the purpose of this paper is to characterize an end-of-life region which insures no interaction with the active geosynchronous zone.

In that way, taking into account the natural perturbations acting on the geostationary orbit, the long term evolution of abandoned satellites has been investigated.

The study has first considered the evolution outside the orbital plan (long term evolution of the inclination) and second, inside the plan (long term evolution of the semi-major axis and eccentricity). For this last point, perturbations have been analysed first separately and second all together to take into account the coupling between the periodic terms.

The final result of this study is to define a "burial" region (based on a minimal perigee altitude) for end-of-life orbits insuring to remain above the geosynchronous area.

<sup>†</sup> Centre National d'Etudes Spatiales - DGA/T/TL/MS/SG - 18 avenue Edouard Belin 31401 Toulouse Cedex 4 FRANCE

# GEOSTATIONARY ORBIT MANAGEMENT

## The Station Keeping Ring

Today, there is no official boundaries for a "station keeping geostationary ring". There is only a current practice of  $\pm 0.1^\circ$  around the station keeping longitude. However, not all active satellites conform to this definition. Some missions (whithout inclination control for example) may enjoy larger limits.

Nevertheless, based upon this current station keeping practice of  $\pm 0.1^\circ$ , the geostationary ring may be taken to be an equatorial annulus with a radial width of  $\pm 37.5$  km around the geostationary altitude (35787 km) and  $\pm 75$  km in the north-south direction.

There is also a need to define the corridor for on-orbit shift of satellites or station acquisition. That will be defined in the next paragraph.

## The drift orbit corridor

This corridor will be mainly used in the following conditions :

- at the end of LEOP (Low Earth Orbit Procedures) to put the satellite into its final station keeping longitude (when it is different than the IOT - In Orbit Test - one),
- for on-orbit shift of satellites when a new generation replaces the old one.

The principle of on-orbit shifts is to increase (respectively to decrease) the semi-major axis of the geosynchronous orbit with an acceleration (resp. deceleration) maneuver in order to create a drift into the west (resp. the east) direction for a terrestrial observer.

As for the station keeping geostationary ring, there is no official boundary for the drift corridor but the following conventional figures :

$$37.5 \text{ km} < |a_d - a_s| < 200 \text{ km}$$

- with
- $a_d$  is the semi-major axis of the drift orbit,
  - $a_s = 42165$  km is the geosynchronous semi-major axis.

These values correspond to the following minimal and maximal drifts :  $d_{\min} = 0.48^\circ/\text{day}$  and  $d_{\max} = 2.57^\circ/\text{day}$ .

These regions around the geosynchronous arc may be drawn in the orbital plan as follows :

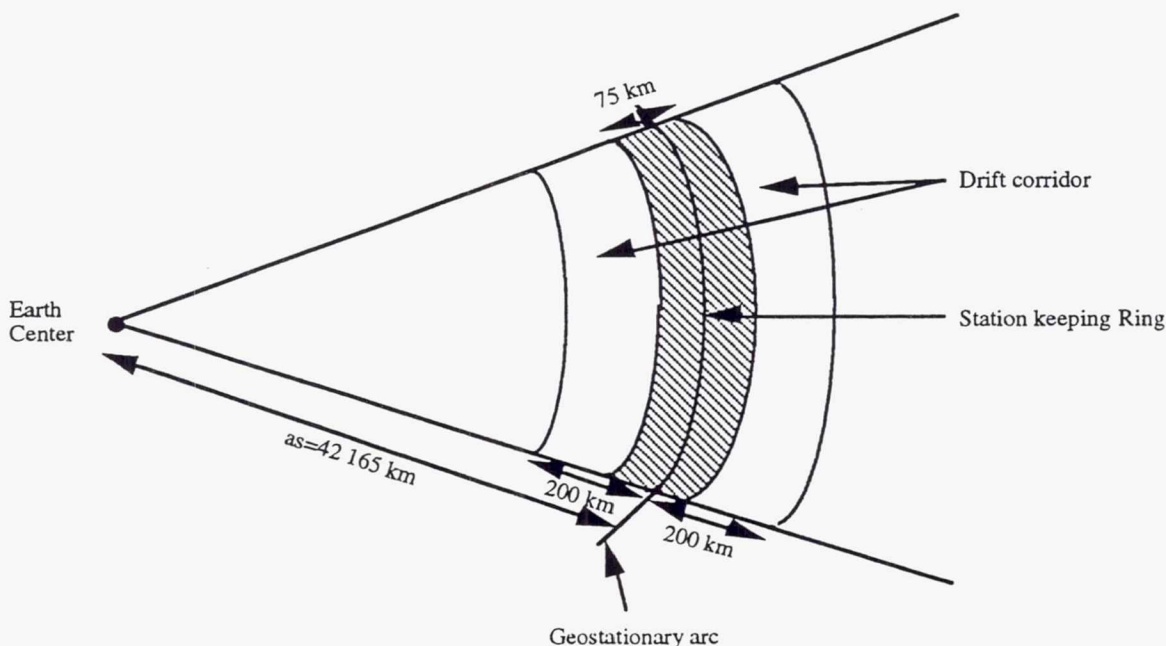


Figure 1

Station keeping and on-orbit shift areas around  $a_s$



## LONG-TERM EVOLUTION OUTSIDE THE ORBITAL PLAN

Due to the luni-solar perturbation, the orbital inclination varies cyclically with an amplitude of about  $15^\circ$  over a period of about 52.5 years<sup>1</sup>. The annual maximum amplitude of this variation is of 0.75 to 0.95°/year. This well-known phenomenon is ruled in classical station keeping strategy by north-south maneuvers.

Consequently, geostationary satellites remaining in the station keeping ring (indeed with inclination lower  $0.1^\circ$ ) will be naturally separated from end-of-life satellites. In other words, whatever end-of-life orbits we take, they only will cross the geostationary station keeping ring twice a day.

However, in order to define dimensional values for collision risks, but also since the end-of-life orbits inclination plan takes cyclically (once every 52.5 years) a zero inclination value, we will only characterize the "burial" region with a minimal perigee altitude. As a consequence, we forget the inclination separation and reduce the three-dimensional problem to a bi-dimensional one in the orbital plan. Nevertheless, we must keep in mind that this separation decreases drastically the collision risks.

## LONG-TERM EVOLUTION IN THE ORBITAL PLAN

### Outline of the study

We now only consider the variation of the perigee altitude.

There is two parameters which may influence the perigee altitude ( $R_p$ ): the semi-major axis ( $a$ ) and the eccentricity ( $e$ ). The variation of perigee altitude ( $\delta R_p$ ) is related to the variation of these two parameters ( $\delta a$  and  $\delta e$ ) by the following equation :

$$\text{since} \quad R_p = a(1 - e) \quad (1)$$

$$\text{we will have} \quad \delta R_p = |\delta a|(1 - e) + a|\delta e| \quad (2)$$

We are going to study the long-term behaviour of the semi-major axis and of the eccentricity in order to estimate  $\delta a_{\max}$  and  $\delta e_{\max}$ . The combination of these two results with equation (2) will permit to calculate  $\delta R_{p_{\max}}$  and draw a conclusion about the minimum perigee altitude which permits to remain above the geostationary drift corridor.

All the long-term evolutions have been performed with a prediction software<sup>2</sup> based upon a semi analytical theory for geosynchronous mean elements. This software has two limitations :

- the inclination is supposed to be low and is only developed until order 2,
- the solar radiation pressure is supposed to be constant.

That could lead to long term perturbations. However, all the behaviours we have observed have been validated on many cases and cross-coupled (for the periodic phenomena) with equations. They are not simple artefacts of the software.

### The evolution of the semi-major axis and mean longitude

The evolution of the semi-major axis ( $a$ ) and of mean longitude ( $l_m$ ) presents a closed dependance. In consequence, we study the behaviour of " $a$ " versus " $l_m$ ".

Taking into account only long-term perturbations (more than one month), both parameters are only affected by the tesseral terms of the terrestrial potential. Short periodic terms induced by the luni-solar perturbation have been quickly analysed and show a very low - less than one kilometer - amplitude<sup>1</sup>. At the accuracy level of our study, they can be neglected.

When a satellite is abandoned at its station keeping position ( $a_{ini}$  closed to the geosynchronous semi-major axis  $a_s$ ), it will follow a oscillation called libration which consists in moving alternatively towards the east or west around the nearest stable point (within one of the two points located at  $76^\circ$  E and  $258^\circ$  E). In other words, the satellite is pushed by the instable point (within  $11^\circ$  W and  $164^\circ$  W) towards the stable point from which it has come.

Such motion is shown in the following figure ( $\Delta l = l_m - l_{stable}$ ,  $\Delta a = a - a_s$ ) :

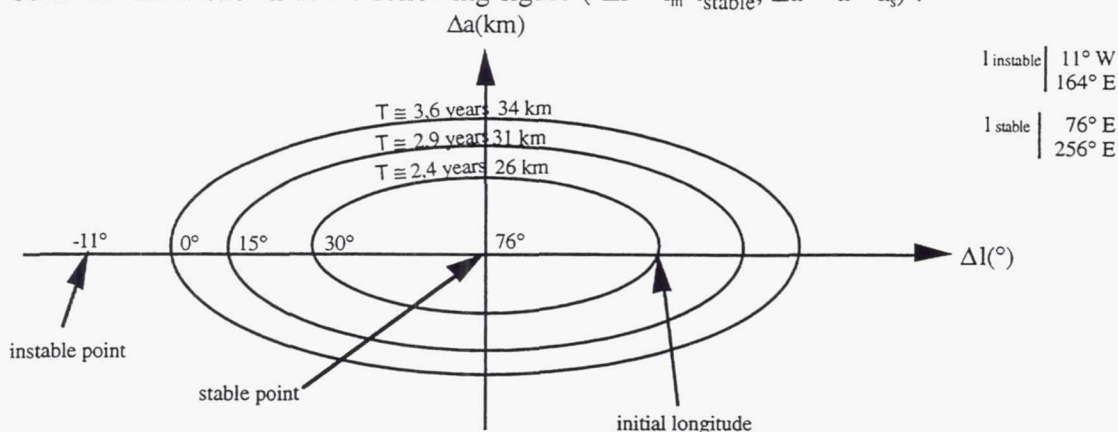


**Figure 2** Semi major-axis versus mean longitude for low  $\Delta a_{ini}$  values

The period of this oscillation depends on the length of the followed way and consequently of the initial longitude. For three longitudes, the results are gathered in the following table :

**Table 1**  
SEMI-MAJOR AXIS EXCURSION AROUND  $a_s$

Initial Longitude ( $^\circ$ )	Period (years)	$\Delta a_{max}$ (km)
0	3.6	34
15	2.9	31
30	2.4	26

If we choose an initial longitude very close from an instable point, the motion is slowed but the maximum semi-major axis variation amplitude remains in all cases lower than 35 km.

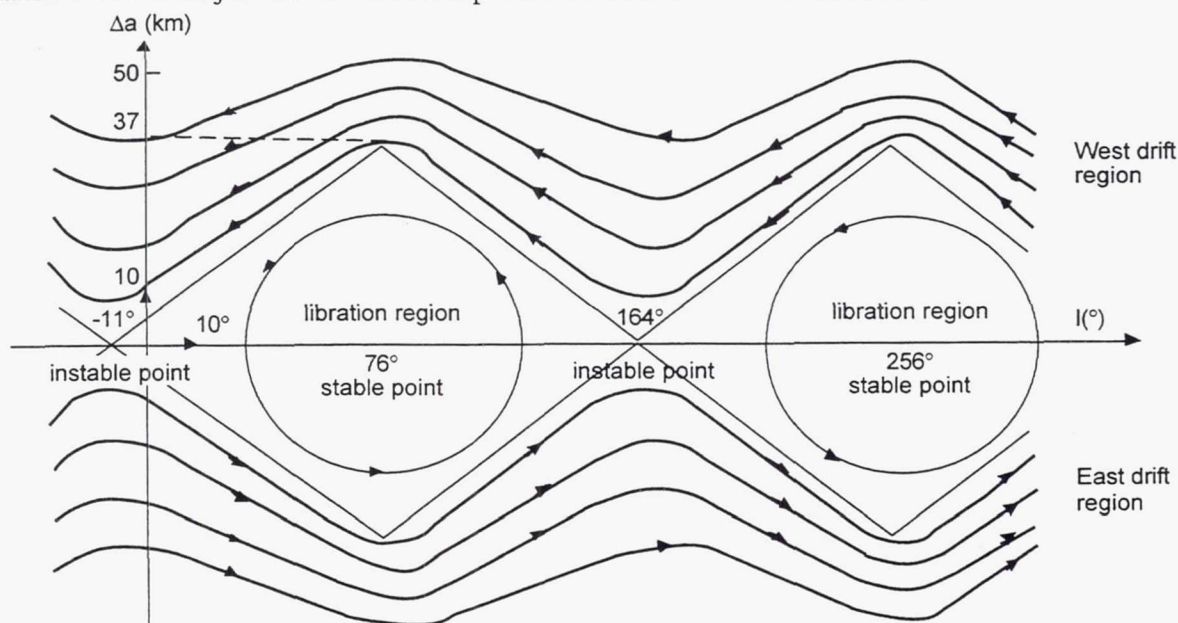


**Figure 3** Semi major-axis versus mean longitude behaviour for high  $\Delta a_{ini}$  values



On the contrary, when a satellite is abandoned with a sufficient  $\Delta a_{ini}$  value, it will only move towards the east or the west as shown above in figure 3.

In the drift regions, the semi-major axis has an oscillation motion of variable amplitude with maxima above stable points and minima above instable points.

Based upon simulations, we have evaluated some  $\Delta a_{min}$  and  $\Delta a_{max}$  and determined the minimum  $\Delta a$  which, for any initial longitude, permits to remain in a drift region and escaping from libration areas. We find a value of 37 km. The results of the simulations are gathered below :

**Table 2**  
**SEMI-MAJOR AXIS EXCURSION BETWEEN  $\Delta a_{Min}$  AND  $\Delta a_{Max}$**

$\Delta a_{max}$ (km)	$\Delta a_{min}$ (km)	$\Delta a_{max} - \Delta a_{min}$ (km)
37	7	30
40	16	24
45	26	19
50	34	16
100	93	7
150	145	5
200	197	3
250	247.3	2.7

$\Delta a_{max}$  value is obtained at 76°E  
 $\Delta a_{min}$  value is obtained at 164°E

The amplitude of the oscillation decreases when we go away from the geosynchronous arc.

The "burial" region we tend to define will be located beyond the on-orbit shifts corridor indeed more than 150 to 200 km above  $a_s$ . Under these conditions, the maximum variation of the semi-major axis can be now evaluated and gives :

$$\delta a_{max} = 5 \text{ km.}$$

## The evolution of the eccentricity

### Solar Radiation pressure perturbation

Under the solar radiation pressure effect, the mainly evolution of the eccentricity is a periodic motion of one year period and  $R_e$  amplitude<sup>1</sup> with :

$$R_e = 1.115 \cdot 10^{-2} \frac{C_p S}{m} \quad (3)$$

where  $C_p$  is the reflectivity coefficient ( $1 < C_p < 2$ ),  
 $S$  is the efficient satellite surface in the sun direction (in  $m^2$ ),  
 $m$  is the satellite mass in kg.

In the classical eccentricity plan ( $e_x = e \cos(\omega + \Omega)$ ,  $e_y = e \sin(\omega + \Omega)$ ), the end of the eccentricity vector traces a circle over the period of a year with center C (depending on the satellite initial position and sun direction) and radius  $R_e$  (depending on the characteristics of the satellite as demonstrated by (3)).

$\bar{e}_0$  represents the initial eccentricity of the orbit,  
 $\lambda_0$  the initial mean longitude of the sun.

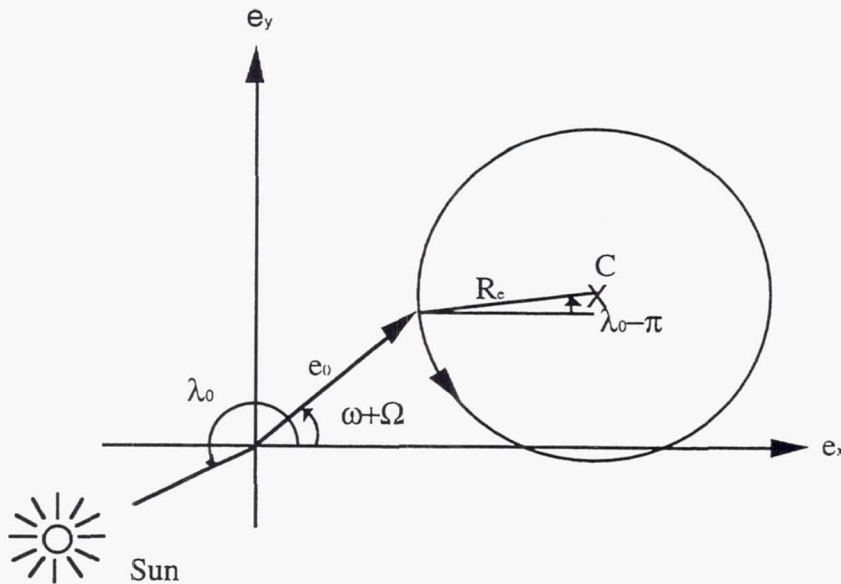


**Figure 4 Evolution of the eccentricity under solar radiation pressure perturbation**

If we consider the dimensioning case ( $\vec{e}_0$  and sun direction in opposite direction), we have an estimation of the maximum variation of eccentricity under solar radiation pressure effect with :

$$\delta e_{\max} = 2 R_e \quad (4)$$

then

$$\delta R_{p\max} = 2 a R_e \quad (5)$$

To have a numerical estimation of  $\delta R_{p\max}$ , we need to make some hypothesis on the maximum  $C_p S/m$  values. We have considered that current values for three axis stabilized satellites are situated around 0.04 and always lower than 0.05 which yields :

$$\begin{aligned} \delta e_{\max} &\approx 11.15 \cdot 10^{-4} \\ \text{and} \quad \delta R_{p\max} &\approx 47 \text{ km} \end{aligned}$$

#### Comments :

1. Relative to end-of-life satellites, a  $C_p S/m$  value of 0.035 would be more realistic (and would give a  $\delta R_{p\max}$  of 33 km). Consequently, 47 km is actually a pessimistic value.

2. The dimensioning case ( $\vec{e}_0$  and sun direction in opposite direction) happens when there is alignment between the initial apogee of end-of-life orbits and the sun. In other words, if we want to prevent of it, we can choose judicious re-orbiting maneuver hours in order to align, for example, the perigee with the sun.

### Luni-solar and earth gravitational potential perturbations

As for the the semi-major axis study, only long periodic terms will be completely examined. A quick evaluation of short-term ones<sup>1</sup> (less than one month) demonstrates that their amplitudes are lower than  $5 \cdot 10^{-5}$ . Nevertheless, they will be considered in our final estimation of  $\delta R_{p\max}$  with a 50% error margin (leading to a value of  $0.75 \cdot 10^{-4}$ ).

Considering the both perturbations (luni-solar and earth gravitational potential), we have showed the existence of a long periodic term of 8.847 years (period of the lunar perigee) of variable amplitude. A plot of  $e_x$  and  $e_y$  evolution versus time (expressed in julian day) over a period of 100000 days (about 274 years) illustrates the behaviour (see figure 5). The maximum amplitude of the oscillation remains in all cases under  $6 \cdot 10^{-4}$ .



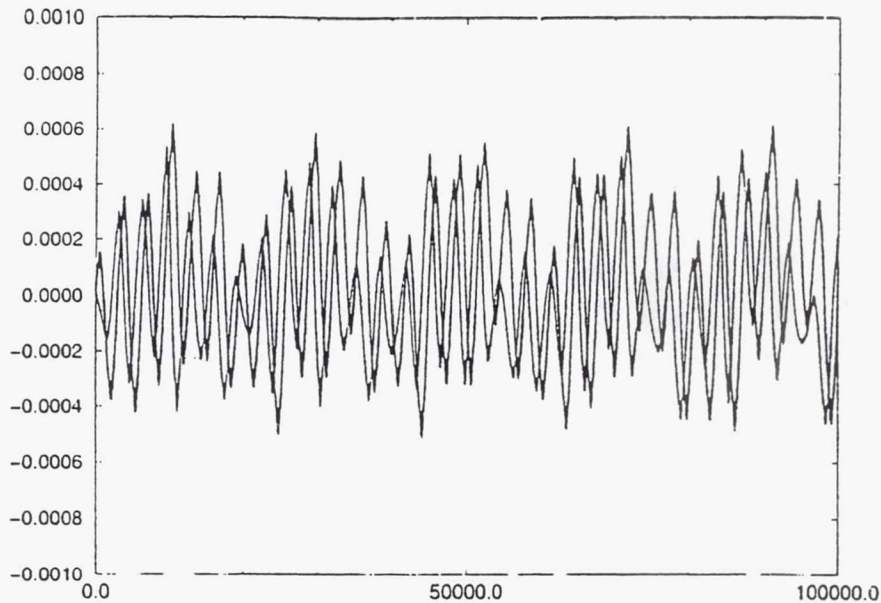


**Figure 5 Evolution of  $e_x$  and  $e_y$  under luni-solar perturbation over 274 years**

An analysis of this behaviour<sup>3</sup> has led to the conclusion that there is a combination effect between both perturbations: the high frequency term (8.847 years) is due to the luni-solar perturbation, whereas the low frequency term (about 53 years) results from the modulation created by the coupling between luni-solar and earth gravitational perturbations.

The maximum amplitude of the periodic term is of the same order than the solar radiation pressure perturbation. However, since it is a long-term period effect which does not interest the station keeping strategy, it is often not considered. Moreover, we must keep in mind, that the behaviour of the eccentricity plotted above is a simple view of spirit. Indeed, we have not considered the solar radiation pressure which acts continuously on geostationary satellites (excepting during the solar eclipses). An other approach would be to consider this behaviour only realistic for spinned-up satellites which have a very low  $C_p S/m$  (about 0.01).

Nevertheless, in the next paragraph, we go back to satellites with high  $C_p S/m$  values (indeed 0.05) in order to analyse the behaviour of the eccentricity when all perturbations are applied together.

#### **Solar radiation pressure, luni-solar and earth gravitational perturbations**

In the next figures, we have plotted the eccentricity ( $e_x$  and  $e_y$ ) evolution versus time (in julian days) over a period of 100000 days (about 274 years).

The conditions of the simulations are :

- initial eccentricity equals to zero,
- $C_p S/m = 0.05$ ,
- date of beginning = 08/18/1997 for figure 6 and 09/21/2037 for figure 7

On both figures, a long periodic term of about 53 years is observable. Many simulations have been performed and have shown that this period is not sensitive with the conditions of the simulation whereas the amplitude of the oscillation is completely conditioned by the beginning date and  $C_p S/m$  value. Lower  $C_p S/m$  values than 0.05 would generate lower amplitudes since this parameter acts as a multiplied factor of the oscillation period. Such results are developed in reference 4.

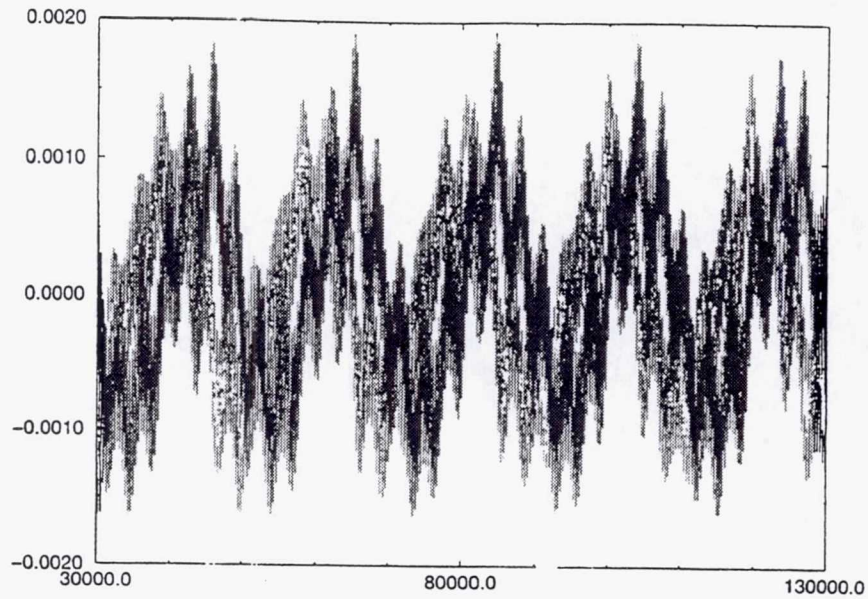


**Figure 6** Evolution of  $e_x$  and  $e_y$  under all perturbations over 274 years

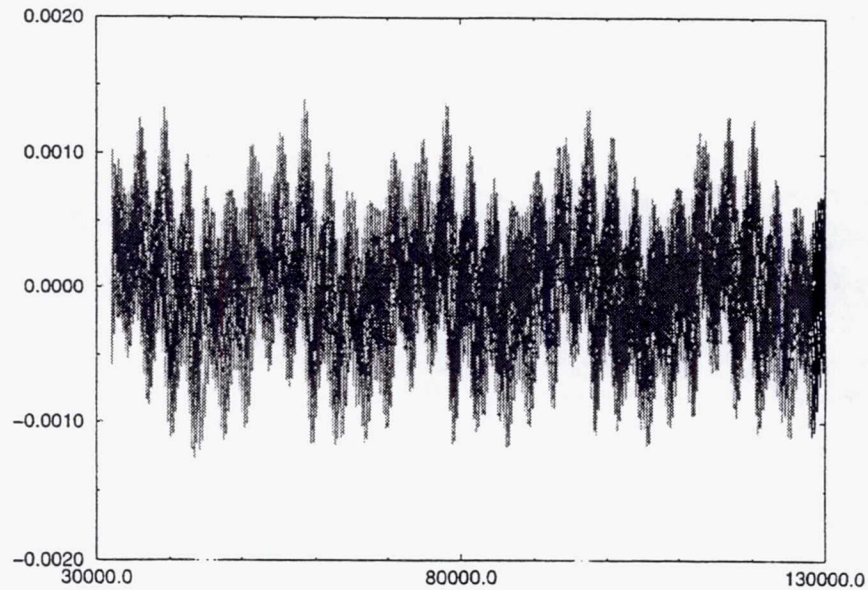


**Figure 7** Evolution of  $e_x$  and  $e_y$  under all perturbations over 274 years

The behaviour has been analysed<sup>4</sup> in order to understand the sensitivity versus the beginning date and find the configuration which generates the maximum amplitude. Taking into account some error margins, this value will permit to estimate directly  $\delta e_{\max}$  and thus  $\delta R_{p\max}$ .

Our explanation is that the 53 years periodic term results from a coupling between the one year term due to the solar radiation pressure and the 8.847 years term due to the luni-solar potential. Thus, the resulting phenomenon (the 53 years term) will be maximum when the one year and 8.847 years terms will be phased and minimum in opposite phase.

First, we have only considered the one year term created by the solar radiation pressure. Under the effect of this sole perturbation, the behaviour of the extremity of the eccentricity vector is perfectly determined following the sun in the eccentricity plan<sup>1</sup>. As a consequence the  $e_x$



component will be maximum at the spring equinox and minimum at the autumn equinox whereas the  $e_x$  component will be maximum at the summer solstice and minimum at the winter one.

Secondly, we have considered that we are close to the spring equinox ( $e_x$  is thus minimum for the one year term) and looked for in the  $e_x$  plot (see figure 8) which of the 8.847 years peaks are extremum around this period. We have found the both values (08/18/1997 and 09/21/2037) corresponding to the simulations plotted in figure 6 and 7.

More details of this analysis can be found in reference 4.

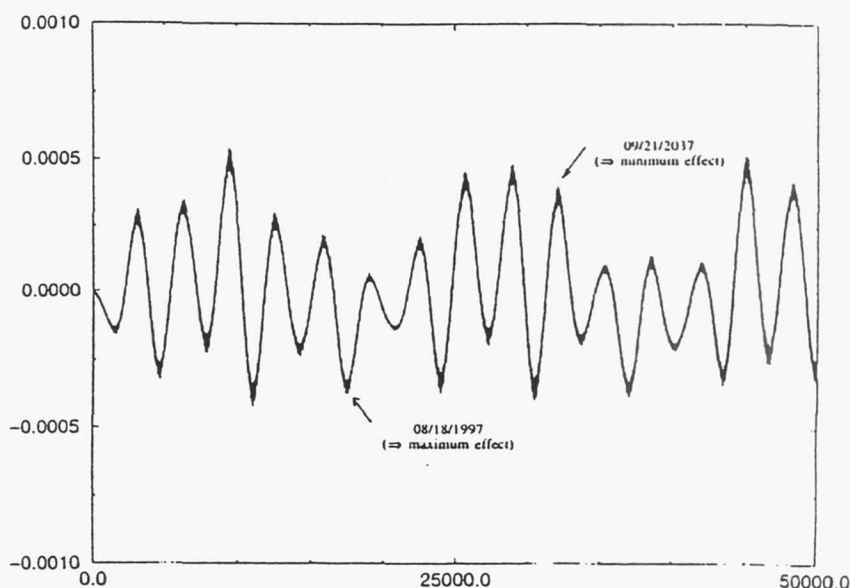


**Figure 8 Evolution of  $e_x$  under luni-solar perturbation over 137 years**

The maximum eccentricity variation value has been only estimated on the case plotted in figure 6 which yields :

$$\delta e_{\max} = 19.3 \cdot 10^{-4}$$

Taking a 10% error margin, we have kept a value of  $20.3 \cdot 10^{-4}$  for the global estimation of  $\delta R_{\text{pmax}}$ . Many other simulations, with different beginning dates, have been tried and confirm the validity of this estimation.

Concerning the 53 years periodic term, we may have the same comments as for the previous term of 8.847 years. Even if this amplitude may be larger than the solar radiation pressure perturbation's, the evolution is so slow that it is not sensitive with current station keeping periods. However, such a behaviour exists and must be taken into account when we study long-term evolutions.

#### Global estimation of maximal variation of perigee altitude

We have now gathered all the elements required to make a complete evaluation of the maximal variation of perigee altitude. Based on equation (2), we have :

$$\delta R_{\text{pmax}} = 5 + 42365 (0.75 \cdot 10^{-4} + 20.3 \cdot 10^{-4}) \text{ km}$$

$$\delta R_{\text{pmax}} \approx 95 \text{ km}$$

Taking an additional error margin of 5%, we can say now that, whatever the initial perigee altitude chosen for end-of-life orbits, the decreasing of this altitude will be of 100 km maximum.

## CONCLUSION

Considering the global value of 100 km and the current figures relative of geostationary orbit management, we can draw the conclusion that the altitude of perigee which prevents us of any risk of collision with active or on-orbit shift satellites is beyond 300 km above the geostationary arc.

Thus, the conclusion of our study is that at end of mission spacecrafts have to be re-orbited with a perigee not less then 300 km above the geostationary arc. This result complies with the IADC recommendation value.

## ACKNOWLEDGEMENT

Paul Legendre is gratefully knowledged as the initiator of the prediction software used for this study and for helpful discussions on the analysis of the results.

## REFERENCES

1. Spaceflight dynamics - Tome II - CNES - Cépaduès Editions  
Station keeping methods for geostationary satellites
2. ORANGE - Documentation Mathématique du modèle  
CT/TI/MS/SG/93.577 du 23/12/93
3. Orbite fin de vie des satellites geostationnaires  
DGA/T/TI/MS/SG/97.208 du 02/07/97 - M. Deleuze
4. Orbite fin de vie des satellites geostationnaires - Compléments d'étude  
DGA/T/TI/MS/SG/97.311 du 13/10/97 - M. Deleuze



## AN AUTONOMOUS NAVIGATOR FOR LEO SATELLITES

Virginie Pascal, Hervé Marcille, Patrice Damilano\*

MATRA MARCONI Space decided in 1996 to initiate the internal development of the LEOSTAR platform dedicated to low Earth orbiting missions. The LEOSTAR innovative approach is characterised by multi-mission, high quality, state of the art technical solutions, while ensuring a low cost access to space.

In this spirit, an original low cost navigator has been designed, based on GPS receiver position fix (Position, Velocity and Time), for low eccentricity and low Earth orbits. Its attractive features are the following : a simple measurement processing (using directly the position/velocity derived by the GPS receiver and expressed in the J2000 inertial frame), the use of constant update gains yet accounting for orbital coupling, and the simplicity of the retained integrator. More precisely, the originality of the proposed approach is to compute steady-state Kalman gains relative to the evolution of the actual position/velocity with respect to the estimated one, assumed to follow Clohessy-Wiltshire equations. The selected integrator is a 4<sup>th</sup> order Runge-Kutta using the inertial position/velocity and taking account of disturbing accelerations reduced to the J2 effect of the Earth potential development.

This navigator allows to deal with no-PVT phases i.e. phases during which less than four GPS satellites are visible, and to upgrade the intrinsic GPS Standard Positioning Service performance by a factor two for the position and a factor ten for the velocity. This last effect is of primary importance for reducing the angular estimation error of the local orbital frame with respect to the inertial frame. The performances can be improved if a more accurate integrator is considered.

For performance validation, an orbit generator has been used to generate many different orbits to which PVT error profiles - obtained from an actual GPS receiver - have been added. The obtained measurements have fed the navigator, allowing to assess performances. Moreover, in the frame of the first flight demonstration (US Shuttle STS-80 flight) of the ATV RendezVous Predevelopment program, actual GPS PVT data from the LABEN Tensor GPS receiver have been collected. Those data correspond to a reference trajectory for which best estimates have been determined by ESOC using DGPS techniques. Both the measurements and the reference trajectory allowed to confirm the predicted performances when using the navigator but also to refine the re-initialisation filter logic.

---

\* Matra Marconi Space, 31 ave des Cosmonautes, 31402 Toulouse Cedex 4, France

e-mail: [firstname.name@tls.mms.fr](mailto:firstname.name@tls.mms.fr)

## INTRODUCTION

The LEOSTAR multi-mission bus development was started by MATRA MARCONI Space in 1996. The LEOSTAR bus is designed to allow low cost access to space for scientific, observation and telecommunication missions. The technical design uses state-of-the art equipment to achieve high performances, and is organized in a modular way to adapt to different mission requirements. Of particular importance for the LEOSTAR bus are the notions of system autonomy and of robust design. In particular, orbit determination is realized on board using a GPS receiver to allow continuous autonomous navigation during nominal operations. The GPS receiver is also used to provide the bus time reference, and the position and velocity data are used to autonomously determine the local orbital frame used for Earth pointing missions.

The use of a GPS receiver presents those significant advantages for the overall system simplification and autonomy, but raises concerns among which the performance when Selective Availability (SA) is ON and during measurement interruptions due to a possible receiver transient lock up. Furthermore, simulations have shown that a zenith oriented GPS antenna only sees two GPS satellites near the poles on a polar orbit during about 5 minutes. On the other hand, since LEOSTAR addresses the commercial market, a solution adapted to the different available receivers is preferred, with no customization to a particular receiver.

A solution to the above mentioned issues, while staying simple and directly adapted to all the available receivers (L1, C/A code), is to use the snapshot navigation output i.e. the Position/Velocity/Time Fix (PVT) obtained through a processing of at least four simultaneous GPS satellites data, and to filter these position and velocity measurements. Those measurements are filtered by an Earth gravity potential model that improves both the position and the velocity receiver output, and propagates the position estimate when less than four satellites are visible. Another advantage of this filter is its particularly adaptive formulation - described hereafter - that allows more or less complex gravity models to be taken into account and therefore improve the restitution and propagation accuracy. The paper describes the filter mathematical formulation, the design and performances in different cases. The performances are also validated by comparison to real flight experiment data from the ESA ARP-K program.



## WHAT KIND OF ORBIT DETERMINATION ?

Between the various types of orbit determination, one can distinguish on-board orbit prediction, precise on-board real-time orbit determination and a posteriori on-ground restitution based on precise differential solutions (post-processing of data). On-board orbit prediction aims basically at providing a long-term reliable navigation solution, for missions that do not require high precision. For example, a simple, autonomous GPS-based navigator<sup>1</sup> has been successfully tested for the PoSAT-1 satellite. The high and growing interest in real-time on-board orbit determination has been demonstrated by the increasing number of the state-of-the-art, high-precision navigators such as DIODE<sup>2</sup> based on the DORIS system (DORIS Doppler data), DIOGENE<sup>2</sup> based on GPS pseudorange data or GEODE<sup>4</sup> also using GPS pseudorange and Doppler. The on-ground orbit restitution is now well mastered : better than one meter accuracy may be obtained with data post-processing using software such as MSODP1<sup>6</sup>, ZOOM<sup>2</sup>, GIPSY-OASIS<sup>3</sup> or GPSBET<sup>5</sup>.

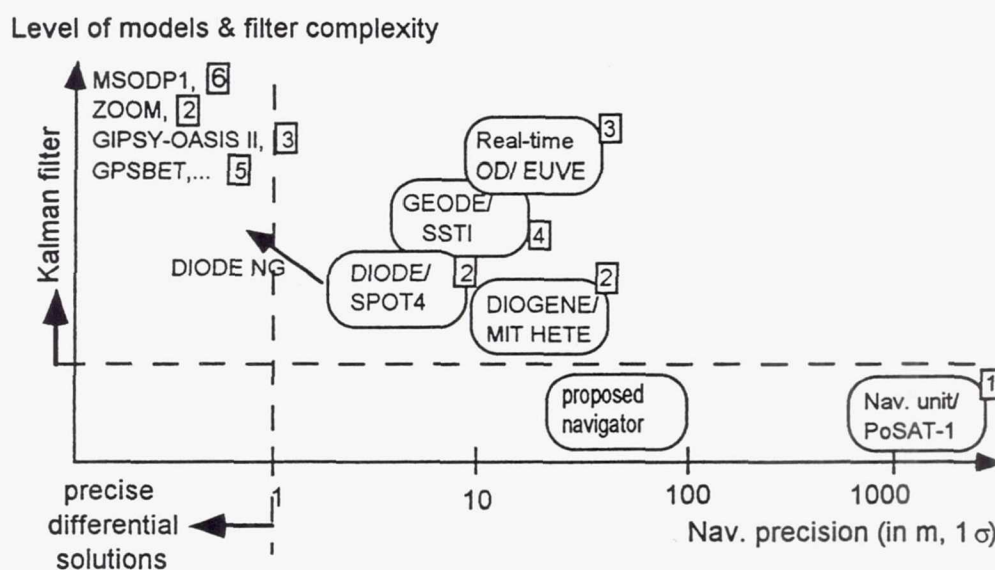


**Figure 1 - Examples of orbit determination software and associated performance**

For missions requiring typically better than one hundred meters orbit knowledge ( $1\sigma$ ), all the proposed algorithms are quite complex (an extended Kalman filter is commonly used) and the models are quite heavy (for example, the GEODE Earth gravitational model is the JGM-2 nonspherical geopotential up to degree 30 and order 30). It is therefore of great interest in this performance range to propose a simple, robust and generic navigator. The LEOSTAR navigator is generic in the sense it is viable for all the LEOSTAR quasi-circular mission orbits from 500 to 2000 km altitude, robust and simple because it uses fixed gains and a simple acceleration model reduced to the Earth gravitational primary effects (Kepler + J2) without considering any drag effect, solar and lunar attraction or solar radiation pressure.

## THE LEOSTAR SOLUTION

### Main characteristics

- The position/velocity in terms of Cartesian coordinates expressed in the J2000 inertial frame (mean equator and equinox of J2000.0) is propagated. The associated integrator is a 4<sup>th</sup> order Runge-Kutta and the spacecraft acceleration model is reduced to Earth point mass and J2 effect. Note that this model may be extended and one of the purposes of this paper (see chapter Performance Upgrade) is also to show the impact on the navigation precision of an acceleration model upgrade. The model may be in fact adapted to the accuracy need.
- To be able to deal with the GPS receiver position fixes, one has to express the PVT in the inertial frame if the GPS receiver does not provide this facility.
- Then concerning the update of the on-board estimate, an attractive idea<sup>7</sup> has been developed : the use of steady-state Kalman gains. Going into this direction, our goal was to find gains related to the physical in-orbit motion explicitly accounting for orbital coupling. This has been made possible by considering that the true motion differs from the on-board estimation through the Clohessy-Wiltshire equations<sup>8</sup> (also known as Hill equations) that usually reflect the evolution of the position/velocity difference of two close quasi-circular orbits and that are commonly used in RendezVous navigation software<sup>10</sup>. Thus the evolution of the cartesian error  $x$  (estimation wrt true motion) follows the equations given hereafter :

$$\begin{cases} \dot{x} = F_{CW}x + Gw \\ z = Hx + v \end{cases}$$

with

$$H = Id_6$$

$$F_{CW} = \begin{pmatrix} 0 & 0 & 0 & 1 & 0 & 0 \\ 0 & 0 & 0 & 0 & 1 & 0 \\ 0 & 0 & 0 & 0 & 0 & 1 \\ 0 & 0 & 0 & 0 & 0 & 2\omega_0 \\ 0 & -\omega_0^2 & 0 & 0 & 0 & 0 \\ 0 & 0 & 3\omega_0^2 & -2\omega_0 & 0 & 0 \end{pmatrix} \quad \omega_0: \text{orbital\_rate}$$

$w$  : acceleration estimation error, mainly due to the Earth gravitational model truncation and the neglected atmospheric drag ;  $E(ww^t) = Q$

$v$  : PVT measurement error ;  $E(vv^t) = R$

The Ricatti equation allows to derive the steady-state solution in terms of covariance matrix (P) and gains (K) of this system :



$$0 = \dot{P} = F_{CW}P + PF_{CW}' + GQG' - PH'R^{-1}HP$$

$$K = P_{\infty}H'R^{-1}$$

The resulting gains are then used for the navigator.

Note that the difficulty in all this process is to characterize the white noise sigma representative of acceleration error (Q) and measurement error (R); this was performed by likening measurement error to a white noise entering a second order filter (certainly not far from the Selective Availability process) and the velocity error to the integration of a white noise.

In theory gains depend on the orbit (because of the acceleration error and the orbital rate  $\omega_0$ ), but the gains obtained for the first study case turned out to be usable for the other ones.

- The filter initialization can be performed on the basis of the first PVT measurement. About half an orbit is necessary to reach the steady-state performance (with Kepler+J2 dynamics model). A simple measurement rejection scheme is applied to avoid state update with potential erroneous measurements: a measurement is rejected if the position (resp. the velocity) residual (difference between the estimate and the measurement) is greater than 500 m (resp. 5 m/s) typically. In the event of too many successive rejections, a filter re-initialization is performed, allowing to recover from wrong initialization or unexpected filter divergence resulting from too long measurement interruption.
- The flight software development has been performed using Ada83 programming language, with a memory utilization not exceeding 20 kilobytes.

## Functional architecture of the navigator

Figure 2 illustrates the structure of the LEOSTAR navigator. First of all, the GPS receiver position fix (computed at  $t_{obs}$ ) has to be propagated until the current on-board time ( $t_n$ ). There is no need of using the same propagator as for the filter estimate : for every study case mentioned in this paper - even the ones related to the section « Performance Upgrade » - the measurement propagation acceleration model is limited to Earth point mass and J2. From the filter side, the estimate is also propagated. The transformation matrix from inertial frame to local vertical/local horizontal (LV/LH) frame and also the orbital rate are then computed, on the basis of the current estimate. This allows to obtain the difference between the estimate and the measurement at the same on-board time and expressed in the LV/LH frame corresponding to the estimate. The gains computed as explained further, apply on this LV/LH difference, giving the updated estimate. The last step consists in expressing the estimate back in the inertial frame.

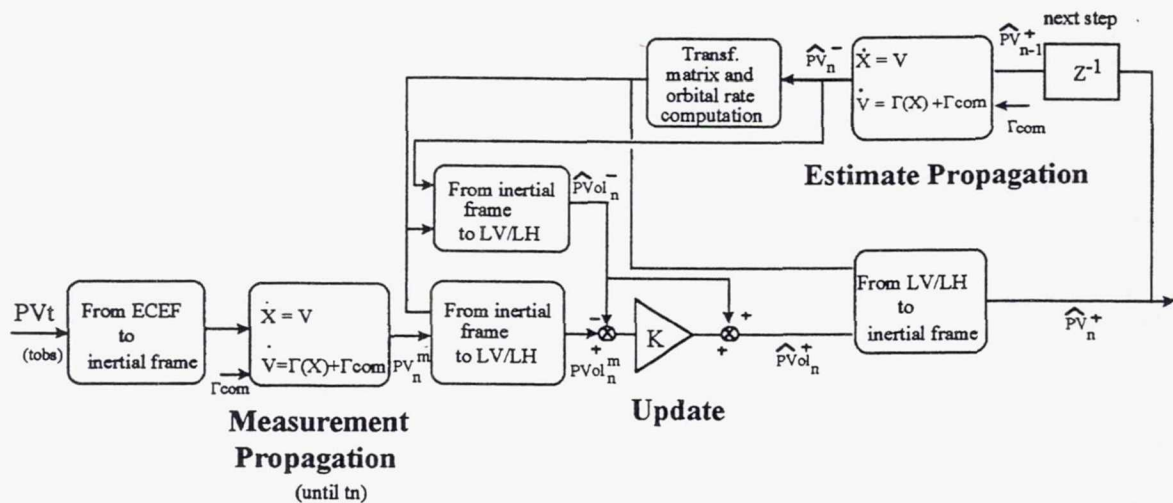
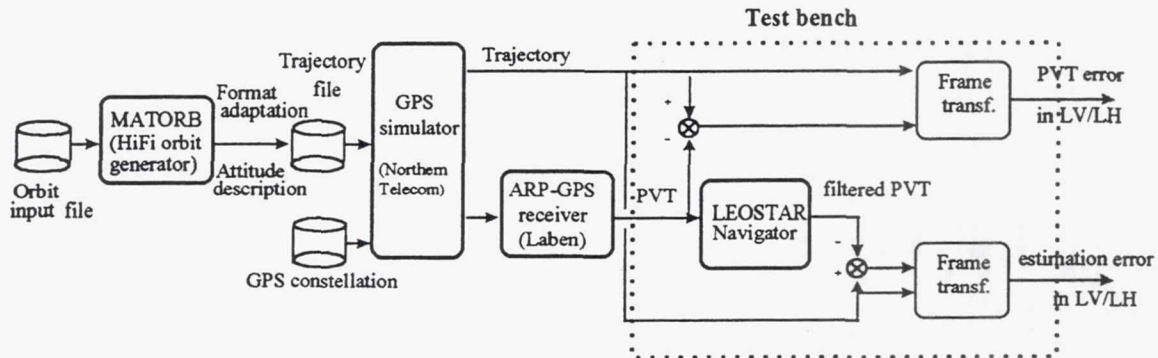


Figure 2 Principle of the LEOSTAR Navigator



## Performances

The navigator has been implemented so as to test the actual behavior of the proposed filter. And test data have been obtained using a Northern Telecom GPS simulator<sup>9</sup>, as explained on the following figure.



**Figure 3 Test of the LEOSTAR Navigator with simulated data**

Four LEOSTAR orbit cases were studied :

- IO1 : a 1000-kilometer-altitude, 60-degree-inclination, circular mission orbit,
- EQO1 : a 500-kilometer-altitude, equatorial, circular mission orbit,
- EQO2 : a 1500-kilometer-altitude, equatorial, circular mission orbit,
- SSO1 : a 700-kilometer-altitude, 98-degree-inclination, heliosynchronous, circular mission orbit.

First of all, LEOSTAR orbits have been generated with the MMS MATORB orbit generator software which allows to generate an orbit taking account of all kinds of perturbations (GEM10 or GEM10B Earth gravitational model, JACCIA 70 or MSIS-86 atmospheric density model, solar and lunar attraction, solar radiation pressure). Then trajectory files have been adapted to the GPS simulator input file format. This allowed to derive representative GPS measurements for the orbits considered, including periods during which less than four GPS satellites were visible i.e. periods without PVT data. Up to 1000 sec without PVT has been observed for the inclined orbit IO1. The GPS simulator re-generates also an orbit file : this is the yardstick of our simulation. The test bench is made of two main chains : one is dedicated to the computation of the PVT error in the actual LV/LH frame and the other one feeds the LEOSTAR navigator and provides the navigation error in the same frame.

A first glance on the figure 4 shows the advantage to filter the PVT measurement, especially for the velocity performance. A comparison between the PVT error and the filter estimation error may be made in terms of cartesian coordinates (position/velocity in LV/LH) or orbital elements. As an example the radial position and velocity on one side and the semi-major axis, inclination and argument of latitude on the other side have been plotted hereafter. Note that the critical period without PVT measurement just before

10000 sec is perfectly handled by the navigator then reduced to a simple propagator.

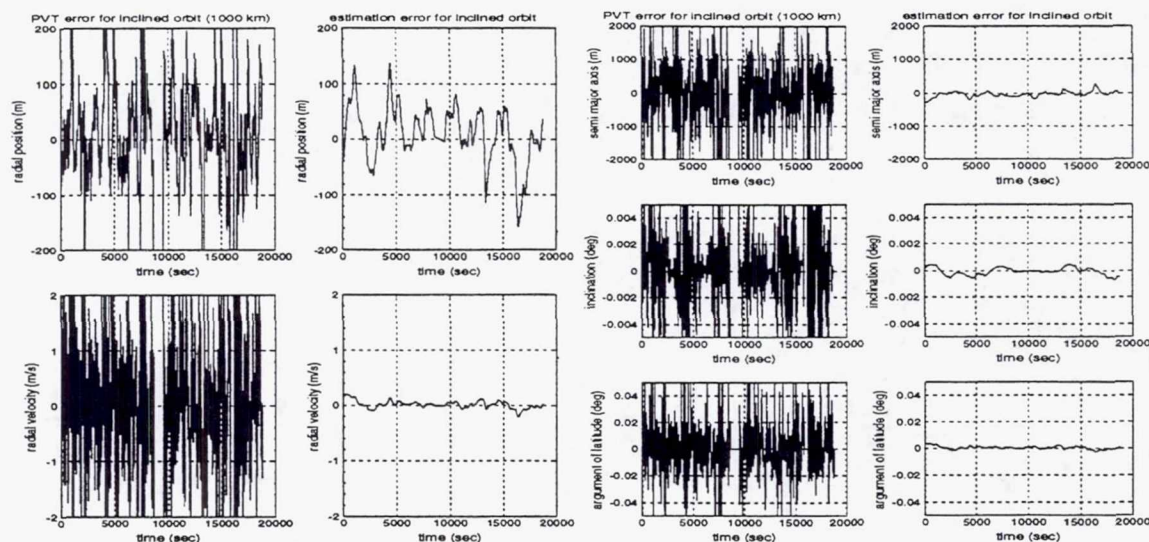


**Figure 4 Comparison between the GPS receiver snapshot navigation output (PVT) and the filtered navigation solution**

**Table 1**

**Performance with simulated data**

<u>Orbit</u>	<u>3D position performance (m, <math>1\sigma</math>)</u>	<u>3D velocity performance (cm/s, <math>1\sigma</math>)</u>
EQO1	51.0	12.5
SSO1	44.2	8.4
IO1	65.6	9.6
EQO2	49.5	9.2

The performance sensitivity to no-PVT periods has been evaluated. Visibility holes up to 1500 sec have been voluntarily added to the available PVT profiles so as to assess the performance in degraded cases. The performance is then roughly obtained by multiplying the velocity estimation error at the beginning of the critical phase by the visibility hole duration, that is a maximum value of 200m in 1000 sec.



In the frame of the first flight demonstration (US Shuttle STS-80 flight, November 1996) of the ATV RendezVous Predevelopment program (ARP), the ARP-GPS LABEN receiver (early TENSOR receiver) mounted on a retrievable platform (ASTRO-SPAS) performed PVT and raw measurements (pseudorange and Doppler) during disposal and retrieval phases with the US Shuttle and those data have been collected<sup>11</sup> in order to feed the ARP Relative GPS Navigation filter<sup>10</sup>. It was also used as an opportunity to test the LEOSTAR navigator with actual GPS PVT data, knowing that ESOC had estimated for this flight demonstration the ASTRO-SPAS reference trajectory (our yardstick) using the already-mentioned software GPSBET<sup>5</sup>. Moreover no modification of the test bench had to be performed (see figure 5).

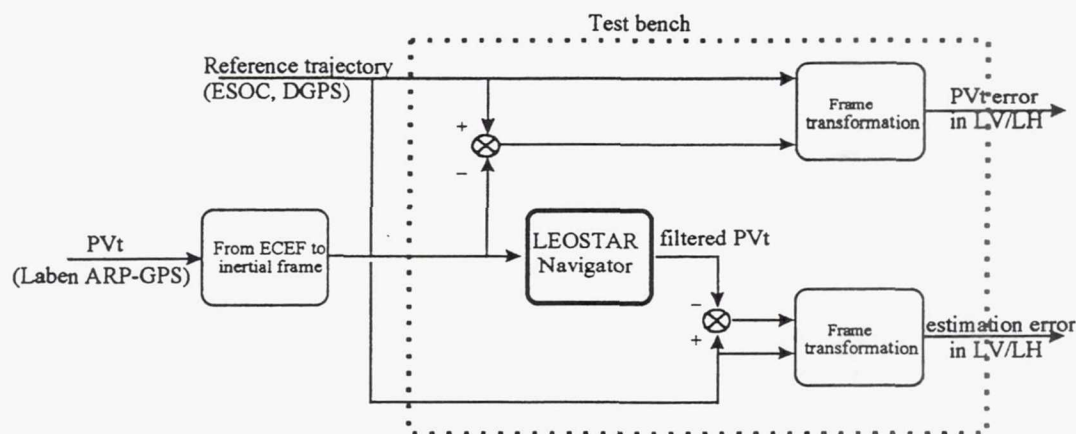


**Figure 5 Test of the LEOSTAR Navigator with actual flight data**

The position and velocity estimation errors are shown on figure 6. It reveals that one begins the phase with a very bad velocity knowledge. It induces at about 400 sec a filter re-initialization. But such an event and the fact that the measurement availability period is quite short (about 7000 sec) do not prevent the filter to converge and to provide a navigation performance of the same order of magnitude as for the simulated data : 40.7 m and 10.5 cm/s (3D RMS values).

Moreover the actual GPS PVT data profile led us to refine the filter re-initialization threshold which had been arbitrarily set to 20 successive rejections i.e. 20 sec since the PVT is computed and delivered at one hertz by the receiver. In fact periods up to 100-150 sec of bad data (more than 300 m and 3 m/s PVT error) have been observed. Therefore despite the reactivity loss, it has been preferred to consider that the filter estimation could differ from measurement information during 200 sec. Otherwise (with a threshold fixed to 20), such a polluted period would induce a filter re-initialization based on a degraded information, which is not safe.

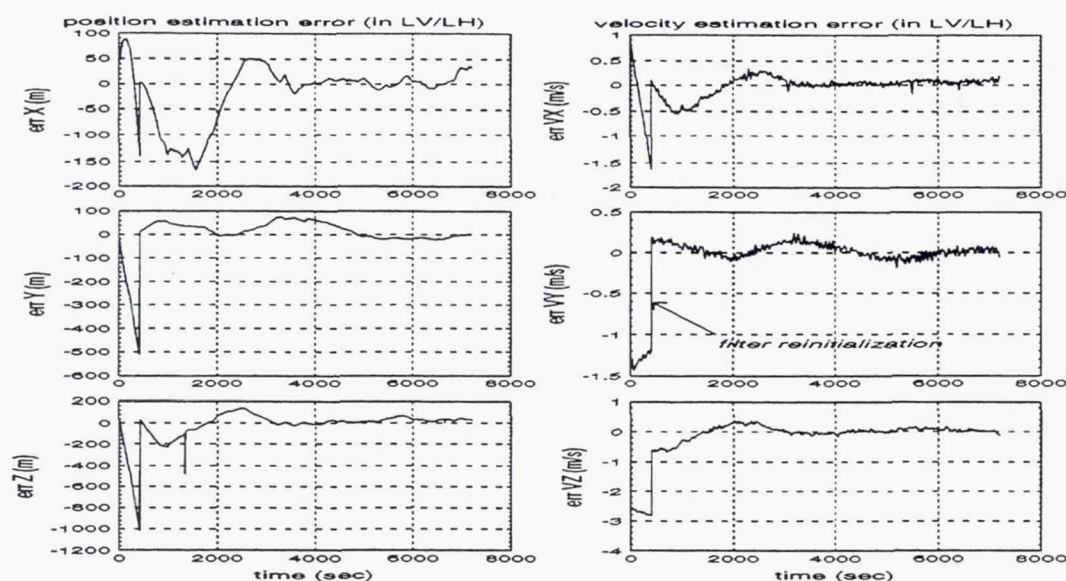


**Figure 6 LEOSTAR Navigator estimation performance with actual flight data**

## PERFORMANCE UPGRADE

It was of course of great interest to test the implementation of a more precise perturbation model. Thus up to the 6<sup>th</sup> order and degree of the GEM10B Earth gravitational model was considered. It has been established that there was no need for augmenting the degree/order of the Earth gravitational model without considering a drag model especially for the considered lower orbits (500 km altitude).

The propagator change induced a new gain computation that was not without impact : as a great confidence is put in the on-board model (low model noise), the convergence is much slower (about one orbit) and the filter is much more sensitive to the transient events. This critical point was solved by gain scheduling that is by considering two sets of gains : one before convergence (the same as the one for a Kepler+J2 propagator) and another one after convergence to take benefit of the improved propagator accuracy. Thus the convergence occurs again after half an orbit (3000 sec) and the performance in the converged state is improved.

Figure 7 compares, for the equatorial orbit EQO1, the navigation estimation errors on the radial position/velocity in the case of a Kepler+J2 propagator and of a 6<sup>th</sup> degree/order Earth potential based propagator with gain scheduling. Table 2 presents the performance reached (after convergence) for the inclined orbit IO1 at 1000 km altitude and for the equatorial orbit EQO1 at 500 km altitude.



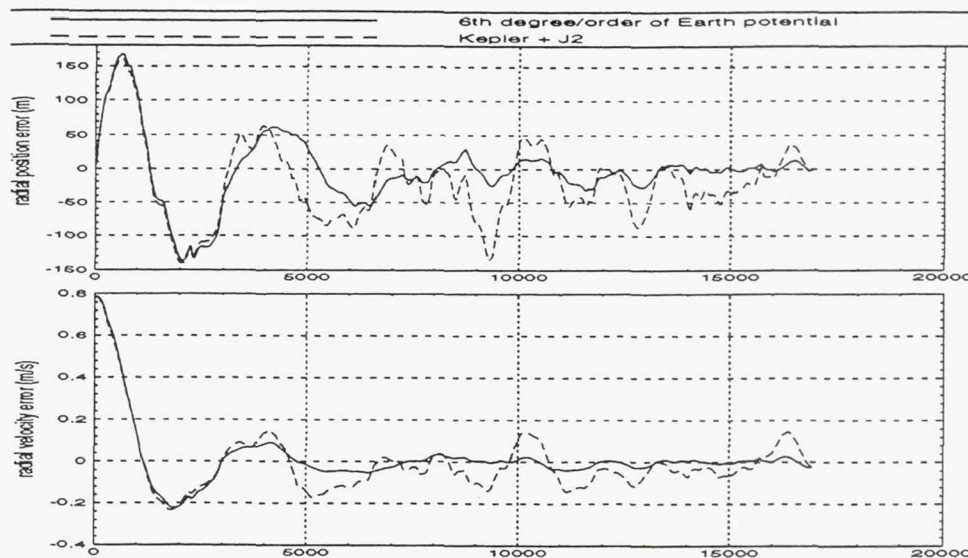


**Figure 7 Interest of upgrading the spacecraft acceleration model**

**Table 2**

**Performances with a 6<sup>th</sup> order/degree propagator**

<u>Orbit</u>	<u>3D position performance (m, 1<math>\sigma</math>)</u>	<u>3D velocity performance (cm/s, 1<math>\sigma</math>)</u>
EQO1	36.5	6.0
IO1	15.3	3.2

The performance gain is significant, especially for « high » altitude orbits for which the drag error is small.

## CONCLUSION

An original compact navigator design based on GPS PVT measurements has been presented in this paper. Basically it consists in a propagation process based on cartesian coordinates and in an update process using fixed gains. The propagator may be adapted to navigation requirement, knowing that gain scheduling is recommended in the case of a « complex » propagator.

In spite of the implementation simplicity, the 50 m / 10 cm/s level performance (3D,  $1\sigma$ ) is reached. This design will be more extensively tested in the frame of maneuvers and through a real-time simulation campaign. However the results already obtained with actual flight data make it an attractive basis to offer a reliable and continuous autonomous navigation service to a large variety of LEO space missions whose localization needs are typically well covered by the proposed performance.

## NOTATIONS

GPS	Global Positioning System
PVT	Position/Velocity/Time fix
ATV	Automated Transfer Vehicle
LEO	Low Earth Orbit
LV/LH	Local Vertical / Local Horizontal frame
ECEF	Earth-Centered Earth-Fixed frame (WGS84 in our case)
$t_n$	current on-board time
$\Gamma_{com}$	commanded accelerations
$PV_n^m$	position/velocity measurement at $t_n$ , in the inertial frame
$Pvol_n^m$	position/velocity measurement at $t_n$ , in the LV/LH frame
$\hat{X}$	estimate of the X entity

## REFERENCES

1. M. Unwin (University of Surrey) : "The Design and Implementation of a Small Satellite Navigation Unit Based on a GPS Receiver", *thesis* September 1995.
2. J.-P. Berthias, P. Broca, J. Fourcade, D. Pradines (CNES) : "General characteristics of real-time on-board orbit determination", *ESOC 12th International Symposium on Space Flight Dynamics*, June 1997.
3. K. Gold, G. Born, K. Larson (University of Colorado), W. Bertiger, S. Wu, T. Yunck, R. Muellerschoen (JPL) : "A Study of Real-Time GPS Orbit Determination For the Extreme Ultraviolet Explorer", *Institute of Navigation National Technical Meeting*, January 1994
4. R. C. Hart, K. R. Hartman (GSFC), A. C. Long, T. Lee, D. H. Oza (CSC) : "Global Positioning System (GPS) Enhanced Orbit Determination Experiment (GEODE) on the Small Satellite Technology Initiative (SSTI) Lewis spacecraft", *ION GPS Meeting*, 1996



5. T.J. Martin Mur, J.M. Dow (ESOC) : "Satellite Navigation Using GPS", *bulletin ESA*, May 1997.
6. G. Davis, J. Ries, H. Rim, B. Schutz, B. Tapley (University of Texas Center for Space Research) : "Orbit Determination Techniques for GPS Tracking of Low Altitude Satellites", *ION GPS Meeting* 1994.
7. Q. M. Lam, R. V. Welch (Welch Engineering), W. Grosman, D. C. Freesland (CTA Space System) : "Development On An  $\alpha$ - $\beta$  Filter Based Orbit Determination System", *AIAA/AAS* 96.
8. *Spaceflight dynamics 1995*, CNES (France).
9. *GPS Simulator System User manual*, Northern Telecom.
10. H. Marcille, G. Moreau, V. Pascal (MMS-France) : "Relative Navigation Design and Validation for ATV Rendez-Vous", *ESA 3rd Symposium on Spacecraft Guidance, Navigation & Control Systems*, November 1996.
11. G. Moreau, H. Marcille (MMS-France) : "RGPS Postflight Analysis of ARP-K Flight Demonstration", *ESOC 12th International Symposium on Space Flight Dynamics*, June 1997.

**Page intentionally left blank**



## Autonomous Acquisition and Maintenance of a Satellite Constellation using LQG/LTR Optimal Controller with GPS Measurements<sup>+</sup>

Guang Q. Xing\* and Shabbir A. Parvez\*\*

The subject of this paper is the autonomous orbit acquisition and maintenance for a satellite constellation. The digital LQG/LTR Optimal Controller using GPS measurements are used for implementing the autonomous onboard real-time closed-loop feedback orbit control for the acquisition and maintenance of a satellite constellation. The input to this autonomous orbit control is the GPS information data (3 or 4 code pseudo ranges) and the output of this system is the optimal LQG/LTR control law for closed-loop feedback. This paper shows that this control system is completely controllable and completely observable and the closed-loop feedback system is asymptotically stable. The Loop Transfer Recovery technique for the discrete-time system is used to enhance the performance and stability robustness of this digital control system.

The measurement and control simulations of the discrete-time system show that the control system design is feasible and the system performance satisfies the design requirements. Various simulation results provided in this paper indicate that this digital GPS optimal output feedback control system can be applied to autonomous orbit acquisition and maintenance control for satellite constellations.

### INTRODUCTION

Since 1984 the use of multiple satellite in formation pattern for future space exploration and commercial space-based communication systems has been proposed. More recently, these ideas have materialized in form of actual space-based global communication systems using constellations of large number of satellites in the Low Earth Orbits (LEOs). Some examples are Motorola's Iridium and Celestri Mobile Communication System and the Teledesic Inc' small satellite global communication system. Development of such space-based communication network require the addressing the following problems related to the Guidance and Control of the satellites:

- (1) Defining the optimal distribution and patterns for constellations and formations
- (2) Acquisition of the designated position in the formation pattern for the spacecraft just separated from the launch vehicle
- (3) Maintenance of the positional relationships between spacecrafts in the formation pattern
- (4) Autonomous orbital control and operations of these missions

The solution to the first problem is dictated by communications requirement of the user, subject to constraints such as sun pointing and other astronomical observation requirement, etc. Problems (2)-(4) are the problems that need to be resolved for the navigation, guidance and control design. Particular emphasis is being given

<sup>+</sup> This work was supported by Air Force Research Laboratory/Phillips Research Site, Kirtland AFB, New Mexico, under Contract F29601-97-C-0029

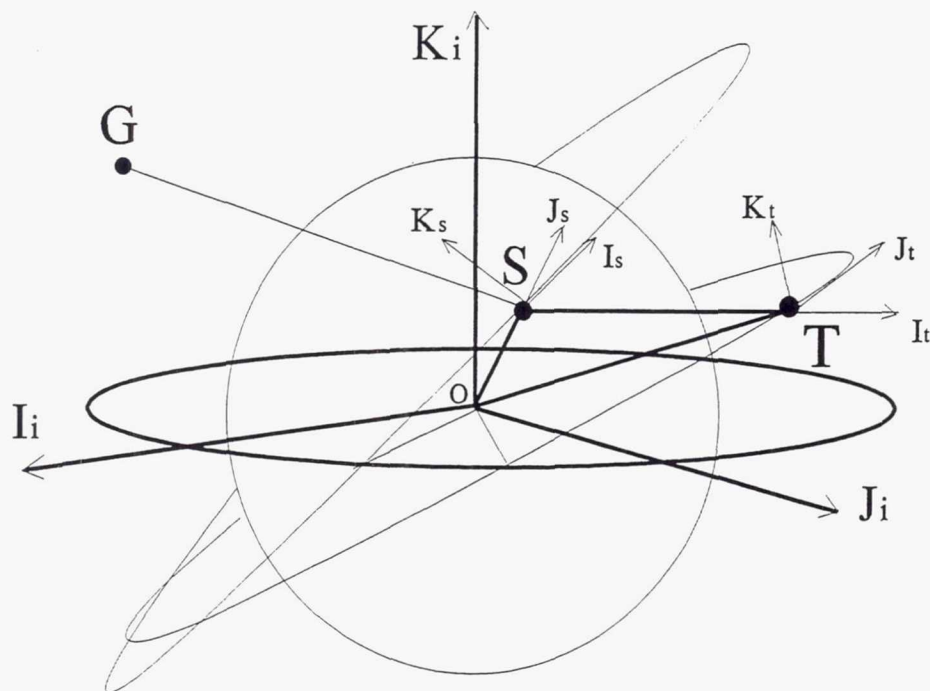
\* Principal Scientist, Space Products and Applications, 3900 Jermantown Road, Ste.300, Fairfax, VA 22030. Phone (703) 934-4619, email: xingspa@erols.com

\*\* President, Space Products and Applications. Phone (703) 934-4619, email: parvzspa@erols.com

here to the last item, which is the requirement for autonomous orbit navigation, guidance and control. It is obvious that due to the sheer number of satellites involved, traditional methods of orbit control involving ground tracking and control stations would be prohibitively expensive, manpower and computer intensive, and in some cases virtually impossible. Therefore, by vastly reducing the ground station involvement, autonomous orbit control and navigation system will be of immense economic and operational benefit.

The pattern in which the multiple spacecraft are arranged can be divided into two category :

- (i) Constellation - the reference base for this pattern is the Earth or an inertial reference;
- (ii) Formation flying - the reference base for this pattern is one of the spacecrafts in the formation. This spacecraft, selected as the reference base, can be referred to as the leader of the



spacecrafts in the formation.

This paper, as the one of a series of research done in this field, will study the autonomous orbit navigation and control for a

**Fig. 1 The Position Relationship of the Pursuit Satellite, The Target Orbit and GPS Satellites**

constellation. Although literature indicates several papers studying the autonomous orbit control, the search did not reveal any paper that addressed the issue of autonomous orbit control using measurement output feedback control that can be realized in practical engineering design. This paper, therefore, addresses this issue of autonomous orbit acquisition and maintenance.

SPA has also filed for a patent for the application of autonomous on-board orbit control that includes the feedback control techniques discussed in this paper.



## STATEMENT OF THE AUTONOMOUS ORBIT CONTROL PROBLEM

It is assumed that the constellation pattern for the global communication is given. The objective of the autonomous orbit control system is to place the satellite, after separation from launch vehicle, in the designated orbit position and to maintain its orbit. It means that all of the control processes have to be realized only by onboard real-time feedback control. The input of the control system is the code pseudorange measurement from GPS satellite, and the output of the control system are the control signals for actuators. The digital LQG/LTR technique is used for the design of the autonomous orbit controller.

## THE LQG/LTR CONTROLLER FOR AUTONOMOUS ORBIT CONTROL

### Orbital control dynamics model

It is well known that the orbit dynamics equations are a set of nonlinear equations, but the equations of relative movement can be treated as a set of linear differential equations. With the goal being implementation of the design, the equations are being set up in form of the difference equations. It is assumed that the difference equation of the relative orbit movement is

$$x(k+1) = \Phi x(k) + \Gamma u(k) + w(k) \quad (1)$$

where  $x$  is the system state vector and  $u$  is the control input vector. In this study,  $u$  represents the radial-tangential-normal for three direction control signal, or only tangential-normal for two direction control signal.  $w(k)$  is a zero-mean white Gaussian discrete-time noise with

$$E[w(i)w(j)^T] = Q\delta_{ij} \quad (2)$$

and assumed to be independent of the initial state condition.  $Q$  is the variance of the system noise and modeling error resulting from the linearization of the nonlinear orbit dynamics equations.  $\Phi$  is the transfer matrix of the discrete-time system and  $\Gamma$  is the control influence matrix.

### GPS measurement and observation equation

In concept defined in [1], GPS observable are ranges, as deduced from measured time or phase differences based on a comparison between received signal and receiver generated signals. Unlike the terrestrial electronic distance measurements, GPS uses the "one way concept" where two clocks are used, one in the satellite and the other in the receiver. Thus, the ranges are biased by satellite and receiver clock errors and, consequently, they are denoted as pseudoranges. Since the bias of the satellite clock can be calculated, most of clock bias can be removed, although small error remain.

Therefore, the pseudorange signal will contain range information and receiver clock bias error. This clock bias error can be removed by using the pseudorange data from four GPS satellites that are observed simultaneously. The pseudorange can then be used as the observational data for estimating the system state. The range observational data is nonlinear function,  $\rho = h(\underline{x}, t)$ , of the orbit state. In order to estimate the state, the observational equation need to be linearized. It is assumed that the linear observational equation is

$$y(k) = H\underline{x}(k) + v(k) \quad (3)$$

where  $H = dh/dx$ .  $V$  is observational zero-mean white noise with

$$E[v(i)v^T(j)] = R\delta_{ij} \quad (4)$$

R is the variance of the observational noise.

It has been proven that the system  $\{\Phi, \Gamma, H\}$  consisting of the orbit control dynamics model and GPS measurement model are completely controllable and completely observable (even when the target orbit is not circular). Therefore, the LQG closed loop system is asymptotically stable.

#### The digital LQG/LTR controller

*LQG Control*<sup>2</sup>. It well known that the system represented in equations (1)-(4) describes a time-invariant system with stationary noise. If the system model is stabilizable and detectable, then there will be constant gains for both the controller and observer dynamics. The stochastic optimal control,  $\underline{u}$ , which will minimize a quadratic cost function of the form

$$J = E\left[\frac{1}{2} \sum_{i=0}^{\infty} (\underline{x}(i)\hat{Q}\underline{x}^T(i) + \underline{u}(i)\hat{R}\underline{u}^T(i))\right] \quad (5)$$

is

$$\underline{u}(k) = -K_c \hat{\underline{x}}(k) \quad (6)$$

$$K_c = (\hat{R} + \Gamma^T P_c \Gamma)^{-1} \Gamma^T P_c \Phi \quad (7)$$

where  $P_c$  satisfies the control algebraic Riccati equation

$$P_c = \Phi^T P_c \Phi + \hat{Q} - \Phi^T P_c \Gamma (\hat{R} + \Gamma^T P_c \Gamma)^{-1} \Gamma^T P_c \Phi \quad (8)$$

The state estimate,  $\underline{\hat{x}}(k)$ , is given by

$$\underline{\hat{x}}(k) = \underline{\hat{x}}(k/k-1) + K_e [y(k) - H\underline{\hat{x}}(k/k-1)] \quad (9)$$

where

$$\underline{\hat{x}}(k/k-1) = \Phi \underline{\hat{x}}(k-1) + \Gamma \underline{u}(k-1) \quad (10)$$

$$K_e = P_e H^T (H P_e H^T + R)^{-1} \quad (11)$$

The covariance of the state estimate,  $P_e$ , satisfies the filtering algebraic Riccati equation

$$P_e = \Phi P_e \Phi^T - \Phi P_e H^T (R + H P_e H^T)^{-1} H P_e \Phi^T + Q \quad (12)$$

*Loop Transfer Recovery (LTR) for discrete-time system*<sup>3-6</sup>. In the typical LQG problem, the parameters

$$\hat{Q}, \quad \hat{R} = \rho^2 I, \quad Q, \quad R = \mu^2 I \quad (13)$$

are the free parameters for adjusting the performance and robustness of the system. It is known that the multivariable linear quadratic (LQ) optimal regulators have impressive robustness properties, including guaranteed classical gain margins of -6db to +∞ db and phase margins of 60 deg. in all channels. But if an Observer or a Kalman filter is used in the implementation of the control, the robustness properties of the system become degraded. The robustness recovery means that if the measurement noise parameter,  $\mu$ , approaches zero, then the loop transfer function of the LQG control at the input loop-breaking point, 1, will approach the loop transfer function of LQR control. That is, the robustness properties for LQG control will be the same as that for the LQR control when the noise parameter,  $\mu$ , approaches zero. The LTR property is also true for the discrete-time system<sup>6</sup>.

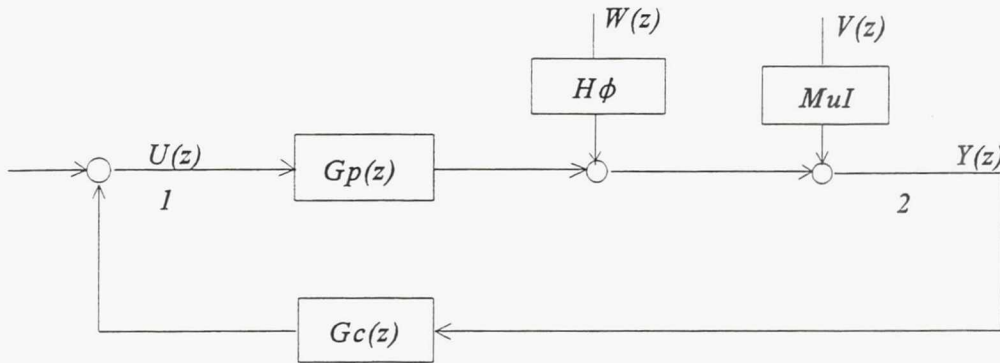


Fig.2 Block Diagram of the optimal LQG digital control with filter observer

Fig.2 shows the block diagram for input and output in terms of the z transformation, where

$$\begin{aligned} \phi(z) &= (zI - \Phi)^{-1} \\ G_c(z) &= zKc[zI - (I - K_e)(\Phi - \Gamma K_c)]^{-1} K_e \\ G_p(z) &= H\phi\Gamma \end{aligned} \quad (14)$$

In terms of mathematical notations, this property can be stated as follows:

If the open-loop transfer function of the system (1-12), has no (finite) zeros in  $\{z: |z| > 1\}$  and  $\det(H\Gamma) \neq 0$ , then

$$\lim_{\mu \rightarrow 0} G_c(z)G_p(z) = K_c\phi(z)\Gamma \quad (15)$$



The  $K_c\phi\Gamma$  is just the open-loop transfer function for the LQR control.

The properties of the loop transfer recovery were also demonstrated through the singular values of the loop transfer functions in the frequency domain in Figs.3 and 4, i.e.,

$$\lim_{\mu \rightarrow 0} \bar{\sigma}(G_c G_p) = \bar{\sigma}(K_c \phi \Gamma) \quad (16)$$

When the sampling time is 1 second for the discrete-time system, as in Fig.3, the frequency  $\omega \in [-\pi, \pi]$ . When the sampling time is 60 seconds, as in Fig.4, the frequency  $\omega \in [-\pi/60, \pi/60]$ . Figs. 3 and 4 show that open-loop property of LQG for this orbit control system are the same as the closed-loop property of their corresponding LQR for most frequencies except the higher frequency region. The variation in the digital LQG open-loop property due to reduction in the value of  $\mu$  is however, less than the variation in a corresponding continuous time system.

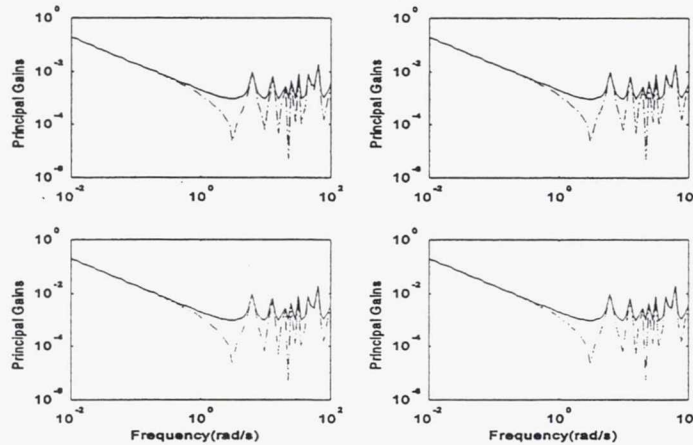


Fig. 3 The Demonstration of the LTR Properties for the Digital Orbit Control system for Sampling time=1 second when  $\mu = 1.0e0, 1.0e-2, 1.0e-4, 1.0e-6$

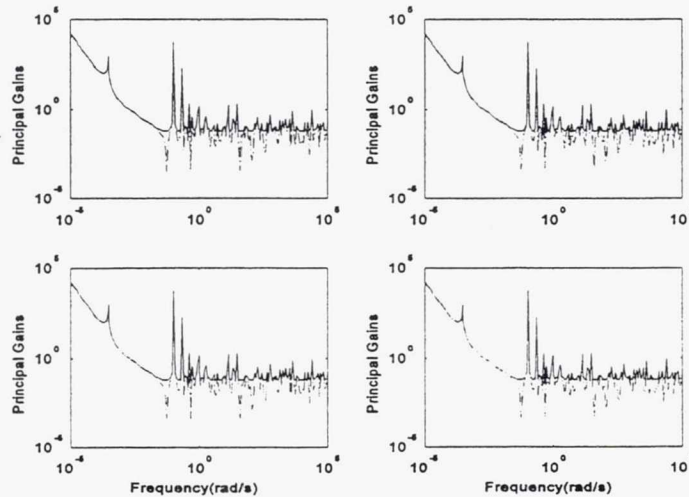


Fig.4 The Demonstration of the LTR Properties for the Digital Orbit Control system for Sampling time=60 second when  $\mu = 1.0e0, 1.0e-2, 1.0e-4, 1.0e-6$

## Implementation of the digital optimal LQG/LTR controller

In order to apply LQG/LTR controller for the autonomous orbit control of a satellite, the constraint of the actuator used for orbit control must be considered. In general, the actuator are constrained by their thrust level and the form of modulation provided by the jets, such as, linear modulation or on-off modulation.

For a given thrust level, the control force compatible with the thrusters can be obtained by adjusting the ratio of the weighting matrices in performance index, i.e. the value of the free parameter,  $\rho$  or by solving saturation constraint LQR problem using Pontryagin's minimum Principle<sup>7,8</sup>.

If the thruster can provide the linear modulation for jet force, it will be compatible with the output of the digital LQG/LTR controller, because this output is pulse-amplitude modulation of the control force. If the thruster is the on-off type, it will be compatible with the pulse-width modulation of the control force, and the original pulse-amplitude modulation of the digital LQG/LTR controller needs to be transformed into pulse-width modulation. This can be done fairly easily, since an equivalent impulse can be provided through pulse-width modulation by the simple division calculation.

The implementation of the autonomous orbit control requires the attitude information of satellite, and attitude control system needs to provide the required attitude for the orbit control. The relationship between orbit and attitude control system is shown in Fig.5.

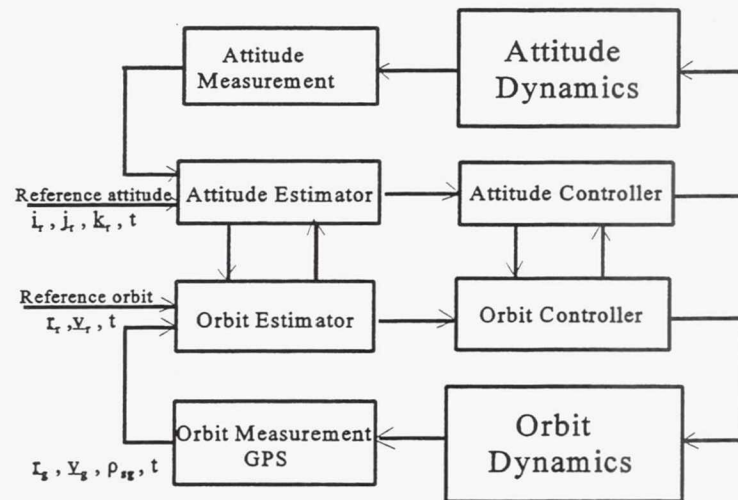


**Fig. 5 The Autonomous Orbit Acquisition/Maintenance System for the Satellite Constellation Using GPS LQG/LTR Controller**

The flow chart of the LQG/LTR controller with GPS measurements for the autonomous orbit control system is shown in Fig.6. The sampling time for the discrete-time orbit dynamics system can be chosen based on the requirements and constraints of an actual satellite design. Simulations have shown that selections of sampling times such as 1 second, 10 second, 1 minute, or a few minutes are all acceptable. This selection will be driven by the memory and speed of the onboard computer.

## SIMULATIONS OF THE LQG/LTR AUTONOMOUS ORBIT CONTROL WITH GPS MEASUREMENTS AND THE NUMERICAL RESULTS

As presented in this paper, the goal of the simulation is to demonstrate the feasibility of the LQG/LTR autonomous orbit control with GPS measurements, and to verify the validity of this controller design. It should, however, be noted that the design being presented in this paper does not minimize the velocity change (and hence the propellant consumption) that will be required for the orbital correction.

The simulations consist of two parts: The first is the simulation of the GPS measurements. These GPS measurements are provided simultaneously by 4 GPS satellites in different orbits of the GPS satellite system. The distance of the GPS satellites from the center of the Earth is assumed to be 26560 km. The target orbit is assumed to be a circular orbit. The height of the target can be assumed based on the standard orbits of the LEOs. The second part of the simulation is the simulation of the digital optimal LQG/LTR controller of the autonomous orbit control system. All these simulations have been done on PC computers in the MATLAB environment.

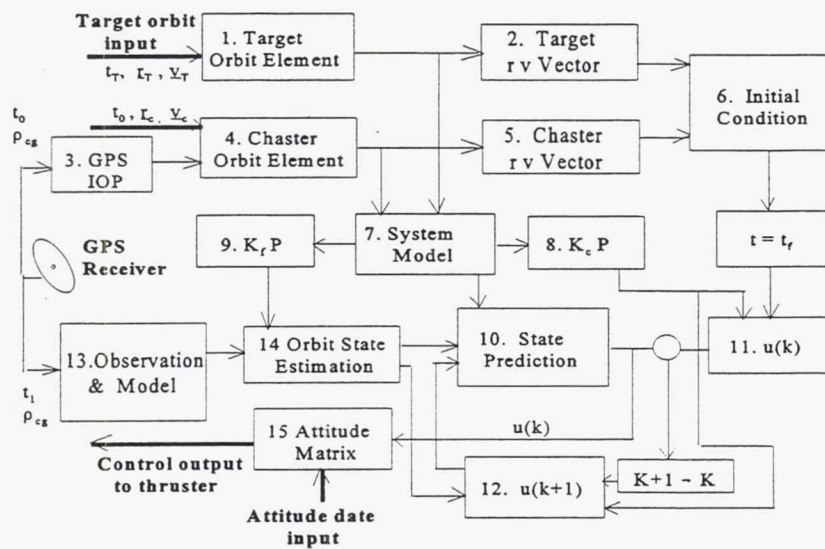


Fig.6 The Flow Chart of the LQG/LTR Controller

The goal of the simulations were:

- i. Study the difference in orbit state transient responses thrust is available only along two axes (tangential and normal) as opposed to availability in all axes.
- ii. Study the difference in the orbit state transient responses to the choice of various sampling times.
- iii. Study the estimation of the orbit state during the control process when there is no information on the initial estimate.



iv. Study the control accuracy and establish that the control system is asymptotically stable.

Fig.7 show the transient responses of the autonomous orbit control for when 3-axes thrust is available. The initial conditions are  $\Delta v_p=49.23\text{m/sec}$ ,  $\Delta r_s=686000\text{ m}$ , and the sampling time  $\Delta T=60\text{ sec}$ . Fig. 7a is the responses for the 6 components of the orbit state vector. Figs.7b and 7c are the estimate and estimate error of the orbit state, respectively. They indicate that the control system is asymptotically stable even with totally unknown initial conditions, and the efficiency of the estimation process is excellent. Fig.7d is the control acceleration and the total  $\Delta v$  for the all control process.

Fig.8 duplicate the simulations for Fig.7, except that in these cases thrusting is available only along two axes. Comparison between Fig.7 and Fig.8 shows that the performance of control system using 3-axes thrusting is better than that of the system with 2-axes thrusting. This is to be expected, since the degree of controllability for 3-axes thrusters is higher than that of 2-axes thruster system. However, it is important to note that both systems are all controllable.

Fig.9 shows the transient responses of the autonomous orbit control for 2-axes thrusters. The initial conditions are  $\Delta v_p=49.23\text{m/sec}$ ,  $\Delta r_s=686000\text{ m}$  and  $\Delta T=30\text{ sec}$ .

Figs.10, 11 and 12 show the transient responses of the orbit state vector and the control accelerations for the various sampling time, i.e.,  $\Delta T = 1\text{ sec.}$ ,  $10\text{ sec.}$ , and  $20\text{ sec.}$  The comparing of these plots show us the obvious - that the performance of the system is the best with  $\Delta T=1\text{ sec.}$  However, longer sampling times will be desirable for implementation, and plots show acceptable performance even with the larger sampling intervals.

## CONCLUSIONS

- (1) This paper the performance of an autonomous orbit acquisition and maintenance for a satellite constellation design that involves a digital LQG/LTR optimal controller with GPS measurements. This design can implement the autonomous on-board real-time closed-loop feedback orbit control for the acquisition and maintenance of a satellite constellation. The input to this control system is the GPS information data (3 code pseudo ranges) and the output of this system is the optimal LQG/LTR control law for closed-loop feedback. It has been shown that this control system is completely controllable and completely observable. The closed-loop feedback system is also asymptotically stable.
- (2) The Loop Transfer Recovery properties for this discrete-time system have been presented. The digital system has very good performance and robustness which is similar to LQR controller for most frequency ranges.
- (3) The simulation of the digital LQG/LTR autonomous orbit control with GPS measurements have been presented. Simulation results confirm that it is feasible to use the digital LQG/LTR controller with GPS measurements for implementing the autonomous orbit maintenance and acquisition system for a satellite constellation. The simulations also show the differences due to differences in thruster availability, and the variations in sampling times. While performances are best with thruster availability along all three axes and with the shortest sampling times, the performances were very satisfactory even with 2-axes thruster availability and larger sampling times. This autonomous control system can be directly applied to low Earth orbits, and would be very suitable for application to the commercial communication satellite systems that are being currently proposed.

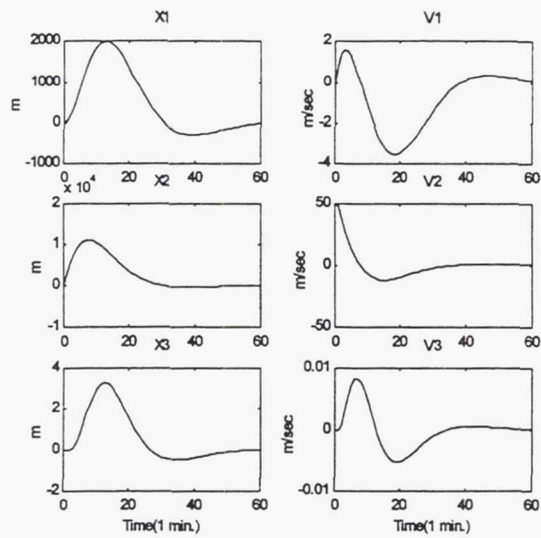


Fig. 7a. The orbit state vector

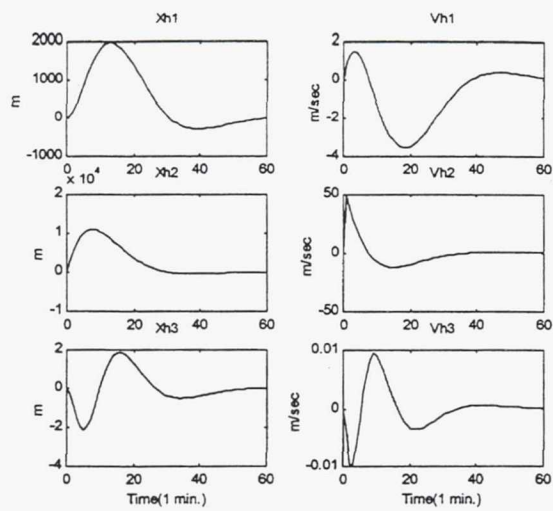


Fig. 7b. The estimate of the orbit state

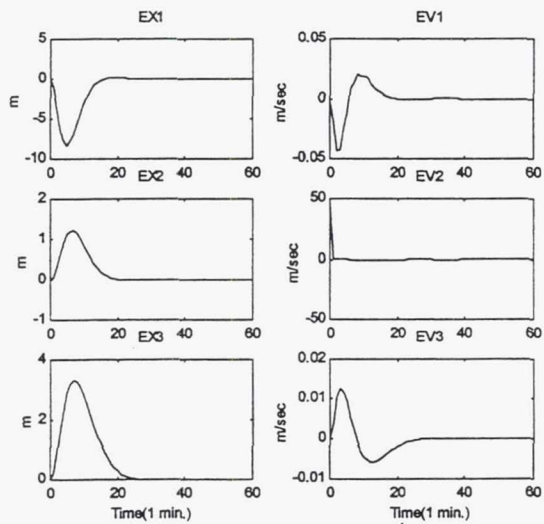


Fig. 7c. The error of the estimation

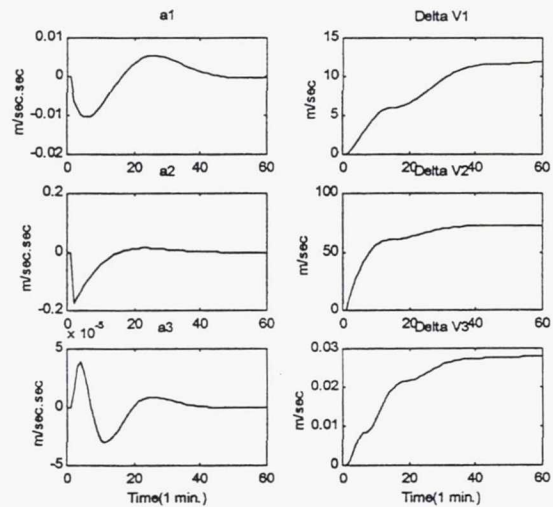


Fig. 7d. The control acceleration and  $\Delta v$

**Fig. 7. The Transient Responses of the Autonomous Orbit control for 3-Thrusters and  $\Delta T=60$  sec**

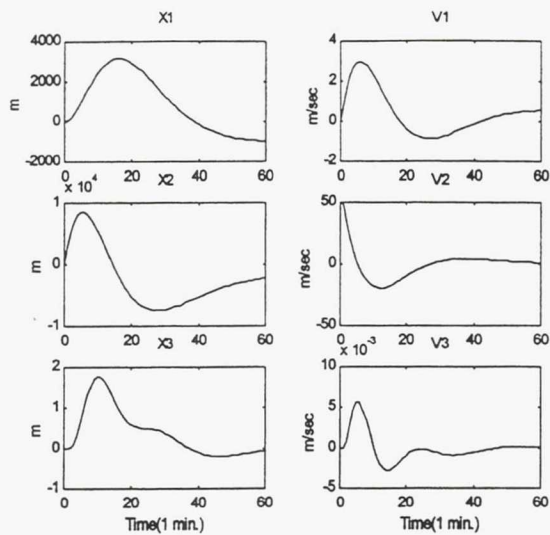


Fig.8a. The orbit state vector

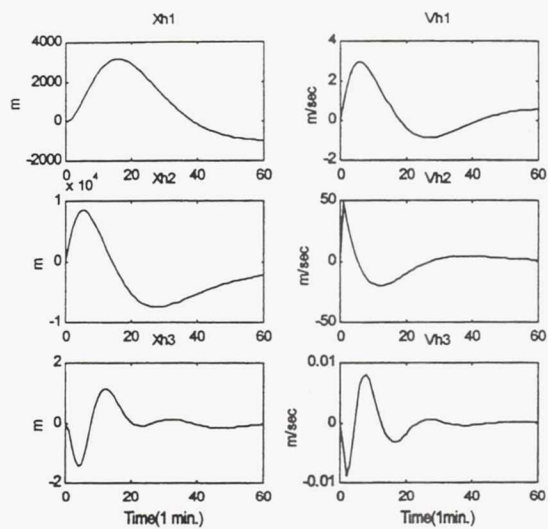


Fig.8b. The estimate of orbit state

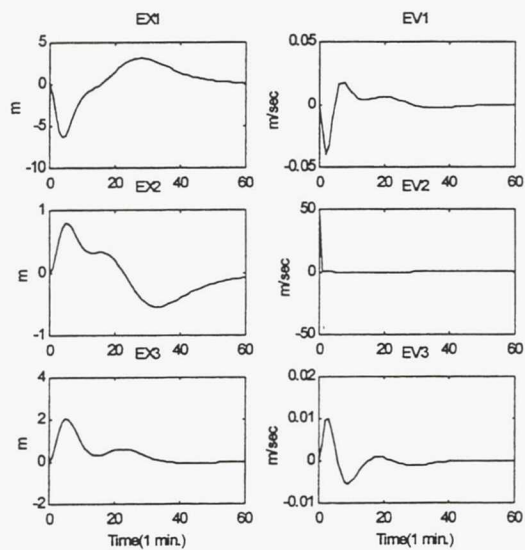


Fig.8c. The error of the estimation

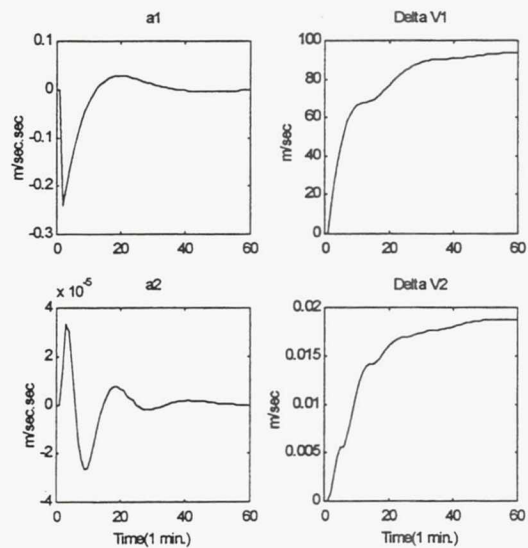


Fig.8d. The control acceleration and  $\Delta v$

**Fig.8 The Transient Responses of the Autonomous Orbit control for 2-Thrusters and  $\Delta T=60$  sec**



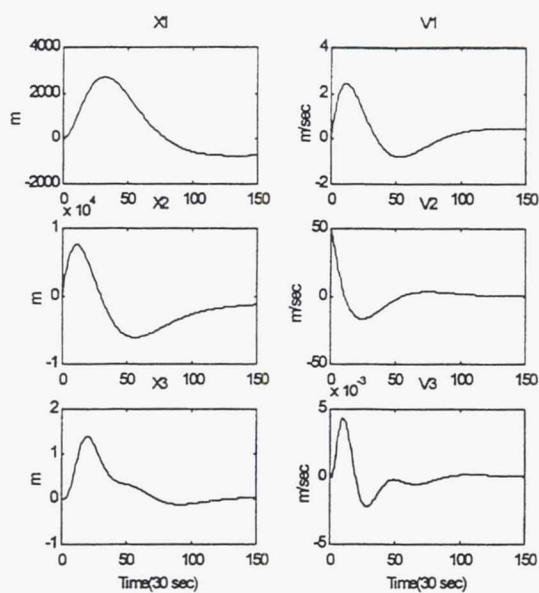


Fig. 9a. The orbit state vector

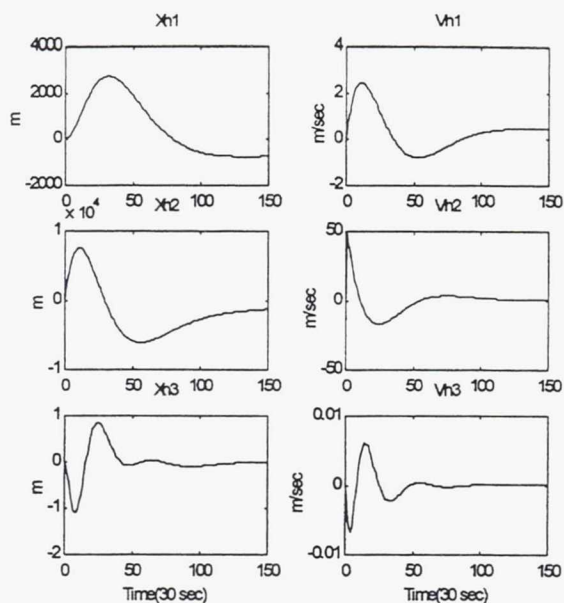


Fig.9b. The estimate of the orbit state

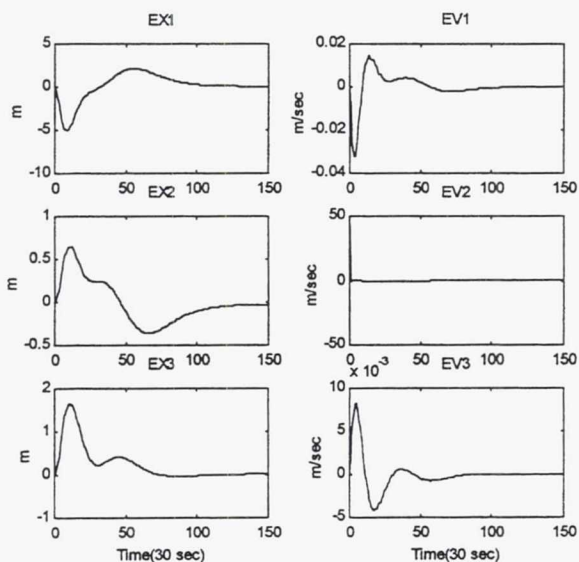


Fig.9c. The error of the estimation

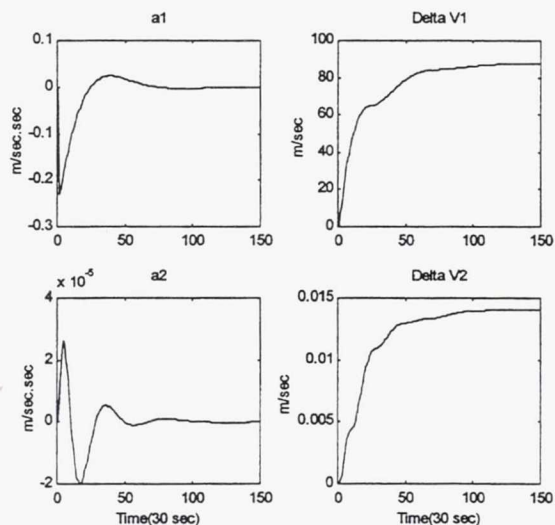


Fig.9d. The control acceleration and  $\Delta v$

**Fig.9 The Transient Responses of the Autonomous Orbit control for 2-Thrusters and  $\Delta T=30$  sec**

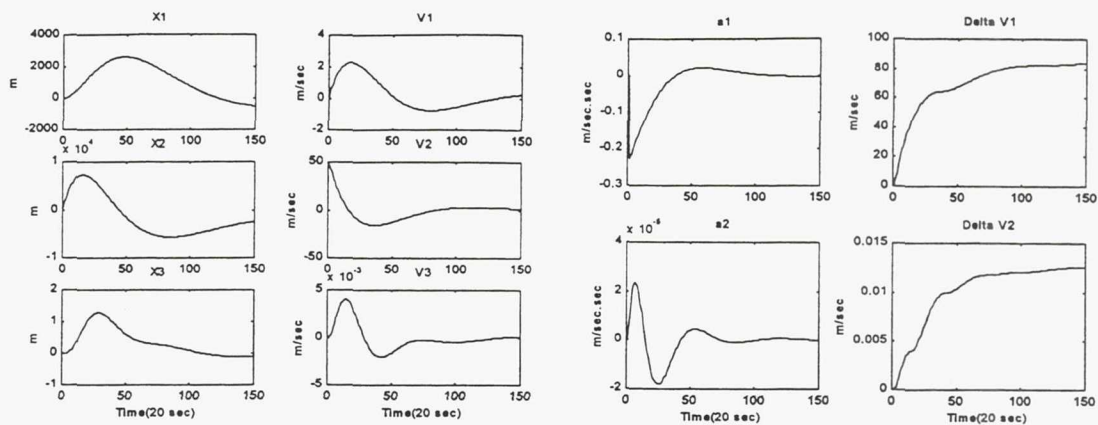


Fig.10 The Transient Responses of the Autonomous Orbit control for 2-Thrusters and  $\Delta T=20$  sec

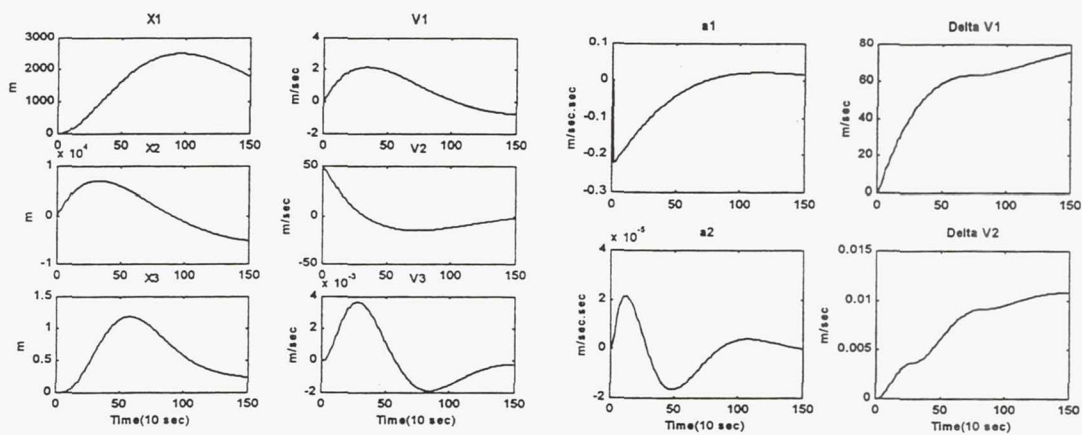


Fig.11 The Transient Responses of the Autonomous Orbit control for 2-Thrusters and  $\Delta T=10$  sec

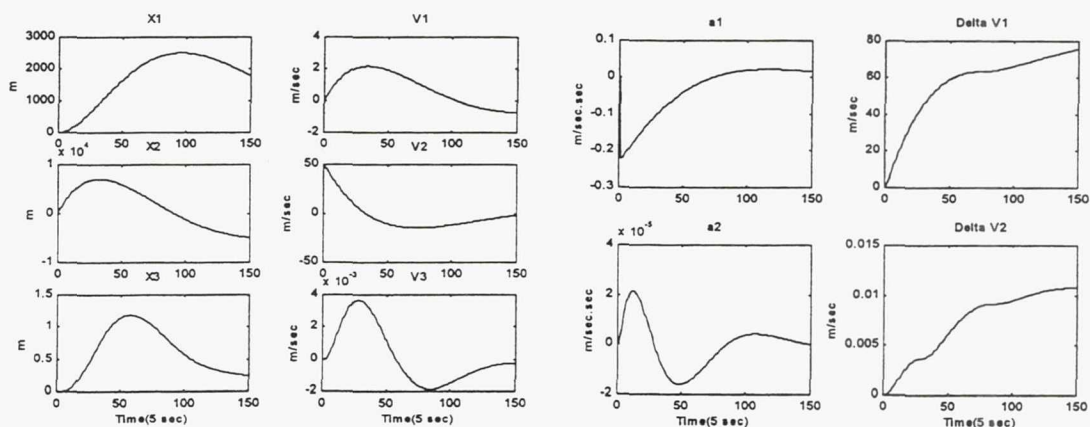


Fig.12 The Transient Responses of the Autonomous Orbit control for 2-Thrusters and  $\Delta T=5$  sec

## ACKNOWLEDGMENT

This paper is based on the Research Project currently being sponsored by the United States Air Force, Air Force Research Laboratory - Phillips Research Site, Kirtland AFB, New Mexico 87117-6008

## REFERENCES

- [1] B. W. Parkinson and J. J. Spilker Jr., Ed., Global Positioning System: Theory and Applications, Vol. 1-2, *Progress in Astronautics and Aeronautics*, Paul Zarchan, Editor-in-Chief, Volume 163, 1996.
- [2] P. S. Mybeck, *Stochastic Model, Estimation and Control*, Vol. 3, Academic Press, New York, 1982.
- [3] J. C. Doyle and G. Stein, "Robustness with Observers," *IEEE Transactions on Automatic Control*, AC-24, No.4, pp. 607-611, Aug. 1979.
- [4] J. C. Doyle and G. Stein, "Multivariable Feedback Design: Concepts for a Classical/Modern Synthesis," *IEEE Trans.*, Vol. 32, No. 1, pp.105-114, Feb. 1987.
- [5] J. M. Maciejowski, *Multivariable Feedback Design*, Addison-Wesley Publishing Company, 1989.
- [6] Guang Q. Xing and Peter M. Bainum, "The LQG/LTR Methodology for Discrete-Time Systems," IAF-92-0039, 43<sup>rd</sup> Congress of the International Astronautical Federation, Aug. 28-Sept. 5, 1992, Washington, DC.
- [7] R. E. Skelton, *Dynamic Systems Control*, John Wiley & Sons, New York, 1988.
- [8] R. J. Helgeson and P. W. Szustak, "Saturation Constrained LQR," *Proceedings of the 10<sup>th</sup> VPI & SU Symposium*, Blacksburg, Virginia, May 8-10, 1995, pp 25-36.



## RELATIVE NAVIGATION FOR SPACECRAFT FORMATION FLYING

Kate R. Hartman,<sup>\*\*</sup> Cheryl J. Gramling,<sup>\*</sup> Taesul Lee,<sup>†</sup>  
David A. Kelbel,<sup>‡</sup> and Anne C. Long<sup>¶</sup>

The Goddard Space Flight Center Guidance, Navigation, and Control Center (GNCC) is currently developing and implementing advanced satellite systems to provide autonomous control of formation flyers. The initial formation maintenance capability will be flight-demonstrated on the Earth-Orbiter-1 (EO-1) satellite, which is planned under the National Aeronautics and Space Administration New Millennium Program to be a coflight with the Landsat-7 (L-7) satellite. Formation flying imposes relative navigation accuracy requirements in addition to the orbit accuracy requirements for the individual satellites. In the case of EO-1 and L-7, the two satellites are in nearly coplanar orbits, with a small difference in the longitude of the ascending node to compensate for the Earth's rotation. The GNCC has performed trajectory error analysis for the relative navigation of the EO-1/L-7 formation, as well as for a more advanced tracking configuration using cross-link satellite communications. This paper discusses the orbit determination and prediction accuracy achievable for EO-1 and L-7 under various tracking and orbit determination scenarios and discusses the expected relative separation errors in their formation flying configuration.

### INTRODUCTION

National Aeronautics and Space Administration (NASA) Enterprises are recognizing the advantages of flying multiple satellites in coordinated virtual platforms and constellations to accomplish science objectives. Formation flying techniques and space vehicle autonomy will revolutionize space and Earth science missions and enable many small, inexpensive satellites to fly in formation and gather concurrent science data.

The Guidance, Navigation, and Control Center (GNCC) at the Goddard Space Flight Center (GSFC) maintains a cutting-edge technology program that enhances satellite performance, streamlines processes, and ultimately enables cheaper science. Technology focus areas within the

---

<sup>\*\*</sup> Assistant Chief for Technology, Guidance, Navigation, and Control Center, Code 570, Goddard Space Flight Center, Greenbelt, Maryland 20771. Phone: (301) 286-5696; FAX: (301) 286-1718. AIAA Member.

<sup>\*</sup> Aerospace Engineer, Flight Dynamics Analysis Branch, Code 572, Goddard Space Flight Center, Greenbelt, Maryland 20771. AIAA and AAS Member.

<sup>†</sup> Senior Principal Engineer, Applied Research Department, Computer Sciences Corporation, 10110 Aerospace Road, Lanham-Seabrook, Maryland 20706. AIAA Member.

<sup>‡</sup> Member of Technical Staff, Applied Research Department, Computer Sciences Corporation, 10110 Aerospace Road, Lanham-Seabrook, Maryland 20706. AIAA Member.

<sup>¶</sup> Senior Consulting Engineer, Applied Research Department, Computer Sciences Corporation, 10110 Aerospace Road, Lanham-Seabrook, Maryland 20706. AIAA and AAS Member.

GNCC encompass control system architectures, sensor and actuator components, propulsion, electronic systems, design and development of algorithms, embedded systems, and space vehicle autonomy. Through collaboration with government, universities, non-profit organizations, and industry, the GNCC incrementally develops key technologies that conquer NASA's challenges.

The GNCC is currently providing innovative technology solutions on two NASA missions associated with formation flying and coordinated virtual platforms. The New Millennium Program (NMP) Earth Orbiter (EO)-1 mission, scheduled for launch in 1999, will demonstrate key aspects of formation flying, and the Earth Observing System (EOS)-AM1, scheduled for launch in 1998, will perform coordinated science observations with Landsat-7 (L-7). The essential formation control requirement on EO-1 is to maintain a 1-minute separation from L-7 to within a tolerance of 6 seconds. In addition, L-7 will fly over the EOS-AM1 groundtrack 15 minutes later to provide coordinated observations between the two satellites. Demonstrations of constellation control of L-7 and EOS-AM1, autonomous navigation of EO-1 using a spaceborne Global Positioning System (GPS) receiver, and aspects of autonomous formation flying on EO-1 are key initial steps toward enabling fully autonomous control of a group of small, single-instrument satellites that can collect scientific data as if all of the instruments were on a single, large platform. This "virtual platform" approach lowers the total risk, increases science data collection, and adds considerable flexibility to future NASA Earth and space science missions.

To support the EO-1/L-7 formation flying experiment, GNCC has performed trajectory error analysis for the relative navigation of EO-1 with respect to L-7. In addition, central to the achievement of the strategic goal of virtual platforms are cross-link satellite communications and autonomous relative navigation. Although neither of these technologies will be demonstrated on the NMP EO-1 flight, the GNCC has investigated an advanced approach for autonomous relative navigation using cross-link satellite measurements. This approach extends the Onboard Navigation System (ONS), developed by GSFC to support single satellite autonomous navigation, to process tracking measurements derived from a cross-link satellite signal. This paper discusses the orbit determination and prediction accuracy achievable for EO-1 and L-7 under various tracking and orbit determination scenarios and discusses the expected relative separation errors in their formation flying configuration.

## **RELATIVE NAVIGATION ACCURACY REQUIREMENTS FOR THE EO-1 AND L-7 FORMATION**

Formation flying refers to the coordinated control of a group of satellites such that the satellite positions relative to a reference position (e.g., one of the satellites) are maintained according to some predetermined constraints dictated by the overall mission goals, usually a separation distance and formation tolerance. The separation distance and formation tolerance for coordinated Earth sensing missions are typically on the order of hundreds and tens of kilometers, respectively, but may reduce to the order of meters in the future.

Formation flying requires both "formation sensing" and "formation control". Formation sensing provides a measure of the satellite relative positions as input to the formation control algorithms, which compute the maneuvers required to maintain the formation. The most straightforward relative navigation approach computes the satellite relative positions by differencing the absolute position vectors of each satellite. In such a case, the target or command satellite would have to obtain accurate position vectors for not only itself, but also for the chase satellites in the formation either via ground uplink or a satellite-to-satellite communications cross-link. While each satellite may have its own onboard ephemeris knowledge or onboard navigation system, a



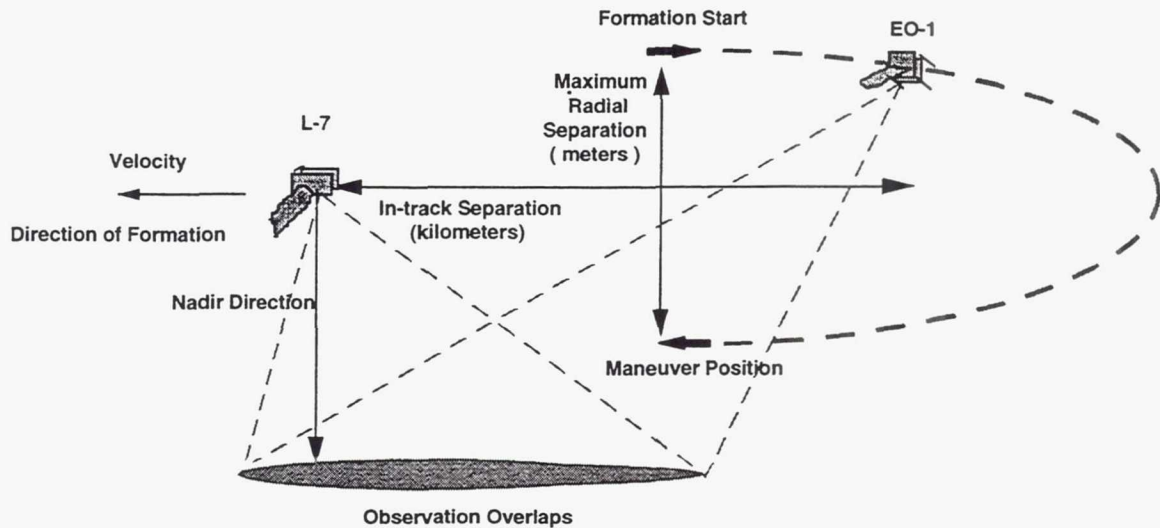


**Figure 1 Example of Relative Separation Evolution For the EO-1/L-7 Formation**

means to communicate the knowledge from one satellite to another is required to determine the relative separations.

Formation flying EO-1 with L-7 will enable coordinated, coregistered observations of the reference geographic sites for scientific comparison of the imaging sensors onboard the satellite. The two satellites will be placed in nearly coplanar orbits, with a 0.25 degree difference in the right ascension of the ascending node to compensate for the Earth's rotation. The separation between the satellites is nominally 450 kilometers ( $\approx 1$  minute). The formation tolerance is approximately  $\pm 40$  kilometers ( $\approx 6$  seconds).

Figure 1 illustrates one proposed formation control strategy for the EO-1/L-7 formation.<sup>1</sup> The initial EO-1 position is behind L-7 at the minimum acceptable in-track separation ( $\approx 410$  kilometers) and the initial altitude is about 25 meters above that of L-7 (nominally at a 705-kilometer altitude). Initially, the relative in-track separation increases because of the longer period of the higher EO-1 satellite. However, due to its larger area-to-mass ratio, the EO-1 orbit decays faster than L-7, which reduces the initial altitude separation and decreases the relative orbital velocities. The proposed strategy is to select the initial altitude separation such that the maximum acceptable separation ( $\approx 490$  kilometers) is not reached before the radial separation reaches zero. When the EO-1 orbit decays below the L-7 altitude, the in-track separation will decrease. When the minimum acceptable separation is reached, a maneuver is executed to restore EO-1 to the initial formation configuration. To reduce the frequency of the formation control maneuvers to approximately weekly, the semimajor axis difference, or equivalently the radial separation, between the two satellite must be maintained within approximately  $\pm 25$  meters. To maintain a radial separation of  $\pm 25$  meters, the relative radial separation must be known to about 5 meters. The change in velocity that is needed to maintain a  $\pm 25$ -meter radial separation is approximately 2.7 centimeters per second in the in-track direction. Therefore, to accurately plan and perform this maneuver, the relative in-track velocity must be known to about 0.5 centimeters per second.

To monitor the state of this formation, the navigation software must compute the relative separations of one satellite with respect to the other. In the planned EO-1/L-7 formation-flying configuration, the L-7 position is periodically determined on the ground using NASA's Tracking



and Data Relay Satellite System (TDRSS). A predicted L-7 state vector is uplinked to EO-1. L-7 executes its nominal mission independent of EO-1, including its ground-track control maneuvers.

EO-1 will use a Global Positioning System (GPS) receiver to compute its real-time position and velocity. NASA's Ground Network (GN) will provide a backup tracking capability for EO-1. The EO-1 satellite will host autonomous formation flying software to adjust its orbit to maintain the desired formation with respect to L-7.

Table 1 lists the relative navigation accuracy requirements for the EO-1/L-7 formation.

**Table 1**  
**RELATIVE NAVIGATION ACCURACY REQUIREMENTS**  
**FOR EO-1/L-7 FORMATION FLYING**

Description	Requirement (3-sigma)
In-track relative separation	1 minute ( $\approx$ 450 kilometers)
Radial separation	$\pm$ 25 meters
Mean radial separation tolerance	$\pm$ 5 meters
In-track separation tolerance	$\pm$ 6 seconds ( $\approx$ 40 kilometers)
Ground-track separation tolerance	$\pm$ 3 kilometers (in cross-track direction)

## RELATIVE NAVIGATION ACCURACY FOR THE EO-1 AND L-7 FORMATION

In this section, accuracy estimates are provided for computation of the relative separation of EO-1 with respect to L-7 in the radial (R), in-track (I), and cross-track (C) directions. It is straightforward to estimate the individual satellite orbit determination and prediction errors. Orbit determination and error analysis programs, such as the Goddard Trajectory Determination System (GTDS) and the Orbit Determination Error Analysis System (ODEAS), are based on the concept of processing one user satellite at a time. To assess the relative positioning errors, these independently-derived errors must be combined. To properly combine independently-estimated orbital errors to get relative errors, a breakdown of the total errors into its component errors is needed. These component errors are contributed by various error sources.

In the case of EO-1 and L-7, the tracking measurement errors for the two satellites are statistically uncorrelated, since they will be tracked using different tracking systems with different tracking schedules. Therefore, the individual satellite errors arising from measurement noise and uncertainties in measurement biases and tropospheric and ionospheric refraction delay are uncorrelated. Such errors can be combined using the root-sum-square (RSS) method.

On the other hand, the satellite orbital errors arising from satellite force model errors can be considered fully correlated since the two satellites are following each other closely in essentially the same orbit, thereby always experiencing the influence of essentially the same dynamic environment. Examples of such errors are those due to uncertainties in geopotential, atmospheric drag, and solar radiation pressure models. When computing the relative errors, the orbital error terms for the two satellites arising from correlated dynamic error sources are algebraically subtracted before combining with those arising from the measurement-related error sources.

This procedure can be symbolically expressed as follows:

$$\text{Relative Error} = \left( \sum_{\text{meas error}} \left[ (\text{EO} - 1)^2 + (\text{L} - 7)^2 \right] + \sum_{\text{dyn error}} \left[ (\text{EO} - 1) - (\text{L} - 7) \right]^2 \right)^{\frac{1}{2}} \quad (1)$$

### Relative Separation Errors Based on Previous Studies

This section presents an estimate of the relative separation errors for the EO-1/L-7 formation based on previous studies of orbit determination (OD) accuracies for the Landsat-4 (L-4) and L-7 missions. These studies assumed TDRSS tracking or GN tracking and used either orbit error covariance analysis or analysis of the orbit determination solutions obtained using real tracking data. The definitive OD accuracy results are presented in Table 2.

**Table 2**  
**DEFINITIVE ORBIT DETERMINATION POSITION ERRORS FOR L-4 AND L-7**

Description	Tracking Schedule	Radial (meters)	In-Track (meters)	Cross-Track (meters)	RSS (meters)
<b>Covariance Analysis Results (Maximum 3σ)</b>					
<u>Arc Length (Hours)</u>					
30	35 TDRSS passes	13	14	6	16
34	12 TDRSS passes	7	33	15	37
34	7 GN passes	10	55	3	56
48	9 GN passes	3.5	30	8	32
<b>Definitive OD Results (Maximum Differences)</b>					
<u>Arc Length (Hours)</u>					
34 (*)	21 TDRSS passes	1.4	x	x	7
34 (+)	11 TDRSS passes	11	50	25	54
34 (\$)	11 TDRSS passes	3	31	8	31

\*: 34-hour high-quality reference solutions ; results shown represent maximum definitive position overlap

+: Maximum position comparison between reference solutions and solutions obtained using nominal TDRS orbit solutions

\$: Maximum position comparison between reference solutions and solutions obtained using high-quality TDRS orbit solutions

x: Data not available

The covariance analysis results listed in Table 2 were based on GSFC Flight Dynamics Division internal memoranda. These covariance results provide maximum 3-sigma error estimates. Radial errors vary from 3.5 to 13 meters and in-track errors vary from 14 to 55 meters. The first of three definitive OD results presented in Table 2 is taken from a study performed using an unusually dense TDRSS tracking of L-4.<sup>2</sup> These solutions were obtained using 21 tracking contacts over the 34-hour OD arc, approximately twice the nominal tracking. These results are the maximum position differences between two consecutive definitive OD arcs in the 10-hour overlapping region. Such overlap comparisons are often used as a measure of definitive OD consistency. These solutions produced maximum radial overlap of 1.4 meters and maximum total overlap of 7 meters. Nominal L-4 definitive OD accuracies would be 5- to 10-times larger than these results. In addition, these solutions were obtained by simultaneously estimating the



user and two TDRS spacecraft that were used as relays. To improve the overall OD accuracy for the user and TDRSs, high-density Bilateral Ranging Transponder System (BRTS) tracking was also included in the solution. In normal operational OD scenarios, TDRS OD solutions are performed first without any user tracking data, and then the user OD is performed using the TDRS OD solutions.

The other two OD accuracy results listed in Table 2 are based on a study in which two sets of L-4 OD solutions (obtained using more nominal OD scenarios) were compared with the solutions obtained using the high-density TDRSS tracking discussed above.<sup>3</sup> The first of the two solutions were obtained using TDRS solutions with nominal accuracy, the second using high-quality TDRS solutions. The radial and in-track position errors associated with these solutions are seen to vary from 3 to 11 meters, and 31 to 50-meters, respectively. These errors are comparable to those obtained using the covariance analysis.

The quality of the orbit determination solutions improves when the number of tracking contacts in a given orbit determination arc increases. In the case of TDRSS tracking, the solutions improve further when better quality TDRS state vectors are used. Except for the special case of high-density tracking of L-4, the number of tracking contacts assumed or used in the studies is approximately 10, and the orbit determination arc lengths chosen were 34 or 48 hours. TDRSS tracking and GN tracking produced solutions with comparable quality. Table 2 shows that the OD accuracies for Landsat spacecraft achievable using nominal TDRSS or GN tracking will be in the range of 3 to 13-meters in the radial direction and 30 to 55-meters in the in-track direction.

Table 3 lists the worst case maximum  $3\sigma$  or position difference errors (in meters) from Table 2. In addition, Table 3 lists the EO-1 orbit determination accuracy expected based on processing GPS Standard Positioning Service (SPS) measurements using a sophisticated Kalman filter based on the ONS algorithms, with GPS Selective Availability (SA) at typical levels. The GPS accuracy estimates are based on GSFC Flight Dynamics Analysis Branch's evaluation of the GPS Enhanced Orbit Determination Experiment (GEODE) capability for the TOPEX/Poseidon and Explorer Platform/Extreme Ultraviolet Explorer satellites.<sup>4</sup> Typically unfiltered GPS receiver satellite solution errors are about ten times larger.

**Table 3.**  
**DEFINITIVE POSITION ACCURACY USING**  
**DIFFERENT ORBIT DETERMINATION OPTIONS**

Orbit Determination Option	Maximum $3\sigma$ Definitive Position Accuracy (meters)			
	Radial	Cross-track	In-track	RSS
Filtered GPS (for EO-1)	11	10	35	35
GN (for EO-1)	10	8	55	56
TDRSS (L-7)	11	25	50	54

A worst case estimate for the relative separation errors associated with the use of these orbit determination options for EO-1 and L-7 can be approximated by forming the root sum square (RSS) of the error for each spacecraft. Comparing the resulting relative position accuracies to the relative separation tolerances listed in Table 1 indicates that even when the worst case position errors given in Table 3 are assumed, the in-track and ground-track separation tolerances can be easily met. However, the requirement on the mean radial separation will not be satisfied easily.



In addition, if the orbit determination solutions are computed on the ground and predicted navigation data are uplinked to the satellite, the prediction accuracy is degraded depending upon the method by which the uplink is prepared. Thus, an additional error margin is needed when the OD solutions are generated on the ground. Reference 5 provides estimates of prediction accuracies for these satellites based on orbit determination experience.

### Covariance Analysis to Estimate Relative Separation Errors

To evaluate the impact of the correlation of the dynamic errors on the relative navigation accuracy, additional covariance analysis was performed using ODEAS. The objective of this new study was to correctly estimate the relative separation errors of EO-1 with respect to L-7 using Equation (1) and to identify the major error sources for the relative separation errors using standard tracking methods. At the time of this analysis, there was an interest in examining the backup to GPS receiver navigation for EO-1, which consists of GN tracking using a maximum of four contacts per day from three ground stations (Wallops, Poker Flat, and Spitzbergen). Tracking for L-7 consisted of eight TDRSS 10-minute contacts per day via two TDRSSs. Table 4 lists the uncertainties used for the major error sources included in this analysis.

**Table 4**  
**3-SIGMA ERROR UNCERTAINTIES**

Error Source	Uncertainties (3-sigma)	
	EO-1	L-7
Range-rate noise (meters per second)	0.001	0.0028
Radial/in-track/cross-track TDRS position (meters)		10/100/40
Ground antenna position per axis (meters)	3.0	3.0
Ground-to-satellite ionospheric delay (percent)	100	100
TDRS-to-satellite ionospheric delay (percent)		100
Ground-to-satellite tropospheric delay (percent)	45	45
Earth's gravitational constant (parts per million)	0.03	0.03
70x70 Joint Goddard Model 2 (JGM2) for Earth's nonspherical gravity (unitless))	3*(JGM2 clone -JGM2)	3*(JGM2 clone -JGM2)
Daily solar flux for mean solar flux of 200 Janskys		
Days 1, 2, 3 of definitive arc (percent)	5	5
Days 1, 2, 3 of prediction (percent)	14, 22, 32	14, 22, 32
81-day solar flux for mean solar flux of 200 Janskys		
Days 1, 2, 3 of definitive arc (percent)	9.1, 9.4, 9.6	9.1, 9.4, 9.6
Days 1, 2, 3 of prediction (percent)	9.8, 10.1, 10.3	9.8, 10.1, 10.3

Orbital elements for the two satellites were chosen such that the two trajectories have a nominal in-track separation of 1 minute and the L-7 ground-track retraces that of EO-1. The EO-1 orbit is initially higher than the L-7 orbit with a mean radial difference of 25 meters. The area-to-mass ratio used for EO-1 (0.0146 meters<sup>2</sup>/kilogram) was about twice that of L-7 (0.0067 meters<sup>2</sup>/kilogram), so the EO-1 orbit decays faster (due to the stronger drag) than the L-7 orbit. Note that the most recent EO-1 satellite design yields an area-to-mass ratio of only 0.008 meters<sup>2</sup>/kilogram.

Over a 6-day period, 3-day-definitive and 3-day-predictive ephemeris errors for both L-7 and EO-1 were computed using the batch covariance analysis capability of ODEAS. These

results are summarized in Table 5. This table consists of three sections: the top section lists the definitive and predictive errors for EO-1, the middle section lists the errors for L-7, and the bottom section the relative separation errors that were computed using Equation (1).

**Table 5**  
**MAXIMUM 3-SIGMA POSITION AND VELOCITY ERRORS**

Description	Definitive Ephemeris		Predictive Ephemeris					
			1 day		2 days		3 days	
	Position (m)	Velocity (cm/sec)	Position (m)	Velocity (cm/sec)	Position (m)	Velocity (cm/sec)	Position (m)	Velocity (cm/sec)
<b>EO-1 Error (Maximum <math>3\sigma</math>)</b>								
Radial	6.8	2.2	7.0	21.0	11.6	101.4	21.0	286.3
In-track	27.1	0.7	197.5	0.7	965.6	1.1	2701.9	1.9
Cross-track	13.5	1.4	11.3	1.2	11.3	1.2	11.3	1.2
<b>L-7 Error (Maximum <math>3\sigma</math>)</b>								
Radial	6.7	4.0	7.3	10.7	8.9	49.0	11.8	134.9
In-track	43.1	0.7	101.7	0.7	467.5	0.8	1272.8	0.9
Cross-track	46.3	4.9	48.5	5.1	51.5	5.4	54.4	5.7
<b>Relative Separation Error (Maximum <math>3\sigma</math>)</b>								
Radial	8.4	4.4	7.4	11.9	9.1	56.1	12.6	155.6
In-track	48.8	0.9	112.1	0.7	534.9	0.8	1468.1	1.1
Cross-track	47.1	4.9	49.3	5.2	52.3	5.5	55.3	5.8

Examination of these results indicates that the definitive EO-1 cross-track and in-track position errors are smaller than those of L-7. This may be explained by observing that the L-7 OD includes TDRSS-related error sources, such as satellite-to-satellite ionospheric refraction errors and TDRS ephemeris errors, which are absent in EO-1 tracking. These TDRSS-related error sources are the major error contributors in the definitive period for L-7. Using the height-of-ray-path (HORP) editing technique may reduce the contributions due to the satellite-to-satellite ionospheric refraction effects. Because HORP editing was not used for these solutions, the L-7 errors may be somewhat pessimistic. In addition, the predictive EO-1 in-track position errors are approximately twice as large as those of L-7. This is due to the fact that at the relatively high solar flux level of 200 Janskys most of the predictive error arises from atmospheric drag modeling errors due to solar flux uncertainty. Because the area-to-mass ratio assumed for EO-1 is about twice that of L-7, the impact of atmospheric drag modeling errors on EO-1 is twice as large as for L-7.

The relative separation errors between EO-1 and L-7, shown in the bottom section of Table 5, were computed by combining the EO-1 and L-7 error budgets such that the errors due to the correlated dynamic errors (such as Earth gravity and solar flux uncertainties) were algebraically subtracted and errors due to the statistically uncorrelated measurement related errors (such as measurement noise and atmospheric refraction effects) were combined using the RSS method.

The maximum radial separation errors for the definitive and 1-day predictive periods are 8.4 meters and 7.4 meters (3-sigma), respectively. Although the first-day predictive error is smaller than the error for the definitive period in this particular simulation, it may not be a



feature that can be expected in general for other simulations. These results show that the predictive radial separation errors increase slowly reaching 12.6 meters for the 3-day prediction, considerably smaller than the individual EO-1 radial position error. Similarly, the predictive cross-track separation errors increase slowly with the length of the prediction period. However, the in-track position separation errors steadily increase outside the definitive period, but remain considerably smaller than the individual EO-1 in-track position errors. This behavior indicates that there is considerable cancellation of correlated dynamic errors in the computation of the relative separation errors.

Because the atmospheric drag coefficient is estimated over the definitive OD arc, the solar flux uncertainties do not contribute significantly to the definitive ephemeris errors. However, beyond the definitive arc, the in-track position errors for low-Earth satellites grow rapidly due to the solar flux uncertainties. The increase in the relative radial and in-track position errors during the prediction period is primarily due to the solar flux uncertainties. On the other hand, the cross-track errors are relatively insensitive to the solar flux uncertainties. Because the actual area-to-mass ratios for EO-1 (0.008) and L-7 (0.0067) will be much closer than the area-to-mass ratios used in this covariance analysis, the cancellation of the individual satellite radial and in-track prediction errors should be more complete and the growth of relative radial and in-track position errors in the 3-day prediction periods should be substantially smaller than those presented in Table 5.

### Relative Navigation Scenarios

Covariance results were used to compute relative navigation accuracies for the following two candidate scenarios for providing relative navigation of EO-1 with respect to L-7:

- Scenario A: The relative separation is computed onboard EO-1 using predicted EO-1 and predicted L-7 navigation data that is computed on the ground and uplinked daily to the satellite.
- Scenario B: The relative separation is computed onboard EO-1 using real-time EO-1 navigation data computed onboard and predicted L-7 navigation data that is computed on the ground and uplinked daily to the satellite.

Table 6 summarizes the resulting relative separation error estimates based on the use of 1-day predicted L-7 ephemerides.

**Table 6**  
**MAXIMUM 3-SIGMA NAVIGATION ERRORS FOR CANDIDATE SCENARIOS**

Error Component	Scenario A Errors			Scenario B Errors		
	EO-1 Predictive	L-7 Predictive	Relative	EO-1 Definitive	L-7 Predictive	Relative
<b>Position (meters)</b>						
Radial	7.0	7.3	7.4	6.8	6.4	6.4
In-Track	197.5	101.7	112.1	27.1	96.7	98.6
Cross-Track	11.3	48.5	49.3	13.5	26.7	28.0
<b>Velocity (centimeters per second)</b>						
Radial	21.0	10.7	11.9	2.2	10.1	10.2
In-Track	0.7	0.7	0.7	0.7	0.7	0.7
Cross-Track	1.2	5.1	5.2	1.4	2.8	2.9



The relative radial errors are similar for both scenarios. In both cases, the relative errors are smaller than the RSS of the individual errors due to the partial cancellation of the dynamic contributions from atmospheric drag modeling errors. These results indicate that a radial separation accuracy of 10 meters is achievable using the nominal tracking configuration for the EO-1/L-7 formation. The relative in-track error for scenario A is much smaller than the RSS of the individual satellite contributions due to the significant cancellation of the contribution from atmospheric drag modeling errors. The relative in-track error for scenario B is nearly equal to the RSS of the individual satellite contributions because the EO-1 in-track dynamic errors are small and therefore provide little cancellation of the L-7 dynamic errors. As a result, the relative in-track separation errors are only slightly larger for scenario A than for scenario B. In both scenarios, the relative cross-track errors are nearly equal to the RSS of the individual satellite contributions because the major cross-track error contributors are uncorrelated measurement-related errors.

The change in velocity that is needed to maintain a  $\pm 25$ -meter radial separation is approximately 2.7 centimeters per second in the in-track direction. Therefore, to accurately plan and perform this maneuver, the relative in-track velocity must be known to about 0.5 centimeters per second. The relative in-track errors for both scenarios are about 0.7 centimeters per second (3-sigma), very close to the accuracy needed to control the formation.

## **AUTONOMOUS RELATIVE NAVIGATION USING CROSS-LINK SATELLITE MEASUREMENTS**

The Flight Dynamics Analysis Branch of GSFC's GNCC has developed an Onboard Navigation System (ONS) for autonomous navigation using TDRSS or GN communications signals.<sup>6,7</sup> The ONS extracts high-fidelity tracking measurements onboard from the forward-link communications signal and processes these measurements to estimate the satellite's current state and to maintain an estimate of the satellite time. By making full use of the communication, time, and computing subsystems already available on many NASA satellites, the ONS is convenient to implement, requiring no additional flight hardware. This section presents a concept for relative navigation using the ONS and projects the navigation accuracy achievable onboard to support formation flying requirements.

The ONS concepts have been extended to support real-time relative navigation to meet formation sensing requirements. Figure 2 illustrates one possible ONS tracking configuration for the coordinated control of a target and one or more chase satellites. In this configuration, the target satellite performs relative navigation of the chase satellites based on Doppler and possibly pseudorange measurements derived from a cross-link communications carrier signal transmitted from the chase to the target satellite. The target satellite hosts the relative ONS algorithms to determine the chase satellite's relative positions with respect to the target. The target state is determined independently using another onboard navigation system (possibly Global Positioning System (GPS) or GN ONS). These orbital state estimates are used in the onboard autonomous maneuver control software hosted on the target satellite to plan the formation maintenance maneuvers for the entire fleet. The target satellite executes the maneuvers required for absolute formation control and the chase satellites execute the maneuvers required to maintain their positions relative to that of the target. In this relative ONS configuration, the ground system's role is reduced to periodic verification of the system performance, providing a significant decrease in operations costs for multiple mission sets.

The GSFC Flight Dynamics Analysis Branch has evaluated the accuracy achievable using a relative ONS for L-7 position determination in support of the EO-1/L-7 formation flying

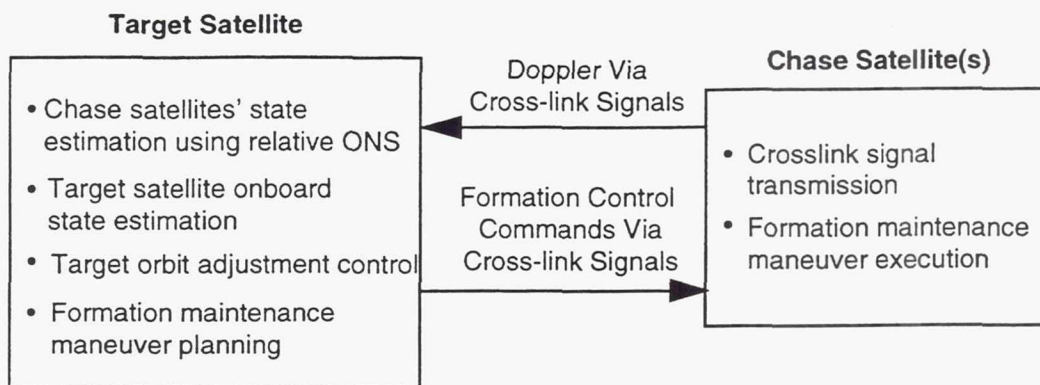


**Figure 2 Relative ONS Tracking Configuration Example**

application. Reference 8 discusses this analysis in detail. In the proposed EO-1/L-7 configuration, L-7 periodically transmits an S-band communications carrier signal that is received by an S-band receiver on EO-1. The receiver on EO-1 accurately measures the relative Doppler and optionally pseudorange on the cross-link signal. The ONS flight software, resident on EO-1, processes the cross-link measurements to compute the L-7 navigation data.

For this evaluation, the reference orbits and cross-link measurements were simulated using nearly identical orbital parameters for the two satellites that produced a 1 minute in-track separation, a 25-meter mean radial separation, and right ascension of the ascending node differences ( $\Delta\text{RAAN}$ ) of 0.0, 0.25, 0.5, 1 and 4 degrees. The relative range-rate between the two satellites results from gravitational acceleration differences due to the satellite relative positions and changing velocity in noncircular orbits and atmospheric drag acceleration differences due to the different area-to-mass ratios of the satellites. The area-to-mass ratio used for EO-1 was approximately twice that of L-7, which augments the relative velocity contribution due to the nonconstant velocity of two noncircular orbits. The drift between the two satellites changes the relative satellite separations inducing a change in the range-rate between the satellites. With these satellites flying relatively close together in identical coplanar orbits, the Doppler profile has low dynamic signature, varying between  $\pm 9$  hertz. Without pseudorange measurements, the relative position of L-7 as the chase vehicle is not directly observable, but must be deduced based on the weak dependence of the relative range-rate on the relative separation.

The performance of the relative ONS was studied as a function of tracking measurement quality, tracking frequency, and relative orbital geometry using simulated tracking measurements. Simulated cases included processing only one-way Doppler and one-way Doppler and pseudorange measurements using prototype relative ONS flight algorithms to estimate the L-7 position and velocity and optionally the atmospheric drag coefficient and measurement biases. The relative ONS algorithms used to process the cross-link data are an extension of the ONS algorithms used with TDRSS and GN carrier signals and GPS navigation signals, modified to process cross-link tracking measurements for estimation of the transmitting (chase) satellite. Two tracking scenarios were studied: 1) two 2-minute cross-link contacts per orbit and 2) three 5-minute cross-link contacts per orbit. Doppler measurements were simulated using three levels of measurement noise: 1 hertz (consistent with nominal temperature compensated crystal oscillator (TCXO) performance), 0.1 hertz (consistent with high quality TCXO performance), and 0.001 hertz (consistent with ultrastable oscillator (USO) performance). Pseudorange measurements were simulated with measurement noise of 5 meters.



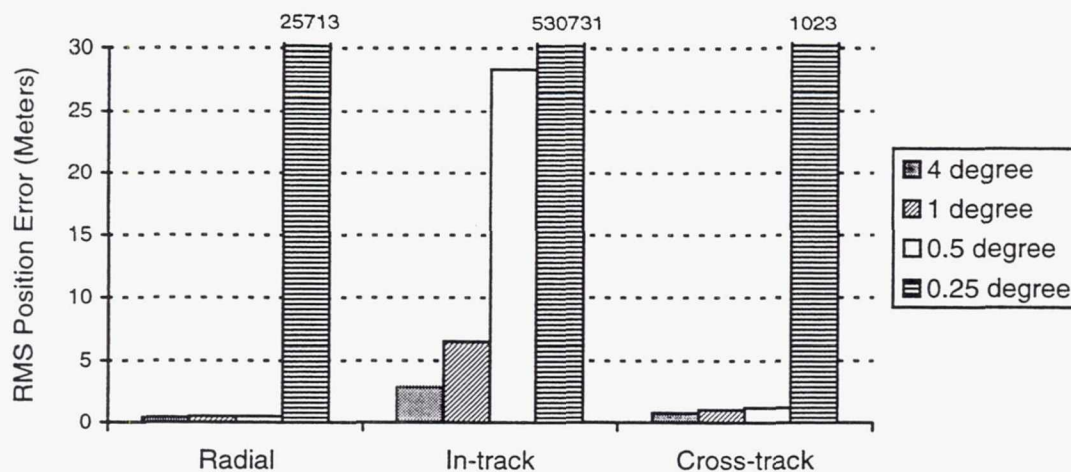


**Figure 3 Comparison of Solutions Obtained Using USO-Quality Doppler Measurements With Plane Separations of 0.25, 0.5, 1 and 4 Degrees**

In the case of coplanar satellites, TCXO-quality Doppler-only simulations using a tracking schedule of two 2-minute contacts per orbit did not provide sufficient observability to achieve filter convergence. When the Doppler measurements were augmented with pseudorange, the radial position could be determined to within 5 meters; however, the in-track position errors showed inconsistent trends and the cross-track position was not observable. In addition, the pseudorange bias and the atmospheric drag coefficient were not observable.

The non-coplanar satellite configurations provided considerably better performance. Solutions were obtained by processing Doppler measurements for these configurations to estimate the position and velocity of the chase satellite and the Doppler measurement bias. Figure 3 compares the root-mean-square (RMS) of the position error components for each solution. The Doppler-only solution for the case of 0.25 degree plane separation diverged. Solutions for the other three cases appear to be stable with errors progressively increasing with decreasing plane separations, well within the separation tolerances listed in Table 1. The cross-track position was observable for the three higher plane separations. The radial and cross-track position errors were relatively insensitive to the plane separations, with RMS errors of about 0.5 meters and 1 meter, respectively. The in-track error variation was larger. The estimated Doppler biases associated with these solutions were seen to be stable as well.

For the case with 0.25 degree plane separation (which is the nominal EO-1/L-7 configuration), stable position, velocity and Doppler bias estimates were achieved when both pseudorange and Doppler measurements were processed. However, when estimation of a pseudorange bias was also attempted, it was not observable. It was also found that stable and accurate position and velocity estimates are achievable if the Doppler bias is not estimated. For all plane separations, position errors were reduced when pseudorange measurements were included in the solutions.

The formation plane separation is not an arbitrary design parameter but is usually selected to achieve groundtrack cross-track coincidence for a specified satellite in-track separation. The above analysis indicates that 0.5 degree is close to the minimal plane separation that permits accurate onboard, real-time estimation of the position, velocity, and Doppler bias of the chase satellite using only Doppler measurements. The relative radial, in-track, and cross-track (RIC) position errors for the 0.5 degree RAAN separation case are presented in Figure 4. This solution



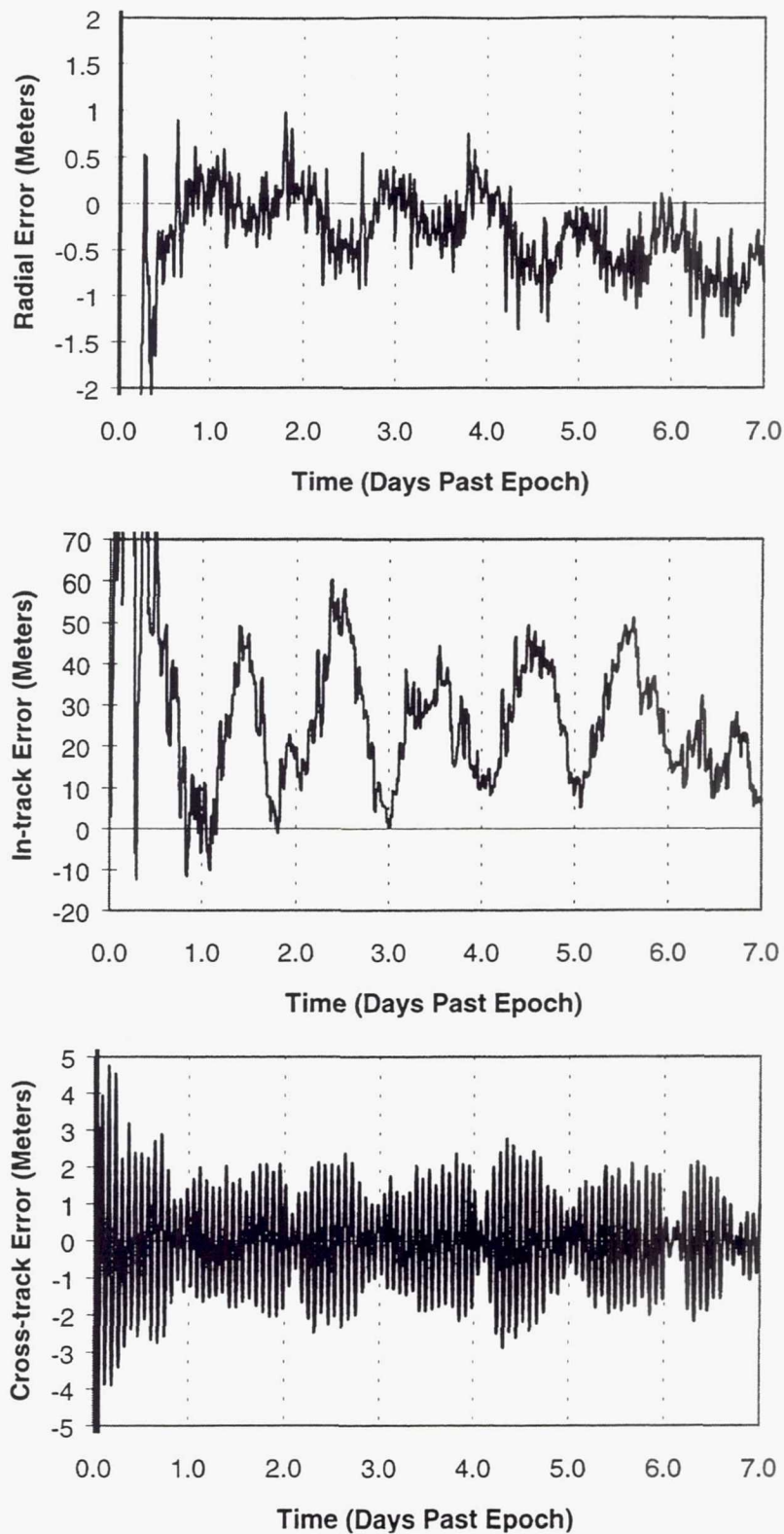


**Figure 4** Relative RIC Position Errors Using USO-Quality Doppler Measurements With 0.5 Degree Plane Separation

was obtained solving for the position, velocity and Doppler bias using USO-quality Doppler measurements. For the same satellite configuration, a solution obtained by processing moderate-quality Doppler measurements (simulated using a Doppler noise of 0.1 hertz), indicated that, with three 5-minute contacts per orbit, the relative radial position can be estimated to better than 3 meters. In similar simulations with a reduced tracking schedule of two 2-minute contacts per orbit providing either the USO-quality or moderate-quality Doppler measurements, the time for the relative ONS filter to converge to an accurate steady state increased, but the accuracy of the solution was not significantly improved.

## CONCLUSIONS

This paper presents a summary of orbit determination and prediction accuracies achievable for EO-1 and L-7 under various tracking and OD scenarios and discusses expected relative navigation errors in their formation-flying configuration.

A survey of orbit determination and prediction accuracy studies previously performed for EO-1 and L-7 indicates that, regardless of tracking measurement type, the expected definitive 3-sigma position errors are approximately 10, 25, and 55 meters in radial, cross-track and in-track directions, respectively. Computation of the relative satellite positions by differencing the independent OD solutions should satisfy all of the formation separation tolerances, regardless of the plane separation, except for the radial separation tolerance of approximately 5 meters. These studies also suggest that the independent OD accuracies can be improved using special tracking and OD scenarios. In the case of TDRSS or GN tracking, this involves using high density tracking (for example, approximately one pass per orbit). In the case of using GPS for EO-1 navigation, it may be necessary to remove the measurement corruption caused by selective availability (for example, using corrections provided by the Federal Aviation Agency's Wide Area Augmentation System (WAAS), use of differential GPS techniques, or the use of dual frequency P-code measurements).

Covariance analysis was performed to investigate the impact of correlated dynamic errors on the relative separation accuracy. These results indicate that the relative separation errors obtained using definitive solutions are 8.5-, 50-, and 47-meters, respectively, in radial, in-track and cross-track directions. Those derived from 1-day-predicted ephemerides are 7.4, 49, and 112 meters, respectively. The results derived from 1-day-predicted ephemerides are applicable to the case where both EO-1 and L-7 ephemeris data are prepared on ground and uplinked to the satellite. The correlation of the dynamic errors due to solar flux uncertainties provides considerable cancellation when the individual satellite position prediction errors are combined to compute the separation errors. When the correlation between satellite dynamic errors is taken into account, the results indicate that a radial separation accuracy of 7.5 meters (3-sigma) and a relative in-track velocity of 7 centimeters per second (3-sigma) are achievable using the nominal tracking configuration for the EO-1/L-7 formation. Because the actual area-to-mass ratios for EO-1 (0.008) and L-7 (0.0067) will be much closer than the area-to-mass ratios used in the covariance analysis, the cancellation of the individual satellite radial and in-track prediction errors will be more complete and the growth of relative radial and in-track position errors in the 3-day prediction periods will be smaller than these estimates.

In addition, the performance of a relative ONS using cross-link measurements was characterized for the relative navigation of a two-satellite formation similar to EO-1 and L-7, with RAAN differences of 0.0, 0.25, 0.5, 1.0 and 4.0 degrees. Because of the limited degree of observability present in the cross-link measurements for coplanar satellites, the associated navigation performance is very sensitive to measurement quality, measurement quantity, and a



priori state knowledge. Increasing the orbit plane separation to 0.5 degree greatly improves the potency of the Doppler measurements by increasing the variation in the relative satellite dynamics from  $\pm 9$  hertz in the coplanar case to a variation of  $\pm 42$  hertz. It was found that position, velocity, and a Doppler bias could be accurately estimated in the real-time relative ONS algorithms using only one-way Doppler cross-link measurements of moderate quality. Increasing the tracking frequency and duration reduced the time for the filter to converge to an accurate steady state, but did not significantly improve the accuracy of the solution. For satellite formations with a plane separation of 0.5 degree or greater, a radial separation accuracy of 2 meters (3-sigma) is achievable using the relative ONS capability with USO-quality Doppler measurements.

## REFERENCES

1. D. Folta and D. Quinn, "Enhanced Formation Flying For the Earth Observing-1 (EO-1) New Millennium Mission," paper presented at the Flight Mechanics Symposium 1997, Goddard Space Flight Center, Greenbelt, Maryland, May 19-21, 1997.
2. D. Oza et al., "Assessment of Orbit Determination Solutions for TDRSS Users", Paper AIAA-95-3242, presented at AIAA Guidance, Navigation, and Control Conference, Baltimore, Maryland August 7-9, 1995
3. E. Santoro, M. Hoppe, J. Lorah, Computer Sciences Corporation internal memorandum titled "GTDS Orbit Accuracy Studies for Landsat-7", October 16, 1996
4. R. C. Hart et al., "Global Positioning System (GPS) Enhanced Orbit Determination Experiment (GEODE) on the Small Satellite Technology Initiative (SSTI) Lewis Spacecraft", ION GPS-96 Technical Meeting, Kansas City, Missouri, September 17-20, 1996
5. Computer Sciences Corporation, CSC-27434-42, *Expected Relative Orbital Accuracy of Earth Orbiter-1 in Formation Flying with Landsat-7*, T. Lee, D. Kelbel, and M. MacWilliams, September 1997
6. C. J. Gramling et al., "TDRSS Onboard Navigation System (TONS) Flight Qualification Experiment," *Proceedings of the Flight Mechanics/Estimation Theory Symposium 1994*, NASA Conference Publication 3265, May 17-19, 1995, p. 253.
7. Goddard Space Flight Center, Flight Dynamics Division, 553-FDD-95/016R0UD0, *Analysis of Ground One-Way Forward Doppler Tracking Data Using the Prototype Filter Smoother (PFS)*, G. Horstkamp and D. Niklewski (CSC), prepared by Computer Sciences Corporation, September 1995.
8. C. J. Gramling et al., "Relative Navigation For Autonomous Formation Flying of Spacecraft," AAS 97-627, presented at the AAS/AIAA Astrodynamics Specialist Conference, Sun Valley, Idaho, August 4-7, 1997



**Page intentionally left blank**

## ONBOARD ORBIT DETERMINATION ALGORITHM BASED ON EARTH REFERENCED ATTITUDE SENSORS

Hiroshi IIDA \*    Tatsuaki HASHIMOTO †    Keiken NINOMIYA ‡

This paper describes onboard orbit determination algorithm and its performance analyses. The algorithm utilizes earth-referenced attitude sensors such as earth sensors or magnetometers together with attitude determination information obtained by inertial-referenced sensors such as star trackers and sun sensors. An extended Kalman filter is applied to estimate real-time position and velocity w.r.t. an inertial frame by processing the data of these attitude sensors.

Several parametric studies are discussed from the standpoint of designing simpler and smaller algorithm that still meets a requirement on accuracy. The achieved accuracy depends on the accuracy of an orbit propagation model, the magnitude of observation errors, and the time step for the Kalman filtering. The studies show that the accuracy by the earth sensor system is about 100 [km], while the accuracy by the magnetometer system is about 1000 [km] even when the simplest orbit propagation model and the worst observation errors are assumed. The achieved accuracy is somewhat coarse, however, it is still effective for calculating the time of umbra and star eclipse by the earth, and for correcting deflected sensors' angle by Doppler shift.

The proposed algorithm is effective for a relatively small and cost efficient satellites, because it requires no additional H/W weight and cost, as well as because it can reduce the efforts in ground operation in which orbital information is updated periodically. Disadvantages lie in the execution of the algorithms by an onboard computer, and an additional memory size to implement the algorithms. However, recent H/W device technology can solve them, and the proposed algorithm becomes available for the near future astronomical satellites of ISAS.

## INTRODUCTION

A variety of schemes have been proposed for onboard orbit determination systems. ([1], [2]) Some schemes require a dedicated hardware such as a GPS receiver. Others require no additional hardware, and utilize the equipment already onboard a satellite. Some are applicable for short-term orbit estimation and some for long-term orbit prediction.

For certain earth observing satellites, GPS-based schemes have been adopted because their missions have required a very accurate orbit determination. On the other hand, in the operation of the astronomical satellites of ISAS launched so far, onboard orbit information

---

\*Engineer, NEC Corporation. 4035 Ikebe-cho, Tsuzuki-ku, Yokohama, Kanagawa 224, Japan. Phone: +81-45-939-2396, Fax: +81-45-939-2399, E-mail: iida@spc.yh.nec.co.jp

†Associate Professor, Institute of Space and Astronautical Science. 3-1-1 Yoshino-dai, Sagami-hara 229, Japan. Phone: +81-427-51-3911, Fax: +81-427-59-4260, E-mail: hashimoto@nnl.isas.ac.jp

‡Professor, Institute of Space and Astronautical Science. 3-1-1 Yoshino-dai, Sagami-hara 229, Japan. Phone: +81-427-51-3911, Fax: +81-427-59-4260, E-mail: ninomiya@nnl.isas.ac.jp

has been periodically updated by ground supports for the purpose of predicting the time of umbra/penumbra and/or star eclipse by the earth. Since accurate orbit determination is not required for such a purpose, a heavy and expensive GPS receiver cannot be adopted for relatively small and cost-efficient astronomical satellites of ISAS. Therefore, the scheme is selected that utilizes the attitude sensors already onboard the satellites for another function such as attitude determination, and the detailed algorithms are studied in order to apply them to ASTRO-F, an infrared observatory of ISAS to be launched in 2003, and other satellites which follow it.

The orbit of ASTRO-F is a sun-synchronous, near-polar orbit whose conditions are listed in Table 1. ASTRO-F is equipped with two star trackers and a fine sun sensor for fine attitude determination w.r.t. an inertial-referenced frame, two conical earth sensors for faulty attitude detection, and a three-axis magnetometer whose data is used for an initial attitude acquisition and for a magnetic torquers' control law dedicated to wheel unloading. Since the earth sensors and the magnetometer can measure the attitude information w.r.t. an earth-referenced frame, onboard orbit determination scheme can be established by combining the inertial-referenced attitude determination with the earth sensors (named as "earth sensor system") or with the magnetometer (named as "magnetometer system").

Table 1: Orbital Conditions for ASTRO-F

Items	Value	(Units)
Altitude	750	[km]
Eccentricity	less than 0.01	[-]
Inclination	98.4	[deg]
Right Ascension of the Ascending Node	6 or 18	LST

This paper is organized as follows. The next section describes the requirements on onboard orbit determination algorithms for the astronomical satellites of ISAS. In the following section, system equations are introduced for the earth sensor system and the magnetometer system. The analyses are performed in the subsequent section, by which the detailed formulae of orbit propagation models and observation models can be specified based on the requirements. The specified algorithms will be verified by numerical simulation from the standpoint of convergence time and robustness against initial conditions. Conclusions are found in the final section.

## REQUIREMENTS

The requirements for designing the onboard orbit determination algorithm should be considered from the standpoints of required accuracy, permissible load and allowable program size. In general, the algorithm needs much load and larger memory as the achieved accuracy becomes better by applying more sophisticated orbit propagation models and/or observation models. On the other hand, the necessary load and program size might be restricted by the onboard computer's performance such as CPU capability and memory size. In this sense, the requirement on the accuracy might be contradictory to the requirements on the others. Therefore, an actual onboard algorithm should be developed by the trade-off of these requirements.

In the following subsections, the requirements on accuracy, load, and program size are



described for low earth orbiting astronomical satellites of ISAS.

### Requirement on Accuracy

Regarding the astronomical satellites of ISAS developed so far, the onboard orbital information is updated for the following two objectives:

- To calculate the time of umbra/penumbra and star eclipse by the earth which are inevitable for satellite operations, especially for AOCS operations,
- To correct attitude sensors' angles deflected by Doppler effect, or offset depending on orbital position.

The requirement on accuracy for the first objective is not so strict. By predicting the time of umbra/penumbra, and by disabling the output data from sun sensors during that period, it becomes possible to protect against misunderstanding that a satellite has lost its attitude or that the sun sensors has been out of order. Similarly, the time of star eclipse can be used to predict the time when the star trackers' data should be disabled. In order to secure a marginal time, the period for disabling the sensors' data has been usually set a few minutes longer than an actual period of umbra/penumbra or star eclipse. It means that about 1000 [km] position accuracy along track direction is good enough for the first objective.

The requirement for the second objective depends on the requirement on the attitude determination accuracy of a satellite. The outputs from the sun sensors and the star trackers are subject to be deflected by Doppler effect, and the deflection angle is about 5 [arcsec] at maximum. In addition, supposing the case that the attitude of the satellite should be determined w.r.t. an inertial frame, the sun sensors' output should be corrected depending on the position of the satellite w.r.t. an earth-centered frame, since it is offset by 10 [arcsec] at maximum. In the case where the requirement on attitude determination accuracy is less than the two values, accurate position information is also required in order to correct the two errors. Figure 1 shows the requirements on the position determination accuracy vs. the required pointing accuracy. The solid line and the dashed line correspond to the deflection angle and the offset angle, respectively. Basically, position accuracy is proportional to the pointing accuracy.

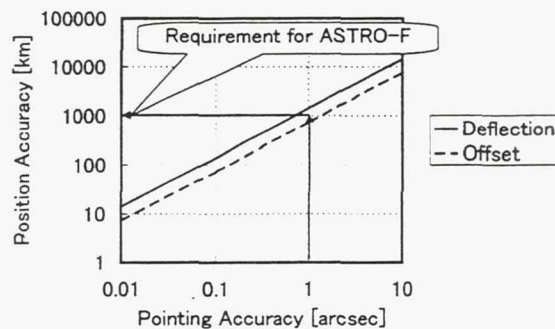


Figure 1: Requirements on Position Accuracy vs. Required Pointing Accuracy

For the case of ASTRO-F, the attitude control accuracy shall be less than 30 [arcsec]. Assuming that at least 1 [arcsec] can be allocated to the error after correcting those effects, the requirement on position accuracy should be about 1,000 [km]. It is now evident, by combining the requirements for the two objectives, the accuracy of the onboard orbit determination shall be less than 1,000 [km] for ASTRO-F.

### **Requirement on Load**

The requirement on the load to CPU shall be to minimize it. The load can be minimized by minimizing the required tasks in a single time step, or by maximizing the time step as far as the achieved accuracy can meet the requirement on accuracy. One of the effective ways to minimize the required tasks in a single time step is to simplify the onboard orbit determination algorithm as much as possible by truncating the higher order terms in an orbit propagation function or in an observation function. This will be discussed later in the analyses of achieved accuracy.

The allowable time step depends on the orbit determination accuracy. The longer the time step is, the more coarse the resolution of orbit determination becomes, and the resolution along track direction can be calculated as a product of 7.5 [km/s] times the time step in second. As stated previously, the requirement on position determination accuracy shall be less than 1,000 [km]. Assuming that the allocation to the resolution shall be 100 [km], and the allowable time step shall be less than 13 [sec].

### **Requirement on Program Size**

The requirement on program size shall be to minimize it. The allowable program size depends on the total memory size of the onboard computers. The size of memory used to be very limited by its expensive cost and by its weight. However, recent device technology has made it possible that more than 128 KB memory size is available by a single RAM device. Compared with the situation that the size was only 32 KB for the computers onboard the satellite of ISAS until 1997 when ASCA, an X-ray observatory satellite was launched, the requirements on program size will be relaxed tremendously. Now, it becomes apparent that the onboard orbit determination algorithm may be implemented as long as it does not have an impact on the memory size.

Here, we will establish the following strategies to make the necessary program size minimized.

- To minimize the algorithm,
- To make a common task executed in a subroutine module, and
- To use a iterative routine.

The above strategies will be taken into account in designing flight software unless they do not sacrifice the execution time.

### **ALGORITHM**

In this section, onboard orbit determination algorithms are described for the earth sensor system and the magnetometer system which will be onboard ASTRO-F. It is assumed that the attitude of a satellite can be determined by an attitude determination system that



utilizes inertial-referenced sensors such as star trackers and sun sensors. It is also assumed that the attitude determination accuracy of the system is so good that the effect to the orbit determination error can be neglected. At first, common algorithms are introduced for both the two systems. Then, respective algorithms are described for each of the two systems. Throughout this section, the formulae are described in continuous forms. In implementing the formulae to actual onboard software, they should be transformed to discrete forms.

## Common Algorithms

The algorithms for the onboard orbit determination systems can be formulated by applying an extended Kalman filter to the system equation expressed as

$$\dot{\mathbf{x}} = \mathbf{f}(\mathbf{x}) + \mathbf{w} , \quad (1)$$

$$\mathbf{y} = \mathbf{h}(\mathbf{x}) + \mathbf{v} , \quad (2)$$

where,  $\mathbf{x}$  is a state vector,  $\mathbf{f}(\mathbf{x})$  is a orbit propagation function,  $\mathbf{y}$  is an observation vector obtained by the earth sensors or the magnetometers,  $\mathbf{h}(\mathbf{x})$  is an observation function, or equivalently a mapping function from the state vector to the observation vector,  $\mathbf{w}$  is a system noise, and  $\mathbf{v}$  is an observation noise.

*State Vector.* The state vector can be a combination of position and velocity in a cartesian coordinate or a spherical coordinate, or it can be a set of equinoctial variables. The selection of the state vector might affect the necessary load and/or the program memory. However, the load and the program size seem to be affected much by the selection of  $\mathbf{f}(\mathbf{x})$  and  $\mathbf{h}(\mathbf{x})$  rather than by the selection of the state vector. Therefore, the combination of position and velocity in a cartesian coordinate is simply selected as the state vector throughout this study. The reason also lies in the fact that the functions of  $\mathbf{f}(\mathbf{x})$  and  $\mathbf{h}(\mathbf{x})$  do not contain time-wasting sine and cosine functions. The state vector defined w.r.t. an inertial frame can be written as

$$\mathbf{x} = \begin{bmatrix} x & y & z & v_x & v_y & v_z \end{bmatrix}^T . \quad (3)$$

*Orbit Propagation Function.* The simplest formula of orbit propagation function can be expressed as

$$\mathbf{f}(\mathbf{x}) = \begin{bmatrix} v_x & v_y & v_z & -x/r^3 & -y/r^3 & -z/r^3 \end{bmatrix}^T , \quad (4)$$

where,  $r = \sqrt{x^2 + y^2 + z^2}$ . Equation (4) neglects  $J_2$  and higher geopotential terms. Roughly speaking, for a short term propagation within an orbital period, neglecting the  $J_2$  term results in the position error about 10 [km], and neglecting the other higher terms results in the position error about 1 [km]. Therefore, when such orbit determination accuracy is required, it is necessary to include the appropriate higher terms in addition to the simplest formula in Equation (4).

The error induced by neglecting higher terms depends on the orbit of a satellite, and extensive simulation study is required to choose the appropriate higher terms. In addition, when non-zonal higher terms need to be included in the function, the onboard orbit determination system requires the information on the right ascension of the Greenwich meridian at a present time or the absolute time by which the meridian can be calculated. It means



that an onboard clock system is required in order to calculate the meridian, and this addition system will also make the onboard orbit determination system more complex than simply adding the non-zonal terms to the orbit propagation function.

*System Noise.* The system noise  $w$  can be described as

$$w = \begin{bmatrix} 0 & 0 & 0 & w_x & w_y & w_z \end{bmatrix}^T, \quad (5)$$

where,  $w_x$ ,  $w_y$  and  $w_z$  are the summations of acceleration by air drag, solar pressure, gravity from the moon, the sun or planets other than the earth, and truncated higher geopotential terms out of the orbit propagation function. Figure 2 shows the normal standard of truncated acceleration along a single axis of the inertial frame vs. the order of geopotential models included in  $f(x)$ . The orbit elements of ASTRO-F listed in Table 1 are assumed in calculating the error.

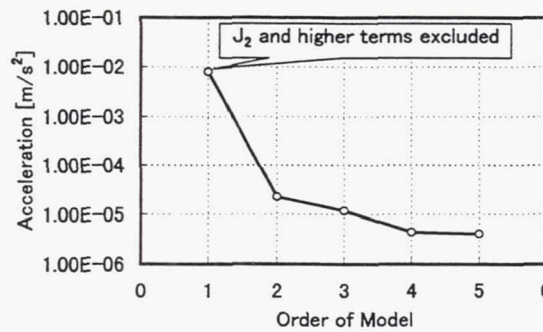


Figure 2: Truncated Geopotential Acceleration

*Linearization of Orbit Propagation Function.* In order to apply an extended Kalman filter to the system equations in Equations (1) and (2), they should be linearized. That is, the derivative of  $f(x)$  and  $h(x)$  should be calculated w.r.t. the state vector. The derivative of  $f(x)$  can be calculated, using Equation (4), as

$$F = \frac{\partial f}{\partial x} = \begin{bmatrix} 0 & 0 & 0 & 1 & 0 & 0 \\ 0 & 0 & 0 & 0 & 1 & 0 \\ 0 & 0 & 0 & 0 & 0 & 1 \\ \mu(3x^2 - r^2)/r^5 & 3\mu xy/r^5 & 3\mu zx/r^5 & 0 & 0 & 0 \\ 3\mu xy/r^5 & \mu(3y^2 - r^2)/r^5 & 3\mu yz/r^5 & 0 & 0 & 0 \\ 3\mu zx/r^5 & 3\mu yz/r^5 & \mu(3z^2 - r^2)/r^5 & 0 & 0 & 0 \end{bmatrix}, \quad (6)$$

where,  $\mu$  is a gravity constant. Even when the  $J_2$  and the higher geopotential terms are included in  $f(x)$ , Equation (6) can still be applied for the linearization. This can be explained as follows: Let

$$f(x) = f_0(x) + f'(x), \quad (7)$$

$$x = x_0 + x' \quad (8)$$

where,  $f_0(x)$  is the basic function defined by Equation (4),  $f'(x)$  is a set of higher geopotential terms,  $x_0$  is a reference state vector, and  $x'$  is a small state vector for linearization. Substituting the above equations into Equation (1) yields

$$\dot{x}_0 + \dot{x}' = f_0(x_0) + f'(x_0) + \frac{\partial f_0}{\partial x} x' + \frac{\partial f}{\partial x} x' + w . \quad (9)$$

Since the term of  $\partial f'/\partial x' \cdot x$  is a product of two small values, it can be neglected. Then the above equation can be divided into two equations as

$$\dot{x}_0 = f_0(x_0) + f'(x_0) , \quad (10)$$

$$\dot{x}' = \frac{\partial f_0}{\partial x} x' + w . \quad (11)$$

The first equation is an orbit propagation function for the reference state vector including the higher geopotential terms, and the second equation is a linearized state equation in which the derivative is obtained solely by deriving  $f_0$ .

### Other Algorithms for Earth Sensor System

*Observation Vector.* The observation vector can be calculated by the output of the earth sensors. Since the output is basically a direction cosine vector from a satellite to the center of the earth which is defined w.r.t. the body frame of a satellite, it should be transformed to an inertial frame as follows:

$$y = T_{\text{INR} \rightarrow \text{BODY}}^{-1} y_{\text{ESA}} , \quad (12)$$

where,  $T_{\text{INR} \rightarrow \text{BODY}}$  is a direction cosine matrix from the inertial frame to the body frame, and  $y_{\text{ESA}}$  is the output from the earth sensors.

*Observation Function.* The simplest observation function for the earth sensors can be written as

$$h(x) = \begin{bmatrix} -x/r & -y/r & -z/r \end{bmatrix}^T . \quad (13)$$

*Observation Noise.* The observation noise is a summation of earth sensors' noise, and a coordinate transformation error induced by an attitude determination error. In addition, the observation function in Equation (13) neglects the earth oblateness, and this also yields an observation error. Furthermore, an ordinarily earth sensor detects infrared emitted from CO<sub>2</sub> about 100 [km] in altitude. Because the radiance fluctuates, this also leads to an observation error. The error due to the earth oblateness is about 0.1 to 0.2 [deg] if no correction is made. The error due to the radiance fluctuation is about 0.1 to 0.3 [deg], and it is almost impossible to correct it because the prediction of the radiance fluctuation is very difficult.

*Linearization of Observation Function.* The derivative of Equation (13) can easily be obtained as

$$H = \frac{\partial h}{\partial x} = \begin{bmatrix} (y^2 + z^2)/r^3 & -xy/r^3 & -zx/r^3 & 0 & 0 & 0 \\ -xy/r^3 & (z^2 + x^2)/r^3 & -yz/r^3 & 0 & 0 & 0 \\ -zx/r^3 & -yz/r^3 & (x^2 + y^2)/r^3 & 0 & 0 & 0 \end{bmatrix} . \quad (14)$$

Again, the above equation is still valid even if the earth oblateness is taken into account in formulating the observation function of  $h(x)$ .

## Other Algorithm for Magnetometer System

*Observation Vector.* The observation vector can be calculated by the output from the magnetometers. Since the output is basically a measured magnetic field vector which is defined w.r.t. the body frame, it should be transformed to the inertial frame as follows:

$$\mathbf{y} = \mathbf{T}_{\text{INR} \rightarrow \text{BODY}}^{-1} \mathbf{y}_{\text{MAG}}, \quad (15)$$

where,  $\mathbf{y}_{\text{MAG}}$  is the output from the magnetometers.

*Observation Function.* A simple formula of observation function for magnetometers can be formulated by assuming a dipole model that can be written as

$$\mathbf{h}(\mathbf{x}) = \frac{a^3 H_0}{r^3} \begin{bmatrix} 3(\hat{m}_1 x + \hat{m}_2 y + \hat{m}_3 z) x/r^2 - \hat{m}_1 \\ 3(\hat{m}_1 x + \hat{m}_2 y + \hat{m}_3 z) y/r^2 - \hat{m}_2 \\ 3(\hat{m}_1 x + \hat{m}_2 y + \hat{m}_3 z) z/r^2 - \hat{m}_3 \end{bmatrix}, \quad (16)$$

where  $a^3 H_0$  is the total dipole strength and is approximately  $7.9 \times 10^{15} [\text{Wb} \cdot \text{m}]$ . The vector  $\hat{\mathbf{m}} = [\hat{m}_1 \ \hat{m}_2 \ \hat{m}_3]^T$  is a dipole unit vector w.r.t. an earth-fixed, earth-centered frame. It can be expressed by using the coelevation  $\theta'_m$  ( $\sim 169$  [deg]) and the right ascension  $\alpha_m$  of the dipole unit vector, as

$$\hat{\mathbf{m}} = \begin{bmatrix} \sin \theta'_m \cos \alpha_m & \sin \theta'_m \sin \alpha_m & \cos \theta'_m \end{bmatrix}^T. \quad (17)$$

To calculate the right ascension of the dipole requires the absolute time or the right ascension of the Greenwich meridian at a present time. If the coelevation  $\theta'_m$  is further approximated to be exactly 180 [deg], then the absolute time is not required for the observation function, because the dipole is assumed to be symmetrically aligned with the earth axis in this case. (We call this dipole as “symmetric dipole”) Therefore, this approximation further simplifies not only the observation function in Equation (16) but also the onboard orbit determination system in a sense that it does not require an onboard clock.

Similar to the discussion of adding higher geopotential terms to the orbit propagation function, higher geomagnetic field terms should be added to the basic observation function in Equation (16) depending on the required accuracy for onboard orbit determination.

*Observation Noise.* The observation noise is a summation of magnetometers' noise, a coordinate transformation error induced by an attitude determination error, and a geomagnetic model error due to the truncation of higher geomagnetic terms.

Figure 3 depicts the truncated geomagnetic field w.r.t the order of the geomagnetic model included in the observation function. The number 0 and 1 on the longitudinal axis corresponds to the symmetric dipole model about the earth axis and the ordinary dipole model, respectively. The errors are evaluated by taking the normal standard over one revolution of the orbit of ASTRO-F.

*Linearization of Observation Function.* Similarly to the discussion on the linearization of the orbit propagation function,  $\mathbf{H} = \partial \mathbf{h} / \partial \mathbf{x}$  can be substituted by the derivative of a basic observation function which omits a set of higher terms. By assuming that  $\theta'_m = 180$  [deg], the derivative of Equation (16) can be simply expressed as

$$\mathbf{H} = \frac{a^3 H_0}{r^7} \begin{bmatrix} -3z(r^2 - 5x^2) & 15xyz & -3x(r^2 - 5z^2) & 0 & 0 & 0 \\ 15xyz & -3z(r^2 - 5y^2) & -3y(r^2 - 5z^2) & 0 & 0 & 0 \\ -3x(r^2 - 5z^2) & -3y(r^2 - 5z^2) & -3z(3r^2 - 5z^2) & 0 & 0 & 0 \end{bmatrix}. \quad (18)$$



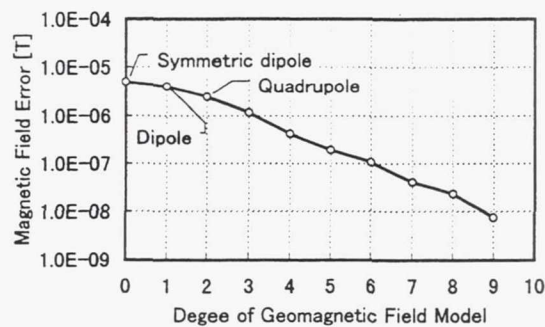


Figure 3: Truncated Geomagnetic Field vs. Degree of Geomagnetic Field Model

## ACCURACY ANALYSIS

In this section, achieved accuracy is investigated for the on-board orbit determination algorithms presented in the previous section. Kalman filtering assumes that the system noise and the observation noise are random, white Gaussian noises, and the resulting error in the estimated state is also a Gaussian noise. However, some of the factors of these noises cannot be regarded as random processes. For example, the errors in the observation models should be regarded as bias noises rather than as random noises for both the earth sensor system and the magnetometer system. Therefore, the achieved accuracy should be analyzed by the combination of a random error analysis and a bias error analysis.

The random error analysis is based on the error covariance at its steady state. That is, the final values after the Kalman filters become convergent are regarded as steady values, and the expected values of the error can be calculated by taking the roots of the corresponding orthogonal elements of the error covariance matrix. If the system is linear, the elements of the matrices  $F$  and  $H$  are constant, and the solution can be obtained analytically by solving the steady state of Riccati equation. However, since the system equations are nonlinear for both the two systems, it is impossible to obtain the solution analytically. Instead, extensive simulation needs to be carried out over the probable ranges of the system noise and the observation noise.

The random error in the estimated state depends on the magnitude of parameters such as the system noise  $w$ , the observation noise  $v$ , and the time step for Kalman filtering. These parameters should be decided not only by the accuracy of the estimated state but also by the convergence time and robustness against the error in an initial state. These characteristics can only be investigated by the simulation. In executing the simulation, sun-synchronous, near-polar, and low-earth orbit is assumed that is exactly the same orbit with ASTRO-F as listed in Table 1.

The bias error analysis is performed based on a geometrical consideration. Since the dominant factor of the bias error in an estimated state seems an observation bias error, or an observation model error rather than the bias error in the orbit propagation function, the bias error analysis is dependent on the type of sensors involved in the algorithm. The details are described in the following subsections for the earth sensor system and the magnetometer system.

## Accuracy Analysis on Earth Sensor System

The parameter ranges for accuracy analysis on the earth sensor system are listed in Table 2, together with the selected values as a result of the analysis. Among the factors of the system noise, the truncated geopotential acceleration is in the range of  $10^{-6}$  to  $10^{-2}$  [m/s<sup>2</sup>] as shown in Figure 2, while other factors such as aerodrag are less than  $1 \times 10^{-6}$  [m/s<sup>2</sup>] for the case of ASTRO-F. Therefore, the range of the system noise is chosen so that it can cover the range of the truncated acceleration. The value of  $1 \times 10^{-2}$  [m/s<sup>2</sup>] corresponds to the case where the  $J_2$  and the higher terms are neglected. The upper value of 1 [m/s<sup>2</sup>] is chosen relatively larger than the actual system noise so as to improve a convergence time with a trade of degrading the achieved accuracy.

The range of the observation noise is chosen so that it can cover the error due to the earth oblateness and the radiance fluctuation, and the error of the earth sensors' output. The error of 1 [deg] is supposed to be the worst error by an ordinary horizon scanner, while the error of 0.01 [deg] is selected as a minimum error that cannot be achieved by any earth sensor ever developed for a low-earth orbit. The time step of 10 [sec] is chosen as the longest time step to keep the resolution of position estimation within 100 [km].

Table 2: Parameters for Accuracy Analysis on the Earth Sensor System

PARAMETER	RANGE	(Unit)	SELECTED VALUE	(Unit)
System Noise	$10^{-6}$ - 1	[m/s <sup>2</sup> ]	$10^{-1}$	[m/s <sup>2</sup> ]
Observation Noise	0.01 - 1	[deg]	1	[deg]
Time Step	10	[sec]	10	[sec]

Figure 4 shows a part of the results for random error analysis obtained by the covariance analysis explained before. In the figure, random errors in position and velocity are plotted vs. the random error in observation. The system noises of  $1 \times 10^{-2}$  and 1 [m/s<sup>2</sup>] are selected as practical examples. The  $x$ ,  $y$ , and  $z$  axes are the along track, the cross track and the radial directions, respectively. From the figure, we can see the following features:

- Roughly speaking, the velocity error can be estimated by the position error divided by 1000 [sec], the inverse of the orbit mean motion for ASTRO-F.
- As the system noise increases, the random error becomes less affected by the observation error.
- The achieved random error satisfies the requirement of 1000 [km] position accuracy even if the worst observation error and a system noise of 1 [m/s<sup>2</sup>] are assumed.

The last feature indicates that it is not necessary to include the  $J_2$  and the higher geopotential terms in the orbit propagation function.

As for the bias error analysis for the earth sensor system, the effect by the observation bias noise and by the system noise should be considered. The bias error in the orbit propagation function leads to the position bias error in radial direction up to 10 [km] even though the  $J_2$  and the higher geopotential terms are neglected. On the other hand, the bias angle error of the earth sensor leads to a bias position error in along track and cross track directions which can be calculated simply as a product of the radius of the satellite and the bias angle error.

Figure 5 shows the bias position error vs. the bias angle error of the earth sensor. For a low earth orbit, the bias angle error is about 0.3 [deg] by the earth oblateness or by the



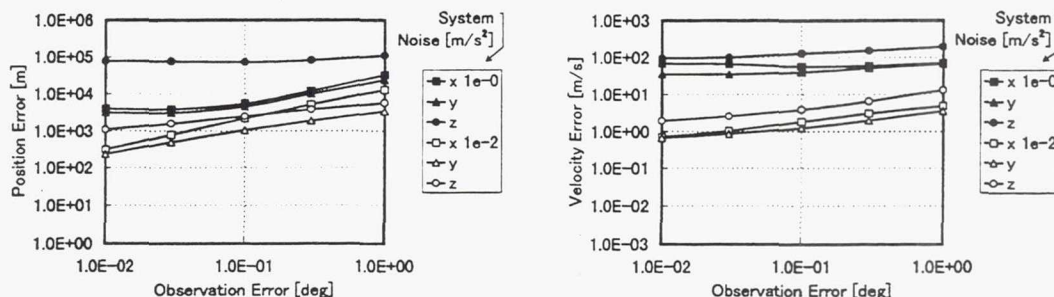


Figure 4: Random Error Analysis for Earth Sensor System

infrared radiance fluctuation. We assume the bias angle error is 1 [deg] at largest for the bias error analysis. Therefore, the bias position error is estimated about 100 [km].

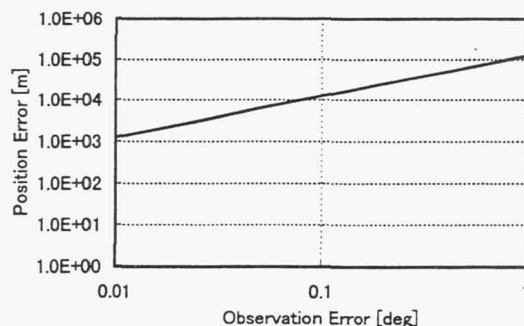


Figure 5: Bias Error Analysis for the Earth Sensor System

Figure 6 shows the result of a numerical simulation in which the selected values listed in Table 2 are applied, and the simplest formula of orbit propagation function in Equation (4) is used. The result of the simulation does not include the effect by the bias angle error in the earth sensor, and it does count in the random noise in the earth sensor and the system noise in the orbit propagation function. An initial position error of 10000 [km] is assumed for each axis, and the Kalman filter becomes convergent after a couple of orbit periods. It means that no a priori state vector is required for a low earth orbit.

Table 3 summarizes the achieved performance described in this subsection and the required conditions for the achievement.

### Accuracy Analysis on Magnetometer System

The parameter ranges for accuracy analysis on the magnetometer system are listed in Table 4, together with the selected values as a result of the analysis. The range of the system noise is chosen in the same manner as is described for the earth sensor system. The range of the observation noise is chosen so that it can cover the truncated geomagnetic field out of



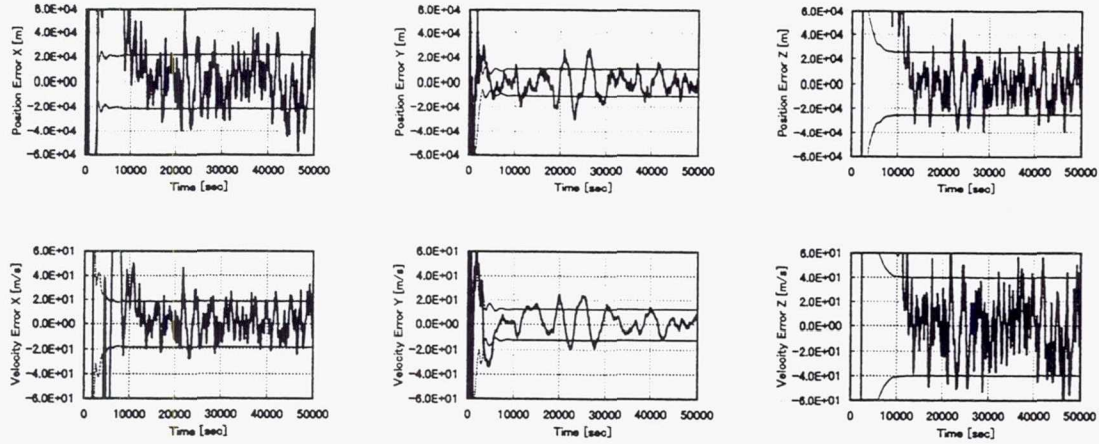


Figure 6: Simulation Results for the Earth Sensor System

the observation equation for the orbital condition of ASTRO-F as shown in Figure 3. The range of the sensor noise, which seems in the range from  $10^{-8}$  to  $10^{-6}$  [T] for an ordinary magnetometer, is within the range of the observation noise.

Figure 7 shows a part of the results for random error analysis. From the figure, we can see the following characteristics:

- The velocity error can be estimated by the same discussion as is described in the analysis on the earth sensor system.
- The achieved random error satisfies the requirement even if the observation error of  $1 \times 10^{-4}$  [T] and a system noise of 1 [m/s<sup>2</sup>] are assumed.

The last feature indicates that the symmetric dipole model is accurate enough as far as the random error is concerned, since the truncation error in the model is less than  $1 \times 10^{-5}$  [T] as depicted in Figure 3.

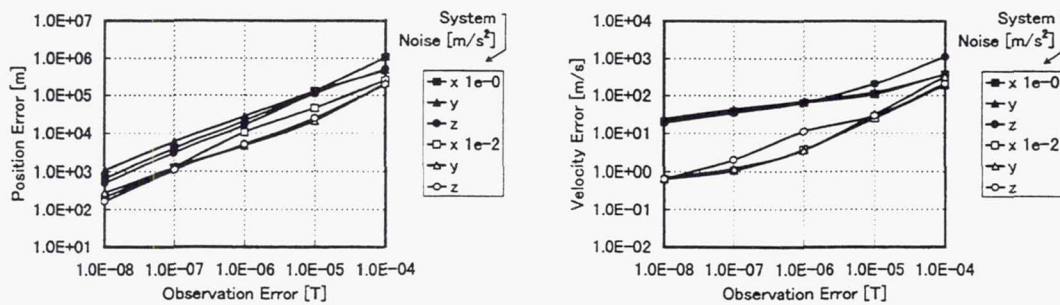


Figure 7: Random Error Analysis for Magnetometer System

As for the bias error analysis for the magnetometer system, the effect by the observation model error can be estimated using numerical simulations. Figure 8 shows the results, in which normal standard of the bias position error over an orbital period is plotted against the

Table 3: Achieved Performance and Required Conditions for Earth Sensor System

ACHIEVED PERFORMANCE		
Position Error	Random Bias	X/Y/Z: less than 20 / 10 / 20 [km] less than 100 / 100 / 10
Velocity Error	Random Bias	X/Y/Z: less than 20 / 20 / 40 [m/s] less than 10 / 10 / 100
Convergence Time		less than 12000 [sec]
A Priori State		Not Required
REQUIRED CONDITIONS		
Earth Sensor Error	Random Bias	less than 1 [deg] less than 1 [deg] (earth oblateness and infrared radiance errors included)
Orbit Propagation Model		(see Equation 4)
Observation Model		(see Equation 13)

Remarks: X/Y/Z = Along Track / Cross Track / Radial directions

Table 4: Parameters for the Accuracy Analysis on the magnetometer System

PARAMETER	RANGE	(Unit)	SELECTED VALUE	(Unit)
System Noise	$10^{-6}$ - 1	[m/s <sup>2</sup> ]	1	[m/s <sup>2</sup> ]
Observation Noise	$10^{-8}$ - $10^{-4}$	[T]	$3 \times 10^{-5}$	[T]
Time Step	10	[sec]	10	[sec]

degree of geomagnetic field model. We can see from the figure that, even if the geomagnetic field model contains up to 6 degrees and the associated orders, the position error is more than 10 [km]. On the other hand, the bias position error due to the system noise in the orbit propagation function is less than 10 [km] as mentioned. Therefore, it is evident that the observation model error has a dominant effect to the bias error in position.

From the figure, we can also see that the normal standard of the position error is still less than the required accuracy even if the symmetrical dipole model is assumed. It is true that the zero-to-peak error might be a couple of times as large as the normal standard. However, it is less expected from the figure that the position accuracy is improved tremendously by adding a couple of higher terms to the simplest observation function. Therefore, numerical simulations are executed by applying the simplest observation function together with the simplest orbit propagation function.

Figure 9 shows the result of a numerical simulation in which the selected values listed in Table 2 are applied. The result of the simulation includes the effect by the observation model error discussed above, as well as the random noise in the magnetometer and the system noise in the orbit propagation function. An initial position errors of 8,000 [km] are assumed for each axis, and the Kalman filter becomes convergent within an orbital period. It means that no a priori state vector is required for a low earth orbit. However, another simulation result proves that an initial position error of 10,000 [km] make the filter divergent instead of convergent. Therefore, the initial condition should carefully be confirmed by a simulation for a different orbit other than that of ASTRO-F.

It might be possible to make the filter convergent in such a case by incorporating the



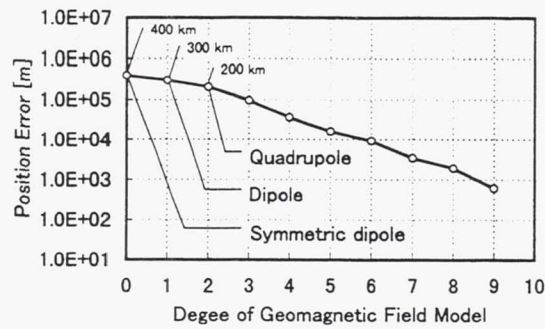


Figure 8: Bias Position Error vs. Degree of Geomagnetic Field Model

earth sensors' data together with the magnetometers' data for a certain period after the filtering starts. This work is left to be investigated for future works.

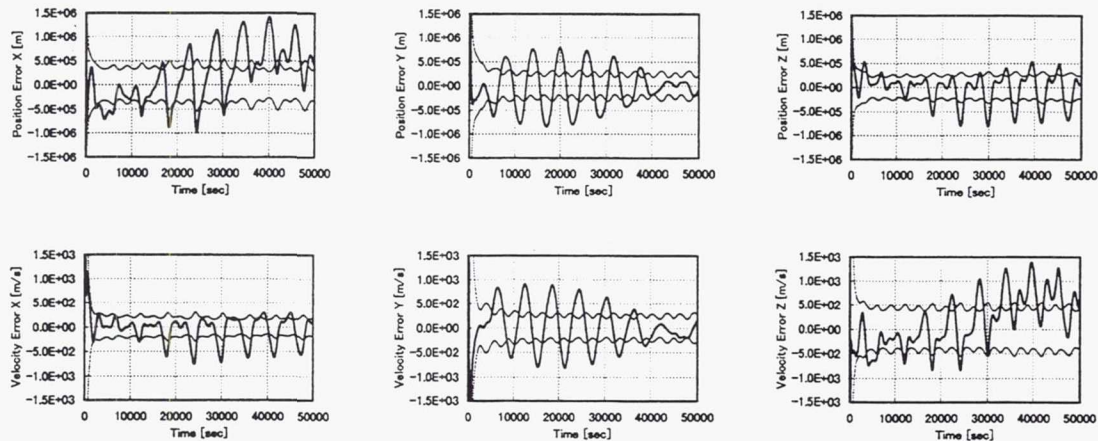


Figure 9: Simulation Results for the Magnetometer System

Regarding the achieved accuracy by the simulation, it does not meet the requirement. Another simulation result proved that 'quadrupole' need to be applied as an observation function, which makes the algorithms more complex. However, the requirement is supposed to be relaxed for ASTRO-F up to the achieved accuracy of 1500 [km]. Therefore, we decided not to modify the observation model and keep it to be the simplest formula as given by Equation 16.

Table 5 summarizes the achieved performance described here and the required conditions for the achievement.

## CONCLUSION

Onboard orbit determination algorithms have been established for two systems in which



Table 5: Achieved Performance and Required Conditions for Magnetometer System

ACHIEVED PERFORMANCE		
Position Error	Random Bias	X/Y/Z: less than 500 / 300 / 300 [km] less than 1500 / 800 / 800
Velocity Error	Random Bias	X/Y/Z: less than 300 / 300 / 500 [m/s] less than 800 / 800 / 1500
Convergence Time		less than 6000 [sec]
A Priori State		Not Required (depending on orbital conditions)
REQUIRED CONDITIONS		
Magnetometer Error	Random Bias	less than $1 \times 10^{-6}$ [T] less than $1 \times 10^{-6}$ [T]
Orbit Propagation Model		(see Equation 4)
Observation Model		(see Equation 16)

Remarks: X/Y/Z = Along Track / Cross Track / Radial directions

earth sensors or magnetometers are applied. An extended Kalman filter has been applied to estimate real-time position and velocity. Orbit propagation function and observation functions for the Kalman filter have been introduced, and their required accuracy has been studied from the standpoint of the requirement on accuracy.

Since the requirement for the astronomical satellites of ISAS shall be less than 1000 [km] and is not so strict, the simplest models for these functions are adopted for both the two systems. The earth sensor system has achieved about 100 [km] position accuracy, and this can satisfy the requirement. On the other hand, it has been analyzed that accuracy for the magnetometer system is about 1,500 [km]. However, the requirement can be relaxed for ASTRO-F, and the simplest algorithm is still valid for the satellite.

Recent device technology has improved the capability of onboard computers, and it is expected that the proposed algorithm becomes available for the near future satellites of ISAS.

## References

- [1] Major C. S. Chory M. A., Hoffman D. P. and Spector V. A. Autonomous navigation-where we are in 1984. In *Guidance and Control Conference*, pages 27-37, New York, 1984. AIAA.
- [2] D.W. Lowrie. Autonomous navigation systems technology assessment. In *17th Aerospace Sciences Meeting*. AIAA, 1979.

**Page intentionally left blank**

## A Low Cost Approach to Simultaneous Orbit, Attitude, and Rate Estimation Using an Extended Kalman Filter

Julie Deutschmann\*, Rick Harman†, and Itzhack Bar-Itzhack‡

An innovative approach to autonomous attitude and trajectory estimation is available using *only* magnetic field data and rate data. The estimation is performed simultaneously using an Extended Kalman Filter, a well known algorithm used extensively in onboard applications. The magnetic field is measured on a satellite by a magnetometer, an inexpensive and reliable sensor flown on virtually all satellites in low earth orbit. Rate data is provided by a gyro, which can be costly. This system has been developed and successfully tested in a post-processing mode using magnetometer and gyro data from 4 satellites supported by the Flight Dynamics Division at Goddard.

In order for this system to be truly low cost, an alternative source for rate data must be utilized. An independent system which estimates spacecraft rate has been successfully developed and tested using only magnetometer data or a combination of magnetometer data and sun sensor data, which is less costly than a gyro. This system also uses an Extended Kalman Filter. Merging the two systems will provide an extremely low cost, autonomous approach to attitude and trajectory estimation.

In this work we provide the theoretical background of the combined system. The measurement matrix is developed by combining the measurement matrix of the orbit and attitude estimation EKF with the measurement matrix of the rate estimation EKF, which is composed of a pseudo-measurement which makes the effective measurement a function of the angular velocity. Associated with this is the development of the noise covariance matrix associated with the original measurement combined with the new pseudo-measurement. In addition, the combination of the dynamics from the two systems is presented along with preliminary test results.

---

\*Aerospace Engineer, Flight Dynamics Analysis Branch, NASA Goddard Space Flight Center, Greenbelt, MD 20771, phone: 301-286-9033, fax: 301-286-0369; email: julie.deutschmann@gsfc.nasa.gov

† Aerospace Engineer, Flight Dynamics Analysis Branch, NASA Goddard Space Flight Center, Greenbelt, MD 20771, phone: 301-286-5125, fax: 301-286-0369; email: richard.harman@gsfc.nasa.gov

‡ Sophie and William Shamban Professor of Aerospace Engineering, Faculty of Aerospace Engineering, Technion-Israel Institute of Technology, Haifa 32000 Israel



## INTRODUCTION

Most missions supported by NASA have an attitude and orbit determination requirement. In most cases, the attitude estimation is performed onboard the satellite. However, the orbit determination is performed primarily on the ground post pass. Efforts are underway to provide for spacecraft onboard autonomous orbit determination. However, these efforts are somewhat expensive and have limited availability which makes them less attractive to the multitude of missions being launched with very modest attitude and orbit requirements as well as modest budget. Up to this point their options were quite limited due to the expense of space qualified attitude determination hardware as well as the expense of ground based and GPS based orbit determination.

In this work, the EKF used to estimate the orbit and the attitude is expanded to include the estimation of the rates. The effective measurement used by the EKF now includes the difference between the observed and expected magnetic field and the derivative of this difference. A corresponding noise covariance matrix is developed. The combined filter dynamics are straightforward and requires input regarding external torques on the spacecraft. Results from simulated data are presented following the theoretical background of the EKF.

The resulting system is expected to provide low cost navigation, i.e. attitude, orbit, and rates, for low earth orbit satellites. The system relies on existing hardware, namely, magnetometers, sensors that are carried on virtually all low earth orbit satellites. There has been only 1 reported failure of a magnetometer for missions supported by NASA/GSFC. Sun sensors, if used, are also extremely reliable. Both sensors are currently available and most importantly, they are flight qualified. Comparable systems, such as GPS, are considerably more expensive and flight qualified receivers are not readily available. Any mission, whether commercial or government, with coarse accuracy constraints or desiring an inexpensive backup method for attitude, rate, and orbit estimation can use this system, provided the satellite has an onboard computer. The impact to the onboard processing will not be significantly more than current onboard processing and can easily be accomplished with current computing technology. Furthermore, utilizing onboard processing reduces the cost of ground operations. Overall, this is an innovative approach for a low cost, coarse attitude and trajectory estimation system.

## THEORETICAL BACKGROUND

Following is a summary of the EKF algorithm. The assumed models of the EKF are given as:

System Model:

$$\underline{X}(t) = \underline{f}(\underline{X}(t), t) + \underline{w}(t) \quad (1)$$

Measurement Model:

$$\underline{z}_k = \underline{h}_k(\underline{X}(t_k)) + \underline{n}_k \quad (2)$$

*Update Stage*

The linearization of equation (2) results in

$$\underline{z}_k = \underline{H}_k \underline{X}_k + \underline{n}_k \quad (3)$$

where  $\underline{H}_k$  is the measurement matrix of the new, combined filter.  $\underline{H}_k$  is composed of submatrices which reflect the dependence of the effective measurement  $\underline{z}_k$  on the state vector,  $\underline{X}_k$  which contains the orbital elements, the attitude quaternion, and the angular velocity.

$$\underline{X}_k^T = [a, e, i, \Omega, w, \theta, C_d, q, \underline{\omega}]$$

where:

$a$  = semi-major axis  
 $e$  = eccentricity  
 $i$  = inclination  
 $\Omega$  = right ascension of ascending node  
 $w$  = argument of perigee  
 $\theta$  = true anomaly  
 $C_d$  = drag coefficient  
 $q$  = attitude quaternion  
 $\underline{\omega}$  = rotation rate

The measurement matrix is

$$\underline{H}_k = \begin{bmatrix} \underline{H}_o & \underline{H}_a & 0 \\ 0 & 0 & [\underline{b} \times] \end{bmatrix} \quad (4)$$

Where  $\underline{H}_o$  and  $\underline{H}_a$  are the submatrices reflecting the dependence of the orbital components<sup>3</sup> and the attitude<sup>4</sup>, respectively, on the effective measurement.

The effective measurement,  $\underline{z}_k$  contains two elements,  $\underline{z}_1$  and  $\underline{z}_2$ . The first is the difference between the measured and observed vector<sup>1</sup> and the second element is the difference in the derivatives of the measured and observed vectors<sup>2</sup>. Taking the derivatives of the observed and measured vectors brings in a dependence on the angular velocity through the formula:

$$\underline{D}_q^I \dot{\underline{r}} = \dot{\underline{b}} + \underline{\omega} \times \underline{b} \quad (5)$$

where:  $\underline{\omega}$  = angular velocity vector

$\underline{r}$  = reference magnetic field vector resolved in inertial coordinates

$\underline{D}_q^I$  = transformation from inertial to body coordinates

$\underline{b}$  = observed magnetic field vector resolved in body coordinates

Incorporating the noise into the reference and observed magnetic field vectors, (5) can be written as

$$\dot{\underline{b}} - D_q^I \dot{\underline{r}} = [\underline{b} \times] \underline{\omega} + [\underline{\eta}_b \times] \underline{\omega} - \underline{\eta}_{\dot{b}} + D_q^I \underline{\eta}_{\dot{r}} \quad (6)$$

where:  $\underline{\eta}_r$  = reference vector noise

$\underline{\eta}_b$  = measurement vector noise

$$\underline{\eta}_{\dot{b}} = (\eta_{1,k} - \eta_{1,k-1})/\Delta$$

$[\underline{b} \times]$  = anti-symmetric matrix composed of the elements of  $\underline{b}$

The second element of the effective measurement is then formally defined as

$$\underline{z}_2 \triangleq (\dot{\underline{b}} - D_q^I \dot{\underline{r}}) - [\underline{b} \times] \underline{\omega}_{est} \quad (7)$$

Where  $\underline{\omega}_{est}$  is the current estimated rate.

Assuming the noise from the reference vector to be zero, the noise terms in (6) can be combined into

$$\underline{\eta}_d = [-\underline{\omega} \times] \underline{\eta}_b - \underline{\eta}_{\dot{b}}$$

The measurement noise,  $\underline{\eta}_b$  is augmented with the noise  $\underline{\eta}_d$  into the noise vector,  $\underline{\eta}$ , of (3). In order to use this in the filter the covariance matrix  $R$  is computed as

$$R \triangleq E \left\{ \begin{bmatrix} \underline{\eta}_1 \\ \underline{\eta}_d \end{bmatrix} \begin{bmatrix} \underline{\eta}_1^T & \underline{\eta}_d^T \end{bmatrix} \right\} - E \left\{ \begin{bmatrix} \underline{\eta}_1 \\ \underline{\eta}_d \end{bmatrix} \right\} E \left\{ \begin{bmatrix} \underline{\eta}_1^T & \underline{\eta}_d^T \end{bmatrix} \right\} \quad (9)$$

If the magnetometer is calibrated such that the measurements have no bias  $E\{\underline{\eta}_1\}$  and  $E\{\underline{\eta}_d\}$  are zero and  $R$  becomes

$$R = \begin{bmatrix} E\{\underline{\eta}_1^T \underline{\eta}_1\} & E\{\underline{\eta}_1^T \underline{\eta}_d\} \\ E\{\underline{\eta}_d^T \underline{\eta}_1\} & E\{\underline{\eta}_d^T \underline{\eta}_d\} \end{bmatrix} \quad (10)$$

The matrix  $E\{\underline{\eta}_1^T \underline{\eta}_1\}$  is the noise covariance matrix for the magnetometer measurement. Based on the assumption that the  $\eta_{1,k}$  and  $\eta_{1,k-1}$  are independent, the  $E\{\underline{\eta}_d^T \underline{\eta}_d\}$  becomes



$$E\{\underline{\eta}_d \underline{\eta}_d^T\} = D R_{TAM} D^T + (1/\Delta^2) R_{TAM} \quad (11)$$

where:  $\Delta$  = the time difference between the current and the previous measurement

The matrix D is computed as

$$D = [\hat{\underline{\omega}} \times] + (1/\Delta) I \quad (12)$$

The noise covariance matrix then becomes

$$R = \begin{bmatrix} R_{TAM} & R_{TAM} D^T \\ -D R_{TAM} & D R_{TAM} D^T + (1/\Delta^2) R_{TAM} \end{bmatrix} \quad (13)$$

The update of the state vector and covariance matrix is performed using the standard EKF equations

$$\underline{x}_k(+) = \underline{x}_k(-) + K_k \underline{z}_k \quad (14)$$

$$P_k(+) = (I - K_k H_k) P_k(-) (I - K_k H_k) + R_k \quad (15)$$

where the gain matrix,  $K_k$  is computed as

$$K_k = P_k(-) H_k^T (H_k P_k(-) H_k + R_k)^{-1} \quad (16)$$

The state vector,  $\underline{x}$ , given in (14) is the internal state used by the EKF. This form is used internally to estimate the angular error in the attitude (in addition to the other state vector elements) which is then converted to the quaternion given in the state,  $\underline{X}$ , above. This is the so-called 'multiplicative' approach<sup>4</sup>.

The above derivation is valid for a magnetometer. For another sensor, such as a sun sensor, the following changes must be made. First, since another sensor is not influenced by the orbit, the measurement matrix in (4) is replaced with

$$H_k = \begin{bmatrix} 0 & H_a & 0 \\ 0 & 0 & [\underline{b} \times] \end{bmatrix} \quad (17)$$

where  $\underline{b}$  is the measured vector. The effective measurement,  $\underline{z}$ , is based on the sensor measurements of the given sensor and is computed as for the magnetometer. The computation of R is as given in (13) with  $R_{TAM}$  replaced with the noise covariance matrix of the given sensor. Based on the results of Reference 4, the 3<sup>rd</sup> and 6<sup>th</sup> rows of  $H_k$  in (17) above and the corresponding rows and columns of R are removed. This is to prevent singularities from a line of sight sensor.

### Propagation stage

The propagation of the state estimate, based on equation 1 is performed as

$$\dot{\underline{\hat{X}}} = f(\underline{\hat{X}}(t), t) \quad (18)$$

The updated estimate of the state vector,  $\underline{\hat{X}}_k(+)$  is propagated from time  $t_k$  to  $t_{k+1}$  by a numerical solution of the continuous dynamics. The orbital dynamics are non-linear and describe a central force including both J2 effects and drag<sup>3</sup>. The differential equation which governs the propagation of the quaternion is linear and is dependent on the estimation of the spacecraft rotation rate<sup>5</sup>. The spacecraft dynamics are used to propagate the rate estimate. The dynamics model of the spacecraft is non-linear and the method of solution is given in Ref. 2.

The propagation of the covariance matrix is performed using the following

$$P_{k+1}(-) = A_k(\underline{\hat{X}}_k(+))P_k(+)A_k^T(\underline{\hat{X}}_k(+)) + Q_k \quad (19)$$

where  $Q_k$  is the spectral density matrix of  $\underline{w}(t)$  and  $A_k$  is the approximated transition matrix.  $A_k$  is computed using the following first order Taylor series expansion

$$A_k = I + F\Delta T \quad (20)$$

where  $\Delta T$  is the time interval between reaction wheel data. The Jacobian  $F$  is derived for the orbital dynamics in Ref. 3, for the attitude dynamics in Ref. 4, and for the spacecraft dynamics in Ref. 2.

## RESULTS

The initial testing of the above EKF was performed with simulated spacecraft data. The spacecraft in the simulation is the Rossi X-ray Timing Explorer (RXTE) satellite. Table 1 specifies the true state, the initial state used by the EKF, the initial covariance, and the initial RSS errors in position, velocity, attitude, and rates. The simulation is based on an actual spacecraft ephemeris, not a two-body propagation. The simulation contains 6 hours of data, which is equivalent to approximately 3.7 orbits. Magnetometer and sun sensor measurements were generated every 2 seconds, without any noise. The spacecraft is inertially pointed in the simulation; there are no attitude maneuvers. Therefore, the control data necessary for propagation of the rate estimate is nominal. The measurement noise for the magnetometer and sun sensor are 0.01 degrees and 50 milliGauss, respectively. The relatively large value chosen for the magnetometer measurement noise is a result of previous testing of the EKF for attitude and orbit estimation and only orbit estimation based on magnetometer data.

Figures 1 and 2 show the errors in the position. Figure 2 shows the position errors with an expanded vertical axis. After 1 orbit the maximum position error oscillates between  $\pm 40$  km, with an average of approximately 0 km. Figure 2 also indicates that the orbit has not yet converged. Due to the low inclination of the RXTE orbit, the orbital elements take a considerable amount of time to reach steady state as shown in Reference 1. Figure 3 is a plot of the attitude errors about each of the spacecraft axes. The values oscillate between approximately  $\pm 1$  degree. The average error is different for each of the three axes. Figure 4 shows the errors in the rate. The rate errors show a significant overshoot at the beginning and then slowly converge throughout the run. Errors in the rate contribute to the errors in the attitude estimate, this is evident in Figure 3. Additional tuning is necessary to determine if the final errors, and the size of the oscillations and initial overshoot can be reduced. Extending the length of the simulated data span is necessary.

**Table 1.** Truth Model and Initial Conditions

State Variable	Truth	Initial State	Initial Covariance	Initial Errors
a (km)	6956.7	7156.74	10000	RSS position error = 1948 km RSS velocity error = 2.1 km/sec
e	0.00197	0.002074	0.0001	
i (deg)	22.96	22.5	1	RSS attitude error = 8.8 deg
$\Omega$ (deg)	109.74	110.735	10	
$\omega$ (deg)	220.04	225.036	100	
$\theta$ (deg)	18.19	28.19	100	
$C_d$	2.2	0.000	0	
q(1)	0	0.0454	.01 <sup>§</sup>	RSS rate error = 8.87 deg/sec
q(2)	0	0.0416		
q(3)	0	0.0454		
q(4)	1	0.99710		
$\omega_x$ (deg/sec)	0	0.0001	$(0.1)^2$	RSS rate error = 8.87 deg/sec
$\omega_y$ (deg/sec)	0	0.0001	$(0.1)^2$	
$\omega_z$ (deg/sec)	0	0.0001	$(0.1)^2$	

## CONCLUSIONS

The initial test results indicate that the EKF has the potential to simultaneously estimate a spacecraft orbit, attitude, and rates. Final position errors less than 40 km, attitude errors less than 1 degree, and rate errors less than  $7e^{-5}$  deg/sec resulted from the

<sup>§</sup>This is the apriori covariance of the angular error in the quaternion, see Ref. 1. This value is used for each component of the error.



first test case based on the simulated RXTE magnetometer and sun sensor measurements. The initial test case consisted of clean, simulated magnetometer and sun sensor data covering approximately 3.7 orbits. Further tuning and additional data are necessary to reduce the final errors.

Future tests will be conducted on noisy, simulated data based on an inertial attitude. Maneuvers will then be inserted into the data to determine if the EKF can detect and follow the maneuver. Finally, the EKF will be tested with real spacecraft data, ideally from a number of missions such as the existing RXTE, Total Ozone Mapping Spectrometer, Gamma Ray Observatory, Transition Region and Coronal Explorer (TRACE) and the future Wide Field Infrared Explorer (WIRE) mission. The final test will consist of a real time test onboard a spacecraft.

## REFERENCES

1. Deutschmann, J. and Bar-Itzhack, I., "Attitude and Trajectory Estimation Using Earth Magnetic Field Data", Paper No. AIAA-96-3631, presented at AIAA/AAS Astrodynamics Conference, San Diego, CA, July 29-31, 1996.
2. Azor, R., R. Harman, and I. Bar-Itzhack, "Satellite Angular Rate Estimation from Vector Measurements", J. Guidance, Control, and Dynamics, Vol. 21, No. 3, May-June, 1998.
3. Shorshi, G., and Bar-Itzhack, I., "Satellite Autonomous Navigation Based on Magnetic Field Measurements", TAE No. 714, Technion-Israel Institute of Tech., Haifa, Israel, April 1994.
4. Deutschmann, J., Bar-Itzhack, I., and Rokni, M., "Comparison and Testing of Extended Kalman Filters for Attitude Estimation of the Earth Radiation Budget Satellite", presented at the GSFC FDD Flight Mechanics/Estimation Theory Symposium 1990, NASA GSFC, Greenbelt, Maryland, May 22-24, 1990.
5. Wertz, James, R., *Spacecraft Attitude Determination and Control*, D. Reidel Publishing Company, Dordrecht, Holland, 1984.

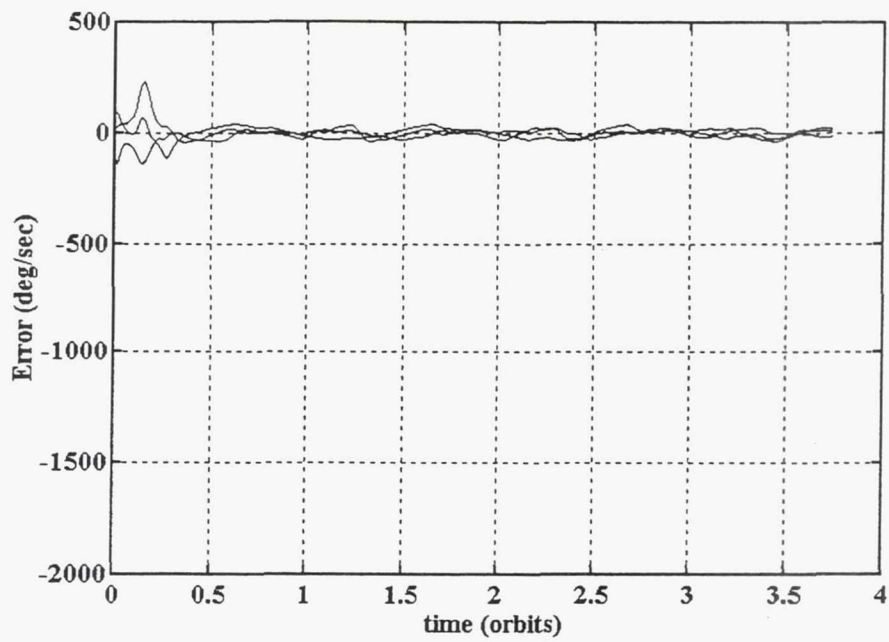


Figure 1. Position Error Components

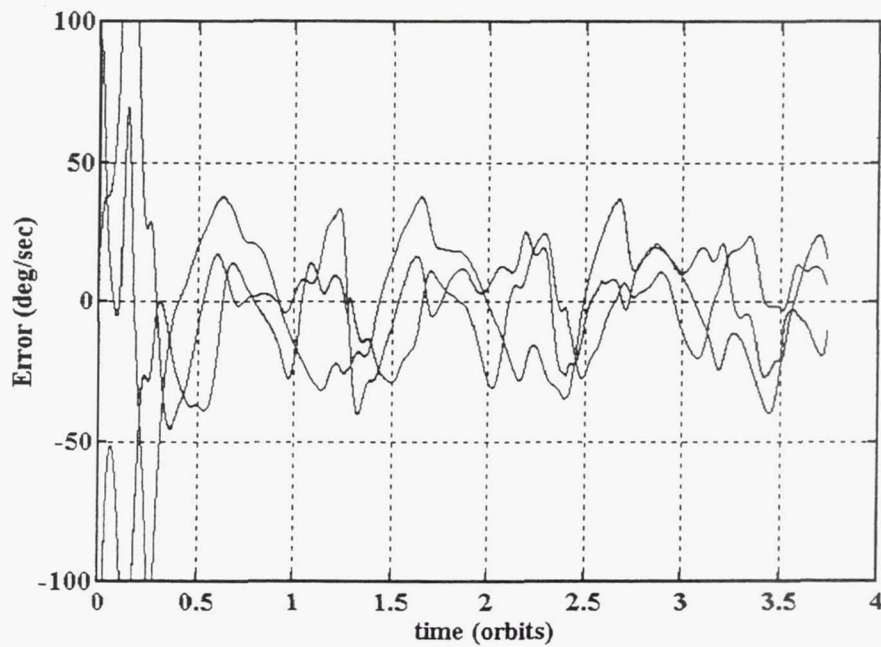


Figure 2. Position Error Components – Expanded Vertical Axis

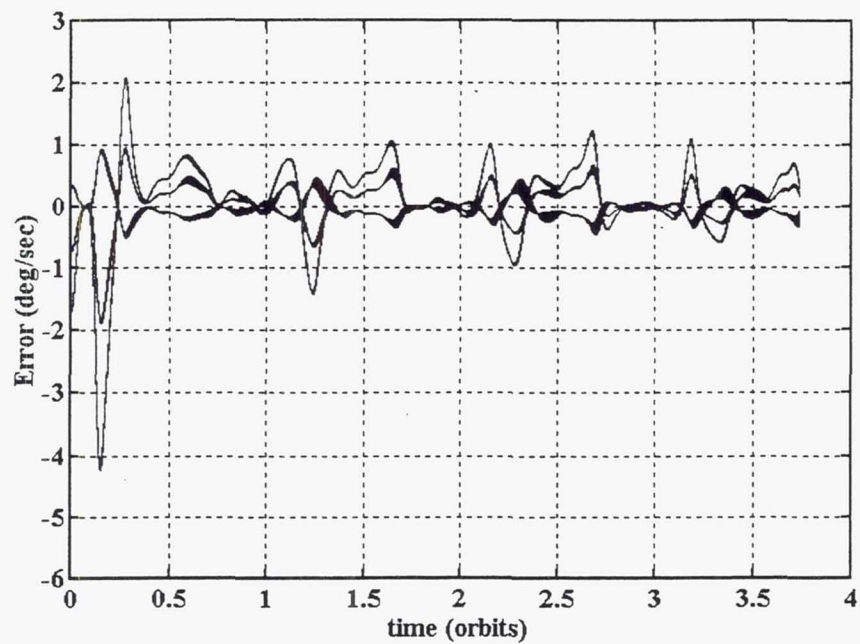


Figure 3. Attitude Error Components

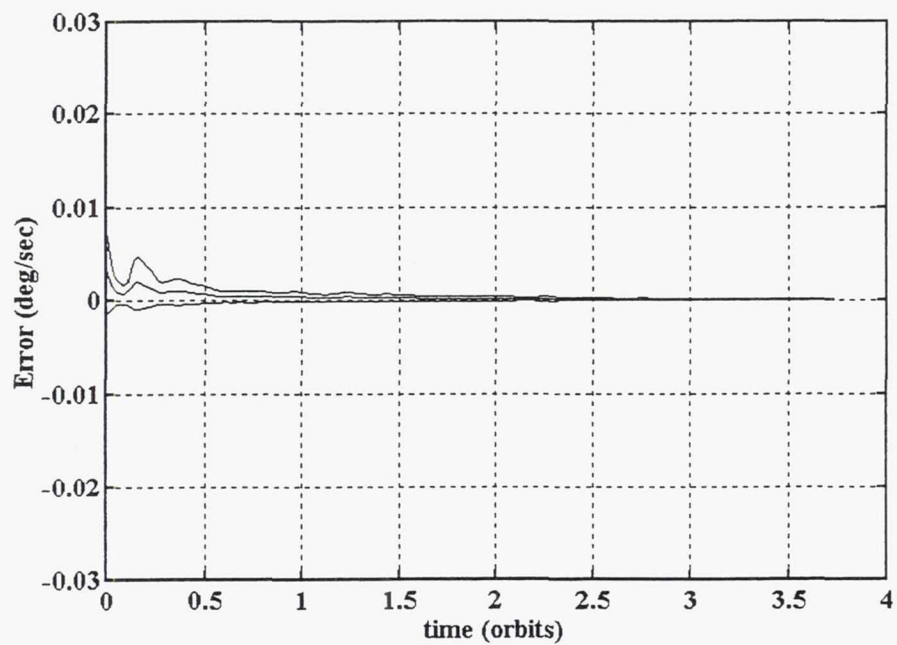


Figure 4. Rate Error Components



## EFFECTS OF ORBIT ECCENTRICITY ON TSS-1 PENDULUM-LIKE OSCILLATIONS

S. Bergamaschi<sup>†</sup>, G. Colombatti<sup>†</sup>  
P. Merlina<sup>\*</sup> and A. Sinopoli<sup>\*\*</sup>

TSS is the largest manned structure to have flown in space to date, and its dynamic behavior involved oscillations over a wide range of frequencies. Although its major dynamic characteristics are readily predicted, advanced applications of long tethers require verification of the theoretical models; moreover, higher frequency oscillations, which are essentially random, are more difficult to predict.

Assuming the experimental data of the TSS-1 mission flown in August 1992 as its starting point, this paper analyzes the effects of the eccentricity of the Shuttle orbit on the plane libration of the tether. Under the assumption of small angles, the study aims to justify the presence of fundamental frequencies, their multiples and combination tones in the experimental spectra in the range between  $10^{-4}$  and  $10^{-3}$  Hz.

First and second order perturbation techniques are then adopted to identify limiting values of the eccentricity for stable motions, an approximate solution and the corresponding spectrum structure.

### INTRODUCTION

The TEID (Theoretical and Experimental Investigation of TSS Dynamics) research, carried out by Silvio Bergamaschi as Principal Investigator along with several co-investigators (\*\*), has analyzed data from a variety of instruments to study Tethered Satellite System dynamics. The primary instruments were the accelerometers and gyros on board the satellite; however, tether tension and length measurements, and magnetic field measurements were also used. The dynamics was observed in real time at the Marshall Space Flight Center (MSFC) Payload Operations Control Center (POCC) and was then subjected to detailed postflight analysis.

The main purpose of the research program to study the dynamics of the tethered satellite system-mission 1 (TSS-1), flown in August 1992, has been to compare the expectations of mathematical models already implemented with the experimental data obtained from the pertinent instruments.

---

<sup>†</sup> Dipartimento di Ingegneria Meccanica, Università di Padova, Via Venezia 1, 35100 Padova (Italy)

<sup>\*</sup> Alenia Aerospazio, Space Division, Corso Marche 41, 10146 Torino (Italy)

<sup>\*\*</sup> Dipartimento di Urbanistica, Istituto Universitario di Architettura, S. Croce 1287, 30135 Venezia (Italy)

It is well known that the study of tethered systems in space is an intriguing problem. In particular, in the case of TSS-1 dynamics, the main simulation difficulty is almost entirely due to the wide spectrum of the oscillatory components of the motion; thus, if purely numerical methods are used to solve the dynamics equations, the integration step must be small and it is likely that a great amount of computer time will be required. This is the reason which motivated the implementation of less general models, usually amenable to semi-analytical solutions, in order to gain deeper insight into some aspects of the motion. This approach has been particularly useful in the case of modal analysis of the system, so that more than one model has been proposed by several authors. Longitudinal and lateral in-plane and out-of-plane vibrations of the tether were then investigated, and the effects of the coupling between different modes evaluated<sup>1-5</sup>.

The first results of the comparison between theoretical and experimental investigation of the TSS-1 mission have been already presented to the scientific community<sup>6</sup>; the main conclusions that can be drawn are as follows:

1. the comparison demonstrates a good agreement between the most important frequencies from mathematical models implemented and those obtained from the mission data;
2. quite frequently, the experimental spectra analyzed exhibit more spikes than expected; among others, this is also the case of frequencies between  $10^{-2}$  and  $10^{-1}$  Hz, which should be linear superposition of fundamentals predicted by linear models and attitude oscillations of the subsatellite, and of frequencies between  $10^{-4}$  and  $10^{-3}$  Hz, which appear to be linear superposition of the fundamental frequency with its multiples, perhaps modulated by tether librations;
3. the presence of several blank time periods in the data flow has been a stringent constraint in the numerical investigation of the experimental values; this has ruled out the possibility of detecting very slow tether librations and considerably reduced the accuracy of the estimation of some harmonic components, because of the relatively poor resolution of the Fast Fourier Transform at low frequencies.

As a consequence, research was recommenced with a twofold purpose<sup>7</sup>:

4. to improve the accuracy of the estimation done so far, by using a more sophisticated method for data analysis;
5. to improve the mathematical models, taking into account possible nonlinearities of the system or other perturbations which can explain the activation of coupling between fundamental frequencies and the presence of combination tones in the spectrum.

As regards points 2, 4 and 5, the nonlinear coupling between attitude motion of the subsatellite and tether vibrations was investigated<sup>7</sup> and the corresponding frequencies obtained theoretically matched the main experimental spikes between  $10^{-2}$  and  $10^{-1}$  Hz well. This work is devoted to the analysis of the effects of the Shuttle orbit eccentricity on the in-plane lateral vibrations of the tether, to justify the experimental spikes between  $10^{-4}$  and  $10^{-3}$  Hz; as a preliminary model, we have studied the eccentricity perturbation on the tether pendulum-like librations.

Few papers in the scientific literature have treated the question of tether systems as well as dumbbells, that is, gravity-gradient stabilized satellites, free to librate in the orbital



plane and moving in an elliptic orbit. Schechter<sup>8</sup> determined a complex solution, evaluated numerically, using a first order perturbation technique. Modi and Brereton, as a first approach<sup>9</sup>, proposed a closed form solution for the libration angle, using the WKBJ method. The solution achieved numerically, by neglecting second and higher-degree terms in the eccentricity, made it possible to determine the structure of the spectrum composed by the orbital frequency  $n$ , the frequency of libration in a circular orbit  $\sqrt{3}n$  and the modulation products of the foregoing two frequencies. Interesting results are obtained in a second paper by the same authors<sup>10</sup>. There, the stability analysis is performed using the concept of invariant surfaces; they permit us to state that the limiting values of eccentricity for stable motions are associated only with periodic solutions of the smallest amplitude. All the families of periodic solutions have thus been identified using the harmonic balance method. However, as emphasized by the authors, the numerical determination of periodic solutions and associated maximum values of the eccentricity involves a prohibitive amount of computational work; for the same reason, no extensive attempt has been made to determine complete sets of periodic solutions.

Finally, Ref. 11 concentrates on the numerical search for periodic solutions with specific initial conditions to evaluate the limiting values of the eccentricity; but the existence of these periodic motions does not necessarily imply their stability.

In this paper the effects induced by the orbit eccentricity  $e$  on the pendulum-like oscillations of TSS-1 are studied using analytical methods. Within the eccentricity first order approximation, the perturbation technique adopted allows discussion of the features of the motion and determination of the limiting values of  $e$  for stable oscillations. A multiple scale method is then used to investigate higher order perturbations; the approximate solution, the corresponding spectrum and the error induced by the approximation adopted are discussed.

## THE PROBLEM

With reference to Figure 1, consider the inertial reference system with its origin on the center of the Earth. Furthermore, let  $(A, x, y, z)$  be a local reference system with its origin on the Shuttle,  $x$  along the local ascending vertical,  $y$  belonging to the orbital plane of the Shuttle and  $z$  completing the right-handed reference system;  $(i, j, k)$  are the unit vectors along the corresponding axes.

The position vector of the free extreme  $P$  of the tether, assumed to be a massless rigid rod, is:

$$r = (r_A + x) i + y j + z k \quad (1)$$

where  $r_A$  is the absolute value of the position vector of the Shuttle along its orbit. Adopt cylindrical coordinates for representing the position of  $P$  with respect to  $A$ ; then:

$$x = l \cos \varphi \cos \theta \quad (2a)$$



$$y = l \cos \varphi \sin \theta \quad (2b)$$

$$z = l \sin \varphi \quad (2c)$$

where  $\theta$  and  $\varphi$  represent the in-plane and out-of-plane libration angles, respectively, and  $l$  is the tether length.

The expression of the kinetic energy  $T$  per unit mass of the sub-satellite is therefore:

$$T = \frac{1}{2} \left\{ \dot{r}_A^2 + r_A^2 \dot{w}^2 - 2 l \dot{r}_A \left[ \dot{\varphi} \sin \varphi \cos \theta + (\dot{w} + \dot{\theta}) \cos \varphi \sin \theta \right] + \right. \\ \left. + 2 l r_A \dot{w} \left[ -\dot{\varphi} \sin \varphi \sin \theta + (\dot{w} + \dot{\theta}) \cos \varphi \cos \theta \right] + l^2 \dot{\varphi}^2 + l^2 (\dot{w} + \dot{\theta})^2 \cos^2 \varphi \right\} \quad (3)$$

where  $w$  is the true anomaly. While, by expanding the position  $|r|$  of  $P$  as a function of  $l/r_A$  as:

$$|r| = r_A \left( 1 + 2 \frac{l}{r_A} \cos \varphi \cos \theta + \frac{l^2}{r_A^2} \right)^{\frac{1}{2}} \quad (4)$$

the potential energy  $V$ , where  $\mu$  is the Earth gravitational constant, becomes:

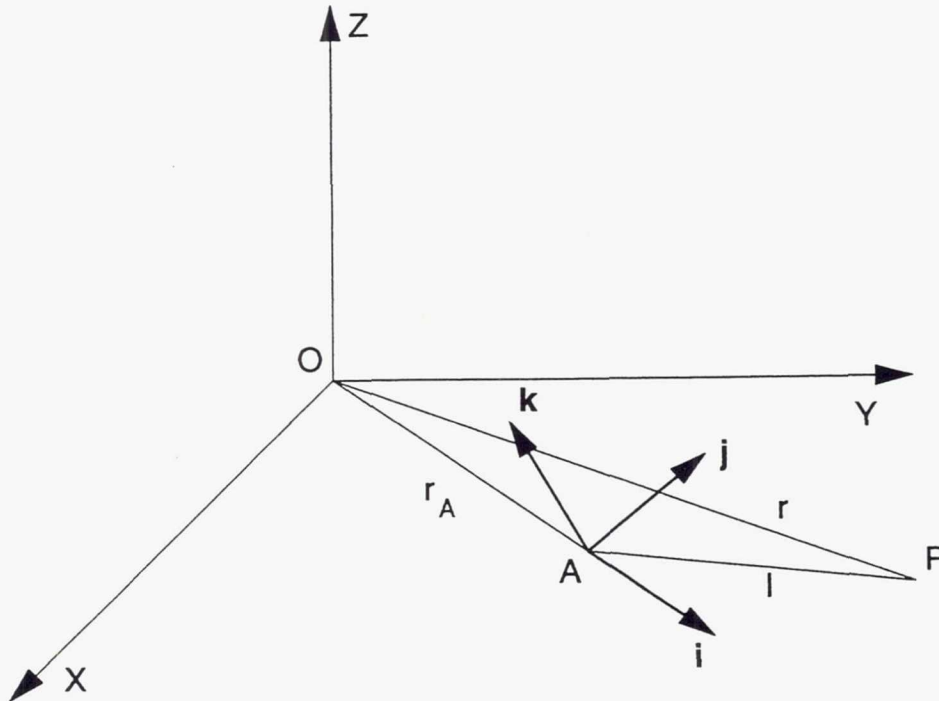


Figure 1

$$V = -\frac{\mu}{r_A} \left( 1 - \frac{l}{r_A} \cos \varphi \cos \theta - \frac{l^2}{2r_A^2} + \frac{3l^2 \cos^2 \varphi \cos^2 \theta}{2r_A^2} \right) \quad (5)$$

Assume small libration angles and investigation of the motion only in the orbital plane; that is:  $\varphi = 0$ ,  $\theta \approx 0 \Rightarrow \cos \theta \approx 1 - \theta^2/2$  and  $\sin \theta \approx \theta$ .

The Lagrangian density  $L$  becomes:

$$L = \frac{1}{2} \left\{ \left[ \dot{r}_A^2 + r_A^2 \dot{w}^2 - 2l \dot{r}_A (\dot{w} + \dot{\theta}) \theta + 2l r_A \dot{w} (\dot{w} + \dot{\theta}) \left( 1 - \frac{\theta^2}{2} \right) \right] + l^2 (\dot{w} + \dot{\theta})^2 \right\} + \frac{\mu}{r_A} \left[ 1 - \frac{l}{r_A} \left( 1 - \frac{\theta^2}{2} \right) - \frac{l^2}{2r_A^2} + \frac{3l^2}{2r_A^2} (1 - \theta^2) \right] \quad (6)$$

and the motion of point  $P$  is characterized by one degree of freedom, namely, the angle  $\theta$  of libration with respect to the local vertical. The corresponding governing equation is:

$$\ddot{\theta} + \ddot{w} + 3\frac{\mu}{r_A^3} \theta - \frac{\ddot{r}_A}{l} \theta + \frac{r_A \dot{w}^2}{l} \theta - \frac{\mu}{l r_A^2} \theta + 2\frac{\dot{r}_A \dot{w}}{l} + \frac{r_A \ddot{w}}{l} = 0 \quad (7)$$

which can be simplified, recognizing that, from the constancy of the angular momentum:

$$h = r_A^2 \dot{w} = \text{const} \quad (8)$$

it follows that:

$$2 r_A \dot{r}_A \dot{w} + r_A^2 \ddot{w} = 0 \quad (9)$$

while, from the accelerations balance in the radial direction:

$$\ddot{r}_A - r_A \dot{w}^2 + \mu/r_A^2 = 0 \quad (10)$$

The small angles plane libration of the tether is therefore governed by:

$$\ddot{\theta} + 3\frac{\mu}{r_A^3} \theta = -\ddot{w} \quad (11)$$

Eq.(11) shows that the oscillations are forced by the second derivative of the true anomaly  $w$ . This is probably the reason which motivated the transformation of the angle  $\theta$  into a new variable only depending on  $w$ , in previous papers on the same subject.

In order to analyze the effects of the eccentricity on the tether motion, we prefer to maintain the dependency of  $\theta$  on time, by adopting the following expression for the Shuttle position, as a function of the semimajor axis  $a$ , the mean anomaly  $M$  and the eccentricity  $e$ :

$$r_A = a (1 - e \cos M + e^2 \sin^2 M) \quad (12)$$

which gives:

$$r_A^{-3} = a^{-3} \left[ 1 + 3e \cos M + \frac{3}{2} e^2 (1 + 3 \cos 2M) \right] \quad (13)$$

Furthermore, from Eq.(12) and the expression of angular momentum (Eq.(8)), the following equation is obtained:

$$\dot{\theta} = \frac{h}{r_A^2} = h a^{-2} \left[ 1 + 2e \cos M + \frac{e^2}{2} (1 + 5 \cos 2M) \right] \quad (14)$$

so that, by putting:  $M = nt$  and  $\mu = n^2 a^3$ , where  $n$  is the mean motion,  $h^2 = \mu a (1 - e^2)$ , and  $\sqrt{1 - e^2} \approx 1 - e^2/2$ , Eq.(11) becomes:

$$\ddot{\theta} + 3n^2 \left[ 1 + 3e \cos nt + \frac{3}{2} e^2 (1 + 3 \cos 2nt) \right] \theta = en^2 [2 \sin nt + 5e \sin 2nt] \quad (15)$$

This represents the equation governing the small angles plane libration assuming an eccentricity perturbation limited to the second order terms; this seems to be a reasonable assumption, since in our problem the typical values of  $e$  range between  $10^{-4}$  and  $10^{-3}$ . Moreover, observe that in the formulation obtained, eccentricity plays the role of an excitation parameter.

## FIRST ORDER PERTURBATION AND STABILITY ANALYSIS

With reference to Eq.(15), first our attention is restricted to the first-order terms on the eccentricity. It is easily recognized that the motion is thus governed by a forced Mathieu equation:

$$\ddot{\theta} + 3n^2 (1 + 3e \cos nt) \theta = 2n^2 e \sin nt \quad (16)$$

which is a special kind of Hill's equation; i.e., a linear differential equation with periodic coefficients. The Floquet theory should therefore be used to analyze the features of the



solutions and their stability. By adopting a new time variable:  $\tau = n t$ , with  $d/dt = d/d\tau (d\tau/dt) = n d/d\tau$  and  $d^2/dt^2 = n^2 d^2/d\tau^2$ , Eq.(14) is thus reformulated in its classical and well known form:

$$\frac{d^2\theta}{d\tau^2} + (\delta + \varepsilon \cos \tau)\theta = f(\tau) \quad (17)$$

where:  $\delta = 3$ ,  $\varepsilon = 3 \delta e$  and  $f(\tau) = 2e \sin \tau$ .

No closed form can be found for the solutions of the homogeneous differential equation associated with Eq.(17):

$$\frac{d^2\theta}{d\tau^2} + (\delta + \varepsilon \cos \tau)\theta = 0 \quad (18)$$

which has been studied very extensively, so that stable and unstable regions in the  $\delta - \varepsilon$  plane have been determined completely for all values of  $\delta$  and  $\varepsilon$  (Figure 2). In particular, two normal solutions can be shown to consist of the product of an exponential function and a periodic function of period  $2\pi$ . In stable regions any periodic motion consequently can exist, which makes it impossible to enumerate a complete set of stable solutions. Nevertheless, if we are particularly interested in the transition curves from stable to unstable motions, it could be demonstrated that, for a given pair of transition values of  $\delta$  and  $\varepsilon$ , Eq.(18) admits a periodic solution with either the period  $2\pi$  or  $4\pi$ . Therefore, the limiting curves can be determined, by developing these periodic solutions in Fourier series and obtaining sets of recurrence relations for the coefficients of the even and odd functions of  $\tau$ , namely  $\sin m\tau$  and  $\cos m\tau$ , with  $m$  integer; the stable regions are connect at the points  $\delta = n^2/4$ ,  $\varepsilon = 0$ .

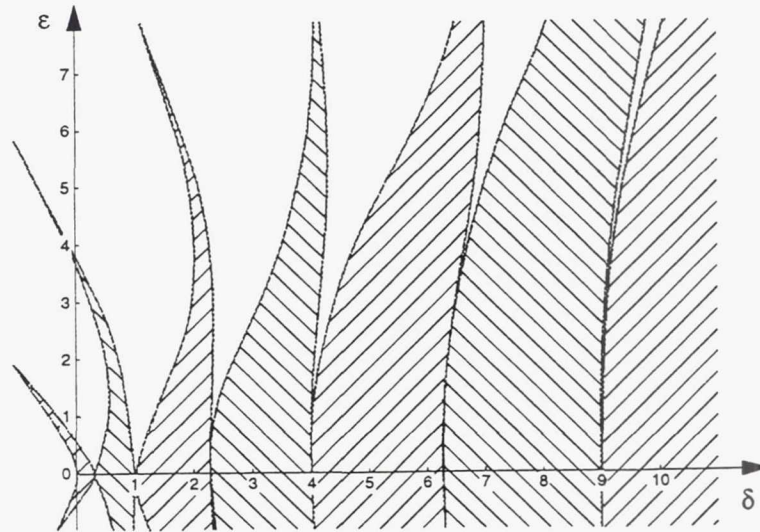


Figure 2. Regions of stable (shaded) and unstable motion in the  $\delta$ - $\varepsilon$  plane.

Since Eq.(17) is linear and the forcing term is periodic, the stability of the general solution depends on the characteristics of the solutions of the associated homogeneous differential equation; while, it could be demonstrated that a forced solution of period  $2\pi$  exists only inside the regions of stable solutions for Eq.(18), with the obvious exclusion of limiting curves.

As the forcing term in Eq.(17) induces a periodic oscillation around a stable configuration, the stability analysis of our problem can be restricted to Eq.(18).

Assume the following values:

$$\mu = 3.986 \cdot 10^5 \text{ km}^3 / \text{sec}^2$$

$$n = 1.158 \cdot 10^{-3} \text{ rad/sec}$$

$$a = 6673.8 \text{ km}$$

$$e = 10^{-3} \div 10^{-4}$$

which correspond to the tether libration excited by the orbital eccentricity in the station-keeping phase of the TSS-1 mission. The values for  $\delta$  and  $\varepsilon$  are, therefore:  $\delta = 3$  and  $\varepsilon = 9 \cdot 10^{-3} \div 9 \cdot 10^{-4}$ , which, as shown in Figure 2, are completely inside the regions of stable motion and far enough from the corresponding limiting curve.

The stability analysis within the first order perturbation terms states the limiting value of eccentricity for stable motions as:  $e \approx 0.3$ ; within the same approximation, the value obtained gives consistency to previous investigations<sup>11</sup>, conducted numerically in an attempt to identify periodic solutions.

## THE MULTIPLE SCALES METHOD

Although the analysis above enables us to state that the eccentricity perturbation does not imply unstable motion during the station keeping phase of the TSS-1 mission, it does not give any information about the features of the motion and the structure of the corresponding spectrum.

To this end, let us use the multiple scales method to obtain an approximate solution within a given order. As is well known, the main feature of the multiple scales method consists in assuming that, given a perturbative small parameter  $\varepsilon$ , the approximate solution depends not only on  $\varepsilon$  and time, but also on their product by introducing new independent time variables:

$$T_K = \varepsilon^K t \quad \text{with:} \quad K = 0, 1, 2, \dots \quad (19)$$

which represent slower times as the order of approximation  $K$  increases.

Therefore, the time derivatives become developments in terms of partial derivatives with respect to  $T_K$ , as follows:

$$\begin{aligned}\frac{d}{dt} &= \frac{dT_0}{dt} \frac{\partial}{\partial T_0} + \frac{dT_1}{dt} \frac{\partial}{\partial T_1} + \dots = D_0 + \varepsilon D_1 + \dots \\ \frac{d^2}{dt^2} &= D_0^2 + 2\varepsilon D_0 D_1 + \varepsilon^2 (D_1^2 + 2D_0 D_2) + \dots\end{aligned}\quad (20)$$

and the approximate solution can be put in the form:

$$\theta(t; \varepsilon; \varepsilon^K t) = \theta_0(T_0, T_1, T_2) + \varepsilon \theta_1(T_0, T_1, T_2) + \varepsilon^2 \theta_2(T_0, T_1, T_2) + O(\varepsilon^3 t) \quad (21)$$

where the development of the solution has been stopped at the second order approximation. The substitution of Eq.(21) in Eq.(15) gives:

$$\begin{aligned}& \left[ D_0^2 + 2\varepsilon D_0 D_1 + \varepsilon^2 (D_1^2 + 2D_0 D_2) \right] (\theta_0 + \varepsilon \theta_1 + \varepsilon^2 \theta_2) + 3n^2 [1 + 3\varepsilon \cos nt + \\ & + \frac{3}{2} \varepsilon^2 (1 + 3\cos 2nt)] (\theta_0 + \varepsilon \theta_1 + \varepsilon^2 \theta_2) = \varepsilon n^2 [2\sin nt + 5\varepsilon \sin 2nt]\end{aligned}\quad (22)$$

By equating the terms of equal powers in  $\varepsilon$  in Eq. (22), and assuming that the perturbation parameter coincides with the eccentricity, the equations of motion at different  $k - th$  orders are obtained.

### Zero Order Equation

At  $0 - th$  order, the equation of free librations in a circular orbit is obtained:

$$D_0^2 \theta_0 + 3n^2 \theta_0 = 0 \quad (23)$$

Note that the fundamentals frequency  $\omega_0 = n\sqrt{3}$  depends on the gravity gradient and the motion amplitude as a function of  $T_0 = t$  is a constant; its dependence on time will be determined at subsequent levels of approximation. The solution of Eq.(23) is therefore:

$$\theta_0(T_0, T_1, T_2) = A_0(T_1, T_2) e^{i\omega_0 T_0} + \bar{A}_0(T_1, T_2) e^{-i\omega_0 T_0} \quad (24)$$

where  $\bar{A}_0(T_1, T_2)$  is the complex conjugate of  $A_0(T_1, T_2)$ , and, from now on, the eccentricity is represented by parameter  $\varepsilon$ , in order to eliminate confusion with the exponential representation.



## First Order Equation

By substituting the solution (24) in the first order equation, we obtain:

$$D_0^2 \theta_1 + \omega_0^2 \theta_1 = -2D_0 D_1 \left[ A_0(T_1, T_2) e^{i\omega_0 T_0} + \bar{A}_0(T_1, T_2) e^{-i\omega_0 T_0} \right] + \\ -9n^2 \cos nt \left[ A_0(T_1, T_2) e^{i\omega_0 T_0} + \bar{A}_0(T_1, T_2) e^{-i\omega_0 T_0} \right] + 2n^2 \sin nT_0 \quad (25)$$

which, after some trigonometric transformations, gives:

$$D_0^2 \theta_1 + \omega_0^2 \theta_1 = -2i\omega_0 D_1 A_0(T_1, T_2) e^{i\omega_0 T_0} + \\ -\frac{9n^2 A_0}{2} \left[ e^{i(\omega_0+n)T_0} + e^{i(\omega_0-n)T_0} \right] + 2n^2 \sin nt + c.c. \quad (26)$$

In order to guarantee that the solution at the first order approximation be also periodic, all the terms directly depending on  $T_0$  on the right-hand side of Eq.(26), that is the secular terms, must be equal to zero. This implies:

$$D_1 A_0(T_1, T_2) = 0 \quad (27)$$

so that the amplitude of the motion does not depend either on  $T_0$  or on  $T_1$ , and:  $A_0 = A_0(T_2)$ . The solution of Eq.(26) is, therefore:

$$\theta_1 = -\frac{9}{22} A_0(T_2) \left[ (1-2\sqrt{3}) e^{i(\omega_0+n)T_0} + \right. \\ \left. + (1+2\sqrt{3}) e^{i(\omega_0-n)T_0} \right] + \sin nT_0 + c.c. \quad (28)$$

It is worthwhile observing that, at the first order approximation, the perturbative effect of the eccentricity induces the appearance of new periodic oscillations in the motion; the corresponding frequencies are equal to the orbital mean motion and to its combinations with the fundamental frequency of free oscillations in a circular orbit. This is in agreement with the conclusions given in Ref. 9.

## Second Order Equation

Consider, now, the differential equation governing the second order motion:

$$D_0^2 \theta_2 + 3 n^2 \theta_2 = -2D_0 D_1 \theta_1 - 2D_0 D_2 \theta_0 - \frac{9n^2}{2} \theta_0 (1 + 3\cos 2nT_0) + \\ - 9n^2 \theta_1 \cos nT_0 + 5 n^2 \sin 2nT_0 \quad (29)$$

Each of the right hand terms needs to be analyzed in order to avoid the presence of secular effects in the solution. For the sake of brevity, we prefer to present the substitutions of solutions (24) and (28) on each term, the determination of the required derivatives and the consequent algebra in the Appendix.

After some calculations, it is possible to demonstrate (see Appendix) that Eq.(29), taking into account only the terms depending on  $e^{i\omega_0 T_0}$ , can be expressed as:

$$D_0^2 \theta_2 + 3 n^2 \theta_2 = -\frac{1}{11} \left[ 22 i \omega_0 D_2 A_0(T_2) + 9n^2 A_0(T_2) \right] e^{i\omega_0 T_0} + c.c. \quad (30)$$

To avoid secular terms in the solution, the expression within the square brackets in Eq.(30) must be zero. To this aim, reformulate the amplitude  $A_0$  as:

$$A_0(T_2) = \frac{1}{2} a(T_2) e^{i\beta(T_2)} \quad (31)$$

so that:

$$D_2 A_0(T_2) = \frac{1}{2} (a' e^{i\beta} + i a \beta' e^{i\beta}) \quad (32)$$

and the right-hand term of Eq.(30) becomes:

$$11 i \omega_0 (a' e^{i\beta} + i a \beta' e^{i\beta}) + \frac{9}{2} n^2 a e^{i\beta} = 0 \quad (33)$$

By separating the real from the imaginary part in Eq.(33), it is obtained that:

$$\omega_0 a' = 0 \quad \Rightarrow \quad a = \text{const.} \quad (34)$$

$$\beta' = \frac{9}{2} n^2 \frac{1}{11 \omega_0} = \frac{9}{22\sqrt{3}} n \quad (35)$$

so that, integrating Eq.(35) over  $T_2$ , the dependency of  $\beta$  on time can be expressed as:

$$\beta = \frac{9}{22\sqrt{3}} n T_2 + \beta_0 \quad (36)$$

while the dependence of  $A$  is:

$$A = \frac{1}{2} a e^{i \frac{9}{22\sqrt{3}} n T_2 + \beta_0} \quad (37)$$

We are now able to determine the solution  $\theta_2$ , since all the secular terms in the right hand of Eq.(29) have been eliminated. The differential equation governing the motion of the second order can be therefore rewritten as:

$$D_0^2 \theta_2 + 3 n^2 \theta_2 = -\frac{27 n^2}{22} A_0(T_2) \left[ (4 + 3\sqrt{3}) e^{i(\omega_0 + 2n)T_0} + (4 - 3\sqrt{3}) e^{i(\omega_0 - 2n)T_0} \right] + \frac{n^2}{2} \sin 2nT_0 + c.c. \quad (38)$$

which, for  $\theta_2$  gives:

$$\theta_2 = -\frac{27}{176} A_0(T_2) \left[ -(\sqrt{3} + 5) e^{i(\omega_0 + 2n)T_0} + (\sqrt{3} - 5) e^{i(\omega_0 - 2n)T_0} \right] - \frac{1}{2} \sin 2nT_0 + c.c. \quad (39)$$

Due to the dependence of  $A_0(T_2)$  on time, the fundamental frequency at the zero order is changed as follows:

$$\omega_0^* = \omega_0 + \frac{9}{22\sqrt{3}} \varepsilon^2 n = \left( \sqrt{3} + \frac{9}{22\sqrt{3}} \varepsilon^2 \right) n \quad (40)$$

and the uniform expansion of the solution up to the second order approximation is:

$$\begin{aligned} \theta = \theta_0 + \varepsilon \theta_1 + \varepsilon^2 \theta_2 = & a \cos(\omega_0^* t + \beta_0) + \varepsilon \sin nt + \\ & -\varepsilon \frac{9a}{22} \left\{ (1 - 2\sqrt{3}) \cos[(\omega_0^* + n)t + \beta_0] + (1 + 2\sqrt{3}) \cos[(\omega_0^* - n)t + \beta_0] \right\} + \\ & -\varepsilon^2 \frac{27a}{176} \left\{ (\sqrt{3} - 5) \cos[(\omega_0^* - 2n)t + \beta_0] - (\sqrt{3} + 5) \cos[(\omega_0^* + 2n)t + \beta_0] \right\} + \\ & -\varepsilon^2 \frac{1}{2} \sin 2nt + O(\varepsilon^3 t) \end{aligned} \quad (41)$$



New frequencies are therefore activated by the eccentricity perturbation; they are equal to the orbital mean motion and its multiples, respectively, and to their linear combinations with the new fundamental frequency  $\omega_0^*$ .

On examining the solution (41), we observe that the error is  $O(\varepsilon^3 t)$ ; this allows us to determine the number of terms for a valid uniform expansion as a function of the order of magnitude of the time interval considered. For example, the error is  $O(1)$ , and hence, the same order of magnitude of the first term  $\theta_0$  when  $t = O(\varepsilon^{-3})$ . The solution (41) is therefore not valid for  $t \geq O(\varepsilon^{-3})$ , a case for which an expansion up to higher order terms is required; on the contrary, for  $t \geq O(\varepsilon^{-2})$ , the error is  $O(\varepsilon)$ , and a valid uniform expansion consists only of the first term  $\theta_0$ .

This implies that a second order approximation, as in our case, gives an expansion for the solution which consists of the zero and first order terms:  $\theta = \theta_0 + \varepsilon\theta_1$ , and is valid for  $t \geq O(\varepsilon^{-1})$ , that is during a few orbital revolutions; the effects of the second order terms are taken into account on  $\theta_0$  and  $\theta_1$ . For larger intervals of time, higher order terms in the uniform expansion of the solution must be taken into account.

## CONCLUSION

The effects of orbit eccentricity on the plane libration of the tethered satellite system have been studied and the stability of the corresponding motion has been investigated.

It has been demonstrated that, within the first order approximation, stable motion is induced by the nominal values of the eccentricity ( $e = 10^{-3} \div 10^{-4}$ ) for the TSS-1 mission in the station-keeping phase; the transition from stable to unstable motion corresponds in this case to  $e \approx 0.3$ .

Second order effects have also been considered and an approximate solution has been obtained using the multiple scales method. This showed that as time increases the motion spectrum is enriched with new frequencies, which are equal to the orbital mean motion and its multiples, plus their linear combinations with the libration's fundamental frequency.

The perturbation induced during a few orbital revolutions on the amplitude of the motion is of the same order of magnitude as the eccentricity, a value which is negligible for nominal values of eccentricity in the TSS-1 mission. However, this perturbation should become more and more appreciable as  $e$  increases to values larger than the nominal ones; in this case, a higher order approximation is required to check stability of the motion during a given number of orbital revolutions.

## ACKNOWLEDGMENT

This paper is part of a research program sponsored by the Agenzia Spaziale Italiana (A.S.I.)

## REFERENCES

1. V. J. Modi and A. K. Misra, "Orbital Perturbations of Tethered Satellite Systems" *The Journal of Astronautical Sciences*, Vol. XXV, N. 3, July-September 1977, pp. 271-278.
2. S. Bergamaschi, S. Cusinato and A. Sinopoli, *A Continuous Model for Tether Elastic Vibrations in TSS*, AIAA Paper N. 86-0087, AIAA 24th Aerospace Sciences Meeting, Reno, Nevada, January 1986.
3. S. Bergamaschi, *Dynamics and Dynamics Experiments in TSS-1*, AGARD-CP-489, Paper N. 19, Proceedings of the AGARD Conference on Space Vehicle Flight Mechanics, Luxembourg, November 1989.
4. M. Pasca, M. Pignataro and A. Luongo, "Three-Dimensional Vibrations of Tethered Satellite Systems", *Journal of Guidance, Control and Dynamics*, Vol. 14, N. 2, March-April 1991, pp. 312-320.
5. S. Bergamaschi and F. Bonon, "Coupling of Tether Lateral Vibration and Subsattellite Attitude Motion", *Journal of Guidance, Control and Dynamics*, Vol. 15, N. 5, September-October 1992, pp. 1284-1286.
6. S. Bergamaschi, F. Bonon and M. Legnami, "Spectral Analysis of Tethered Satellite System Mission-1 Vibrations", *Journal of Guidance, Control and Dynamics*, Vol. 18, N. 3, May-June 1995, pp. 618-624.
7. S. Bergamaschi, P. Zanetti and C. Zottarel, "Nonlinear Vibrations in the Tethered Satellite System-Mission 1", *Journal of Guidance, Control and Dynamics*, Vol. 19, N. 2, March-April 1996, pp. 289-296.
8. H. B. Schechter, "Dumbbell Librations in Elliptic Orbits", *AIAA Journal*, Vol. 2, N. 6, 1964, pp. 1000-1003.
9. V. J. Modi and R. C. Brereton, "Libration Analysis of a Dumbbell Satellite Using the WKBJ Method", *Journal of Applied mechanics*, Transactions of the ASME, September 1966, pp. 676-678.
10. V. J. Modi and R. C. Brereton, "Periodic Solutions Associated with the Gravity-Gradient-Oriented System: Part I. Analytical and Numerical Determination", *AIAA Journal*, Vol. 7, N. 7, July 1969, pp. 1217-1225.
11. E. B. Crellin and F. L. Janssens, *Some Properties of the In-Plane Motion of a Dumbbell in Elliptic Orbit*, Internal ESTEC Working Paper n. 1888, Noordwijk, May 1996.
12. J. J. Stoker, *Non linear vibrations*, Interscience Pub., New York, 1950.
13. A. H. Nayfeh, *Introduction to Perturbation Techniques*, John Wiley & Sons, Inc., New York, 1993.

## APPENDIX

*First term.* The substitution of solution (28) in the first term  $-2 D_0 D_1 \theta_1$  of Eq.(29) implies that it is zero:

$$D_0 D_1 \theta_1 = D_0 D_1 \left\{ -\frac{9}{22} A_0(T_2) \left[ (1-2\sqrt{3}) e^{i(\omega_0+n)T_0} + \right. \right. \\ \left. \left. + (1+2\sqrt{3}) e^{i(\omega_0-n)T_0} \right] + \sin nT_0 + c.c. \right\} = 0$$

since both the exponential and harmonic terms depend only on  $T_0$ , and  $A_0 = A_0(T_2)$  is independent of both  $T_0$  and  $T_1$ .

*Second term.* The second term contains secular perturbations, since it is:

$$-2D_0 D_2 \theta_0 = -2i\omega_0 [D_2 A_0(T_2) e^{i\omega_0 T_0} - D_2 \bar{A}_0(T_2) e^{-i\omega_0 T_0}]$$

*Third term.* This term also can induce secular effects; it can be expressed as:

$$\begin{aligned} (1 + 3\cos 2nT_0)\theta_0 &= \left[1 + \frac{3}{2}(e^{i2nT_0} + e^{-i2nT_0})\right] [A_0(T_2) e^{i\omega_0 T_0} + \bar{A}_0(T_2) e^{-i\omega_0 T_0}] \\ &= [A_0(T_2) e^{i\omega_0 T_0} + \bar{A}_0(T_2) e^{-i\omega_0 T_0}] + \frac{3}{2} A_0(T_2) [e^{i(\omega_0+2n)T_0} + e^{i(\omega_0-2n)T_0}] + \\ &\quad + \frac{3}{2} \bar{A}_0(T_2) [e^{-i(\omega_0+2n)T_0} + e^{-i(\omega_0-2n)T_0}] \end{aligned}$$

*Fourth term.* Finally the fourth term  $\cos nT_0 \theta_1$  can be transformed as:

$$\begin{aligned} \cos nT_0 \theta_1 &= \left( \frac{e^{inT_0} + e^{-inT_0}}{2} \right) \left\{ -\frac{9}{22} A_0(T_2) [(1-2\sqrt{3}) e^{i(\omega_0+n)T_0} + \right. \\ &\quad \left. + (1+2\sqrt{3}) e^{i(\omega_0-n)T_0}] + \sin nT_0 + c.c. \right\} \\ &= \frac{-9}{44} A_0(T_2) \left[ (1-2\sqrt{3}) (e^{i(\omega_0+2n)T_0} + e^{i\omega_0 T_0}) + (1+2\sqrt{3}) (e^{i\omega_0 T_0} + \right. \\ &\quad \left. + e^{i(\omega_0-2n)T_0}) \right] - \frac{9}{44} \bar{A}_0(T_2) \left[ (1-2\sqrt{3}) (e^{-i(\omega_0+2n)T_0} + e^{-i\omega_0 T_0}) + \right. \\ &\quad \left. + (1+2\sqrt{3}) (e^{-i\omega_0 T_0} + e^{-i(\omega_0-2n)T_0}) \right] + \frac{1}{4i} (e^{i2nT_0} - e^{-i2nT_0}) \end{aligned}$$



**Page intentionally left blank**

## Control of the XMM orbit using momentum dumping manoeuvres

Mats Rosengren<sup>1</sup>

XMM is a space telescope for the X-ray frequency band to be launched in August 1999. It will be operated in an elliptic Earth synchronous 48 hours orbit with an apogee altitude of about 114000 km and a perigee altitude of about 7000 km. Because of the Earth synchronous orbital period the triaxiality of the Earth will cause a secular perturbation of the orbital period. The size of this secular perturbation of the period will depend on the phase of the orbit relative to the Earth rotation, i.e. on the apogee longitude. Regular orbit maintenance manoeuvres will therefore be necessary to maintain the Earth synchronisation.

The attitude is controlled with reaction wheels. Because of the non-cyclic components of the torque caused by the solar radiation pressure and the gravity gradient these wheels will have to be off-loaded at least once per orbit. This is done by exerting small torques on the spacecraft with thruster burns. These burns should be made below 40000 km altitude outside the period of science observation but within ground station coverage.

It is shown in this paper that although the attitudes in which the momentum dumping manoeuvres can be made in are severely constraint to avoid blinding of attitude sensors and although the size of the momentum dumping manoeuvres are small (typically 2-4 mm/s) it is possible to design these manoeuvres such that they also will correct the orbital period

This is an innovation compared to the orbit control of the ESA space telescope ISO for which special orbit control manoeuvres had to be made.

### Introduction

The scientific observations with XMM will only be made at an altitude above 40000 km. There will at the very least be 55 minutes<sup>2</sup> between the end of these operations and the loss of ground station coverage before the perigee passages. In this time the following operations will take place:

- 
1. European Space Operations Centre,  
Robert Bosch Str. 5  
D-64293 Darmstadt, Germany  
mrosengr@esoc.esa.de
  2. In general between 120 and 150 minutes

- slew to an attitude suitable for the perigee passage
- make a momentum dumping manoeuvre
- hibernate the spacecraft

The ground station coverage will then be regained after the perigee passage at least 70 minutes<sup>1</sup> before the start of the scientific operations at an altitude of 40000 km. In this time the following operations will take place:

- de-hibernate the spacecraft
- make a momentum dumping manoeuvre
- slew to the attitude for the first scientific observation

These momentum dumping manoeuvres having magnitudes in the order of a few mm/s will slightly modify the orbital period. The purpose of this study is to investigate if these manoeuvres can be designed to maintain a perfect synchronisation with the rotation of the Earth making special orbit maintenance manoeuvres superfluous.

## Avionics design

The pointing of the telescope is determined by a star tracker looking in the direction of the telescope. The roll angle around the viewing direction of the telescope is determined by a slit sun sensor. The normal attitude control mode is to operate the reaction wheels such that the image of a guide star on the focal plane of the star tracker is kept on a given fixed position and that the Sun is in the meridian plane of the spacecraft corresponding to the slit of the sun sensor.

The spacecraft will have a blow-down hydrazine Reaction Control System with 2 redundant sets of thrusters each consisting of 4 thrusters. All thrusters will give a force off-set with only 12 deg from the direction of view of the telescope. The thrusters have different lever arms and can be operated to impart any torque to the spacecraft (Yaw, Pitch, Roll) but the direction of the resulting force will always be within 12 deg of the direction of view of the telescope.

## Requirements on the perigee passage attitude

During the perigee passage the star sensor shall stay locked on a star. Bright objects like the Sun, the Earth and the Moon would blind the starsensor and prevent it from seeing the star.

The angle between the viewing direction of the starmapper/telescope and the direction to the Sun shall take a value between 70 deg and 110 deg at all times. With this requirement fulfilled the Sun will not disturb the functioning of the starmapper/telescope, the sun sensor will see the Sun (with an adequate roll control around the x-axis) and the thermal balance on-board the spacecraft will be adequate. The viewing direction must also be off-set from the rim of the Earth with a separation angle of at least 35 degrees. Because of the large apparent radius of the Earth at low altitudes and the large off-set required a large portion of the direction sphere is prohibited. The Moon being less bright shall have a separation angle of at least 3 degrees. This requirement is in general easy to fulfil because of the small apparent radius of the Moon and the small off-set required.

---

1. In general between 120 and 150 minutes



The possibilities to fulfil both the solar aspect angle constraint and the earth aspect angle constraint depends on the orientation of the orbit relative to the direction to the Sun. To illustrate this dependence it is useful to introduce a right hand rectangular coordinate system  $\bar{a}, \bar{b}, \bar{c}$  defined by the orientation of the orbit with the c-axis in the direction of the orbital pole and with the a-axis in the direction from the centre of the Earth to perigee.

In figure 1 the viewing directions of the starmapper/telescope fulfilling these Sun/Earth/Moon constraints for the reference orbit from an altitude of 40000 km before the perigee passage 1999/8/7 to the same altitude after the perigee passage are displayed. It can be seen that the right ascension relative the  $\bar{a}, \bar{b}, \bar{c}$  system has to be in the interval from -73 deg to 58 deg and the declination between 19 deg and 63 deg. In figure 2 the viewing directions fulfilling these conditions for the whole orbit following this perigee passage are displayed. It can be seen that the declination now is restricted to the range between 38 deg and 63 deg.

### The gravity gradient torque

In the annex the following formula for the perturbing torque caused by the gravity gradient is derived:

$$\bar{T} = \frac{3\mu}{r^3} \times (\beta\gamma(I_3 - I_2), \gamma\alpha(I_1 - I_3), \alpha\beta(I_2 - I_1))$$

where

$\mu$  is the gravitational constant of the Earth (398601.3 km\*\*3/sek\*\*2)

$r$  is the distance from the Earth centre to the spacecraft

$\alpha, \beta, \gamma$  are the direction cosinus relative the principal axis system for the direction (unit vector) from the Earth centre to the spacecraft

$I_1, I_2, I_3$  are the principal moments of inertia

The approximate numerical values of  $I_1, I_2, I_3$  are 5000, 28000 and 29000 kg m\*\*2. As  $I_2$  is close to  $I_3$  the gravity gradient torque component around principal axis number 1 (the x-axis) will be rather low. The products  $\beta\gamma, \gamma\alpha$  and  $\alpha\beta$  are always in the interval from -0.5 to 0.5. The maximal torque component that can be obtained around a principal axis is therefore obtained around the spacecraft y-axis at a low perigee passage ( $r=12500$  km) with an attitude such that the local vertical is in the plane defined by the x-axis and the z-axis making an angle of 45 deg to these axis. This is illustrated in figure 3. This maximal torque around the z-axis is 0.007 Nm while the torques around the x and the y axis are zero. The accumulated torque around the z axis is zero over any orbital arch that is symmetric around perigee for such an attitude. The accumulated torque around the y axis over the orbital arch from true anomaly -90 deg to 90 deg is 18 Nms for the attitude of fig 3. This is largest accumulated torque that is possible over this orbital arch. The intermediate accumulated torques in this attitude over this orbital arch are displayed in figure 4. The z-component of the accumulated torque is cyclic with a maximal value of 7 Nms at perigee. Defining the x-axis to be positive along the viewing direction of the starmapper/telescope (i.e. opposite to the conventional definition defined by the s/c contractor) the attitude of fig 3 corresponds about to the mid-point of the area of attitudes adequate for the perigee passage displayed in figures 1 and 2 (right ascension 0 deg, declination 45 deg).

## The orbital effects of momentum dumping manoeuvres

As said in the introduction it is planned to make momentum dumping manoeuvres to off-load the reaction wheels below the altitude of 40000 km when anyway no scientific observations are done. As these momentum dumping manoeuvres have to be executed within ground station coverage they will typically be made at an altitude between 30000 and 40000 km before and/or after a perigee passage. The delta-V resulting from such a manoeuvre will have a direction close to the direction of view of the telescope. Figure 5 shows the change in semi-major axis resulting from such a momentum dumping manoeuvre in the range of possible perigee passage attitudes displayed in figure 1 under the following assumptions:

- The dumping is made at 40000 km altitude in the attitude for perigee passage
- The dumping is made for the accumulated gravity gradient torque passing from 40000 km altitude down to perigee and then back up to 40000 km altitude
- For any possible right ascension (in the  $\bar{a}, \bar{b}, \bar{c}$  coordinate system) the declination is chosen as close to zero as possible, i.e. the x-axis is as close as possible to the orbital plane. This maximises the orbital effects of the dumping manoeuvre.

It is seen that any change in semi-major axis between an increase with 219 m (entire dumping before perigee and a decrease with 217 m (entire dumping after perigee) can be obtained. The data for these cases are

Table 1:

Case	1	2
True anomaly	-126.9 deg	126.9 deg
Right ascension	29.00 deg	-30.00 deg
Declination	36.66 deg	37.24 deg
$H_x^a$	0.64 Nms	-0.34 Nms
$H_y$	14.56 Nms	16.01 Nms
$H_z$	7.39 Nms	-4.45 Nms
$DV_x$	3.8 mm/s	3.7 mm/s
$DV_y$	-0.3 mm/s	0.2 mm/s
DA	219 m	-217 m

a. x- in the direction of view of the telescope. y/z in the orthogonal plane.

Other additional torques like solar radiation torque and magnetic torque will tend to increase the sizes of the momentum dumping resulting in a somewhat larger delta-v i.e. the control authority will in reality be somewhat larger!

Figure 6 shows the same for the perigee passage attitudes satisfying the Earth aspect angle constraints for the full orbit as displayed in figure 2. It can be seen that also in this more restrictive



case the full range of possible changes to the semi-major axis is available.

Figure 7 shows the effect of a simulated momentum dumping strategy for the reference orbit aiming at

- to get a maximal increase in semi-major axis
- to have no average effect of the momentum dumping, i.e a situation similar to “free drift”
- to get a maximal decrease in semi-major axis

It can be seen that the control authority of the momentum dumping manoeuvres by far exceeds what is necessary to maintain a perfect Earth synchronisation and to maintain an optimal ground station coverage.

## Conclusions

After the initial orbit acquisition there should be no need for orbit manoeuvres to maintain the synchronisation of the orbital period with the Earth rotation. This will instead be achieved by the optimal design of the momentum dumping manoeuvres.

## Annex: The gravity gradient torque

If  $\bar{r}$  is the radius vector from the centre of the Earth to the centre of mass of the spacecraft and  $d\bar{r}$  is the radius vector from the centre of mass of the spacecraft to a mass element with the mass  $dm$  the force on the mass element due to the Earth gravitation can be written

$$d\bar{f} = -\mu \frac{\bar{r}}{r^3} dm - \mu \frac{d\bar{r} dm}{r^3} + \frac{3\mu}{r^3} \hat{r} \langle d\bar{r} | \hat{r} \rangle dm$$

where  $\hat{r}$  is the unit vector in the direction of  $\bar{r}$  and  $r$  is the distance between the spacecraft and the centre of the Earth

Forming the cross product  $d\bar{r} \times d\bar{f}$  and integrating over all mass elements one gets the total torque

$$\int d\bar{r} \times d\bar{f} = \frac{3\mu}{r^3} \int d\bar{r} \times \hat{r} \langle d\bar{r} | \hat{r} \rangle dm$$

Introducing a right handed orthogonal coordinate system with  $z$  axis in the direction of  $\hat{r}$  this integral takes the form



$$\frac{3\mu}{r^3} \cdot \langle \int yz dm, -\int xz dm, 0 \rangle$$

If the same spacecraft rotates around the z axis with an angular rate  $\omega$  the angular momentum is body is

$$\omega \cdot \langle -\int xz dm, -\int yz dm, \int x^2 + y^2 dm \rangle$$

As the rotation vector has the components  $\langle 0, 0, \omega \rangle$  it follows that

$$\bar{\omega} \times \bar{M} = \omega^2 \langle \int yz dm, -\int xz dm, 0 \rangle$$

In the principal axis system the components of  $\bar{\omega} \times \bar{M}$  are

$$\omega^2 \langle \beta\gamma(I_3 - I_2), \gamma\alpha(I_1 - I_3), \alpha\beta(I_2 - I_1) \rangle$$

where  $\alpha, \beta, \gamma$  are the direction cosinus of the rotation vector which is in the direction of  $\hat{r}$ . It follows that the gravity gradient torque in the principal axis system is

$$\bar{T} = \frac{3\mu}{r^3} \times (\beta\gamma(I_3 - I_2), \gamma\alpha(I_1 - I_3), \alpha\beta(I_2 - I_1))$$

where

$\mu$  is the gravitational constant of the Earth (398601.3 km\*\*3/sek\*\*2)

$r$  is the distance from the Earth centre to the spacecraft

$\alpha, \beta, \gamma$  are the direction cosinus relative the principal axis system for the direction (unit vector) from the Earth centre to the spacecraft

$I_1, I_2, I_3$  are the principal moments of inertia

Introducing coordinate axis  $\bar{a}, \bar{b}, \bar{c}$  defined by the orbit such that  $\bar{a}$  points from the centre of the Earth to perigee and  $\bar{c}$  is in the direction of the orbital pole then

$$\alpha = x_a \cos \theta + x_b \sin \theta$$

$$\beta = y_a \cos \theta + y_b \sin \theta$$

$$\gamma = z_a \cos \theta + z_b \sin \theta$$

where  $\theta$  is the true anomaly and  $x_a, x_b, x_c, y_a, y_b, y_c$  and  $z_a, z_b, z_c$  are the direction cosinus of

the principal axis with respect to the  $\bar{a}, \bar{b}, \bar{c}$  axis.

As the change of integration variable from time  $t$  to true anomaly  $\theta$  is made by the transformation

$$dt\sqrt{\mu p} = d\theta r^2$$

and as

$$\frac{1}{r} = \frac{1 + e \cos \theta}{p}$$

the time integral of  $\bar{T}$  along a Kepler orbit from true anomaly  $\theta_1$  to  $\theta_2$  can be computed analytically by finding the primitive function to a trigonometric polynomial. This primitive function is

$$\frac{3}{p} \times \sqrt{\frac{\mu}{p}} ((I_3 - I_2)(F_1(\theta) + eG_1(\theta)), (I_1 - I_3)(F_2(\theta) + eG_2(\theta)), (I_2 - I_1)(F_3(\theta) + eG_3(\theta)))$$

where

$$F_j(\theta) = A_j\theta + B_j\sin(2\theta) - C_j\cos(2\theta)$$

and

$$G_j(\theta) = A_j\sin\theta + B_j\left(\frac{\sin(3\theta)}{3} + \sin\theta\right) - C_j\left(\frac{\cos(3\theta)}{3} + \cos\theta\right)$$

where

$$A_1 = \frac{(y_a z_a + y_b z_b)}{2}$$

$$A_2 = \frac{(z_a x_a + z_b x_b)}{2}$$

$$A_3 = \frac{(x_a y_a + x_b y_b)}{2}$$

$$B_1 = \frac{(y_a z_a - y_b z_b)}{4}$$

$$B_2 = \frac{(z_a x_a - z_b x_b)}{4}$$

$$B_3 = \frac{(x_a y_a - x_b y_b)}{4}$$

$$C_1 = \frac{(y_a z_b + y_b z_a)}{4}$$

$$C_2 = \frac{(z_a x_b + z_b x_a)}{4}$$

$$C_3 = \frac{(x_a y_b + x_b y_a)}{4}$$



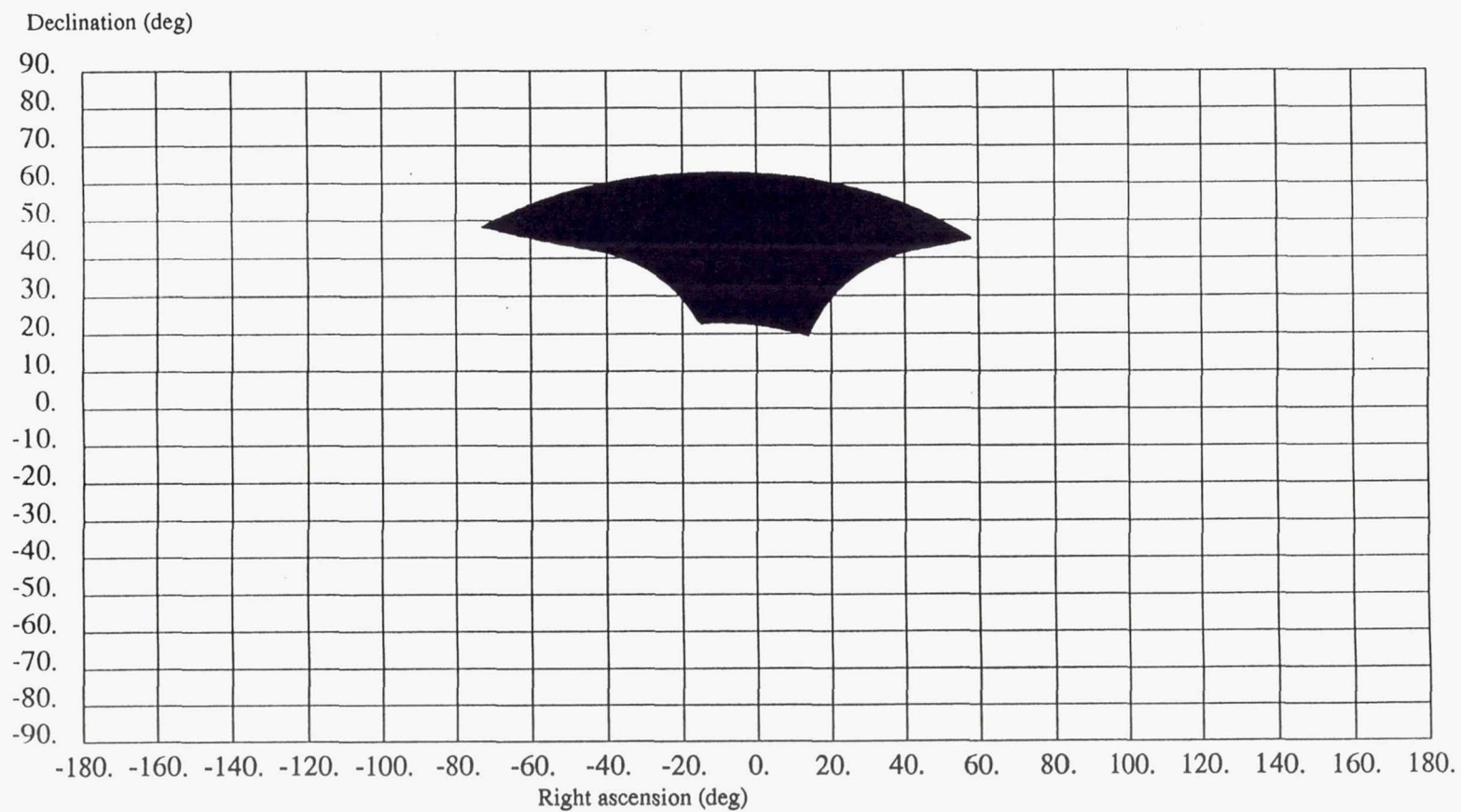


Figure 1: The possible viewing direction of the starmapper/telescope during the perigee passage of the reference orbit 99/08/07. Earth aspect angle constraint fulfilled up to altitude 40000 km.

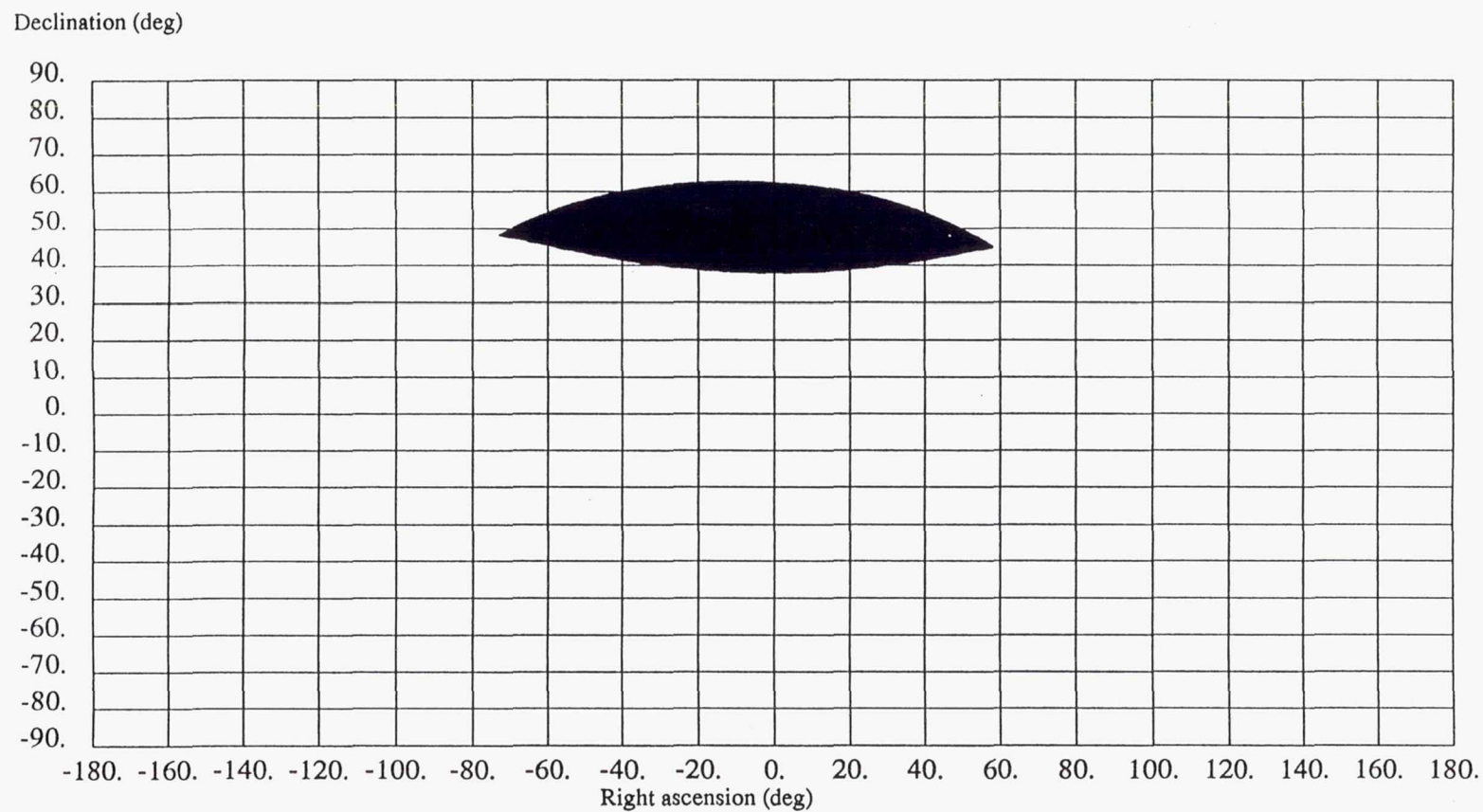


Figure 2: The possible viewing direction of the starmapper/telescope during the perigee passage of the reference orbit 99/08/07. Earth aspect angle constraint fulfilled the whole following orbital revolution

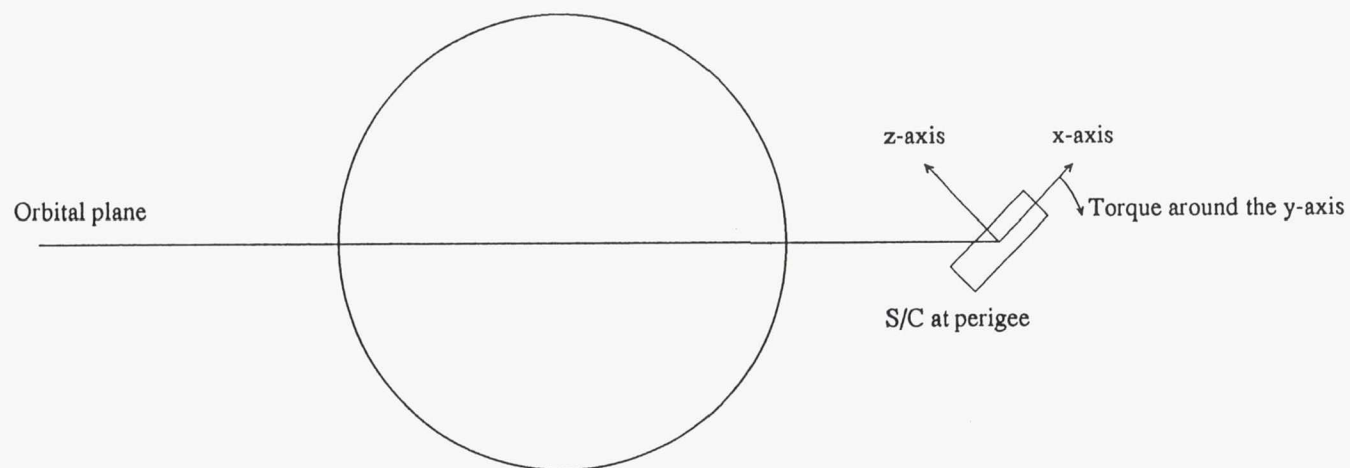


Figure 3: The attitude resulting in a maximal gravity gradient torque. The torque is in the directed to align the x-axis with the local vertical. This attitude also gives the maximal accumulated torque from -90 deg to 90 deg true anomaly.



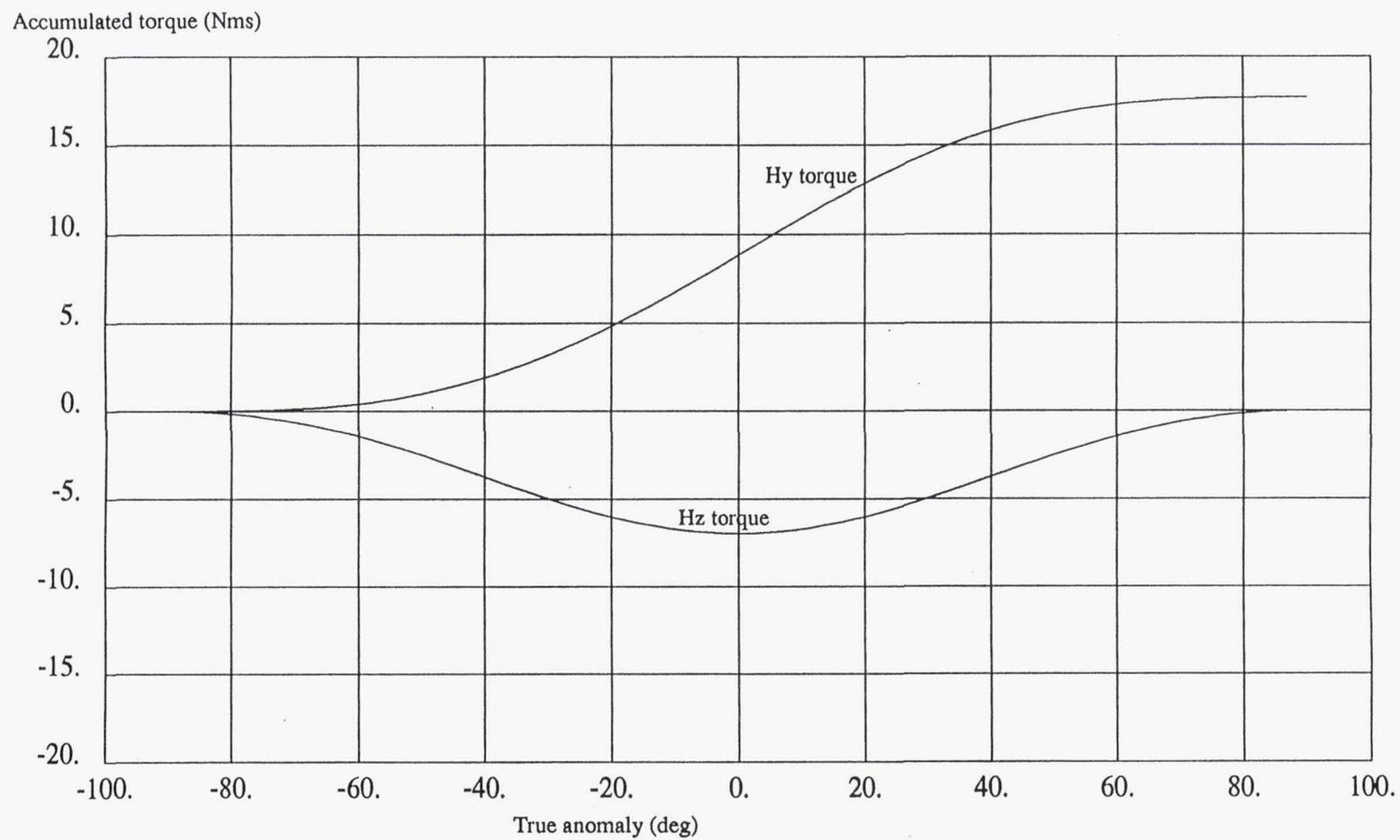


Figure 4: The accumulated torque with an attitude as in figure 3 from true anomaly -90 deg to 90 deg. The accumulated Hy torque increases continuously to 19 Nms while the accumulated Hz torque is cyclic with final value zero

Change in semi-major axis (km)

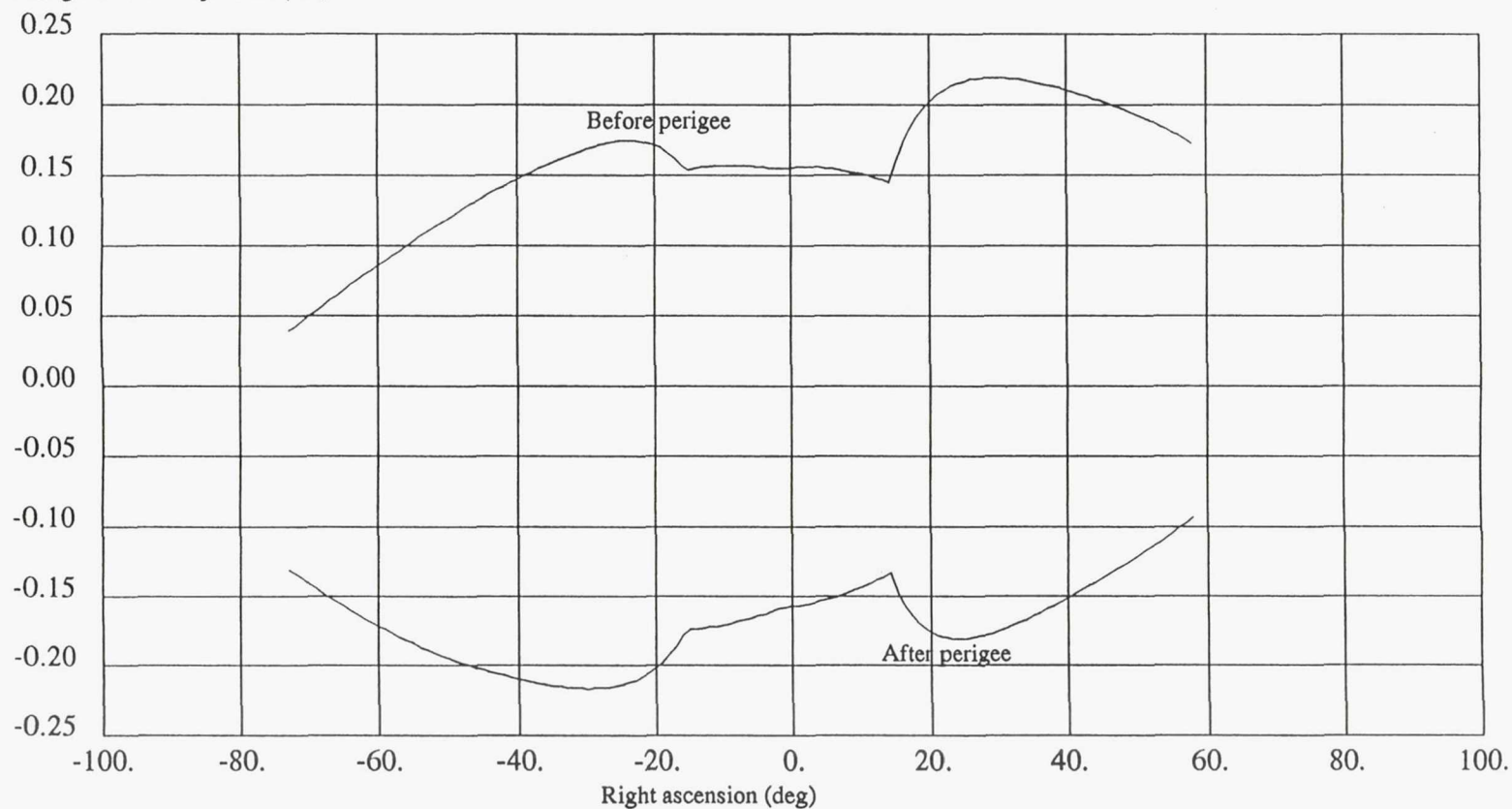


Figure 5: The range of the possible changes in semi-major axis that can be obtained with a momentum dumping manoeuvre at 40000 km altitude before and after perigee with the attitudes of figure 1. For given r.asc. the decl. is chosen as close as possible to zero

Change in semi-major axis (km)

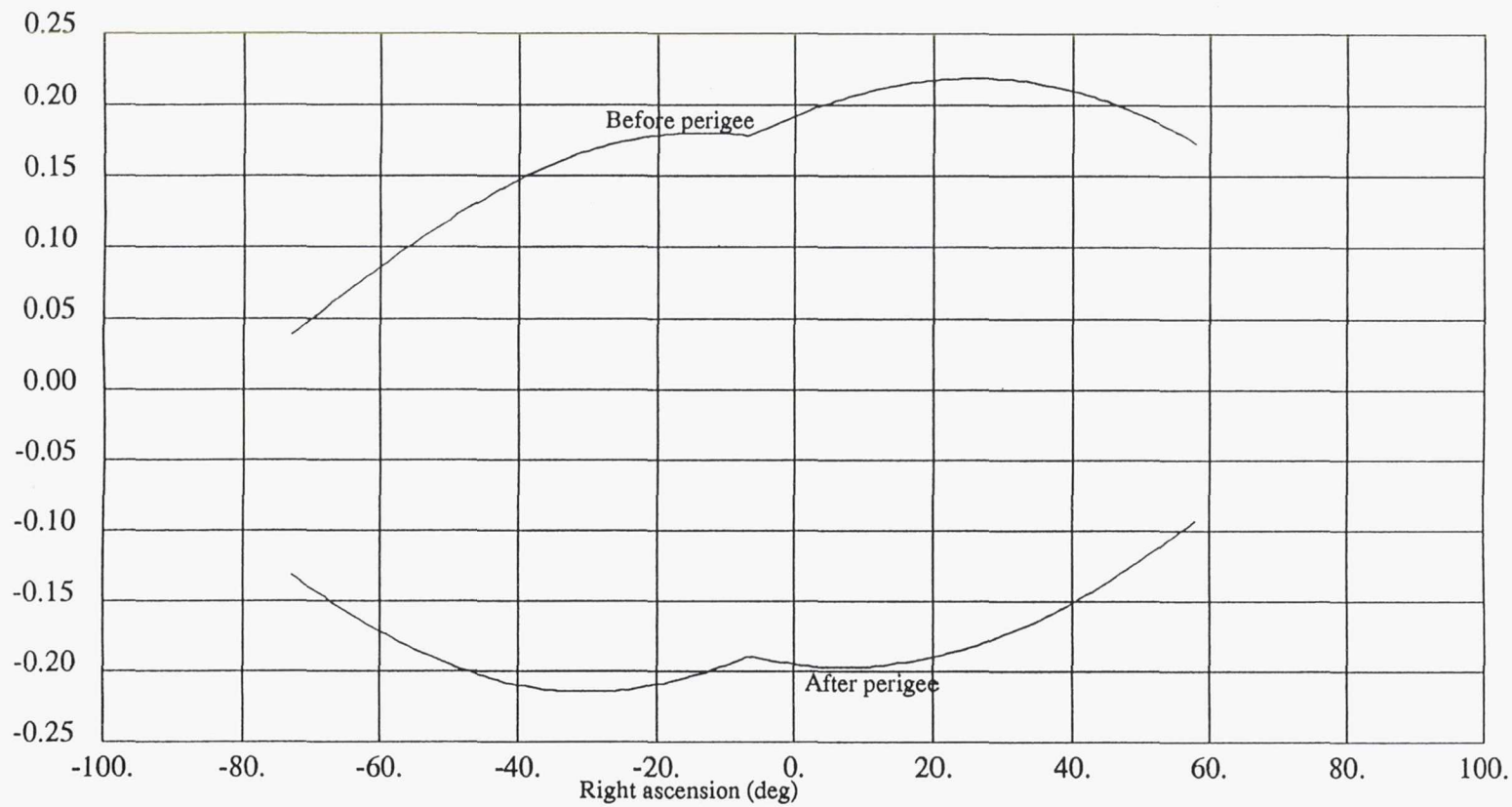


Figure 6: The range of the possible changes in semi-major axis that can be obtained with a momentum dumping manoeuvre at 40000 km altitude before and after perigee with the attitudes of figure 2. For a given right ascension the declination is chosen as close as possible to zero



Semi-major axis (km)

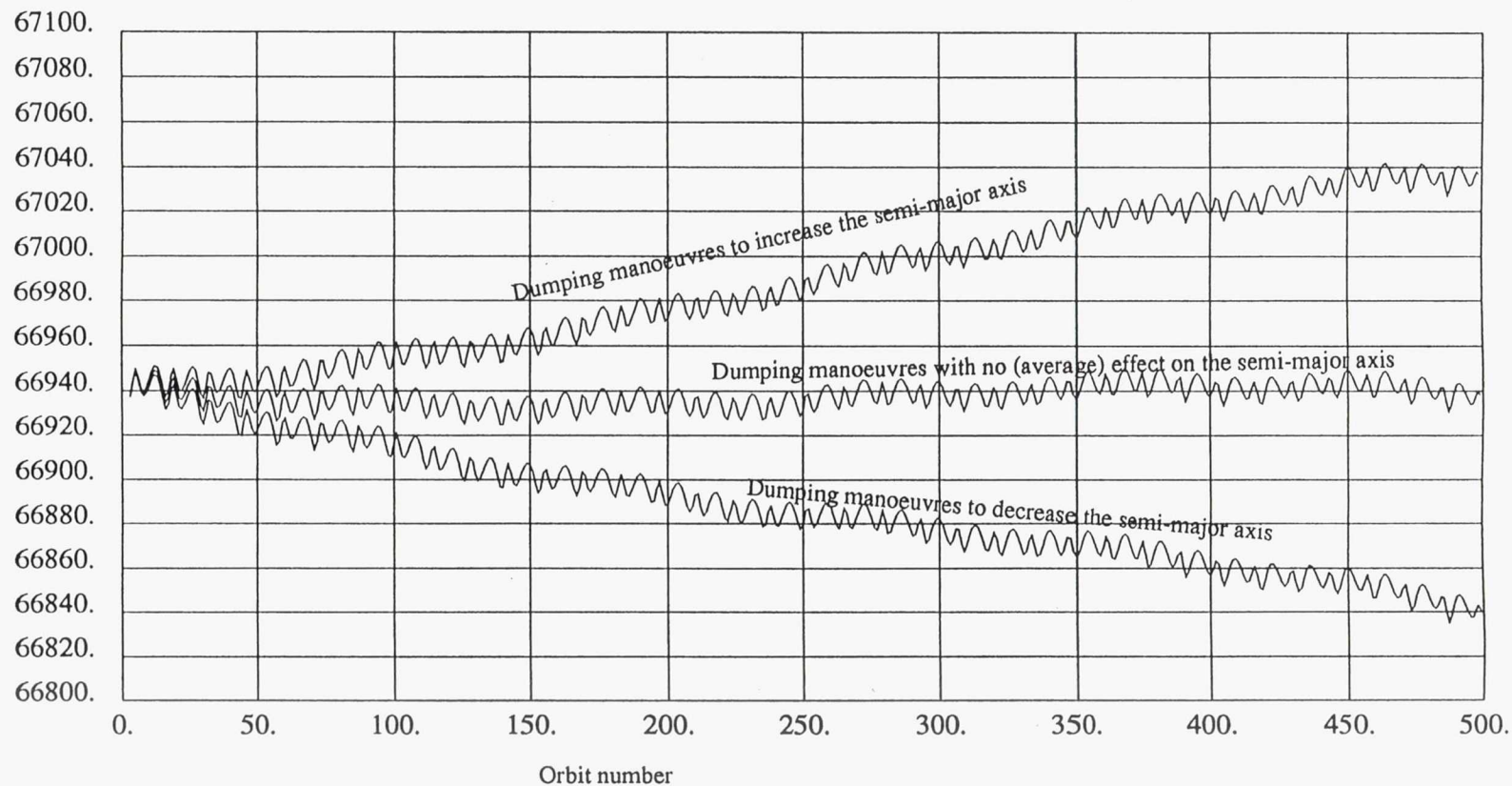


Figure 7: The range of possible semi-major axis developments (osculating at apogee) that can be obtained with momentum dumping manoeuvres at 40000 km altitude in permissible perigee passage attitudes.

**Page intentionally left blank**

## RADARSAT TIME RATE OF MEAN SEMI-MAJOR AXIS DUE TO DRAG

Said R. Marandi \*

A model of time rate of the mean semi-major axis due to radiation drag versus day of year and orientation of RADARSAT is developed. This model takes into account the periodic shadowing of the satellite by the earth during the summer months. Through use of this model, the flight orbital data from 1996-98, and a number of assumptions, the following parameters are extracted via a least squares technique: (i) the aerodynamic drag formed only about 39% of the net drag on the satellite in 1996; (ii) 21% of the radiation on the cell side of the solar array was reflected.

Four pieces of evidence are offered for the accuracy of the tuned model: (1) the flight measured time rate of mean semi-major axis prior, during and after a ten day solar array articulation maneuver versus the predictions of the tuned model, (2) the vendor absorptance values for the cell side of the solar array versus the deduced reflected portion of the incident radiation, (3) the increase of the average aerodynamic drag from year 1996 to 97 deduced from this model versus the rise of the solar flux at 10.7 cm wave length and (4) qualitative agreement between the model and the measured data during 1996-98.

Aside from the operational significance of (i), once proven accurate by accounting for the remaining fuel of RADARSAT in year 2001 and the effect of solar cycles on the atmospheric drag, this intelligence, markedly different from the values estimated by previous studies, opens the door to the following consideration: an effective use of radiation pressure may be made in the design of satellites with large surface to mass ratio to reduce the needed fuel for periodic orbit corrections.

---

\*Spacecraft Dynamics Engineer with Canadian Space Agency, 6767 route de l'Aéroport, Saint-Hubert, Quebec J3Y 8Y9, Canada. Phone: (514) 926-4691, FAX: (514) 926-4695.



## INTRODUCTION

In the following paragraphs, the motive behind this work is given. Throughout this paper semi-major axis is short for mean semi-major axis of RADARSAT<sup>†</sup>.

The problem facing the flight dynamics group in preparation for the Antarctic Mapping Mission of RADARSAT was to ensure that the ground track of the satellite remained within  $\pm 5$  km of the nominal track during the sixty days of the mission. In Antarctic orientation one can only lower the altitude of the satellite; in this orientation the thrust vector is along the velocity vector of the satellite. A reliable estimate of daily drop in the altitude of the satellite in the Antarctic orientation, for which there was no prior data, was needed. This estimate allowed the operators to raise appropriately the altitude of the satellite prior to the Antarctic Mapping Mission.

The initial aim of the study reported in this paper was to estimate the daily drop in the semi-major axis of the satellite in the Antarctic orientation.

## METHODOLOGY

In the following paragraphs, the method employed to estimate the constituents of drag on the satellite is outlined.

The *modus operandi* in this study was to base all estimates on the flight data collected during the first two years of the operation of the satellite. Furthermore, I considered the solar radiation phenomenon much better understood than the atmospheric conditions in exosphere. As a result, I wrote a model of time rate of semi-major axis  $\dot{a}(\alpha, \rho, t)$  due to the solar radiation as a function of two parameters: articulation angle of the solar array  $\alpha$  and the ratio of the reflected to incident radiation on the cell side of the solar array  $\rho$ . This model naturally depends upon time  $t$  which ties the phenomena such as sun declination and distance with  $\dot{a}$ . The sun declination in combination with the particular orbit of RADARSAT dictate eclipse periods which are taken into account in the model.

The component of the net force due to the solar radiation along the inertial velocity of the satellite averaged over an orbit with due regard to eclipse periods is computed as a function of time  $t$ . I refer to this component as the radiation drag. The radiation force is due to the reflection of the solar radiation off the solar array wings and the SAR antenna. The component of the portion of the solar force due to the absorption of the radiation by the satellite along the velocity vector averaged over an orbit is about zero and plays no role in  $\dot{a}$ . In this analysis, reflected intensity refers strictly to specular reflection: the portion of the scattered energy in the incident plane reflected at an angle equal to the incident angle. The diffuse reflection is of secondary importance.

---

<sup>†</sup>RADARSAT is a Canadian-led cooperative program with the U.S. to launch and operate a remote sensing satellite with a synthetic aperture radar. The launch was on 4 November 1995.

The available flight data is in the form of mean semi-major axis given at intervals of about one day. The time rate of mean semi-major axis  $\dot{A}(t_i)$  computed from the flight data constitute the measurement in this analysis. The family  $(t_i)_{i=1}^n$  is the sequence of time tags at which a measurement is available.

To find the time rate of semi-major axis due to aerodynamic drag  $D$  and  $\rho$  minimize

$$\sum_{i=1}^n \left( \dot{a}(\alpha, \rho, t_i) + D - \dot{A}(t_i) \right)^2$$

with respect to these two parameters. This method yields a constant value  $D$  over the period under consideration  $t_n - t_1$ . One year was the adopted period in this study. A year is long enough to average out the diurnal, 27-day, seasonal-latitudinal and semi-annual variations in the aerodynamic drag and short enough to reflect the 11-year variation due to the solar cycles. The named atmospheric phenomena are reported in Ref. [1].

## RESULTS

The results of the analysis outline in the previous section is given below.

Figures 1 and 2 show the results of the least squares fit of the model and the data for years 1996-97. For 1996 data  $\rho = 0.21$  and  $D = -0.47$  m/day. For 1997 data  $\rho = 0.20$  and  $D = -0.54$  m/day. Assuming that we have a moderately good fit to the data one may estimate standard deviations of 0.26 m/day and 0.28 m/day for data from these two years. The relatively large dispersion in the measured data is, possibly, a result of the particular choice of mean semi-major axis. I suspect that the orbital period, as a proxy for the altitude of the satellite, would show a smaller relative dispersion.

The marked minimum in the time rate of semi-major axis near summer solstice corresponds to the season when part of the satellite orbit is eclipsed by the earth. The large gaps in the data are from periods when the articulation of the solar array was other than nominal.

## VERIFICATION

In this section pieces of evidence which lend credence to the results are presented.

To verify the accuracy of the model with the determined parameters, I have computed the effect of the articulation of the solar array to body aligned orientation during days 42 to 52 of 1996 and compared to the available data. Figure 3 contains the results of this comparison. The three constant values of the measured time rate of semi-major axis are obtained from three separate linear fits to the measured semi-major axis over periods 35 to 45, 45 to 52 and 55 to 62 days of 1996. There were eight samples in each step. Hence the standard deviation associated with ordinate of

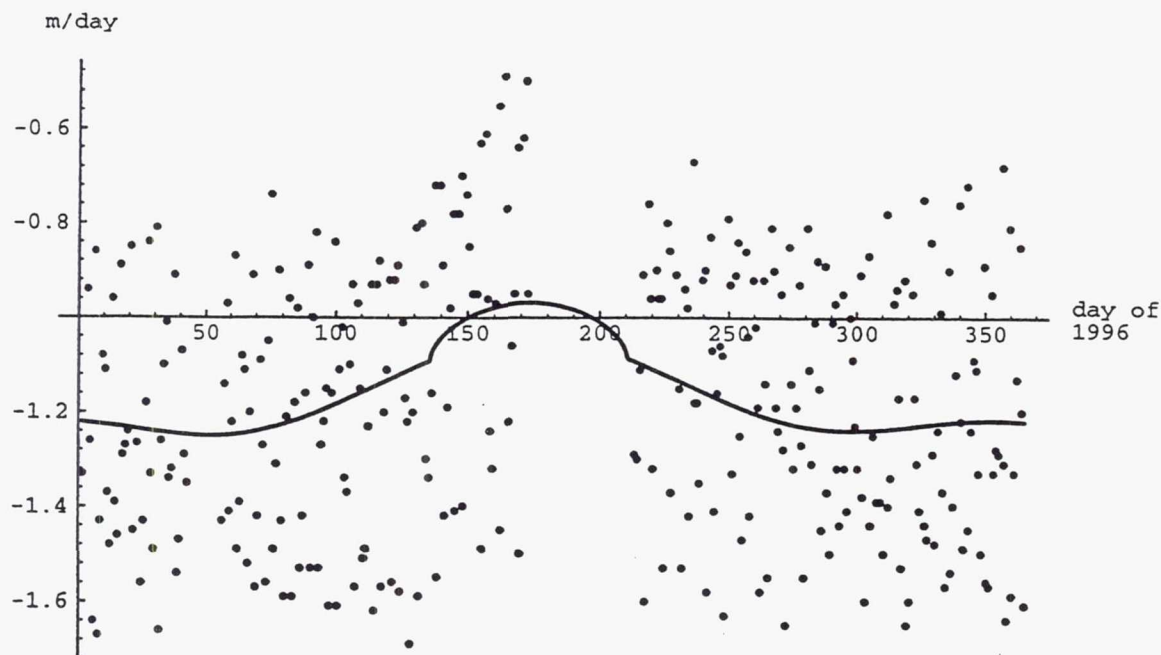


Figure 1: The measured time rate of RADARSAT mean semi-major axis (dots) versus day of year 1996. The line is the best fit of the model to the measured data.

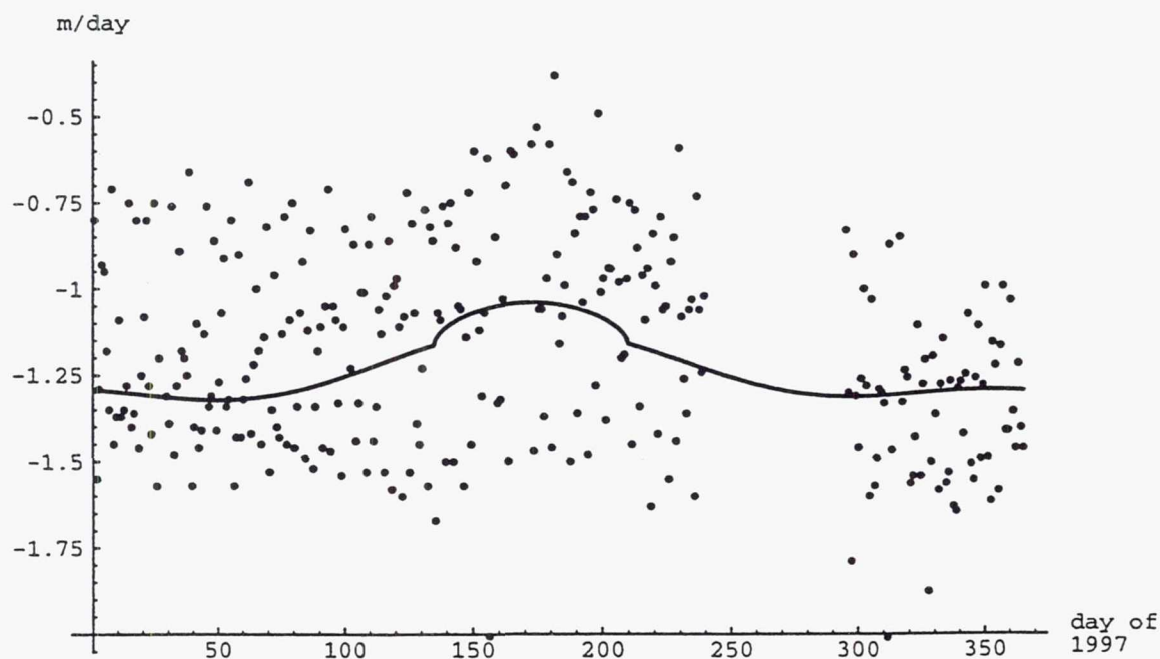


Figure 2: The measured time rate of RADARSAT mean semi-major axis (dots) versus day of year 1997. The line is the best fit of the model to the measured data.



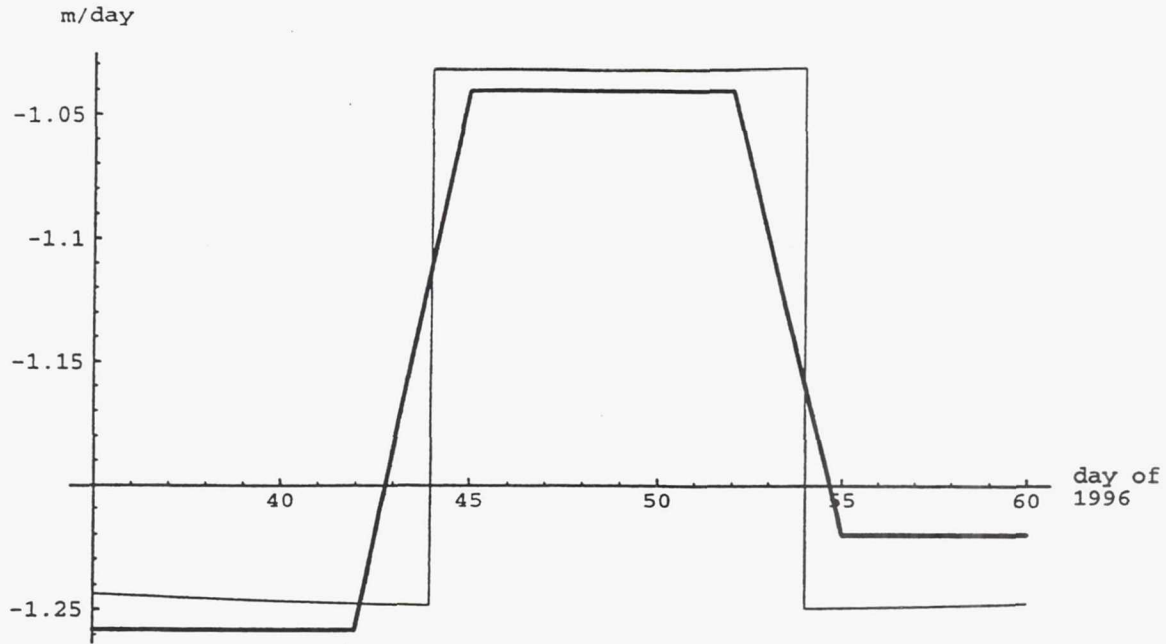


Figure 3: The measured (thick) and the model time rate of mean semi-major axis of RADARSAT versus day of year 1996.

each step, computed from the standard deviation of the data (0.26 m/day) and the sample size, is 0.09 m/day. Therefore, we have an agreement between the model and the data well within one standard deviation. Note that the model was independent of the data from days 35-62 of 1996.

The obtained ratio of the reflected to incident radiation intensity for solar array  $\rho = 0.21$  is consistent with the manufacturer reported solar absorptance of 0.645 (beginning of life) and 0.69 (end of life) for solar cells. The gap between one minus absorptance values and  $\rho$  is attributed to the diffuse reflection of about 0.14 of the incident radiation. Furthermore, the minor reduction of  $\rho = 0.21$  in 1996 to  $\rho = 0.20$  in 1997 is also consistent with the expected increase in the absorptance values of solar cells.

From the aerodynamic contribution to the rate of semi-major axis one may find, through the standard drag equation, an atmospheric density value. Then using the basic static model of L.G. Jacchia reported in Ref. [2] one may adopt a corresponding exospheric temperature. Based on  $D = -0.47$  m/day for 1996 and  $D = -0.54$  m/day the exospheric temperatures of 1107 K and 1127 K are found for years 1996-97.

The solar flux at 10.7 centimeter wave length  $F$ , based on Penticton Observatory measurements, averaged over years 1996 and 1997 are, respectively, about 72.03 and 80.97 ( $10^{-22} \frac{\text{Watts}}{\text{m}^2 \text{Hz}}$ ). Ignoring all but the mean yearly variation of the exospheric

temperature one may estimate the expected difference in the exospheric temperature over the two year from Ref. [3]

$$3.24(F(1997) - F(1996))$$

to be 29 K. This accords well with the exospheric temperatures deduced from our aerodynamic drag estimates, considering the gross nature of our calculations.

The available literature on aerodynamic drag correlates the sun activity with the mean rate of semi-major axis in satellites over a year. However, the intermediate steps used in this correlation, such as exospheric temperature, atmospheric density and aerodynamic drag equation, are not a logical outcome of this correlation. The accepted values of exospheric temperature and atmospheric density and the validity of aerodynamic drag equation in exosphere may come under question if independent means of verifying them is adopted.

## CONCLUSION

In 1996 the aerodynamic drag of RADARSAT was about 39% of the total drag. The preponderance of the radiation drag over aerodynamic in RADARSAT is due to an 11° offset between the spine of the solar array and the velocity vector of the satellite.

If the solar array is designed with significant component of the unit normal vector to the cell side along the minus velocity vector, in the future versions of the satellite, the solar radiation could dramatically reduce the amount of fuel required for raising of the satellite altitude.

## REFERENCES

1. James R. Wertz, Editor, *Spacecraft Attitude Determination and Control*, Kluwer Academic Publishers, Boston, 1978, p. 109.
2. L.G. Jacchia, "Thermospheric Temperature, Density, and Composition," Smithsonian Astrophysical Observatory special report No. 375, 16 March 1977.
3. J.O. Cappellari, "Mathematical Theory of the Goddard Trajectory Determination System," Goddard Space Flight Center, 1976, section 4.5.4.

## REENTRY ALGORITHM FOR RESCUE REENTRY VEHICLE

Y.G.Sikharoulidze, Y.N.Kaluzhskikh\*

The paper discusses the main principles of a reentry algorithm for a rescue reentry vehicle with the average lift-to-drag ratio (about 0.5). The rescue reentry vehicle must realize a mission in a short time. So the reentry algorithm must provide a high accuracy (about 1 km) that allows to use not 1...2 landing places, but one order more. A high activity of mission assumes the autonomous reentry guidance including a solution of two-point boundary problem on a choice of a reference (command) roll angle function. The reference roll angle function is a piecewise constant with three roll overturns. This allows to reduce to zero downrange miss and crossrange miss simultaneously. The developed method permits quickly to obtain a solution within the guaranteed zone of vehicle manoeuvre. It is possible also to take into account a limitation on a maximal value of a load factor that is important for a rescue reentry vehicle.

The mathematical simulation of a reentry in the disturbed atmosphere for different location of a landing point confirms a high accuracy of developed algorithm.

### INTRODUCTION

The problem of an emergency return of one astronaut or the whole crew during near the Earth manned mission may sometimes arise. The transport spacecraft "Soyuz - TM" is intended for both this purpose and for delivery of the crew on the orbital station "Mir". But "Soyuz" type reentry vehicle has a relatively non-high landing accuracy, so a number of landing places is limited. As a result it is necessary to wait for the special conditions on the orbit which allow to land in a given place. Waiting time may reach many hours that is inadmissible in some situations.

An advanced rescue spacecraft for emergency evacuation of orbital station's crew must have two new capabilities. The first one is an increase of a propellant reserve to realize rendezvous and docking with the orbital station in a limited time. A rendezvous manoeuvre will be noncoplanar in a general case. The second capability is an increase of a landing accuracy up to 1 km. Such an accuracy allows significantly to increase a number

---

\* Keldysh Institute of Applied Mathematics RAS, Russia  
phone: (095)333-7177, fax: (095)972-0737, e-mail: sikh@kiam1.rssi.ru



of landing places. As a result time for delivery of crew on the Earth essentially decreases. Thus capabilities of advanced rescue spacecraft mentioned above allow to increase its operativeness and efficiency. A high accuracy of landing is necessary for any reentry vehicle because it excludes a lot of restrictions on the choice of landing place.

Let us assume that for the most part of trajectory the vehicle has a constant trim angle of attack and is static neutral with a respect to a velocity roll angle. It realizes the single channel roll control as reentry vehicles "Soyz" and Apollo.

## ZONE OF MANOEUVRE

A zone of manoeuvre is a set of points on the Earth surface or on the equidistant sphere with altitude of 5...10 km, which are accessible for a reentry vehicle. Let us construct a zone of manoeuvre in the following coordinate system. The origin of coordinates coincides with a point of intersection of ballistic reentry trajectory with the equidistant sphere (or the Earth surface). Axis X is in the local horizontal plane and passes through projection on the plane of a terminal point of a trajectory with a zero roll angle ( $\gamma=0$ ) when lift force is up. Axis Y is directed along the local vertical and axis Z forms the right coordinate system.

For given reentry conditions the size of zone of manoeuvre depends essentially on available lift-to-drag ratio. For example, if a reentry angle is  $-1^\circ$  and a vehicle has average lift-to-drag ratio  $K = 0.5$ , downrange from a ballistic landing point is about 4000 km and crossrange is more than 400 km (Figure 1). The maximal load factor during reentry is of 2 for a large range and increases up to 6...9 for a short range. If a value of reentry angle increases the size of manoeuvre zone decreases.

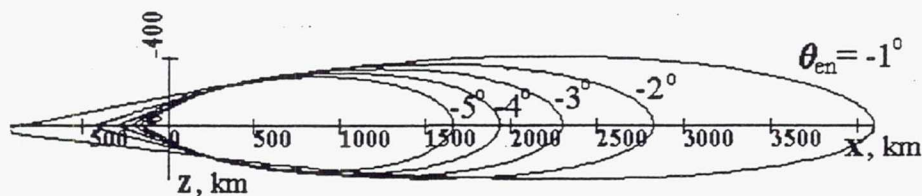


Figure 1 Landing zones

For reentry with a constant roll angle in the disturbed atmosphere, a downrange dissipation is about 300 km and a crossrange dissipation is near 30 km. Therefore the guaranteed zone of manoeuvre of reentry vehicle decreases. The guaranteed zone is inner envelope of disturbed landing points (Figure 2). We shall consider only the guaranteed zone of manoeuvre.

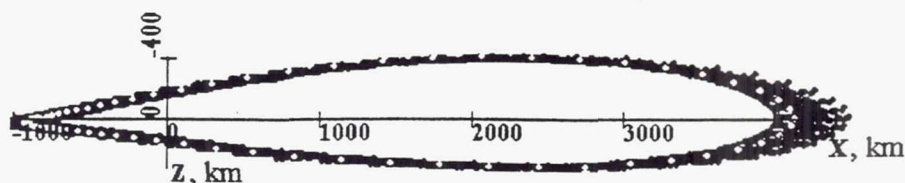


Figure 2 The guaranteed zone of manoeuvre

If the initial orbit of a reentry vehicle is known and value of deboost impulse is given, the geometry of a zone of manoeuvre is determined uniquely. When a deboost point is removed along the orbit the zone of manoeuvre removes respectively on the surface of equidistant sphere (or the Earth). Deboost of reentry vehicle is possible at the time when one of given landing points is found inside the zone of manoeuvre. In a general case it is necessary to carry out both downrange manoeuvre and crossrange one for landing in a given place. The downrange manoeuvre depends on a value of a roll angle mainly. The crossrange manoeuvre is determined by a number of roll overturns (i.e. change of sign of a roll angle with a constant value of angle) and time of overturns.

## THE REFERENCE ROLL ANGLE FUNCTION

The reference roll angle function on phantom velocity (or time) is determined as a solution of the two-point boundary problem. It provides landing in a given place if the atmosphere is standard (or monthly average). A piecewise constant roll angle function with three overturns is necessary to provide a high (about 1 km) accuracy of landing<sup>1</sup>. In the simplest consideration we can assume instantaneous roll overturn (dotted line in Figure 3). But it is more useful to take into account a duration of overturn phase according to available efficiency of the roll control channel (solid line in Figure 3). The value of roll angle  $\gamma_0$  and overturns location on phantom velocity  $V_1, V_2, V_3$  of reference function depend on a position of a landing point in the zone of manoeuvre. These parameters must be chosen before the beginning of roll control, i.e. before reentry in the atmosphere. Results of a preflight calculation are used to simplify an onboard solution of two-point boundary problem. Thus during investigation of a zone of manoeuvre for a given reentry angle it is possible to determine a function  $\gamma_0 = f_0(X_L)$ , where  $X_L$  is downrange of a landing point. Then, by statistical simulation of reentry trajectories in the disturbed atmosphere it is possible to calculate reference values of phantom velocity  $V_1, V_2, V_3$  at overturns for fixed downrange  $X_L$  in assumption that crossrange of a landing point  $Z_L = 0$ .

Preliminary calculated function  $\gamma_0 = f_0(X_L)$ ,  $V_1 = f_1(X_L)$ ,  $V_2 = f_2(X_L)$ ,  $V_3 = f_3(X_L)$  are used in the onboard software as initial values for determination of a reference function  $\gamma_{\text{ref}} = F(V_{\text{ph}}, \gamma_0, V_1, V_2, V_3)$ . The function is calculated by a standard



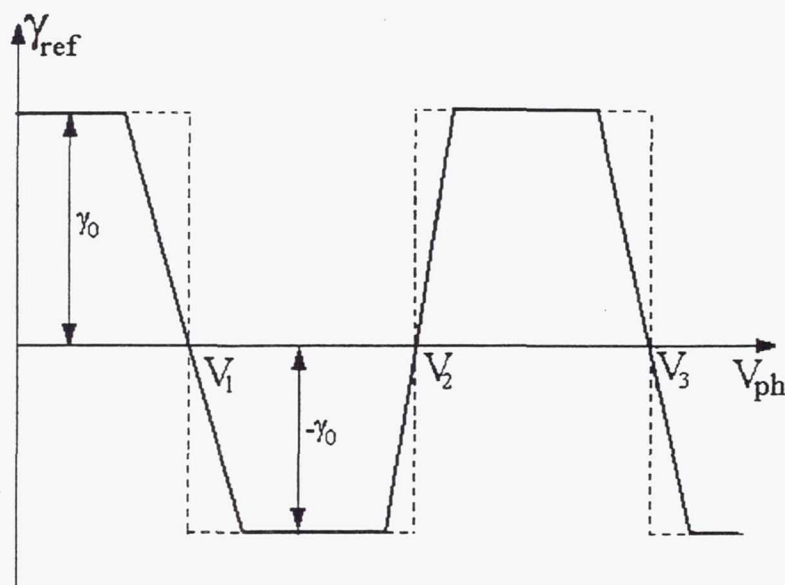


Figure 3 The reference functions of roll angle

procedure of control parameters choice at each step of control update. Simulation confirms that an algorithm has quick convergence and provides determination of a reference function by 1...3 iterations. All calculations are fulfilled after deboost and before reentry (the boundary of conditional atmosphere is at altitude of 100 km). The reentry point location and reentry parameters are updated simultaneously. Results of a phantom velocity measurement during a deboost phase and navigation at a passive flight phase by Glonass or GPS are used for this purpose. As a result, it is possible to provide near zero initial errors at reentry. Then a landing error will depend on the disturbed atmosphere and non-nominal aerodynamic characteristics mainly. But a regular component of non-nominal aerodynamics may be selected during flight tests and updated characteristics will be used in a control process. Thus the disturbed atmosphere is the most essential for landing accuracy.

## TERMINAL GUIDANCE ALGORITHM

Let us suppose that a control system of a reentry vehicle includes the three-axis gyroplatform with accelerometers along each axis. Thus it is possible to solve an onboard complete navigational task and determine a three-dimensional reentry trajectory. At altitudes above 80 km and below 40 km, i.e. outside of blackout zone, it is possible to use navigational systems Glonass and GPS. Consequently the accuracy of a navigational task will be some tens meters on position and some centimeters per second on velocity. This allows to realize a high accuracy terminal control.

At each step of a control correction for a center mass trajectory (with duration of 1...2 sec) an updated set of parameters  $\gamma_0$ ,  $V_1$ ,  $V_2$ ,  $V_3$  of reference function is chosen.



The set provides guidance of a vehicle from the current position to a given landing point with an accuracy of 1 km if at the remaining part of trajectory parameters of the disturbed atmosphere (density, temperature, pressure, wind) correspond to a monthly average model of the atmosphere. Systematic errors of guidance algorithm, errors of control realization, atmospheric and aerodynamic disturbances are compensated due to a multistep control process<sup>2</sup>.

Let us discuss a procedure of a control choice at the current step. Before realization of the first roll overturn we suppose that the second and third overturns are fixed. Then a reference roll function is two-parameter. Parameters are a value of roll angle and time of the first overturn. Two control parameters allow to reduce to zero a downrange miss and crossrange miss simultaneously. Let us note that the control system of "Soyz" and Apollo reentry vehicles compensate only downrange miss and limit value of crossrange miss.

So-called method of modulating functions<sup>3</sup> is used for a control choice. A predicted command control is looked for in the form

$$\gamma(V_{ph}) = \gamma_{ref}(V_{ph}, \varepsilon)(1 + \beta). \quad (1)$$

Here  $\gamma_{ref}(V_{ph}, \varepsilon)$  is a reference function of a roll angle (see Figure 4),  $\varepsilon$  is a parameter of phase modulation for correction of a point  $V_1$  of overturn,  $\beta$  is a parameter of amplitude modulation for "contraction" or "expansion" of a function  $\gamma(V_{ph})$  with respect of abscissa axis.

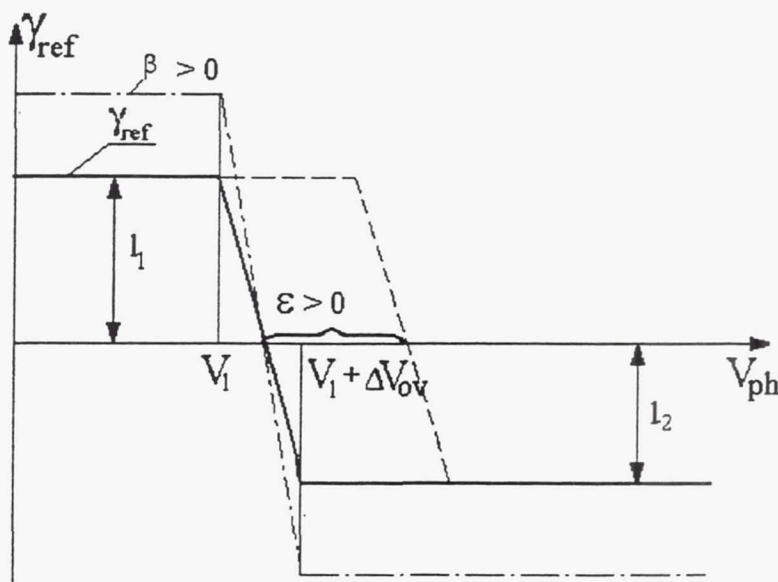


Figure 4 Modulation of reference function

The parameter  $\beta$  affects downrange motion mainly. If  $-1 \leq \beta \leq 0$ , the command roll function contracts to abscissa axis and value of roll angle decreases. Therefore a steepness of the trajectory decreases and downrange increases. If  $\beta > 0$ , a downrange decreases.

If  $\varepsilon > 0$ , a roll overturn takes place later and in the case  $\varepsilon < 0$  overturn takes place earlier.

Now let us discuss a control correction procedure in detail. An initial radius vector  $\vec{r}_0$  and velocity vector  $\vec{V}_0$  are known from the solution of a navigation task. Control parameters  $\beta_0$  and  $\varepsilon_0$  at previous step are known also. A reference prediction with parameters  $\beta_0$  and  $\varepsilon_0$  is run initially to determine downrange miss  $L_0$  and crossrange miss  $B_0$  from a given landing point. Then two predictions are run with parameters

$$\beta_1 = \beta_0 + \delta\beta, \quad \varepsilon_1 = \varepsilon_0 \quad (2)$$

and

$$\beta_2 = \beta_0, \quad \varepsilon_2 = \varepsilon_0 + \delta\varepsilon, \quad (3)$$

where  $\delta\beta$ ,  $\delta\varepsilon$  are small variations for calculation of partial derivatives.

Let us assume that  $L_1$  and  $B_1$  are components of miss for the second prediction and  $L_2$ ,  $B_2$  for the third prediction. We solve a two-parameter boundary problem, so the number of predicted trajectories is equal to three. Then in linear approximation it is possible to obtain a system of algebraic equations for determination of corrections  $\Delta\beta$  and  $\Delta\varepsilon$  those provide zero miss:

$$\begin{aligned} \frac{\partial L}{\partial \beta} \Delta\beta + \frac{\partial L}{\partial \varepsilon} \Delta\varepsilon + L_0 &= 0, \\ \frac{\partial B}{\partial \beta} \Delta\beta + \frac{\partial B}{\partial \varepsilon} \Delta\varepsilon + B_0 &= 0. \end{aligned} \quad (4)$$

Here partial derivatives are determined by a method of finite differences

$$\begin{aligned} \frac{\partial L}{\partial \beta} &= \frac{L_1 - L_0}{\delta\beta}, \quad \frac{\partial L}{\partial \varepsilon} = \frac{L_2 - L_0}{\delta\varepsilon}, \\ \frac{\partial B}{\partial \beta} &= \frac{B_1 - B_0}{\delta\beta}, \quad \frac{\partial B}{\partial \varepsilon} = \frac{B_2 - B_0}{\delta\varepsilon}. \end{aligned} \quad (5)$$

A solution of system (4) allows to find updated control parameters

$$\beta = \beta_0 + \Delta\beta, \varepsilon = \varepsilon_0 + \Delta\varepsilon \quad (6)$$

for a current step.

Time is necessary for calculation of updated parameters. Thus a solution for a current step may be used not earlier than at the following step due to discreteness of terminal control. Consequently a minimal delay in use of update control is equal to a step, i.e. 1...2 sec. If delay is a step, we can realize only piecewise constant control (Figure 5), when a command roll function has ordinary discontinuities at each step.

If delay is two steps we can connect a previous command roll angle with updated one. Then we have a continuous piecewise linear control function (Figure 6) that simplifies the problem of stabilization of attitude motion.

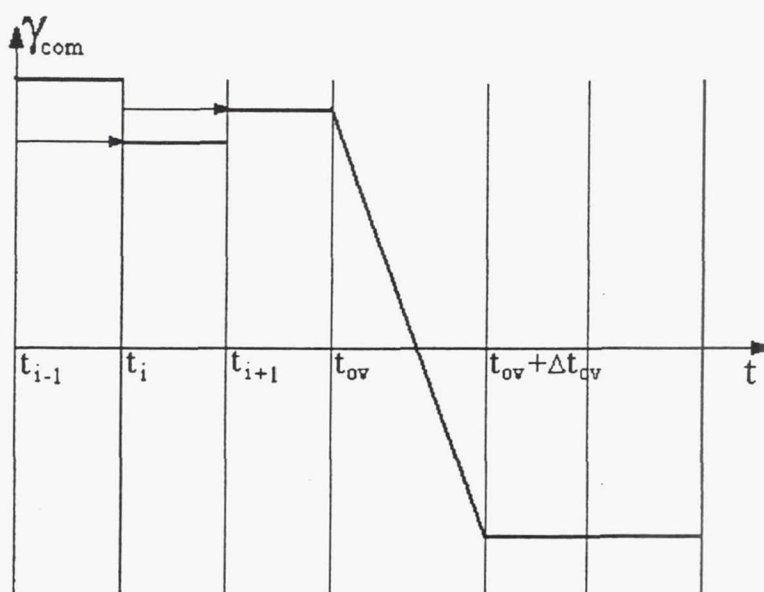


Figure 5 The piecewise constant control

After the first overturn we fix on phantom velocity the third overturn ( $V_3$ ) and update location of the second overturn ( $V_2$ ), etc. Finally, after realization of the third overturn the two-parameter control transfers in one-parameter control. A single parameter ( $\beta$ ) is used for correction of downrange miss.



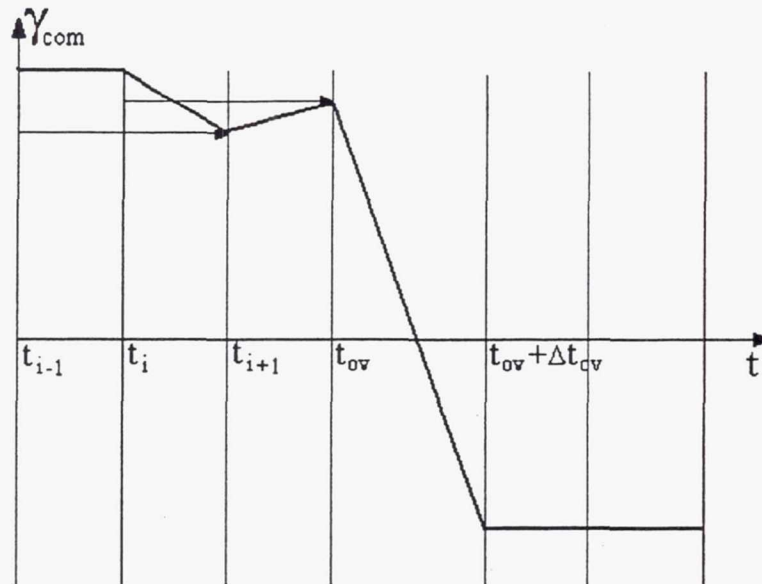


Figure 6 The piecewise linear control

## SINGULARITY OF CONTROL

The third overturn  $V_3$  of reference function should be placed as close as possible to the end of trajectory to reduce a crossrange miss. But during reentry in the disturbed atmosphere the third overturn can remove beyond the end of trajectory in a process of a control correction. Such a control can not be realized and solution of two-parameter boundary problem has singularity. Careful analysis allowed to find out a reason of singularity and the method to eliminate it was suggested.

Let us suppose that at the phase of reentry after the second overturn and before the third overturn we have a trajectory with undershoot (due to a high density of the disturbed atmosphere, headwind, etc.). For compensation of undershoot the guidance algorithm tries to reduce a value of a roll angle. Simultaneously a side component of control force decreases and efficiency of crossrange control decreases as well. Really, it is impossible to regulate crossrange miss if a roll angle reduces to zero. As a result the third overturn quickly moves to the end of reentry trajectory and may be on phantom velocity outside of a trajectory.

The revealed reason of control singularity permitted to suggest a simple and reliable way of its elimination. Instead of a given landing point we introduce coordinates of point with larger downrange  $\Delta X > 0$  in algorithm. Usually  $\Delta X = 1...3$  km. Some value of phantom velocity  $V_{bias}$  is chosen simultaneously in the range from  $V_2$  to  $V_3$ . A biased landing point is retained till achievement of velocity  $V_{bias}$ . At that velocity the targeting

point is superposed with the given landing point. It is clear that up to this time we have a trajectory with overshooting. Thus at the current control step algorithm increases a value of roll angle to compensate "arisen" overshooting. An efficiency of crossrange control is increased simultaneously, and the third overturn displaces not to the end but to the beginning of trajectory. Control parameters  $\Delta X$  and  $V_{bias}$  are chosen by mathematical simulation at an adjustment of guidance algorithm.

In a special case we can remove a target point in downrange direction ( $\Delta X$ ) and crossrange direction ( $\Delta Z$ ). In addition the downrange correction of a landing point  $V_{bias}(\Delta X)$  and crossrange correction  $V_{bias}(\Delta Z)$  may be different. Two additional control parameters  $\Delta Z$  and  $V_{bias}(\Delta Z)$  increase capability of guidance algorithm but simultaneously complicate its adjustment.

## PREDICTION OF REENTRY TRAJECTORY

To choose control parameters according to a method of modulating functions it is necessary to make three predictions of remaining reentry trajectory. For high accuracy terminal guidance we can't use simplified explicit formulas or preliminary calculated partial derivatives  $\frac{\partial L}{\partial b}$ ,  $\frac{\partial L}{\partial e}$ ,  $\frac{\partial B}{\partial b}$ ,  $\frac{\partial B}{\partial e}$  for a nominal reentry trajectory. A variety of possible reentry trajectories for a rescue vehicle and a high landing accuracy require only numerical prediction by an onboard computer. Developed algorithm of terminal control allows parallel calculations, so a multi-processor computer is preferable. Then during a control step (1...2 sec) three predicted trajectories are calculated in parallel and this reduces requirements to calculation speed of computer.

If a calculation speed of an available computer is not enough for realization of a terminal control algorithm it is possible to fix a maximal admissible number of integration steps to guarantee all calculations within a control step. Then at initial phase of reentry an integration step may be big and accuracy of calculation may be found to be low. The nearer to the end of reentry trajectory, the shorter predicted trajectory. Thus an integration step decreases and accuracy of calculation increases respectively. As a result it is possible to provide a required landing accuracy.

Phantom velocity is suitable independent variable for numerical integration. A constant step on phantom velocity automatically decreases a step on time in the region of high aerodynamic load and increases if load is low. Thus an accuracy of prediction increases.

## RESULTS OF SIMULATION

Developed algorithm of terminal control was tested by the mathematical simulation of reentry trajectories of vehicle in the disturbed atmosphere. We considered center mass trajectories with simplified description of a roll angle change in process of overturn (as an aperiodic link with constant of time 3 sec and maximal roll rate of 10 degrees per second). It was assumed that reentry vehicle has the average lift-to-drag ratio  $k=0.5$  and ballistic coefficient  $\sigma_D = \frac{C_D S}{m} = 1,1 \times 10^{-3} \text{ m}^2/\text{kg}$ . Altitude of conditional boundary of atmosphere is 100 km, inclination of orbit  $51.6^\circ$ , reentry angle  $-0.9^\circ$  at velocity 7.87 km/sec. Coordinates of a reentry point are  $20^\circ$  of Northern latitude and  $20.2^\circ$  of Eastern longitude. A terminal point is at altitude of 10 km where a parachute system is operated. The computational model of disturbed atmosphere<sup>1</sup> includes season-latitude, diurnal and random variations of density and field of zonal (along a parallel) and meridional winds. For reentry at mean latitudes extremal disturbances of atmospheric parameters take place in winter (January) and in summer (July). Both months were considered. Figure 7 illustrates dispersion of

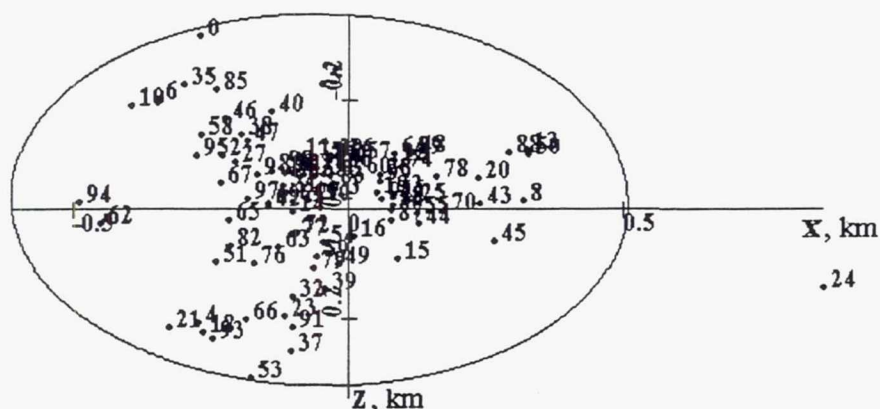


**Figure 7** Dispersion of terminal points for  $X_T = 3500$  km,  $Z_T = 0$  km (January)

terminal points for 100 reentry trajectories in January. Landing point has downrange coordinate  $X_T = 3500$  km and crossrange one  $Z_T = 0$ . This is approximately a maximal downrange inside of guaranteed zone of manoeuvre. Figure 8 shows simulation results for 100 reentry trajectories in July. A landing point has coordinates  $X_T = 2500$  km and  $Z_T = -400$  km. This is middle of downrange manoeuvre and limit of crossrange approximately. Figure 9 gives an example of landing accuracy in January for minimal downrange ( $X_T = 500$  km,  $Z_T = 0$ ) when maximal load factor is limited by value 5.

Simulation results show that majority of landing points are deep inside of a circle with a diameter of 1 km. This confirms a high accuracy of a developed reentry algorithm.



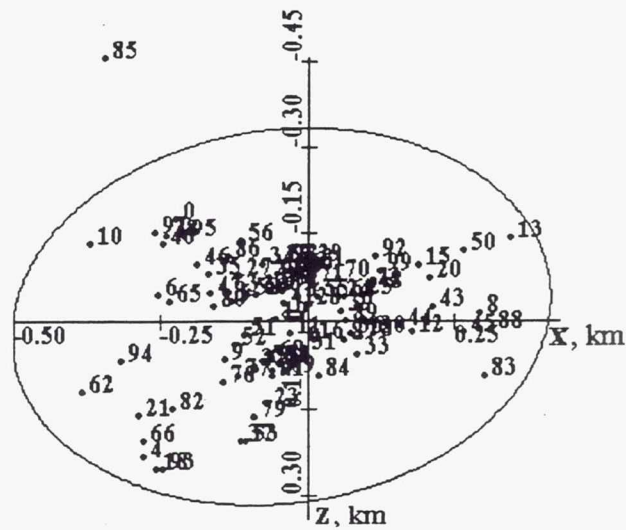


Figure 8 Dispersion of terminal points for  $X_T = 2500$  km,  $Z_T = -300$  km (July)

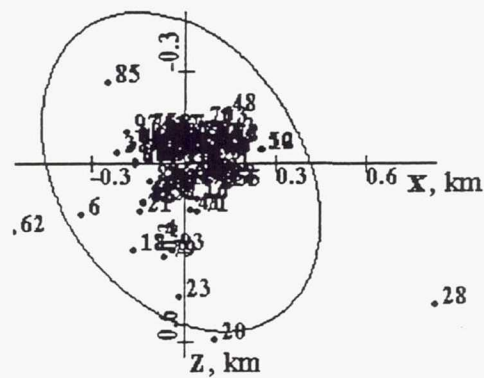


Figure 9 Dispersion of terminal points for  $X_T = 500$  km,  $Z_T = 0$  km (January)

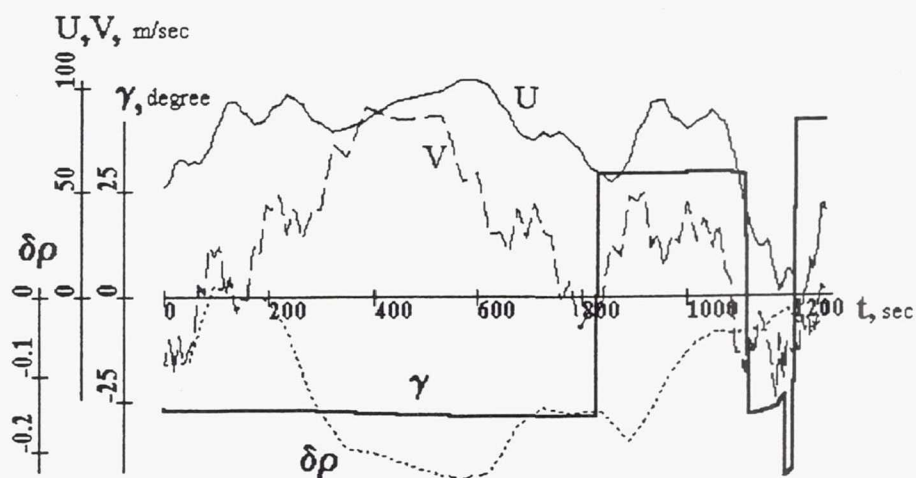


Figure 10 An example of roll control and parameters of disturbed atmosphere

An example of roll angle control and parameters of the disturbed atmosphere (January, variant N 94) is given in Figure 10. Here  $\delta_\rho = \frac{\rho - \rho_{st}}{\rho_{st}}$  is variation of density,  $U$  is zonal wind,  $V$  is meridional wind. A roll angle function on time is sufficiently smooth that provides a small propellant consumption for attitude stabilization.

## REFERENCES

1. Sikharoulidze Y.G., Kaluzhskikh Y.N., Kostochko P.M. Computational model of the Earth disturbed atmosphere and a high accuracy reentry guidance for a vehicle with middle lift-to-drag ratio. Proceedings of the 12th International Symposium on Space Flight Dynamics, ESOC, Darmstadt, Germany, 2-6 June 1997.
2. Mostovoy D.Y., Sikharoulidze Y.G. High Accuracy Guidance Algorithm for Reentry of Spacecraft with Low Lift-to-Drag Ratio. Proceedings of the International Symposium on Space Flight Dynamics, 1994, May 22-26, St-Petersburg-Moscow.
3. Okhotsimski D.E., Golubev Y.Ph., Sikharoulidze Y.G. Control algorithms for spacecraft entry into atmosphere. Moscow, Nauka, 1975 (book in Russian)

# **FLIGHT DYNAMIC DESIGNING OF MANNED RETURN SPACE VEHICLE FOR HYPERBOLIC ENTRY**

N.M. Ivanov, M.N. Kazakov, A.N. Rumynskiy, V.G. Sobolevskiy, V.A. Udaloy

Mission Control Center

Pionerskaya str. 4, 141070, Korolyov, Moscow region, Russia  
phone: +7 095 586 94 04, fax +7 095 274 00 25, e-mail nmi@mcc.rsa.ru

The paper presents materials on development of a future manned returned space vehicle included into a complex for the Martian mission. The basic points of the developed aerothermodynamic and flight dynamic method for designing of the unwinged returned vehicle performing an entry to the Earth atmosphere at hyperbolic velocities are presented. The results of the comparative thermal and mass analysis are given for three unwinged returned vehicles and for the entry velocities 13-17 km/s, longitudinal ranges of descent 3000-5000 km (providing the accuracy of landing within 1 km), satisfying the temperature constraint at a characteristic point on the windward surface of the vehicle and also providing admissible g-loads for the crew (taking into account the 'withstandability' factor).

## **INTRODUCTION**

During the last years one of the most important directions of modern cosmonautics - the interplanetary Martian missions with a return to the Earth has obtained a new development. First of all it is connected with the announced program of Mars explorations with automatic and manned vehicles for the period till 2015.

This direction was developed rather intensively in 60-th years [6-10,17,18] at the initial phase of manned space explorations but then the associated studies and design works were stopped due to different political, economical and technological reasons. The comprehensive studies conducted at that time in all important directions of implementation of the interplanetary Martian mission with a return to the Earth produced the fundamental for the applied cosmonautics results that are still significant at the present time.

It was found that in order to perform a 'capture' of the vehicle by the Earth atmosphere and to satisfy the admissible thermal and load factor constraints on the descent trajectory one of the most important design flight dynamic tasks is to find the minimally sufficient available lift to drag ratio  $(K_p)_{\min}$  for studied return vehicle of any configuration. One of results of the conducted studies was that for the future unwinged vehicles it is necessary



to provide  $(K_p)_{\min}$  not less than 0.4 [6]. This result lead to a need to consider candidate return vehicles of non standard (for that period of time) configurations - vehicles of the 'conical segment' class [5, 10, 18], biconical configuration [18], segmetal-conical configuration [10] (different by its geometry shape from the Soyuz and Appolo configurations [18]) and many other original configurations.

The longitudinal range  $L_{\text{LONG}}$  of the atmospheric descent phase belongs to important initial parameters characterizing a relative position of the required area of landing and phase position of the vehicle at the entry point (or basic parameters of the approach hyperbola). It was established that for an arbitrary specification of the  $L_{\text{LONG}}$  range the direct landing of the return vehicle (without exiting out of the atmosphere) may not be provided. Then in order to provide the direct landing of the return vehicle on the USSR territory the longitudinal range  $L_{\text{LONG}}$  was taken within the interval 3000-5000 km, and the most important obtained result [7,10] is that a necessary condition of landing in a required area of the USSR territory (at the latitude  $50^\circ \text{ N}$ ) is a nonpositivity of the initial declination angle on the infinity

$\delta_\infty \leq 0$  (the angle  $\delta_\infty$  characterizes a position of the asymptote of the vehicle's approach hyperbola). For the unfavorable combination of the initial parameters  $V_\infty$  and  $\delta_\infty$  (first of all for the values  $\delta_\infty > 0$ ) the direct landing of the return vehicle is not always possible and so it is necessary to take into account the alternative way of the orbital landing (with preliminary insertion of the vehicle to the Earth orbit).

The safe landing of the manned return vehicle requires to take into account and solve the problem of an admissible load factor profile that is first of all connected with the account of an admissible duration of high g-loads acting on the crew at the atmospheric phase [17]. This problem of the g-load 'withstandability' was formalized with the analytic relation [9] that takes into account an integral effect of g-loads during the atmospheric deceleration phase and allows to design the required descent trajectory and guidance law with an obligatory fulfillment of the final 'withstandability' condition  $\Phi_{\text{FIN}} < 0$ . The use of the given criterion allows to provide a flight dynamic solution of the problem of the return vehicle safe landing in the required area of the USSR [10].

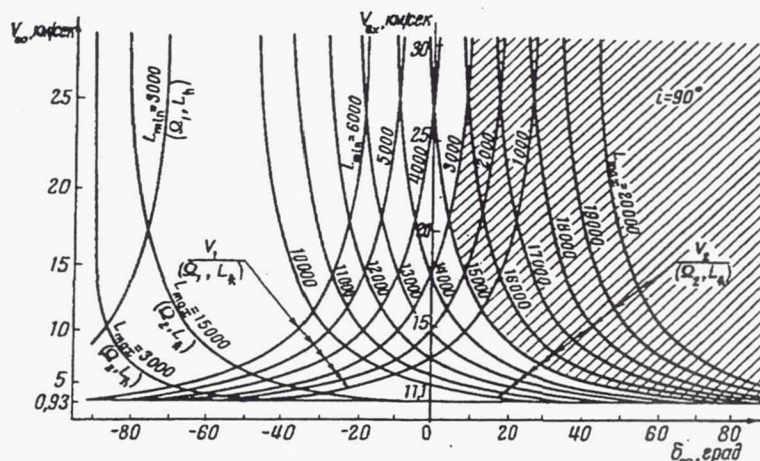


Figure 1

It should be noted that the choice of a shape (configuration) of RV was considered at that time as one of the most important design tasks since the required mass of the RV thermal protection coating was estimated as  $\approx 40\%$  of the total RV mass. Then the main task during choice of the RV configuration was to minimize the total required mass of the vehicle's thermal protection coating (also satisfying all imposed constraints and conditions of landing in a given area) [10, 14].

### BASIC POINTS OF AEROTHERMODYNAMIC AND FLIGHT DYNAMIC DESIGNING OF RETURN VEHICLE.

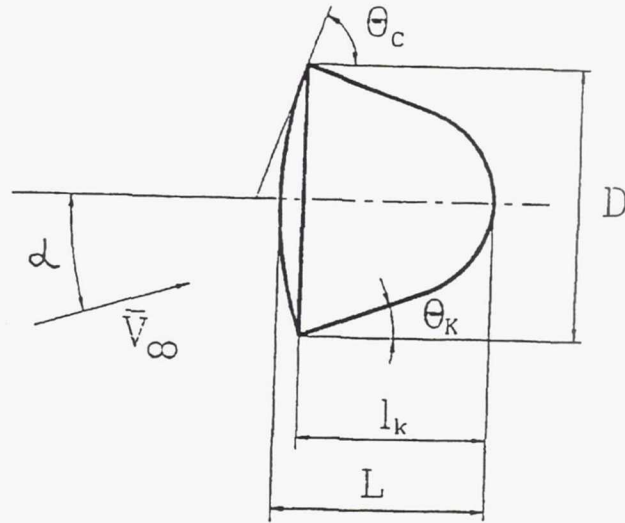
At the present time an important task of the space technology for the manned missions is to provide an accurate landing of the return vehicle in any given area of the Earth surface, i.e. to provide a highly accurate landing (within a circle of 1 km in diameter) of the vehicles returned from the Earth surface [1]; to provide an accurate landing of the interplanetary vehicles in a give area of the Earth or other explored planet (for example Mars) [3].

In order to develop a successful (in technical and economical respects) return vehicle of any configuration and to do it quickly it is necessary to form the mutually coordinated and technically feasible geometry, flight dynamic and aerothermodynamic parameters of the return vehicle at the initial phase of a design work [1-4]. This approach to the comprehensive designing of the vehicle guarantees obtaining of noncontradictory and feasible technical characteristics of the vehicle and facilitates further successful detailed designing.

The aerothermodynamic and flight dynamic designing of a future returned space vehicle is a development of mutually agreed basic flight-dynamic, aerothermodynamic and geometry parameters of the vehicle, which feasibility is verified during the flight dynamic modeling of the return vehicle motion on every phase of a flight.

The initial stage of the flight dynamic designing of RV of a specified configuration is to develop the basic initial data for performing an analysis on finding the feasible geometry and aerodynamic parameters of the vehicle to be developed. The basic initial data for the manned unwinged return vehicle of a segmental-conical configuration (Fig. 2) are: number of crewmembers, parameters of the configuration describing the vehicle's geometry shape (parameters  $\theta_c$ ,  $\theta_k$ ,  $\lambda_k$ ), a volume  $W$  (corresponding to the external shape of the vehicle) or a characteristic linear dimension of RV, an initial mass  $G_0$  (or a payload mass  $G_{pl}$ ) of the developed RV.





Characteristic parameters of configuration

$\lambda_k = l_k/D$	$\theta_c$	$\theta_k$
0.70	70.0	20.0

Figure 2

The determination of the basic geometry dimensions of the developed RV is done using the so called configuration equation [10,11]:

$$W = C_f \cdot D^3, \quad (1)$$

where  $W$  is a vehicle's volume, m<sup>3</sup>;

$D$  is a characteristic linear size of the vehicle, m;

for the RV of the considered shape  $D$  is a diameter of the head spherical segment (Fig.2);

$C_f$  is a shape coefficient functionally depending on initial characteristic parameters of the configuration.

For the RV of a considered type the configuration equation is the following:

$$C_f = \frac{\pi}{24} \cdot \left[ \frac{(1 - \sin \theta_c)(2 + \sin \theta_c)}{(1 + \sin \theta_c) \cos \theta_c} + \frac{1 - B_k^3}{\tan \theta_k} + B_k F_k^2 (2 + \sin \theta_k) \cos \theta_k \right] \quad (2)$$

where

$$\begin{cases} F_k = 2\lambda_k \cdot \tan \theta_k, \\ B_k = F_k (1 + \sin \theta_k) \end{cases} \quad (3)$$

It should be noted that for each RV of a given geometry shape the corresponding analytic relation can be obtained.

Basing on equations (1)-(3) all geometry parameters of the considered RV can be obtained uniquely that allow to calculate the 'maximum section area' parameter  $S_{mid}$  (necessary for the further analysis of the flight dynamic parameters) and the design parameter [4,11]:

$$k_{vol} = \frac{4.836 \cdot W^{2/3}}{S_\Sigma} \quad (4)$$

characterizing a level of the vehicle's design quality, here  $S_\Sigma$  is a full surface of the vehicle calculated by the obtained geometric parameters.

It should be mentioned that in a case of the obligatory satisfaction of a design constraint on the maximum admissible diameter  $D$  (the requirement on the RV placement in a launcher payload module) the configuration equation (1) gives a unique value of the vehicle's volume  $W$ . Also an additional constraint on the large-size loads ( $D < 4.1m$ ) limits an available volume of the vehicle:  $W = 22.5m^3$ .

The main feature in an analysis of the available aerodynamic parameters of the RV to be developed is to find a range of the trim angle of attack  $\alpha_s$  for which the vehicle has the longitudinal static stability during the atmospheric deceleration. As it is known a criterion of the longitudinal static stability of any flying vehicle is to satisfy the condition

$\frac{dm_z}{d\alpha} = m_z^\alpha < 0$  at  $m_z = 0$ . The profiles for the available lift to drag ratio  $K_p = f(m_z^\alpha)$  and trim angle of attack  $\alpha_s = f(K_p, m_z^\alpha)$  can be obtained for each RV and for different values of the center of gravity coordinate  $\bar{x}_t$  (fig.3). The use of these graphic profiles allow to determine not only an available range of the trim angle of attack  $\Delta\alpha_s$  but also a range of the available lift to drag ratio [2,4,5].

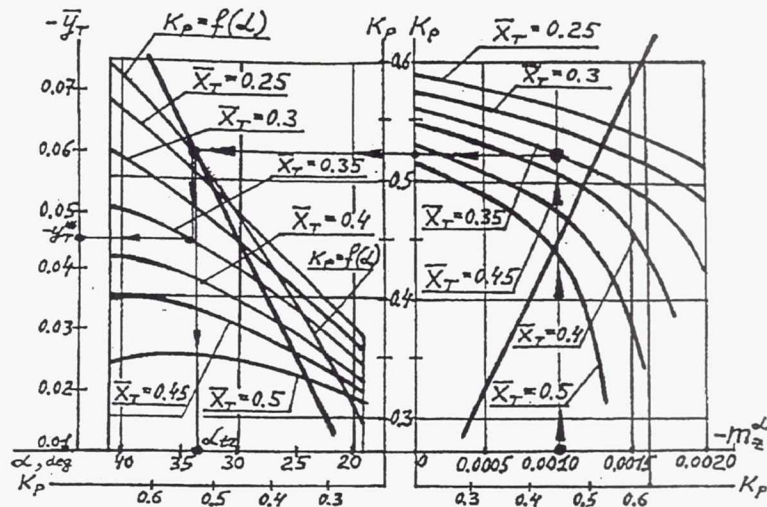


Figure 3

A process of obtaining the graphic profiles  $K_p = f(m_z^\alpha)$  and  $\alpha_s = f(K_p, m_z^\alpha)$  (fig.3) requires rather long computations. In order to be able to estimate quickly a 'flyability' of the developed vehicle (at an admissible trim angle of attack  $\alpha_s$ ) a new analytic relations [11,12] have been obtained. The generalized flyability criterion combines both the design geometric, aerodynamic parameters and basic flight dynamic parameters of RV (the lift to

drag ratio  $K_s$  and ballistic coefficient  $\sigma_x = \frac{C_{xa} \cdot S_{mid}}{G_0}$ , where  $G_0$  is an initial design mass

of RV). The use of the generalized flyability criterion [11,12] allow to obtain a quantitative estimation of a quality of the adopted design solution of RV for each trim angle of attack  $\alpha_s$ . If the generalized flyability criterion is satisfied for each of candidate trim angles of attack (within the range  $\Delta\alpha_s$ ) it can be stated that the obtained design geometry and aerodynamic parameters are mutually coordinated and feasible, and the developed RV can accomplish the required task.

An important stage of the flight dynamic designing of the developing RV is to find such flight dynamic parameters of the vehicle that allow both to accomplish a formulated task and to satisfy all constraints during descent in the atmosphere, in particular the constraints connected with the thermal and load factor profiles. This task is accomplished using the flight dynamic modeling of the RV motion that allow at the same time to produce a program of the vehicle's guidance and a trajectory of the RV descent to a required geographic point.

All constraints connected with the admissible deceleration profile and conditions of the vehicle's functioning [10,14] are to be taken into account in the guidance program and during analysis of the RV descent trajectory. It should be mentioned that the RV of an unwinged configuration is controlled during motion in the atmosphere by variation of its bank angle  $\gamma$  (here the vehicle is stabilized on a required trim angle of attack  $\alpha_s$ ).



The basic constraints in the algorithm of solution are a one side limitation on the maximum admissible equilibrium radiation temperature  $(T_w^*)_{\max}$  in a characteristic point on the head surface of the vehicle and a two side limitation on the load factor  $(n_\Sigma)_{\min} \leq n_\Sigma \leq (n_\Sigma)_{\max}$ . Here the limitation on the minimum admissible load factor is introduced to guarantee a non-exit of RV out of the atmosphere that is especially critical when the vehicle is moving near an upper border of the entry corridor.

The generation of the guidance law  $\gamma(t_i) \equiv \gamma_i$  (at a current moment in time  $t_i$ ,  $i=1, \dots, n$ ) and of the RV state vector at the same moment in time is based on a special prediction module [10] which predicts and estimates possible variants of the current guidance (with necessary checking of the mentioned above constraints). From the algorithmic point of view the RV motion prediction is done using the second system of the equations of motion (on the prediction interval that is equal to 100 integration steps of the first basic system), and here a predicted estimation of all admissible values of the bank angle  $\gamma_i$  is provided with further analysis and choice of the best value of the angle  $\gamma_i^*$ . The obtained guidance (value of the angle  $\gamma_i^*$ ) corresponding to the minimum temperature value  $(T_w^*)_{\min}$  is then used in the basic (first) system of RV motion equations only on the current step of solution (till the moment  $t_{i+1}$ ), then the procedure of the quick prediction and choice of a new bank angle value  $(\gamma_{i+1})^*$  is repeated.

It should be noted that in order to increase a speed of the described algorithm for obtaining the guidance law  $\gamma(t)$  and nominal descent trajectory of RV the new analytic relations [15,16] are applied, first of all in the prediction module of the second system of the vehicle's equations of motion. A distinctive feature of the new method of RV motion prediction is a substantial reduction in computation time while keeping a required accuracy of solution (in comparison with the solution obtained using the numerical integration of the motion equations).

## COMPARATIVE THERMAL AND MASS ANALYSIS OF RETURNED UNWINGED CONFIGURATIONS

Fig. 4 shows [4,5] the experimental dependencies of the lift to drag ratio with respect to the drag coefficient for the segmental-conical vehicle that demonstrate a possibility and/or appropriateness to consider RV of the given configuration as a promising vehicle for return to the Earth (if the lift to drag ratio  $K_\delta > 0.4$  is provided).

Three types of RV of the unwinged configuration that are the most studied aerodynamically have been compared: a vehicle with the head thermal protection screen (the segmental-conical vehicle, fig.3) and two lifting body vehicles (the 'conical segment' type vehicle [10] and the 'conical segment with a superstructure' type vehicle [5], fig.5).

The following parameters have been taken as the basic initial data: the number of crewmembers is 6 (2 pilots and 4 passengers), the vehicle's volume  $W=20.2 \text{ m}^3$ , the initial mass of the vehicle before its entry to the atmosphere is 7.012-8.645 t, here the lowest

value of the initial mass corresponds to the entry velocity 13 km/s and the highest one corresponds to the entry velocity 17 km/s.

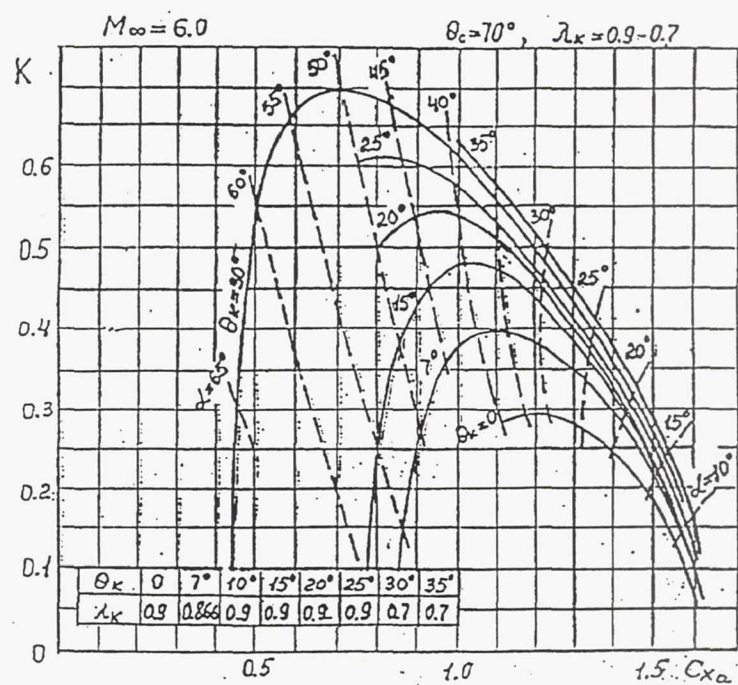
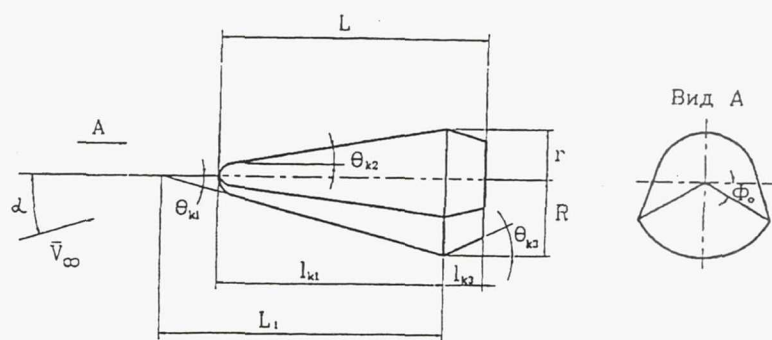


Figure 4



Characteristic parameters of configuration

$\bar{l}_w = \frac{l_w}{L_1}$	$\theta_w, \text{град}$	$\Phi, \text{град}$	$\theta_{K2}, \text{град}$	$\bar{l}_w = \frac{l_w}{L}$	$\theta_{K2}, \text{град}$
0.79	15.0	30.0	10.0	0.152	25.0

Figure 5

The methodology of the aerothermodynamic and flight dynamic designing of RV developed for the solution of the given problem has some specific features typical only to the hyperbolic entry vehicles: to provide a 'capture' of the vehicle (non-exit of RV out of the atmosphere) and an admissible integral level of high g-loads acting on a crew  $(n_{\Sigma})_{\max} > 6$ . The load factor  $(n_{\Sigma})_{\max} = 8$  was taken as a maximum admissible limit and a level of the load factor influence on the crew was estimated using the integral criterion of the load factor withstandability  $\Delta\Phi$  [9,10,17], and here the minimum value  $\Delta\Phi_{\min}$  was provided during analysis of the basic aerothermodynamic and flight dynamic parameters of each vehicle. It should be mentioned that the design geometry parameters for each of the compared vehicles were obtained basing on solution of the corresponding configuration equations (1) while satisfying the given design criteria.

In order to obtain basic mutually coordinated aerothermodynamic and flight dynamic parameters the criterion of 'drag efficiency'  $S_T$  (the first time introduced in [10]) was applied for each of the considered vehicles:

$$S_T = \frac{K_p}{C_{X_A} \cdot S_{\text{mid}}} \quad (5)$$

The profiles  $S_T = f(\alpha)$  and  $S_T = f(\theta_0)$  obtained for each vehicle and each value of the entry velocity  $V_{\text{en}}$  (here  $\alpha$  is the angle of attack and  $\theta_0$  is the entry angle) allow to form the required flight dynamic parameters  $(\alpha_6, K_6, \sigma_x, \theta_0)$  that provide the minimum value of the load factor withstandability criterion  $\Delta\Phi_{\min}$ . Thus the analyzed segmental-conical vehicle has the non-standard (in comparison with the Soyuz RV) design geometry parameters:  $\theta_c = 57^\circ$ ,  $\theta_k = 35^\circ$  [10].

Fig. 6 presents the mentioned profiles  $S_T = f(\alpha)$  and  $S_T = f(\theta_0)$  for the considered vehicle of the segmental-conical configuration. Using these profiles it is possible to determine the trim angle of attack  $\alpha_6$  and entry angle  $\theta_0$  corresponding to a minimum level of the integral load factor effect on the initial phase of the RV deceleration  $\Delta\Phi_{\min}$ .



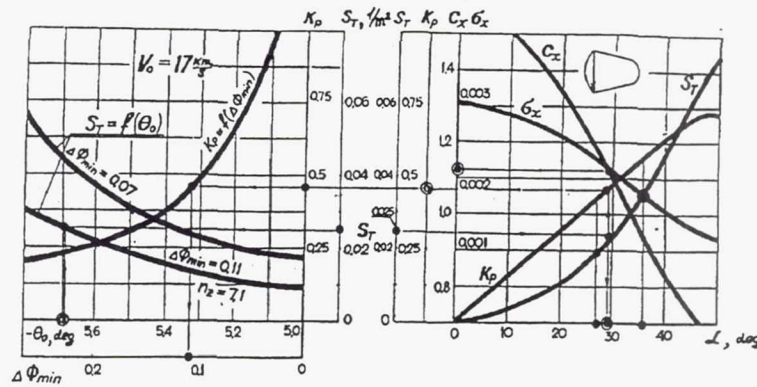


Figure 6

Fig. 7 gives a relative mass of the thermal protection  $G$  as a function of the entry angle  $\theta_0$  and values of the drag efficiency criterion  $S_T$  at different values of the entry velocity  $V_0$ , longitudinal range of the atmospheric phase  $L_{LONG}$  and different models ( $\Phi_1, \dots, \Phi_7$ ) of the load factor withstandability. The given graphic profiles were built solving the thermal and mass trajectory optimization problem [14] minimizing the thermal protection weight  $G$  at the characteristic point of the windward surface of the considered segmental-conical configuration. The similar profiles were obtained also for the other considered vehicles. It should be noted that the applied analytic relations [14] for determination of the mass  $G$  are based on the results of fundamental studies in the area of the radiation and convective heat exchange of entry vehicles [13].

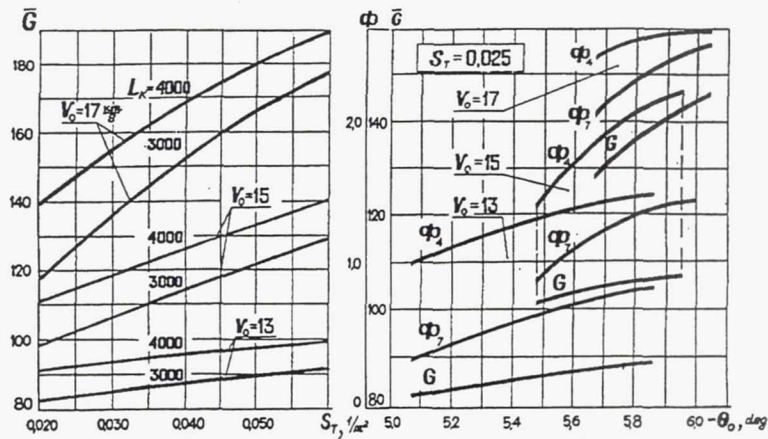


Figure 7

Table 1 contains for each of the considered return vehicles the obtained values of the maximum lift to drag ratio  $K_{max}$ , trim angle of attack  $(\alpha)_{K_{max}}$  corresponding to  $K_{max}$ , values of the drag efficiency criterion  $S_T$  (also corresponding to  $K_{max}$ ), range of the lift to drag ratio  $K_p$  variation (corresponding to the optimum available range of the drag

efficiency criterion  $S_T=0.020-0.035$ ) and range of the trim angle of attack  $\alpha_s$  variation (also corresponding to the optimum available range of the drag efficiency criterion  $S_T=0.020-0.035$ ).

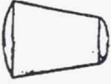


Shape	$K_{\max}$	$\alpha_{K_{\max}}$	$(St)_{K_{\max}}$	Range $St=0.020-0.035$	
				Range $K_p$	Range $\alpha_\sigma$
	0.725	50°	0.075	0.40-0.55	27.0°-36.0°
	0.565	15°	0.146	0.43-0.58	51.0°-41.0°
	1.525	0°	0.340	0.43-0.62	33.0°-26.0°

Table 1

The obtained in such a way flight dynamic parameters of RV was used then to form the nominal guidance profile  $\gamma(t)$  and descent trajectory to satisfy a terminal condition to provide a longitudinal range of the atmospheric phase  $L_{LONG}=3000-5000$  km.

## CONCLUSION

Fig. 8 presents the final results of the comparative thermal and weight analysis performed for the three RV of unwinged configurations, and graphs in the right part of Fig. 8 corresponds to the case when the drag efficiency criterion  $S_T$  (5) has been applied in determination of the basic flight dynamic and aerodynamic parameters for each vehicle and graphs in the left part of Fig. 8 corresponds to the case when this criterion has not been applied.

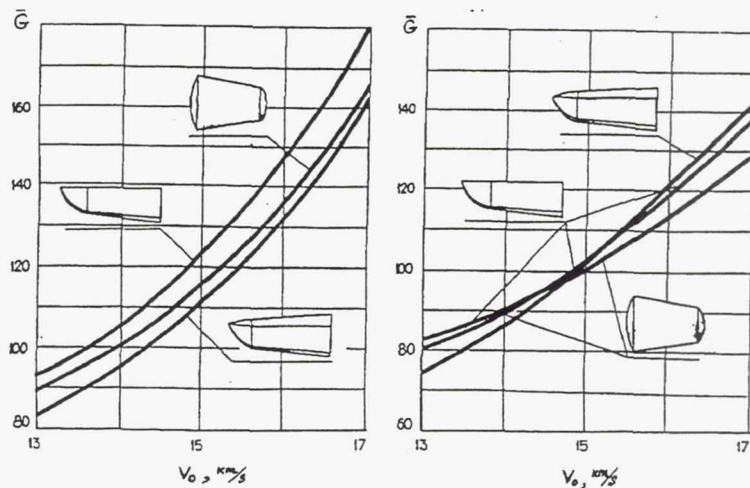


Figure 8

The main result of the performed studies is a conclusion about the competitiveness of the segmental-conical configuration RV in comparison with the considered lifting body vehicles (using the criterion of the minimum required mass of the thermal protection coating in the characteristic point of the vehicle's surface). It should be especially stressed that this conclusion is done at the accurate forming of the basic aerothermodynamic and flight dynamic parameters of RV (using the drag efficiency criterion  $S_T$ ) and at accurate solution of the trajectory thermal/mass optimization problem during the RV motion in the atmosphere.

#### REFERENCES

1. N.M.Ivanov, V.A. Korsakov, S.I. Kudriavtsev, A.A. Savchenko, V.G. Sobolevskiy, N.L. Sokolov. Problem of landing of unwinged reentry vehicle to return site of small size. XI International Symposium on Space Flight Dynamics, CNES, Toulouse, France, 1995.
2. N.M.Ivanov, M.N. Kazakov, V.E. Minenko, A.N. Rumynskiy, V.G. Sobolevskiy. Designing shape of advanced reentry vehicle. 'Kosmonavtika i raketostroenie', 9, 1997.
3. N.M.Ivanov, M.N. Kazakov, A.N. Rumynskiy, V.G. Sobolevskiy. Formulation of requirements to parameters of thermal protection and aeroballistic parameters of future Martian return vehicle. 'Kosmonavtika i raketostroenie', 11, 1997.
4. M.N. Kazakov, V.E. Minenko, V.G. Sobolevskiy. Preliminary aeroballistic designing of advanced unwinged reentry vehicles. I International Conference on Microminiaturization and New Space Technologies, Korolev, Russia, 1997.
5. M.N. Kazakov. Choice of shape of unwinged reentry vehicle with increased lift to drag ratio. 'Kosmonavtika i raketostroenie', 3, 1995.



6. N.A. Anfimov, N.M.Ivanov, V.G. Sobolevskiy and others. Basic theory of space vehicle flight. Under editorial of G.S. Narimanov and M.K. Tikhonravov. Moscow, 'Mashinostroenie', 1972.
7. N.M.Ivanov, V.G. Sobolevskiy. Analytic estimation of descent range of space vehicle for hyperbolic return trajectories. 'Kosmicheskie issledovania', vol. X, ed. 3, 1972.
8. V.A. Yaroshevskiy. Entry of space vehicles to atmosphere. Moscow, 'Nauka', 1988.
9. A.V. Klimin. Manned space vehicle braking in atmosphere after interplanetary flight. 'Kosmicheskie issledovania', vol. XI, ed. 1, 1973.
10. V.G. Sobolevskiy. Studying problems of ballistic designing of reentry vehicles for return to the Earth. Candidate of technical sciences dissertation. Kaliningrad, Russia, 1973.
11. V.G. Sobolevskiy. Analysis of problems of ballistic designing of future reentry vehicles. Moscow, TSNTI RKA 'Poisk', 1997.
12. V.G. Sobolevskiy. Analytic methods in ballistic designing of future reentry vehicles. I International Conference on Microminiaturization and New Space Technologies, Korolev, Russia, 1997.
13. N.A. Anfimov, A.N. Rumynskiy. Radiation-convective heat exchange and thermal protection of space vehicles descending on the Earth and other planets of Solar system. Moscow, 'Mashinostroenie', 1982.
14. N.M.Ivanov, A.N. Rumynskiy, V.G. Sobolevskiy. Numerical thermal and weight optimization of descent trajectory of blunted body. 'Raketno-kosmicheskaya tehnika', ser. IX, ed. 1, Kaliningrad, Russia, 1993.
15. V.G. Sobolevskiy. Analytic prediction of reentry vehicle motion. 'Kosmonavtika i raketostroenie', 10, 1997
16. N.M.Ivanov, V.G. Sobolevskiy. Operational prediction of reentry vehicle motion. XII International Symposium on Space Flight Dynamics, ESOC, Darmstadt, Germany, 1997.
17. A.S. Barer, E.I. Sorokina, K.I. Murakhovskiy. To the problem of human withstandability to g-loads after long presence in conditions simulating weightlessness. 'Kosmicheskaya biologiya i meditsina', vol VI, 3, 1972.
18. D.J. Shapland, W.F. Munroe. Comparison of three configurations of manned vehicles for entry to the Earth atmosphere at hyperbolic velocities. 'Astronautics and rocket dynamics', Moscow, VINITI, 39, 1967.

### Improved Instrumental Magnitude Prediction Expected from Version 2 of the NASA SKY2000 Master Star Catalog\*

C.B.Sande†, D.Brasoveanu, A.C.Miller, A.T.Home, (Computer Sciences Corp.),  
D.A.Tracewell (NASA/GSFC), W.H.Warren Jr. (Raytheon STX)

The *SKY2000 Master Star Catalog (MC)*, *Version 2* and its predecessors have been designed to provide the basic astronomical input data needed for satellite acquisition and attitude determination on NASA spacecraft. Stellar positions and proper motions are the primary *MC* data required for operations support followed closely by the stellar brightness observed in various standard astronomical passbands. The instrumental red-magnitude prediction subsystem (REDMAG) in the MMSCAT software package computes the expected instrumental color index (CI) [sensor color correction] from an observed astronomical stellar magnitude in the *MC* and the characteristics of the stellar spectrum, astronomical passband, and sensor sensitivity curve. The computation is more error prone the greater the mismatch of the sensor sensitivity curve characteristics and those of the observed astronomical passbands. See Figure 3 for comparison of the sensitivity curve of a typical new-generation red-sensitive charge-coupled-device (CCD) star tracker (ST) with the standard passbands (*UBVRI*). Here, the effective wavelength of the very broad sensor curve is shifted well away from that of the much narrower visual (*V*) passband.

This paper presents the preliminary performance analysis of a typical red-sensitive CCDST during acquisition of sensor data from the two Ball CT-601 ST's onboard the Rossi X-Ray Timing Explorer (RXTE). A comparison is made of relative star positions measured in the ST FOV coordinate system with the expected results computed from the recently released *Tycho Catalogue* (Reference 1). The comparison is repeated for a group of observed stars with nearby, bright neighbors in order to determine the tracker behavior in the presence of an interfering near neighbor (NN). The results of this analysis will be used to help define a new photoelectric photometric instrumental sensor magnitude system (*S*) that is based on several thousand bright star magnitudes observed with the RXTE ST's. This new system will be implemented in *Version 2* of the *SKY2000 MC* to provide improved predicted magnitudes in the mission run catalogs.

---

\* This work was supported by the National Aeronautics and Space Administration (NASA)/Goddard Space Flight Center (GSFC), Greenbelt, Maryland, USA, under Contract GS-35F-4381G, Task Order No. S-03365-Y.

† e-mail: csande@cscmail.csc.com

## INTRODUCTION

The current operational version of the *SKYMAP MC*, known as *SKY2000 MC, Version 1* was produced in 1996-7 and represents the last version of the *MC* to contain data solely from ground-based sources. It is to be replaced by *SKY2000 MC, Version 2*, which will incorporate data from several newly available spaceborne sources, including astrometric and photometric data from the European Space Agency (ESA) Hipparcos mission and sensor photometric data acquired from the RXTE spacecraft. This catalog is to be a comprehensive all-sky star catalog down to approximately visual magnitude 9 that includes astrometric, photometric, and many other types of stellar data for approximately 300,000 stars. The MMSCAT software package is used to generate specialized subcatalogs called mission run catalogs for satellite attitude support using the *SKY2000 MC, Version 2* as input. All mission run catalog stars include a predicted sensor magnitude ( $m_s$ ) calculated by the REDMAG subsystem. The observed sensor magnitudes from the RXTE ST's will provide an additional group of input magnitudes to the software for several thousand of the brightest stars.

## BACKGROUND

### Rossi X-Ray Timing Explorer:

The RXTE spacecraft was launched by a Delta II ELV on December 30, 1995, to study the time variability in emissions of x-ray sources over the spectral range 2-250 keV. Two Ball CT-601 CCDST's were carried as part of the spacecraft's attitude control system (ACS). Each tracker is capable of identifying up to five stars simultaneously for use in attitude determination (see Figure 1). Beginning in March, 1997, the Attitude Model Support Task began collecting additional star observations from both star trackers to refine the sensor calibration, to define a new observed photometric sensor system (*S*) for the *MC, Version 2*, and to determine near neighbor (NN) effects on measured sensor positions and magnitudes. In less than six months, more than 7700 observations have been obtained of several thousand different stars. Sky coverage has not been uniform because of mission constraints, but enough sensor magnitudes have been obtained to allow the creation of a new observed RXTE photometric sensor system. Stars having observed RXTE magnitudes will have magnitudes available that will more nearly match the effective wavelength and bandwidth of other CCDST's than those observed in the standard *UBVRI* passbands. Predicted instrumental  $m_s$ 's based upon RXTE input magnitudes are expected to be improved over those based upon the *UBVRI* passbands. The data acquired permit an examination of CCDST performance, primarily in the areas of measured star positions and measured sensor magnitudes, which are the most important pieces of information coming out of the ST's from the operational standpoint. The knowledge gained will be of use in improving the generation of future mission run catalogs for other satellites using CCDST's.



## XTE Spacecraft

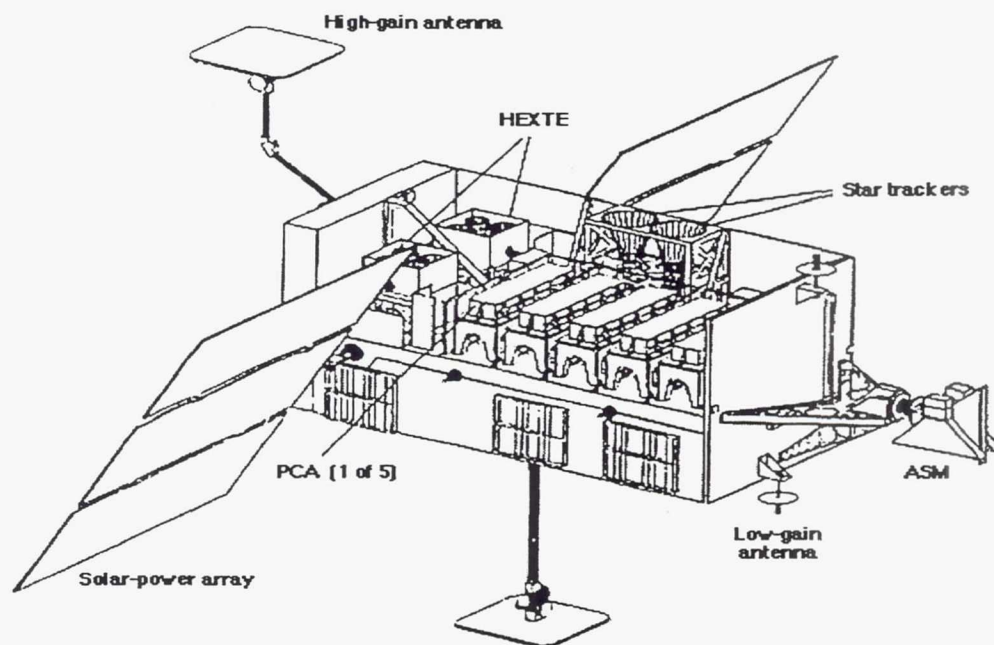


Figure 1 Rossi X-ray Timing Explorer

### Characterization of the CCDST Data:

The body of data acquired by the Attitude Model Support Task includes measured positions in field of view (FOV) coordinates and measured instrumental magnitudes with data points at two-second intervals during periods of successful star identification. Observations were acquired both during periods of spacecraft inertial pointing and during slews between points. Up to five stars may be identified simultaneously by each star tracker. The trackers are mounted with a boresight separation of 9.9 degrees along the diagonal of each FOV, so that there is a little more than one degree in common between the nominal 8x8 degree FOV's at the overlapping corners. This arrangement allows for the possibility of simultaneous observation of the same star by both trackers.

Each star image detected by the CCDST is defocused so that its image is spread over 4x4 to 5x5 pixels. Each pixel on the CCD is approximately 60x60 arcsecond. The calculated centroid of this defocused image over 16 to 25 pixels yields a position in FOV coordinates and integration of the flux over the same image yields a sensor magnitude. Since a real-time spacecraft attitude was not recorded during the data acquisition, only the angular separation of neighboring pairs of stars in the FOV at the same time is useful in comparison with other independent source catalog positions (e.g., the *Tycho Catalogue* [Ref. 1]).

Stars which were mis-identified in the attitude determination software used to process the star tracker data were identified by the large deviations in the measured angular separation from that predicted for the

pair. These large deviations were typically on the order of several degrees and were well outside the range of variation examined for NN effects.

A comparison of the observed RXTE magnitudes with the predicted REDMAG subsystem values was done to validate the REDMAG algorithms. For the purposes of this analysis, a group of stars observed simultaneously in the FOV of RXTE ST 1 was chosen and divided into two subgroups, one of the stars not expected to have NN-related identification problems and the other stars in which at least one star of the pair has a bright NN. These stars were identified in the *Tycho Catalogue* and independent *Tycho* positions and *V* magnitudes were obtained.

## TRACKER POSITION PERFORMANCE COMPARED WITH *TYCHO*

### Star-Pair Angular Separations:

Angular separations of star pairs were calculated both from the RXTE FOV coordinates and from the *Tycho* positions. For the stars with NN's brighter than approximately  $V = 10.0$ , the effects on the observed RXTE star by its near-neighbor were measured in a shift in position relative to another observed RXTE star in the FOV at the same time.

Figure 2 shows the effects of NN interference on the measured position of the centroid by plotting the deviation of the predicted pair separation from the measured separation (taken as measured minus predicted) as a function of NN angular separation ( $\Delta\theta$ ) and the magnitude difference ( $\Delta m$ ) of the primary and secondary NN stars. The horizontal axis represents the NN  $\Delta\theta$  in arcseconds, while the vertical axis represents the component  $\Delta m$  (in magnitudes), and the contours are the measured  $\Delta\theta_o$  minus the predicted  $\Delta\theta_p$  in arcseconds. The horizontal axis is marked in one-pixel increments. The location of each data point used in the plot has been superimposed over the contours as an oval symbol. The region in the lower left-hand corner corresponds to stars with small NN separations and a bright companion star. Due to these characteristics, this region ( $0 \leq \Delta m \leq 1$ ;  $0 \leq \Delta\theta \leq 60$ ) is devoid of features because the attitude determination software rejected the stars seen by the star tracker for identification. The difference between the  $\Delta\theta_o$  and  $\Delta\theta_p$  separations is probably not bounded; the maxima and minima in Figure 2 probably indicate regions in which star identification often fails in the software. The 10-arcsecond or less contours correspond to the noise (standard deviation between the  $\Delta\theta_o$  and  $\Delta\theta_p$  values for the group of stars without interfering NN's). This number is in good agreement with the 6 arcsecond error (in each coordinate) found during calibration maneuvers early in the RXTE mission (Ref. 2).



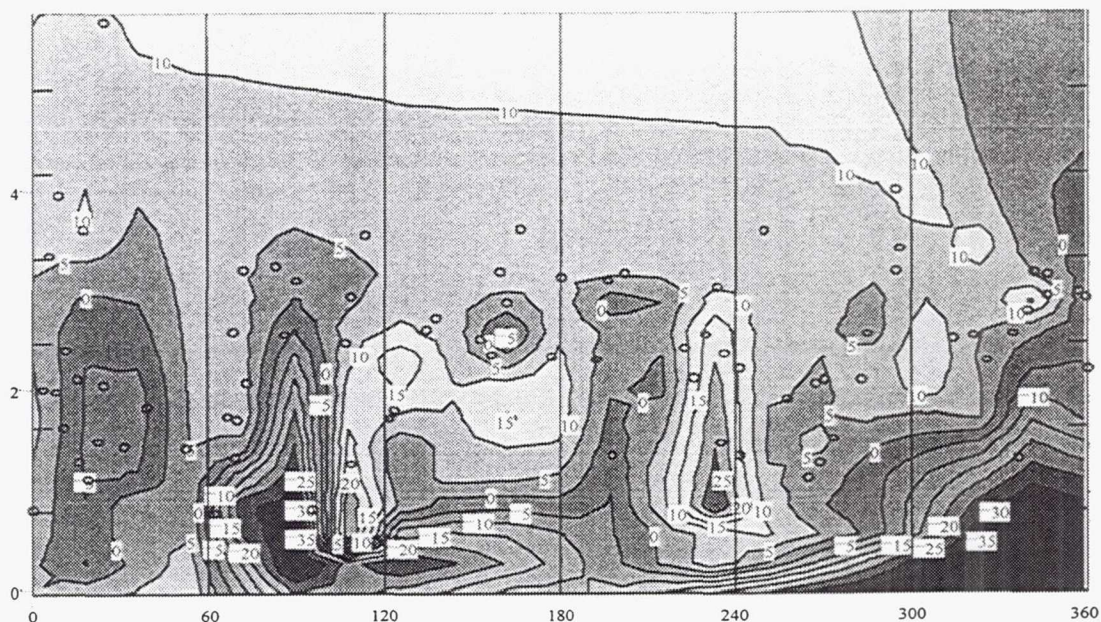


**Figure 2 Near-Neighbor Effects on Measured Separations (Arcseconds)**

## CCDST MAGNITUDE MEASUREMENT COMPARED TO PREDICTION

### Star-Pair Magnitude Differences:

All observed RXTE stars have  $V$  magnitudes obtained either from the *Tycho Catalogue*, the *Catalog of Red Magnitudes* (Ref. 3), or from the *Mermilliod UBV Catalogue* (Ref. 4). These magnitudes are not directly useful, as the sensitivity curves of the CCDSTs on RXTE are not close to that of the Johnson  $V$  passband (see Figure 3). However, these magnitudes together with available Johnson and Cousins red magnitudes from Reference 3 ( $R$  passband) could be used as input to the REDMAG magnitude prediction subsystem of the MMSCAT catalog generation software. REDMAG uses the sensitivity curve of the RXTE CCDSTs (an average of the curves for trackers 1 and 2) together with spectrophotometric scans of different stellar spectral types to calculate a color correction (CI) to the input astronomical magnitude in order to predict the instrumental RXTE  $m_s$ . See the Appendix and Ref. 5 for discussions of REDMAG algorithms. The residuals between measurement and prediction were investigated for the stars without an interfering near neighbor and found to be in accordance with results documented elsewhere (Ref. 6), and then separately for the subgroup where at least one star of the pair was expected to show the effects of NN interference.



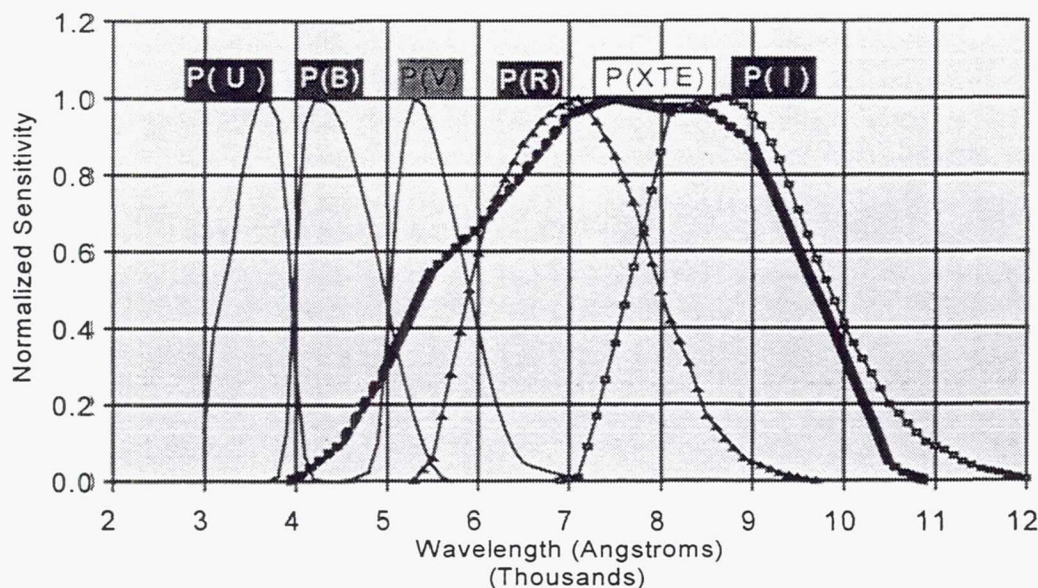


**Figure 3 Johnson Standard UBVRI Passbands Compared to Ball Aerospace CT-601 Sensitivity Curve (Rossi XTE)**

For the stars with interfering NN's, the magnitude residuals were then related to separations and magnitude differences obtained from various catalog sources, usually *Tycho* or the *Washington Catalog of Visual Double Stars 1994.0* (Ref. 7), with the qualifier that predicted sensor magnitudes for the primaries and secondaries were used to generate sensor passband magnitude differences for the pairs involved. Also, it was apparent that the observed sensor magnitudes from the defocused CCDST images can be modeled better by using the standard astronomical formula for a blended pair magnitude with the standard astronomical passband magnitudes and magnitude differences replaced by predicted sensor magnitudes and magnitude differences (compare Figures 4 and 5, see Eq. 1).

$$m(\text{blend}) = m(\text{primary}) - 2.5 \log_{10}(1 + 2.5119^{-\Delta m}) \quad (1)$$

Figure 4 shows the effects of NN interference on the measured CCDST magnitudes, expressed as the difference between the measured sensor magnitude and the unblended predicted magnitude. The horizontal and vertical axes are the same as in Figure 2, but the contours in Figure 4 represent the difference between the measured and predicted magnitudes of the stars. The magnitude difference on the vertical axis is the sensor passband magnitude difference, and the horizontal axis represents the separation in arcseconds between the primary and secondary components of the pair.

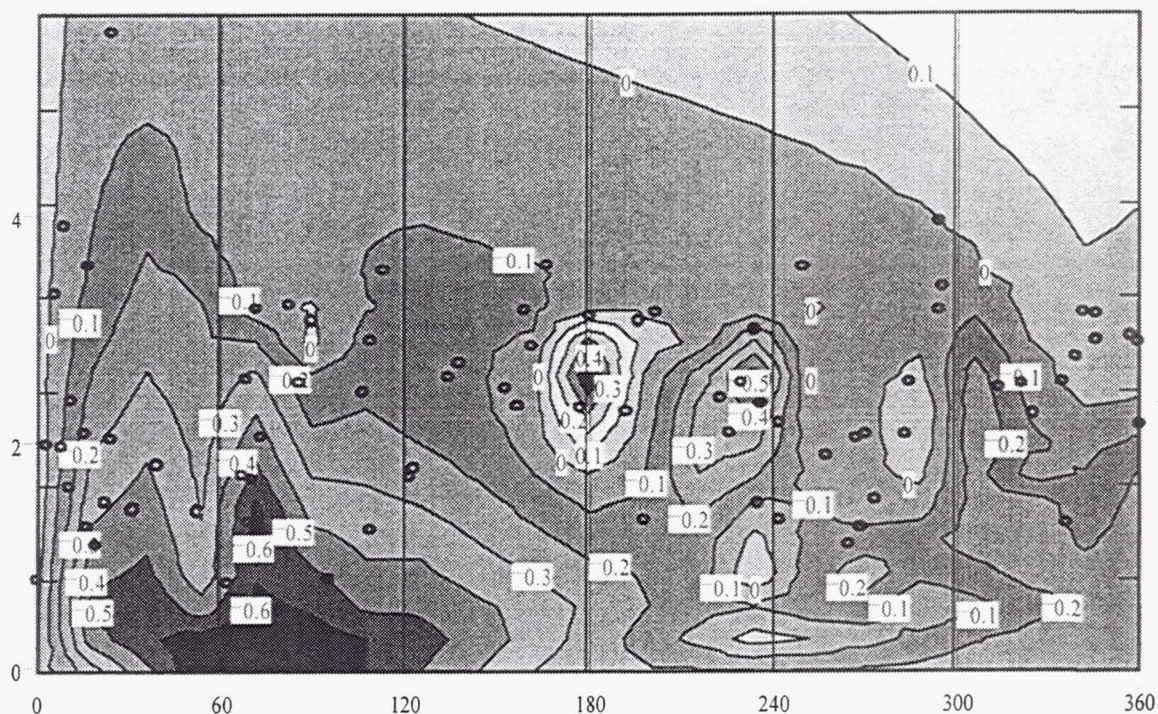


**Figure 4 Near-Neighbor Effects on Measured Magnitude, Non-Blended Predicted Magnitudes**

Figure 5 is the same plot, but using blended predicted magnitudes, where the blended magnitude is computed from the predicted primary magnitude and the sensor passband magnitude difference. Both figures show features near the CCDST pixel boundaries which may be associated with the algorithm used by the manufacturer to sum the incident flux and produce a measured sensor magnitude. Further analysis of this effect may require knowledge of the manufacturer's algorithm, which is not available at present. Figure 5 shows an improvement in the agreement of the predicted magnitudes with the measured magnitudes over the region in which a blended image is seen by the tracker, but the blended predicted values become too bright in the region in which the tracker begins to separate the images (4-5 pixels separation).



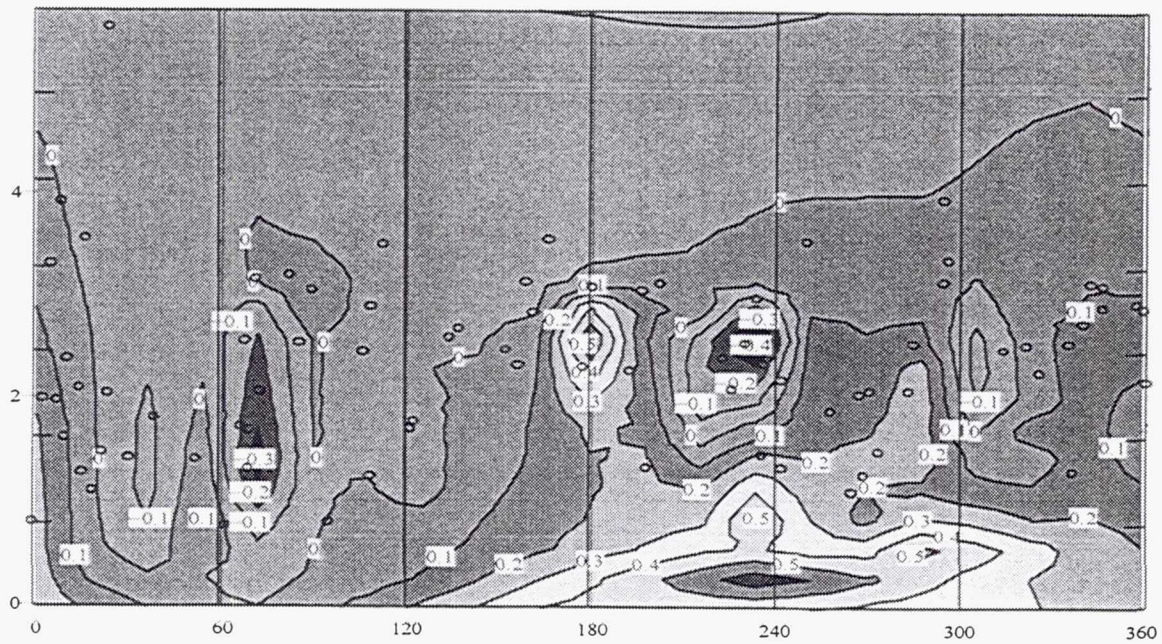


**Figure 5 Near-Neighbor Effects on Measured Magnitude, Blended Predicted Magnitudes**



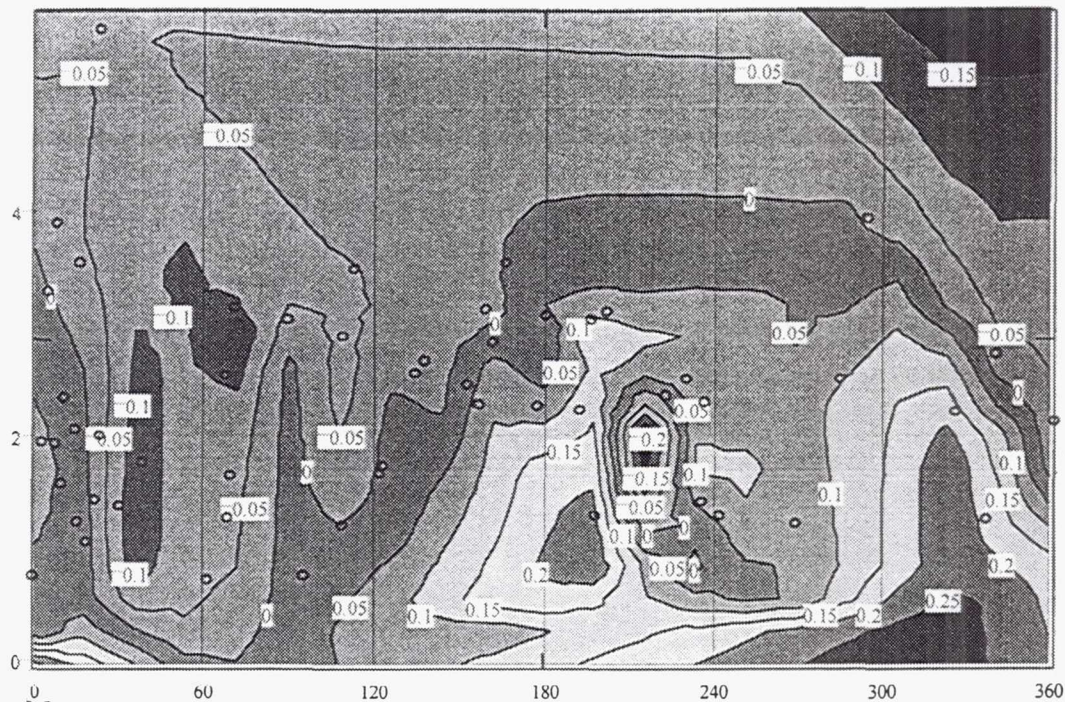


**Figure 6 Near-Neighbor Effects on Measured Magnitude, Blended Predicted Magnitudes (Spectral Types O-F)**

Since the CT-601 CCDST is known to be selectively more sensitive in red wavelengths, the stars plotted in Figures 4 and 5 were further separated into two groups, one composed of stars with spectral types between O and F, and one composed of stars with spectral types K, M, or redder. Figures 6 and 7 highlight the fact that the predicted magnitudes are not as accurate for the redder stars, as expected (Ref. 6). The region in Figure 7 corresponding to NN's brighter than two magnitudes fainter than the primary and closer than 4 pixels (240 arcseconds) is devoid of data points, which may indicate that the star identification software fails for red primary stars in this region.





**Figure 7 Near-Neighbor Effects on Measured Magnitude, Blended Predicted Magnitudes (Spectral Types K, M, and Redder)**

## DISCUSSION

The manufacturer of the CT-601 CCDST states that NN's separated by more than four pixels (240 arcseconds) from a measured star should have a greatly reduced effect on the position determination. This appears to be well borne out by the data. For example, replacement of primary component positions with center-of-light positions showed no significant improvement in the residuals in the region where blended magnitudes improved the magnitude residuals (less than four pixels NN separation). Calculated positions can deviate by tens of arcseconds from predicted values in cases of extreme interference, but most attitude determination software applies constraints to the identification process and properly setting them can eliminate many of the affected stars from an attitude solution. Also, there does seem to be a significant pixel edge-related effect on the measured positions, but at this point in the analysis it has not been examined closely (Figure 2).

The manufacturer also recommends that no star brighter than 4 magnitudes fainter than a potential candidate catalog star be located within 0.1 degree (6 pixels) of that candidate star in order to reduce the contamination of the image. Within this 0.1-degree region, it appears that stars 3 or more magnitudes fainter than the catalog star produce little or no observable interference (Figure 5). As the NN brightness

and position approaches the catalog star, the interference increases until the image measured by the star tracker deviates too much from the catalog prediction, whereupon most attitude software will reject the star. This situation can be improved by the use of blended sensor magnitudes for pairs separated by approximately 3 pixels (compare Figures 4 and 5), but the blended magnitudes are less accurate than unblended predictions at separations of approximately four or more pixels (Figure 5). The positive deviations in Figure 5 indicate that the blended predictions are brighter than what is observed, possibly indicating that the tracker no longer sees a blended image.

The recommendation from the manufacturer that stars with NN's violating the preceding constraints be excluded from a mission star catalog would probably be too harsh a restriction. Instead, alterations in the NN data fields of the input MC and in the REDMAG subsystem of the MMSCAT software could be made in order to produce better predictions for CCDST's. Catalog entries could be blended into single entries for stars with significantly interfering NN's, which would also eliminate a problem seen for stars with NN separations of around four pixels, in which the identification produced by the attitude software "flip-flops" between the two stars of the pair. A single, blended catalog entry would obviously eliminate the possibility of a "flip-flop" in the software and is probably a better prediction of what the CCDST will see for stars with interfering NN's.

## ACKNOWLEDGMENT

The authors wish to acknowledge the contributions of the following personnel to this paper:

- Joseph A. Hashmall
- Joanne R. Myers
- Flight Dynamics Attitude Operations personnel, notably Jonathan S. Landis and Craig U. Woodruff

## REFERENCES

- 1.) European Space Agency, *Hipparcos and Tycho Catalogues*, ESA SP-1200, 1997.
- 2.) Goddard Space Flight Center, Flight Dynamics Division, CSC 10032526, Rossi X-Ray Timing Explorer (RXTE) Postlaunch Report, D. Fink, W. Davis, et al. (CSC), June, 1996.
- 3.) Warren Jr., W., *Northern Hemisphere Catalog of Red Magnitudes*, 1994.
- 4.) Mermilliod, J.C., *Catalogue of Homogeneous Means in the UBV System*, Institut d'Astronomie, Universite de Lausanne, 1994.
- 5.) Goddard Space Flight Center, Flight Dynamics Division, CSC-27434-41, SKYMAP Requirements, Functional, and Mathematical Specifications, Volume 2, Revision 1, Instrumental Red Magnitude Prediction Subsystem, A.C. Miller, D. Brasoveanu, C. Sande, (CSC), D.A. Tracewell (NASA/GSFC), W.H. Warren Jr. (Raytheon STX), prepared by the Computer Sciences Corporation, June 1997, pp. 4.6-4 & 4.6-5.
- 6.) Goddard Space Flight Center, Flight Dynamics Division, 56830-04, SWAS Run Catalog Prelaunch Analysis, A.C. Miller, R. Nieman, prepared by the Computer Sciences Corporation, September, 1996.
- 7.) Worley, C.E. and G.G. Douglass, *Washington Catalog of Visual Double Stars 1994.0*, United States Naval Observatory, 1994.



## APPENDIX

### Instrumental Magnitude Prediction Algorithm

The instrumental red-magnitude prediction subsystem (REDMAG) in the MMSCAT software package computes the expected instrumental color index ( $CI_{SZ}$ ) [sensor color correction] from a stellar magnitude ( $m_Z$ ) observed through an astronomical passband ( $Z$ ) and the spectral type (MK) both recorded in the *Master Star Catalog (MC)*, and the characteristics of the  $Z$  passband response curve ( $P_Z$ ) and sensor passband ( $S$ ) sensitivity curve ( $P_S$ ).  $m_Z$  is corrected by  $CI_{SZ}$  to give the expected sensor magnitude ( $m_S = m_Z + CI_{SZ}$ ). The  $CI_{SZ}$  algorithm follows from Reference 5:

$$CI_{SZ} = -25 \log_{10} \left\{ \frac{\langle\langle P_S \bullet N \otimes 10^{-0.4W(\lambda)A_V} \rangle\rangle}{\langle\langle P_Z \bullet N \otimes 10^{-0.4W(\lambda)A_V} \rangle\rangle} \frac{\langle\langle P_Z \bullet N^{A_V} \rangle\rangle}{\langle\langle P_S \bullet N^* \rangle\rangle} \frac{\langle\langle P_V \bullet N^* \rangle\rangle}{\langle\langle P_V \bullet N^{A_V} \rangle\rangle} \right\}$$

where each set of double brackets  $\langle\langle \bullet \rangle\rangle$  gives the energy flux of the stellar spectrum ( $N$ ) intercepted by the response curve ( $P$ ). The Morgan-Keenan-Johnson (MK) spectral type gives access to the proper spectrophotometric spectrum in the REDMAG scan file. Each scan is normalized to 1.0 at the effective wavelength ( $\lambda_{eff}^V$ ) of the visual passband ( $V$ ) and each response curve is normalized to 1.0 at its maximum value. All  $N$ 's and  $P$ 's are functions of wavelength ( $\lambda$ ) and their product function is defined as

$$\langle\langle P \bullet N \rangle\rangle = \int_0^\infty P(\lambda)N(\lambda)d\lambda \approx \sum_{i=1}^{np} P(\lambda_i)N(\lambda_i)\delta\lambda_i$$

where

$np$  = the total number of data points in the summation

Specific variables and functions are defined as

$CI_{SZ}$  = notation for the ( $S$ - $Z$ ) sensor color

$Z = V$ (typically); the preferred order of use for the RXTE mission is red ( $R$ ) first, then  $V$  when  $R$  is not available, then photovisual ( $pv$ ), followed by infrared ( $I$ ), blue ( $B$ ), photographic ( $ptg$ ), or ultraviolet ( $U$ ) as available

$P_V$  = response curve of the  $V$  passband

$P_S$  = sensitivity curve of the sensor ( $S$ )

$P_Z$  = response curve of an observed standard astronomical passband ( $Z$ )

$N$  = normalized stellar spectrophotometric scan

$A_V$  = interstellar absorption index in the  $V$  passband is computed using the difference between the observed color  $(B-V)_{\text{obs}}$  and intrinsic [standard] color  $(B-V)_{\text{int}}$ ; the MK spectral type of the star in the MC gives access to the REDMAG standard colors file.

$W(\lambda)$  = Whitford interstellar reddening function normalized to  $\lambda_{\text{eff}}^V$

$N \otimes 10^{-0.4W(\lambda)A_V}$  = stellar spectral scan reddened by interstellar absorption

$N^{A0V}$  = spectral scan of an  $A0V$  reference type

$(*)$  = typically  $A0V$ ,  $G0V$ ,  $K0V$  or other reference selected for the mission sensor; frequently different from the standard  $A0V$  reference used for astronomical passbands ( $UBVR_I$ )

$N^{(*)}$  = normalized spectral scan for the mission sensor reference type  $(*)$

In general, the contribution from each of three ratios in the  $CI_{SZ}$  expression above is given by

$$\Delta CI_{SZ}(\text{ratio}) = -2.5 \log_{10}(\text{ratio value})$$

Once the value of  $(*)$  has been selected for the mission, the contribution of the last ratio is a constant, unchanged for all stars and all observed astronomical passbands. [Examples:  $(*) = A0V$  and  $\Delta CI_{SZ}(\text{last}) =$  zero for the RXTE;  $(*) = G0V$  and  $\Delta CI_{SZ}(\text{last}) = 0.455$  magnitude for the SWAS.] Similarly,  $\Delta CI_{SZ}(\text{middle})$  is unchanged for all stars but does change with the observed astronomical passband used in each computation.  $\Delta CI_{SZ}(\text{first})$  changes with each star and the observed passband ( $Z$ ) used. Due to the non-flat stellar spectrum of the typical star, it is clear that the closer  $\lambda_{\text{eff}}^Z$ , effective bandwidth ( $\Delta \lambda_{\text{eff}}^Z$ ), and shape of  $P_Z$  is to  $P_S$  the closer  $\Delta CI_{SZ}(\text{first})$  comes to zero and the less critical the uncertainty in the computation. See Figure 8 for the product functions  $P_S \bullet N$  and  $P_V \bullet N$  for RXTE.

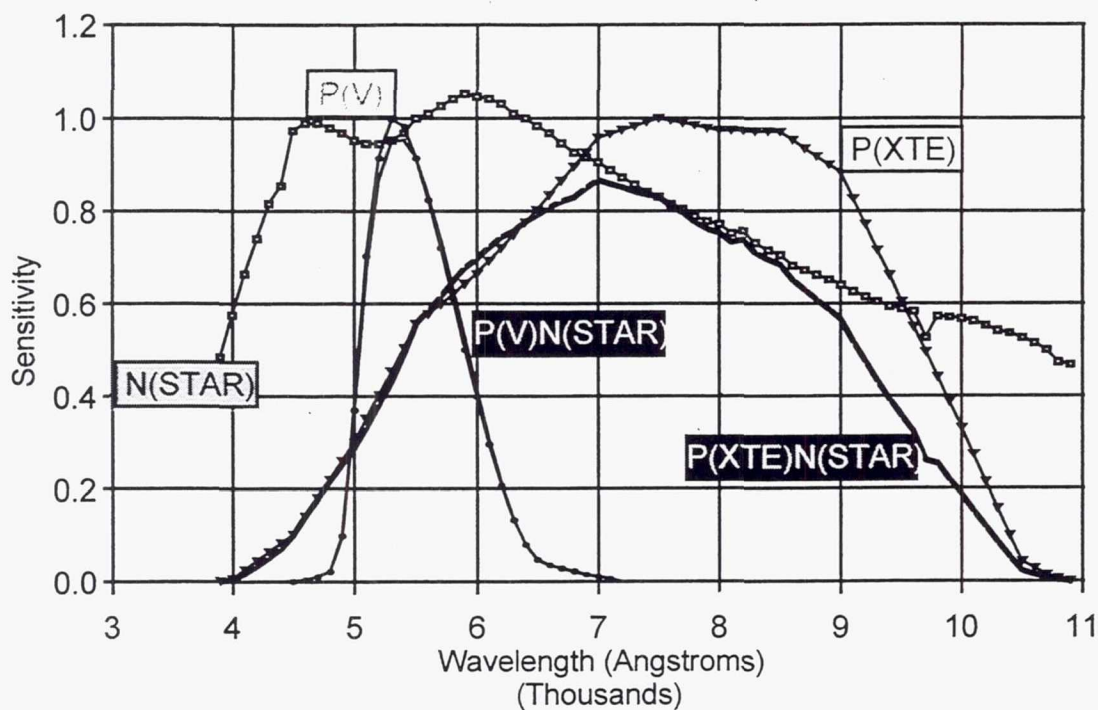


FIGURE 8 TYPICAL STAR MEASURED IN V & XTE (BALL CT-601) BANDS

Usually  $Z = V$  and  $P_Z$  becomes  $P_V$  since there are many more accurate, observed  $m_V$ 's in the  $MC$  than any other magnitude. The first equation above reduces to the following:

$$CI_{SV} = -25 \log_{10} \left\{ \frac{\left\langle \left\langle P_S \bullet N \otimes 10^{-0.4W(\lambda)A_V} \right\rangle \right\rangle}{\left\langle \left\langle P_V \bullet N \otimes 10^{-0.4W(\lambda)A_V} \right\rangle \right\rangle} \frac{\left\langle \left\langle P_V \bullet N^* \right\rangle \right\rangle}{\left\langle \left\langle P_S \bullet N^* \right\rangle \right\rangle} \right\}$$

The  $CI_{SV} = m_S - m_V$  is the sensor color correction supplied by the vendor which includes the effect of the reference spectral type (\*) selected for the mission. At the selected reference,  $CI_{SV} = 0$  ( $m_S = m_V$ ). Note that at the selected reference, when  $Z \neq V$ , in general  $CI_{SZ} \neq 0$  ( $m_S \neq m_Z$ ).



## **AUTONOMOUS STAR TRACKER**

### **Performance versus cost effective A-STR**

**A. Landi / D. Procopio / M. Lucarini**

**Alenia Difesa, Un'Azienda Finmeccanica, Divisione Sistemi Avionici ed  
Equipaggiamenti, Unita Officine Galileo, via A. Einstein 35, 50013 Campi Bisenzio,  
Italy**

#### **ABSTRACT**

As an evolution of activities performed in the frame of an ESTEC contract for the development and realization of an autonomous star sensor for interplanetary and scientific mission, OG is now developing a compact autonomous star tracker useful for commercial applications where reduced mass, power consumption and recurring cost are driving requirements, rather than accuracy.

Through proper on-board star catalogues and pattern recognition and attitude estimation algorithm, the sensor is capable to quickly determine attitude and rate of S/C with respect to inertial reference frame without any a priori attitude knowledge. The sensor is designed to allow an updating rate of 10 Hz (or higher) to be competitive with the faster sensor on board of a S/C (i.e. gyro) and then to be used as part of a gyroless attitude control system.

New Electronic packaging technology and VLSI components are used to reduce electronic volume to the minimum extent.

This paper presents the description of the sensor H/W and S/W, a summary of the functionality and the performance analysis as obtained via a high fidelity simulator.

**Page intentionally left blank**

## AUTONOMOUS STAR IDENTIFICATION USING FUZZY NEURAL LOGIC NETWORK

Jian Hong\* and Julie A. Dickerson\*

Star observation is widely used by spacecraft for attitude determination. Star sensors are used by spacecraft to measure star magnitude and star coordinates in the spacecraft frame. The measurements are then compared with a reference star catalog to obtain the attitude information of the spacecraft. Most "quaternion-out" star recognition systems use direct match algorithms to search a database of star patterns. These methods are inefficient in both search time and memory requirements. Fuzzy Neural Logic Networks (NLN) can through their internal parallelism speed up the search process and deal with measurement uncertainty. It also requires no a-priori attitude knowledge for the star identification. We use a set of NLNs that divide the data into eleven subnetworks based on the distance between the two brightest stars in a star triplet. On a set of 9050 star triplet patterns generated from the SKY2000 database, the network recognition accuracy was better than 99% even when measurement errors up to 72 arcsec were present. With the proposed star recognition algorithm, errors due to star magnitude measurement can also be minimized.

### INTRODUCTION

Star observation is widely used by spacecraft for attitude determination. Star sensors measure star magnitude and star coordinates in the spacecraft frame. The measurements are then compared with a reference star catalog to obtain the attitude information of the spacecraft. Autonomous star identification is important for spacecraft navigation since it reduces the influence caused by the system failure and the spacecraft is less dependant on the ground communication links.

Most of the current autonomous star identification systems use direct-match algorithms that store the star feature vectors in a database<sup>1,2</sup>. During recognition, the measurements are compared with the reference feature vectors in sequence<sup>2</sup> or by using binary-tree search<sup>3</sup>, until a correct match is found. The computation time for star recognition with direct-match algorithms is high and it increases as the number of the feature patterns in the database increases.

---

\* Electrical and Computer Engineering Department, Iowa State University, Ames, IA 50010



Fuzzy logic and neural networks can help deal with these problems. The parallelism of neural networks can help speed pattern search and fuzzy logic can help deal with measurement uncertainty. However, star recognition is very different from other pattern recognition problems in that the number of star patterns is quite large. For example, the number of star triplet patterns in the SWAS Catalog is 9050. Therefore, when applying neural network models to star recognition, network complexity and recognition speed are two major concerns.

The Neural Logic Network (NLN) is a neural network model which combines the strength of both neural networks and rule-based systems<sup>4</sup>. In our research, we proposed an autonomous star identification system by using a fuzzy NLN. The algorithm used by the fuzzy NLN for pattern matching is called Supervised Clustering and Matching (SCM)<sup>5</sup>. During training, a specific hidden node learns and encodes the input pattern only when both the input and output patterns match well enough. With fuzzy NLN, no-apriori attitude knowledge is required. The simulation results based on SKY2000 Master Star Catalog<sup>6</sup> shows that fuzzy NLN has the advantage of fast learning speed and high accuracy in star pattern recognition.

## NEURAL LOGIC NETWORK

The Neural Logic Network (NLN) is a neural network model that combines the strength of both neural networks and rule-based expert systems. Artificial neural networks are computational models that have the capability of learning and adaptation, but they can not reason with symbolic languages. Rule-based expert systems simulate the human problem solving process in the form of heuristic rules, but they can not respond to the new inputs. A NLN combines the two systems to incorporate human problem solving skills to the area of pattern recognition and information evaluation.<sup>4</sup>

A NLN builds up its inference engine with the neural network as its underlying structure. So it can simulate human decision making behavior as well as learn adaptively. In star identification, NLN is used as a neural network model, where parallel pattern learning and recognition is most important.

There are three types of NLNs: Boolean NLN, 3-valued NLN, and fuzzy NLN<sup>5</sup>. In a Boolean NLN, "0" is used to denote "True" and "1" for "False". In a 3-valued NLN,  $\{(1,0), (0,1), (0,0)\}$  are used as the truth values, where (1,0) denotes "True", (0,1) denotes "False", and (0,0) denotes "Unknown". In a fuzzy NLN, the truth value domain  $A$  is defined by<sup>5</sup>:

$$A = \{(x, \bar{x}) : x \in [0,1], \bar{x} \in [0,1], x + \bar{x} = 1\} \quad (1)$$

where  $x$  represents on-response and  $\bar{x} = 1 - x$  is the complement of  $x$ , representing the off-response. Complement coding preserves both the on-response and the off-response to

an input vector. It shows if a feature is present or absent and to what degree. It helps fuzzy NLN to handle measurement uncertainty.

The structure of a fuzzy NLN for star pattern recognition is similar to that of the three-layer feed-forward neural networks (Figure 1). The hidden nodes are called cluster nodes, since one hidden node may be used to encode more than one pattern. Each input and output pattern can be represented by:

$$X = ((x_1, \bar{x}_1), (x_2, \bar{x}_2), \dots, (x_M, \bar{x}_M)) \quad (2)$$

$$Y = ((y_1, \bar{y}_1), (y_2, \bar{y}_2), \dots, (y_N, \bar{y}_N)) \quad (3)$$

where  $(x_i, \bar{x}_i)$  denotes the truth value of the  $i$ th input node and  $(y_j, \bar{y}_j)$  denotes the truth value of  $j$ th output node.

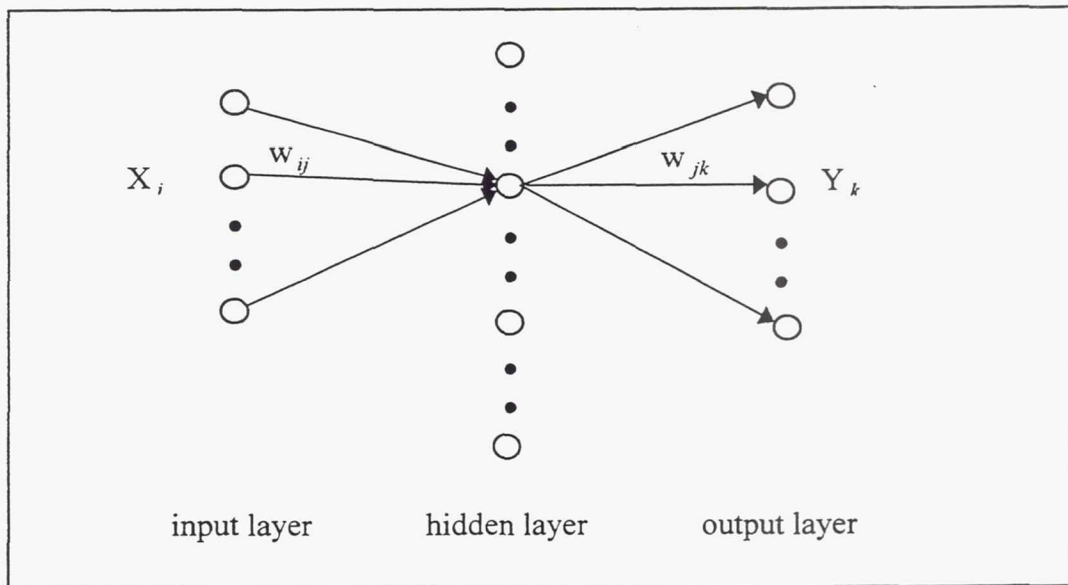


**Figure 1 Structure of Fuzzy NLN**

The fuzzy NLN is trained with the Supervised Clustering and Matching (SCM) algorithm.<sup>5</sup> SCM is derived from the Adaptive Resonance Associative Map (ARAM)<sup>7</sup>, which is a model from the supervised Adaptive Resonance Theory (ART) network family<sup>8</sup>. During training, a cluster node is chosen if both its input and output templates match the input and output patterns to a certain degree. The match similarity is measured as follows<sup>5</sup>:

$$m_j^x = \frac{\sum_i (w_{ji}^x x_i - \bar{w}_{ji}^x \bar{x}_i)}{|W_j^x|_2 |X|_2} \geq \rho_x \quad \text{and} \quad m_j^y = \frac{\sum_i (w_{ji}^y y_i - \bar{w}_{ji}^y \bar{y}_i)}{|W_j^y|_2 |Y|_2} \geq \rho_y \quad (4)$$

where  $m_j^x$  and  $m_j^y$  are the match degrees for input and output patterns,  $\rho_x \in [0,1]$  and  $\rho_y \in [0,1]$  are the recognition thresholds for the input and output layer,  $(w_{ji}^x, \bar{w}_{ji}^x)$  and  $(w_{ji}^y, \bar{w}_{ji}^y)$  are the  $J$ th weights for the input and output layer. In Eq. (4),  $w_{ji}^x x_i$  is the correlation measurement between the input pattern and the input weight template, so the bigger  $\sum_i (w_{ji}^x x_i - \bar{w}_{ji}^x \bar{x}_i)$  means the input pattern is more similar to the input weight template. This measurement is then normalized by the multiplication of the L2-norm of the input and weight vectors. The L2-norm function  $|\bullet|$  is defined as:

$$|X|_2 = \sqrt{\sum_i (x_i^2 + \bar{x}_i^2)} \quad (5)$$

If both the input and output matches exceed the thresholds, the cluster node learns the input and output pattern by updating its weight vectors as follows:

$$(w_{ji}^x, \bar{w}_{ji}^x)^{new} = (1 - \beta_x)(w_{ji}^x, \bar{w}_{ji}^x)^{old} + \beta_x(x_i, -\bar{x}_i) \quad (6)$$

$$(w_{ji}^y, \bar{w}_{ji}^y)^{new} = (1 - \beta_y)(w_{ji}^y, \bar{w}_{ji}^y)^{old} + \beta_y(y_i, -\bar{y}_i) \quad (7)$$

where  $\beta_x \in [0,1]$  and  $\beta_y \in [0,1]$  are the learning rates for the input and output layer respectively. The learning moves the weight vectors  $W_j^x$  and  $W_j^y$  towards the input and output vectors  $X$  and  $-Y$  respectively. Large learning rates result in fast learning speed. Small learning rates can result in more accurate learning, but the learning speed is quite slow.

If the node does not satisfy the threshold in Eq. (4), the network selects another node. If no existing cluster nodes satisfy the above condition, a new cluster node is added to encode the given input and output pattern. The advantage of using two different thresholds is to allow the network to respond properly to different pattern recognition problems. Higher values can impose a stricter matching criteria, which in turn partitions the input set into finer categories. Lower vigilance values tolerate greater mismatch, which will result in a coarse recognition. In star recognition, we used high input and output thresholds, since very similar triplet features may correspond to different triplet patterns due to the measurement errors.

## SYSTEM DESIGN

Since a single star does not have enough distinctive features to classify it from thousands of other stars, successful star identification algorithms often use features



generated by a group of stars. Previous studies show that star triplets work well for star identification<sup>3,9</sup>. We use star triplets for feature extraction in our system, then the features are sent to the fuzzy NLN to get the recognition result.

## Feature Selection

Star features that can be used for recognition include star magnitude, angular separation, the group geometry, or the variations of these features, such as the square of the separation. Star magnitudes can be difficult to determine accurately, since different star spectral types can cause shifts in intensity measurements unique to particular imaging systems<sup>3</sup>, and star magnitudes can change over a short period of time. Data from the XTE (X-ray Timing Explorer) showed that the observed magnitude difference could be greater than 1.0 relative to the predicted magnitude<sup>10</sup>. Therefore star magnitude may not be a very reliable parameter. For recognition, the angular separation has small variation and can be measured with high accuracy. So we use the angular separation between the stars in a triplet as the feature vector. The geometry of the triplet is determined by reordering the stars according to their magnitudes. The procedure to generate the triplet feature vector is as follows:

1. Choose a reference star from the central portion of Field of View (FOV).
2. Select the two brightest neighbors within the FOV. For SWAS CT-601 star tracker<sup>11</sup>, the FOV is 8x8 degree.
3. Reorder the triplet from brightest to faintest according to star magnitude, i.e.

$$m_1 < m_2 < m_3 \quad (8)$$

4. Calculate the angular separations between each pair of the stars, which is denoted by  $d_{ij}$ . Therefore, the input feature vector to the fuzzy NLN network is (Figure 2):

$$\langle d_{12}, d_{23}, d_{31} \rangle$$

where,  $d_{12}$ ,  $d_{23}$  and  $d_{31}$  are the distances between the three vertices.

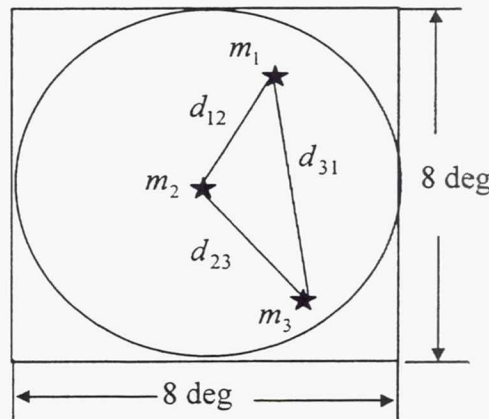


Figure 2 Star Triplet Attributes

## System Structure

The reference star catalog used by our research is the SWAS star catalog, which is a run catalog created from SKY2000 Master Catalog. The original SWAS star catalog contains 33,379 stars. Considering only those stars whose magnitudes are brighter than 6.5, the total number of triplet patterns generated is 9,050. With this large number of patterns, it is inefficient to train a single neural network. The solution is to divide the problem into smaller NLNs that can be trained more efficiently.

From analysis, we know the angular separation is a more reliable parameter than star magnitude. The histograms of the three angular separations of the triplet (Figure 3, 4 and 5) show that  $d_{12}$  (the distance between star1 and star2 in a triplet) is the most evenly distributed attribute, therefore we used  $d_{12}$  to select which NLN to use. During recognition, direct match is first used on  $d_{12}$  to decide which fuzzy NLN to enter, then the corresponding NLN will give the classification result as shown in Figure 6.

The range for  $d_{12}$  is [0.0031, 7.855] deg. The overlap of each interval for  $d_{12}$  ensures an error tolerance capability up to 0.3 deg for angular separation at this step. The number of triplet patterns in each NLN is (from NLN-1 to NLN-11): 914, 1048, 1300, 1495, 1544, 1697, 1626, 1131, 1027, 889, and 1047 respectively. The average of pattern stored in each fuzzy NLN is 1247. This is a very quick and efficient method in dividing the total triplet patterns, which also maintains the error tolerance performance.

Due to the overlap between each two nearby intervals of  $d_{12}$ , one triplet may fall into two NLNs. For example, assume the original angular separation  $d_{12}$  is 2.6, due to the measurement error, it is changed to  $2.6-0.3=2.3$  (suppose the maximum angular separation error is 0.3). So this pattern will fall into two NLNs: NLN-3 and NLN-4, which correspond to  $d_{12}$  interval of [1.7, 2.5] and [2.3, 3.0] respectively. However, the correct pattern should belong to NLN-4. The method to decide which classification result is the correct one depends on the calculation of the maximum hidden node truth value  $T_j$ :

$$T_j = \frac{\sum_i (w_{ji}^x x_i - \bar{w}_{ji}^x \bar{x}_i)}{|W_j^x|_2 |X|_2} \quad (9)$$

Here,  $w_{ji}^x$  is the weight connecting  $i$ th input node and  $j$ th hidden node,  $x_i$  is the  $i$ th input feature value.  $W_j^x$  is the weight vector connecting input vector with the  $j$ th hidden node.  $X$  is the input vector.  $T_j$  is a similarity measurement between input pattern and the stored pattern. A larger value of  $T_j$  means that the input is more similar to the stored pattern. For example, in our experiment, the pattern mentioned before ( $d_{12}=2.3$ ) has the maximum

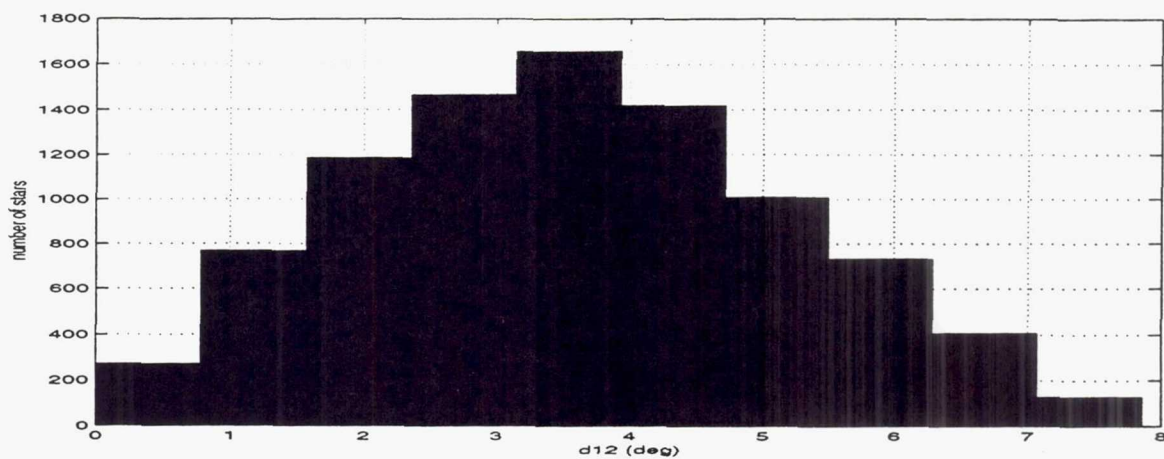


Figure 3 Histogram of  $d_{12}$

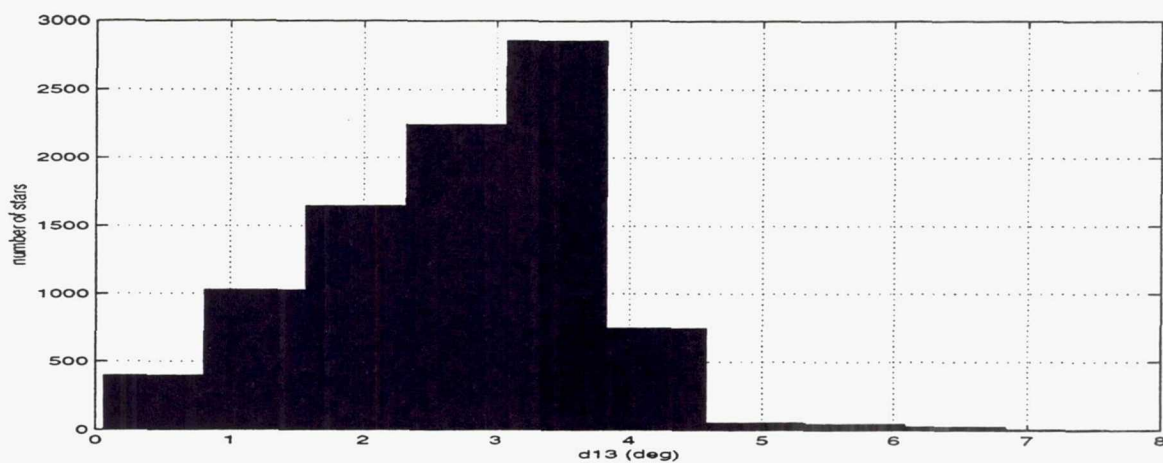


Figure 4 Histogram of  $d_{23}$

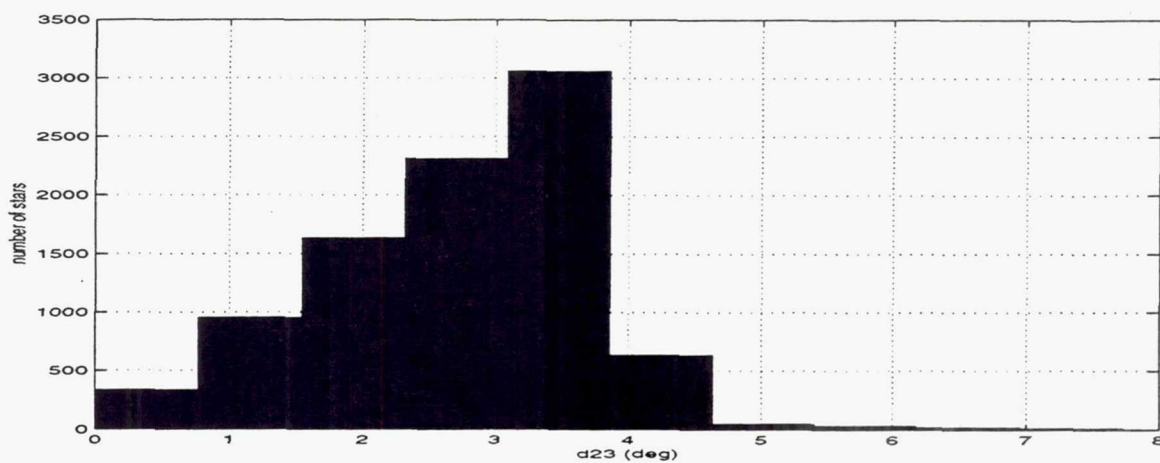
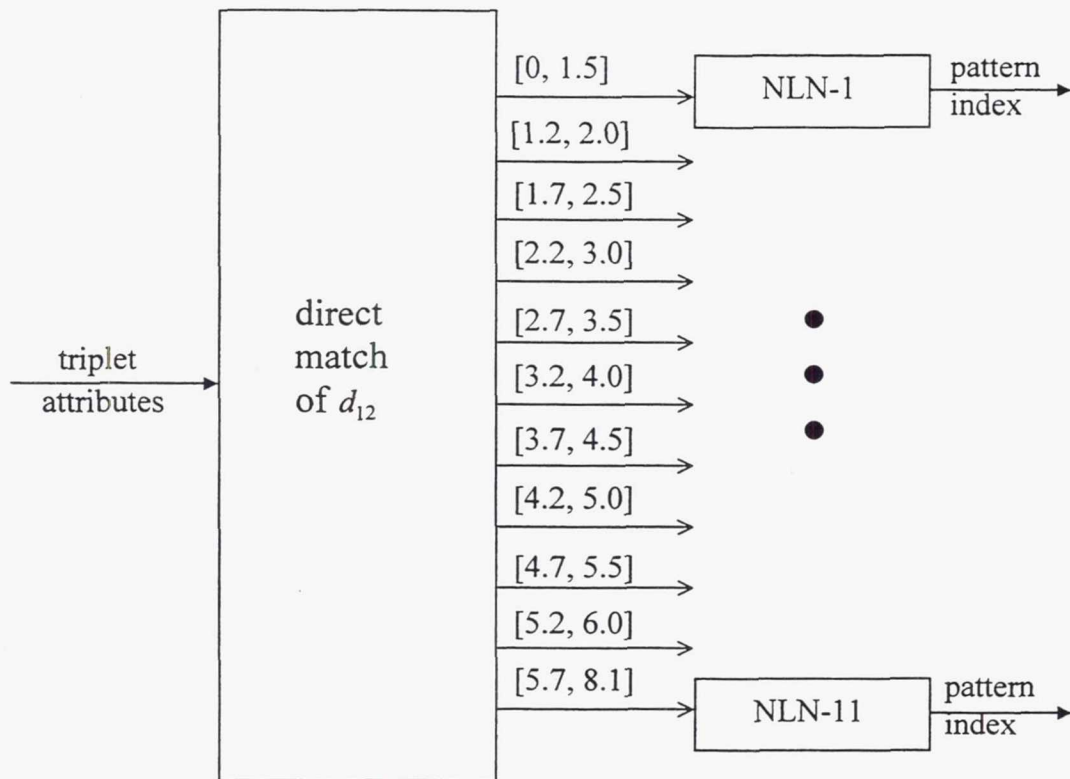


Figure 5 Histogram of  $d_{31}$





**Figure 6 System Structure for Star Recognition ( The triplet measurement  $d_{12}$  selects which NLN to use. The numbers in [ ] give the range of  $d_{12}$  for a NLN )**

hidden node truth value of 0.999148 for NLN-4 and 0.998707 for NLN-3. Therefore, the classification result from NLN-4 is considered to be the correct one.

### Star Identification Algorithm

Based on the analysis and system design described above, we propose the algorithm for autonomous star identification as follows:

1. Generate a triplet for the reference star that is in the central portion of FOV. Reorder the triplet according to the star magnitude.
2. Calculate the angular separation for the triplet to get the feature vector:  $\langle d_{12}, d_{23}, d_{31} \rangle$ .
3. Use direct match on  $d_{12}$  to choose a proper NLN for identification.

4. If more than one NLN is used, calculate the hidden node truth value of each NLN. Choose the NLN with the largest hidden node truth value.
5. Get the identification result by using Eq. (10):

$$(y_i, \bar{y}_i) = f^s \left( \sum_j w_{ji}^y t_j, \sum_j \bar{w}_{ji}^y \bar{t}_j \right) \quad (10)$$

where  $(t_j, \bar{t}_j) = (1, 0)$  if it is the maximum hidden node, otherwise  $(t_j, \bar{t}_j) = (0, 0)$ .  $(Y, \bar{Y})$  is the output truth vector. The slope threshold function  $f^s$  is defined by

$$f^s(a, \bar{a}) = \begin{cases} (1, 0) & \text{if } a - \bar{a} \geq 1 \\ (0, 1) & \text{if } a - \bar{a} \leq -1 \\ (a, 1 - a) & \text{otherwise} \end{cases} \quad (11)$$

Then translate this binary representation of  $(Y, \bar{Y})$  to get the SKY2000 index number of the reference star.

In the SCM algorithm, only the cluster node  $J$  that receives the maximum hidden node truth value predicts the output. For fuzzy identification, the highest two or three maximum truth value nodes were chosen to predict the results. For example, when the angular separation error was 60 arcsec, the first two maximum hidden node truth values for an input corresponding to reference star 6376 were 0.999997 and 0.999994 respectively, where “6376” is the SKY2000 index number. The recognition result from the first hidden node was star 2102, while the result from the second hidden node was star 6376. In fuzzy recognition, the truth value  $T_j$  was used as a confidence level. By using fuzzy recognition, we obtained more accurate results. This is especially useful for the situation where the measurement error is big enough that one pattern can easily fall into another class.

## SIMULATION RESULTS

The simulation is done in three steps. First, generate a reference catalog of star triplets from the SWAS star catalog. Second, train the fuzzy NLNs using triplet feature vectors. Third, test the system using simulated observation data.

The procedure for creating a triplet catalog from SWAS star catalog is shown in Figure 7. In SWAS star catalog, flag7 is the trackability near-neighbor flag. This flag maps the angle to the nearest star either brighter than or up to 4.0 magnitude fainter. Flag8 is the identifiability near-neighbor flag. It maps the angle to the nearest star within 1.0 magnitude. In Figure 7, the comparison for flag7 and flag8 is to ensure that a reference star has no neighbors within 0.1 degree that are within 4 magnitude of the

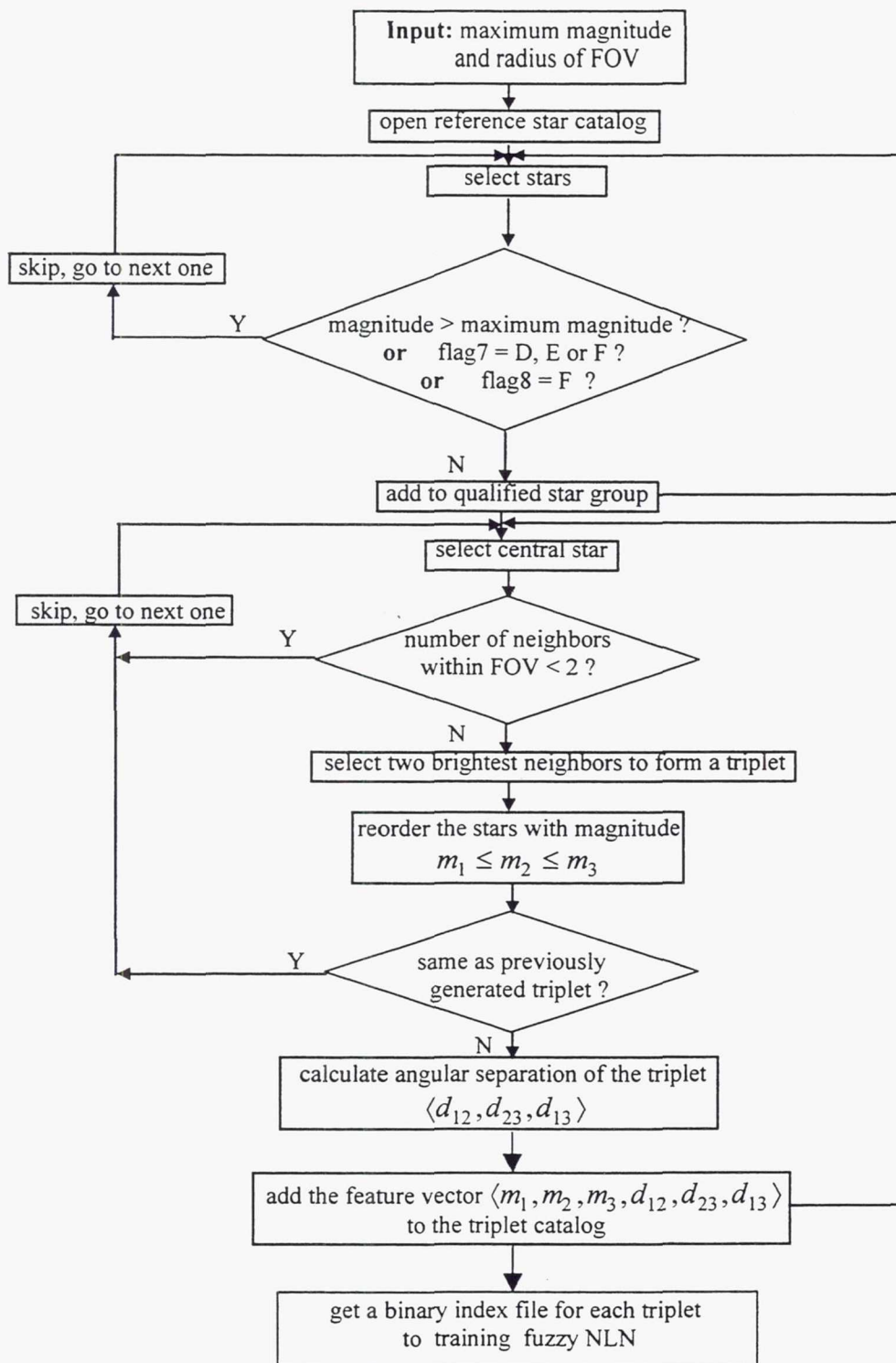


Figure 7 Diagram for Generating Triplet Catalog



reference star brightness, according to the CT-601 star tracker's manual<sup>11</sup>.

After obtaining the triplet feature vector, the second step is to train the fuzzy NLNs. The procedure for training fuzzy NLN is introduced in the second part of this paper. The inputs to each of the fuzzy subnets are the angular separations, so there are three input nodes. The hidden nodes are dynamically created during the training. Since there are 9050 triplet patterns, the binary representation for each pattern can be done by using 14 binary digits:

$$N = \lfloor \log_2 9050 \rfloor + 1 = 14 \quad (12)$$

So the number of output nodes for each fuzzy NLN is 14. Other parameters for training fuzzy NLN are:

$$\beta_x = 0.15, \quad \beta_y = 0.15, \quad \rho_x = 0.9, \quad \rho_y = 1.0 \quad (13)$$

We used small learning rates to get more stable learning results. For star recognition, high input and output vigilance values were used to ensure high recognition accuracy.

The feature vector used to train the fuzzy NLN consists of 9 training samples for each pattern. The training samples are generated by adding random noise to the original feature vectors. The intensity of the noise is up to 2% of the maximum feature value. The training time for each NLN was about 3 hours.

Finally, we used the flight data from SWAS star catalog to test the system performance. Simulations were done on SGI workstations by using C/C++. The maximum error for angular separation is set to 72 arcsec in the simulated data. The recognition results are shown in Table 1.

Table 1 shows that the proposed system has star recognition accuracy higher than 99% even when the angular separation error is 72 arcsec. The recognition is also very fast. The major computations for average NLN include  $3 \times 1049 \times 2 + 1049 \times 14 \times 2 = 35,666$  multiplications, where 1049 is the average number of stored patterns, 3 is the number of input nodes, 14 is the number of output nodes, 2 accounts for the complement coding. The storage required for the system includes the weights connecting the input layer with the hidden layer and the weights connecting the hidden layer with the output layer for each NLN.

Although by using angular separations for star pattern recognition, the magnitude error will not have direct influence on the performance of fuzzy NLN, it can affect the system performance if the magnitude error is big enough that the star triplet is improperly ordered. To illustrate the influence of the magnitude error on the system performance, histograms of the absolute magnitude difference between each two stars in a triplet are

**Table 1**  
**RECOGNITION RESULTS FOR AUTONOMOUS STAR RECOGNITION**

	Error Range for Angular Separation (arcsec)				
	[0,0]	[0,36]	[0,54]	[0,61]	[0,72]
<b>9 Training Samples</b>					
Misclassification/ Number of Samples	0/1047	0/1047	0/1047	9/1047	
Correct (%)	100	100	100	99.14	
<b>16 Training Samples</b>					
Misclassification/ Number of Samples	0/1047	0/1047	2/1047	5/1047	
Correct (%)	100	100	99.81	99.52	
<b>25 Training Samples</b>					
Misclassification/ Number of Samples	0/1047	3/3141	6/3141	7/2094	14/4188
Correct (%)	100	99.90	99.81	99.67	99.67

shown in Figure 8, 9, and 10. Table 2 lists the statistical information of the star magnitude difference based on the histograms.

From Table 2, we can see the magnitude error has more influence on the order of the first and second brightest stars in a triplet geometry. For example, if star1 or star2 has the magnitude error of up to 0.3, then the probability of misordering can increase to 28.17%. But the third star is usually much fainter than the first two stars, so the possibility of error is reduced.

An effective solution for this problem is to represent the triplet patterns in different ways to the recognition system. For example, assume the original feature vector is  $\langle d_{12}, d_{23}, d_{31} \rangle$ , we present it to the recognition system and get **solution I**. Then we present the feature vector  $\langle d_{12}, d_{31}, d_{23} \rangle$  to the system, in case star2 is actually brighter than star1 (so we switch star1  $\leftrightarrow$  star2). We obtain **solution II** through this way. Next, we

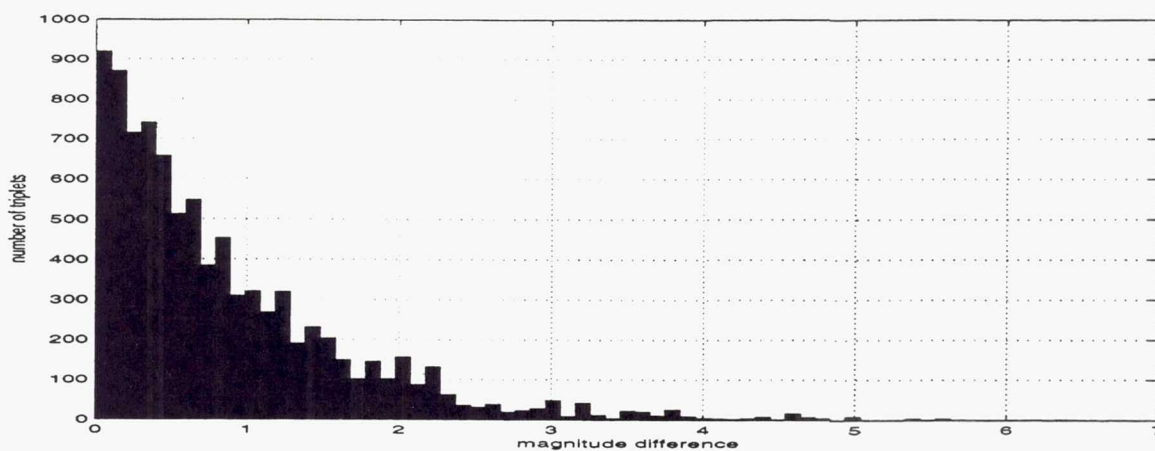


Figure 8 Histogram of  $|M_1 - M_2|$ , the absolute magnitude difference between the first and second brightest stars in a triplet

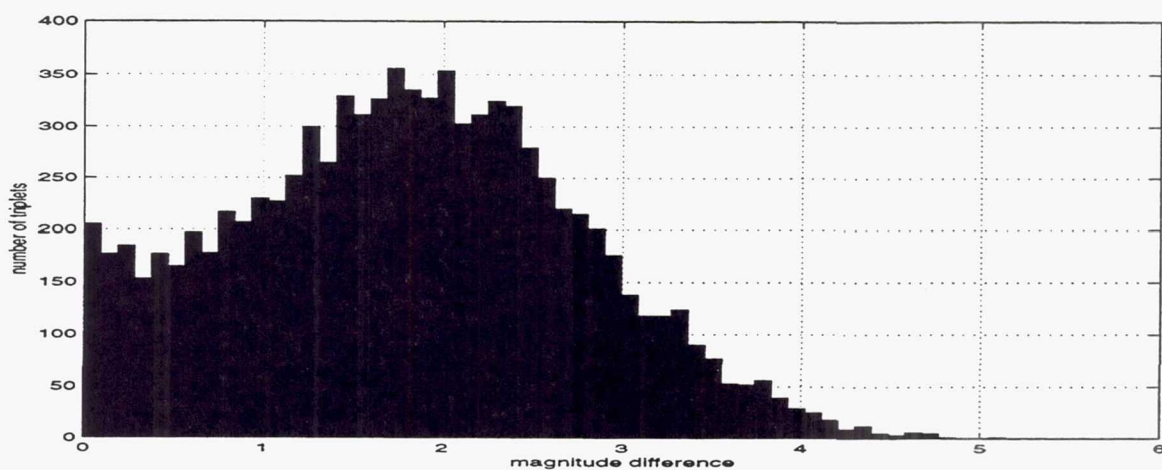


Figure 9 Histogram of  $|M_2 - M_3|$ , the absolute magnitude difference between the second and third brightest stars in a triplet

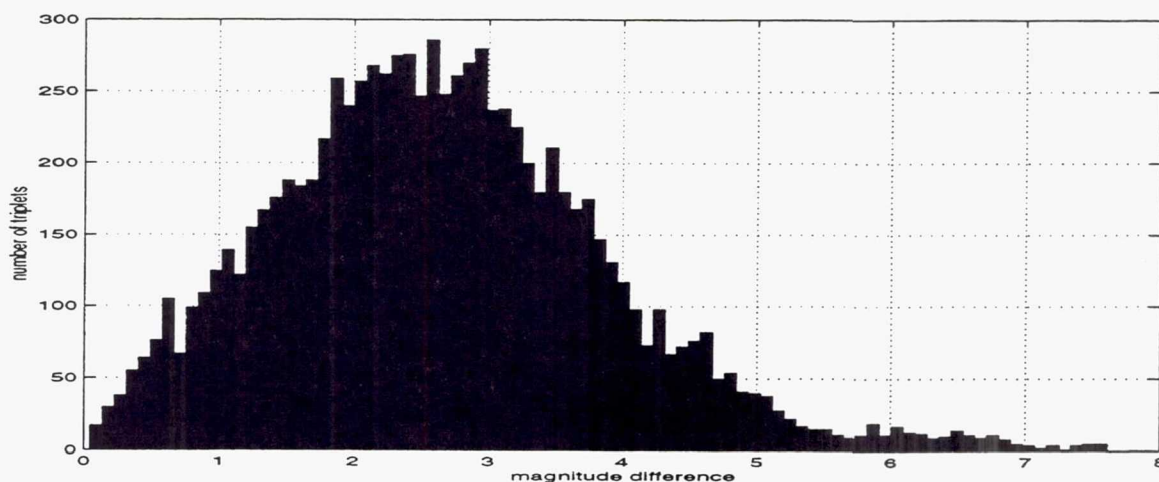


Figure 10 Histogram of  $|M_1 - M_3|$ , the absolute magnitude difference between the first and third brightest stars in a triplet



**Table 2**  
**MAGNITUDE DIFFERENCE OF STAR TRIPLETS\***

Range of Magnitude Difference	Number of Star Triplets					
	$ M_1 - M_2 $		$ M_2 - M_3 $		$ M_1 - M_3 $	
[0, 0.1]	930	(10.28%)	209	(2.31%)	9	(0.1%)
[0, 0.2]	1799	(19.88%)	405	(4.48%)	34	(0.38%)
[0, 0.3]	2549	(28.17%)	599	(6.62%)	77	(0.85%)
[0, 0.4]	3274	(36.18%)	764	(8.44%)	138	(1.52%)
[0, 0.5]	3929	(43.41%)	956	(10.56%)	213	(2.35%)

\*  $M_1$ ,  $M_2$  and  $M_3$  are the magnitudes of the brightest, the second brightest and the faintest star in a triplet

reorder the triplet feature to  $\langle d_{31}, d_{23}, d_{12} \rangle$  and get **solution III**. This result is possible if star3 is in fact brighter than star2. The choice of the final solution depends on the maximum hidden node truth value. The solution with the biggest maximum hidden node truth value is considered to be the correct one. In this way, the influence of the magnitude error on the system performance can be minimized. This technique is to be incorporated into our system.

## CONCLUSIONS

In our research, we proposed an autonomous star identification system that uses fuzzy NLN. The system performance was successfully tested using SWAS star catalog. Compared with the direct match algorithms, this system can obtain both high accuracy and fast recognition speed when a large star catalog is used. When new patterns are added to the catalog, the NLN can learn the new pattern by adding another cluster node to the network. In contrast, the binary-tree search algorithm<sup>3</sup> needs to update the entire tree. It also requires a much smaller FOV (8x8 deg) when compared with Williams et al. neural network star identification algorithm<sup>12</sup>, which requires a FOV as wide as 20x20 deg. With the proposed algorithm, the influence caused by the magnitude error can also be minimized. Therefore, the proposed system should have a great promise for star identification in the real world.

With large reference catalog, the memory requirement is a bit high in order to store the weight vectors for each NLN. The total memory required for all the NLNs is over 3M bytes. Although the recognition speed is not slowed down, further work will be done to seek a solution for this problem for implementation on-board spacecraft.

## ACKNOWLEDGEMENTS

The authors would like to express their appreciation to Mark Woodard with the NASA Goddard Space Flight Center for his valuable assistance in this research.

## REFERENCES

1. W. K. Daniel, T. E. Correll and M. O. Anderson, "Development of a Direct Match Technique for Star Identification of the SWAS Mission," presented at *NASA/GFSC Flight Mechanics Symposium*, Goddard Space Center, 1995.
2. R. W. H. Van Bezooijen, "True-sky Demonstration of an Autonomous Star Tracker," *SPIE*, Vol. 2221, 1996, pp. 156-168.
3. B. M. Quine and H. F. Durrant-Whyte, "A Fast Autonomous Star-acquisition Algorithm for Spacecraft," *Control Engineering Practice*, Vol. 4, No. 12, Dec. 1996, pp. 1735-1740.
4. C. L. Tan, T. S. Quah and H. H. Teh, "An Artificial Neural Network that Models Human Decision Making," *Computer*, March 1996, pp. 65-70.
5. A. H. Tan and L. N. Teow, "Inductive Neural Logic Network and the SCM Algorithm," *Neurocomputing*, No. 14, 1997, pp. 157-176.
6. J. R. Myers, C. B. Sande, A. C. Miller, W. H. Warren, and D. A. Tracewell, "The SKY2000 Master Star Catalog," presented at *AAS/AIAA Space Mechanics Symposium*, Goddard Flight Space Center, 1997.
7. A. H. Tan, "Adaptive Resonance Associative Map," *Neural Networks*, Vol. 8, No. 3, 1995, pp. 437-446.
8. G. A. Carpenter, S. Grossberg, N. Markuzon, J. H. Reynolds and D. B. Rosen, "Fuzzy ARTMAP: A Neural Network Architecture for Incremental Supervised Learning of Analog Multidimensional Maps," *IEEE Trans. on Neural Networks*, Vol. 3, No. 5, Sept. 1992, pp. 698-712.
9. E. A. Ketchum and R. H. Tolson, "Onboard Star Identification without A Priori Attitude Information," *Journal of Guidance, Control, and Dynamics*, Vol. 18, No. 2, March-April 1995, pp. 242-246.
10. M. H. Lee, "A Simplified Pattern Match Algorithm for Star Identification," *Flight Mechanics/Estimation Theory Symposium*, May 1996, pp. 3-14.
11. "User's Manual for the SWAS CT-601 Star Tracker", Ball Aerospace Systems Division, Boulder, Co. Feb. 1994.
12. K. E. Williams, T. E. Strikwerda, H. L. Fisher, K. Strohbehn and T. G. Edwards, "Design Study: Parallel Architecture for Autonomous Star Pattern Identification and Tracking," *Advances in the Astronautical Sciences*, Feb. 1993, pp. 93-102.

**Page intentionally left blank**



# **Probability Analysis For Spacecraft Attitude Acquisition Using Star Pattern Match Algorithm**

Garry Didinsky  
Hughes Telecommunications and Space Company

Andy Wu  
Hughes Aircraft Company  
EO/E1/D125  
P. O. Box 902  
El Segundo, CA 90245

## **Abstract**

Star trackers have recently been used to determine spacecraft attitude by identifying and matching the observed stars in the tracker field of view (FOV) against onboard catalog stars. Many algorithms to perform initial attitude acquisition using star sighting data have been developed [1-6] for autonomous attitude determination. However, none of these papers provides analytical methods to predict the attitude acquisition algorithm performance. This paper presents a probabilistic model that can accurately predict the probability of a successful attitude acquisition using star pattern match algorithms. A lower bound of successful attitude acquisition probability is also derived in the paper to assess the worst case performance. Statistics generated from Monte Carlo simulations are used to validate the derived probabilistic model. The results demonstrate the usefulness of the probabilistic model for performing system performance trades against many attitude acquisition design parameters such as star tracker FOV, maximum tracked stars, star magnitude sensitivity and accuracy, star position accuracy, and number of catalog stars.

---

Key words : Attitude acquisition and determination, star pattern match algorithm, probabilistic model.

## 6.0 References :

- [1] : Eleanor A. Ketchum and Robert H. Tolson, "Onboard Star Identification Without A Priori Attitude Information," *Journal of Guidance, Control, and Dynamics*, Vol. 18, No. 2, 1995, pp. 242-246.
- [2] : M. S. Scholl, "Star-Field Identification for Autonomous Attitude Determination," *Journal of Guidance, Control, and Dynamics*, Vol. 18, No. 1, 1995, pp. 61-65.
- [3] : Carl Christian Liebe, "Pattern Recognition of Star Constellations for Spacecraft Applications," *IEEE AES Magazine*, June 1992, pp. 34-41.
- [4] : R. W. H. Van Bezeooijea, "Autonomous Star Referenced Attitude Determination," *Journal of Guidance, Control, and Dynamics*, Vol. 68, 1989, pp. 31-52.
- [5] : Curtis Padgett and Suraphol Udomkesmalee, "Evaluation of Star Identification Techniques," *Journal of Guidance, Control, and Dynamics*, Vol. 20, No. 2, 1997, pp. 259-267.
- [6] : Michael H. Lee, "A Simplified Pattern Match Algorithm for Star Identification," *NASA Goddard Flight Mechanics/Estimation Theory Symposium*, 1996, pp. 3-14.

## STAR IDENTIFICATION FOR THREE-AXIS ATTITUDE ESTIMATION OF FRENCH-BRAZILIAN SCIENTIFIC MICRO-SATELLITE

Roberto V. F. Lopes\*, Gustavo B. Carvalho† and Adenilson R. Silva†

This paper investigates full sky star identification methods envisaging their application to attitude determination of the French-Brazilian scientific micro-satellite. A statistical analysis gives a suitable framework to select and adapt an algorithm based on the relationship between star sensor specification and the achievable star identification confidence level under the mission constraints. Attitude determination global performance is presented for a one year long digital simulation, which is intended to give subside to the AOCS design.

### INTRODUCTION

In the context of CNES-INPE cooperation protocol, Brazil and France are going to jointly build and operate a micro-satellite for scientific purposes. As far as the Brazilian side experiments are concerned, the  $\mu$ -satellite will be in a low inclination and low altitude orbit, with three-axis, Sun oriented attitude stabilization, the z-axis towards the ecliptic north. In a preliminary conception, the AOCS contains a three-axis reaction wheel and a three-axis magnetic coil for wheel desaturation. During the routine phase mode, the attitude kinematics will be measured by a three-axis rate gyro. The gyro drift will be updated by a Kalman filter primarily fed by a CCD star tracker. Whenever the star tracker field of view (FOV) is obliterated by the Earth, secondary rough attitude sensors (namely a sun sensor and a magnetometer) would supply the necessary three-axis attitude information to the Kalman filter.

The main attitude control specification is  $0.5^\circ$  around each axis, as long as the Sun remains at sight. The on board computer should be able to perform full sky identification autonomously, without any a priori attitude information. Such capability would contribute to reduce charge on ground support segment as well as to qualify the platform for multi-mission future applications. There are however restrictions due to the memory budget of the on board computer. So, a trade off between the size of the on board star catalog and the average processing time of the star identification algorithm is an important element to the AOCS design. The star tracker must be also compatible with the low cost concept of the  $\mu$ -satellite. This represents an additional constraint for the selection of a star identification method. A statistical analysis is accomplished which gives insight to the whole problem. The selected algorithm is specially adapted to the current platform specification.

---

\*Aerospace Engineer, Division of Space Mechanics and Control, Instituto Nacional de Pesquisas Espaciais - INPE, CP 515, 12.201-970 São José dos Campos - SP, Brazil, e-mail: rvf@dem.inpe.br

†Graduate Student on Engineering and Aerospace Technology, Instituto Nacional de Pesquisas Espaciais - INPE, CP 515, 12.201-970 São José dos Campos - SP, Brazil



## OVERVIEW ON STAR IDENTIFICATION METHODS

Stars are the most accurate and abundant natural source of attitude reference spread all over the sky. Consequently, star sensors may achieve the highest accuracy level among spacecraft attitude sensors and are suitable for multi-mission purposes. Processing star sensor observations is however a much more complicated task than processing Sun sensor or magnetometer observations. It requires a star catalog and a star identification software, besides the attitude determination software, which may also include after-launch calibration of distortion and misalignment.

When a priori attitude information is available, the star identification task may be performed by the direct match method<sup>1</sup>. It matches each observed star with the respective guide star from the star catalog in an optimized neighborhood of its a priori coordinates. This situation may apply ordinarily whenever a new star enters the sensor FOV during safe routine phase, or after attitude acquisition by means of secondary attitude sensors.

If no a priori attitude information is available, then a full sky star identification procedure must be used. Unfortunately, identifying a star name (or equivalently its catalog number) from a star image only is still out of the scope of current star sensor technology. The existing procedures identify not properly a star, but a constellation - a set of two or more neighbor stars - basically by the angular separation match method<sup>1</sup>. This method matches the angular separation between each observed star pair with their respective values from star catalog. Star instrumental magnitude information may also be taken into account in order to improve the identification success rate. This however may require post launch calibration of the predicted instrumental magnitude of the cataloged (guide) stars.

Procedures using the angular separation match method may be classified as iterative or non iterative procedures. Iterative procedures<sup>2-6</sup> usually start with a pair match and next search for a triplet match and so on. The search domain may be considerably reduced, as well as the search time, if magnitude information is taken into account<sup>7</sup>. Non iterative procedures<sup>8,9</sup> match the constellation at once by maximizing a matching function with respect to the candidate guide stars for every observed star. They are potentially faster than iterative procedures, but at memory expense.

Some procedures<sup>8,9,10</sup> are more indicated to a large FOV application, while others<sup>7</sup> are able to deal with huge guide stars catalog and a narrow sensor FOV, which are more likely to offer high accuracy. Therefore, the choice of a star sensor for a given space mission is strongly connected not only with the required attitude accuracy but also with the star identification procedure. This connection may be highlighted by a statistical analysis.

## STATISTICAL ANALYSIS

Since star catalogs and star sensors are not perfectly reliable, any star identification procedure is subject to failure. The expected success rate of such procedures are limited by the probability of uniqueness of observed star patterns under the applicable uncertainty level. Star patterns whose representation are unique are called unambiguous and the probability of observing an unambiguous star pattern depends mainly on the sensor accuracy, the sensor FOV, the range of magnitudes which can be observed by the sensor and the maximum number of stars which can be simultaneously tracked by the sensor.

This relationship is not straightforward. The expected number of stars at sight on a wide FOV, for instance, is larger than on a narrow one. This should make unambiguous star patterns likely to be found at wide FOV values. Nevertheless, because the CCD matrix size of currently available star trackers are roughly in the same range of hundreds of thousands of pixels, increasing the sensor FOV has a negative impact on sensor accuracy. The supposed advantage of a wide FOV may thus be vanished. The expected number of stars at sight could also be increased by extending the sensor

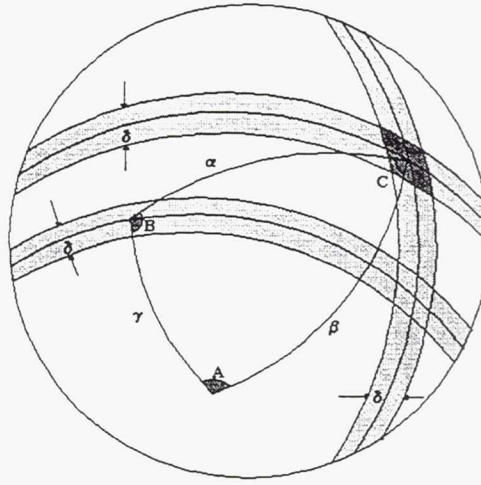


Fig. 1: Star Pairs Star Triplets and their Uncertainty Bandwidth

range of magnitudes but again this apparent profit is compensated by the exponential growth at the required catalog size, since ambiguous star pattern probability increases with the amount of candidate guide stars.

In order to get insight in this subject, this section evaluates the probability of unambiguous star pairs and unambiguous star triplets observations as a function of pertinent sensor characteristics. The numerical results were obtained using MATLAB.

## Sky Model

Assuming a Poisson model for space distribution of stars at the celestial sphere, the expected number of stars on a certain distance range  $[\gamma - \frac{1}{2}\delta, \gamma + \frac{1}{2}\delta]$  from a given star is given by (see Figure 1):

$$\frac{N(M_V)}{4\pi} 2\pi \sin(\gamma) \delta, \quad (1)$$

where  $N$  is the number of stars with visual magnitude less or equal to  $M_V$ .

Let be  $Q_P$  the number of guide star pairs in this  $\delta$ -bandwidth. The expectance of  $Q_P$  is :

$$E\{Q_P\} = N_P \equiv \frac{1}{2} N^2(M_V) \frac{2\pi \sin(\gamma) \delta}{4\pi}, \quad (2)$$

where  $E\{\cdot\}$  represents the expectance operator.  $N_P$  may be written in a compact way as:

$$N_P(p, \gamma) = p \sin(\gamma), \quad (3)$$

where  $p$  is a sensor parameter which represents the maximum expected number of candidate pairs:

$$p = \frac{1}{4} N^2(M_V) \delta. \quad (4)$$

In order to discard the star pairs which could not be fitted at the sensor FOV, one imposes the constraint  $\gamma \leq \gamma_{\max}$  where  $\gamma_{\max}$  is the distance between opposite corners of sensor FOV. The probability density function of  $\gamma$  is then:

$$f_\Gamma(\gamma) = \frac{\sin(\gamma)}{1 - \cos(\gamma_{\max})}, \quad \forall \gamma \in [0, \gamma_{\max}], \quad (5)$$



while the probability distribution function is:

$$F_{\Gamma}(\gamma) = \frac{1 - \cos(\gamma)}{1 - \cos(\gamma_{\max})}, \quad \forall \gamma \in [0, \gamma_{\max}] . \quad (6)$$

This agree with real data up to visual magnitude  $M_V = 5$  from SKY2000 star catalog<sup>11</sup> for a  $20^\circ \times 20^\circ$  square FOV (see Figure 2a). Such agreement does not mean that the star distribution over the sky follows the Poisson model. Indeed the star density is clearly higher at the galactic plane than at the neighborhood of the galactic pole, for instance. Furthermore, the analysis is based on visual magnitude though CCD's are more sensitive to the red or infra-red range of the spectrum. One should keep this in mind when analyzing the quantitative information of this section. Nevertheless, the presented results are primarily intended to illustrate the qualitative relationship between sensor parameters and their correspondent capability to identify stars. More realistic numerical evaluation for a specific sensor configuration is carried out at the next section.

Figure 2b shows the exponential growth of the amount of real stars against the maximum visual magnitude from SKY2000 star catalog. According to this data, the number of stars follows an empirical law:

$$N(M_V) = 6.5e^{1.107M_V} . \quad (7)$$

Angular separation between star pairs does not have the same distribution for both observed star pairs and guide star pairs, specially for distances close to  $\gamma_{\max}$  (compare Figures 2a,2c). The distribution  $F_{\Gamma_o}(\gamma)$  for observed star pairs was evaluated numerically by the Monte Carlo method for different square FOV values.

For a triplet, it would be hard to show the distribution function, since it depends on three angular separations. Fortunately it is needless for the present purpose. It is more convenient in this case to focus on the number  $Q_T$  of triplets  $(\alpha, \beta, \gamma)$  of guide stars which could not be distinguished from each other due to sensor inaccuracy. From the Poisson model, considering an uncertainty band  $\delta$ , the expectance of  $Q_T$  is given by (see Figure 1):

$$E\{Q_T\} = N_T \equiv \frac{N}{2 \times 3} \left( \frac{2\pi N \sin(\alpha)}{4\pi} \right) \left( \frac{N\delta^2}{4\pi \sin(A)} \right) . \quad (8)$$

$N_T$  may be rewritten in the following compact way:

$$N_T(r, r^*) = \frac{r}{r^*} , \quad (9)$$

where  $r$  is the sines ratio of the triplet spherical triangle; and  $r^*$  is a sensor parameter which gives the sines ratio of triplets whose expected number amounts one. They are respectively given by:

$$r \equiv \frac{\sin(\alpha)}{\sin(A)} = \frac{\sin(\beta)}{\sin(B)} = \frac{\sin(\gamma)}{\sin(C)} , \quad (10)$$

$$r^* \equiv \frac{48\pi}{[N(M_V)\delta]^3} . \quad (11)$$

The probability distribution of  $r$  for observed triples,  $F_{R_o}(r)$  was numerically evaluated for different values of sensor FOV by the Monte Carlo method. The results are shown on Figure 2d. One should remark that, analogous to the star pair case, sines ratio of star triplets would not present the same distribution for both observed stars and guide stars.

## Observation Constraints for Star Sensors

According to the Poisson model, the expected number of stars at a square FOV obeys:

$$m = N(M_V) \frac{2\pi - 4 \arccos[\sin^2(\frac{1}{2}\phi)]}{4\pi} , \quad (12)$$



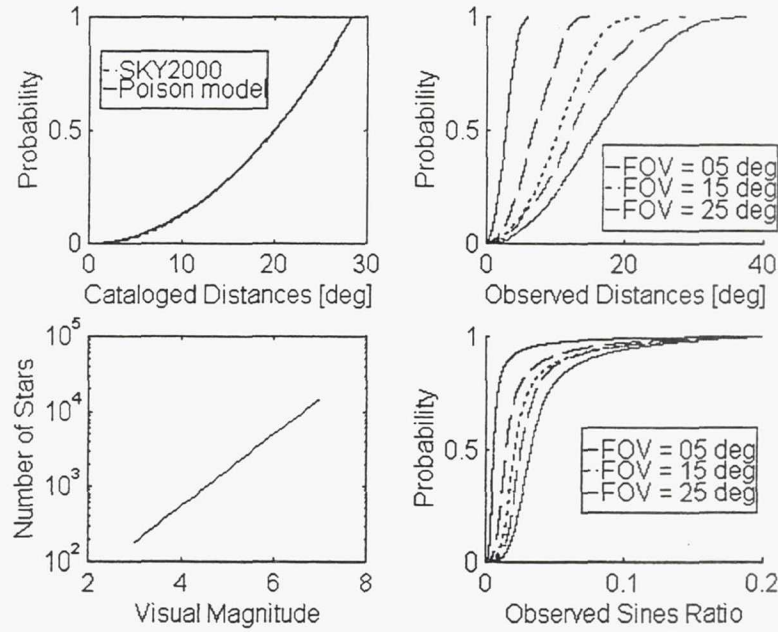


Fig. 2: **The Sky Model:** a) Probability distribution of distance between guide stars; b) Size of star catalog; c) Probability distribution of distance between observed stars; d) Probability distribution of sines ratio for observed star triplets.

where  $\phi$  represents the sensor FOV. Figure 3a shows how  $m$  changes with the sensor magnitude limit and the sensor FOV. The probability of the number  $N_o$  of observed stars is:

$$P[N_o = n] = \frac{m^n}{n!} e^{-m}, \quad (13)$$

while the probability of observing at least  $n$  stars is:

$$P[N_o \geq n] = 1 - \sum_{i=0}^{n-1} \frac{m^i}{i!} e^{-m}. \quad (14)$$

which is plotted on Figure 3.b for different values of  $m$ .

Figure 3c presents the relationship of sensor accuracy  $\sigma_*$  and sensor FOV for some typical star trackers. In order to simplify the analysis, the sensor accuracy will be assumed to be one arc-second per degree of the FOV. In view of Figure 3c, such naive empirical law seems to give a conservative approximation.

Figure 3d combines information from Figures 3a,b and show the number of stars with 95% of probability to be observed, as a function of sensor FOV and magnitude limit. Figures 3c,d, in connection with Figure 2b, characterize the observation constraints for a star tracker. From them one can conclude that in order to assure a reasonable number of star observations (5, for instance), a highly accurate sensor would have a narrow FOV and a large magnitude limit, which consequently would require a large star catalog, and vice versa.

## Identification Capability of Star Sensors

The last step is to evaluate the uniqueness probability for star pairs and star triplets. With this purpose, the uncertainty  $\delta$ -bandwidth is taken as twice the maximum error on the angular separation

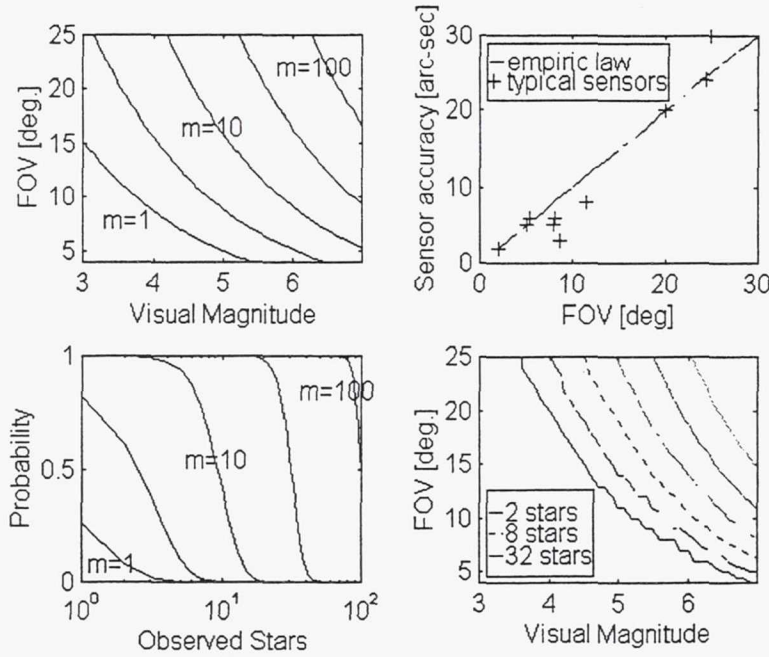


Fig. 3: **Sensor Constraints:** a) Average number of stars at sight; b) Probability distribution of number of stars at sight; c) Characteristics of typical star trackers; d) Number of stars at sight with 95% of confidence.

of a star pair, usually taken as three times the standard deviation of the error distribution. Since such error is composed of two primary errors (related to the position of each star), its standard deviation is bigger than the sensor one by a factor of  $\sqrt{2}$ , which yields:

$$\delta = 2 \times 3\sigma_* \sqrt{2} . \quad (15)$$

According to the Poisson distribution, the probability of  $Q_P$  obeys:

$$P[Q_P = n] = \frac{N_P^n}{n!} e^{-N_P} . \quad (16)$$

Therefore, the probability that a given guide star pair is unambiguous is:

$$P[Q_P = 1 | Q_P > 0] = \frac{P[Q_P = 1]}{1 - P[Q_P = 0]} = \frac{N_P}{e^{N_P} - 1} . \quad (17)$$

The probability that an observed star pair  $\mathcal{O}_{i,j}$  is unambiguous is:

$$\begin{aligned} P[\mathcal{O}_{i,j}^*] &= \int_0^1 P[Q_P = 1 | Q_P > 0] dF_{\Gamma_o} \\ &= \left\langle \frac{N_P}{e^{N_P} - 1} \right\rangle_{\Gamma_o} , \end{aligned} \quad (18)$$

where \* denotes unambiguity and  $\langle \cdot \rangle_{\Gamma_o}$  represents the arithmetic average for observed star pairs computed by Monte Carlo method. For currently available star trackers the uniqueness probability of a star pair resulted too small.

For a given set  $\mathcal{O}_P = \{\mathcal{O}_{i,j}, i = 2, \dots, n, j = 1, \dots, i\}$  of observed star pairs, the probability that none of them is unambiguous is

$$P[\bar{\mathcal{O}}_P^* | N_o = n] = \{1 - P[\mathcal{O}_{i,j}^*]\}^{\frac{1}{2}n(n-1)}, \quad \forall n \geq 2, \quad (19)$$

where the bar indicates the complement event. Finally, the probability that at least one of the observed star pairs is unambiguous is:

$$\begin{aligned} P[\mathcal{O}_P^*] &= 1 - \sum_{n=2}^{n^*} P[\bar{\mathcal{O}}_P^* | N_o = n] P[N_o = n] \\ &= 1 - \sum_{n=2}^{n^*} \left\{ 1 - \left\langle \frac{N_P}{e^{N_P} - 1} \right\rangle_{\Gamma_o} \right\}^{\frac{1}{2}n(n-1)} e^{-m} \frac{m^n}{n!}, \end{aligned} \quad (20)$$

where  $n^*$  is the maximum number of stars which can be simultaneously tracked by the sensor. Unfortunately such probability was less than 5% for all the analyzed values. This indicates that for the current star tracker technology, full sky star identification procedures based on star pair matches only would be likely to be quite disappointing. Star magnitudes or star triplet matches should be considered if high success rates have to be assured. Otherwise, star pairs seems to fit better for applications where the uncertainty search area is smaller than full sky in order of magnitude.

For a triplet the situation is much more favorable. The development is similar to the star pair case. The probability of  $Q_T$  obeys:

$$P[Q_T = n] = \frac{N_T^n}{n!} e^{-N_T}. \quad (21)$$

Therefore, the probability that a given guide star triplet is unambiguous is:

$$P[Q_T = 1 | Q_T > 0] = \frac{P[Q_T = 1]}{1 - P[Q_T = 0]} = \frac{N_T}{e^{N_T} - 1}. \quad (22)$$

The probability that an observed star triplet  $\mathcal{O}_{i,j,k}$  is unambiguous is:

$$\begin{aligned} P[\mathcal{O}_{i,j,k}^*] &= \int_0^1 P[Q_T = 1 | Q_T > 0] dF_{R_o} \\ &= \left\langle \frac{N_T}{e^{N_T} - 1} \right\rangle_{R_o}, \end{aligned} \quad (23)$$

where  $\langle \cdot \rangle_{R_o}$  represents the arithmetic average for observed star triplets computed by Monte Carlo method. The uniqueness probability of a star triplet resulted typically very high.

For a given set  $\mathcal{O}_T = \{\mathcal{O}_{i,j,k}, i = 3, \dots, n, j = 2, \dots, i, k = 1, \dots, j\}$  of observed star triplets, the probability that none of them is unambiguous is

$$P[\bar{\mathcal{O}}_T^* | N_o = n] = \{1 - P[\mathcal{O}_{i,j,k}^*]\}^{\frac{1}{6}n(n-1)(n-2)}, \quad \forall n \geq 3. \quad (24)$$

The probability that at least one of the observed star triplets is unambiguous is:

$$\begin{aligned} P[\mathcal{O}_T^*] &= 1 - \sum_{n=3}^{n^*} P[\bar{\mathcal{O}}_T^* | N_o = n] P[N_o = n] \\ &= 1 - \sum_{n=3}^{n^*} \left\{ 1 - \left\langle \frac{N_T}{e^{N_T} - 1} \right\rangle_{\text{FOV}} \right\}^{\frac{1}{6}n(n-1)(n-2)} e^{-m} \frac{m^n}{n!}, \end{aligned} \quad (25)$$



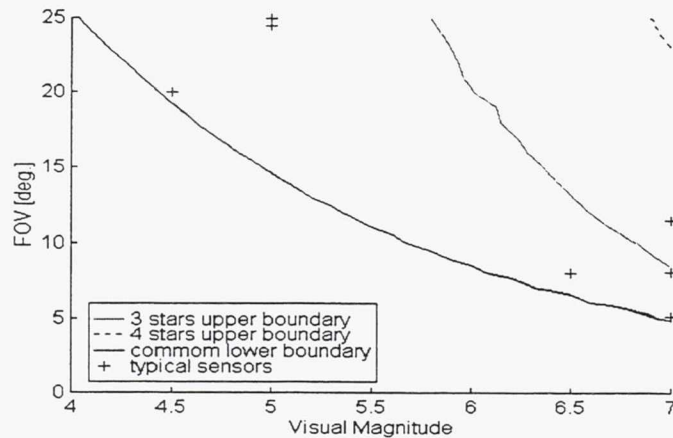


Fig. 4: Boundaries for design parameters of star trackers which assure star identification with a 99% confidence level based on star triplets for different values of maximum number  $n^*$  of stars which can be simultaneously tracked.

Figure 4 shows the boundaries of the areas at the magnitude limit and sensor FOV map with 99% of success rate of a triplet identification for two values of  $n^*$ . The results indicates that typical star trackers assure unambiguous identification from a single observed star triplet. Of course for the sake of safeness, a bigger value of  $n^*$  is recommended, since non cataloged bodies such as planets and variable stars, which often have low magnitudes, may appear in the sensor FOV. The value  $n^* = 5$  found in many star trackers seems to satisfy this recommendation.

## THE IDENTIFICATION ALGORITHM

As aforementioned, for a low cost mission with moderate accuracy requirements for attitude determination, a wide FOV star tracker would be suitable. It does not need too many guide stars - typically up to visual magnitude 4 is good enough to assure a number of stars at sight most of the time. In this case, the number of guide star pairs is manageable by the on board computer memory and can be pre-stored, sorted by angular separation. This is supposed to be the case for French-Brazilian  $\mu$ -satellite. For this reason, the Bezooijen's approach<sup>9</sup> was selected for the present analysis.

Bezoijen's approach is subdivided into a special algorithm, which is intended to work for small uncertainty areas (typically ten times the sensor FOV); and a general algorithm for full sky star identification. In few words, both algorithms are based on the "confirmation value" of every candidate star match. For every star pair match (under a given tolerance bandwidth), the confirmation value of the related candidate star matches are incremented by one.

The special algorithm is very simple and basically selects a star match as the candidate one with higher confirmation value. A number of sanity checks completes the special identification algorithm. Ideally, if  $n^*$  stars are observed, and  $i$ -th observed star corresponds to  $I$ -th guide star, then  $M_{I,i} = n^* - 1$ , while  $M_{K \neq I,i} = 0$ , where  $M_{I,i}$  is the confirmation value of star match  $(I, i)$ . Of course, the confirmation value is affected by sensor inaccuracy which could ultimately lead to misidentification, specially for large uncertainty areas. The general algorithm copes with this problem by carefully taking into account information about match groups headed by kernel matches. In this way, candidate match kernels with unacceptably low confirmation values are considered spurious and their related match groups are excluded from the identification process. The same is true if the match group does not satisfy a geometry check. Such high efficient approach represents however an increasing in the algorithm complexity.

In this section one proposes a modification of Bezooijen's special algorithm which extends its identification capability to the full sky uncertainty area case and keeps its simplicity when compared to the general algorithm. The challenge for full sky identification using the special algorithm is to avoid spurious pair matches to score. The proposed solution is to replace unit scores by weighted iterative scores. The match matrix  $\mathcal{M}$  is initialized with equal confirmation values for every candidate star match. At next iterations, for every star pair match (under a given tolerance bandwidth), the confirmation value of the correspondent candidate star matches are incremented proportionally to the product of last iteration confirmation values of both candidate star matches:

$$\begin{aligned} \begin{Bmatrix} \mathcal{M}_{I,i}^k \\ \mathcal{M}_{J,j}^k \end{Bmatrix} &\leftarrow \begin{Bmatrix} \mathcal{M}_{I,i}^{k-1} \\ \mathcal{M}_{J,j}^{k-1} \end{Bmatrix} + \frac{D \mathcal{M}_{I,i}^{k-1} \mathcal{M}_{J,j}^{k-1}}{\sum_{I'} \sum_{J' \neq I'} \mathcal{M}_{I',i}^{k-1} \mathcal{M}_{J',j}^{k-1}}, \\ D &= \begin{cases} 1 & , \text{ if } |\gamma_{i,j}^o - \gamma_{I,J}| < \frac{1}{2}\delta \\ 0 & , \text{ otherwise} \end{cases} \end{aligned}$$

where  $D$  is the uniform discriminating function. In this way, if any of candidate star matches related with a given star pair match is found to be spurious, such star pair match will not score any more. It means that spurious star matches are intrinsically excluded from the identification process. The match matrix is normalized at the end of each iteration so that the sum of each column is always one. At the beginning of each iteration one sets  $\mathcal{M}^k = 0$ . Note that first iteration is equivalent to the original special algorithm.

The triplet with higher confirmation values is taken as a triplet match. Actual implementation of the algorithm takes profit of the pre-stored catalog of guide star pairs angular separation, and convergence ( $\mathcal{M}_{I,i} = 1$ ) is often achieved in less than five steps. The number of iterations was limited to  $k_{max} = 10$ . By setting  $k_{max} = 1$  one reproduces the results of Bezooijen's special algorithm.

Alternatively a gaussian discriminating function was also tested:

$$D_{\text{Gauss}} = \exp \left\{ -\frac{1}{2} \left( \frac{\gamma_{i,j}^o - \gamma_{I,J}}{\frac{1}{2}\delta} \right)^2 \right\}.$$

Numerical results for several simulation cases, one hundred trials each, considering the current specification of the French-Brazilian  $\mu$ -satellite star tracker are summarized in Table 1. In the first simulation battery, about 800 guide stars have been considered. The advantage of the iterative algorithm is clear: it increases the confidence degree of the identification algorithm from less than 80% to close to 95%. The results were not very sensitive to the shape of the discriminating function. Since the uniform is the simplest one, it turns to be the natural choice. The increased FOV size had a minor negative impact on the algorithm performance.

The last simulation battery considered about 1600 guide stars up to visual magnitude 4.5 and has shown that the number of guide stars has a strong effect on the algorithm performance. The confidence of the proposed iterative algorithm resulted about 90%. In order to improve this value, information about the star magnitude was included in the discriminating function as follows:

$$\begin{aligned} D &= \begin{cases} 1, & \text{if } |\gamma_{i,j}^o - \gamma_{I,J}| < \frac{1}{2}\delta \quad \& \quad |M_{V_i}^o - M_{V_I}| < \delta_{\text{mag}} \quad \& \quad |M_{V_j}^o - M_{V_J}| < \delta_{\text{mag}} \\ 0, & \text{otherwise} \end{cases} \\ D_{\text{Gauss}} &= \exp \left\{ -\frac{1}{2} \left[ \left( \frac{\gamma_{i,j}^o - \gamma_{I,J}}{\frac{1}{2}\delta} \right)^2 + \left( \frac{M_{V_i}^o - M_{V_I}}{\delta_{\text{mag}}} \right)^2 + \left( \frac{M_{V_j}^o - M_{V_J}}{\delta_{\text{mag}}} \right)^2 \right] \right\}. \end{aligned}$$

where  $\delta_{\text{mag}}$  was taken equal to 0.5. The discriminating power was suitably improved, as one can see from Table 1. Uniform discriminating function was confirmed as the right choice from which identification failure reports were virtually eliminated.



Table 1: CONFIDENCE OF MODIFIED BEZOOIJEN'S ALGORITHM

$k_{max}$	Discrim. Function	$N = 800, \sigma^* = 24''$		$N = 1600, \sigma^* = 20''$	
		FOV $20^\circ \times 20^\circ$	FOV $30^\circ \times 20^\circ$	FOV $20^\circ \times 20^\circ$	FOV $20^\circ \times 20^\circ$ <sup>(1)</sup>
1	Uniform	73%	79%	21%	90%
1	Gaussian	80%	72%	42%	87%
10	Uniform	97%	94%	89%	100%
10	Gaussian	96%	94%	89%	97%

(1) Star magnitude included in the discriminating function

## ADDITIONAL DEVELOPMENTS: High Accuracy Application Case

At this point it is convenient to introduce a variation of Bezooijen's modified approach. The algorithm presented on the previous section has a natural limitation: the on board guide star pairs catalog must be manageable. Even though the current design of the multi-mission platform for the French-Brazilian  $\mu$ -satellite is in fully compliance with this constraint, future applications may require attitude determination with higher accuracy. In terms of star sensor parameters it means a narrow FOV, a high boundary for observable star magnitudes and consequently a huge on board guide star catalog which ultimately makes any star pairs catalog based algorithm virtually unfeasible. Nevertheless, by partitioning conveniently the celestial sphere, the problem falls into a sequence of sub-problems whose related guide stars sub-catalogs are small enough to assure manageability of the corresponding guide star pairs sub-catalogs. Of course the processing time may increase considerably.

A genetic algorithm<sup>12</sup> is proposed to solve this problem. The result is also supposed to be useful to cope with star identification reported failures at moderate accuracy applications. The standard procedure under a identification failure report is to commute the spacecraft control to contingency mode, if secondary attitude sensors are available and to emergency mode otherwise, and so wait for ground based commands. A small attitude maneuver may also be commanded in order to change the observed star pattern. However, attitude maneuvers from an initial attitude which is unknown by assumption may be hazardous. Furthermore, interruption of routine operation mode represents a waste of payload lifetime and possibly a waste of fuel too. Therefore, the genetic algorithm as a back up procedure offers an appealing solution, despite the possibility of a higher processing time.

In order to apply the genetic algorithm, small guide stars sub-catalogs  $\mathcal{G}_k$  are represented by chromosomes. The goal function is given by:

$$f(\mathcal{G}_k) = \mathcal{F}(\mathcal{G}_k) P_*^{\bar{n}}, \quad (26)$$

where  $\mathcal{F}(\mathcal{G}_k)$  is the product of the confirmation values of each identified star from the Bezooijen's modified approach considering the stars in  $\mathcal{G}_k$ ,  $P_*$  is the probability of observing a false star, and  $\bar{n}$  is the number of observed stars which could not be identified yet. Since the goal function can be seen as an approximation of the correct identification probability, the convergence criterion is achieved when  $f$  is higher then a given confidence level.

The phenotypes have been codified by a special curve named *Cocoon*<sup>13</sup> (see Figure 5) based on the Hilbert curve<sup>14</sup>. The *Cocoon* is a closed fractal curve without knots or crossings, which fills the sphere with arbitrary resolution level. In other words, it is able to map star angular coordinates on scalar coordinates over the unit circle. Such mapping also preserves closeness of neighbor stars in most of its domain.

One took advantage of the referred property and set the initial population with sub-catalogs composed by guide stars which are neighbors on the *Cocoon*. The sub-catalogs all together cover the whole sky. Since the stars composing an observable constellation look necessarily close to each



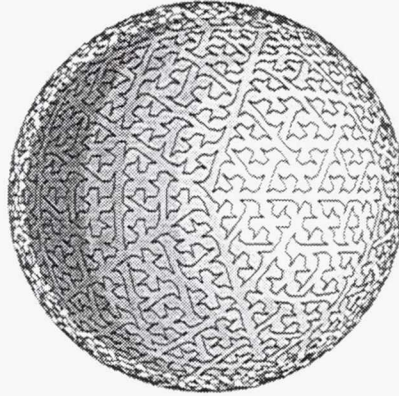


Fig. 5: **The Cocoon**: adaptation of Hilbert curve over the isocohedrom faces projected on a sphere.

other on space, they are likely to be found in a same sub-catalog. Indeed, convergence was achieved in less than 10 generations for nearly 70% of tested cases. Considering that more than 9000 guide stars with visual magnitude up to 6.5 has been put in the core catalog, it represents an encouraging result. Further analysis are currently being carried out by the second author on his master thesis, in order to better explore this new approach.

## ATTITUDE ESTIMATION: Algorithm and Simulation Results

Having a star triplet been identified, three-axis attitude determination can be accomplished and the gyro drift calibration updated. A digital simulation was carried out which takes into account sensor obliteration by Earth presence. In such case the attitude is updated by a three-axis magnetometer and a Sun sensor, when available. The geomagnetic field is taken from the IGRF-95 spherical harmonic model up to order 10. In this section one describes the attitude estimation process and show the related numerical results.

The satellite has inertial three-axis stabilization. Its attitude is supposed to be on a nominal steady state equilibrium due to the action of attitude control,  $X$ -axis pointed directly to the Sun,  $Z$ -axis towards the Ecliptic North Pole and  $Y = Z \wedge X$ . To maintain Sun orientation, the angular velocity rate is  $\omega = 2\pi$  rad/year around  $Z$ -axis.

The attitude kinematics is described by the following uncoupled model, based on a discrete version of Markley & Lefferts & Shuster's approach<sup>15</sup> for small attitude deviations:

$$\theta_{k+1} = \theta_k + \omega_k \Delta t \quad , \quad (27)$$

$$\omega_g = \omega_k + d_k + \mathcal{N}[\sigma_g^2 I_{3 \times 3}] \quad , \quad (28)$$

$$d_{k+1} = \exp\{-\Delta t/\tau\} d_k + \mathcal{N}[\sigma_d^2 (1 - \exp\{-2\Delta t/\tau\}) I_{3 \times 3}] \quad , \quad (29)$$

where  $\theta \in \mathbb{R}^3$  represents the small attitude error vector around the body axes;  $\omega_g \in \mathbb{R}^3$  represents the rate gyro output;  $d \in \mathbb{R}^3$  is the gyro drift;  $\mathcal{N}[\cdot]$  represents a gaussian white sequence with given covariance matrix;  $\sigma_g$  is the standard deviation of gyro noise output;  $\sigma_d$  is the standard deviation of long term gyro drift;  $\tau$  is the long term time constant of the gyro drift model; and  $I$  is the identity matrix.

Let the state vector be:

$$\mathcal{X} \equiv \{\Delta\theta' : \Delta d'\}' \quad , \quad (30)$$

where ' indicates the transpose operator and the deviation  $\Delta \cdot$  is taken with respect to the expected values:

$$\Delta \theta \equiv \theta - \hat{\theta} \quad , \quad (31)$$

$$\Delta \omega \equiv \omega - \hat{\omega} \quad . \quad (32)$$

By taking the estimate of  $\omega$  as the gyro output corrected from the estimated gyro drift:

$$\hat{\omega}_k = \omega_g - \hat{d}_k \quad , \quad (33)$$

the state propagation obeys:

$$\mathcal{X}_{k+1-} = \Phi \mathcal{X}_k + \mathcal{N}[Q] \quad , \quad (34)$$

where the transition matrix  $\Phi$  and the state noise matrix  $Q$  are:

$$\Phi = \begin{pmatrix} I_{3 \times 3} & -\Delta t I_{3 \times 3} \\ 0_{3 \times 3} & \exp\{-\Delta t/\tau\} I_{3 \times 3} \end{pmatrix} \quad , \quad (35)$$

$$Q = \text{diag}\{\Delta t \sigma_g^2 [1 : 1 : 1] : \sigma_d^2 (1 - \exp\{-2\Delta t/\tau\}) [1 : 1 : 1]\} \quad . \quad (36)$$

The attitude observation model may be written as:

$$\mathcal{Y}_k = H_k \mathcal{X}_k + \mathcal{N}[R_k] \quad , \quad (37)$$

where the observation matrix  $H_k$  and the observation error covariance matrix  $R_k$  depend of which attitude sensors are switched on. Three-axis attitude determination is performed by the singular value decomposition method<sup>16</sup> (see also<sup>17</sup>) based on star observations only, whenever they are available. Such static estimate works as the attitude observation to the Kalman filter estimation process which takes into account the kinetic model. If the star sensor field of view is obliterated by the Earth presence, then secondary attitude sensor observations may be taken into account in either of the following ways. If Sun sensor observations are available, a rough three-axis attitude determination is carried out from both Sun sensor and magnetometer observations. In this case, the attitude observation to the Kalman filter estimation process is the same as for the previous case except for the worst attitude error covariance matrix. Finally, if only magnetometer observations are available, they fed the Kalman filter directly, since there is a lack of instantaneous observability in such case. Therefore, one has:

$$H_k = \begin{cases} [I_{3 \times 3} : 0_{3 \times 3}] , & \text{if stars or Sun observations are available;} \\ [\Omega(\mu) : 0_{3 \times 3}] , & \text{otherwise;} \end{cases} \quad (38)$$

$$R_k = \begin{cases} \sigma_\star^2 \mathcal{A}_\star \begin{pmatrix} 1 & 0 & 0 \\ 0 & 1 & 0 \\ 0 & 0 & 10 \end{pmatrix} \mathcal{A}_\star' , & \text{if star observations are available;} \\ [\sigma_\odot^{-2} (I_{3 \times 3} - s s') + \sigma_\mu^{-2} (I_{3 \times 3} - \mu \mu')]^{-1} , & \text{if Sun is the only star at sight;} \\ \sigma_\mu^2 (I_{3 \times 3} - \mu \mu') , & \text{otherwise,} \end{cases} \quad (39)$$

where  $s$  is the sun direction at body frame, nominally  $\{1 : 0 : 0\}'$ ;  $\mu$  is the observed magnetic field unit vector;  $\sigma_\mu$  is the magnetometer uncertainty;  $\sigma_\star$  is the star sensor uncertainty;  $\Omega(\cdot)$  is the vector product operator matrix, and  $\mathcal{A}_\star$  is the star sensor attitude matrix with respect to the body frame:

$$\mathcal{A}_\star = \begin{pmatrix} \cos \psi & 0 & \sin \psi \\ 0 & 1 & 0 \\ -\sin \psi & 0 & \cos \psi \end{pmatrix} \quad , \quad (40)$$

and  $\psi$  is the star sensor tilt angle, intended to minimize the sensor obliteration problem during payload Sun observations.

Table 2: ATTITUDE SIMULATION PARAMETERS

$\Delta t$	$\sigma_\omega$	$\sigma_d$	$\tau$	$\psi$	FOV	$\sigma_*$	$\sigma_\odot$	$\sigma_\mu$
5s	.05°/s	17°/hr	1000s	20°	20° × 20°	24''	1°	2°

Based on Equations 34 and 37, a Kalman filter<sup>18</sup> was implemented and a one year long simulation was carried out, one orbit every five days. The satellite is in a circular orbit with 800Km of altitude, 7° of inclination and initial ascending node of 0°. Table 2 presents the attitude relevant parameters. The overall performance is shown at Figure 6. The two plots on the page bottom correspond to an increased sensor FOV which simulates the worst possible effect of control degradation due to star sensor obliteration. It yielded a small increasing on the length of occultation periods.

Unfortunately, with the current AOCS specification, attitude errors soon became bigger than 0.5° (3 $\sigma$ ) during unavoidable periods with lack of star observations. Nevertheless, such performance should be considered acceptable since the pointing accuracy specification refers to the illuminated orbit phase only. Furthermore, error overflow effect is conditionally periodic due to the seasonal apparent motion of the Sun throughout the ecliptic and the orbit precession motion, whose period is about 50 days. It means that a suitable attitude maneuver every six months could reduce the problem.

## CONCLUSIONS AND RECOMMENDATIONS

A numerical analysis was carried out on star identification algorithms applied to attitude determination of a  $\mu$ -satellite being jointly designed by Brazil and France. The main conclusions and recommendations are:

- The use of star pairs only is not recommended for full sky star identification with currently available star trackers;
- The use of star triplets is reliable for a wide range of existing star trackers;
- The proposed Bezooijen's modified algorithm is a simple and still fast solution for full sky star identification for moderate accuracy level applications;
- For the French-Brazilian  $\mu$ -satellite, star magnitude information seems to be necessary to increase the discriminating power of the proposed identification algorithm;
- For smaller guide star catalogs, magnitude information could be relegated to the sanity checks of a pattern match;
- For highly accurate applications, on board guide star pairs catalog may grow up to an unmanageable size. So, alternative solutions such as the Ketchum&Tolson and the Williams et al ones seems to be necessary. Preliminary results using genetic algorithms indicate however that the Bezooijen's modified algorithm could also be used in a partitioned way.
- Using the currently AOCS specification of French-Brazilian  $\mu$ -satellite, the analysis indicate preliminary that, due to star sensor obliterating periods, attitude accuracy requirements would not be fulfilled during less than 10 minutes per orbit, at the worst case. Since roughly 50% of the orbit is left for payload scientific experiments, the performance could be still considered acceptable for practical purposes. Periodic orbit maneuvers should be carefully analyzed as a way to minimize the problem without AOCS design modifications.



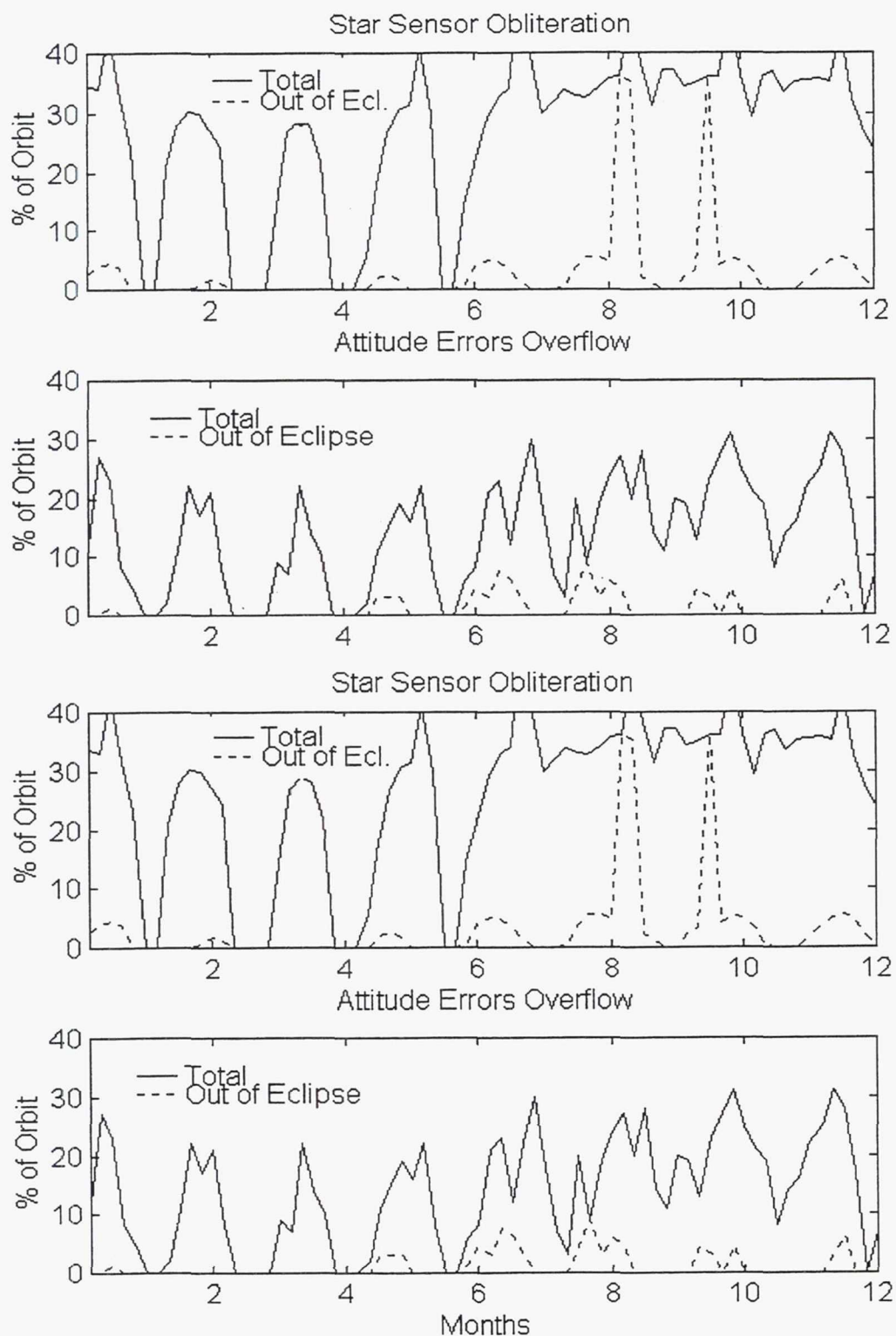


Fig. 6: Summary of Results for FOV 20 deg (a) and FOV 22 deg (b)

## ACKNOWLEDGEMENT

This work has been supported by a grant from the Brazilian agencies CAPES and CNPq, contract number 300388/95-0 (NV).

## REFERENCES

1. J. R. Wertz (ed.) *Spacecraft attitude determination and control*. D. Reidel, Boston, 1978.
2. D. Baldini; M. Barni; A. Foggi; G. Benelli and A. Mecocci "A New Star-Constellation Matching Algorithm for Satellite Attitude Determination." *ESA Journal* 1993, 17(2):185-198.
3. T. Bank "All Stellar Attitude Estimation Using a Ball CT-633 Star Tracker." (AAS 95-004) *Advances in the Astronautical Sciences* Vol. 88, 1995, pp. 59-66.
4. J. C. Kosik "Star Pattern Identification Aboard an Inertially Stabilized Spacecraft." *Journal of Guidance, Control and Dynamics* 14(2):230-235, Mar.-Apr., 1991.
5. M. S. Scholl "Star-Field Identification for Autonomous Attitude Determination." *Journal of Guidance, Control and Dynamics* 18(1):61-65, Jan.-Feb. 1995.
6. T. E. Strikwerda; H. L. Fisher; C. C. Kilgus and L. J. Frank "Autonomous Star Identification and Spacecraft Attitude Determination with CCD Star Trackers." *Proceedings of 1st ESA International Conference on Spacecraft Guidance, Navigation and Control Systems*. ESTEC, Noordwijk, the Netherlands, 4-7 June, 1991. pp. 195-200.
7. E. A. Ketchum and R. H. Tolson "Onboard Star Identification Without A Priori Attitude Information." *Journal of Guidance, Control and Dynamics* 18(2):242-246, Mar.-Apr. 1995.
8. K. E. Williams; T. E. Strikwerda; H. L. Fisher; K. Strohbehn and T. G. Edwards "Design Study: Parallel Architectures for Autonomous Star Pattern Identification and Tracking." (AAS 93-102) *Advances in the Astronautical Sciences* Vol. 82, Part I, 1993 pp. 43-58.
9. R. W. H. Van Bezooijen "Autonomous Star Referenced Attitude Determination." (AAS 89-003) *Advances in The Astronautical Sciences* Vol. 68, 1989, pp. 31-52.
10. D. Mortari "A Fast On-Board Autonomous Attitude Determination System Based On A New Star-Id Technique For A Wide FOV Star Tracker." (AAS 96-158) *Advances in The Astronautical Sciences*, Vol 89, 1996, pp. 893-903.
11. Sky Publishing Corporation, *SKY Catalogue 2000.0*, Vol.1, 2nd ed., Sky Publishing Corporation, Belmont-MA, USA, 1991.
12. M. Mitchell, *An introduction to genetic algorithm*. The MIT Press, Cambridge, MS, USA, 1996.
13. R.V.F. Lopes, and A.S.F. Salles "Elaboration of Star Catalogs Dedicated to Artificial Satellites." *VIII Brazilian Colloquium on Orbit Dynamics*, section B, p. 90 (poster). Santos, SP, Brazil, November 18-22, 1996. (in Portuguese)
14. H-O. Peitgen, H. Jürgens, and D. Saupe, *Chaos and fractals: new frontiers of science*. Springer Verlag, N.York, 1992.
15. E. J. Lefferts, F. L. Markley, and M. D. Shuster, "Kalman Filtering for Spacecraft Attitude Estimation," *Journal of Spacecraft, Control and Dynamics*, 5(5):417-429, Sept.-Oct. 1982.
16. F. L. Markley, "Attitude Determination Using Vector Observations and the Singular Value Decomposition" *The Journal of Astronautical Sciences*, 36(3):245-258, July-Sept., 1988.
17. M. D. Shuster "Maximum Likelihood Estimation of Spacecraft Attitude." *The Journal of Astronautical Sciences* 37(1):79-88, Jan.-Mar. 1989.
18. P. S. Maybeck *Stochastic models, estimation and control* N.York, NY, Academic Press, Vol.1. 1979 (*Mathematics in Science and Engineering*).

**Page intentionally left blank**



## A ROBUST STAR ACQUISITION ALGORITHM FOR THE WIDE-FIELD INFRARED EXPLORER

Eric T. Stoneking

Mission requirements for the Wide-field Infra-Red Explorer (WIRE) motivate an autonomous star acquisition algorithm which is flexible and robust. WIRE uses one Ball CT-601 CCD Star Tracker for fine attitude determination, and will observe 8–10 inertial targets per orbit. Each target is defined by an uploaded list of 2–5 guide stars. The star acquisition algorithm described in this paper is based on the Submillimeter Wave Astronomy Satellite (SWAS) algorithm, with additional features added to improve its reliability under WIRE's more demanding acquisition requirements. The algorithm first looks for one guide star, accepting up to four candidates in a reduced field of view which satisfy a magnitude check. It then uses a pattern match to find a second guide star and confirm one of the candidates for the first star. The remaining guide stars are then acquired by directed search. Attitude determination is enabled as soon as enough stars have been acquired to provide adequate attitude information about the axis of the star tracker boresight. Noting that the Rossi X-ray Timing Explorer uses two CT-601's which have exhibited anomalous Loss Of Track (LOT) events, the WIRE algorithm includes LOT-handling logic. Performance is demonstrated with nominal and difficult starfields, and guide star selection guidelines are discussed.

### INTRODUCTION

The Wide-field Infra-Red Explorer (WIRE) is a Small Explorer mission slated for launch in the fall of 1998. During its four-month mission, the spacecraft will point a cryogenically-cooled telescope to observe starburst galaxies. Eight to ten inertially-fixed targets will be studied per orbit. Each target is defined by an uploaded list of two to five guide stars.

Fine attitude determination is performed using a Ball CT-601 CCD Star Tracker aligned with the science instrument. For thermal control reasons, the instrument, and therefore the star tracker, must always point within  $30^\circ$  of zenith. The initial acquisition of stars must be performed while using the coarse attitude estimate, based on sun sensor, magnetometer, and gyro information. Once stars have been acquired, fine attitude estimation is performed using star tracker and gyro information. During slews between targets, the fine attitude estimate is propagated using gyro inputs.

The CT-601 tracker can simultaneously track up to five stars in its  $8^\circ \times 8^\circ$  field of view. The tracker can be commanded to perform a Full FOV Search, a Directed Search, or a

Reduced FOV Search. The Full FOV Search takes about 25 seconds to scan the entire field of view for stars. The Directed Search, which searches an area 8 arcmin on a side, takes only a few tenths of a second.

The Reduced Field of View (RFOV) is a window of intermediate, commandable size, developed for SWAS. WIRE uses two typical sizes of RFOV: a  $2^\circ \times 6^\circ$  window which assures that the window doesn't miss the sought star due to coarse attitude estimation errors, or a  $0.5^\circ$  square window which reduces the search time when the fine attitude estimate is used.

Stars found by any of these search functions are tested against the guide star's instrument magnitude before the search is deemed successful. On SWAS and WIRE, a tolerance of  $\pm 0.75$  instrument magnitudes is used.

The Rossi X-Ray Timing Experiment (RXTE) was launched in 1995, and carries two CT-601's. These trackers have exhibited Loss Of Track anomalies (LOT's), characterized by unexplained loss of a tracked star.

These factors impose a set of constraints on the star acquisition algorithm. The acquisition process must acquire a new target ten times per orbit, so it must be autonomous. It must be rapid, to maximize science. It must be robust to attitude estimation errors, star misidentification, and LOT's. These are accomplished through a sequence of steps, using a strategy of provisional acceptance and verification.

## SWAS BACKGROUND

Consistent with the Small Explorer philosophy, WIRE re-uses as much of the SWAS algorithms as possible. The star acquisition algorithm keeps the basic outline of the SWAS algorithm, but WIRE's more demanding acquisition requirements make necessary some significant modifications. We outline the SWAS procedure here to present the basis for the WIRE algorithm, and to point out some of the reasons why modifications were required. A more complete description of the SWAS algorithm is presented in [2].

SWAS uses two special targets for acquisition, one near the north ecliptic pole and one near the south ecliptic pole. These targets are chosen so that, from any orbit position and at any time of year, one of them will always be visible. (SWAS will fly in a near-polar orbit, as will WIRE.) One star in each acquisition target is identified as the Base Star. The Base Star is chosen to differ sufficiently in brightness from all other stars in the field of view, so that a magnitude check will reliably identify it.

To acquire the Base Star, a Reduced Field of View (RFOV) search is conducted. The RFOV is sized so that the only star in the RFOV bright enough for the tracker to track is the Base Star. Once the Base Star is acquired, directed searches are commanded to find the other guide stars. Offsets of the observed Base Star position from its predicted position are used to correct the positions of the directed search commands for the remaining stars. Completion of the acquisition phase is achieved through a criterion on the separation of the acquired guide stars.



# THE WIRE STAR ACQUISITION ALGORITHM

Modifications in the star acquisition sequence for WIRE are driven by the more severe constraints on spacecraft pointing, and by the short mission lifetime. Since the star tracker must always point near zenith, the ecliptic poles are only visible to the tracker for portions of the orbit. Since the mission is only four months long (limited by cryogen supply), it is desirable not to have to wait for an acquisition target. These considerations lead us to the goal of using any science target as an acquisition target. This in turn leads us to maximize the algorithm's flexibility and robustness. This is done by allowing for multiple base star candidates, performing a search for a second star to confirm the base star choice, and by allowing any of the uploaded stars to function as a base star.

## Obtaining a Base Star

As for SWAS, the first step in the WIRE algorithm is to acquire a base star. SWAS uses a RFOV search, keeping the one star found that meets its criterion on instrument magnitude. For WIRE, this is inadequate, since we cannot expect that a general starfield will have so distinct a star in it.

By default, WIRE uses the first star in the guide star list as a base star. To maximize robustness, however, any guide star may be called upon to act as the base star should preceding stars not be found.

The base star is sought using an RFOV search, with the window centered on the expected location of the base star in the tracker FOV. The size of the RFOV is determined by the performance of the attitude estimator; the RFOV must be large enough that the base star will lie in it despite the worst-case attitude estimation errors. For the initial acquisition, WIRE's RFOV size is  $2^\circ \times 6^\circ$ . The rectangular shape occurs because the coarse attitude estimate accuracy about the X axis is driven by digital sun sensor errors, while accuracy about the Y axis is driven by magnetometer errors. Once the fine attitude estimator has converged, a smaller RFOV is used to speed the RFOV search and reduce the chance of having multiple candidates. This window size is commandable, with a typical expected value of  $0.5^\circ \times 0.5^\circ$ .

With the large window, and a general star field, it is possible that more than one star which is near the base star's magnitude will lie in the RFOV. (SWAS and WIRE have a  $\pm 0.75$  magnitude tolerance on their magnitude matching checks.) The SWAS algorithm would stop on finding the first of these matches. The WIRE algorithm continues, assigning a tracking slot to each star it finds in the RFOV which satisfies the magnitude check, until it has acquired four such stars, or has searched the entire RFOV. The stars found are labeled as base star *candidates*. Up to four candidates may be tracked because the tracker can track up to five stars simultaneously, and we reserve one tracking slot for the next step in the acquisition procedure.

In the event that no base star candidates are found, the guide star list is "cycled"; the pointer which identifies the base star is incremented to point at the next guide star in the list. Then the acquisition is restarted, and an RFOV search is conducted to find candidates for the new base star. This continues as needed until base star candidates are found.



It is also possible, though rather unlikely, that there are more than four base star matches in the RFOV, and the true base star is not one of the first four found in the RFOV search. This case will be handled by the next step, Base Star Verification.

## Verifying the Base Star

Having found at least one, and up to four, base star candidates, the next step is to determine which one, if any, is the base star. This is done using the simplest form of a pattern match. Using the first candidate, a directed search is commanded for another guide star. This guide star carries the functional tag "Guide Star #2" (GS#2). Like "base star", this is a functional tag which may point to any of the uploaded guide stars; by default it is the last star in the guide star list. If the directed search returns a successful result before a timeout occurs, then the base star candidate is confirmed as the base star. If not, the GS#2 pointer is incremented, and another directed search is commanded. This continues until a GS#2 is found, or the list of guide stars is exhausted. If the former, we have succeeded in verifying the base star, and proceed to the next step, acquiring the remaining guide stars. If the list of guide stars is exhausted, we consider the next base star candidate and conduct another GS#2 search. If the candidate list is exhausted, then we cycle the guide stars and begin again with an RFOV search for the new base star.

Once the base star and GS#2 are found, break track commands are issued to those windows tracking the remaining base star candidates. These windows will be needed to find and track the remaining guide stars.

## Acquiring Remaining Guide Stars

At this point the base star has been found, and confirmed by finding a second star. All that remains is to find the remaining guide stars and enable attitude updates.

The remaining guide stars are sought using directed search commands. The positions of the directed search windows are corrected using the differences between the observed and predicted locations of the base star and GS#2. To guard against the unlikely event of a misidentified base-GS#2 pair, at least one of the remaining guide stars must be found before a timeout. If none are found, the base-GS#2 pair is assumed to be misidentified, the guide stars are cycled, and the process begins again with an RFOV search for a new base star.

There are two cases where the algorithm cannot perform this final check on the base-GS#2 pair, and so must assume that they have been correctly identified. The first case is when there are only two guide stars. The second is when the predicted position of the remaining guide stars, corrected by the observed positions of the base star and GS#2, lies outside the tracker's FOV. Although not likely, this condition could occur due to coarse attitude estimation errors.

To provide useful information to the attitude estimator, it is not necessary for all of the guide stars to be found. Since the tracker is used to generate a three-axis attitude estimate, at least two stars, sufficiently separated, are sufficient. Thus, following SWAS, we define a criterion on the separation of the acquired stars which defines the completion of the star

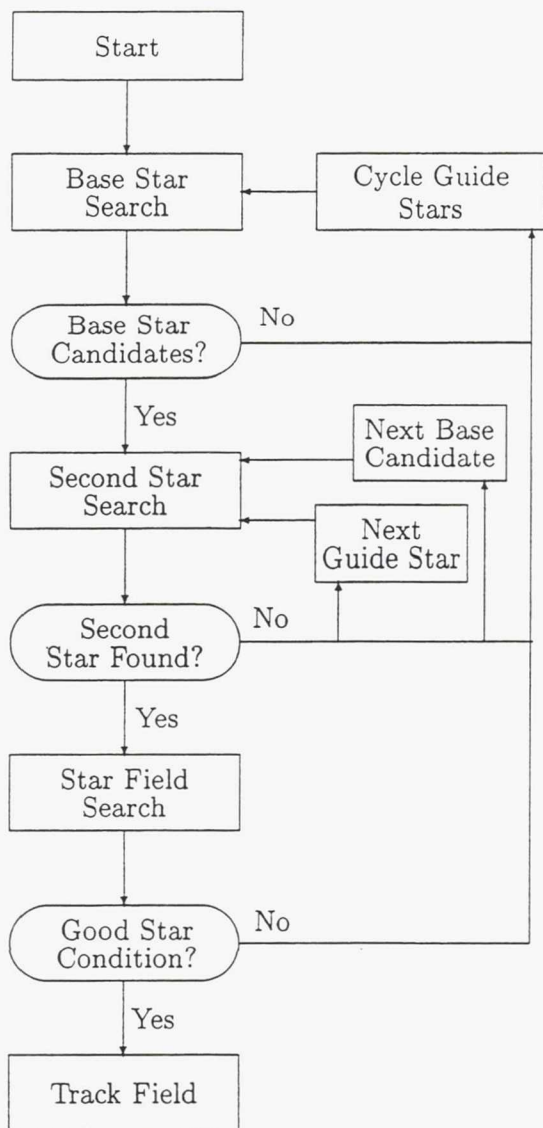
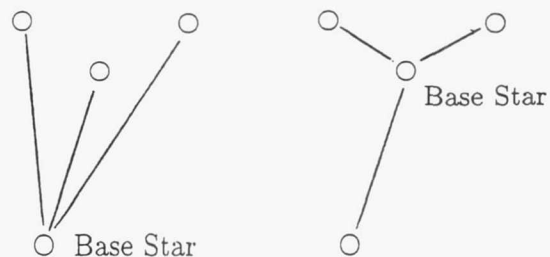
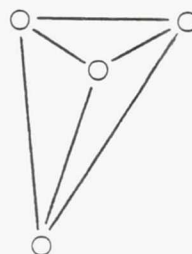


Figure 1: Star Acquisition Flowchart



SWAS: Same stars, different  
Good Star Condition



WIRE resolves ambiguity  
by using all chords

Figure 2: SWAS and WIRE Separation Criteria

acquisition process. This criterion is called the Good Star Condition.

The SWAS algorithm used the sum of the squares of the chords between the base star and each of the other acquired guide stars. This sum had to be larger than a threshold ( $4 \text{ deg}^2$ ) for the Good Star Condition to be true. For WIRE, this criterion is modified. The SWAS method yields different sums for the same set of stars, depending on which one is the base star. But the attitude estimator accuracy doesn't change depending on which star is the base star, so the distinction serves no purpose. So, the WIRE algorithm measures the sum of the squares of all chords between all pairs of acquired guide stars. If this sum is above a threshold, the criterion is satisfied and Good Star Condition is set to True.

## HANDLING LOSS OF TRACK EVENTS

The Rossi X-Ray Timing Experiment (RXTE) was launched in December 1995. It has experienced Loss of Track (LOT) anomalies with its two CT- 601 star trackers[3]. Some of these events are attributable to debris floating across the field of view, but some remain unexplained.

While the cause is unknown, the solution for LOT's is simple. When the LOT is detected, a break track command is sent, then the tracking window is re-commanded to search for the lost star. Since the LOT is a transient event, the star should be recovered immediately. RXTE, SWAS, and WIRE have all implemented similar solutions. The WIRE algorithm is written so that this recovery is transparent to the attitude estimator and to the taking of science data. Failure Detection and Handling logic does monitor the star processing, but only acts if the Good Star Condition is violated for a period of time. If this occurs, the ground is notified, and the star acquisition process is re-initialized.

## PERFORMANCE

The star processing modules of the WIRE flight algorithm have been modelled in detail in the WIRE high-fidelity dynamics simulation, both to show the typical behavior of the star acquisition process and to test the flight algorithm prior to real-time testing. We present here the results of two acquisition cases: a nominal acquisition starting from a coarse attitude estimate, and a rather difficult case which shows the robustness of the algorithm. In both cases, LOT events were simulated at 60-second intervals, so that each tracker slot suffered a LOT every five minutes. This is a much higher rate than is expected on orbit, and was shown to have no impact on the acquisition or maintenance of a stellar attitude.

To help interpret the behavior of the acquisition process, the acquisition states are plotted. Table 1 presents the state numbers and the corresponding labels. Comparison with figure 1 shows that the three search phases of the algorithm are comprised of two states each. In the "Init Search" state, commands are formulated and issued to the tracker, and in the "Search" state the tracker results are received and interpreted.



StarSearchMode Number	State Name
1	Standby
2	InitBaseStarSearch
3	BaseStarSearch
4	InitSecondStarSearch
5	SecondStarSearch
6	InitStarFieldSearch
7	StarFieldSearch
8	TrackField

Table 1: Star Search States

## Nominal Acquisition

Figures 3–5 show a nominal acquisition case. This case simulates the initial acquisition of an inertial stellar attitude, starting from a zenith-pointing attitude and a coarse attitude estimate using sun sensor, magnetometer, and gyro measurements. The slew to the target occurs in the first 25 seconds, and the starfield acquisition is completed in the following 13 seconds. The majority of the acquisition time is spent performing the Reduced Field of View search for the base star. Upon completion of the acquisition, the fine attitude estimator is enabled, and the estimation errors about the X and Y axes drop immediately to the arc-second range. Estimation errors about the Z axis converge more slowly because this is the tracker boresight axis, and observability is poor. Figure 5 shows the state of the algorithm as a function of time.

## Acquisition with Ambiguous Base-Second Star Pairs

Figures 6–8 show a difficult acquisition case. In this case, there are two field stars which match the first guide star, and two field stars which match the second guide star. One 1-2 pair is the intended pair, and one 1-2 pair is a spurious pair, offset from the intended pair and having the same relative spacing. The stars are arranged so that a Reduced Field of View search finds the spurious star before it finds the intended star. A search for the remainder of the field will be required to avoid a misidentification.

The acquisition state history is shown in figure 8. To interpret this plot, it is helpful to trace the use of the guide star slots. Remember, the terms “base star” and “second star” are functional tags. The “base star” may be any of the stars in the uploaded guide star list. The term “guide slot” will refer to the position of a particular guide star in that list. For example, the base star and second star may be the stars in guide slots 4 and 2, respectively. (The tracker slots are yet another matter, not to be confused with guide slots.)

The first RFOV search finds both candidates for guide slot #1. Using the spurious candidate, a directed search is commanded at the expected location of guide slot #5 (the default slot for the “second star”, as guide slot #1 is the default slot for the “base star”). This search fails, and the next directed search is at the expected location of guide slot #2. This search succeeds, only because we have placed a spurious “second star” to accompany

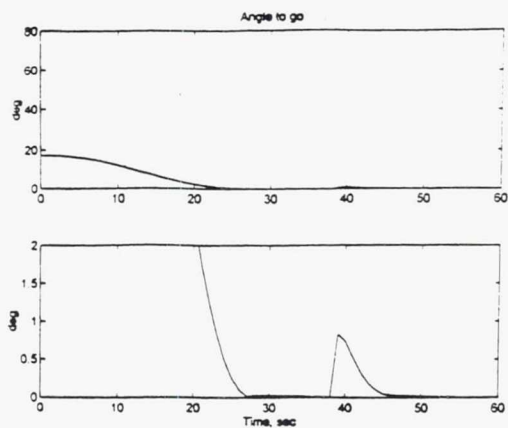


Figure 3: Nominal Acquisition, Angle to Go

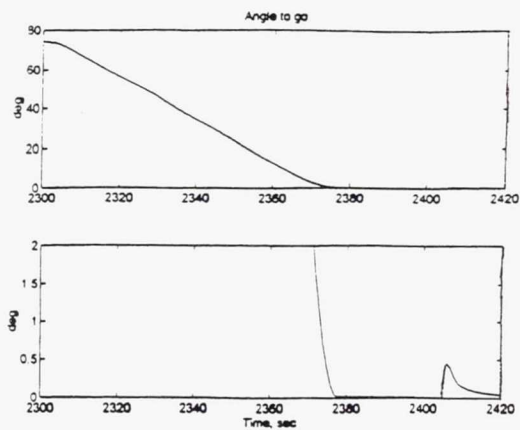


Figure 6: Difficult Acquisition, Angle to Go

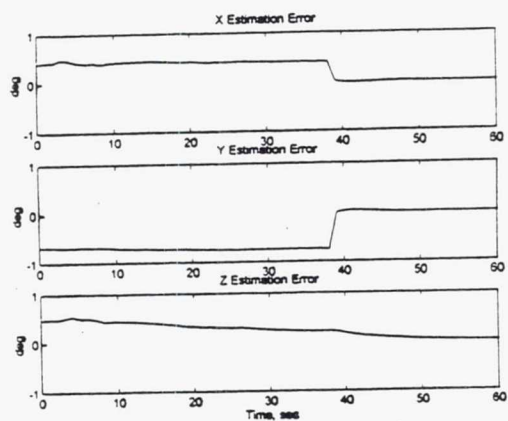


Figure 4: Nominal Acquisition, Estimation Errors

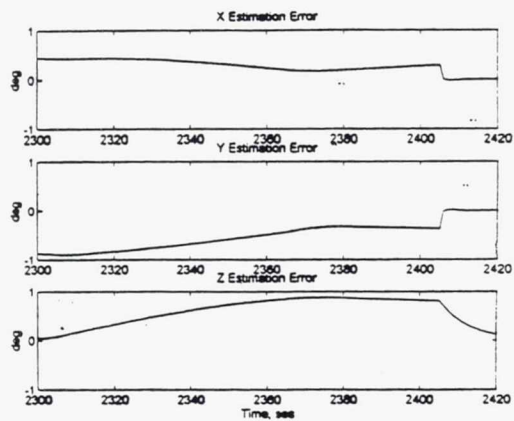


Figure 7: Difficult Acquisition, Estimation Errors

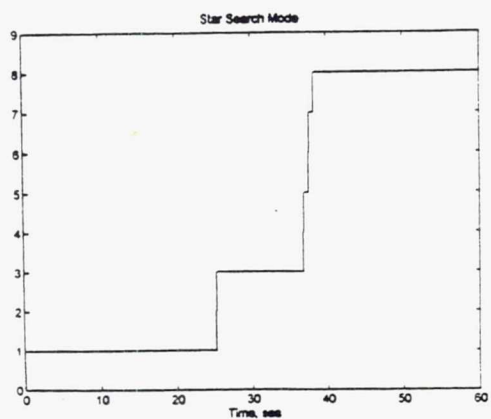


Figure 5: Nominal Acquisition, Star Search State

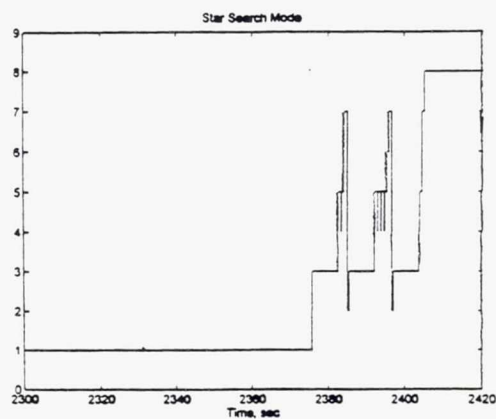


Figure 8: Difficult Acquisition, Star Search State

our spurious "base star". The next step is to search for the remaining guide stars. This search fails, forcing a return to the InitBaseStarSearch state, where the "base star" tag is reassigned to guide slot #2 and the "second star" tag is reassigned to guide slot #3. Then the second RFOV search is performed. It finds two candidates for the base star, the true and spurious stars we provided for guide slot #2. Using the spurious candidate, a search is performed for a second star, failing to find one for guide slots #3,4, and 5 before finding the spurious star for guide slot #1. Again, a search is performed for the remaining guide stars, which once again fails. This forces another return to InitBaseStarSearch, where the "base star" tag is assigned to guide slot #3 and the "second star" tag is reassigned to guide slot #4. With this unambiguous pair, the acquisition proceeds as in the nominal case.

## GUIDE STAR SELECTION

In conjunction with algorithm design, intelligent selection of the uploaded guide stars is also required in order to ensure acquisition of the star field. Both the algorithm design and guide star selection guidelines have been tailored to the capabilities and limitations of the CT-601 star tracker. In this section, some of the star guidelines are discussed.

Some guidelines are obvious, and do not require much discussion:

1. Each target must have 2-5 guide stars. Two guide stars are required to provide a three-axis attitude solution, and five is the maximum number which may be simultaneously tracked by the CT-601.
2. All guide stars must have instrument magnitudes in the range  $1.0 \leq M_i \leq 6.0$ . This is the sensitivity range specified by Ball Aerospace.
3. Guide stars must have a minimum separation of  $0.15^\circ$ . This is a limitation of the tracker.

Additional guidelines bear more on how the tracker is used, and must be crafted in conjunction with the acquisition algorithm:

1. No guide star may have a neighbor within 3 instrument magnitudes within  $0.1^\circ$ .

This guideline is the result of a trade-off between star availability and accuracy of the measurement. A dim star near a tracked star shifts the perceived location of the tracked star, degrading the accuracy of the measurement. Ball recommends a  $4M_i$  minimum separation, neglecting altogether stars with  $M_i > 9$ . This yields a maximum centroiding error of 4 arcsec, but it reduces the number of available guide stars. For WIRE, the typical science target is already in a sparsely-populated area of the sky, such that this constraint became a concern. Fortunately, WIRE's pointing requirements do not require this level of accuracy. Relaxing the minimum brightness separation to  $3M_i$  yields an 8 arcsec centroiding error, which is acceptable, and greatly increases the availability of guide stars.

2. At least two guide stars per target should be at least  $0.5^\circ$  from the edge of the tracker's field of view when the tracker is centered on the target attitude.



This guideline is a reflection of the expected estimator errors at the end of a large slew. Between targets, the fine attitude estimate is propagated using gyroscope rate measurements. Uncompensated scale factor errors may lead to estimation errors of up to  $0.28^\circ$  after a  $60^\circ$  slew. Since a minimum of two stars is required for a successful acquisition, at least two stars must be far enough away from the FOV edge to insure that they will still be in the FOV after such a slew. Once these stars are acquired, the star acquisition algorithm has provision for then acquiring any additional stars which may have drifted out of the FOV. This guideline may be modified as the mission progresses, as the gyro properties are better characterized.

3. The instrument magnitude of all guide stars must be known to within 0.75 at observation time.

Magnitude checks are performed on all stars found by the tracker. The CCD star tracker has a somewhat different spectral response than the human eye, however, so the instrument magnitude of a star varies from the visual magnitude as a function of its spectrum. While this dependence has been characterized [4] for the RXTE tracker, WIRE still allows large tolerances on magnitude checks. The trade-off is between finding more base star candidates and rejecting valid guide star matches. Since the WIRE algorithm provides for rejection of false positive matches, tight magnitude tolerances are not required.

4. Guide stars must be spaced to insure satisfaction for the Good Star Criterion,

$$\sum_{i=1}^{n-1} \sum_{j=i+1}^n |r_i - r_j|^2 \geq 4 \text{ deg}^2$$

where  $r_i$  is the two-dimensional position vector of the  $i$ th star in the tracker FOV, and  $n$  is the number of guide stars being tracked.

Assuming an 8 arcsec error on the placement of any star, this separation criterion assures that the attitude measurement error about the tracker boresight is less than 15 arcmin.

5. At least one target in any  $120^\circ$  orbit segment should have two guide stars separated by no more than  $2.8^\circ$ .

This condition allows the target to be used as an acquisition target, despite worst-case coarse attitude estimation errors (assumed to be  $2^\circ$  about the sun line). With this estimation error, the directed search for the second guide star may miss the star if it is more than  $2.8^\circ$  from the base star. Recalling that the goal of the star acquisition algorithm is to allow acquisition more quickly than could be done with the SWAS strategy using dedicated targets at the North and South ecliptic poles, at least three acquisition-quality targets per orbit are desired. Star catalog studies suggest that this is not a difficult condition to satisfy.

Note that this guideline, combined with the guideline above, indicate that targets with only two guide stars are less likely to make good acquisition targets than target with more guide stars.

## CONCLUSION

Building on SWAS heritage and RXTE flight experience, an autonomous star acquisition algorithm has been developed for the WIRE spacecraft. This algorithm first searches a reduced field of view (RFOV) for one star, using a loose magnitude match criterion. Accepting up to four candidates for this "base" star, it then searches for a second star, using a pattern match for verification. The algorithm makes use of the capability of the tracker to track multiple stars, and to limit its search to a reduced field of view. This latter capability was added for SWAS, and included in the WIRE star tracker. The algorithm is robust to initial attitude estimation errors, bad uploaded stars, multiple matches for guide stars, and Loss of Track anomalies.

## References

- [1] Ball Aerospace and Technology Corporation. "User's Manual for the WIRE CT-601 Star Tracker", prepared for NASA Goddard Space Flight Center, Contract No. NAS5-32995, May 1997.
- [2] Daniel, Walter K., Correll, Thomas E., Anderson, Mark O. "Development of a Direct Match Technique for Star Identification on the SWAS Mission". Proceedings of the 1995 Flight Mechanics/Estimation Theory Symposium, NASA Goddard Space Flight Center, May 1995.
- [3] Fink, Chapman, Davis, *et al.* "Experience Gained from Launch and Early Orbit Support of the Rossi X-Ray Timing Explorer (RXTE)". Proceedings of the 1996 Flight Mechanics/Estimation Theory Symposium, NASA Goddard Space Flight Center, May 1996.
- [4] Computer Sciences Corp. "SMEX Flight Dynamics Analysis: SWAS Run Catalog Prelaunch Analysis". Memo 56830-04 under contract NAS 5-31000, to Mr. R. Kieckhefer, September 9, 1996.
- [5] Hacking, P., Gautier, T. N., *et al.* "The Wide-Field Infrared Explorer (WIRE) Mission". Proceedings of the Moriond Astrophysics Meeting on Extragalactic Astronomy in the Infrared, Moriond, France, March 1997.
- [6] Fennell, Michael D., Untalan, Victoriano Z., and Lee, Michael H. "The Attitude Control System Design for the Wide-Field Infrared Explorer Mission". Proceedings of the 11th Annual AIAA/USU Conference on Small Satellites, Logan, Utah, September 1997.
- [7] Lee, Michael H. "A Simplified Pattern Match Algorithm for Star Identification". Proceedings of the 1996 Flight Mechanics/Estimation Theory Symposium, NASA Goddard Space Flight Center, May 1996.

**Page intentionally left blank**



# PERFORMANCE OF LEAST SQUARES AND KALMAN FILTER ALGORITHMS FOR ORBIT DETERMINATION USING SINGLE- AND MULTI-STATION TRACKING OF GEOSTATIONARY SATELLITES

J.P. Halain <sup>1</sup>, T. Welter <sup>2</sup>, P. Francken <sup>2</sup>, G. Krier <sup>2</sup>, P. Wauthier <sup>2</sup> and P. Rochus <sup>1</sup>

## ABSTRACT

This paper provides a comprehensive overview of the Least Squares (LS) and Extended Kalman Filter (EKF) orbit estimation algorithms and their current software implementations at Société Européenne des Satellites (SES). We present how a LS orbit determination program has been adapted to yield the implementation of a continuous-discrete EKF, making maximal re-use of computer code between the two formulations. We discuss how the performances of both methods have been assessed using a dedicated Monte-Carlo analysis software. Our implementations of the two methods are also compared from an operational standpoint. Finally actual orbit determination results using single-station tracking based on range and angle data as well as a new multi-station tracking system developed by SES are presented and discussed.

## INTRODUCTION

SES has realized a safe co-location of 7 satellites in a longitude and latitude window of  $\pm 0.1$  using a conventional single station tracking system composed of accurate spread-spectrum ranging units and of a single antenna tracking successively the different satellites<sup>1</sup>. In order to support the future development of its fleet, SES has developed and installed a so-called trilateration network. Operational since February 1998, this system consists in a master tracking station located in Betzdorf, Luxembourg and a set of three slave ranging stations - including a backup - located close to the edges of the ASTRA system footprint. Each station provides a continuous flow of range data with an accuracy better than one meter. The system was designed to provide an improvement in orbit determination accuracy of one order of magnitude compared to the single station tracking system.

---

<sup>1</sup> Université de Liège, Centre Spatial de Liège  
Parc Industriel du Sart Tilman, Avenue du Pré-Aily, B-4031 Angleur-Liège, Belgium  
tel : +32 41 67 67 75 fax : +32 41 67 56 13

<sup>2</sup> Société Européenne des Satellites  
L-6815 Château de Betzdorf, Grand-Duchy of Luxembourg  
tel : +352 710 725 1 fax : +352 710 725 390

In order to comply with the high accuracy of this new tracking system, the overall trajectory and measurement models in the DLR program ORBIT<sup>2</sup> have been improved<sup>3</sup>. As a result, the thrust-free trajectory of a geostationary satellite can be modelled with an accuracy better than 1 m (effective range error) over a 2 weeks orbit estimation.

In parallel, SES analyzed if further improvements in estimation accuracy could be obtained by using an Extended Kalman Filter (EKF) *in lieu* of the current Least Squares (LS) estimator. In the present paper, we describe our prototype of a continuous-discrete EKF, as well as a dedicated Monte Carlo simulation software used to compare the accuracy of the estimations provided by the LS and EKF methods. Both methods are also compared in terms of their operational implementations. Finally we present actual operational experience with both the LS and EKF methods, using single- as well as multi-station tracking systems. The results confirm the accuracy of the trilateration system and the conclusions of our simulations regarding the relative performances of the LS and EKF techniques and their implementations.

## THEORY

The equations of motion of the satellite can formally be written as

$$\dot{\mathbf{y}}(t) = \mathbf{f}(\mathbf{y}, t) + \mathbf{w}(t) \quad (1)$$

where the generalized state vector  $\mathbf{y}(t)$  includes the position and velocity vectors as well as a set of model parameters;  $\mathbf{w}(t)$  denotes Gaussian white process noise with

$$E[\mathbf{w}(t)] = \mathbf{0}, \quad E[\mathbf{w}(t)\mathbf{w}^T(\tau)] = \mathbf{Q}(t)\delta(t - \tau). \quad (2)$$

A particular solution of Eqs. (1) is defined by initial conditions  $\mathbf{y}(t_0) = \mathbf{y}_0$ . The set of measurements  $\{z_k(t_k)\}$  collected at discrete times  $t_1 \leq t_2 \leq \dots \leq t_n$ , forms a  $n$ -dimensional vector  $\mathbf{z}$ , which is related to the state vector by means of a measurement model :

$$\mathbf{z} = \mathbf{h}(\mathbf{y}_0) + \mathbf{v} \quad (3)$$

where  $\mathbf{h}$  implicitly depends on  $\mathbf{y}_0$  through  $\mathbf{y}(t_k)$ ,  $k = 1, \dots, n$  and  $\mathbf{v}$  is Gaussian noise with

$$E(\mathbf{v}) = \mathbf{0}, \quad E(\mathbf{v} \cdot \mathbf{v}^T) = \mathbf{R}. \quad (4)$$

In the absence of process noise,  $\mathbf{w} = \mathbf{0}$ , the *maximum likelihood estimator* is the one that minimizes the  $\chi^2$  function :

$$\chi^2 \equiv [\mathbf{z} - \mathbf{h}(\hat{\mathbf{y}}_0)]^T \cdot \mathbf{R}^{-1} \cdot [\mathbf{z} - \mathbf{h}(\hat{\mathbf{y}}_0)]. \quad (5)$$

The dependency upon the estimate  $\hat{\mathbf{y}}_0$  is non-linear so the problem is solved iteratively. At each iteration, a linearisation is performed around the reference trajectory  $\mathbf{y}_{ref}$  obtained from the estimation of the previous iteration and it is required to compute the correction  $\mathbf{x}$  to be applied to the current reference trajectory :

$$\mathbf{x}(t_0) = \hat{\mathbf{y}}(t_0) - \mathbf{y}_{ref}(t_0). \quad (6)$$

The *normal equations* provide a mean to solve the linear LS sub-problem :

$$\hat{\mathbf{x}} = (\mathbf{A}^T \cdot \mathbf{R}^{-1} \cdot \mathbf{A})^{-1} \mathbf{A}^T \cdot \mathbf{R}^{-1} \cdot \mathbf{b} \quad (7)$$

where we have defined

$$\mathbf{A} \stackrel{\text{def}}{=} \left. \frac{\partial \mathbf{h}(\mathbf{y}_0)}{\partial \mathbf{y}_0} \right|_{\mathbf{y}_0 = \mathbf{y}_{ref}(t_0)}, \quad \mathbf{b} \stackrel{\text{def}}{=} [\mathbf{z} - \mathbf{h}(\mathbf{y}_0)] \Big|_{\mathbf{y}_0 = \mathbf{y}_{ref}(t_0)}. \quad (8)$$

We get for the covariance matrix :

$$\mathbf{P} = E[(\hat{\mathbf{x}} - E(\hat{\mathbf{x}}))(\hat{\mathbf{x}} - E(\hat{\mathbf{x}}))^T] = (\mathbf{A}^T \mathbf{R}^{-1} \mathbf{A})^{-1} . \quad (9)$$

Assuming now that a priori information on  $\mathbf{x}$  is available in the form of an a priori estimate  $\mathbf{x}_a$  and an associated covariance matrix  $\mathbf{P}_0(t_0) = \text{Cov}(\mathbf{x}_a, \mathbf{x}_a)$ , this information can be handled by analogy with additional observations of  $\mathbf{x}$  through

$$\mathbf{x} = \mathbf{x}_a + \tilde{\mathbf{v}} \quad \text{with} \quad E(\tilde{\mathbf{v}}) = \mathbf{0} , \quad E(\tilde{\mathbf{v}} \cdot \tilde{\mathbf{v}}^T) = \mathbf{P}_0(t_0) . \quad (10)$$

In consequence the LS with a-priori information can be deduced from the standard formulation through the substitutions

$$\mathbf{A} \longrightarrow \begin{pmatrix} \mathbf{I} \\ \mathbf{A} \end{pmatrix} \quad \mathbf{b} \longrightarrow \begin{pmatrix} \mathbf{x}_a \\ \mathbf{b} \end{pmatrix} \quad \mathbf{R}^{-1} \longrightarrow \begin{pmatrix} \mathbf{P}_0^{-1}(t_0) & \mathbf{0} \\ \mathbf{0} & \mathbf{R}^{-1} \end{pmatrix} . \quad (11)$$

The normal equations Eqs. (7) and (9) then become

$$\hat{\mathbf{x}}(t_0) = [\mathbf{P}_0^{-1}(t_0) + \mathbf{A}^T \mathbf{R}^{-1} \mathbf{A}]^{-1} \cdot [\mathbf{P}_0^{-1}(t_0) \mathbf{x}_a + \mathbf{A}^T \mathbf{R}^{-1} \mathbf{b}] , \quad (12)$$

$$\mathbf{P}(t_0) = [\mathbf{P}_0^{-1}(t_0) + \mathbf{A}^T \mathbf{R}^{-1} \mathbf{A}]^{-1} . \quad (13)$$

This formulation allows the LS to be implemented in a recursive way; whenever a new measurement is collected at time  $t_k$  the a priori information is taken from the previous estimation at  $t_{k-1}$  and the process is repeated. The a priori estimate  $\mathbf{x}_a(t)$  and covariance matrix  $\mathbf{P}_0(t)$  are then replaced by  $\hat{\mathbf{x}}(t|t_{k-1})$  and  $\mathbf{P}(t|t_{k-1})$ , while the new estimates  $\hat{\mathbf{x}}(t)$  and  $\mathbf{P}(t)$  are now denoted  $\hat{\mathbf{x}}(t|t_k)$  and  $\mathbf{P}(t|t_k)$ . The matrix  $\mathbf{R}$  becomes the scalar quantity  $R(t_k) = E\{v^2(t_k)\}$  while the matrix  $\mathbf{A}$  and the vector  $\mathbf{b}$  become  $\mathbf{A}(t_k, t) = \partial h[\mathbf{y}(t_k), t_k] / \partial \mathbf{y}(t)$  and  $b(t_k) = z_k - h[\mathbf{y}(t_k), t_k]$ , respectively. In general  $\mathbf{A}(t_k, t)$  may be obtained as

$$\mathbf{A}(t_k, t) = \frac{\partial h[\mathbf{y}(t_k), t_k]}{\partial \mathbf{y}(t)} \bigg|_{\mathbf{y}(t)=\mathbf{y}_{ref}(t)} = \frac{\partial h[\mathbf{y}(t_k), t_k]}{\partial \mathbf{y}(t_k)} \bigg|_{\mathbf{y}(t)=\mathbf{y}_{ref}(t)} \cdot \Phi(t_k, t) \quad (14)$$

where the transition matrix  $\Phi$  is obtained from the matrix differential equation:

$$\frac{d}{dt'} \Phi(t', t) = \mathbf{F}(t') \Phi(t', t) \quad \text{with} \quad \Phi(t, t) = \mathbf{I} \quad (15)$$

and  $\mathbf{F}(t)$  is the Jacobian of the vector function  $\mathbf{f}[\mathbf{y}(t), t]$

$$\mathbf{F}(t) \stackrel{\text{def}}{=} \frac{\partial \mathbf{f}[\mathbf{y}(t), t]}{\partial \mathbf{y}(t)} \bigg|_{\mathbf{y}(t)=\mathbf{y}_{ref}(t)} . \quad (16)$$

Defining the *Kalman gain*

$$\mathbf{K}(t) \stackrel{\text{def}}{=} \mathbf{P}(t|t_{k-1}) \mathbf{A}^T(t_k, t) \cdot [\mathbf{A}(t_k, t) \mathbf{P}(t|t_{k-1}) \mathbf{A}^T(t_k, t) + R(t_k)]^{-1} \quad (17)$$

we can rewrite Eqs. (12, 13), after some algebraic manipulations, as the *filtering equations*

$$\hat{\mathbf{x}}(t|t_k) = \hat{\mathbf{x}}(t|t_{k-1}) + \mathbf{K}(t_k) [b(t_k) - \mathbf{A}(t_k, t) \hat{\mathbf{x}}(t|t_{k-1})] , \quad (18)$$

$$\mathbf{P}(t|t_k) = [\mathbf{I} - \mathbf{K}(t_k) \mathbf{A}(t_k, t)] \cdot \mathbf{P}(t|t_{k-1}) . \quad (19)$$

For  $t = t_0$  this formulation is equivalent to the initial LS parameter estimation problem. By contrast, setting  $t = t_k$  in the above equations leads to a filtering problem. In this case the integration of the



variational equations Eqs. (15) is avoided, but the values of  $\hat{\mathbf{x}}(t_k|t_{k-1})$  and  $\mathbf{P}(t_k|t_{k-1})$  need to be computed from the values  $\hat{\mathbf{x}}(t_{k-1}|t_{k-1})$  and  $\mathbf{P}(t_{k-1}|t_{k-1})$  obtained at the previous time  $t_{k-1}$  through a *prediction step*. Taking now additional process noise  $\mathbf{w}$  into account, the quantity  $\mathbf{x}(t)$  appearing in Eq. (6) satisfies the equation :

$$\dot{\mathbf{x}}(t) = \mathbf{F}(t)\mathbf{x}(t) + \mathbf{w}(t) \quad (20)$$

where  $\mathbf{F}(t)$  is given by Eq. (16). The solution of the linearised system Eq. (20) can be expressed between the observation times  $t_{k-1}$  and  $t_k$  as

$$\mathbf{x}(t_k) = \Phi(t_k, t_{k-1})\mathbf{x}(t_{k-1}) + \mathbf{w}'(t_k) \quad (21)$$

where  $\Phi(t_k, t_{k-1})$  is the transition matrix of Eq. (15) and  $\mathbf{w}'(t_k) = \int_{t_{k-1}}^{t_k} \Phi(t_k, t)\mathbf{w}(t)dt$  is a stochastic integral with

$$E[\mathbf{w}'(t_k)] = \mathbf{0}, \quad E[\mathbf{w}'(t_k)\mathbf{w}'^T(t_{k+l})] = \mathbf{Q}'(t_k)\delta(l). \quad (22)$$

The discrete noise covariance matrix  $\mathbf{Q}'(t_k)$  satisfies the matrix differential equation

$$\frac{d}{dt}\mathbf{Q}'(t) = \mathbf{Q}(t) + \mathbf{F}(t)\mathbf{Q}'(t) + \mathbf{Q}'(t)\mathbf{F}^T(t) \quad \text{with} \quad \mathbf{Q}'(t_{k-1}) = \mathbf{0}. \quad (23)$$

The prediction equations for the estimated state-vector and error covariance now become

$$\hat{\mathbf{x}}(t_k|t_{k-1}) = E\{\Phi(t_k, t_{k-1})\mathbf{x}(t_{k-1}) + \mathbf{w}'(t_k)\} = \Phi(t_k, t_{k-1})\hat{\mathbf{x}}(t_{k-1}|t_{k-1}), \quad (24)$$

$$\mathbf{P}(t_k|t_{k-1}) = \Phi(t_k, t_{k-1})\mathbf{P}(t_{k-1}|t_{k-1})\Phi^T(t_k, t_{k-1}) + \mathbf{Q}'(t_k). \quad (25)$$

The filtering equations from  $\hat{\mathbf{x}}(t_k|t_{k-1})$  to  $\hat{\mathbf{x}}(t_k|t_k)$  are similar to the recursive LS estimation, Eqs. (17), (18), (19). We have the discrete KF equations:

$$\mathbf{y}(t_k|t_{k-1}) = \mathbf{y}_{\text{ref}}(t_k) + \mathbf{x}(t_k|t_{k-1}) \quad (26)$$

$$b(t_k) = z(t_k) - h[\mathbf{y}(t_k|t_{k-1}), t_k] \quad (27)$$

$$L(t_k) = \mathbf{A}(t_k, t_k)\mathbf{P}(t_k|t_{k-1})\mathbf{A}^T(t_k, t_k) + R(t_k) \quad (28)$$

$$\mathbf{K}(t_k) = \mathbf{P}(t_k|t_{k-1})\mathbf{A}^T(t_k, t_k)L^{-1}(t_k) \quad (29)$$

$$\hat{\mathbf{x}}(t_k|t_k) = \hat{\mathbf{x}}(t_k|t_{k-1}) + \mathbf{K}(t_k)[b(t_k) - \mathbf{A}(t_k, t_k)\hat{\mathbf{x}}(t_k|t_{k-1})] \quad (30)$$

$$\mathbf{P}(t_k|t_k) = \mathbf{P}(t_k|t_{k-1}) - L(t_k)\mathbf{K}(t_k)\mathbf{K}^T(t_k) \quad (31)$$

The *extended* discrete Kalman-Filter relinearises about each new estimate :

$$\mathbf{y}_{\text{ref}}(t) = \hat{\mathbf{y}}(t|t_{k-1}), \quad \mathbf{x}(t) = \mathbf{y}(t) - \hat{\mathbf{y}}(t|t_{k-1}) \quad \text{for } t_{k-1} \leq t \leq t_k \quad (32)$$

Equations can now be rewritten in terms of the original state vector  $\mathbf{y}$  instead of the auxiliary vector  $\mathbf{x}$ . Indeed,  $\mathbf{y}(t_k|t_{k-1})$  may be obtained through integration of the equations

$$\frac{d}{dt}\hat{\mathbf{y}}(t|t_{k-1}) = \mathbf{f}[\hat{\mathbf{y}}(t|t_{k-1}), t]. \quad (33)$$

From Eq. (32) one has  $\hat{\mathbf{x}}(t_k|t_{k-1}) = \mathbf{0}$  so using the explicit form of  $b(t_k)$  in Eq. (27) the filter update equation Eq. (30) becomes, adding  $\hat{\mathbf{y}}(t_k|t_{k-1})$  to both sides :

$$\hat{\mathbf{y}}(t_k|t_k) = \hat{\mathbf{y}}(t_k|t_{k-1}) + \mathbf{K}(t_k)\{z(t_k) - h[\hat{\mathbf{y}}(t_k|t_{k-1}), t_k]\}. \quad (34)$$

In the *continuous-discrete* EKF, differential equations for the covariance matrix can also be derived from Eq. (25) by differentiation with respect to  $t_k$ , using Eqs. (15), (23) and (25) :

$$\frac{d}{dt}\mathbf{P}(t|t_{k-1}) = \mathbf{F}(t)\mathbf{P}(t|t_{k-1}) + \mathbf{P}(t|t_{k-1})\mathbf{F}^T(t) + \mathbf{Q}(t). \quad (35)$$

## DEVELOPMENT OF A CONTINUOUS-DISCRETE EKF

DLR's program ORBIT<sup>3</sup>, which is in use at SES, implements a Square Root information filter formulation of the LS method, wherein tracking data are treated sequentially. Each time a new measurement is processed the QR-factorization of the design matrix Eq. (8),  $A = Q \cdot R$ , where  $Q$  is an orthogonal matrix constructed by the accumulation of Givens rotation matrices and  $R$  is an upper triangular factor, is updated. By contrast to a recursive LS, the resulting system of equations is only solved once after all measurements have been processed in order to obtain the desired estimates. This feature made it quite easy to implement an EKF with maximum re-use of the existing ORBIT code; the sequential accumulation step was replaced by the Kalman filtering step of Eqs. (28, 29, 34, 31), while propagation of the state and transition matrix between measurements in the LS, Eqs. (1, 15), was replaced by the propagation of the estimate and covariance matrix, Eqs. (33, 35). Note that in practice the LS code splits the transition matrix of Eq. (15) into a  $6 \times 6$  state transition matrix associated to the position/velocity vector and a so-called sensitivity matrix  $S$  associated to the model parameters; this feature does not apply to the EKF formulation.

A main orbit estimation package ORBIT\_OD, shown in Figure 1, implements functions to initialize the filter, loop over measurements, propagate differential equations to the new measurement time (through procedures in package ORBINT) and process the data. Since further interpolation of the state and covariance matrix is required for light-time correction<sup>3</sup>, the time update of the EKF (which consists in assigning propagation results to private internal structures of the filter) is not performed directly after the propagation step but only after light-time correction. Measurement processing also involves computing  $h[y(t_k), t_k]$  and  $A(t_k, t) = \partial h[y(t_k), t_k] / \partial y(t)$  and subsequently realizing the filter measurement update, Eqs. (28, 29, 34, 31), through a KALMANLIB procedure.

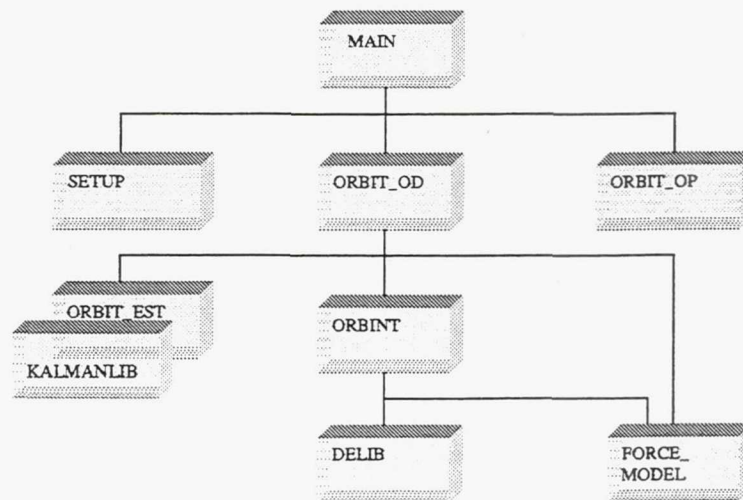


Fig. 1.— Package dependencies in program ORBIT. SETUP: process user inputs; ORBIT\_OD: orbit determination; ORBIT\_OP: orbit propagation; ORBIT\_EST: non-linear LS; KALMANLIB: Kalman filtering; ORBINT: integration and interpolation of trajectory and covariance or transition matrix; FORCE\_MODEL: computation of differential equations right hand side; DELIB: numerical integrator.

Compared to the LS version of ORBIT\_OD, the procedure contains one less level of iteration, and no further processing is required on exit of the main measurements loop, while the LS implementation



calls a set of ORBIT\_EST procedures to solve for the estimates, compute the covariance matrix and update estimation parameters with the solution of the LS system. Another major difference is that for the EKF, the multi-step numerical integrator needs to be restarted at each new measurement due to the update of the reference trajectory, Eq. (32). Like the LS version of ORBIT, our EKF implementation has the capability to estimate the 6 components of the position/velocity vector, the 2 in-plane components of the solar radiation force and a drag coefficient. It also involves the 3 components of a maneuver thrust vector, for a total of 12 solve-for parameters.

The original ORBIT code comprises 47 Ada packages, 4 of which required modification:

- Main program : involved very limited changes, concerning mainly the size of the covariance matrix which was extended from  $6 \times 6$  to  $12 \times 12$ .
- ORBIT\_OD package : reflects the changes mentioned above
- Integrator package ORBINT : the sensitivity matrix was removed as argument of the various procedures; the state transition matrix was replaced by the covariance matrix.
- FORCE\_MODEL package : the sensitivity matrix was removed as argument of the various procedures and the state transition matrix was replaced by the covariance matrix. The procedure that integrates the variational equations Eq. (15) was replaced by a corresponding procedure that integrates the covariance matrix equation, Eq. (35). Since the same partial derivative information, Eq. (16), is required in both cases on the right hand side of the equations, modifications were again minimized.

The specific package KALMANLIB was finally implemented to replace the package ORBIT\_EST of the LS version. It defines specific data structures for the EKF and procedures for EKF initialization, time update, measurement update and retrieval of estimation results from private EKF structures. In total about 630 lines of code were changed in existing packages and 290 lines of code were added in new packages.

## ESTIMATOR ACCURACY EVALUATION USING SIMULATIONS

In this chapter, we will describe how the performances of the LS and EKF estimators were compared in a systematic way using Monte Carlo simulations. The comparison greatly takes advantage of the large commonality between the software implementation of the two algorithms, so that any bias related to the use of different propagation or observation models is avoided. Artificial trajectories - which may include dynamical effects not actually modelled in the estimation software - are generated and subsequently observed through an observation function, which includes a model of random and systematic measurement errors. The observations are then processed by the LS and EKF versions of the ORBIT program, and estimated trajectories are compared to the reference artificial trajectory. Comparison results are accumulated over a large sample of realizations of the tracking data and are analyzed statistically. This process has been systematized through a dedicated simulation software, whose architecture is depicted in Figure 2.

Actual tracking data are used as a reference and processed through our standard LS version of ORBIT. The estimation residuals are stored, and an artificial trajectory corresponding to the observed tracking data arc is generated, along with a set of "perfect" artificial tracking data (without observation errors) and a dense interpolation table of the reference trajectory, to be used for subsequent comparison with estimation results.



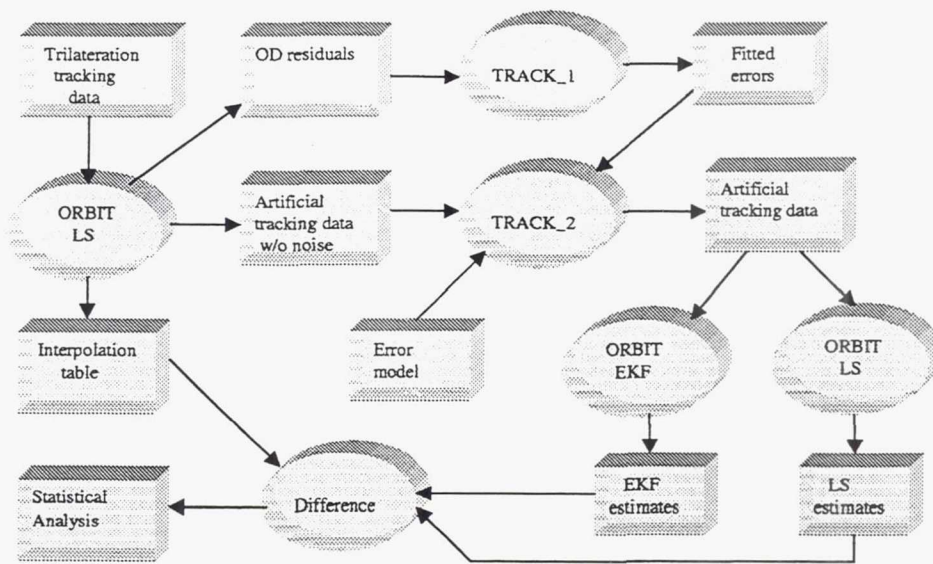


Fig. 2.— Data flow diagram of the tracking data simulation software.

In a second step, the estimation residuals are analyzed through a module TRACK\_1, which fits the observed statistical distribution of residuals as a function of time and models the observed temporal distribution of the tracking data. In a third step, a module TRACK\_2 adds random noise to the “perfect” artificial tracking data; this noise corresponds to the residual distribution model generated previously - which is conservatively considered to be part of the observation error model. It also filters the tracking data according to the temporal distribution model and, last but not least, superimposes an a-priori model of the observation errors. This model is meant to account for errors which may not be directly observable in OD residual patterns, but can be assumed from a physical knowledge of the observation process, like unmodelled ionospheric refraction, station calibration or spacecraft delay uncertainties. This model takes the form

$$\delta_i = \eta_i^1 + \eta_i^2 t + \eta_i^3 \sin(\psi t - \eta_i^4) + [\Theta(\varphi_i) \eta_i^5 + \Theta(-\varphi_i) \eta_i^6] \sin \varphi_i, \quad \varphi_i \equiv \psi t - \eta_i^7 \quad (36)$$

where the index  $i$  runs over the different measurement stations,  $t$  is the observation time,  $\psi$  denotes the Earth's angular velocity,  $\Theta(x) = 0$  if  $x < 0$  and  $\Theta(x) = 1$  if  $x \geq 0$  and each of the coefficients  $\eta_i^j$ ,  $j = 1, \dots, 7$  is a Gaussian random variable characterized by its mean and standard deviation. These parameters remain constant over each realization of the full tracking data set, and different realizations of these random variables are obtained by repeating a number of times the whole artificial tracking data generation process.

Once the artificial tracking data have been generated, they are processed using both the LS and EKF versions of the ORBIT program. The EKF produces a new estimation after each tracking data while, for the LS, the estimation is repeated over increasing slices of the data and the estimated orbit is propagated up to the end of the data slice. The estimated position and velocity vectors at the successive times are then compared to the true reference trajectory by using the interpolation table generated in the first step, and the resulting errors are stored for subsequent statistical analysis. The whole process is then repeated until enough data have been accumulated to yield statistically significant results.

The statistical analysis proceeds by propagating, for each estimate, the difference between the true and estimated spacecraft positions over one orbital period and extracting the minimum and maximum position discrepancies along each of the three axes of the spacecraft local frame. Minimum and maximum values contribute together to the position error statistics along each axis. Population parameters are then computed along with an associated confidence interval estimate. The number of samples needed to obtain the confidence interval corresponding to a fixed confidence level can then be computed, directing the system whether or not to proceed with further simulations. The Kolmogorov-Smirnov test is finally applied to test the normality of the populations.

## SIMULATION RESULTS AND DISCUSSION

For single-station tracking, simulations were performed for a station located in Betzdorf (Luxembourg), using spread-spectrum ranging and an accurate tracking antenna providing azimuth and elevation data with an accuracy better than  $0^{\circ}.01$ . For trilateration, simulations were performed assuming a master station located in Betzdorf and three slave stations, ranging successively each of the 7 ASTRA satellites for about 10 minutes.

In both cases a real data span of 2 days without maneuver was used as input for residuals analysis. The resulting a-posteriori measurement error statistics was combined with an a-priori error model characterized by the parameters of Table 1 in order to generate the artificial data. Coefficient  $\eta_i^1$  was assumed to represent station calibration and position errors;  $\eta_i^2$  was used to represent equipment drifts,  $\eta_i^3$  and  $\eta_i^4$  represent daily variations of satellite transponder delays and possibly solid Earth tides and  $\eta_i^5$ ,  $\eta_i^6$  and  $\eta_i^7$  are dedicated to the modelling of day and night components of the ionospheric refraction. Other sources of error, like inaccuracies in the modelling of the tropospheric refraction, may also be considered to be included in these coefficients.

Table 1: Error model parameters used in simulations. The factor  $\rho_i$  in the range error coefficients  $\eta_i^5$ ,  $\eta_i^6$  is defined as  $\rho_i = \sin^{-1} \epsilon_i$  where  $\epsilon_i$  is the spacecraft elevation at the  $i$ -th station.

Model parameter	range		azimuth		elevation	
	mean	rms	mean	rms	mean	rms
$\eta_i^1$	0.00 m	2.00 m	0".00	4".00	0".00	6".00
$\eta_i^2$	0.00 m/day	0.10 m/day	0".00 /day	3".00 /day	0".00 /day	5".00 /day
$\eta_i^3$	0.00 m	0.20 m	0".00	4".00	0".00	5".00
$\eta_i^4$	1.57 rad	1.00 rad	1.57 rad	1.00 rad	1.57 rad	1.00 rad
$\eta_i^5$	$\rho_i \times 0.53$ m	$\rho_i \times 0.37$ m	0".00	0".00	0".00	0".00
$\eta_i^6$	$\rho_i \times 0.05$ m	$\rho_i \times 0.04$ m	0".00	0".00	0".00	0".00
$\eta_i^7$	1.57 rad	0.26 rad	0.00 rad	0.00 rad	0.00 rad	0.00 rad

In addition to the measurement error model, simulations discussed in this paper take into account an imperfect modelling of the trajectory in the estimation softwares. To this end, the reference trajectory was generated by using a modified version of the ORBIT propagator, which models the solar radiation force applied on the reflectors of the satellite. By contrast, this dynamical effect is not modelled by the estimators, which only have the capability to estimate inertially fixed components of the solar pressure. Orbit estimations were started with an initial guess error consistent with typical estimation accuracies shown below, namely in the order of 1000 m for the position and



10 mm/s in velocity in each direction for single-station tracking and 100 m and 1 mm/s respectively for trilateration. The initial covariance matrix was input to be  $(10 \text{ km})^2$  for the position and  $(1 \text{ m/s})^2$  for the velocity vector components. For single-station tracking a Kalman filter input noise covariance of  $(10^{-7} \text{ m s}^{-2})^2$  was applied to each component of the velocity vector; for trilateration this value was reduced to  $(10^{-9} \text{ m s}^{-2})^2$ . These values were optimized based on simulation results so as to avoid divergence of the filter while maximising the estimation accuracy.

Simulation results were statistically analysed as described in the previous chapter. As a first example, Table 2 shows the mean and standard deviations of the LS and EKF estimation errors along the three directions, for 2 days of single- and multi-station tracking. The LS appears to yield better estimates for single-station tracking while both estimators provide similar results for trilateration. Trilateration is also seen to provide an improvement of more than an order of magnitude in accuracy.

Table 2: Accuracy of the LS and EKF for single- and multi-station tracking (100 realizations).

tracking system/ method	mean position diff. [m]			rms position diff. [m]		
	radial	tangential	normal	radial	tangential	normal
single-station / LS	0.60	-31.69	0.06	131.33	298.99	1036.59
single-station / EKF	1.57	-73.70	0.04	194.23	754.40	1526.83
multi-station / LS	0.57	-5.67	-0.82	3.98	85.32	21.74
multi-station / EKF	0.39	-2.78	-1.70	4.55	73.99	30.33

More detailed analysis results will now be presented for the case of trilateration. Figure 3 shows the evolution of the normal component of the position estimation error for the LS and EKF, sampled over successive tracking intervals of 3, 6, 9, 12, 18, 24, 36 and 48 hours. The figure shows the mean error and its associated confidence interval computed from Student's distribution, corresponding to a confidence level of 99.9%, along with the  $3\sigma$  error band. Note that as in most cases the Kolmogorov-Smirnov test did not allow to conclude to the normality of the populations, corresponding statistics and confidence intervals for the standard deviation are difficult to obtain. No significant estimation

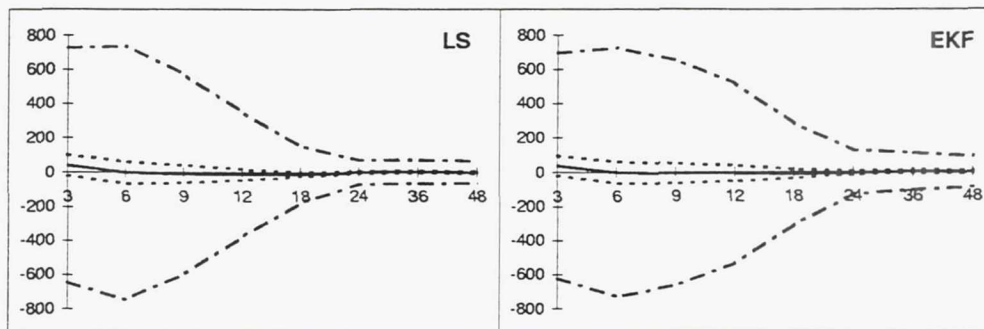


Fig. 3.— Evolution of the normal component of the position estimation error (in m) for the LS and EKF as a function of the tracking interval (in hours). Solid line: mean position error; dotted lines: associated confidence interval at 0.1%, dash-dotted lines:  $3\sigma$  error band. Statistics are over 100 realizations.

bias can be detected; the behaviour of both estimator looks rather similar, although it may be observed that the  $3\sigma$  error band of the LS reduces slightly faster than that of the EKF.



In order to further compare the two estimators, we introduced the concept of a worst-case error estimate defined as the sum of the absolute values of the error mean, half-width of the associated confidence interval and 3 times the observed standard deviation of the estimates. Figures 4 shows the evolution of this worst case error for both estimators and all three components of the position.

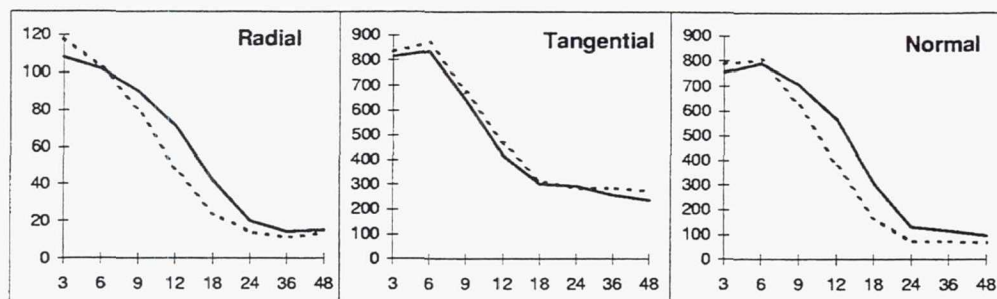


Fig. 4.— Evolution of the worst case estimation errors along the radial, tangential and normal directions (in m) as a function of the tracking interval (in hours). Solid line: EKF; dashed line: LS. Statistics are over 100 realizations.

Both estimators are seen to be almost equivalent for the estimation of the tangential component. There seems to be a slight advantage to the LS in terms of the two other components; the difference is however not large enough to draw any definitive conclusion.

Note that in addition to the simulations presented above, a significant number of other simulation cases were analysed, for different values of the initial guess error, of the Kalman filter's input spectral density matrix, of the error model parameters and different combinations of tracking stations. In general, however, the results confirm the above conclusion that none of the methods seems to exhibit a significant advantage over the other one.

## OPERATIONAL IMPLEMENTATION OF THE ALGORITHMS

Kalman Filters are often considered operationally superior to Batch LS algorithms due to their capability to provide a real-time update of the estimate triggered by the arrival of new measurements. However, for geostationary satellites, the time elapsed between consecutive measurements is typically a very small fraction of the orbital period and there is practically no advantage in getting an update at each measurement. On the other hand the performances of modern computers make the frequent processing of a large batch of data quite feasible. For example a typical Orbit Determination using the LS version of the ORBIT software and 4 days of trilateration data takes in the order of 10 seconds on a DEC/AXP 233MHz workstation. Based on these considerations, SES undertook some years ago the development of a quasi real-time orbit determination application (QRTOD) based on the ORBIT program. This application acts as a scheduler for ORBIT, which processes tracking data arcs over a moving time window. The previous estimate is usually taken as the new initial guess which guarantees convergence of the LS in only a few iterations. The overall architecture of this system is depicted in Figure 5. It is written in Ada, and reuses functions of the ORBIT application library for orbit propagation, database access and time format conversions. It contains 10 packages and some 3100 lines of code.

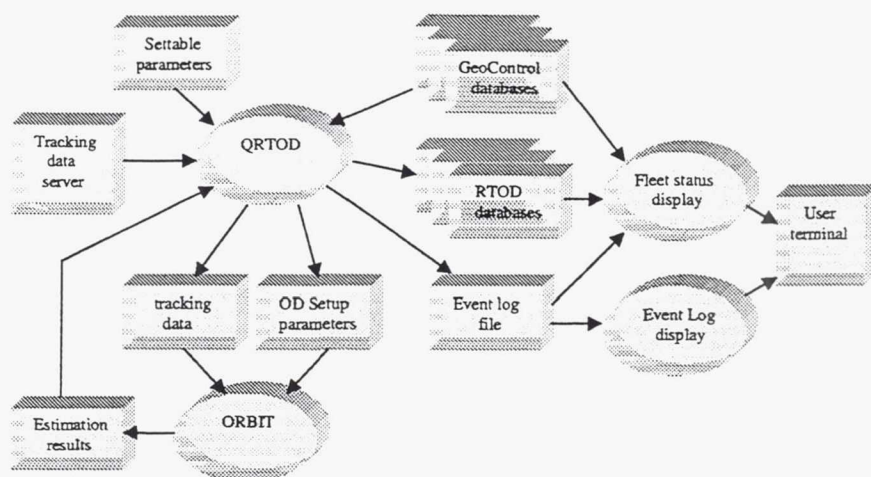


Fig. 5.— Data flow diagram of the QRTOD software.

The system operates in 4 modes: an initialisation mode with typically minimal number of solve-for parameters and modest accuracy requirements, a calibration mode used to calibrate biases over long coast arcs and E/W and N/S maneuver assessment modes. The system is fully integrated with the best knowledge orbit and maneuver database system of the *GeoControl* environment<sup>2</sup>. It automatically detects the occurrence of maneuvers and decides to solve for maneuver parameters as required. Its internal logic allows the determination of optimum tracking arcs based on criteria like maximum arc length and minimum data span before and after any maneuver, for each operating mode. Once the optimum tracking arc has been determined, the system propagates its latest state vector estimate to the beginning of the arc and retrieves all relevant tracking information from the tracking data server. Based on the particular circumstances, *e.g.* if it detects a long enough coast arc, it automatically decides to calibrate antenna angular biases. It has embedded self-correction algorithms which analyse the quality of the last orbit determination and takes appropriate measures to cure problems by *e.g.* modifying its set of solve-for parameters.

The system offers maximum flexibility as the user can fully configure the parameters like (1) the tracking data sources and types, (2) the corresponding default bias and standard deviation values, (3) the OD frequency, (4) the nominal tracking arc length, (5) the nominal duration of stay in maneuver assessment mode, (6) the maximum number of LS iterations, (7) culling limits, (8) dynamical model parameters, (9) the nominal list of solve-for parameters and (10) a list of thresholds on parameters like mean and standard deviation of residuals for each measurement type or state vector convergence parameters as used for quality estimation. Most of these parameters can be specified separately for each operating mode.

Once all Orbit Determination parameters have been established the QRTOD spawns the execution of the ORBIT program and retrieves its results upon completion of the task. Based on the quality estimation the system then decides whether or not to (1) update the external database, (2) update its internal state vector estimate, (3) update internal maneuver estimates, (4) update internal bias estimates, (5) retrieve new estimates from the external database, (6) reload default parameters, (7) return to robust initialization mode.

The system maintains its own best knowledge database by merging at all times in a consistent



way its most up-to-date estimation information with the most up-to-date planning information available in the standard *GeoControl* database<sup>2</sup>. It involves several display functions which allow to either monitor the correct behavior of the system or get a summary status of the latest orbit and maneuvers estimation for the entire fleet, by comparing assessment to prediction information.

The EKF code currently in use at SES does not have the same level of sophistication as the QRTOD system, as it is essentially being used for evaluation purposes. Note that a limitation of our current EKF implementation is its capability to evaluate a single maneuver at a time; once a new maneuver takes place the filter's covariance matrix needs to be updated, which can be done in practice by stopping the filter once the estimation of the previous maneuver has converged and restarting it with the new maneuver prediction. Furthermore our EKF does not have the capability to estimate measurement biases. Finally our EKF implementation does not include the type of self-correcting algorithms embedded in the QRTOD. It may be envisaged, in the future, to implement such actions as modifying the filter's input spectral density matrix based on a monitoring of the residuals behaviour. However the implementation of the EKF is intrinsically simpler software-wise than that of the QRTOD, as neither the specific tracking arc selection logic nor the upper software layers contained in the QRTOD implementation for the sake of events scheduling and monitoring is required. Instead, a simple infinite loop waits for new measurements and processes them.

## OPERATIONAL EXPERIENCE

From an operational point of view, the single-station tracking system consists in a set of ranging units and a single antenna tracking successively the different satellites; trilateration consists in 4 stations ranging successively each satellite for about 10 minutes and sending the tracking data, along with local meteorological data used for tropospheric refraction correction, via a satellite transponder back to the master station in Betzdorf. Figure 6 shows typical range residuals, corresponding to a LS orbit determination performed using 4 stations over a period of 8 days; the initial state vector, 2 in-plane components of the solar radiation force and a satellite transponder delay were estimated. The assumption of white Gaussian measurement noise as the dominant error source cannot be confirmed, as systematic errors with characteristic periods of fractions of one day can be observed. However the residuals amplitude over this period (about 1 m) is remarkable, demonstrating the accuracy of the measurement device as well as of the ORBIT propagation and observation models.

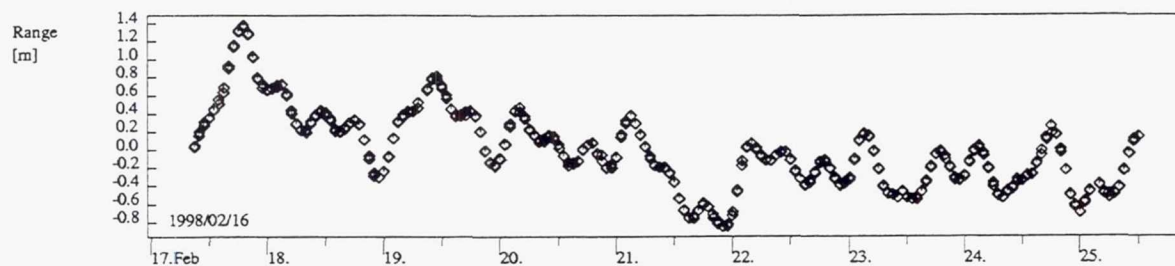


Fig. 6.— Example of LS range residuals from a trilateration slave station.

A way to practically assess the OD accuracy is to perform an estimation, propagate the estimate at a future time and subsequently verify this prediction. The following procedure was applied:



1. perform an orbit determination for a first 3-day tracking interval  $[t_{a_1}, t_{a_2}]$
2. predict the state vector  $\mathbf{y}_a(t)$  at the future epoch  $t = t_{a_2} + 5 \text{ days}$ .
3. perform an orbit determination for a second 3-day tracking interval  $[t_{b_1}, t_{b_2}]$  centered around  $t$  and determine the state vector  $\mathbf{y}_b(t)$  at epoch  $t$ .
4. propagate the relative state vector  $\mathbf{y}_b(t) - \mathbf{y}_a(t)$  over one orbital period and compute the maximum difference along each component in the spacecraft local reference frame.

Table 3: Accuracy of orbit prediction (see explanation in the text) resulting from an average over 7 satellites. The EKF input noise variance was taken to be  $(3 \times 10^{-8} \text{ m s}^{-2})^2$ .

tracking system/ method	max. position diff. [m]			max. velocity diff. [mm/s]		
	radial	tangential	normal	radial	tangential	normal
single-station / LS	84	428	620	5.9	12.1	45.2
multi-station / LS	5.0	87.0	6.0	0.24	0.67	0.44
multi-station / EKF	5.1	71.3	5.8	0.24	0.68	0.42

Table 3 summarizes the differences so obtained; the multi-station tracking system is seen to be almost two orders of magnitude more accurate than the single-station system for the estimation of the normal component and one order of magnitude more accurate for the two in-plane components. Results are seen to be almost similar for the LS and EKF estimators, and confirm the simulation results presented above.

Beside an accurate estimation of the satellite position and velocity vectors, it is operationally important to be able to accurately assess maneuver performances. For instance, accurate estimation

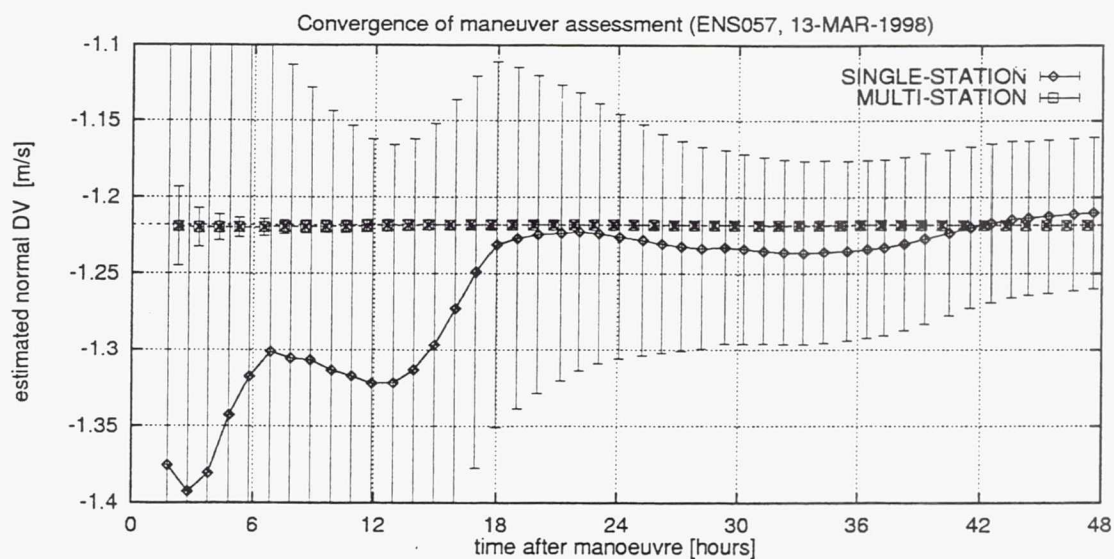


Fig. 7.— Convergence of Astra N/S maneuver estimations using single- and multi-station tracking. Shown are the estimated normal velocity increment and the associated  $3\sigma$  confidence interval.

of maneuver parameters is required to properly calibrate thrusters, assess the seasonal variations of thruster performances or monitor the health of the propulsion subsystem. Another important aspect of the problem is the amount and the time-span of post-maneuver tracking data required to be able to assess a maneuver with a given accuracy level. Indeed, the faster the maneuver can be assessed, the safer the satellites can be co-located, since one can react faster to misperformances or anomalies. While from this point of view single-station tracking is satisfactory for E/W-maneuvers, N/S maneuvers are difficult to assess in a reasonably short period after the maneuver as typically 24 to 48 hours of data are required. Here again, multi-station tracking substantially improves the situation. This can be seen in Figure 7, which shows the typical evolution of QRTOD maneuver estimates as a function of time, for the two tracking systems. It can be observed that three hours of post maneuver tracking using the trilateration system yield more accurate results than two days of single station tracking.

## CONCLUSIONS

We have described the actual implementation of LS and EKF estimators at SES; we have emphasized how both implementations were derived from a common basis and how differences were limited, software-wise, to only a few specific estimation modules. We have described the dedicated simulation software developed to compare our implementations of both estimators, and concluded that in the context of SES's trilateration tracking system our LS and EKF estimators were essentially equivalent in terms of accuracy. We have also compared our implementations of the two methods from an operational point of view, showing that the specific QRTOD software built by SES around the LS software could provide a flexibility equal or superior to that of our current EKF implementation. We have also presented actual operational experience, which confirms the conclusions of our simulations and demonstrates the significant enhancement of orbit determination accuracy, brought by the trilateration system. We showed in particular that this system allowed to greatly improve the monitoring of the station-keeping maneuver performances as well as their calibration.

## REFERENCES

1. P. Wauthier, P. Francken and H. Laroche, *Co-location of 6 Astra satellites : assessment after one year of operations*, Proceedings of the 12th International Symposium on Space Flight Dynamics, Darmstadt, 1997.
2. O. Montenbruck, M.C. Eckstein and J. Gonner, *The GeoControl System for Station Keeping and Colocation of Geostationary Satellites*, Second Symposium on Ground Data Systems for Space Mission Operations (Spaceops), Pasadena, 1992.
3. P. Francken, P. Wauthier and O. Montenbruck, *Advanced Tracking and Orbit Determination for Geostationary Satellites with Ionic Propulsion*, Proceedings of the 12th International Symposium on Space Flight Dynamics, Darmstadt, 1997.



## SOHO AND WIND ORBIT DETERMINATION USING A SEQUENTIAL FILTER

Richard Hujsak<sup>1</sup>, Ned Stein<sup>2</sup>, William Chuba, Todd Rose  
Logicon<sup>3</sup> Geodynamics, Exton, PA. & Sunnyvale, CA.

SOHO and WIND are solar observing satellites which can be characterized as deep space orbits which remain in the vicinity of the Earth. They are tracked via NASA's Deep Space Network and operated from Goddard Space Flight Center. The orbits for SOHO and WIND are operationally determined by the Goddard Trajectory Determination System (GTDS) using batch least squares. For this analysis the orbits are determined with a sequential filter, a modified version of RTOD<sup>®</sup>, and the ephemerides are compared to GTDS-derived products. The SOHO case was uneventful and provided the basis for verifying the new DSN measurement models in RTOD<sup>®</sup>. The test case for WIND contained three maneuvers, a perigee passage, an outgoing lunar fly-by, and a leap second. The filter successfully processed through all events, including maneuvers, without manual intervention, and generated a single continuous ephemeris file, while GTDS was run in five batches to work around maneuver events. Differences between the filter ephemeris and the five GTDS ephemerides were generally smaller than the abutment error between successive GTDS ephemerides, with no appreciable degradation in the RTOD<sup>®</sup> ephemeris during or following maneuver events. These results demonstrate that a filter is a robust alternative to least squares for this class of orbits. These results also demonstrate a level of automation in the presence of maneuvers which is generally unachievable with least squares methods, implying that a filter is a strong candidate for NASA's effort to achieve a "lights out" operational capability.

### INTRODUCTION

The authors have spent much of the last decade demonstrating that orbit determination using a sequential filter is a viable alternative to orbit determination based on least squares methods. Filter-derived ephemerides have proven to be as accurate or more accurate than those generated with least squares. More importantly the filter has been demonstrated to be a fully automated process, and should be a viable candidate for fully automated, or "lights out", satellite operations. This particular analysis addresses solar observing satellites SOHO and WIND, which are tracked through NASA's Deep Space Network (DSN). This is the first attempt by the authors to process DSN tracking data and the first attempt to determine orbits for this class of objects. Our objective is to once again demonstrate the accuracy and degree of autonomy that can be achieved with filter-based orbit determination.

---

<sup>1</sup>760 Constitution Dr. Suite 30, Exton, PA, 19341, (610) 458-3330, dhujak@logicon.com.

<sup>2</sup> 1150 N. Fair Oaks Ave., Sunnyvale, CA, 94089, (408) 745-1310, nstein@logicon.com.

<sup>3</sup> Logicon is a wholly owned subsidiary of Northrop Grumman.



The sequential filter used for this analysis is an engineering variant to our proprietary orbit determination product, RTOD<sup>®</sup>, which was originally developed in 1988 through a Small Business Innovative Research (SBIR) project funded by NASA Goddard Space Flight Center (GSFC). At that time GSFC was investigating simultaneous sequential orbit determination as an alternative to the Goddard Trajectory Determination System (GTDS) when applied to the Tracking and Data Relay Satellite System (TDRSS) and the user satellites serviced by TDRSS. GSFC and Computer Sciences Corporation (CSC) tested<sup>1,2,3,4,5</sup> an early version, called RTOD/E over a period of three years. In the final report<sup>6</sup> they say "The comparison of the RTOD/E estimates for EUVE, ERBS, COBE, Landsat-4, and TOPEX/Poseidon with external results shows the filter capable of quite accurate results, and can certainly meet the accuracy requirements for daily operational support for the TDRSS user spacecraft and the TDRSs". The same report does note a deficiency in RTOD/E in processing through TDRS maneuvers. These reports do not indicate the degree of automation that a filter brings to satellite operations. That is unfortunate, considering that NASA now seeks to automate satellite operations on a large scale, with a stated objective of "lights-out" operations.

Since that time RTOD<sup>®</sup> has matured and evolved into a true real-time process with the capability to process tracking data from multiple systems. RTOD<sup>®</sup> has been applied, sometimes as an engineering variant, to TDRSS, AFSCN, SSN, GPS, and SLR applications. The filter now processes through all forms of TDRS maneuvers automatically (provided that a TDRS Maneuver Message is input automatically). In an study of military geosynchronous satellites<sup>7</sup>, the filter was shown to provide recovery-of-accuracy with a minimum of post-maneuver tracking data. When an engineering variant of the RTOD<sup>®</sup> filter was mated to a matching smoother and applied to SLR data for TOPEX, with the TOPEX yaw profile incorporated, the resultant ephemeris proved to be as accurate as the NASA POE<sup>8</sup>.

For the SOHO and WIND missions accuracy is not an issue. It appears that GTDS fully satisfies all of the operational requirements for accuracy. Our analysis shows RTOD<sup>®</sup> and GTDS to have comparable accuracy, so RTOD<sup>®</sup> accuracy is not an issue for these missions. NASA has requirements other than accuracy, and now seeks to fully automate orbit determination, including an active investigation of AI methods of controlling and monitoring GTDS processing for resident missions. Orbit determination for these solar observing missions can be automated most of the time, but events such as maneuvers still require orbit analyst attention. Maneuvers also pose challenging problems for AI rules. Our analysis will demonstrate how the filter can process through a variety of events (maneuvers, a lunar swing-by, perigee passage and even a leap second) without manual intervention and without an AI process control. It is in this automation of orbit determination that the filter appears to have some distinct advantages over least squares.

This analysis was performed using Logicon IR&D funding. Release of tracking data to Logicon was authorized by Tom Stengle, NASA GSFC.

## DATA DESCRIPTION

Test data was requested from NASA GSFC and, upon approval, provided by CSC personnel. This data consisted of initial conditions, force modeling parameters, GTDS ephemerides, tracking data for key segments of the NASA SOHO and WIND missions, and tracking data format definitions. The GTDS ephemerides which were provided were generated by CSC personnel in an off-line activity and are not necessarily the same as the operational ephemerides over the same time period.

Deep Space Network (DSN) has a variety of formats, providing Doppler in the DT-2 format and/or in the Universal Tracking Data Format (UTDF) and range in the DT-5 format. Due to limited resources this analysis was restricted to DT-5 range data (however GTDS solutions used all available range and Doppler data).

### SOHO Data

SOHO mission data consists of initial trajectory and force model parameters, DT5 range data from days 196-239 (Jul. 15 to Aug. 27), and a single GTDS ephemeris for days 209-274 (Jul. 28 to Oct. 1). At this time SOHO was orbiting between the earth and Sun at a distance of approximately 230 earth radii from the Earth. There were no maneuver events in this data set.

The SOHO filter used all of the DT-5 range tracking data, while the GTDS fit interval was shorter. The majority of the data was collected from the 34-meter STD antenna at Canberra and the 26-meter antennas at Canberra and Madrid. Some addition, passes were collected from the 34-meter STD antenna at Madrid, the Goldstone 26-meter antenna, and the 34-meter BWG Goldstone antenna.

### WIND Data

Data for the WIND mission was made available just prior to completion of this study and was included without special tuning of the filter. This consisted of DT5 measurement data from days 161-226 (Jun. 10 to Aug. 14) and associated GTDS ephemerides spanning days 161-263 (Jun. 1 to Sept. 20.)

The key events in this test case are summarized in Table 1, below.

**Table 1 "WIND ORBIT AND TRACKING EVENTS"**

Event	Date (1997)	Day-of-Year
Start Tracking Data	June 10	161
Perigee	June 12	163
Perigee Maneuver P20	June 12 03:25:16	163
Leap Second	June 30 24:00:00	181
Perigee	July 4	185
Perigee Maneuver P21	July 9 14:45:03	190
Perigee	July 26	207
Outbound Lunar Swingby	July 29	210
Correction Maneuver	Aug 12 15:00:40	224
End of Tracking Data	Aug 14	226



The WIND satellite maneuvered at one perigee (on June 12) and after the next perigee (on July 4) in preparation for a double lunar swingby. The outgoing lunar swingby is covered by the tracking data span. Each perigee occurs at roughly ten earth radii and the outgoing lunar swingby comes within seven earth radii of the Moon (approximately).

An overview of the WIND data processing timeline is depicted in Figure 1, below. The perigee passages are denoted by the letter "P". Vertical bars denote the start and end times of GTDS ephemerides.

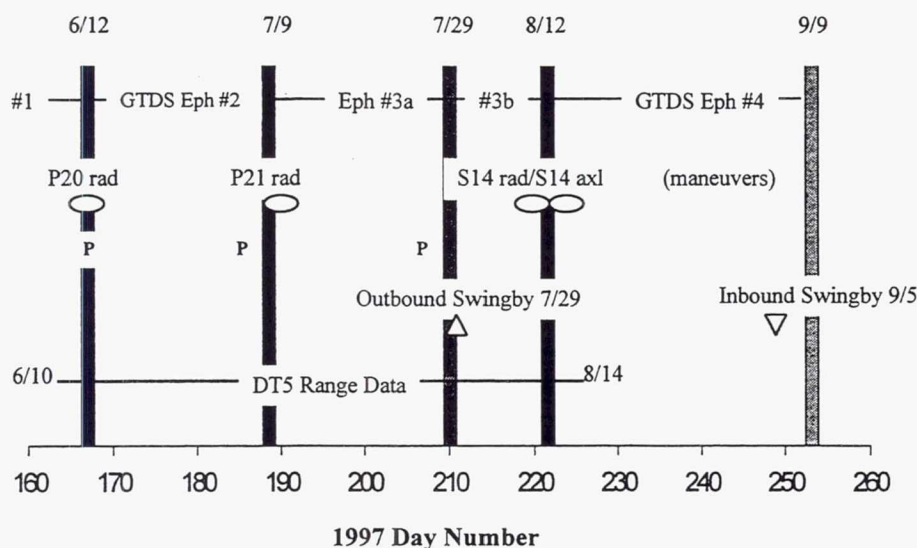


**Figure 1 "WIND Event Timeline"**

DT-5 range tracking data for WIND was collected primarily from two DSN sites, the 34-meter STD antenna at Madrid and the 34-meter BWG antenna at Goldstone. Other passes were contributed by the 34-meter STD antenna at Canberra, the 26-meter antenna at Canberra, and the 26-meter antenna at Goldstone.

## SOFTWARE MODIFICATIONS AND VERIFICATION

The baseline RTOD<sup>®</sup> was modified in several ways, resulting in an engineering variation on the configuration-controlled baseline. These modifications: (a.) changed the entire representation for state and covariance from equinoctial orbital elements to earth centered inertial position and velocity, (b.) replaced the Variation of Parameters orbit integrator with a Cowell Runge-Kutta algorithm, (c.) modified the input processor to read



the DSN DT-5 format for range and pass the ambiguous range and the ambiguity interval to the filter and (d.) modified the RTOD<sup>®</sup> filter range measurement model to resolve the DT-5 range ambiguity and generate a complete range measurement. Several references were useful in defining these changes<sup>9,10,11,12</sup>.

Software validation included: (a.) testing Cowell Runge-Kutta versus the baseline RTOD<sup>®</sup> Variation of Parameters integrator on a LANDSAT test case for accuracy and closure, (b.) testing a variety of Runge-Kutta algorithms for speed and accuracy, (c.) comparing force models between GTDS and RTOD<sup>®</sup>, (d.) comparing RTOD<sup>®</sup> to GTDS in a straight prediction for SOHO, and (e.) evaluating DT-5 range residuals for modeling errors (means and trends). Some of these verification analyses are discussed below.

For this analysis, the filter used a Runge-Kutta (8,12) integrator (eighth order, twelve force model evaluations), using a fixed step size of 600 minutes for SOHO and 60 minutes for WIND. (GTDS ephemerides were generated with a 12<sup>th</sup> order variable step predictor-corrector.)

RTOD<sup>®</sup> ephemeris predictions matched the GTDS SOHO predictions to within 1.5 meters over a 65 day predict span for SOHO, with slightly different solar pressure coefficients.

## FORCE MODEL AND COORDINATE SYSTEMS

The force model parameters are enumerated for each trajectory in Table 2.

Table 2 "FORCE MODEL CONTROLS"

<u>SOHO</u>	<u>GTDS</u>	<u>RTOD</u>
Geopotential	JGM 2, 8X8	EGM-96, 8X8
Solar Radiation, $C_R$	1.41	1.393 (Filter) <sup>4</sup>
SLP Bodies	Sun, Moon, Jupiter, Venus, Saturn, Mars	Sun, Moon, Jupiter, Venus, Saturn, Mars
<u>WIND</u>	<u>GTDS</u>	<u>RTOD</u>
Geopotential	JGM 2, 8X8	EGM-96, 8X8
Solar Radiation, $C_R$	1.67 - 1.70	1.69 (Filter)
SLP Bodies	Sun, Moon, Jupiter, Venus, Saturn, Mars	Sun, Moon, Jupiter, Venus, Saturn, Mars
Thrust	acceleration profile	constant acceleration

<sup>4</sup>  $C_R$  values used for RTOD/GTDS prediction comparisons were tuned to get the best agreement. The initial values for the final RTOD filter runs were not tuned and are indicated by the appellation, (Filter).

There are differences between RTOD<sup>®</sup> and GTDS models, the most significant being the solar pressure and maneuver models. RTOD<sup>®</sup> uses a sphere for a solar pressure model, as does GTDS, however some of the fundamental constants may be different, since it was necessary to fractionally increase the RTOD<sup>®</sup> value for  $C_R$  to obtain a good predictive match with GTDS, yielding the values quoted in Table 2. NASA provided thrust accelerations in tabulated form as is used in GTDS. RTOD<sup>®</sup> does not presently utilize tabulated thrust acceleration profiles, so a constant acceleration was used, defined as the time-average of the tabulated values.

## CALIBRATING THE FILTER

### Range Bias Calibration

The biggest concern in calibration of the range biases is the effects of the bias solutions on satellite position in intrack and crosstrack directions. For both SOHO and WIND trajectories, small changes in range bias can significantly affect both crosstrack and intrack position estimates. A change in a range bias on the order of 5 meters can change the SOHO orbit in the cross track direction by more than 2 kilometers.

Range bias calibration was complicated by a tendency for DSN tracking passes to have significant errors in reported range over the first few and last few minutes of each track. After confirming this behavior with CSC we simply omitted the "tails" in each tracking pass, both in calibration and in performance analyses.

The filter includes range biases as time-varying solve-for parameters for each station. A constant bias for each DSN antenna was determined using SOHO and removed. The remaining "bias" is treated as time-varying with a slow variation on the order of a few hours. Table 3 tabulates the fixed biases and the time-varying bias characteristics assigned to the filter.

**Table 3 "FILTER SOLVED-FOR RANGE BIASES"**

ANTENNA	BIAS (meters)	GAUSS-MARKOV SIGMA (meters)	GAUSS-MARKOV HALF LIFE (hours) <sup>5</sup>
DSS 16	0	5	3
DSS 24	0	5	3
DSS 46	-4	5	3
DSS 42	-3	5	3
DSS 66	0	5	3
DSS 61	0	5	3

Range noise statistics were set in two ways. Initially we applied a fixed noise of 0.5 meters, but the analyses presented here apply range noise statistics calculated on a

<sup>5</sup> Initial biases determined using 30 day half life.

measurement-by-measurement basis from the signal-to-noise statistics in the DT-5 message. The assignment of a time-varying range bias with amplitude of 5 meters is somewhat ad hoc. Calibration over a longer span would be required to provide significant gains.

The bias calibration exercise was performed with SOHO data, but it was later verified by processing SOHO and WIND in a simultaneous filter, solving for a common bias. The simultaneous solution found the biases to be independent of the mission over this data set. This is in contrast to information<sup>13</sup> indicating a 100 +/- 30 meter bias on the Goldstone 34-meter antenna (DSS-24) reported by the operational software supporting the WIND mission over this interval.

### **Solar Pressure Process Noise**

The solar pressure solve-for is an additive correction to  $C_R$ , and is treated as a Gauss-Markov process with exponentially correlated process noise. For SOHO this state was given an r.m.s. value of 0.01 and a half-life of 20 days. For WIND the r.m.s. was 0.10 and the half-life was assigned at one-half day.

### **Thrusting Process Noise**

The accuracy of the thrust acceleration profile was unknown, as was the accuracy of ignition time and burn duration, however we treated these as well-calibrated quantities, and assigned thrust magnitude sigmas as 2% of thrust and an ignition time uncertainty of 1 second (we were using telemetry values for ignition and duration).

### **FILTER PERFORMANCE - SOHO**

Figure 4 provides the differences between RTOD<sup>®</sup> and GTDS ephemerides over the RTOD<sup>®</sup> fit interval. The differences are presented in satellite-centered rotating coordinates, with radial (R) and crosstrack (C) directions properly named and with intrack (I) positive in the direction of motion but constrained to complete the orthonormal basis. The differences fall well within the operational requirements to support SOHO. Nevertheless we are tempted to closely examine the differences. Recall that there is just one GTDS ephemeris, the result of a fit to a set of tracking data, followed by a prediction. The filter solution, on the other hand, is a continually changing ephemeris, predicting between tracking passes and correcting during tracking. In addition the filter processes tracking data throughout the entire interval (RTOD<sup>®</sup> prediction testing is discussed above).



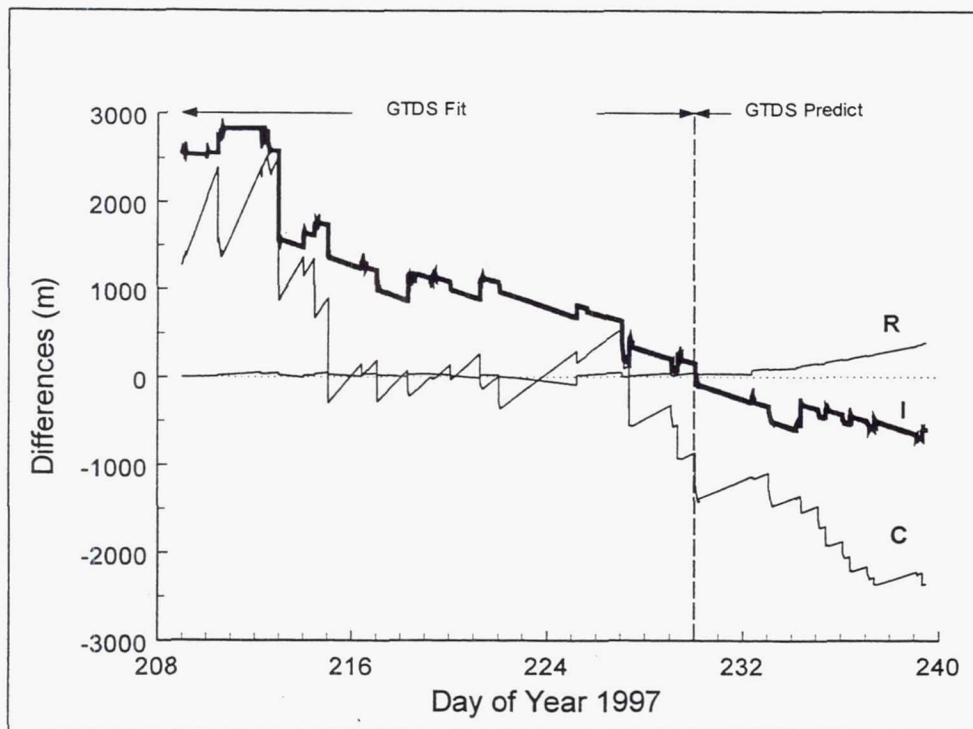


**Figure 2 "SOHO: RTOD® versus GTDS"**

The most noticeable feature of Figure 2 is the persistent trend in crosstrack and intrack differences. It would have been useful to have a second, abutting GTDS ephemeris to help determine whether this trend is due to GTDS or due to RTOD®. The trend is similar to one we will see later in the WIND results where it is clear that it is an artifact of the least squares fit. The intrack and crosstrack ephemeris differences between the RTOD® and GTDS solutions are consistent with a 5 meter uncertainty in range biases. The saw-toothed pattern is due to the filter continuously correcting the orbit plane, reflective of the uncertainty in the plane for SOHO at these very long tracking ranges.

Radial differences agree very nicely over the GTDS fit span and it is quite likely that the increase in radial differences over the prediction in Figure 2 is due to GTDS.

### SOHO Covariance

Figure 3 presents the two-sigma values as generated by the filter while processing SOHO data. The saw-toothed pattern is typical of a filter, with the covariance increasing during predictions and collapsing when tracking data is processed. If the filter is properly tuned and is complete in its statistical representation of significant error sources, then the covariance should be a realistic representation of the orbit errors. If we compare these covariance bounds to the RTOD® versus GTDS differences (Figure 2) and focus on the GTDS fit interval, we see that the differences fall within the covariance bounds. This comparison serves two purposes, it gives confidence that the differences between RTOD® and GTDS fall within the uncertainty in either process, and, conversely, provides some confidence that the covariance is a reasonable measure of the performance of the filter.

The latter conclusion is important in that it provides a measure of performance which can be monitored automatically, which is critical in a "lights-out" operational concept.

Notice that the covariance values do bound the differences between RTOD® and GTDS, except for the crosstrack difference during the GTDS prediction. If the covariance is realistic then we might conclude that the crosstrack tail in Figure 2 is due to the GTDS fit. Again it would be useful to have a second contiguous GTDS ephemeris.

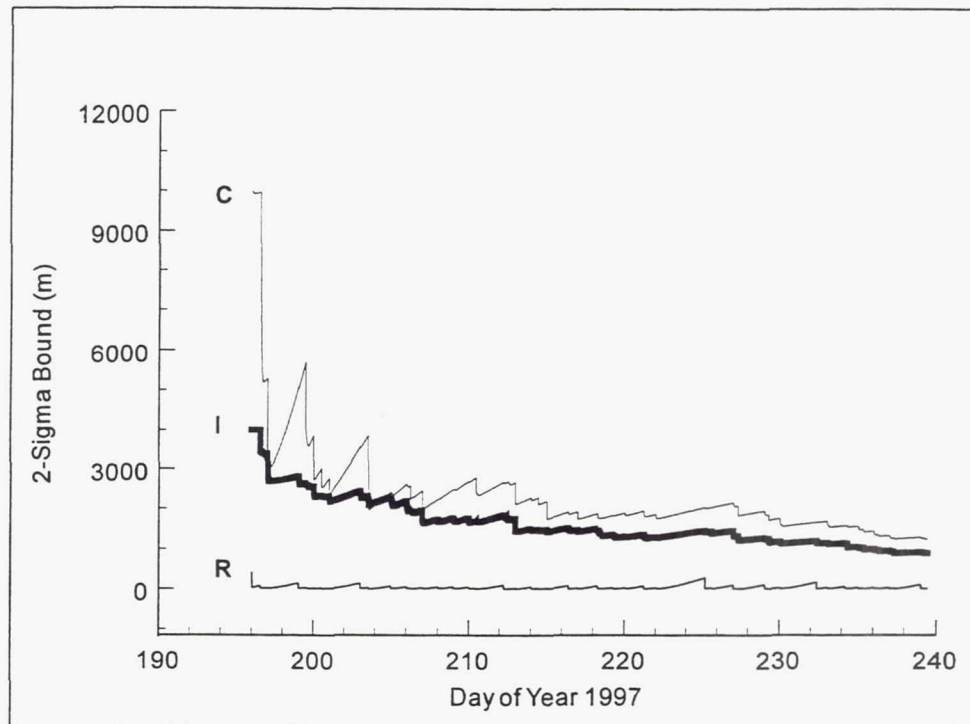


Figure 3 " RTOD® Radial Intrack / Crosstrack Covariance for SOHO"

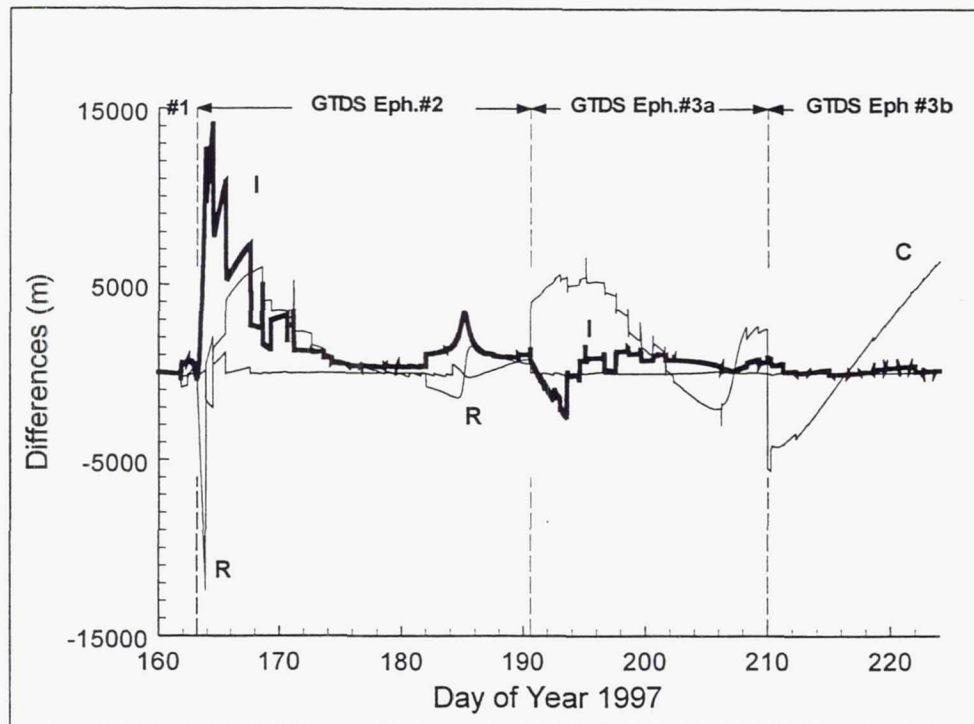
#### FILTER PERFORMANCE - WIND

Figure 4 provides a comparison of the RTOD® trajectory solution to for GTDS ephemerides for the WIND mission. Radial and crosstrack differences are both represented by thin lines, but the radial error is almost always close to zero, so these lines are easily distinguished. The intrack difference is the thicker line. All of the differences presented on this graph are well within the operating requirements for WIND, and in this case the filter provides an independent check of GTDS performance.

At the beginning of Figure 4 the large radial and intrack differences are probably due to the fact that the filter had not converged two days after initialization when a perigee maneuver occurred. (The abutment error between GTDS ephemeris #1 and #2 was less than 1 km.) At the second maneuver (day 190) the radial and intrack differences are well-behaved, which is expected for a converged filter.

The crosstrack differences show several kilometers of abutment error in successive GTDS ephemerides, first at the perigee maneuver time (day 190) and then

later at lunar swingby (day 210). These step functions were investigated to ensure that the step functions graphed were actually due to GTDS abutment errors and not due to some discontinuity in the filter. The magnitude of the step function in crosstrack was confirmed to be the magnitude of the abutment error.



**Figure 4 "WIND: RTOD® versus GTDS"**

Smaller scale features in Figure 4 are also worth noting. There is a bizarre "blip" in the graph following the leap second on day 181, which is probably due to an inconsistency in leap second processing. Since both processes fit tracking data across the leap second, it is difficult to determine where the error lies. It is possible that the filter introduces an error, however the peculiar behavior "magically" disappears at the abutment with GTDS ephemeris #3a.

Note too the sinusoidal behavior of crosstrack differences over GTDS ephemeris #3a. This behavior is a typical least squares response when the plane and intrack errors are poorly separated. While there is no proof that this particular sinusoid is due to the GTDS fit it is a reasonable hypothesis considering that the intrack difference also appears to be biased over this time period.

Finally the crosstrack difference over the last GTDS ephemeris span, after lunar swingby, has a pronounced slope. This too is a typical characteristic of a least squares fit when there are force model errors. Since this slope starts with a large GTDS abutment error on day 210, it is reasonable to assign the slope as an error in the GTDS ephemeris. A converged filter actually has an advantage for such transitional events; the filter is a continuous process with the covariance acting as a constraint on the estimate which tends



to keep slow moving parameters associated with orbit plane from overcorrecting. Successive least squares solutions, on the other hand, are independent, and the plane can change arbitrarily from batch to batch.

### WIND Covariance

The positive portion of the covariance for WIND is given in Figure 5, below. The scales are the same as the those in Figure 4, above, for easy comparisons. The two-sigma bound for intrack is the bold line, while crosstrack and radial two-sigma bounds are thinner. The two perigee maneuvers and the lunar swingby events are indicated by vertical dashed lines, and are coincidentally the abutment points for successive GTDS ephemerides.

Chronologically, the filter starts with a fairly large covariance, which collapses rapidly (WIND is approaching perigee, so there is a lot of dynamical motion and the orbit is easy to determine). The first perigee maneuver (P20) occurs on day 163 and the covariance responds to maneuver process noise by increasing the error covariance. Note the spiking radial covariance values over 6 days. Once the filter has resolved the radial error then the intrack and crosstrack errors begin to collapse. The covariance response to the second perigee maneuver (P21), on day 190, is similar to the first, and requires roughly the same time interval to recover. If the filter had used the DSN Doppler data we would expect the covariance to collapse more quickly.

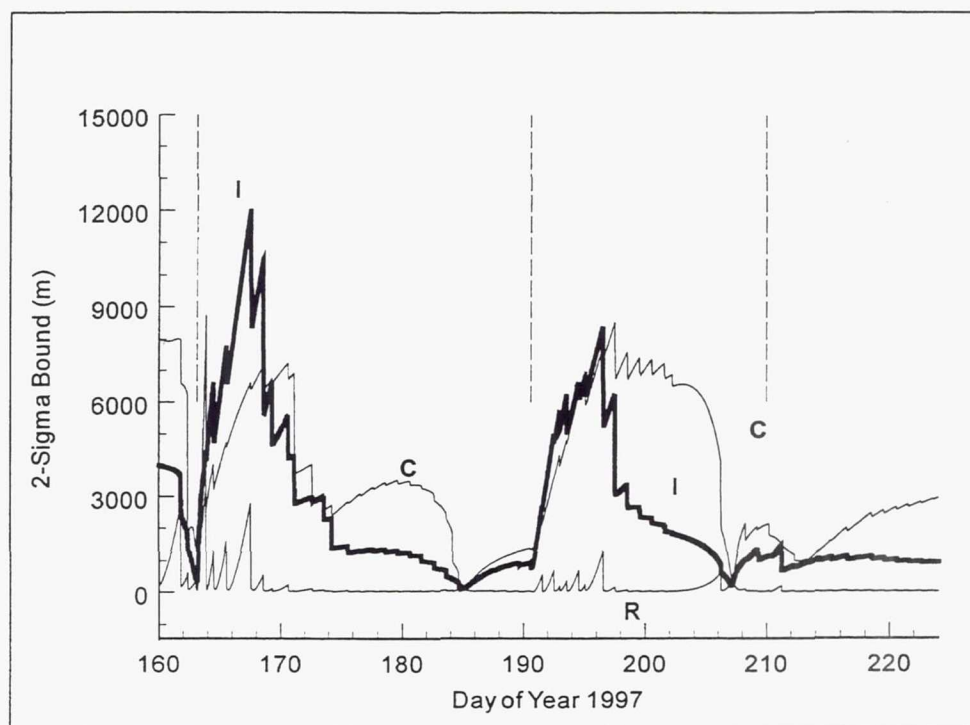


Figure 5 " RTOD® Position 2-Sima Bounds for WIND"

The covariance collapses in all three components on days 163, 185, and 207, when there is a perigee passage and the tracking geometry is most favorable. On the other hand, it is not clear why the covariance collapses slightly on days 211-212, just after the lunar swing-by, perhaps there is a favorable change in the ranging geometry.

### WIND Residual Analysis

Figure 6 provides a sample of the residuals displayed by the filter while it is processing. These residuals are predicted residuals, with the first residual the result of predicting the orbit from a previous tracking pass, but subsequent residuals are obtained by predicting over the short spans between measurements. The 3-sigma bounds are affixed to the plot. The values are obtained through the classical Kalman measurement residual calculation, projecting the full covariance into the range direction and adding the measurement noise variance to it. The 3-sigma bound is important to the filter operation, because residuals which exceed the 3-sigma threshold are autonomously rejected.

The most pronounced feature of Figure 6 is the step decrease in the 3-sigma bound just after 08:35. At this time the signal-to-noise statistic in the DT-5 increased, and the computed measurement error variance (for white noise) dropped. Before 08:35 the 3-sigma calculation was dominated by the white noise contribution, hence the "ratty" bound, but after 08:35 the 3-sigma bound is dominated by the projection of the orbit covariance into range, and the bound is smooth. Note that the residual distribution is really more compact after 08:35, indicating that there is value in dynamically computing the 3-sigma bound from signal-to-noise statistics in the DT-5 message.

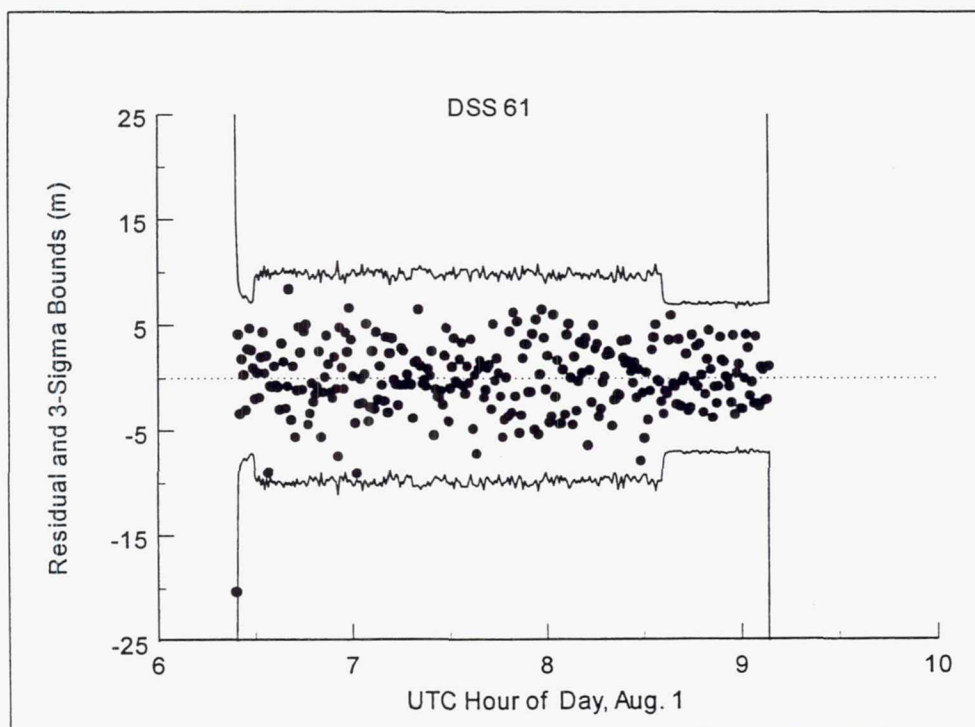


Figure 6 "WIND Predicted Range Residuals"

Note the minor over-correction in the 3-sigma bound just after the first measurement. This is due to the linearization of the measurement correction process. This effect can be removed with classical text-book estimation techniques.

The Measurement Residual Test is constructed by dividing each predicted residual by the computed range sigma and binning in a histogram. If the filter estimate is optimal, then a zero-mean Gaussian histogram will be produced. Unfortunately the converse is not necessarily true, it is possible to generate a Gaussian histogram and have a non-optimal estimate, however it is difficult to do so. Figure 7 was generated for all range data processed in the WIND test case and is remarkably Gaussian, which we interpret as an indicator, but not proof, of a realistic covariance. The dots in Figure 7 are the ideal Gaussian histogram for an infinite sample size.

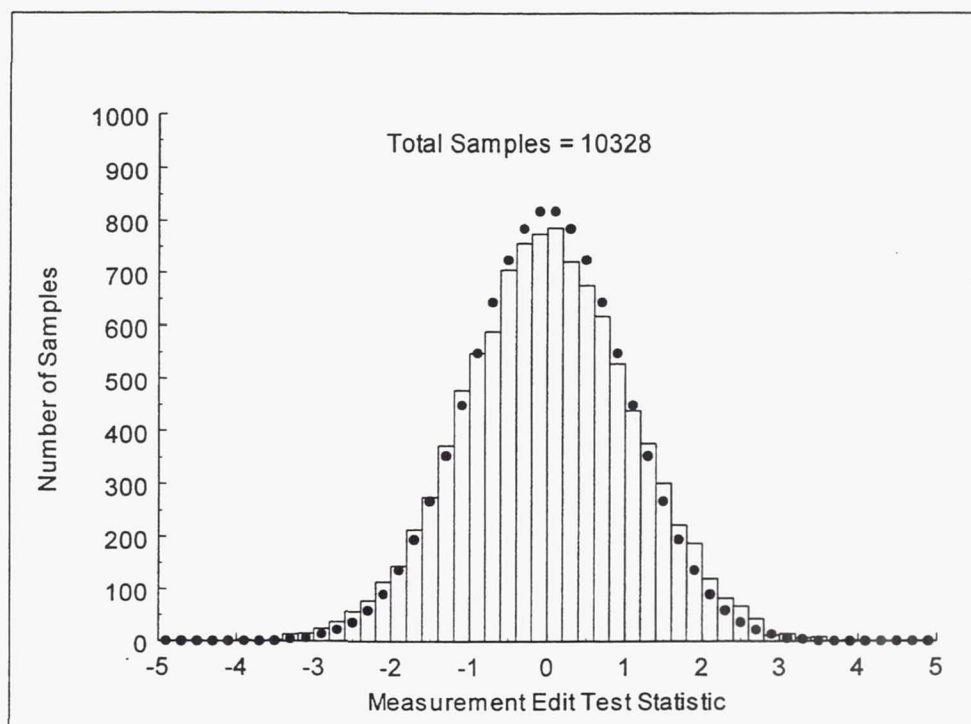


Figure 7 "WIND Measurement Residual Test (All Stations)"

## CONCLUSIONS

We have once again demonstrated the filter to be a powerful alternative to least squares orbit determination. The filter appears to meet NASA accuracy requirements for both missions, as does GTDS. These test cases include many aspects of space craft operations, including maneuvers, a lunar swing-by, very long range operations, and even a leap second. More important than the accuracy achieved is the demonstration of automated processing through all events, and particularly through maneuvers. This is particularly rewarding considering we have never processed this tracking data type before, nor this orbit class, and considering that we did not use the Doppler data, which may improve accuracy and the speed of post-maneuver accuracy recovery.



Given that this is a first attempt to process this class of data and missions we expect that better performance can be achieved with more tracking data and some analysis. These tracking data sets are representative, but are not encompassing, and the SOHO case leaves questions unanswered whether the observed trend is due to RTOD<sup>®</sup> or to GTDS. The filter is also a powerful analysis tool, and when coupled with a smoother can be used to optimize the orbit determination process. Recommended analyses include:

- Further calibration of range biases
- Incorporation of integrated Doppler measurements
- Automated filter initialization techniques
- Addition of adaptive integration controls and techniques
- Refinements and calibration of maneuver models
- Implementation of an optimal filter-smoother configuration

We have, over the last decade, used RTOD<sup>®</sup> and engineering variants on RTOD<sup>®</sup> to demonstrate the accuracy, reliability, and autonomy of filter-based orbit determination. These demonstrations have been performed for a host of tracking systems, including TDRSS, AFSCN, SSN, GPS, SLR, and now DSN. In almost every historical demonstration the issues were filter accuracy and reliability. In every case the filter has proved to be as accurate and as reliable as legacy least squares orbit determination methods, and if there are significant events (maneuvers) or mismodeled forces (drag, solar pressure) then the filter has proved to be more accurate and more reliable. Now autonomy is an important requirement, and NASA seeks "light out" operations for resident satellites. Legacy orbit determination systems can be automated through queuing and even through application of AI techniques, however these efforts "work around" the problem and are severely stressed when events like maneuvers occur. This filter has been demonstrated to be a natural solution for all three requirements, accuracy, reliability, and autonomy.

## **ACKNOWLEDGEMENTS**

We wish to thank Tom Stengle for releasing the tracking data and GTDS ephemerides to Logicon for this analysis. In addition, this work would not have been possible without the cooperation of CSC, and in particular Darryl Carrington and his staff; who collected the data and then explained the data to us; their effort is appreciated. Thank you.

## REFERENCES<sup>6</sup>

- 1 D. Oza, T. L. Jones, et al, "Comparison of ERBS Orbit Determination Using Batch Least-Squares and Sequential Methods," NASA Conference Publication 3123, *Proceedings of Flight Mechanics / Estimation Theory Symposium*, p. 79, Paper No. 5, presented at Goddard Space Flight Center, May 21-23, 1991.
- 2 D. Oza, T. L. Jones, et al, "Evaluation of TDRSS-User Orbit Determination Accuracy Using Batch Least-Squares and Sequential Methods," paper presented at Third International Symposium on Spacecraft Flight Dynamics, Darmstadt, Germany, Sep. 30 - Oct. 4, 1991.
- 3 D. Oza, T. L. Jones, et al, "Landsat-4 (TDRSS-User) Orbit Determination Using Batch Least-Squares and Sequential Methods," Paper No. 92-4432, presented at the AIAA/AAS Astrodynamics Conference, Hilton Head, South Carolina, Aug. 10-12, 1992.
- 4 D. Oza, T. L. Jones, et al, "Evaluation of Landsat-4 Orbit Determination Accuracy Using Batch Least-Squares and Sequential Methods," Paper No. 93-161, presented at the AIAA/AAS Spaceflight Mechanics Meeting, Pasadena, CA, Feb. 22-24, 1993.
- 5 D. Oza, T. L. Jones, et al, "Tracking Schedule Dependence of High-Accuracy TDRSS-User Orbit Determination Solutions," Paper No. 93-600, presented at the AAS/AIAA Astrodynamics Specialist Conference, Victoria, BC, Canada, Aug. 16-19, 1993.
- 6 "Sequential Orbit Determination Final Analysis Report," 553-FDD-93/100R0UD0 and CSC/TM-93/6100R0UD0, April 1994.
- 7 R. Hujsak, "Geosynchronous Satellite Orbit Determination for Maneuvering Satellites," Presented at Lincoln Laboratory Space Surveillance Workshop, 1995.
- 8 R. Hujsak, G. C. Gilbreath, "Filtering TOPEX SLR Data," American Astronautical Society Space Flight Mechanics Meeting, AAS-95-230, Albuquerque, N. M., Feb. 1995.
- 9 D. Folta, C. Knapp, "Trajectory State Estimation for a Translunar and Weakly Bound Spacecraft in the Earth-Moon-Sun System," AAS/AIAA Spaceflight Mechanics Meeting, Feb. 12-15, 1996.
- 10 W. Lear, "Accuracy and Speed of 38 Self-Starting Integrators," TRW Report 3075-6007-TU-00, Jan. 1978.
- 11 A. Kwok, "Deep Space Network Flight Project Interface Design Handbook," (JPL Doc. 810-5), DSN Coverage and Geometry (GEO-10), Rev. E, Jul. 15, 1997.
- 12 R. W. Sniffin, Deep Space Network Flight Project Interface Design Handbook (JPL Doc. 810-5): DSN Tracking System, Ranging (TRK-30), Rev. E, Jan. 15, 1997.
- 13 C. Knapp, Private Communication, Sep. 25 1997.

---

<sup>6</sup> Our apologies to multiple authors, this is a page-limited report.

**Page intentionally left blank**



## NAVIGATION AND MUSES-B MISSION-HALCA

**Tsutomu Ichikawa<sup>†</sup> and Takaji Kato<sup>†</sup>**

MUSES stands for Mu space Engineering Satellite, where Mu is the name of the ISAS's satellite launch rocket. The satellite launched in February 12, 1997 from the Kagoshima Space Center(JKSC) of the ISAS. After injection, three perigee raising maneuvers placed Muses-B into an eccentric orbit ( about 560km by 21,000km ) and carried with 8m antenna for Space Very Long Baseline Interferometry(S-VLBI) science.

This satellite renamed "HALCA". And HALCA is part of an international collaborative effort which includes facilities in the U.S., Canada, Australia, and Europe. The objective of HALCA consists of two aspects: engineering experiments and Space VLBI radio astronomical observations. The engineering experiments are a development antenna using servo mechanism, the stable phase lock system, and the precise orbit determination using radiometric data and on-board GPS receiver. From a point of the navigation technology, the requirement of orbit determination is very stringent for the ground VLBI correlation system. This satellite has both Ku-band and S-band frequency transponders. Namely, the availability of two different frequencies communication between this satellite and the ground station makes it obtain the different radiometric data. And also radiometric data has been exchanged between ISAS two stations and several DSN stations (Included Greenbank station). It can be performed orbit determination by using all station in the world. This paper describe result and evaluation of orbit determination by using Japanese two stations radiometric data for this satellite. And describe the correlation result based on the orbit solutions.

### INTRODUCTION

After three orbit maneuvers HALCA was injected into the elliptical earth orbit and the 8 m diameter radio telescope was successfully deployed. And also the first fringe detected between HALCA 8m antenna and UDSC 64m antenna. UDSC 64m antenna and on-board

---

<sup>†</sup> The Institute of Space and Astronautical Science.  
3-1-1 Yoshinodai, Sagami-hara, Kanagawa 229, Japan

8m antenna tracked same quasar. In this test, the space VLBI technology was proofed.

In mission phase, the requirement of the orbit determination accuracy is precise for the ground VLBI correlation system in order to detect the correlation data. The tracking and control for HALCA is carried out at JKSC in the S-band frequency. The VLBI data acquired with on-board are transmitted to the ground link stations in the Ku-band frequency. Figure 1 shows outline of TT&C and VLBI data acquisition system for HALCA. In the phase, three types of tracking data are used for orbit determination, that is, S-band range and 2-way coherent Doppler data from JKSC, and Ku-band Doppler data from Usuda Deep Space Center (UDSC) in Japan. Especially, Ku-band Doppler data is observed with a mode of two types. These observation model describe next section in this paper.

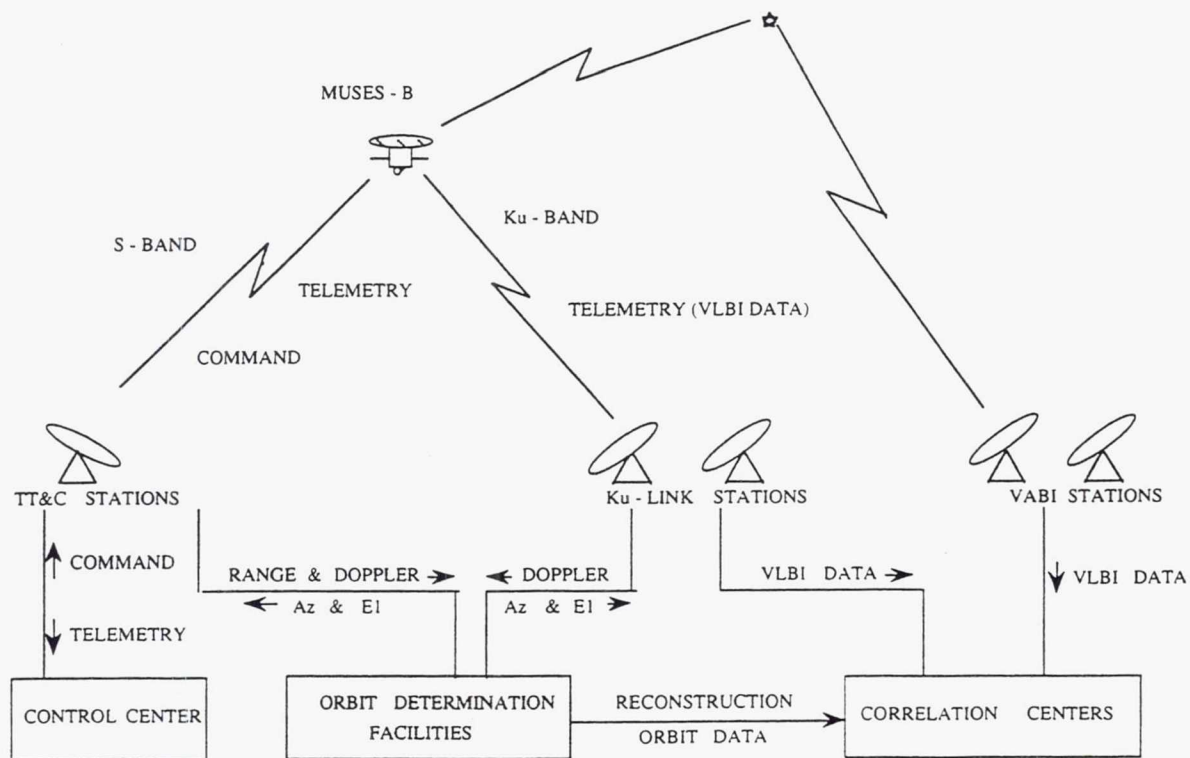


Figure 1 Outline of TT&C and VLBI acquisition system for HALCA

## MEASUREMENT MODEL OF THE DOPPLER DATA

This satellite has both S-band and Ku-band frequency transponders. In the VLBI observation phase, three types of tracking data are used for orbit determination, that is, S-band range and 2-way coherent Doppler data from JKSC, and Ku-band Doppler data from Usuda Deep Space Center (UDSC). Especially, the measurements of Ku-band Doppler data is following as two modes.

(1) 2-way coherent Doppler mode with the fixed Up-link frequency.

(2) 2-way coherent Doppler mode with the Doppler compensated Up-link frequency so that a nearly constant frequency is received at the satellite.

The first mode is same as the mode of S-band Doppler received at JKSC and is used in the test phase. The Second mode is new mode required by Science ( VLBI ) observation and is usually used in the mission phase.

### Measurement modes of Doppler

#### 2-way coherent Doppler mode with the fixed Up-link frequency

Figure 2 shows the measurement scheme of 2-way coherent Doppler mode with the fixed Up-link frequency. In this mode the received frequency  $f_{R0}$  at the ground station is given by

$$f_{R0}(t_3) = k \times f_{T0}(t_1) + k \times f_{dop(up)0} + f_{dop(down)0} \quad (1)$$

where  $t_1, t_3$  : the transmission time and the reception time at the station, And relating equations are as following.

$f_{T0}$  : Up-link frequency (fixed Up- link frequency mode (  $= f_{up0}$  )).

$f_{up0}$  : constant up link frequency

$k$  : the ratio of trasmitted frequency to received frequency at the satellite.

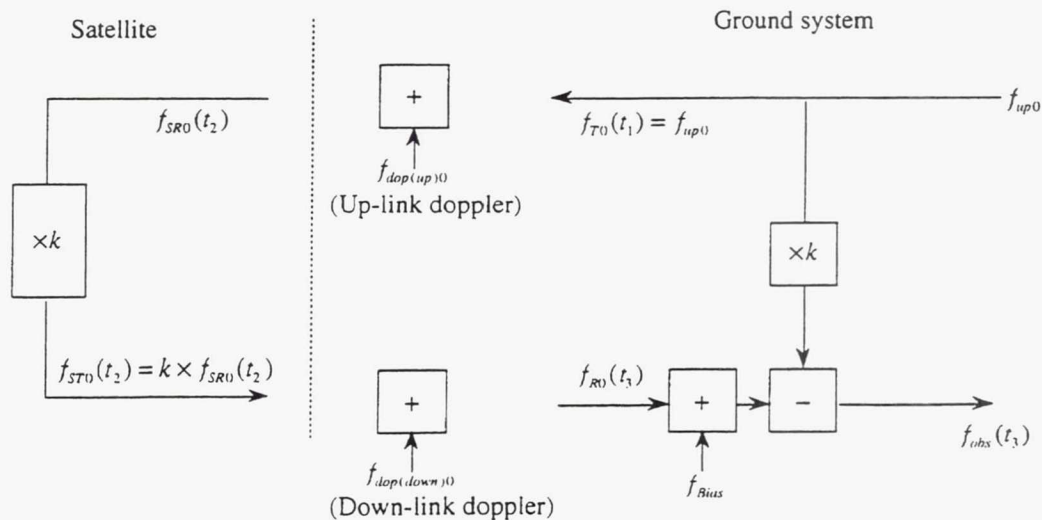


Figure 2 2-way coherent Doppler mode with the fixed up-link frequency



$f_{dop(up)0}$ : up link doppler frequency in the fixed up-link frequency mode.

$f_{dop(down)0}$ : down link doppler frequency in the fixed up-link frequency mode.

The observed frequency  $f_{obs0}$  is

$$\begin{aligned} f_{obs0}(t_3) &= f_{R0}(t_3) - k \times f_{T0}(t_1) + f_{Bias} \\ &= k \times f_{T0}(t_1) \times (f_{R0}(t_3) / (k \times f_{T0}(t_1)) - 1) + f_{Bias} \\ &= k \times f_{dop(up)0} + f_{dop(down)0} + f_{Bias} \end{aligned} \quad (2)$$

where  $f_{Bias}$  is the bias frequency.

The integrated doppler observable ID0 is given by

$$\begin{aligned} \frac{ID(t_b) - ID(t_a)}{T_c} - f_{Bias} &= \frac{1}{T_c} \int_{t_a}^{t_b} (f_{obs0}(t) - f_{Bias}) dt_3 = \frac{1}{T_c} \int_{t_a}^{t_b} (k \times f_{dop(up)0} + f_{dop(down)0}) \\ &= \frac{k \times f_{up0}}{T_c} \int_{t_a}^{t_b} \{ f_{R0}(t_3) / (k \times f_{T0}(t_1)) - 1 \} dt_3 \end{aligned} \quad (3)$$

where  $T_c (= t_b - t_a)$  is the integration time.

## 2-way coherent Doppler mode with the Doppler compensated Up-link frequency

Figure 3 shows the measurement scheme of 2-way coherent Doppler modes with the Doppler compensated Up-link frequency. In this mode the received frequency  $f_{R2}$  at the ground station is given by

$$f_{T2}(t_1) = f_{dop(up)0} - f_{dop(uc)}(t_1) \quad (4)$$

$$f_{R2}(t_3) = k \times f_{T2}(t_1) + k \times f_{dop(up)2} + f_{dop(down)2} \quad (5)$$

where  $f_{dop(uc)}$ : Doppler compensated frequency

$f_{T2}$ : Up-link frequency in the Doppler compensated up-link frequency mode

$f_{dop(up)2}$ : Up-link frequency in the Doppler compensated Up-link frequency mode.

$f_{dop(down)2}$ : Down-link Doppler frequency in the Doppler compensated Up-link frequency mode.

The observed frequency  $f_{obs2}$  of 2-way coherent Doppler mode is

$$\begin{aligned} f_{obs2}(t_3) &= f_{R2}(t_3) - k \times f_{T2}(t_1) + f_{Bias} \\ &= f_{R2}(t_3) - k \times f_{T2}(t_1) + k \times (f_{dop(uc)}(t_3) - f_{dop(uc)}(t_1)) + f_{Bias} \\ &= k \times f_{dop(up)2} + f_{dop(down)2} + k \times (f_{dop(uc)}(t_3) - f_{dop(uc)}(t_1)) + f_{Bias} \end{aligned} \quad (6)$$

The following equation holds good status.

$$\begin{aligned} (f_{R2}(t_3) - k \times f_{T2}(t_1)) / (k \times f_{T2}(t_1)) &= (k \times f_{dop(up)2} + f_{dop(down)2}) / (k \times f_{T2}(t_1)) \\ &= (k \times f_{dop(up)0} + f_{dop(down)0}) / (k \times f_{T0}(t_1)) = f_R / f_T - 1 \end{aligned} \quad (7)$$

Consequently Eq.(6) is written b

$$f_{obs2}(t_3) = k \times (f_{dop(up)0} - f_{dop(uc)}(t_1)) \times (f_R / f_T - 1) + k \times (f_{dop(uc)}(t_3) - f_{dop(uc)}(t_1)) + f_{Bias} \quad (8)$$

The integrated Doppler observable  $ID$  is given by

$$\begin{aligned} \frac{ID(t_b) - ID(t_a)}{T_c} - f_{Bias} &= \frac{1}{T_c} \int_{t_a}^{t_b} (f_{obs2}(t) - f_{Bias}) dt_3 \\ &= \frac{k \times f_{dop(up)0}}{T_c} \int_{t_a}^{t_b} (f_R / f_T - 1) dt_3 - \frac{k}{T_c} \int_{t_a}^{t_b} f_{dop(up)0}(t_1) \times (f_R / f_T) dt_3 + \frac{k}{T_c} \int_{t_a}^{t_b} f_{dop(uc)}(t_3) dt_3 \\ &= \frac{k \times f_{dop(up)0}}{T_c} \int_{t_a}^{t_b} (f_R / f_T - 1) dt_3 - \frac{k}{T_c} \int_{t_a - \tau_a}^{t_b - \tau_b} f_{dop(uc)}(t_1) dt_1 + \frac{k}{T_c} \int_{t_a}^{t_b} f_{dop(uc)}(t_3) dt_3 \end{aligned} \quad (9)$$

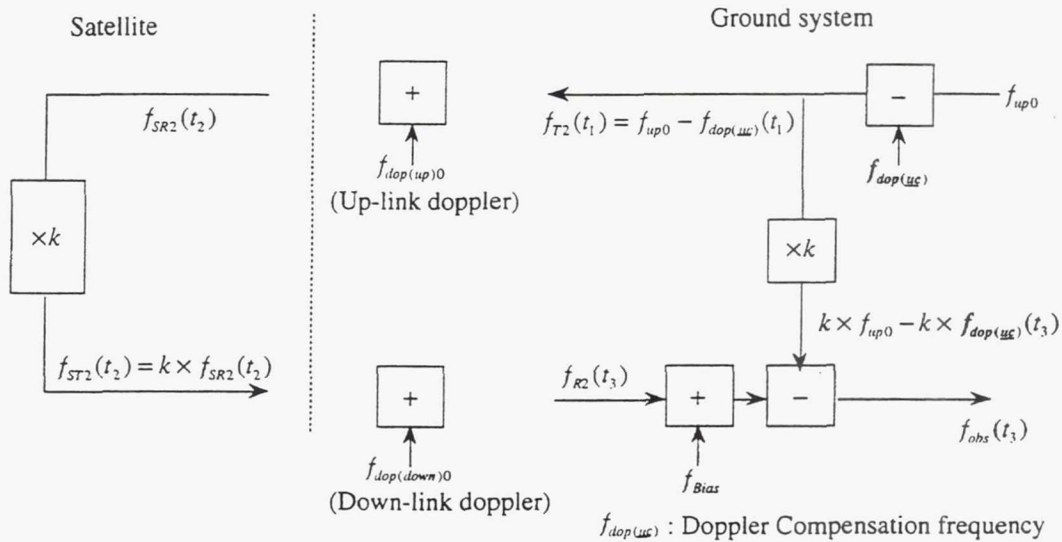


Figure 3 2-way coherent Doppler with variable Up-link frequency

## EVALUATION OF KU-BAND DOPPLER DATA

In the early operation phase Ku-band Doppler measurements were carried out at UDSC in the fixed Up-link frequency mode in order to test Ku-band Doppler measurements system. Fig. 3 shows an example of estimation residuals of Ku-band Doppler data which mean the difference between observation data (O) and expected calculation value (C) so called O-C. The residuals are of the order of 1 mm/s (1 sigma) for Ku-band Doppler data.

In observation phase Ku-band Doppler measurements are carried in the Doppler compensated up link frequency mode so that a nearly constant frequency is received at the satellite.

This nearly constant frequency decreases the loop stress of the receiver at the satellite and observation accuracy will improve. But in this mode the prediction error deteriorates observation accuracy. The integrated Doppler observable data is corrected as follows.

$$\begin{aligned} \frac{ID(t_b) - ID(t_a)}{T_c} - f_{Bias} + \frac{k}{T_c} \int_{t_a - \tau_a}^{t_b - \tau_b} f_{dop(uc)}(t_1) dt_1 - \frac{k}{T_c} \int_{t_a}^{t_b} f_{dop(uc)}(t_3) dt_3 \\ = \frac{k \times f_{dop(up)0}}{T_c} \int_{t_a}^{t_b} (f_R / f_T - 1) dt_3 \end{aligned} \quad (10)$$

So  $\tau_a$  and  $\tau_b$  are calculated used orbit prediction value, the prediction error may have bad effect on the third term in the left part of Eq.(10).

If predicted position error is 1 km, maximum Doppler data error is 1 mm/s at the perigee region. Figure 4 shows example of estimation residuals of Ku-band Doppler data in this mode. The residuals are of the order of 0.5 mm/s (1 sigma) for Ku-band Doppler data. From comparison between Figure 4 and Figure 3 the influence of compensation of Up-link frequency is shown, and the observation accuracy of Ku-band Doppler data in the Doppler compensated Up-link frequency mode is better than that in the fixed Up-link frequency mode.

Consequently, the measurements of 2-way coherent Ku-band Doppler data with the Doppler compensated Up-link frequency is proper.

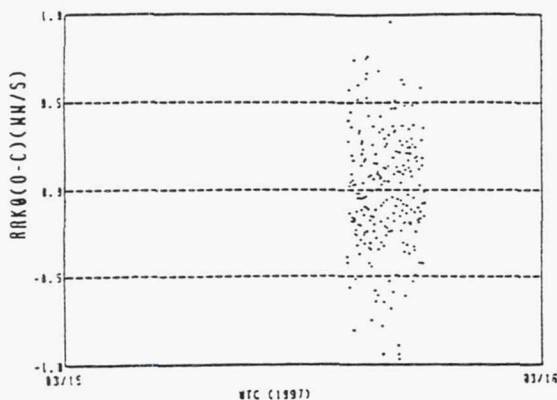


Figure 3 Ku-band Doppler residual with fixed Up-link frequency

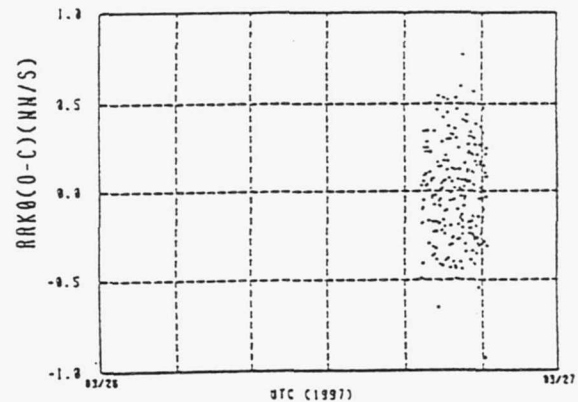


Figure 4 Ku-band Doppler residual with variable Up-link frequency

## ORBIT ESTIMATION RESULT

The orbit element and solar radiation pressure coefficient estimate by using SQRT(Square Root) Filter.

The orbit solution is two phases. One is prediction phase, and the other is reconstruction phase. In the prediction phase, the orbit is estimated by using S-band range and 2-way coherent Doppler data at JKSC station and Ku-band Doppler data at USUDA station during two passes (About four revolution orbit). In the reconstruction phase, the solution is more



precise accuracy based on priori information which the solution is prediction phase. Namely it is solved by using Ku-band Doppler data and S-band Doppler data during one pass that included data in the prediction phase.

The estimation residuals of Ku-band Doppler data and S-band Doppler data which means the difference between observation data ( O ) and calculation value ( C ) so called O-C are shown Figure 5 and Figure 6.

The summary of orbital element.

Epoch : 1997-5-22 19H00M0.0S(UTC) J2000 coordinate system (Center : Earth)

Semi-major axis : 17394.0 ( km )  
 Eccentricity : 0.59991137 ( - - )  
 Inclination : 31.33438 ( deg )  
 Argument of perigee : 198.21592 ( deg )  
 Long. of ascending node : 190.17254 ( deg )  
 Mean Anomaly : 338.0019 ( deg )  
 Perigee height : 573.168 ( km )  
 Apogee height : 21420.137 ( km )  
 Orbit period : 6.33 ( hour )

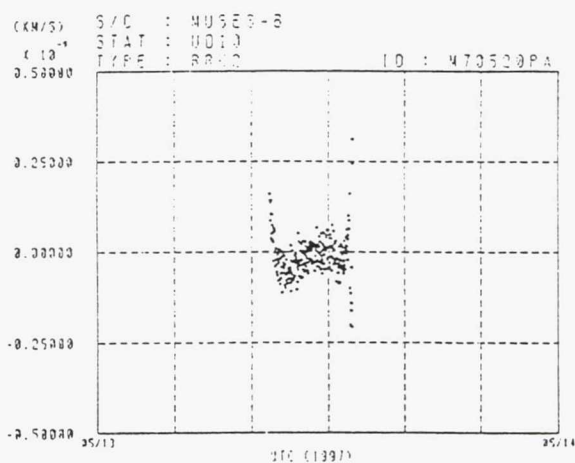


Figure 5 Ku-band coherent Doppler residual at Up-link frequency control

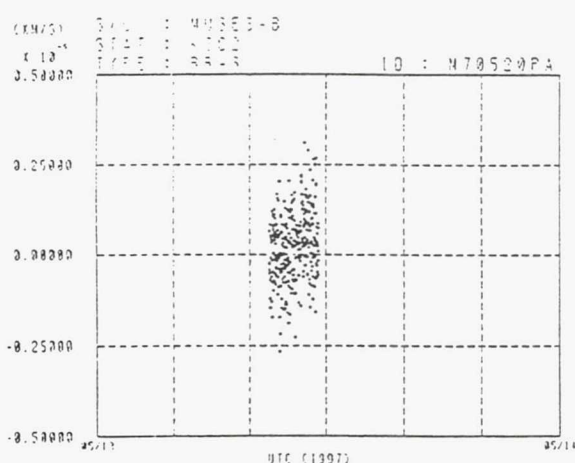


Figure 6 S-band 2-way coherent Doppler residual

This orbit element estimated at the epoch of previous description. The accuracy is 212.34 ( m ) in position and 3.432 ( cm/s ) in velocity ( 1 sigma ). It is shown the result of correlation output based on this reconstruction orbit solution as following ( Fig.7 and Fig.8 ) Fig.7 is shown delay to VLBI observation (1.6GHz). And Fig.8 is shown delay rate as same as VLBI observation time. In the case of change to inertial coordinate system of this satellite, it shows accuracy of maximum 320.4 ( m ) in position and maximum 4.345 ( cm/s ) in velocity.

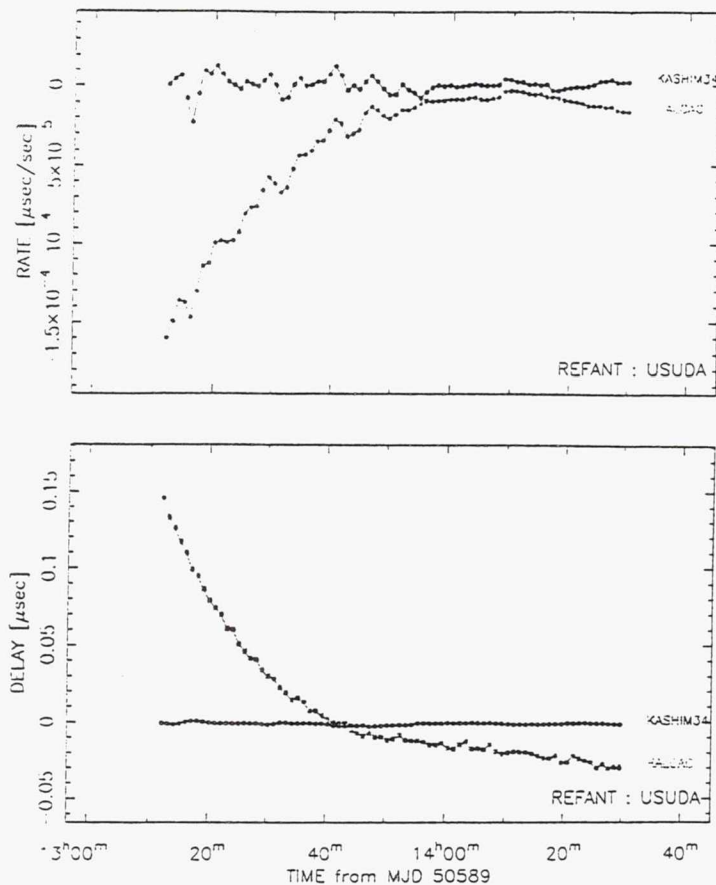


Figure 7 Delay time and Delay rate from the Japanese correlation system

## CONCLUSION AND REMARKS

It is described to orbit estimation result in final section . This reconstructed solution is preliminary result. We study optimal parameter estimation of solar radiation pressure and air drag models for dynamics with orbital element. And consider VLBI observation model. It is expect to more precise accuracy to orbit estimation.

## ACKNOWLEDGMENTS

We express our special thanks to JPL Navigation team for the tracking support and discussion with outside regarding to navigation accuracy.

## REFERENCES

1. C.Tausworthe ' Theory and Practical Design of Phase-Locked Receivers' JPL Technical Report, 1966.
- 2.Bryson A.E.Yu C.H "Applied Optimal Control. Hemisphere Publishing Co. 1975.
3. Maybeck, P.S. "Stochastic Models, estimation, and Control" Vol 3' Academic Press,1982
- 4.T.Ichikawa, and T.Kato: The study of orbit estimation for near earth satellite by using Doppler measurements, Proceedings of 9th guidance and control symposium,1992.

## NAVIGATION OF THE SPACE VLBI MISSION - HALCA<sup>1</sup>

Tung Han You<sup>2</sup>, Jordan Ellis<sup>3</sup> & Neil Mottinger<sup>2</sup>

In February '97, the Japanese Space Agency ISAS launched the first space VLBI satellite, HALCA, with an 8 meter diameter wire mesh antenna and radio astronomy receivers capable of observing at 1.6, 4.8, and 22 GHz. In a 560 by 21000 km orbit with a 6 hour period and 31 degree inclination, it observes celestial radio sources in conjunction with a world wide network of ground radio telescopes as part of an international collaborative effort which includes facilities in Japan, the U.S., Canada, Australia, and Europe. JPL is providing tracking and navigation support using a dedicated subnet of 11 meter antennas as well as co-observations using the DSN 70 meter antennas. This paper describes the spacecraft dynamics model and orbit determination strategies developed to meet the stringent trajectory accuracy requirements for generating predicts for the transfer of a stable uplink frequency to the spacecraft and for determining reconstructed orbits for delivery to the NRAO VLBI correlator and the international VLBI science community.

### INTRODUCTION

Very Long Baseline Interferometry (VLBI) techniques have been extensively used from ground based radio telescopes to map celestial radio sources. The angular resolution is limited by the maximum baseline between sites, which for Earth based antennas, is the diameter of the Earth. Longer baselines and thus increased resolution and sensitivity can be attained by placing one of the antennas in Earth orbit. In February 97 the Japanese Institute of Space and Astronautical Science (ISAS) launched the first VLBI Space Observatory Program (VSOP) satellite using the newly developed M-V launch vehicle. A second VLBI satellite, Radioastron, is scheduled to be launched by the Russian Space Agency in the year 2000. The ISAS satellite, renamed HALCA, is an 800 kg spacecraft with an 8 meter diameter

---

<sup>1</sup>This work was carried out at the Jet Propulsion Laboratory, California Institute of Technology, Pasadena, California under contract to National Aeronautics and Space Administration

<sup>2</sup>Member of Technical Staff

<sup>3</sup>Multi-Mission Navigation Group Supervisor



wire mesh antenna and radio astronomy receivers capable of observing radio sources at 1.6, 4.8 and 22 GHz. HALCA was initially injected into a 200 by 21000 km orbit. Three perigee raising maneuvers placed HALCA into a 560 by 21000 km orbit with a 6 hour period and 31 degree inclination. Approximately two weeks after launch, the critical deployment of the 8 meter mesh antenna was successfully completed. Perigee, initially in the northern hemisphere for communications with the command site in Japan during the orbit transfer, precesses at a rate of 0.96 degrees per day. Communication for commanding and engineering data is at S-band (2.3 GHz). VLBI science data and two-way Doppler are collected at Ku-band frequency (15.3 GHz).

The Space VLBI program is an international collaborative effort which includes facilities in Japan, the U.S., Canada, Australia, and Europe. ISAS provided the spacecraft and the launch vehicle, and is responsible for operating the spacecraft and coordinating the observation sequence of the orbiting antenna with the network of tracking stations and radio telescopes. The U.S. has constructed a network of dedicated Orbiting VLBI tracking stations to support the space VLBI missions, is providing Jet Propulsion Laboratory (JPL) tracking and navigation services, co-observation with the Deep Space Network (DSN) 70-meter antennas, and correlation using facilities of National Radio Astronomy Observatory (NRAO).

The VLBI observation requires lengthy uninterrupted reception of a radio signal at the radio telescope receiving sites. During the VLBI session, uplink phase control must be maintained for the ground to spacecraft link. To satisfy this requirement for nearly continuous contact, a world wide network of five Ku-band tracking stations has been committed to supporting the mission. The DSN has constructed an Orbiting VLBI subnet of three 11 meter stations at sites in Goldstone, Madrid, and Australia. A 14 meter antenna at the NRAO Green Bank site was modified to support HALCA and a new 10 meter station was constructed by ISAS at the Japanese Usuda site. The tracking stations transfer a stable uplink reference frequency to HALCA, record the VLBI data which is downlinked in real time from the spacecraft and collect two-way Ku-band Doppler for orbit determination.

This paper describes the orbit determination strategies developed at JPL to satisfy the prediction and reconstruction accuracy requirements. Orbit determination for the Space VLBI missions is unique because it involves a highly elliptic Earth orbiter with relatively stringent prediction and reconstruction accuracy requirements. These requirements are dictated by the characteristics of the Ku-band tracking stations and the correlation process. The primary data type for determining the orbit is the two-way Ku-band Doppler which is generated by the reference phase transfer operation. The most challenging aspect of the strategy entailed modelling the dynamic effects due to solar pressure and drag acting on the 8 meter mesh antenna. The next section describes the source of the accuracy requirements and details of the support plan. Dynamic and observation models and estimation strategies are discussed in subsequent sections.

<b>Predicts</b>	
Position	170 <i>m</i>
Velocity	27 <i>cm/s</i>
<b>Reconstruction</b>	
Position	80 <i>m</i>
Velocity(22 Ghz)	0.43 <i>cm/s</i>
Velocity(5 Ghz)	1.9 <i>cm/s</i>
Acceleration(Weak Sources)	$6 \times 10^{-8} \text{ m/s}^2$
Phase Residual(Weak Sources)	1.2 <i>mm</i>
Acceleration(Routine Ops)	$4 \times 10^{-7} \text{ m/s}^2$
Phase Residual(Routine Ops)	14 <i>mm</i>

Table 1: HALCA ORBIT ACCURACY REQUIREMENTS (1 SIGMA)

## MISSION SUPPORT

### Navigation Accuracy Requirements

The Space VLBI missions have science and operational objectives which translate into comparatively stringent navigation requirements. A continuous uplink of a ground reference frequency is required to provide a stable reference for the on-board receiver. This signal is the source of the timing information for the VLBI data received at the spacecraft. The uplink is phase compensated to remove the effects of the uplink Doppler shift. This signal is coherently retransmitted by the spacecraft to the tracking site where a predicted downlink Doppler shift is removed to minimize the ground receiver tracking loop degradation. The phase is sampled at the tracking site 400 times per second which translates into a requirement that the error in the predicted received frequency at the spacecraft be less than 175 Hz (3 sigma).

Table 1 summarizes the (one sigma) accuracy requirements imposed by the U.S. Space VLBI project for the predicted and reconstructed orbits. Accuracies for predicted orbits are based on translating the frequency error into equivalent position and velocity errors. Position, velocity, (and acceleration) requirements are expressed as one-dimensional errors. The predicted velocity error represents the component along the tracking station to spacecraft line of sight and the predicted position error the component along the projection of the velocity vector in the plane of sky. Accuracies for reconstruction orbits are defined for the component along the direction to the observed radio source.

Requirements for the reconstructed orbit, derived by R. Linfield (Ref. 1), are governed by the the design of the VLBA correlator. The limit of 128 delay lags per frequency channel translates into an 80 meters (1-sigma) reconstruction requirement. The velocity error is fixed by the maximum fringe rate of the correlator. The requirement for the acceleration accuracies (Ref. 2) is expressed for routine viewing of strong and intermediate strength sources and for viewing of weak sources. The most stringent acceleration accuracies result



from experiments for mapping weak sources at 5 GHz with integration times greater than 300 seconds. The acceleration error is the resulting rms error derived from fitting the phase residuals at the correlator to a first order polynomial. The error can either be expressed as a residual (after the fit) phase error or as a one-dimensional pseudo acceleration error. The latter interpretation is based on equivalencing the second order error to an acceleration.

Since reconstruction requirements are defined by the characteristics of the VLBI correlator, the requirements are only meaningful when HALCA is observing a radio source. A minimum spacecraft altitude of 2500 km is assumed for usable VLBI data. (Reconstruction accuracy requirements imposed by ISAS are significantly less stringent ( $\sim 800$  meters) due to the difference in design of ISAS correlator which processes station and spacecraft signals in separate passes.)

## Navigation Operations Procedures

Extensive coordination between JPL navigation, the ISAS Mission Control Center, and the ISAS navigation center is required for orbit determination. ISAS provides JPL a sequence of events with information needed to model spacecraft dynamics, and the times of any thruster events and momentum dumps. This includes HALCA Antenna pointing angles and a schedule for radio source observations. Twice each week JPL navigation generates a 7 day predicted orbit using the Doppler data received daily from the DSN Orbiting VLBI and Green Bank stations. The predicted trajectory is delivered to the DSN and Green Bank sites. (ISAS navigation is responsible for delivering predicts to the Japanese stations.) The agencies exchange tracking data and orbit solutions weekly. Since the reconstructed orbit is delivered one week from the time of the last data point collected, tracking from all sites, including Usuda, is available for orbit determination. Reconstructed orbits covering a seven day span are delivered in a standard portable format to the U.S. Space VLBI Project for use at the VLBI correlators.

## Navigation Operation Tools

In the early stages of designing an operating system to support orbit determination, it became apparent that graphical user interfaces (GUI) were needed to simplify case setup and execution. The GUIs created enable the user to visualize the processing activities for the current week in the context of prior weeks' activities. A new case can be initialized using a designated previous case as a reference. Other data which must be updated, for example the ISAS file containing the HALCA antenna pointing angles, is acquired from the U.S. Space VLBI project. Access to three different computer platforms is provided by GUIs to gather all the data needed to setup a new case.

As data are gathered in preparation for trajectory product generation, a visualization program displays: (1) station view periods, planned tracking times, and tracking data currently available; (2) spacecraft 8 meter antenna source pointing and VLBI activities; (3) the time when various trajectory events occur, e.g., periapsis, apoapsis, and eclipses. From



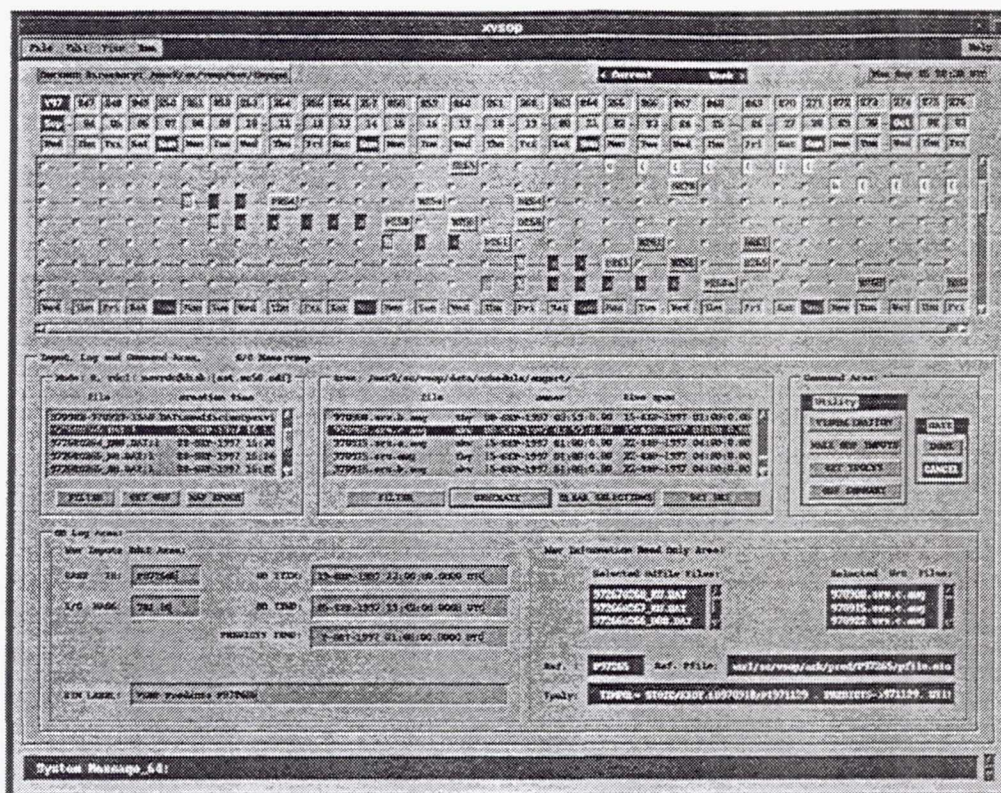


Figure 1: Sample GUI Used in the HALCA Operations

this it is possible to easily verify that the necessary data are available. Then navigation software is activated through other GUIs, including a menu driven interactive data selection and display program for orbit estimation and solution validation.

When trajectory products are created, other GUIs are used to transfer them to the proper platform, a DSN computer for predicts generation and a U.S. Space VLBI computer. The later is accessed by Green Bank, users of the NRAO VLBI correlator, or other members of the VLBI science community.

Overall, the GUIs have reduced the processing time by a factor of four. They provide efficient ways to gather the information needed to conduct and validate the orbit determination activities and disseminate navigation products. Figure 1 demonstrates a sample GUI used in HALCA operations.

## MODELS FOR ORBIT DETERMINATION

### Dynamic Models

Precision orbit determination requires detailed models for the spacecraft dynamics and the observations. A primary factor contributing to the orbit determination difficulty for HALCA is the uncertainty in modelling the nongravitational accelerations. This includes

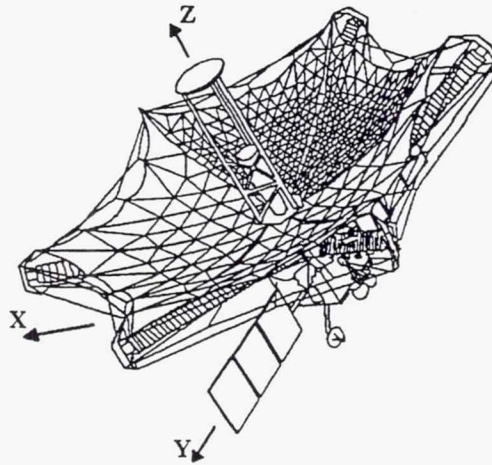


Figure 2: HALCA Structure

the effects of solar pressure acting on the large antenna and solar panels, atmospheric drag at periapsis passage, autonomous thruster firings for transfer to and from safe hold mode, and any outgassing effects. The dominant nongravitational acceleration is expected to be the solar pressure. Modelling this requires a measure of the effective area of the "transparent" mesh VLBI antenna, knowledge of the orientation and the reflectivity properties of the antenna and other spacecraft components. Because only apriori values for these parameters were available prior to launch, our estimation strategy initially attempted to improve the values during the early phases of the mission.

JPL's Double Precision Orbit Determination Program (DPODP) (Ref. 3, 4) is used to model spacecraft dynamics and observations. The trajectory is expressed in the J2000 Solar System Barycentric Reference frame. The spacecraft dynamics models for HALCA include the following:

- central body perturbation due to the Earth and third body perturbations due to Sun, Moon and planets (JPL Ephemeris DE403 is the source of masses and ephemeris )
- General relativistic effects due to Earth, Sun, and Moon using Solar System Barycentric formulation
- Earth geopotential model JGM3  $50 \times 50$  (truncated from  $70 \times 70$ )
- Solid Earth Tide Deformation
- Solar pressure acceleration modeled using antenna, solar panels, and bus components
- Atmospheric drag using a Harris Priester atmosphere

### Spacecraft Component Model



The key to modelling the nongravitational accelerations due to drag and solar pressure is to decompose the complex physical structure of the HALCA spacecraft into five representative component areas. These include the 8 meter mesh antenna, solar panels, and three flat plates which are used to model the central bus. The structures are defined in an orthogonal spacecraft fixed frame as shown in Figure 2 with the antenna bore sighted along the Z axis, and the solar panels, which rotate about the Y axis, oriented so that the front side of the panel faces the Sun. Orientation information for the spacecraft is obtained from the radio source observing scheduling which defines the spacecraft Z direction. Approximate values of the solar pressure constants (i.e., the diffuse and spectral reflectivities) were available before launch along with an estimate of 85 to 90% antenna transparency. This estimate of the antenna transparency was revised during the early phase of mission to 65%.

The total solar radiation force,  $F_{solar}$ , experienced by spacecraft is expressed as

$$F_{solar} = \left( \frac{C_{sf} K_{solar}}{R_{sp}^2} \right) \left( \sum_{i=1}^5 A_i f_i(\mu_i, \nu_i, \phi_i \dots) \right) \quad (1)$$

where  $C_{sf}$  is the solar flux at one AU,  $K_{solar}$  is the shadow factor,  $R_{sp}$  is the Sun-probe distance,  $A_i$  is the area of spacecraft component  $i$ , and  $f_i(\mu_i, \nu_i, \phi_i \dots)$  a collective function of specular and diffuse reflectivity coefficients,  $\mu_i$  and  $\nu_i$ , illumination angle  $\phi_i$  and others (shape, i.e., flat plate or parabolic antenna) of each spacecraft component  $i$ . The effective area for each component is determined from knowledge of the spacecraft orientation. The Harris-Priester atmosphere (HP) model is used for computing the atmospheric drag force on HALCA. The total atmospheric drag force,  $F_{atm}$ , is expressed in terms of the drag coefficient  $C_D$ , the atmospheric density,  $\rho_{atm}$ , and the effective cross-sectional area  $\bar{A}_i$  of spacecraft component  $i$  in the direction of the body-fixed spacecraft velocity vector  $\vec{V}_{sc}$  as

$$F_{atm} = -\frac{\rho_{atm} V_{sc}^2}{2} C_D \left( \sum_{i=1}^5 \bar{A}_i \right) \vec{V}_{sc} \quad (2)$$

## Measurement Models

The Doppler observables from the dedicated DSN Orbiting VLBI stations, Green Bank, and the ISAS stations are modeled using the differenced range formulation in the DPODP. The transformation of the location of the tracking station from body fixed to inertial coordinates includes polar motion calibrations and UT1-TAI timing corrections, solid Earth tides, and an Earth center of mass correction. Troposphere calibrations are computed using a seasonal model. The Earth Orientation file is the source of polar motion and timing data.

Although the uplink frequency is continuously varying to compensate for the uplink Doppler shift, software at the receiving station transforms the accumulated phase data to the equivalent phase for a constant uplink frequency. Consequently, a constant uplink frequency is assumed in the computation of the Doppler shift. The Doppler is sampled every 10 seconds and compressed to 60 seconds.



Parameter	Predicted Strategy	Reconstructed Strategy	A-Priori $\sigma$
<b>Constant Parameters</b>			
epoch state			
position(km)	✓	✓	$10^5$
velocity(km/sec)	✓	✓	$10^2$
solar radiation coefficient			
$\mu_i$	✓		$5 \times 10^{-2}$
$\nu_i$	✓		$5 \times 10^{-2}$
atmospheric drag coefficient			
$C_D$	✓		$5 \times 10^0$
<b>Stochastic Parameters</b>			
stochastic acceleration			
S/C X(km/sec <sup>2</sup> )		✓	$10^{-10}$
S/C Y(km/sec <sup>2</sup> )		✓	$10^{-10}$
S/C Z(km/sec <sup>2</sup> )		✓	$10^{-10}$

✓ parameter is estimated

Table 2: ESTIMATED PARAMETERS

## ESTIMATION METHODS

Uncertainties of solar pressure, atmospheric drag, and nonspherical geopotential perturbations are the major contributors to the errors in estimating the orbit. Analysis by *Tapley et al.* (Ref. 5), demonstrated that the JGM3 gravity field significantly reduced the errors due to gravity mismodelling. Use of this field reduced the errors due to the gravity mismodelling to acceptable levels, directing our attention to developing estimation strategies to reduce the mismodelling effects of solar pressure, atmospheric drag, and other small forces.

Estimation strategies to determine the HALCA orbit are based on the results of covariance studies and modelling sensitivity studies (Ref. 6-10) conducted at JPL and ISAS. The goal of the navigation task is to create simple and efficient orbit determination strategies to meet the accuracy requirements of the predicted and reconstructed trajectories. To meet these requirements, different data processing and filtering strategies were developed for orbit prediction and reconstruction.

### Predicted Filter Strategy

The objective of predicted trajectory generation is to provide a trajectory which satisfies the 175 Hz (3 sigma) accuracy requirement for tracking station frequency predicts. The strategy focuses on estimating the minimum parameter set consistent with achieving valid mapping results.

A six day data arc is used with a simple single batch filter (subsequently called the

*predicted filter strategy*) to estimate the spacecraft epoch state and selected solar pressure and atmospheric drag parameters (see Table 2, column 2). Values of estimated parameters are constrained to maintain "realistic" values of the spacecraft dynamic constants. The new estimated values form the basis of integrating the predicted, one week trajectory. Nominally, the predicted orbit is updated twice each week and delivered to the DSN and Green Bank.

## Reconstructed Filter Strategy

The objective of trajectory reconstruction is to determine the best local fit within the data arc. Reconstructed solutions are initiated using the results of the predicted filter strategy. There are several advantages gained in starting from the solution obtained by the predicted filter strategy, namely, (1) easy setup (same data arc); (2) updated dynamic models (i.e., estimates); (3) un-corrupted observables; and (4) reduced nonlinearities. Using the same data arc as the predicted filter strategy, a stochastic process can be utilized to refine the spacecraft ephemeris.

Typically, the reconstructed orbit is determined by fitting a data arc of 6 days while maintaining a two to three day overlap between the data arcs of each reconstructed orbit. Position and velocity differences in the overlapping data arcs are used as a measure of the solution accuracy. Orbit reconstruction uses a batch-sequential filter (subsequently referred to as *reconstructed filter strategy*) and smoother driven by process noise to reduce the sensitivity of orbit solutions to dynamic mismodelling effects. The reconstructed filter strategy features: (1) a six day data arc; (2) three hour batches; (3) epoch state formulation; and (4) stochastic three dimensional acceleration estimation (see Table 2, column 3). A Markov first order colored noise model is used for stochastic process noise with a constant value assumed in each batch interval and a three day correlation time.

The process noise sigma,  $\sigma$ , can be expressed in terms of the steady state sigma,  $\sigma_{ss}$ , the batch length  $\delta T$ , and the correlation time,  $\tau$ , of the form

$$\sigma = \sigma_{ss} \sqrt{1 - e^{-2\delta T/\tau}} \quad (3)$$

Optimum smoothed estimates are determined by a batch-sequential filter/smoothing algorithm developed by Bierman (Ref. 11). Reconstructed orbits are delivered weekly covering the 7 day period of the previous week.

Table 2 summarizes the estimated parameters in the predicted and reconstructed filter strategies. The dynamic parameters, solar pressure and atmospheric drag coefficients are estimated as constant parameters in the predicted filter and updated later in the reconstructed filter. Typically, for a six day data arc, three hour batches and three day correlation times are used in the HALCA reconstructed filter strategy. For simplicity and efficiency, three dimensional accelerations are estimated as stochastic parameters. It has been proven that this simple design is adequate to absorb the dynamic mismodellings.

Figure 3 illustrates the iteration procedure for the correlated stochastic process. The process noise time update is performed at the end of each batch and the pseudo-epoch



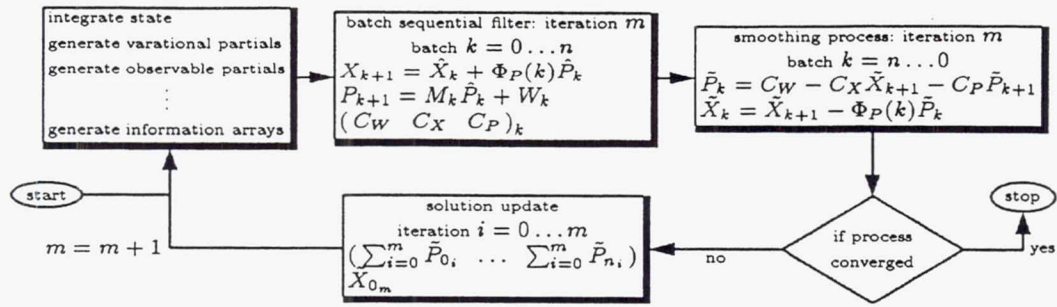


Figure 3: Stochastic Iteration Block Diagram

state  $\hat{X}_k$  and the process noise (stochastic) parameters  $\hat{P}_k$  are mapped to batch  $(k+1)$ . The smoothing coefficients (Ref. 12)  $(C_W, C_X, C_P)_{k+1}$ , are also generated and saved for backward smoothing. The symbol  $\hat{\cdot}$  represents parameters updated with new measurements. By recursively applying the measurement updates and time updates, the square root information filter (SRIF) matrix for the last batch,  $n$ , can be obtained. Along with the estimates, covariance, and smoothing coefficients, Bierman's improved Rauch-Tung-Streibel (RTS) smoothing algorithm is then applied recursively to obtain the smoothed epoch-state  $\tilde{X}_0$  and smoothed process noise parameters  $(\tilde{P}_0 \dots \tilde{P}_n)$ . The symbol  $\tilde{\cdot}$  represents backward smoothed estimates,  $\Phi_P$  is the state transition mapping matrix,  $M$  is a diagonal correlation matrix,  $W$  is filter process noise, and  $m$  is the number of stochastic iterations. Typically, convergence of the stochastic process takes three to five iterations.

## NAVIGATION RESULTS

This section summarizes the orbit determination results for trajectory prediction and reconstruction activities. The performance of the estimation strategies is illustrated by plots of Doppler residuals and estimated values of selected dynamical constants. Plots of position and velocity differences during overlapping segments of reconstructed trajectories are also used as a means for evaluating the accuracy of these orbits.

### Prediction Results

For the predicted strategy, constant values are estimated for the drag,  $C_D$ , and solar pressure reflectivity parameters  $\mu_i$  and  $\nu_i$ , for selected components. These estimates are compromised, however, due to limitations in the ability to update the effective area as the spacecraft orientation changes. Figure 4(a) plots the history of the atmospheric drag coefficient estimates,  $C_D$ , for a five month span. The secular trend may be attributed to seasonal changes. The fluctuations may be due to (1) short term atmospheric density changes, (2) compromised effective antenna transparency values as described above and/or, (3) incorrect spacecraft attitude information.

Similarly, Figure 4(b) plots the history of estimates for the solar radiation coefficient of the solar panels. The mean value of specular reflectivity coefficient is about 0.35. The



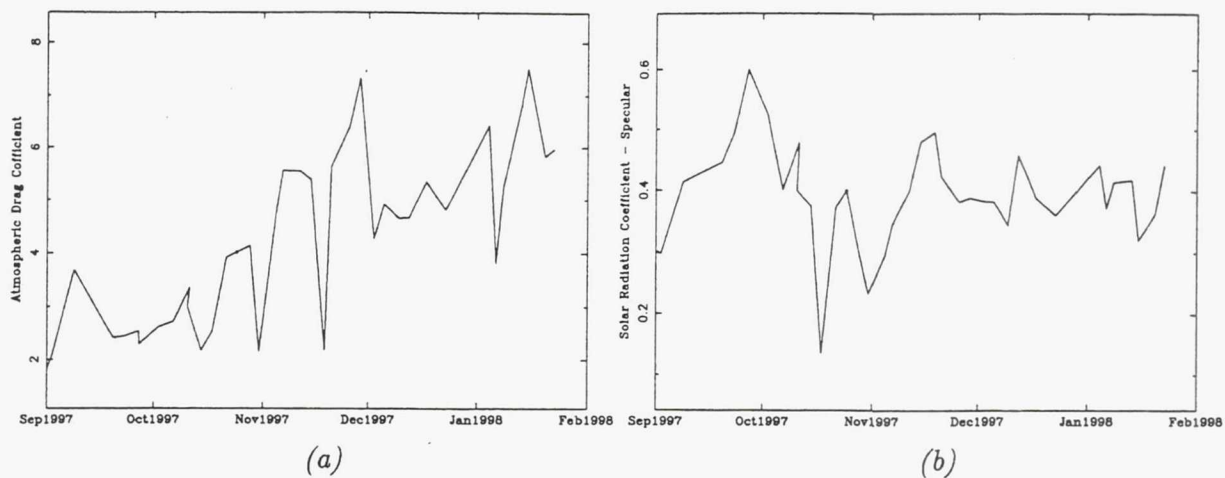


Figure 4: Estimated Values of Atmospheric Drag Coefficient  $C_D(a)$  and Solar Panel Radiation Coefficient  $\mu(b)$

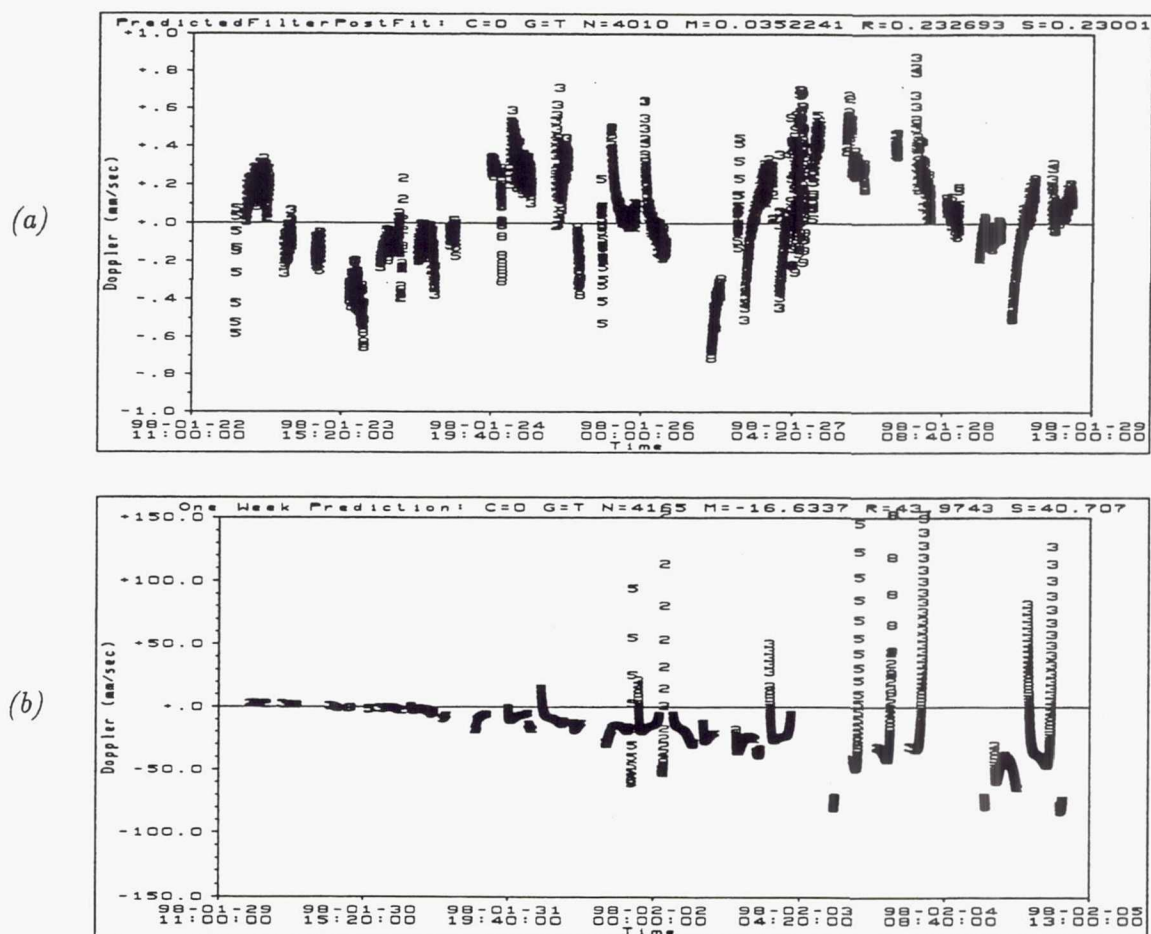


Figure 5: Predicted Filter Strategy, Ku-band Two-Way Doppler Post-Fit Residuals(a) and One-Week Predicted Residuals(b)

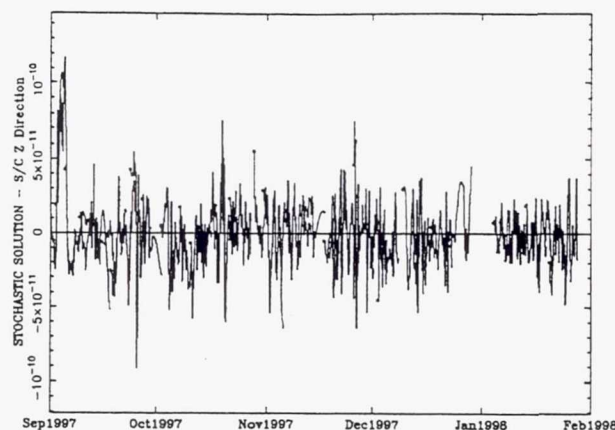


Figure 6: Estimates of Stochastic Acceleration,  $km/sec^2$

spikes from the middle of September through the middle of October are caused by incorrect attitude information. The fluctuations may reflect the effective antenna area mismodelling described above.

Figure 5(a) shows typical post-fit Doppler residuals from the predicted filter strategy. Tracking data is from multiple tracking stations. The data signatures imply dynamic mismodelling is still present. As discussed in previous sections, the main purpose of this strategy is not to obtain a perfect local fit, but to obtain reasonable global estimates of spacecraft constants which can be used to generate a one-week satellite ephemeris that will meet the accuracy requirements.

Figure 5(b) shows typical predicted Doppler residuals for one week. Over this span the mean residual is 80 mm/sec with the maximum deviations occurring near periapsis (for Ku-band two-way Doppler,  $1\text{ mm/sec} = 0.0947\text{ Hz}$ ). The standard procedure is to update the predicts every three or four days, in which case the mean residual is about 40 mm/sec.

## Reconstruction Results

To meet the more stringent orbit accuracy requirements for the reconstructed orbit, a filter strategy using stochastic processes is employed to obtain the best possible local fit. These processes are estimated as accelerations along the spacecraft X, Y, and Z directions.

The function of the stochastic processes is to absorb dynamical effects of: (1) unmodeled spacecraft orientation, particularly in the intervals when the antenna is moving from one celestial source to another; (2) mismodeled spacecraft attitude due to antenna area uncertainty and incorrect attitude information; (3) short term dynamic perturbations, especially atmospheric density fluctuations, higher order nonspherical geopotential mismodellings, and other unmodeled small accelerations. A history of stochastic acceleration is shown in Figure 6. The large initial biases in the September 1997 estimates, were due to an interval in which there was no tracking data. Recall that the initial setup of reconstructed filter strategy

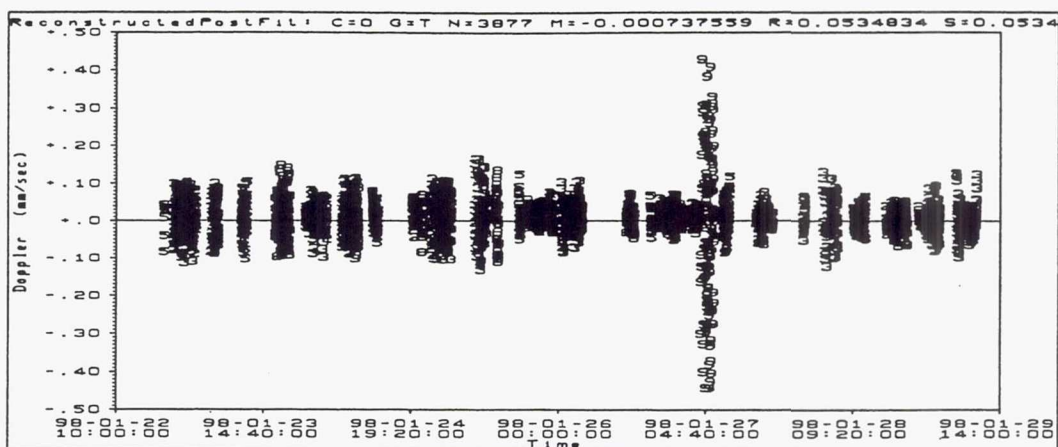


Figure 7: Reconstructed Filter Ku-band Two-Way Doppler Residuals

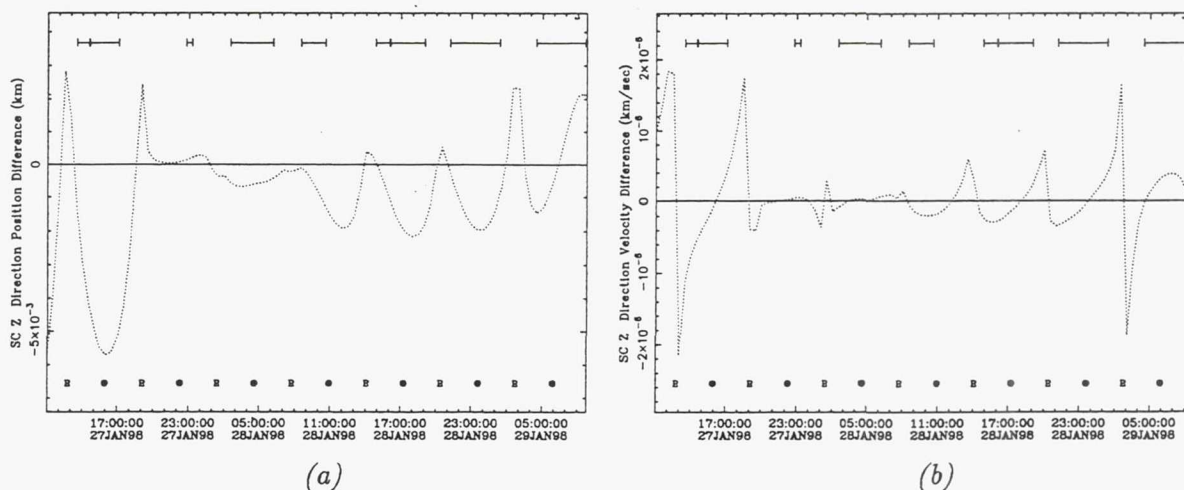


Figure 8: Reconstructed Trajectory Relative Errors along the observing direction

inherits the results of predicted filter strategy. For instance, Figure 5(a) shows the post-fit Doppler residuals of the predicted filter strategy and it also represents pre-fit residuals of a reconstructed case. Figure 7 shows the post-fit reconstructed Doppler residuals for this case. Obviously, the reconstructed filter strategy has significantly improved the local fit by a factor of 5. All tracking data is compressed to 60 second count time except for the one pass with the largest data noise which is 1 second. Normally, 0.1 mm/sec data noise is expected for a count time of 60 seconds.

Evaluation of the reconstructed accuracy is based on differencing the overlapping segment of two reconstructed trajectories. Figure 8 shows the relative errors for a typical week. The symbol  $\vdash\vdash$  indicates spans corresponding to navigation only passes or passes in which science observations are collected. The peaks in the plot correspond to periapsis and apoapsis. The maximum relative position error is 8 meters and the maximum relative



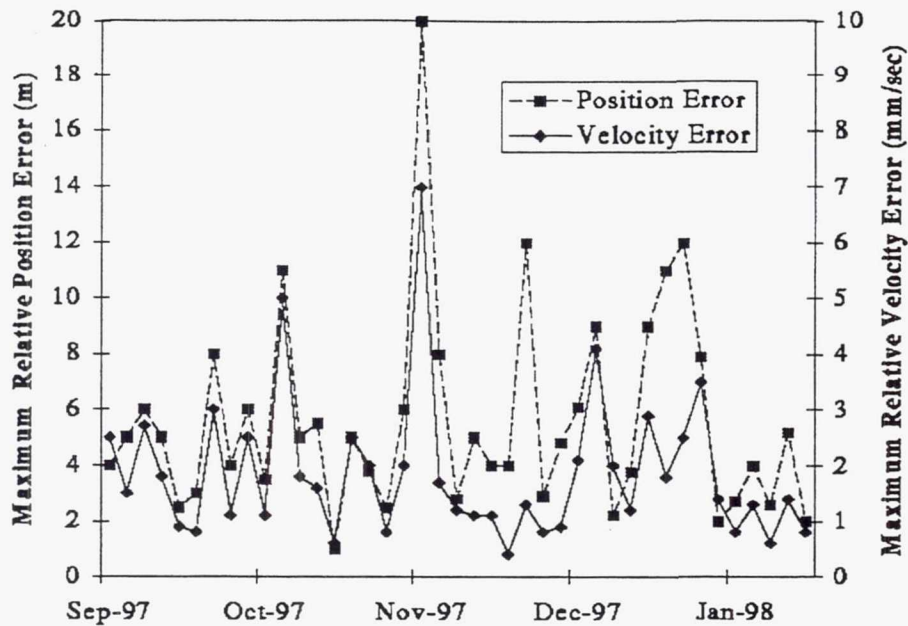


Figure 9: Maximum Reconstruction Errors

error is 2 mm/sec for this case. Figure 9 plots the estimate of the maximum reconstructed orbit errors for a five month span. The maximum position error is approximately 20 meters and the maximum velocity error 6 mm/sec. It should be noted that the maximum errors (ie. the spikes in Fig 9) correspond to either time spans in which there is no tracking data or periods for which the spacecraft attitude is unknown. The most critical test of the reconstructed orbit accuracy is the use of the orbit for the VLBI correlation process. Exceeding the requirements would result in a failure to correlate the VLBI data collected at the spacecraft or in excessive correlator run times. The successful trouble-free use of the reconstructed orbits at the correlator is another demonstration of the ability to satisfy the accuracy requirements.

## CONCLUSIONS

HALCA is the first mission to extend VLBI techniques to incorporate an observing antenna in Earth orbit. The stringent orbit accuracy requirements for an orbiting VLBI antenna were satisfied by developing a detailed model of the spacecraft structure to model the drag and solar pressure accelerations and by developing filter strategies which reduced the sensitivity to these effects.

For orbit prediction the best strategy was determined to be a simple batch filter which estimated the spacecraft state and constrained the estimates of the solar pressure and drag parameters. For the reconstructed orbit, a batch sequential filter/smoothen was required, in which stochastic accelerations were estimated in place of drag and solar pressure. The accuracy of the orbit was limited by: (1) the lack of continuous tracking passes; (2) incorrect

or incomplete knowledge of the spacecraft orientation; and (3) the absence of the data in the vicinity of perigee. The VLBI correlation process, which is very sensitive to any errors in the orbit estimates, was able to successfully utilize the reconstructed orbits to produce the expected high resolution images of the observed sources. The modeling and filtering strategies developed for HALCA are expected to be useful for application to other missions such as Russian Radioastron VLBI mission and the Space Interferometry Mission which have stringent navigation accuracy requirements and complex spacecraft dynamics.

## ACKNOWLEDGMENTS

This work was carried out at the Jet Propulsion Laboratory, California Institute of Technology, Pasadena, California under contract to the National Aeronautics and Space Administration. The authors would like to acknowledge the assistance of the U.S. Space VLBI project and the following people in the Navigation and Flight Mechanics Section at JPL: Mark Ryne for assisting in the checkout of the DSN OVLBI Doppler subsystem; Gene Goltz, KJ Lee, Margaret Medina, Laura Campanelli, and Cheryl Stonebraker in the generation of radio metric Doppler files; Len Efron, Earl Higa, Kevin Criddle, and Kuen Wong for launch support.

## REFERENCES

1. Linfield, R., "Orbit Reconstruction Requirements for VSOP and Radioastron", JPL IOM 334.6-93-001, Feb 23, 1993.
2. Linfield and J. Ulvestad, "Science Loss vs Reconstruction Orbit Acceleration Error for VSOP and Radioastron" IOM 335.1-94-018, May 27, 1993.
3. "DPTRAJ-ODP User's Reference Manual, Vol. 1", JPL Internal Document, Pasadena, CA, May 1993.
4. Moyer, T. D. "Mathematical Formulation of the Double-Precision Orbit Determination Program (DPODP)", JPL Technical Report: 32-1527, Pasadena, CA, May 1971.
5. Tapley, B.D., M. M. Watkins, J. C. Ries, G. W. Davis, R. J. Eanes, S. R. Poole, H. J. Rim, B. E. Schutz, C. K. Shum, R. S. Nerem, F. J. Lerch, J. A. Marshall, S. M. Klosko, N. K. Pavlis, and R.G. Williamson "The Joint Gravity Model 3", Journal of Geophysical Research, vol. 101, no. B12, Dec. 10, 1996.
6. Ellis, J., "Reconstructed Acceleration Errors for SVLBI Missions", IOM 314.7-290, Jun 27, 1994.
7. Ellis, J., "Navigation of Space VLBI Missions: Radioastron and VSOP", Proceedings Second International Symposium on Ground Data Systems for Space Mission Operations, JPL Pub 93-5, March1, 1993.
8. Estefan, J., "Orbit Determination of Highly Elliptical Earth Orbiters Using Improved Doppler Data-Processing Modes", TDA Progress Report 42-120, Feb 15, 1995.

9. Ichikawa, T., and T. Kato "Orbit Determination for MUSES-B Mission", ISTS Paper 94-c-21, 19th International Symposium on Space Technology, May 1994.
10. You, T. H., "VSOP Orbit Accuracy Analysis", IOM 312.C-96-003, Feb 29, 1996.
11. Bierman, G. J. *Factorization Methods for Discrete Sequential Estimation*, Academic Press, New York, NY, 1977
12. Wang, T. C., J. B. Collier, J. E. Ekelund, and P. J. Breckheimer "Applications of Square-Root Information Filtering and Smoothing in Spacecraft Orbit Determination", Proceedings of the 27th IEEE conference on Decision and Control, Vol. I, pp.825-830, Dec. 1988.



# REENTRY PREDICTION METHOD USING PLURAL TWO LINE ELEMENTS

Hiroyuki Konno<sup>†</sup>, Toru Tajima<sup>†</sup>, Masao Hirota<sup>†</sup>

The uncontrolled reentry of space objects is one of the serious problems that the space agencies in the world face. This paper presents a new reentry prediction method, which estimates the reentry time using multiple sets of orbital information and an error-propagation model.

In the low-altitude orbit, the dominant perturbing force for object's motion is air drag. Analyzing how the air drag affects the accuracy of the orbit propagation, we constructed an error-propagation model. Combining the multiple orbital information with this model, this method estimates the optimal air drag and predicts a reentry time accurately.

To demonstrate the performance of this method, a reentry prediction experiment was performed. The experimental prediction took an example of the Chinese satellite FSW1 that actually reentered on 12 March, 1996. Results show that the method can provide accurate predictions of reentry time.

## INTRODUCTION

Recently, the atmospheric reentry of the risk objects has been considered as a consequential problem for which immediate measures should be taken. The high-risk reentry event is defined as (a) the reentry event that may result in radioactive contamination, and (b) the reentry event in which a reentry object may survive to cause a significant damage (Ref.1). When such an event is going to occur, every space agency is supposed to share the information of the reentry object and predict the reentry time and the location of impact. To accomplish this requirement, some agencies have already organized reentry prediction teams (Ref.2 and 3). A major activity has been carried out by the United

---

<sup>†</sup> National Space Development Agency of Japan (NASDA), Sengen 2-1-1, Tsukuba, Ibaraki, 305-8505, Japan

States. The U.S. Space Command (USSpaceCom) periodically monitors more than 8,000 space objects using space surveillance sensors, and determines their orbits (Ref.4). In the case of reentry, they perform reentry prediction based on these observation. The National Aeronautics and Space Administration (NASA) also releases the reentry information in addition to the orbital information.

On the other hand, space agencies which do not possess sensors capable of continuous observation have to predict reentry time based on the orbital data provided by other space agencies (Ref.5 and 6). European Space Agency (ESA) has a system that predicts reentry time by processing other agencies' orbital data such as Tow Line Elements (TLE) from USSpaceCom and orbit determination results from USSR (Ref.5). For the high-quality prediction, this system uses an accurate air density model and an accurate drag coefficient which is well fitted to the semi-major axis reduction history.

This paper describes a prediction method that estimates reentry time using multiple sets of TLE. To predict the reentry time accurately, this method performs an estimation of an optimal air drag and a modification of TLE.

Consider an object in a low orbit. Air drag mainly causes its altitude decrease. Therefore, an accurate reentry prediction requires accurate air drag estimation. To deal with the uncertainty of air drag, we define a parameter " $\rho_1$ ", which involves all the errors related to air drag and adjusts these errors in the numerical integration for orbit propagation. Based on the analysis of the way how the error of  $\rho_1$  and the error of the initial orbit affect the precision of the propagated orbit, an error-propagation model is derived. Combining the plural sets of TLE with the error-propagation model, this method estimates the  $\rho_1$  error and the initial orbit error. Using the improved values with these errors, the accurate reentry time is predicted.

Presented below are a definition of  $\rho_1$ , an error-propagation model, a reentry prediction algorithm, and a reentry prediction experiment.

### DEFINITION OF $\rho_1$

The acceleration by air drag  $\dot{V}_d$  is expressed as

$$\dot{V}_d = -B \cdot \rho \cdot V^2, \quad (1)$$

where  $\rho$  is the air density at an object's position,  $V$  is the velocity of the object, and  $B$  is the ballistic parameter.  $B$  is expressed as

$$B = \frac{1}{2} \cdot C_d \cdot \frac{A}{M}, \quad (2)$$

where  $C_d$  is the drag coefficient,  $A$  is the effective cross-section, and  $M$  is the mass. The ballistic parameter  $B$  includes the uncertainties of the physical characteristics and the attitude of the object. The  $\rho$  has a modeling error of air density. The errors in  $B$  and  $\rho$  are major error sources of air drag, and mainly causes an orbit propagation error.

In this method, the parameter  $\rho_1$  is defined to handle these errors simultaneously. Eq.(1) is reformulated to

$$\dot{V}_d = -B \cdot \rho \cdot (1 + \rho_1) \cdot V^2. \quad (3)$$

This equation makes the  $\rho_1$  represent the major errors related to air drag.

### ERROR-PROPAGATION MODEL

In the orbit propagation, the effect of air-drag error mainly appears as an error of propagated orbital position in the forward direction. In addition to air drag, the accuracy of the initial orbit, from which the orbit is propagated, affects the accuracy of the propagated orbital position. Therefore, an error-propagation model expresses a relationship between the propagated orbit position, air drag, and the initial orbit.

This section describes a set of assumptions made for the model and gives a detailed explanation of the model.



## Assumptions

In order to avoid an excessive complication, three assumptions are made.

### *Assumption 1: Air drag error is constant*

The acceleration by actual air drag (Eq.(3)) varies at every instant, depending on the air density, the attitude of the object, and so on. This means that the air-drag error is not constant. However, the variations mentioned above occur due to complicated physical phenomena so that it is difficult to model the continuous variation of air drag. Therefore, this method assumes that the air drag error is constant in the considered duration.

### *Assumption 2: Neglecting the impact of change in semi-major axis*

The decrease of a semi-major axis changes various physical quantities such as the object velocity and the air density. When we estimate the model the variations due to the decrease of the semi-major axis are neglected in the considered period for convenience. In reality, if a semi-major axis decreases by 60km, the percentage of the change is less than 1% (Note that the semi-major axis is at least more than 6,380km). Therefore, neglecting the impact due to the reduction of semi-major axis has little effect on the accuracy of the reentry prediction, compared with other error sources.

### *Assumption 3: The object is in a circular orbit*

This method assumes that an object is in a circular orbit. If we combine this assumption and Assumption 2, air drag can be assumed to be constant in the considered duration.

## Establish an error-propagation model

This method pays attention to how an air-drag error and an initial orbit error have an effect on a propagated orbital position. The acceleration by air drag is expressed by Eq.(3). Assuming that only air drag causes a change in the object's velocity, we have

$$\Delta V = \dot{V}_d \Delta t, \quad (4)$$

where  $\Delta V$  is the variation in the object's velocity. On the other hand, the Vis-Viva's formula is

$$V^2 = \mu \left( \frac{2}{r} - \frac{1}{a} \right), \quad (5)$$

where  $\mu$  is the gravitational constant of the Earth,  $r$  is the geocentric radius,  $a$  is the semi-major axis. Assuming that the acceleration by air drag immediately affects the orbit in every  $\Delta t$ , Eq(5) can be partially differentiated with respect to the  $a$  while fixing the position where the change in velocity occurs. That is,

$$2V \frac{\partial V}{\partial a} \bigg|_{r=\text{constant}} = \frac{\mu}{a^2}. \quad (6)$$

Based on Eqs.(4) and (6), the change of the  $a$  is expressed by the following relationships:

$$\begin{aligned} \Delta a &= \frac{2a^2V}{\mu} \Delta V, \\ \dot{a} &= \frac{2a^2V}{\mu} \dot{V}_d. \end{aligned} \quad (7)$$

Combining Eqs.(3) and (7),

$$\dot{a} = -B\rho(1+\rho_1) \frac{2a^2V^3}{\mu}. \quad (8)$$

Assumption 2 neglects every variations caused by the reduction of the  $a$ . Therefore, Eq.(8) is approximately constant.

$$-B\rho \frac{2a^2V^3}{\mu} = \text{constant}. \quad (9)$$

Therefore, the error of the  $\rho_1$  (i.e.,  $\Delta\rho_1$ ) is in proportion to the error of the  $\dot{a}$ .

$$\Delta\dot{a} \propto \Delta\rho_1 . \quad (10)$$

Next, assuming that the object is in a circular orbit (Assumption 3), its orbital position in the forward direction is equal to the mean anomaly. The following relationship is derived.

$$\dot{\phi} = \sqrt{\frac{\mu}{a^3}} ,$$

where  $\phi$  is the orbital position in the forward direction. Differentiating this equation with respect to  $a$ , the relationship between the error in  $a$  and the error in  $\dot{\phi}$  is given by

$$\Delta\dot{\phi} = -\frac{3}{2} \sqrt{\frac{\mu}{a^5}} \Delta a . \quad (11)$$

Based on Assumption 2, the coefficient of Eq.(11) is approximately constant and the following relationship is derived.

$$\Delta\ddot{\phi} \propto \Delta\dot{a} \quad (12)$$

Combining Eqs.(10) and (12),

$$\Delta\ddot{\phi} \propto \Delta\rho_1 . \quad (13)$$

Assumption 1 yields  $\Delta\rho_1$  to be constant. Therefore, integration of this differential equation results in the error of the propagated orbital position, which is expressed as a quadratic function of propagation time:

$$\Delta\phi(t) = C_0 + C_1 t + C_2 t^2 . \quad (14)$$

The  $\Delta\phi(t)$  is calculated as the difference between the propagated orbital position, that has some errors, and the determined orbit position, that is a real value. The least square method estimates the coefficients ( $C_0 \sim C_2$ ) by using multiple sets (more than three sets) of the propagation time and the  $\Delta\phi(t)$ .



The following subsections explain the relationships between the coefficients ( $C_0 \sim C_2$ ) and the sources of the orbital position error  $\Delta\phi(t)$ : the error in the  $\rho_1$  ( $\Delta\rho_1$ ), the error in the initial semi-major axis (expressed as  $\Delta a_i$ ), and the error in the initial orbital position (expressed as  $\Delta\phi_i$ ).

*Relationship between  $C_0$  and  $\Delta\phi_i$ :*

The  $\Delta\phi_i$  corresponds to the error in the orbital position at the initial time ( $t = 0$ ). Based on Eq.(14), it is given by

$$\Delta\phi(0) = \Delta\phi_i = C_0 . \quad (15)$$

*Relationship between  $C_1$  and  $\Delta a_i$ :*

The  $\Delta a_i$  corresponds to the error in the semi-major axis at the initial time ( $t = 0$ ). Based on Eqs.(11) and (14), it is derived as

$$\dot{\Delta\phi}(0) = C_1 = -\frac{3}{2} \sqrt{\frac{\mu}{a^5}} \Delta a .$$

Therefore,

$$\Delta a_i = -\frac{2}{3} \sqrt{\frac{a^5}{\mu}} C_1 . \quad (16)$$

*Relationship between  $C_2$  and  $\Delta\rho_1$ :*

Eqs.(13) and (14) yields

$$\ddot{\Delta\phi}(0) = 2C_2 \propto \Delta\rho_1 . \quad (17)$$

The proportional coefficient between the  $C_2$  and the  $\Delta\rho_1$  (i.e., Eq.(9)) depends on an internal calculation method which is used in an orbit propagator. Therefore, it can not be formulated easily. Instead, this method calculates the  $\Delta\rho_1$  by using a differential coefficient of  $C_2$  and  $\rho_1$ :

$$\frac{\partial C_2}{\partial \rho_1} = \frac{C_2(\rho_1 + \varepsilon) - C_2(\rho_1)}{\varepsilon} , \quad (18)$$

$$\Delta\rho_1 = \frac{1}{\frac{\partial C_2}{\partial \rho_1}} C_2 , \quad (19)$$

where  $C_2(\rho_1)$  is the  $C_2$  that is estimated by using an arbitrary value as the  $\rho_1$ .  $C_2(\rho_1 + \varepsilon)$  is estimated by using the  $\rho_1 + \varepsilon$  that is obtained from varying the  $\rho_1$  by an infinitely small amount.

## REENTRY PREDICTION ALGORITHM

This section describes the reentry prediction algorithm that uses the error-propagation model and plural TLE data.

1. Obtain  $n$  sets of TLE ( $n \geq 4$ ) and exchange the orbit type from mean orbital element to osculate orbital element<sup>1</sup>. The TLE that has the newest epoch time is regarded as an initial orbit (Initial TLE) and the others are regarded as data orbits (Data TLE).
2. Assume an arbitrary value as an initial  $\rho_1$ , propagate the Initial TLE to each Data TLE's epoch time, and calculate the difference of the orbital positions:  $\Delta\phi_k$  ( $k=1,2,\dots,n$ ).
3. Substitute these  $\Delta\phi_k$  in the error-propagation model (Eq.(14)) and estimate the coefficients ( $C_0 \sim C_2$ ) with the least square method.
4. Estimate  $\Delta\alpha_i$  and  $\Delta\phi_i$  based on the Eqs.(15) and (16).
5. Change the  $\rho_1$  by a minute amount ( $\rho_1 + \varepsilon$ ) and conduct the process 2, 3, and 4 over again.
6. Estimate  $\Delta\rho_1$  by substituting the pair of  $C_2$  into Eqs.(18) and (19), and calculate an optimal  $\rho_1$  ( $= \rho_1 - \Delta\rho_1$ ).
7. Improve the initial orbit with  $\Delta\alpha_i$  and  $\Delta\phi_i$ , and propagate the improved orbit to the reentry time using the optimal  $\rho_1$ .

Principal features of this method are that the error-propagation model estimates the air-drag error ( $\Delta\rho_1$ ) and the initial orbit error ( $\Delta\alpha_i$  and  $\Delta\phi_i$ ) as the origins of the propagated orbital position error ( $\Delta\phi(t)$ ), and that the statistical processing of a large amount of orbital data provides stable results that are not influenced by the uncertainty of individual orbital data.

---

<sup>1</sup> The orbit propagation considered in this method is based on the special perturbation method. Therefore, TLE, that is the mean orbital element, has to be transformed into the osculate orbital element.

## EXPERIMENT

A reentry prediction experiment was conducted to examine the performance of the presented method. This experiment uses an example of the Chinese satellite (FSW1) whose orbit actually decayed into atmosphere over the Southern Atlantic Ocean on 12 March, 1996. The reentry time that was officially announced is 4:05 UTC of 12 March, 1996 (Ref.7). The solar activity remained stable during the last months of its lifetime.

This section describes an experimental procedure and discusses results.

### Experimental procedure

In this experiment, four cases were simulated: the reentry prediction at 6 days before the reentry (Case1), 5 days before the reentry (Case2), 3 days before the reentry (Case3), and just before the reentry (Case4). For each case, 10 sets of TLE (one of them is Initial TLE and the others are Data TLE) were selected. Table 1 shows the TLE sets used in each case. The physical parameters of the satellite were assumed as  $C_d=2.5$ ,  $A=6$  (m<sup>2</sup>), and  $M=1000$  (kg). This method requires two values for initial  $\rho_1$ 's. In the experiment,  $\rho_1=0$  and  $\rho_1+\varepsilon=-0.5$  were used as the initial  $\rho_1$ . Two initial  $\rho_1$ 's provide two sets of  $\Delta\phi_k$  ( $k=1,2,\dots,9$ ), which result in two set of  $C_0\sim C_2$ . In the experiment, the set of  $C_0\sim C_2$  derived from the smaller  $\Delta\phi_k$  was used to estimate  $\Delta\alpha_i$  and  $\Delta\phi_i$ .

Table 1 : TLE sets used for each case

Case	Prediction Date (Days to Reentry)	Data TLE Duration	Initial TLE Epoch
1	6 Mar. (6days)	Mar. 4 - 6	6 Mar. at 12:28
2	7 Mar. (5days)	Mar. 5 - 7	7 Mar. at 12:21
3	9 Mar. (3days)	Mar. 5 - 9	9 Mar. at 11:55
4	11 Mar. (5hours)	Mar.10-11	11 Mar. at 22:50

### Discussion of results

Table 2 shows the estimated values ( $\rho_1$ ,  $\Delta\alpha_i$ , and  $\Delta\phi_i$ ). Figure 1 shows the prediction error corresponding to each case. Figure 2 shows the ratio of the prediction error and the propagation run-time.



The maximum prediction error is 2.8hr.. The maximum error ratio is 22% and the average error ratio is 6.7%. In particular, the predictions at about a week prior to the reentry are quite good: the prediction error of 0.2hr. for the Case1 and the Case2.

On the other hand, the Figure 2 shows a degradation of the prediction performance at the very last day (Case4). A comparison of the estimated  $\rho_1$ 's shows that the Case4 is different from other cases (see Table 2). This suggests that, in Case4, the prediction method failed to estimate the  $\rho_1$ . The following subsections examine this phenomena.

Table 2: Estimated parameters

Case	$\rho_1$	$\Delta a_i$ (km)	$\Delta \phi_i$ (deg)
1	-0.548	-0.726	0.253
2	-0.562	0.139	-0.028
3	-0.559	-0.596	0.524
4	-0.408	-0.709	0.010

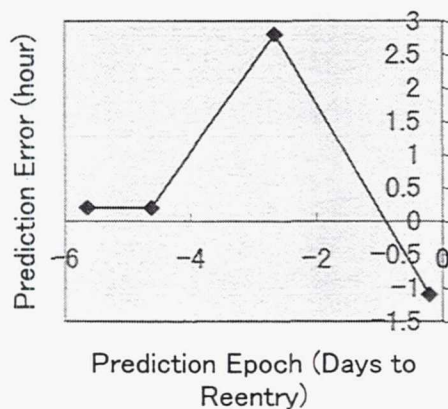


Figure 1: Prediction error

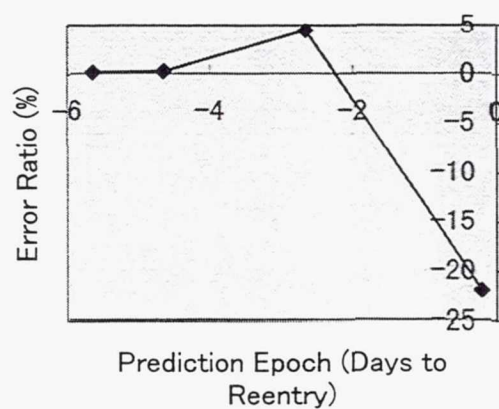


Figure 2: Prediction error ratio

#### *Analysis of TLE data quality*

If there are some sets of Data TLE which have low grade precision compared with other sets, such sets have an undesirable effect on the

estimation of the  $\Delta\phi(t)$  curve (Eq.(14)). Moreover, the precision of the estimated  $\rho_1$  is deteriorated. To confirm the existence of the low-quality data, Figure 3 shows the  $\Delta\phi_k(k=1,2,\dots,9)$  overlapped with the estimated  $\Delta\phi(t)$  curve. As Figure 3 shows, for all the cases, the  $\Delta\phi_k$ 's( $k=1,2,\dots,9$ ) are completely fitted to the curves, and no low-quality data is observed. Therefore, the possibility that the low-quality Data TLE affected the  $\rho_1$  estimation is not the case here.

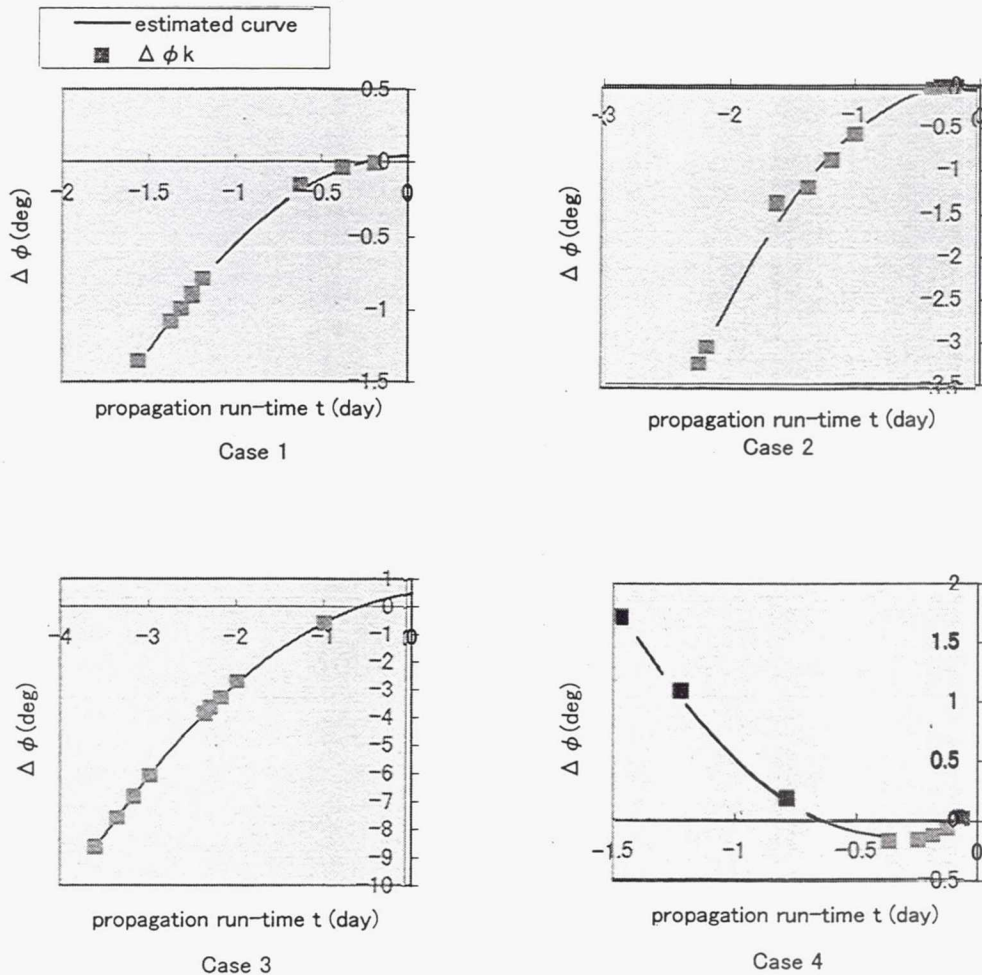


Figure 3:  $\Delta\phi_k$  overlapped with estimated  $\Delta\phi(t)$  curve

#### *Effect of the air drag changing*

This method assumes the air drag is approximately constant within the considered duration (Assumption 2 and 3). However, as the object's altitude decreases, the air drag gradually increases. Moreover, the in-

crease rate becomes higher at a lower altitude. Case4 is the prediction just before the reentry, so that the satellite is at a very low altitude. Therefore, for the Case4, there is a possibility that air drag increased drastically in the considered duration.

Table 3 shows the highest and the lowest altitudes in the each case's Data TLE and the corresponding air densities. The air densities are estimated, based on the Jacchia-Roberts air density model. As Table 3 shows, the air density at the lowest altitude is 11.7 times higher than the highest altitude in the Case4. This difference is significant, compared with other cases. It suggests that a large change in the air density invalidated Assumption 2 and results in the poor estimation of  $\rho_1$ .

Table 3: Altitude and air density

Case	Max. Altitude TLE Altitude (km) Air density ( $\times 10^{-11} \text{ kg/m}^3$ )	Mim. Altitude TLE Altitude (km) Air density ( $\times 10^{-11} \text{ kg/m}^3$ )	Density Change Rate
1	282.860 1.0957	267.132 1.7518	1.6
2	279.879 1.1953	256.210 2.4493	2.0
3	273.504 1.4441	229.743 6.0156	4.1
4	212.381 11.575	159.253 135.424	11.7

#### *Additional experiment*

This method deals with the multiple Data TLE in a certain extent of duration statistically. Therefore, averaging time-to-time variations of ballistic parameter error and air density error should result in the stable  $\rho_1$ . The estimated  $\rho_1$ 's of Case1~3 are, indeed, very stable. It suggests that these  $\rho_1$ 's might be useful for the prediction just before the reentry.

On the other hand, in the initial orbit,  $\Delta a_i$  and  $\Delta \phi_i$  are small for all cases (see Table 2). It suggests that the TLE is very precise. Therefore,



though the Initial TLE is not improved with  $\Delta\alpha_i$  and  $\Delta\phi_i$ , the result is little affected.

Based on the above discussion, an additional experiment was conducted to reduce the prediction error of Case4. In this experiment, the orbit propagator propagated the Case4's Initial TLE to the reentry time. Its calculation used the mean value of the estimated  $\rho_1$ 's of Case1~3 as an optimal  $\rho_1$ . Table 4 shows the result. As Table 4 shows, a more accurate result is obtained, compared with the original Case4.

Table 4: Result of additional experiment

$\rho_1$ (mean of Case1~3)	Initial Orbit	Prediction Error (hour)	Error Ratio (%)
-0.556	Case4 Initial TLE	0.1	2.0

## CONCLUSION

This paper described the reentry prediction method. Processing plural sets of TLE with an error-propagation model, this method estimates the optimal  $\rho_1$  that is viable for the accurate reentry prediction. An experiment shows that the method provides the high quality results, especially when it is performed with the data of days before the reentry.

The experiment also shows that the estimation gradually deteriorates just before the reentry. The reason is surmised that the drastic variation of air drag due to the object's altitude decrease makes the model's assumption invalid. However, the very last day's prediction can be improved by using  $\rho_1$ 's that have been estimated in the earlier prediction.

National Space Development Agency of Japan (NASDA) plans to implement this method in the Space Debris Orbit Analysis Test System (Ref.8). To obtain some know-how of the reentry prediction, the actual prediction work is necessary. By accumulating the prediction experiences and improving the method based on the experiences, we expect this method to contribute the world-wide reentry prediction activities in near future.

## REFERENCES

1. *Proceedings of the 14<sup>th</sup> IADC Meeting*, Inter-Agency Space Debris Coordination Committee, 1997.
2. L. Anselmo, C. Pardini and A. Rossi, "Reentry Predictions for COSMOS 398, FSW-1 5 and TSS-1R", *Proceeding of the 2<sup>nd</sup> European Conference on Space Debris*, 1997, pp. 559-564.
3. J. J. Velasco and H. Conessa, "Organization and Surveillance Concerning the Atmospheric Re-entry of Potentially Dangerous Bodies", *Proceeding of the 2<sup>nd</sup> European Conference on Space Debris*, 1997, pp. 565-572.
4. *ORBITAL DEBRIS*, National Academy Press, Washington D.C., 1995.
5. H. Klinkrad, "SALYUT-7/KOSMOS-1686 Re-Entry Prediction Activities at ESOC", *Proceeding of International Workshop on Salyut-7/Kosmos-1968 Reentry*, 1991, pp.17-34.
6. L. Anselmo, et.al., "SALYUT-7/KOSMOS-1968 Re-entry Predictions for The Italian Civil Defence Authority", *Proceeding of International Workshop on Salyut-7/Kosmos-1968 Reentry*, 1991, pp.45-50.
7. *US SPACE COMMAND NEWS Release*, 11 Mar., 1996.
8. H. Konno, T. Tajima and S. Mori, "Conceptual Study of Space Debris Orbit Analysis Test System", *Proceeding of the 2<sup>nd</sup> European Conference on Space Debris*, 1997, pp. 573-580.

## **EUVE Reaction Wheel Assembly Calibration for Improved Spacecraft Slews**

**Robert Bauer\*, Christopher Smith†, Robert Nevitt‡**

An innovative approach to reaction wheel assembly (RWA) calibration has resulted in improved slew performance of the Extreme Ultra-violet Explorer (EUVE) spacecraft. Calibration tests were performed using an approach which allows the science mission to proceed without interruption and unaffected by the tests. The parameter calibrated was the RWA torque command scale factor. Spacecraft slews confirm improved performance using the calibrated scale factor.

The EUVE spacecraft was launched in June 1992. During the in-orbit check-out the RWA scale factors were calibrated based on data taken during spacecraft slews. However, the accuracy of the scale factor calibration was affected by uncertainties in spacecraft inertia, structural dynamics, attitude determination, and RWA drag variation with wheel speed. To separate the command scale factor from other parameters effecting slews a novel in-flight testing approach was developed. EUVE has four RWAs, three of which are used for attitude control at any given time. The extra degree of control freedom afforded by the fourth RWA is used to issue torque commands to all RWAs in such a way that the net torque on the spacecraft is zero. Thus, spacecraft inertia and structural dynamics uncertainty are eliminated from the calibration process. The change in RWA momenta as observed by the wheel tachometer is used to derive the torque command scale factors. Since attitude determination information is not used, it too is eliminated as a source of errors. To separate effects due to drag, the drag variation with wheel speed is calibrated. By disabling commands to a given RWA, the RWA is allowed to coast down under the sole influence of drag while the other RWAs maintain control of the spacecraft. Drag is deduced from the slope of the momentum versus time.

The tests were performed with minimal burden on the flight operations. More importantly, the science mission was able to proceed completely unaffected by the RWA calibration test. This salient feature of the tests is due to the use of the extra degree of control freedom afforded by four RWAs to exercise them according to a tell tale scenario while imparting zero net torque onto the spacecraft.

This paper presents the test plan and data reduction methods used to calibrate the RWAs. The resulting scale factors are compared with those found during RWA testing in the factory and with the baseline scale factors found from calibration slews performed a few weeks after launch. For completeness, drag is plotted versus wheel speed as deduced from in-flight data for one of the four RWAs. A comparison is made between slews performed using the baseline scale factors and those found using the calibration approach given herein.

---

\* Principal Engineer, Bauer Engineering Enterprises, 13272 Summit Sq., Rt. 413 & Doublewoods Rd., Langhorne, PA 19047 USA, (215) 860-6390.

† Engineer, Center for Extreme Ultraviolet Astrophysics, University of California, 2150 Kittredge Street, Berkeley, CA 94720 USA, (510) 643-7388.

‡ Engineer, Center for Extreme Ultraviolet Astrophysics, University of California, 2150 Kittredge Street, Berkeley, CA 94720 USA, (510) 643-3029.



## INTRODUCTION

Slews are an important part of many spacecraft missions. Typically, payload fields of view are a small fraction of the observational field of interest. Therefore maneuvers are required to collect data from disperse targets. It is desirable to minimize the time spent to maneuver in order to allow more time for observation. Indeed, for some missions time is of the essence since the targets of interest may be fleeting. "Slew" is the general term given to maneuvers which rapidly reposition the payload field of view without regard to collection of mission data during the maneuver. A slew typically has four phases: acceleration, coast, deceleration, and settling. This paper discusses a method demonstrated on the Extreme Ultraviolet Explorer (EUVE) spacecraft to improve the slew performance. Specifically, the attitude errors due to uncertainty in reaction wheel assembly (RWA) torque command scale factors and bearing drag are greatly reduced by an innovative RWA calibration technique which can be performed without impact to the on-going science mission.

EUVE, shown in Figure 1, is a NASA spacecraft which was launched on 7 June 1992 into a low Earth orbit of approximately 528 km altitude and  $28.5^\circ$  inclination<sup>1</sup>. Its principal mission was completed at the end of 1995. Rather than decommission a healthy spacecraft which could still collect valuable science data, EUVE's operation was contracted to the Center for EUV Astrophysics at the University of California Berkeley under a program to demonstrate low cost spacecraft operation and to provide a flight test bed for spacecraft design and performance investigations.

EUVE uses a body mounted payload to make astronomical observations in the extreme ultraviolet band. Four RWAs provide fine attitude control and the torque required to perform slews. As shown in Figure 2, three of the RWAs are arranged with their spin axes along the attitude control X, Y, and Z axes respectively. The fourth is skewed such that its spin axis is equi-angle from the control axes. Normally all four RWAs are on. The net system momentum is maintained near zero using magnetic torquers to counter environmental torque. The momentum of the skew RWA is held at a prescribed level to act as "ballast". The momenta of the other three RWAs are thereby biased away from zero so that they may provide control torque without crossing through zero wheel speed, thus avoiding the disturbance torque caused by zero crossings<sup>2,3</sup>.

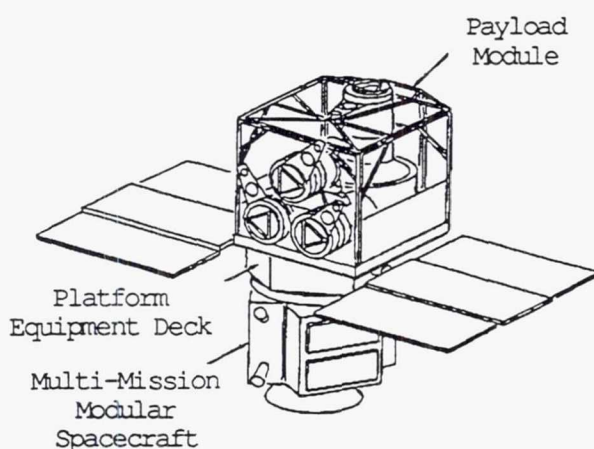


Figure 1 Extreme Ultra-Violet Explorer

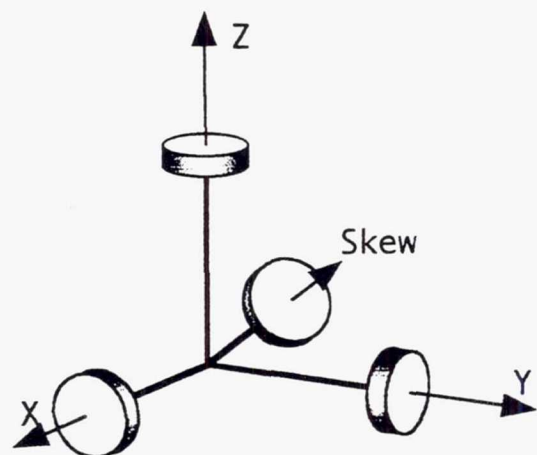


Figure 2 Redundancy allows RWA testing while performing the mission

In a manner typical of many spacecraft, EUVE performs slews to re-position the payload field of view. To slew the spacecraft, the flight software generates RWA commands consisting of a *feed forward* profile and a *feedback* compensation. The scheme described in Figure 3 generates the feed forward profile<sup>4</sup>. This simple scheme accounts for the spacecraft inertia matrix and the RWA scale factors. A high performance slew scheme using RWAs must account for these and other factors summarized in Table 1.

Ideally the feed forward profile by itself should result in a perfect slew. However, imperfect knowledge in the factors in Table 1, or a total failing to account for them, results in slew errors. To compensate for these errors feedback is employed. In doing so, the quality of the attitude determination becomes a factor. The two most important aspects of the attitude determination affecting the slew performance is the gyroscope scale factors and feedback latency. Each of the factors in Table 1 are discussed below.

**Figure 3. EUVE Slew Feed Forward Profile<sup>4</sup>** is found by first determining the Euler axis  $\mathbf{e}$  and angle  $\theta$  which carries the initial attitude to the desired final attitude. An acceleration profile a) is then generated which conforms to several constraints: its second integral equals the Euler angle, and the peak RWA torque and momentum required to achieve the slew are less than specified maxima. Then the feed forward RWA command profile  $\mathbf{c}_p(t)$  is found according to:

$$\alpha_p(t) = \mathbf{e} \alpha_p(t)$$

$$\tau_p(t) = \hat{\mathbf{J}} \alpha_p(t)$$

$$\mathbf{c}_p(t) = \hat{\mathbf{S}}^{-1} \tau_p(t)$$

where  $\alpha_p$  is the scalar acceleration profile,  $\mathbf{e}$  is the Euler axis,  $\hat{\mathbf{J}}$  is the spacecraft inertia matrix,  $\tau_p$  is the torque profile, and  $\hat{\mathbf{S}}$  is the diagonal matrix of RWA torque command scale factors. Body rate and attitude profiles, b) and c), are generated consistent with the acceleration profile to act as a reference for the attitude control feedback, which is used to compensate for slew errors.

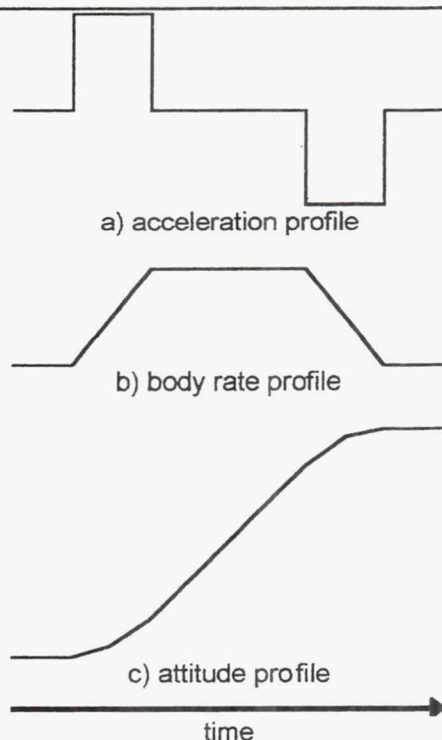


**Table 1 Factors Affecting High Performance Slews**

**Feedforward Factors:**

- Spacecraft main body and movable appendages inertia matrices
- Structural bending dynamics
- Stored momentum
- RWA spin axis alignment
- RWA torque command scale factor
- RWA drag

**Feedback Factors:**

- Gyroscope scale factor
- Feedback latency



This paper focuses on slew errors due to RWA scale factor and drag uncertainty and how to reduce these errors by RWA calibration. Using the innovative method described below, the RWA scale factors and drag are easily calibrated in flight *without* impact to the on-going mission. The extra degree of control freedom afforded by the four RWAs is exploited to exercise a given RWA according to a tell tale scenario while using the other RWAs to maintain three axis spacecraft control. To measure drag versus wheel speed all four RWAs are run-up to near their maximum operational speeds in such a way that their net momentum is held constant. Then, commanding to one RWA is inhibited allowing it to coast down under the sole influence of drag while the other three RWAs maintain attitude control. The RWA tachometer telemetry is recorded and later passed through a non-causal filter to estimate the drag<sup>5</sup>.

The RWA scale factors are measured using torque pulse tests. Simultaneous torque command pulses are sent to all four RWAs such that the net torque on the spacecraft is zero, thereby allowing the mission to proceed unaffected. By recording the commanded torque and RWA tachometer telemetry as a function of time it is possible to extract the torque scale factor for each RWA. The tachometer data is multiplied by the wheel inertia to find the RWA momentum. The delivered motor torque is then derived from the slope of the momentum versus time (reaction torque) and from knowledge of the drag versus wheel speed gained from the coast down tests. A least squares linear fit of the motor torque to command voltage is performed to find the scale factor for a given RWA.

It is possible to calibrate RWA scale factors using momentum and torque command telemetry recorded during initial in-orbit test slews, or during nominal mission slews. In this way the scale factors can be calibrated without impact to the on-going mission and without any special RWA tests. However, with such an approach the calibration is subject to happenstance torque levels, which may not provide information rich enough to yield good observability of the scale factors. Furthermore, the RWA drag torque cannot be calibrated from slew data, and knowledge of the drag torque is needed to accurately calibrate the scale factors.

After the initial calibration of the factors affecting slews, RWA scale factor calibration offers the greatest benefit to maintaining good slew performance. The RWA scale factors are subject to change as electronics age in space flight. Depending on exposure and susceptibility to radiation and extreme thermal environments, the RWA scale factors can be expected to change as much as 10% over the life of a typical mission<sup>6</sup>. As discussed below, the other factors affecting slews (Table 1) may require in-flight calibration at the beginning of the mission, but thereafter remain constant over the life of the spacecraft.

RWA drag must be modeled as part of a high precision slew scheme to account for the dependence of drag on wheel speed, especially when the wheel speed reverses direction<sup>3</sup>. It is best to base such models on flight data since drag tests conducted in the factory are subject to influences from the terrestrial environment. Gravity and atmospheric pressure on the RWA housing affect the preload on the bearings<sup>5,8</sup> which in turn affects the drag. Also, windage due to the atmosphere surrounding the wheel can be greater on the ground than in flight where the RWA housing is vented to the hard vacuum of space. Before calibrating the drag in-flight, the bearings must be allowed to "run-in". The vibration due to launch will disturb the bearing lubrication causing an initially elevated level of drag. After a few days to a few weeks of operation, depending on wheel speed, the drag will diminish. Thereafter the drag as a function of wheel speed will remain fairly constant, although some additional run-in may be observed for several months or more.<sup>3</sup>

The inertia matrices of the main body and appendages (e.g. solar arrays) are typically calibrated to within 2% during spacecraft integration and test. The calibration may be refined by in-flight slew tests<sup>7</sup> to within a fraction of a percent before the primary mission commences. There-



after, these factors remain constant throughout the life of the spacecraft\*, and hence there is no need to re-calibrate. Similarly, the dominant structural bending dynamics and RWA spin axis alignments can be calibrated and expected to remain constant.

A high precision slew scheme must account for stored momentum by adding an  $\omega_p \times H$  term to the RWA commands where  $H$  is the stored momentum and  $\omega_p$  is the spacecraft slew rate. The stored momentum is measured in-flight by reading the RWA tachometers and multiplying by the wheel inertias and by a matrix of spin axis alignment vectors. Assuming a digital tachometer is used (one which counts pulses from an optical encoder or Hall effect sensors) the stored momentum uncertainty is due mainly to the uncertainty in the wheel inertia (about 0.5% per Ref. 8) and spin axis alignments (about  $5 \times 10^{-3}$  radians per Refs. 2 and 6). The magnitude of the slew torque error due to these uncertainties is  $\mu_H |\omega_p \times H|$ , where  $\mu_H$  is about 0.7%. The peak value of this term is typically smaller than other slew torque error terms depending on the magnitude of the stored momentum and slew rate. Even if the slew profiling does not account for the stored momentum ( $\mu_H = 1$ ) as is the case for EUVE, the  $|\omega_p \times H|$  term ramps down to zero during the deceleration phase of the slew. Thus by the end of the slew when pointing errors are of real concern, the torque error due to stored momentum is no longer present.

The feedback needed to compensate for the uncertainties in the feedforward factors discussed above introduces two more important sources of slew errors: gyroscope scale factor uncertainty and feedback latency uncertainty. Gyroscope scale factor uncertainty is typically less than 200 ppm (0.02%) resulting in an error less than 60  $\mu$ rad for a 180 degree slew. This uncertainty, while subject to change over time, is a small influence compared with the RWA scale factor uncertainty.

A more important aspect of the feedback is its latency, i.e. the delay  $\lambda$  from when gyroscope data is taken to when the flight software determines the body rates and attitude based on that data. For high precision slews, a model of this latency must be applied to the body rate and attitude profiles of Figure 3 to make them temporally commensurate with the feedback†. Latency uncertainty  $\epsilon\lambda$  results in a body rate disturbance  $\delta\omega$  and attitude disturbance  $\delta\theta$  to the attitude control loop given by

$$\begin{aligned}\delta\omega &= \alpha_p \epsilon\lambda \\ \delta\theta &= \int \delta\omega dt\end{aligned}$$

where  $\alpha_p$  is the slew acceleration profile of Figure 3. These disturbances return to zero at the end of the slew, but they cause a control transient which increases the slew settling time. The latency is measured by timing tests of the flight software and data system and remains constant over the life of the spacecraft. The uncertainty is typically 10% to 50% of an attitude determination sampling cycle. Using EUVE values for the acceleration profile and sampling cycle the peak attitude transient at the end of the slew is less than 100  $\mu$ rad.

RWA scale factor uncertainty is the slew error source most subject to change after initial in-flight calibration. Therefore only the RWA scale factor needs to be calibrated on and on-going basis to maintain good slew performance. In the next section the RWA calibration method is explained in detail and results given for the EUVE RWAs. Thereafter, results of slew test performed to validate the RWA calibration are discussed.

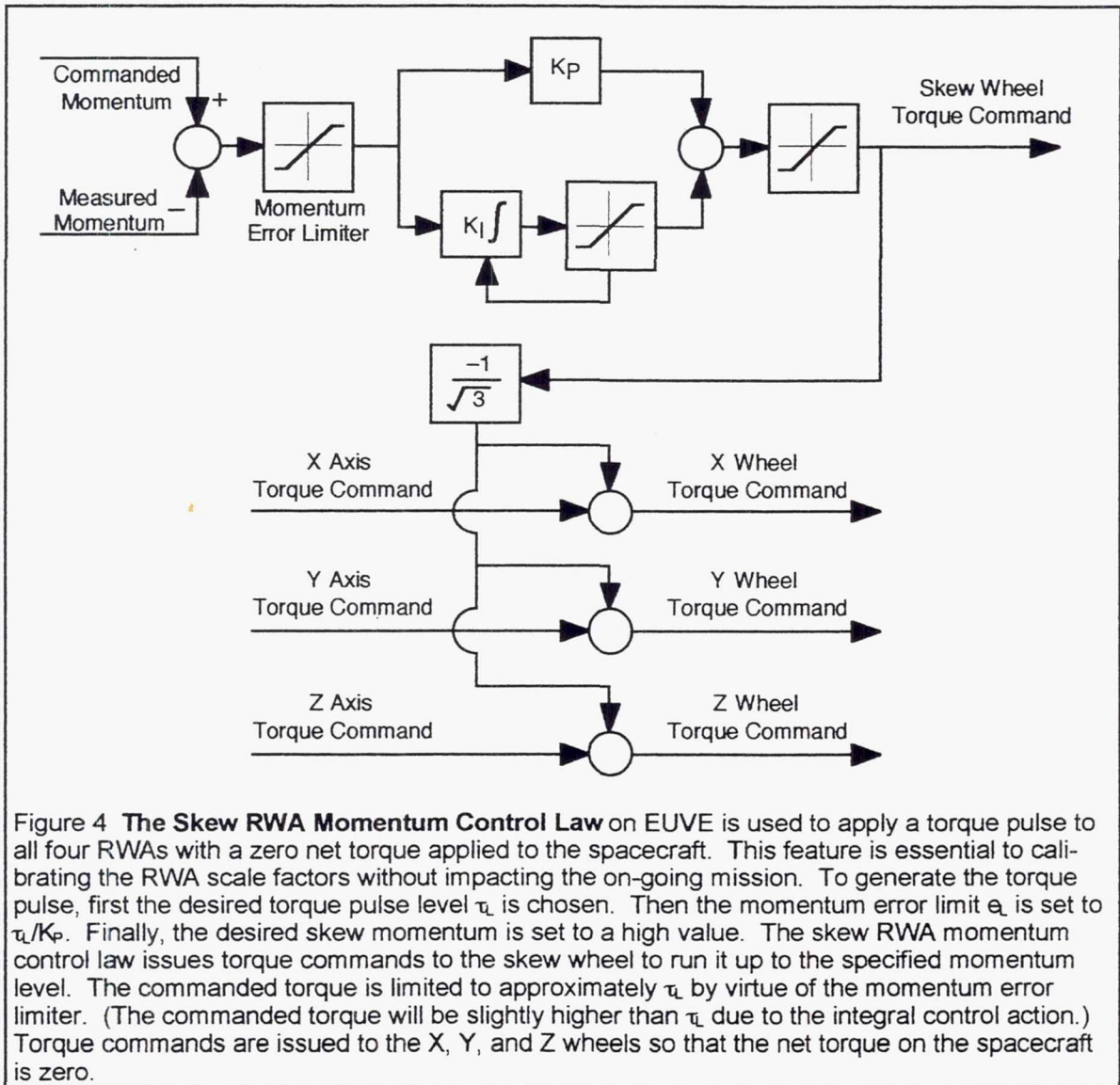
\* Assuming the spacecraft does not use mass expulsion methods for attitude and orbit control the main body inertia matrix will remain constant. If mass expulsion methods are used, propulsion fuel usage estimates are often accurate enough to maintain good knowledge of the spacecraft inertia matrix.

† There is also a delay between the time the RWA command profile is generated and when it is executed by the RWAs. Since what is at issue is the total *uncertainty* in command and sensing delays, it is assumed without loss of generality that the command delay is zero and the total uncertainty is attributed to the sensing delay.

## RWA CALIBRATION

Fundamental to the RWA calibration technique presented here is the ability to command all four RWAs such that the net torque is zero. On EUVE this ability is provided by the skew RWA momentum control shown in Figure 4. In general the spacecraft design features needed to perform RWA calibration without impact to the mission are:

- At least one redundant RWA
- RWAs with high precision tachometers
- A software algorithm to issue torque commands to all RWAs such that the net torque on the spacecraft is zero.
- The ability to disable the motor for any one of the RWAs while leaving its tachometer enabled





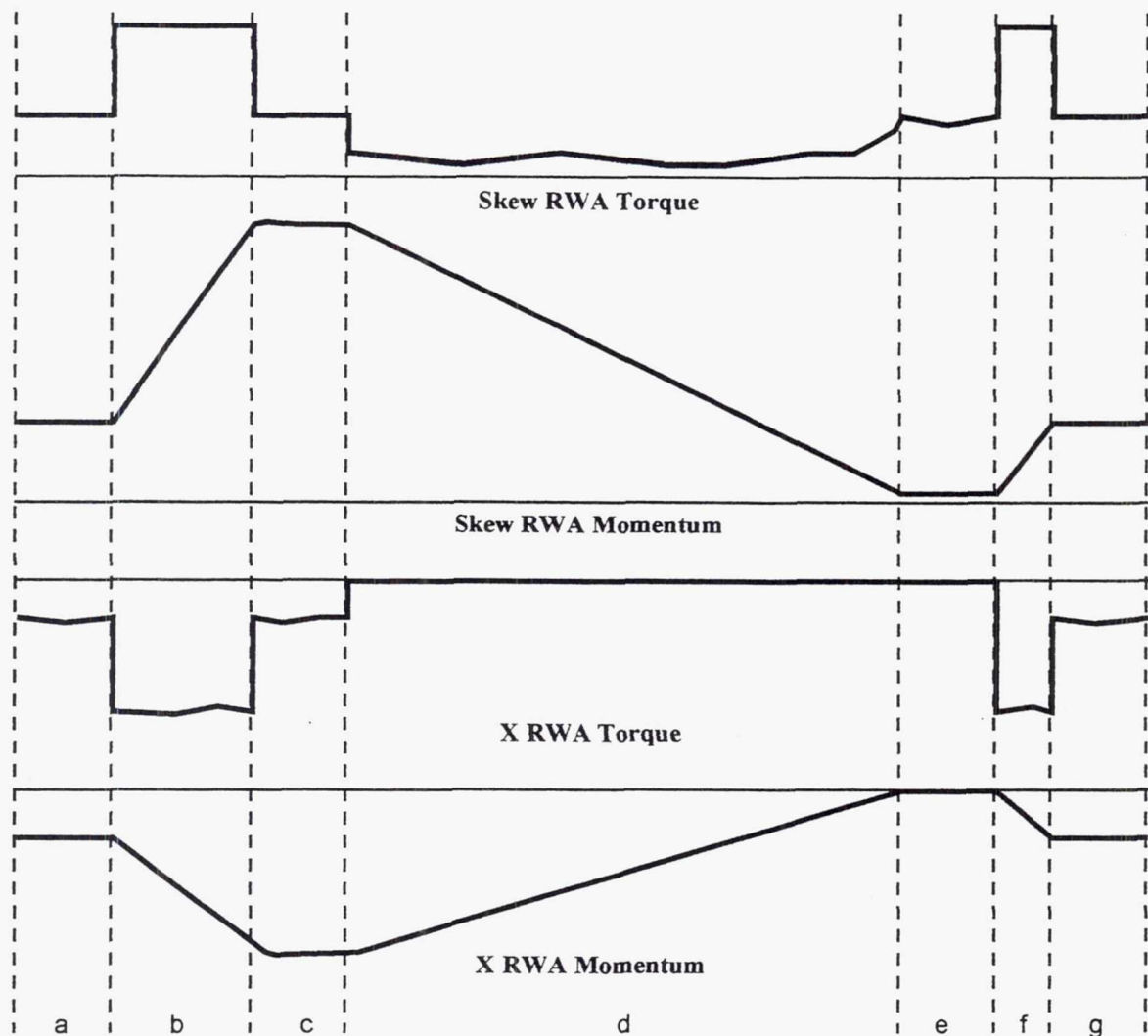
The calibration test consists of a sequence of run-up, coast-down, and run-down phases. To calibrate the RWA scale factor, the drag must also be calibrated to isolate its effect on the wheel momentum. The drag is estimated from coast down data, while the run-up and run-down data are used in conjunction with the estimated drag to calibrate the scale factor. Figure 5 shows a time line for a run-up/coast-down test. This scenario is executed a total of four times so that data can be collected for a range of torque levels during the run-up phases and to allow each wheel to coast down from a high momentum to zero. Figure 6 shows a time line for a run-up/run-down test. During the run-down phase, the commanded torque is in opposition to the wheel momentum causing the motor to operation in "generator" mode. The run-up/run-down test is executed a total of three times to gather data over a range of torque levels during the run-down.

To measure drag in flight, the RWAs are run-up near their maximum operational speed (about half their rated speed of 6000 RPM on EUVE). Then a given RWA is allowed to coast down while the other RWAs maintain control of the spacecraft. RWA momentum telemetry is recorded versus time during the coast down. The drag is estimated from the coast down data using a non-causal estimation filter<sup>5</sup>. Figure 7 shows the in-flight drag for one of the four RWAs. For comparison, the drag measured during unit level testing in the factory is also shown<sup>9</sup>. The in-flight drag is significantly lower than the drag measured in the factory. The lower drag is attributed to the lack of windage since the atmosphere within the RWA has been vented to space, and to bearing run-in<sup>5</sup>. The venting occurs during the first few hours after launch, whereas the run-in process takes several weeks as seen in Figure 8. Seeing the dramatic reduction in drag during the first three weeks, it would be prudent to wait until after this run-in is complete before attempting to calibrate the RWAs.

The RWA torque command scale factor is calibrated using data from the run-up and run-down phases of the tests. The reaction torque is derived at a number of points from the slope of the momentum versus time. Then the delivered motor torque is found by subtracting an estimate of the drag versus wheel speed gained from the coast down tests. A least squares linear fit of the motor torque to command voltage is performed to find the scale factor. The results for RWA calibration performed in January 1995 and October 1997 are summarized in Figure 9. Also given are the scale factors determined during the final factory tests<sup>9</sup> conducted in the first quarter of 1990 and from spacecraft slews performed to calibrate the gyroscopes during the in-orbit check-out<sup>1</sup> shortly after launch (June 1992). It should be noted that the scale factor reported herein is for the attitude control electronics (ACE) and RWA combined. The ACE converts counts from the flight computer to a voltage command to the RWA at a nominal scaling of 10 Volts per 512 counts = 0.01953125 V/cnt. The nominal scale factor for the RWA alone is 0.3661 N·m per 10 Volts = 0.03661 N·m/V. The nominal combined scale factor is 715.0  $\mu$ N·m/cnt.

The most striking result seen in Figure 9 is that the RWA calibration based on the method presented herein gives very different results than the RWA calibration based on slew data performed during the in-orbit check-out. As will be seen in the next section, the scale factors based on the present method also yield better slew performance. Thus one may reasonably conclude that the present method is superior. In all fairness it should be noted that the slews performed during in-orbit check-out were not designed to calibrate the RWA scale factors per se, but rather were meant to calibrate the gyroscope scale factors. The RWA scale factor was deduced from gyroscope data and RWA torque commands observed during the slew. Even when compared to an appropriately designed slew test, one can expect the present method to be superior for two reasons. First, as mentioned before, RWA drag is not observable from slew tests, and knowledge of the drag is need to accurately calibrate the scale factors. Second, the calibration presented herein uses RWA tachometer data, which provides a much more direct observation of the RWA behavior than gyroscope data collected during slews. The gyroscopes are subject to their own residual calibration errors, and observe spacecraft body behavior which is influenced by factors other than RWA scale factors, e.g. mass property uncertainties, structural bending dynamics, and environmental torque.

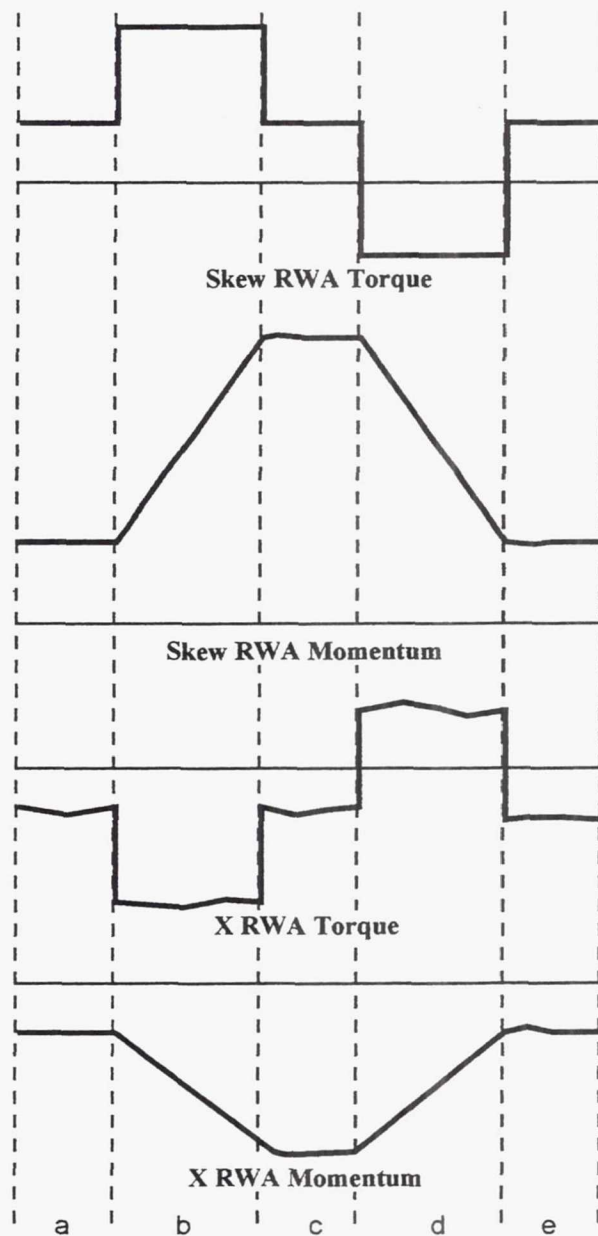




**Figure 5 RWA Run-up/Coast-down Time Line.** To observed RWA drag the wheels are allowed to coast down from a high speed to zero under the sole influence of drag. Data taken during the run-up is used to calibrate the RWA scale factor when the motor drive electronics are in "motor" mode. The time line is as follows: a) The attitude control system is in four RWA mode. The skew RWA momentum control law (see Figure 7) compensates the drag to hold the momentum steady. The spacecraft attitude is controlled by the X, Y, and Z RWAs to compensate for environmental and drag torque. Limits are set in the skew momentum control law to achieve the desired torque range during the up-coming run-up. b) The run-up is initiated by setting the desired skew momentum to a high value. The skew torque command jumps to its limit and the wheel accelerates. The skew momentum control law issues torque commands to the X, Y, and Z RWAs to maintain zero net torque on the spacecraft. c) The skew momentum reaches its desired value and the torque commands to the four RWAs drop back to nominal levels. A few minutes elapse while the skew momentum control law reaches steady state. d) The attitude control system is set to three RWA mode with the X RWA disabled to let its wheel coast down to zero. The X RWA remains powered on to allow wheel speed data to be collected. e) The X RWA reaches zero wheel speed and stops. The desired skew momentum is reset to its nominal value. f) Four RWA mode is re-established and the skew momentum control law accelerates the wheels as it brings the skew momentum back up to its nominal value.

**Figure 6 RWA Run-Up/Run-Down Time Line.** In order to observe the RWA scale factor when the motor drive electronics are in "generator" mode, the RWAs must be commanded to run down. The time line is similar to the run-up/coast-down time line except that the RWAs are commanded to run down rather than allowed to coast down under the sole influence of drag.

a) The attitude control system is in four RWA mode. Limits are set in the skew momentum control law to achieve the desired torque range during the up-coming run-up. b) The run-up is initiated by setting the desired skew momentum to a high value. The skew torque command jumps to its limit. Torque commands are issued to the X, Y, and Z RWAs to maintain zero net torque on the spacecraft. c) The skew momentum reaches its desired value and the torque commands to the four RWAs drop back to nominal levels. d) The run-down is initiated by setting the desired skew momentum back to its nominally low value. The skew torque command jumps to its limit. Torque commands are issued to the X, Y, and Z RWAs to maintain zero net torque on the spacecraft. e) The RWAs reach their nominally low momenta.



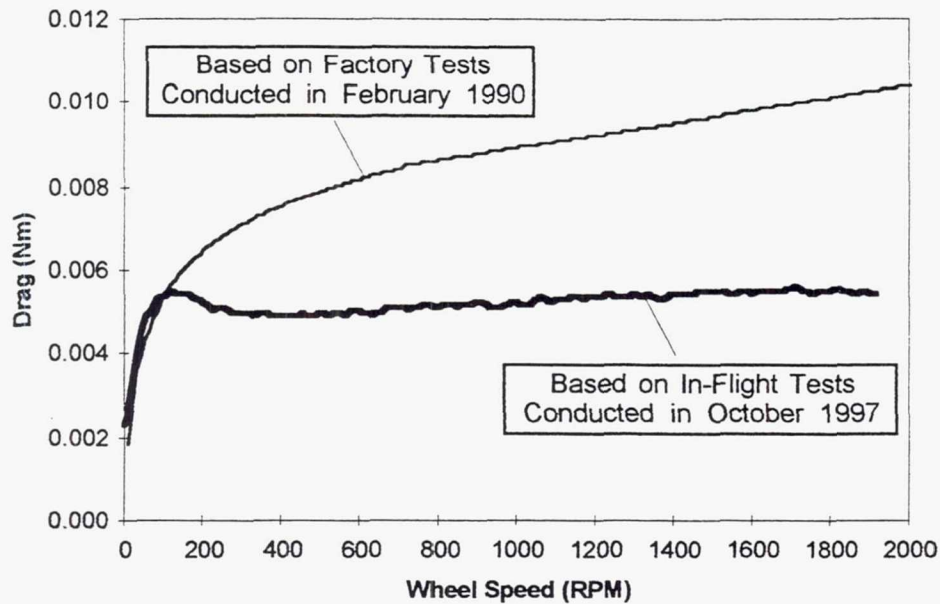


**Figure 7 EUVE RWA Drag versus Wheel Speed** as measured during unit level tests in the factory<sup>9</sup> and by in-flight calibration tests conducted more than five years after launch. The lower drag observed in flight is attributed to lack of windage and to bearing run-in<sup>5</sup>. Data shown is for the Y RWA. The X, Z, and Skew RWAs show similar behavior.

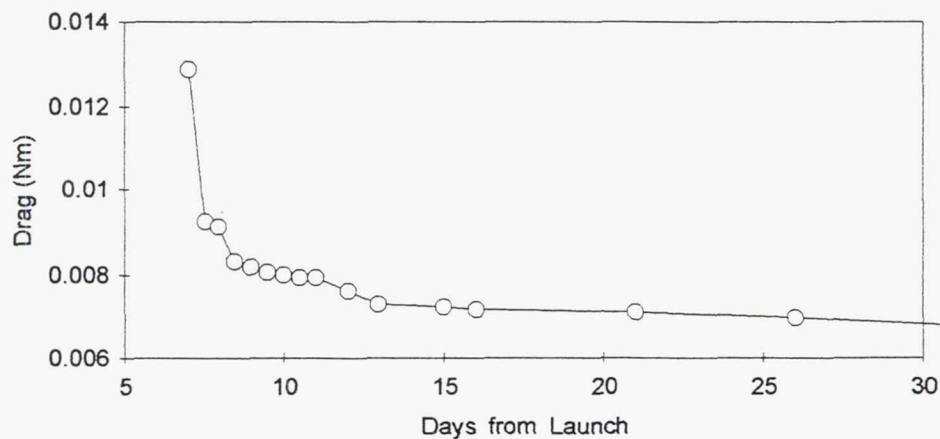


**Figure 8 EUVE RWA Drag Trend over the First Month of In-Flight Operation** exhibits the bearing run-in. Data shown is for the skew RWA which was held at a constant speed of 1000 RPM throughout the run-in.



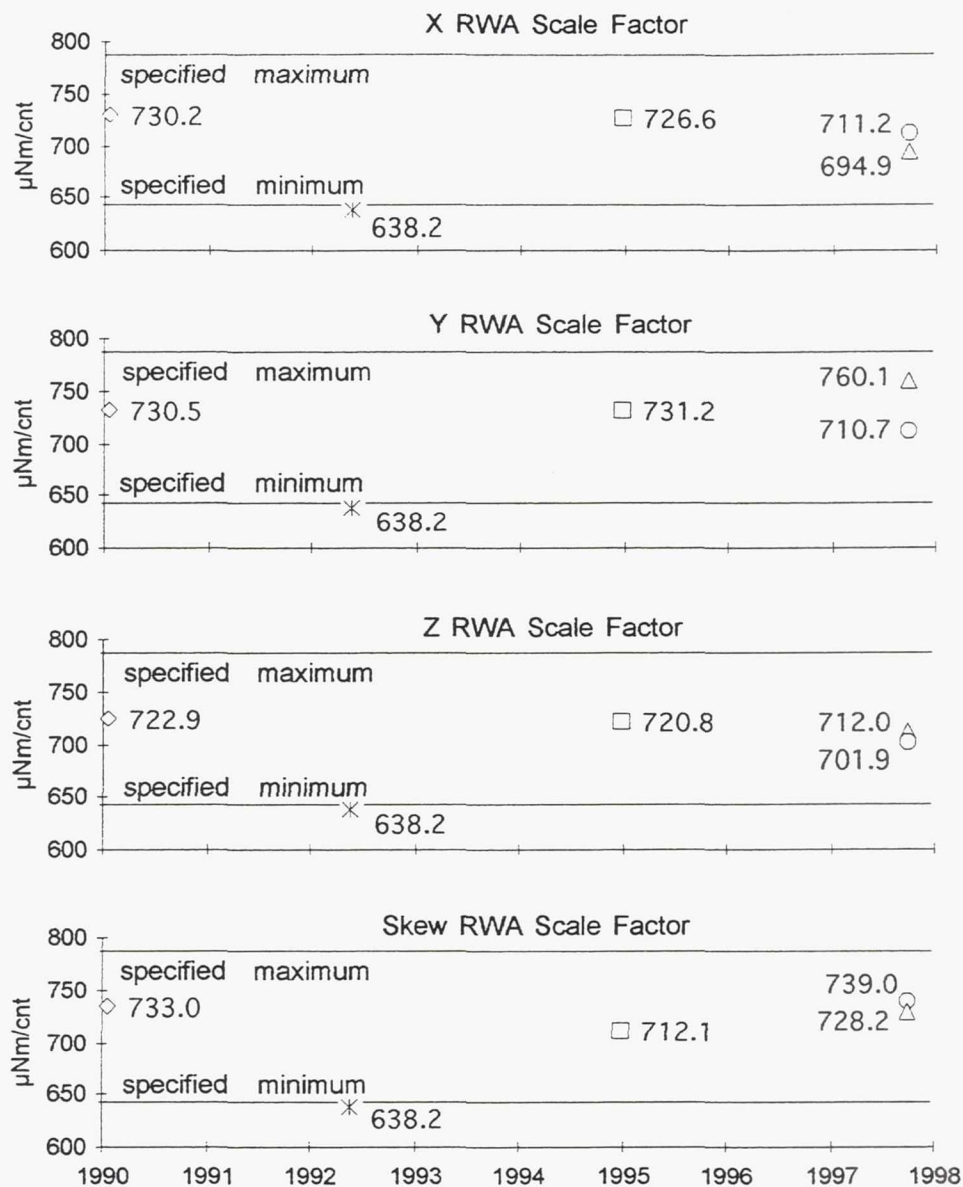


**Figure 9. EUVE RWA Scale Factors** determined by several methods throughout the life of the RWAs. The scale factors for the motor and generator modes were trimmed in the factory at the sub-assembly level to the value in the specification. They were then measured during factory testing in early 1990 at the RWA level by torque pulse tests. For each RWA one scale factor (diamonds) was found using a least squares fit to both motor and generator mode data. During the in-orbit check-out<sup>1</sup> conducted in June 1992 a single scale factor (asterisks) for all four RWAs was deduced from slew data. In January 1995 RWA in-flight performance testing was conducted<sup>5</sup>. For each RWA one scale factor (squares) was found using a least squares fit to both motor and generator mode data. In October of 1997 RWA in-flight tests were repeated. Again using a least squares fit scale factors were found, but this time separate scale factors were found for motor mode (circles) and generator mode (triangles). Discounting the scale factors found during the in-orbit check-out, the scale factors have remained remarkably constant over the life of the RWAs.

Another interesting result seen in Figure 9 is that, discounting the scale factors found during the in-orbit check-out, the scale factors have remained remarkably constant over the life of the RWAs. One should not expect this lack of change to always be the case. Seldom do performance parameters degrade as much as worst case analysis predicts. Even so, one must be prepared for that eventuality.

The final result to be noted is that the scale factor for the motor mode (torque command and wheel speed have the same sign) and generator mode (torque command and wheel speed have the opposite sign) are not the same. Most of the slews examined for the present study exhibited behavior attributable to this difference. This characteristic of the RWA has an important implication for the design of a high precision slew scheme: it should determine whether the RWA is in motor or generator mode and use the appropriate scale factor.

The EUVE flight software has only a single scale factor parameter used for all RWAs. Since the scale factors have changed so little from the original values found during testing in the factory, it was decided to use the average of these original values for the single flight parameter. On 28 February 1998 a new scale factor of 728.2  $\mu\text{N}\cdot\text{m}/\text{cnt}$  was uploaded to the flight software.

## SLEW TESTS

Slew tests were performed on the EUVE spacecraft to demonstrate the improvement to slew performance using scale factors found by the RWA calibration method described above. In December 1997 slews were performed using the baseline RWA scale factor of 638.2  $\mu\text{N}\cdot\text{m}/\text{cnt}$  determined in June 1992 during the in-orbit check-out. Figure 10 shows the results for one of these baseline slews performed about the Y axis using primarily the Y RWA<sup>‡</sup>. The attitude error is approximately -0.020 degrees during the acceleration phase and +0.035 degrees during the deceleration phase. In February 1998 a new RWA scale factor of 728.2  $\mu\text{N}\cdot\text{m}/\text{cnt}$  was uploaded into the flight software. Figure 11 shows results for a slew about the Y axis using the new RWA scale factor. The attitude error with the new scale factor is approximately +0.003 degrees during the acceleration phase and +0.015 degrees during the deceleration phase. The new scale factor has resulted in improved slew performance in the Y axis. Similar improvement has been observed in X and Z axis slews.

A large part of the residual attitude error seen in Figures 10 and 11 can be attributed to the difference between the scale factor used in the flight software and the scale factor found from the RWA calibration. Recall that EUVE has only one RWA scale factor parameter which is used for all four RWAs. So even with calibration an average scale factor must be used, and one can expect some residual error. The attitude error  $\varepsilon$  during slew acceleration/deceleration phases resulting from the difference between the actual scale factor  $\sigma$  and the scale factor  $\hat{\sigma}$  used in the flight software is given by

$$\varepsilon = (\sigma / \hat{\sigma} - 1) \tau_p / K$$

where

$\tau_p$  = torque applied to spacecraft during slew acceleration/deceleration, and

$K$  = 0.47  $\text{N}\cdot\text{m}/\text{deg}$  = attitude control law proportional gain

Table 2 compares the attitude error predicted using the equation above and the attitude errors actually observed for the slews of Figures 10 and 11. In using the equation,  $\sigma$  is set to the value found during the October 1997 calibration for the Y RWA. The generally good agreement between the predicted and observed attitude errors validates the RWA calibration scheme. A properly designed high performance slew scheme could easily account for individual scale factors among the RWAs and for motor and generator mode operation. For such a scheme the slew errors due to RWA scale factor uncertainty would be reduced to negligible levels.

<sup>‡</sup> Some slew torque must be provided by the X and Z RWAs to account for stored momentum and inertia matrix off-diagonal terms.

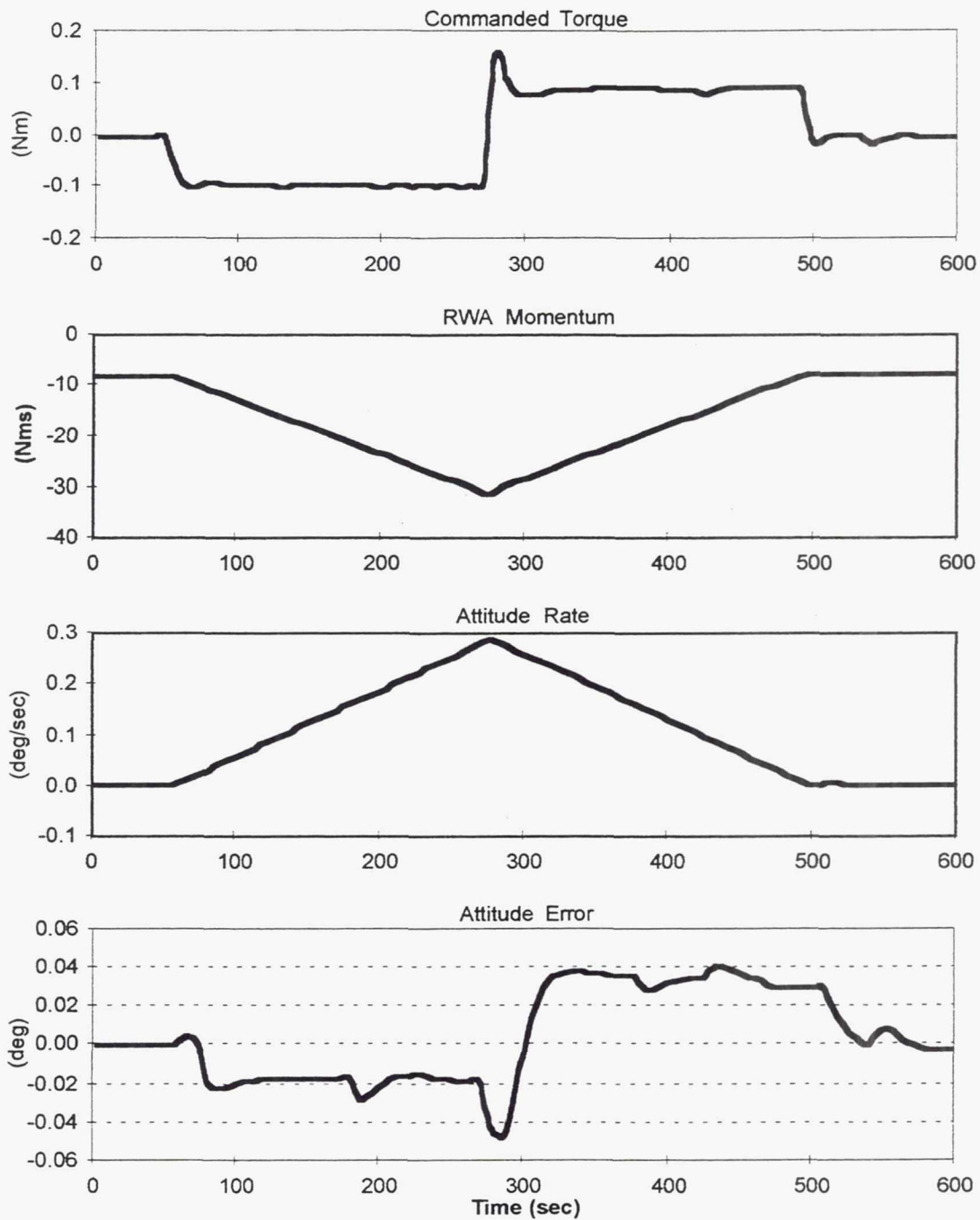


**Figure 10 Y Axis Slew Performed Using Baseline RWA Scale Factor of 638.2  $\mu\text{N}\cdot\text{m}/\text{cnt}$  found during the in-orbit check-out in June 1992. Variables plotted are for the Y axis.**



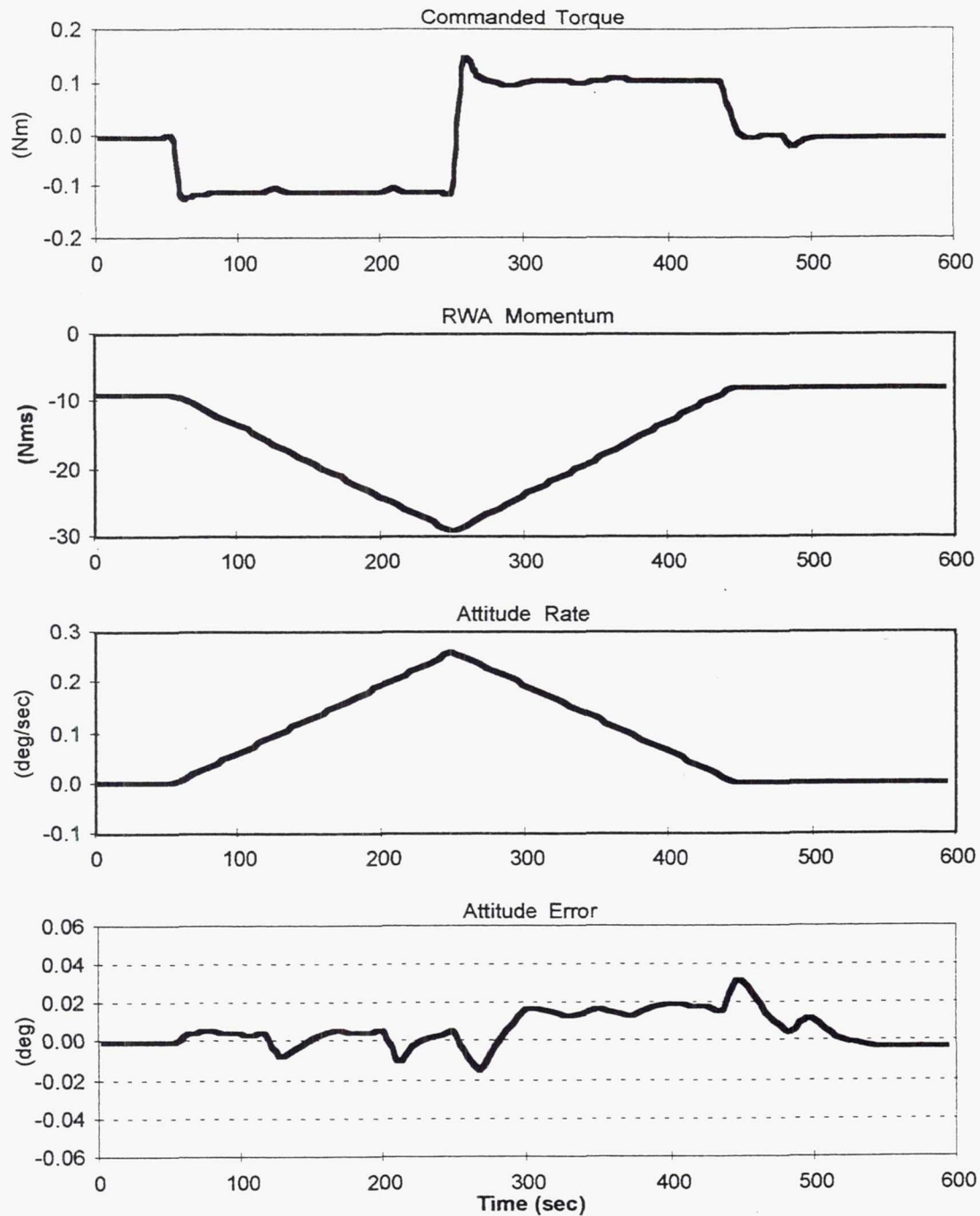


**Figure 11 Y Axis Slew Performed Using New RWA Scale Factor of 728.2  $\mu\text{N}\cdot\text{m}/\text{cnt}$  based on results of in-flight calibration performed in January 1995 and October 1997 using the method presented herein. Variables plotted are for the Y axis.**

**Table 2 Attitude Error due to RWA Scale Factor Error**

Slew Phase	Spacecraft Torque (N·m)*	Scale Factor ( $\mu\text{N}\cdot\text{m}/\text{cnt}$ )		Attitude Error (degree)	
		Found from Calibration	Used in Flight Software	Predicted	Observed
Acceleration	-0.105	710.7	638.2	-0.0228	-0.0200
Deceleration	+0.105	760.1	638.2	+0.0359	+0.0350
Acceleration	-0.105	710.7	728.2	+0.0055	+0.0025
Deceleration	+0.105	760.1	728.2	+0.0094	+0.0150

\* Spacecraft torque differs from commanded torque shown in Fig. 10 and 11 due to the scale factor errors.

## CONCLUSIONS

Many parameters affect slew performance. Of these parameters RWA scale factors are subject to the most change over the life of the spacecraft, and hence their periodic calibration offers the greatest benefit to maintaining good slew performance. The innovative method presented herein allows the RWA scale factors to be calibrated *without* impact to the on-going mission by taking advantage of the extra degree of control freedom afforded by a redundant RWA. Slews performed on EUVE have demonstrated improved performance using the calibration RWA scale factors.

## REFERENCES

1. Class, B., Whitacre, J., and Graham, R. "EUVE Attitude Control Subsystem In-Orbit Check-out Report," Fairchild Space Company, Germantown MD, December 1992, Contract # NAS-5-31786, Task # 074, Report # GNC:EP:92-038.
2. "Explorer Platform User's Guide," prepared for NASA Goddard Space Flight Center by Fairchild Space Company (now Orbital Sciences Corporation) under Contract NAS5-30075, Document Number 408-EP-403-001, August 1989.
3. Pistiner, Josef Siegfried, "Minimization of spacecraft attitude error due to wheel speed reversal," Patent No. 3998409, issued Dec. 21, 1976.
4. "EUVE Attitude Control Subsystem CDR Presentation Package," Fairchild Space Company (now Orbital Sciences Corporation), 27 October 1988.
5. Bauer, Robert, "EUVE Reaction Wheel Assembly In-Flight Performance," Paper No. AAS 97-071, 20th Annual AAS Guidance and Control Conference, February 5-9 1997, Breckenridge, Colorado.
6. "Item Development/Product Specification for a Reaction Wheel Assembly for the Explorer Platform MACS", SVS-11310-A, 20 February 1990, General Electric Space Division (now Lockheed Martin Astro Space), Valley Forge, Pennsylvania.
7. Bergmann, E., and Dzielski, J., "Spacecraft Mass Property Identification with Torque-Generating Control," *Journal of Guidance, Control, and Dynamics*, Vol. 13, No. 1, Jan.-Feb. 1990, pp. 99-103.
8. "EUVE Reaction Wheel Assembly Critical Design Review Data Package," Honeywell Satellite Systems, Glendale AZ, 20-21 April 1988
9. Thames, Mike "EUVE RWA [ATP] Summary", U 1K30 EUVE 221, General Electric Space Division (now Lockheed Martin Astro Space), Valley Forge PA, 4-11-90.

**Page intentionally left blank**



# **SOLAR TORQUE COMPENSATION DETERMINATION SYSTEM FOR THE GOES I-M SERIES WEATHER SATELLITES**

**Jonathan D. DeGumbia\***

**Yo-Kung J. Tsui†**

The Geostationary Operational Environmental Satellite [GOES] I-M series geostationary, three-axis stabilized, weather satellites utilize an optically reflective panel known as a trim tab to minimize the solar pressure imbalance caused by optical and geometric differences between the north panel mounted solar sail and the south panel mounted solar array. The trim tab is mounted on the south end of the solar array and is adjustable rotationally through one degree of freedom via a stepping motor mounted at the hinge point. Daily trim tab adjustments serve to balance the solar pressure throughout the Sun's annual declination cycle and compensate for changes in center of mass location and optical properties throughout the spacecraft life. This is necessary to minimize the requirements on thruster firings and magnetic torquer coils used to relieve momentum. Since the launch of the first spacecraft of this series on April 13, 1994, the trim tab daily slew commanding system has undergone several redesigns. The current method of determining the daily slews is an open-loop system requiring recalculation every 2 to 3 days. The inaccuracy of this system and its reliance on frequent engineering interaction has spawned a need for a self-contained method of control with improved performance. This new method will utilize the existing and proven performance analysis routine and will have the ability to be integrated into the current ground system software with minimal effort. This paper describes the closed-loop trim tab daily slew determination algorithm derived through these efforts, summarizes a proposed method of ground system integration, and discusses the results of initial on-orbit tests.

## **INTRODUCTION**

The GOES I-M series spacecraft, shown in Figure 1, are three-axis stabilized platforms capable of producing a continual stream of earth images used primarily for weather forecasting, severe storm tracking, and meteorological research. The first spacecraft in the series, GOES-I, later designated GOES-8, was launched on April 13, 1994 and is stationed at 75° west longitude. The second, GOES-J, now called GOES-9, was launched on May 23, 1995 and is stationed at 135° west longitude. The two spacecraft provide a continuous region of coverage from

---

\* GOES Attitude and Orbital Controls Systems Engineer Lockheed Martin Space Mission Support and Services, Seabrook, MD 20706

† GOES Engineer, NESDIS, NOAA, Suitland, MD 20746

approximately 15° west to 195° west at the equator, encompassing the contiguous United States, Hawaii, and the continent of South America. GOES-K (GOES-10) was launched April 25, 1997 and is to be placed into an on-orbit storage mode at 105° west until it is called into service.

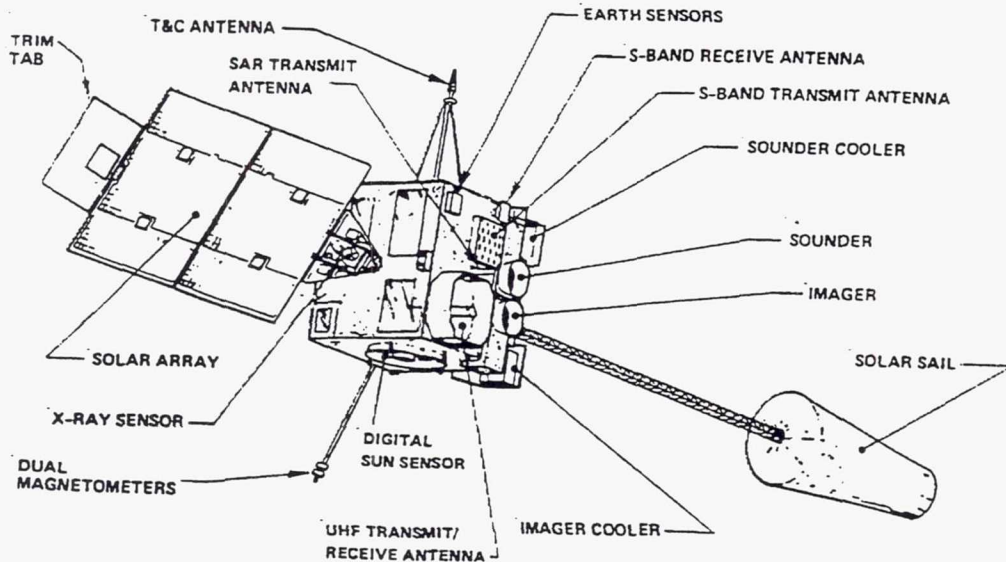


Figure 1 GOES I-M Series Spacecraft

## ATTITUDE CONTROL SYSTEM

During normal operations, spacecraft attitude is controlled primarily through the use of two momentum wheels that provide gyroscopic stiffness and pointing control about the spacecraft pitch and roll axis. The 51 Newton-meter-second (Nms) continuously operating momentum wheels are skewed at  $\pm 1.66^\circ$  off the pitch axis in the pitch/yaw plane. A 2.1 Nms reaction wheel is mounted along the yaw axis and is used to control yaw momentum in the event of a momentum wheel failure. To help alleviate momentum from the wheels, two 100 Ampere-Turn-meter<sup>2</sup> magnetic torquer coils provide roll and yaw torque as necessary. A fully redundant system of twelve 22-N bipropellant thrusters provide attitude control during special operations, translational thrust during stationkeeping maneuvers, and momentum relief during normal operations.

## TRIM TAB

Cooling requirements of the primary payload restrict the use of two symmetrically placed solar arrays. Instead, a single solar array is mounted on the south panel. To balance the force of solar radiation, a solar sail is mounted on the end of a 58-foot boom on the north panel. Seasonal variations in Sun declination relative to the spacecraft cause a seasonally varying solar radiation pressure torque on the spacecraft. This torque is counteracted with a highly reflective aluminized panel, called the trim tab, mounted on the end of the solar array. The trim tab, shown in Figure 2, may be rotated through one-degree of freedom, about its hinged point of attachment, via a precision stepping motor. The trim tab rotational position is monitored by two course position potentiometers and two fine position potentiometers. To make up for deficiencies in the magnetic torquers and to reduce the need for thruster yaw momentum unloading, the trim tab position is adjusted once a day. This is done in such a way so as to minimize the spacecraft environment induced moment arm by varying the effective surface area presented to the Sun.



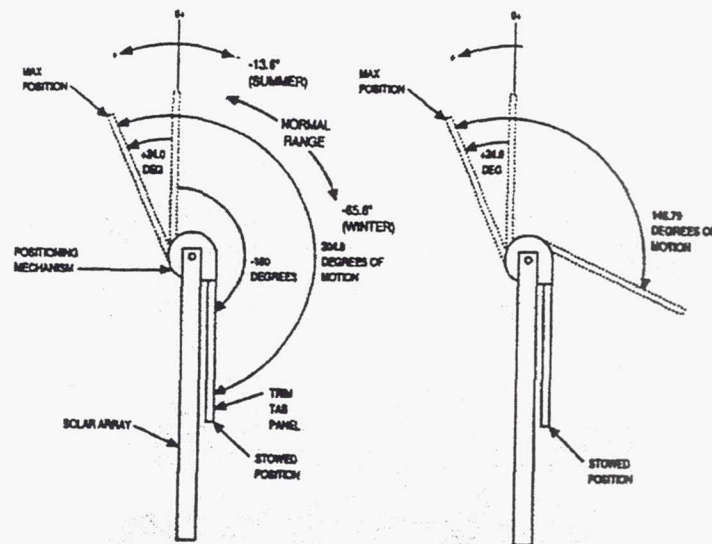


Figure 2 Trim Tab Position Convention

## OATS TRIM TAB COMMAND SYSTEM

The daily calculation of the environmentally induced torque on the spacecraft, determination of necessary trim tab slews, and generation of uplink commands are the responsibility of the ground based, Orbit and Attitude Tracking System [OATS]. Since shortly after the launch of GOES-8, the trim tab slew determination system has undergone several re-designs and major improvements. The currently used system calculates a daily average roll torque created by the momentum wheels, by the magnetic torquers, and by thruster firings and converts them to the Sun Pointing coordinate System [SPS]. The sum of the three torques is the total daily average, control system induced, spacecraft roll torque. The sign opposite of this sum is known as the roll residual torque and represents the rotational force on the spacecraft caused by the environment. Assuming that the majority of external forces are due to solar radiation pressure, the roll residual torque is an indication of trim tab performance. The resultant torque along with trim tab position data, and sun declination information are logged into a scrolling 60-day, history file. A linear least squares fit [LSQ] algorithm generates a 3<sup>rd</sup> order polynomial curve fit to the archived trim tab position data, over a user defined number of days, while providing compensations for the roll residual torque. This produces predicted trim tab positions for the next 10 days. The daily commanded slew is simply the difference between the two consecutive predicted positions for the days in question. Information for each day's trim tab command is automatically sent at a user defined time to the GOES I-M Telemetry And Command System [GIMTACS] to be uplinked to the spacecraft. The OATS commanding system also provides a method of commanding a manual slew, whereby the user may specify the exact position change. Since its inception, the OATS system has been capable of commanding the trim tab to maintain the residual torque within the operational limits of  $\pm 1.0 \times 10^{-6}$  Nm.



## NEED FOR IMPROVEMENT

Although the currently used command system is capable of controlling the trim tab to a degree of accuracy within its originally defined operational limits, it has several shortcomings that have hindered trim tab operations. The intention of the LSQ algorithm was to predict daily trim tab slews for up to 10 days in to the future. Should the residual torque grow to an unacceptable level, a manually entered slew would be sent to override LSQ determined slew. A new LSQ curve would then need to be calculated. In practice, the LSQ routine required recalculation every 2-3 days, and it exhibited a large dependence on manual slews. Off-line analysis tools were developed to calculate ideal trim tab commands to aid in choosing optimum LSQ fits. The efforts to qualify the accuracy of the fits were the original drivers that lead to the development of the newly proposed command determination system.

During various times through out the yearly trim tab cycle, the LSQ algorithm is unable to produce trim tab angles which match the Sun's motion. This is particularly true during Winter and Summer solstices when the Sun's daily change in position relative to the spacecraft reverses direction. For several weeks following the event, the algorithm under commands the trim tab causing the roll residual torque to deviate from zero. A manual command must be sent whenever the torque approaches the operational limits. Other, less predictable, times through out a yearly cycle, the LSQ is unable to control the trim tab to within its limits. Rarely does the LSQ produce an ideal curve. More often, it contains within it some error. Because the curve fit is based on archived slew data, any error in the commanded slew will be re-introduced into the curve fit further perpetuating the problem. In this case, again, manual slews must be used to control trim tab positioning.

Since, during normal operations, spacecraft pointing is controlled using an earth sensor, the spacecraft is not actively controlled in yaw of the spacecraft body coordinant frame. Roll momentum will translate into yaw error every 6 hours as the spacecraft pitches  $15^\circ/\text{hr}$  to maintain earth pointing. Much of the perceived yaw pointing error can be attributed to trim tab misalignment. Improvements in Image Navigation and Registration [INR], a system of compensations applied to an image based on past observations of the pixel locations of stars and earth landmarks, have reduced the noise levels to the point where spacecraft yaw pointing error is evident. Improvements in trim tab positioning will improve the quality of the spacecraft products by reducing pointing error and increasing the consistency of INR performance.

The LSQ routine relies on an archived history file of 40-60 days of consecutively commanded trim tab slews to function optimally. If this is not available, cumbersome off-line analysis tools, and manually entered spacecraft commands must be used. There are three scenarios when this is necessary. First, the trim tab for a newly launched spacecraft would have to be commanded in this fashion until sufficient data is archived. Also, whenever a spacecraft is brought out of on-orbit storage, an off-line method must be used until the telemetry history file is brought up to date. Lastly, due to an early on orbit problem with GOES-10, the ground system was modified to allow operation of the GOES I-M series spacecraft while turned  $180^\circ$  about its yaw axis. There are thermal advantages to flipping the spacecraft seasonally to keep the primary payload instruments cooler. Since this ability now exists, routine yaw flipping is a possibility. Whenever the spacecraft is flipped, the history file cannot be used, as the direction the trim tab moves relative to the Sun movements is changed. All of these events represent a significant amount of time that the LSQ algorithm cannot be used.

To make-up for the shortcomings of the LSQ routine, off-line analysis tools were developed to determine the ideal daily slew given a set of initial conditions. With the notion of eventually replacing the least squares fit routine, they have evolved to the point where they now improve upon the shortcomings of the current system. If implemented properly, they can form the basis of a closed-loop command determination system, reducing the need for frequent engineering interaction.

## FUNDAMENTALS OF THE NEW DETERMINATION METHOD

Many of the inadequacies of the current trim tab slew determination routine, LSQ, stem from its reliance on a large amounts of past commands. In developing an alternative system, a different approach was used. The components that comprise each day's trim tab command were separated. Compensations using the most reliable and accurate telemetry points and calculations were then developed for each. The sum of these compensations would then be used as a daily command. Unlike the least squares fit method, the basis of the calculations was chosen to be calculated in the change in trim tab position rather than predicted positions. This is because, the stepping motor can be commanded to within 0.001 degrees, and the fine position potentiometer has an accuracy of only 0.1 degrees. Calculating and expressing the values of the compensations using commanded position changes negates the need for reliance on the less accurate potentiometers. The new slew determination algorithm,

$$\Delta\gamma_i = G_{SA}\Delta\gamma_{i_{SunAngle}} + G_{TQ}\Delta\gamma_{i_{ResTorque}} - \Delta\gamma_{i_{PrevTorque}}, \quad (1)$$

calculates the change in the daily trim tab position,  $\Delta\gamma$ , for day  $i$  as the sum of three components, each compensating for a different effect, multiplied by the gains,  $G_{SA}$  and  $G_{TQ}$ , where necessary. The components are defined as the Sun declination change compensation,  $\Delta\gamma_{SunAngle}$ , the roll residual torque compensation,  $\Delta\gamma_{ResTorque}$ , and the previous day torque compensation,  $\Delta\gamma_{PrevTorque}$ .

The first component of Eq. (1) compensates for the daily change in the Sun declination. Sun declination angle,  $SA$ , information is taken from the spacecraft ephemeris at 12:00 satellite local time [SLT] for the day of interest and for the following day. The difference in these angles is multiplied by a partial derivative relating the angle change of the trim tab to the angle change of the Sun declination, see Eq. (2).

$$\Delta\gamma_{i_{SunAngle}} = (SA_{i+1} - SA_i) \left. \frac{\partial\gamma}{\partial SA} \right|_i \quad (2)$$

The partial derivative used in Eq. (2) is estimated using GOES-8 & 9 flight history data. The curve, formed by plotting the trim tab position against the solar declination angle, is approximated using,

$$\gamma = \left( \frac{\partial\gamma}{\partial SA} \right) SA + \gamma_{Equinox}, \quad (3)$$

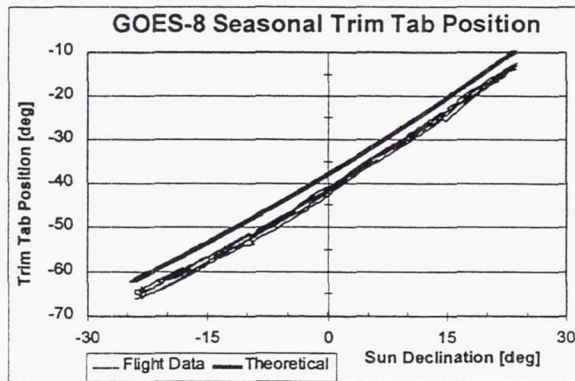
where the slope of the line, the partial derivative, varies linearly from its value at summer solstice [SS] to its value at winter solstice [WS] and the y-intercept,  $\gamma_{Equinox}$ , is the average trim tab



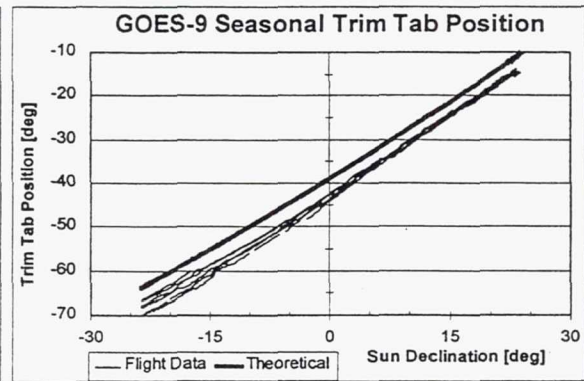
position at the vernal and autumnal equinoxes. The slope at any particular position,  $i$ , along the curve may then be found using,

$$\left. \frac{\partial \gamma}{\partial SA} \right|_i = \left. \frac{\partial \gamma}{\partial SA} \right|_{SS} + \left[ \frac{\left. \frac{\partial \gamma}{\partial SA} \right|_{WS} - \left. \frac{\partial \gamma}{\partial SA} \right|_{SS}}{SA_{WS} - SA_{SS}} \right] (SA_i - SA_{SS}) \quad (4)$$

Figures 3 and 4 show how identical curves scribed by Eq. (3) match the flight history data for GOES-8 and GOES-9. Scale factors have been added to the y-intercepts of each for displaying purposes. Note how the data changes only slightly over time and between spacecraft. For this reason, older satellite data may be used for newly launched spacecraft until sufficient flight data is archived.



Figures 3 Theoretical Curve compared to GOES-8 Flight History Data



Figures 4 Theoretical Curve compared to GOES-9 Flight History Data

The second component of Eq. (1) compensates for the roll residual torque. It is intended to remove errors in the trim tab position caused by the inaccuracies of the sun declination change compensation and by the changes in the relationship between the spacecraft and its environment. The roll residual torque,  $T$ , calculated by the OATS trim tab system, is multiplied by a partial derivative relating trim tab positional error to the torque.

$$\Delta \gamma_{i_{ResTorque}} = T_{i-1} \left( \frac{\partial \gamma}{\partial T} \right) \quad (5)$$

where,

$$\frac{\partial \gamma}{\partial T} \approx -4.1 \times 10^5 \text{ deg/Nm} \quad (6)$$

This trim tab position to torque derivative,  $\partial \gamma / \partial T$ , found through solar torque modeling, is approximated as a constant as it changes only slightly from winter to summer solstice.

The trim tab must be slewed near the time the roll residual torque is calculated. In effort to increase the available time for engineering interaction, the trim tab is adjusted approximately 24 hours after the calculation. This makes the available daily average residual torque one day old at the time of the adjustment and not indicative of the present day average torque. For this



reason, another correction is needed to prevent from redundantly compensating for the residual torque. This is accomplished by taking the part of the previous day's adjustment that compensates for the residual torque and subtracting it from the current day's torque compensation. To do this, the sun declination change compensation for yesterday is subtracted from yesterday's slew, taken from archived data (not the potentiometers.)

$$\Delta\gamma_{i_{\text{PrevTorque}}} = \Delta\gamma_{i-1} - (SA_i - SA_{i-1})G_{SA} \left. \frac{\partial\gamma}{\partial SA} \right|_{i-1} \quad (7)$$

Eq. (7) results in the part of the previous day's slew used to compensate for the residual torque. By subtracting that value from the current day's residual torque compensation, as in Eq. (1), redundant compensation is avoided.

The inclusion of gains in Eqs. (1) and (7), allow the compensations to be fine-tuned to account for deficiencies in the individual compensations, for degrading optical properties, and for changing center of gravity. The solar declination change compensation gain,  $G_{SA}$ , may be calculated using data for any two consecutive days in which the residual roll torque compensation was not used, using the equation,

$$G_{SA} = \frac{\Delta\gamma_i + (T_{i-1} - T_i) \frac{\partial\gamma}{\partial T}}{\Delta\gamma_i} \quad (8)$$

This calculation assumes that the derivative relating the trim tab positional error to the torque is exactly correct.

The roll residual torque compensation gain,  $G_{TQ}$ , may be calculated using data from any two consecutive days in which only the sun declination change compensation is used on day  $i-1$ , and the residual torque compensation along with the Sun angle compensation is used on day  $i$ . The equation,

$$G_{TQ} = \frac{\Delta\gamma_{i_{\text{ResTorque}}} + [T_{i+1} - 2(T_i - T_{i-1})] \frac{\partial\gamma}{\partial T}}{\Delta\gamma_{i_{\text{ResTorque}}}} \quad (9)$$

normalizes any error made by the sun declination change compensation over the last two days and can be used regardless of whether or not  $G_{SA}$  is exact. As with Eq. (8), Eq. (9) requires that the positional error to torque partial be exact. Therefore, it should be calculated several times, each time multiplying the resulting  $G_{TQ}$  by the partial, until a value with an adequate number of significant digits is converged upon. In practice sufficient accuracy is achieved the first time the calculation is performed.

## PROPOSED NEW SLEW DETERMINATION SYSTEM

The new slew determination equations will form the basis for a closed-loop, trim tab command system. It will require minimal engineering interaction and be flexible enough to handle all foreseeable events. For ease of integration, the new command system will utilize many of the features of the current system. The routine that calculates the roll residual torque has proven to be robust and accurate. It will fail only if momentum wheel speed data is missing from the archived telemetry. With proper checks in the new system, this routine does not need to be modified.

The new slew determination system will replace the entire LSQ routine. It will be compatible with the OATS timer function so that it may run without engineering interaction. The slew command will be used one day following its calculation, so time is available to check or override it as needed. The values for the various partial derivatives, winter and summer sun declination angles, gains, and violation thresholds will be stored in the OATS database and available for change as necessary.

The new routine always computes the sun declination change compensation in its routine configuration. This compensation comprises the bulk of the trim tab movements. Its calculation is based on the spacecraft orbit and has no reliance on spacecraft telemetry. It is therefore not likely to fail or give inaccurate results. The roll residual torque compensation will be applied only if the residual torque exceeds a threshold value that will be defined in the OATS database. This will allow room for fluctuations in the accuracy of the torque calculation due to environmental changes such as electromagnetic storms. The previous day torque compensation may be applied every day. It is designed to correct the residual torque compensation only on the day after it is used, and will otherwise yield a value of exactly zero.

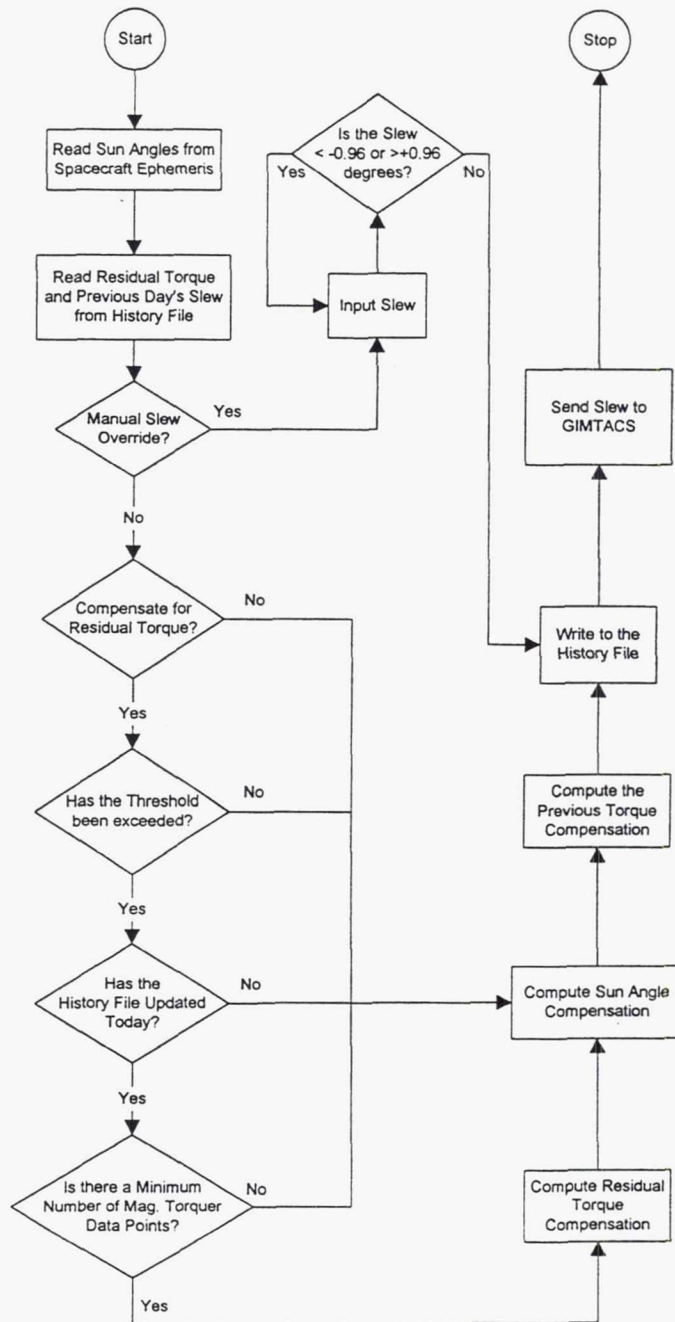


Figure 5 Proposed New Slew Determination System



Figure 5 is the flowchart of the new slew determination system. After reading the spacecraft ephemeris information and archived history file data, the routine will encounter its first user defined path choice, the manual slew override. This option, with a default setting of *off*, is reserved for special operations when a normally calculated command is not adequate. If this option is chosen, the user will be able to input the exact angle he wishes the trim tab to move. The routine will check that the slew is not greater than  $\pm 0.96^\circ$ , the limit of the command procedure, before it is sent to GIMTACS.

If the manual slew is not chosen, the user will have a choice to include the roll residual torque compensation in the calculation of the slew. If this option is not chosen, the routine will by-pass the torque compensation. If it is chosen, a series of checks will determine if the roll residual torque compensation is needed and if it is usable. Its usability will depend on whether or not the calculation had successfully completed that day, whether or not there is enough magnetic torquer data to make the calculation accurate, and whether or not the torque threshold has been exceeded. If all the checks are passed, the torque compensation is computed using Eq. (5). The result, if any, along with the sun declination change compensation as in Eq. (2) and the previous day torque compensation as in Eq. (7) are multiplied by their appropriate gains and added to yield the day's commanded slew.

Once the commanded slew is calculated, the routine will write the results to a record file. This file will contain information about each day's calculation for later analysis. The daily entries will include a time tag, the numeric value of the three compensations, the determination inputs, and the day's trim tab slew.

Next, OATS will send the calculated trim tab slew to the GIMTACS where it will be stored until the daily command is sent to the spacecraft. From this step onward, the operation will not differ from the currently used method.

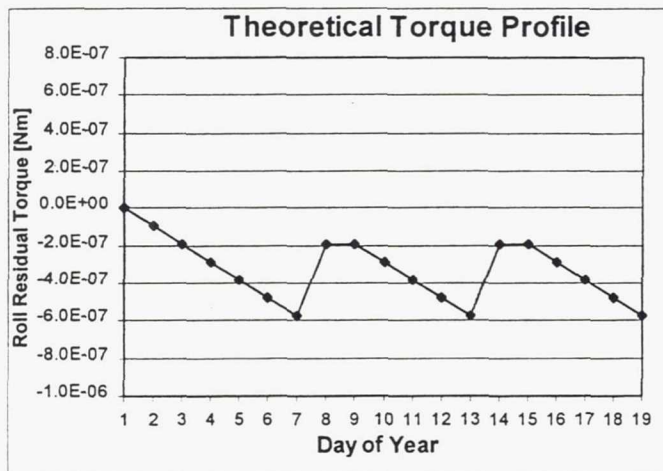


Figure 6 Theoretically expected results of initial test.

Because the Sun declination change compensation is not perfect, the residual torque can be expected to change from the previous day's value by approximately the same magnitude each day. Figure 6 shows the theoretical results of the above logic for the case where the sun compensation is too large during the period after summer solstice and before winter solstice. Each data point represents one day of spacecraft roll residual torque. It is important to note that the torque for any given day is not known until the following day; that is, on day  $i$ , only the torque from previous day  $i-1$  is available. Every day, the residual torque error increases by an amount proportional to the sun declination change compensation error. Figure 6 shows that on day 7 the available torque from day 6 breaks the threshold set at  $\pm 4.0 \times 10^{-7}$ . The torque compensation is used to reset the torque to zero. Since the actual, and unknown, torque on day 7 has worsened, the torque compensation will be inadequate by the change in the torques from day 6 to 7 plus the amount caused by the error in the



sun declination change compensation. On day 8, the torque on day 7 becomes available. Here the observed torque is worse than the day before, so the torque compensation is used. Now, the previous day's command compensation kicks in to subtract the torque compensation on day 7 from the day 8 command. This should improve the torque, but as always, we add in the sun declination change compensation error to get virtually no change in torque. On day 9, the observed torque is within limits and only the sun compensation is used. The cycle continues.

The proposed slew determination algorithm is capable of controlling daily trim tab operations through all foreseeable events. There are two instances when this system will require engineering interaction. The first is the day following a stationkeeping maneuver. The residual torque calculation algorithm can not conclude an accurate number for a time spanning such an event. In this case, the user would have to turn off the roll residual torque compensation for the following day to avoid the compensation of improperly calculated errors. Also, the residual torque calculation is susceptible to error during periods of high magnetic field variance. Here the user would have to determine the times when such magnetic storms have effected the torque calculation, and again, disable the torque compensation.

## TESTS AND RESULTS

Beginning on November 1, 1997, a fourteen-day test of the proposed slew determination system was performed on both GOES-8 and GOES-9. The goal of the test was to prove the feasibility of such a command system by testing the accuracy of the equations, the variance in the roll residual

**Table 1**  
**SETTINGS FOR INITIAL TEST**

Partials and Gains		Logical Parameters	
$\frac{\partial \gamma}{\partial SA}_{WS}$	1.0	Manual Slew	off
$\frac{\partial \gamma}{\partial SA}_{SS}$	1.2	Torque Compensation	on
$SA_{WS}$	$-23.44^\circ$	Torque Threshold	$\pm 4.0 \times 10^7 \text{ deg/Nm}$
$SA_{SS}$	$23.44^\circ$	Torquer Data Minimum	390 points
$\frac{\partial \gamma}{\partial T}$	$-4.5 \times 10^5 \text{ deg/Nm}$		
$G_{SA}$	1.0		
$G_{TQ}$	1.0		

torque calculation, and the repeatability of the gain calculations. Commands were calculated using the above equations. The logic from the flowchart in Figure 5 was followed to simulate the proposed OATS routine. Each day's command was sent to GIMTACS using the OATS manual slew method. For comparison purposes, identical logical parameters and partial derivatives were used for both spacecraft. The gains, although calculated, were not re-introduced into the equations. Table 1 lists the values used for the initial test. The torque compensation threshold

was set to a higher value than it would be operationally. This was done to increase the number of days where only the sun declination change compensation was used.

GOES-8 test data is shown in Figure 7. The steep downward trend from days 308 to 311 and from days 313 to 318 is caused by moving the trim tab too much each day. This suggests that the sun declination change partial was too large. For days 308 to 311, the error was on average about 39%, and from day 313 to day 318 it was approximately 9%. The torque compensation was used on day 311. Analysis shows that this compensation was approximately 90% too large.

GOES-9 data is shown in Figure 8. For this spacecraft, the sun declination change partial was also too high. From days 305 to 309, the partial was on average 28% too large, and from days 315 to 318, the partial was an average of 16% too large. Torque compensation was used on days 309, and 313. It was found to be an average of 66% too large. The torques on days 312 and 313, caused by commands on day 311 and 312, respectively, could not be explained.

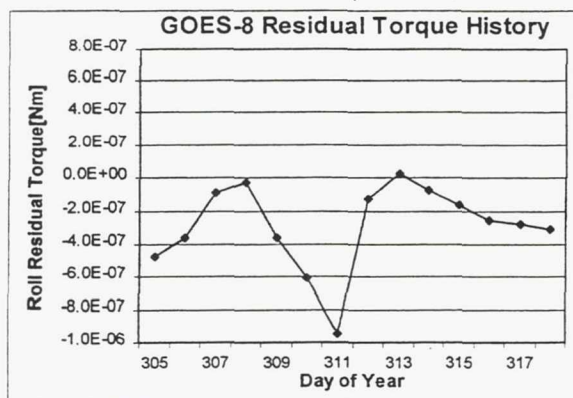


Figure 7 GOES-8 Test Results

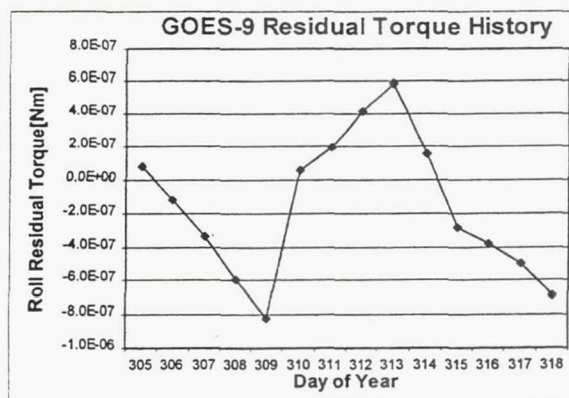


Figure 8 GOES-9 Test Results

Test results revealed a larger reliance on gains than anticipated. The use of the  $G_{SA}$  gain would alleviate the average error in the sun declination change compensation. The variance in the average sun compensation error over a short term of approximately four days represents the noise of the system. This could be caused by spacecraft environmental changes and by trim tab positioning error due to the limitations of the stepping motor. Over a period of several weeks, the variance in the sun compensation error represents the error in the curve fit fitted to flight history data in Eq. (3). This longer-term error is corrected by the roll residual torque compensation by optimizing the trim tab position whenever it breaks the torque threshold.

The errors in the torque compensation could also be relieved though the use of gains. Since, however, it is only necessary for this compensation to reset the torque to its approximate optimum position, it is not necessary to achieve an exact value for this partial. More data is required to determine the annual variance in the derivative relating the trim tab position to the residual torque

The two unexplainable GOES-9 data points on days 312 and 313 may be caused by a change in the spacecraft environment, although this has thus far not been proven. Further tests would be necessary to determine the frequency of such events and their impact on the proposed commanding system. It is important to note that the self-healing nature of the system allowed it to compensate for the effect while maintaining trim tab performance to a degree of accuracy well within acceptable limits.



## FUTURE PLANS

A second series of tests will be performed on GOES-8, GOES-9, and the inverted GOES-10, if available. These tests will be similar to the first except they will span many more days and include the sun compensation gain,  $G_{SA}$ . This will increase the number of data points between torque compensations to get a better feel for the potential accuracy of the system. The accuracy of this system is limited only by the accuracy of the partial derivatives and by the ability to model the seasonal trim tab position curves as in Figures 3 and 4. The next test will also determine if the torque compensation threshold can be tightened in effort to reduce the maximum roll residual torque allowed.

Pending acceptable results, the trim tab command determination system will be proposed for integration into the OATS ground system where it will determine the daily trim tab command for all current and future GOES I-M series spacecraft.

## CONCLUSION

Thermal and attitude requirements of the GOES I-M series spacecraft require the use of a trim tab to balance the environmentally induced torque throughout the yearly solar cycle. A new method of determining the daily position of the trim tab has evolved from off-line analysis tools developed to aid the OATS ground system calculations. This system will alleviate many of the shortcomings of the current least-squares-fit system. For ease of integration, it has been designed to utilize many of the proven features of the currently used method. A test using two operational spacecraft has shown the system to be capable of controlling the trim tab to well within acceptable limits. Another series of tests, better mimicking the proposed system, will control the trim tabs of several spacecraft. If the results of the future tests yield adequate results, the system will be proposed for integration into the OATS ground system.

## ACKNOWLEDGMENTS

The authors wish to give thanks to Scott Miller, Perry Baltimore IV, Edwin Harvie, and Richard James for all their contributions.

## REFERENCES

1. GOES Program Spacecraft Operations Handbook, DRL 503-02, vol. III, revision G – Spacecraft Description, Space Systems/Loral, August 31, 1995.
2. GOES IJK/LM Operations Ground Equipment and Maintenance Manuals, DRL 504-06, Space Systems/Loral, April 1997.
3. Havie, E., J. Rowe, and Y.J. Tsui "Performance Analysis of the GOES Trim Tab Solar Pressure Torque Angular Momentum Control," in *GOES-8 and Beyond*, Edward R. Washwell, Editor, Proc. SPIE 2812, pp. 741-752(1996).



## USE OF MICROGRAVITY SENSORS FOR QUANTIFICATION OF SPACE SHUTTLE ORBITER VERNIER REACTION CONTROL SYSTEM INDUCED ENVIRONMENTS

Robert B. Friend<sup>†</sup>

In the modeling of spacecraft dynamics it is important to accurately characterize the environment in which the vehicle operates, including the environments induced by the vehicle itself. On the Space Shuttle these induced environmental factors include reaction control system plume. Knowledge of these environments is necessary for performance of control systems and loads analyses, estimation of disturbances due to thruster firings, and accurate state vector propagation.

During the STS-71 mission, while the Orbiter was performing attitude control for the mated Orbiter/Mir stack, it was noted that the autopilot was limit cycling at a rate higher than expected from pre-flight simulations. Investigations during the mission resulted in the conjecture that an unmodelled plume impingement force was acting upon the orbiter elevons. The in-flight investigations were not successful in determining the actual magnitude of the impingement, resulting in several sequential post-flight investigations.

Efforts performed to better quantify the vernier reaction control system induced plume impingement environment of the Space Shuttle orbiter are described in this paper, and background detailing circumstances which required the more detailed knowledge of the RCS self impingement forces, as well as a description of the resulting investigations and their results is presented. The investigations described in this paper applied microgravity acceleration data from two shuttle borne microgravity experiments, SAMS and OARE, to the solution of this particular problem. This solution, now used by shuttle analysts and mission planners, results in more accurate propellant consumption and attitude limit cycle estimates in preflight analyses, which are critical for pending International Space Station missions.

---

<sup>†</sup> Flight Control Systems Engineering Manager, Boeing North American Reusable Space Systems

## INTRODUCTION

Reaction jet plume characterization is often performed using computational fluid dynamics and associated techniques. This characterization includes the self impingement components of the rocket plume which impact the orbiter surfaces each time an attitude control engine is fired. The inclusion of these effects becomes extremely difficult when uncertainties in the position of articles in the engine plume are included. For the orbiter aft down firing vernier thrusters, the subject of this investigation, this includes main engine bells, the body flap, and the elevons. The Space Shuttle has been flying for 17 years, yet it was discovered on the STS-71 mission that the induced vernier reaction control system environments and associated plume self-impingement had been poorly quantified.

## PROBLEM DESCRIPTION

The Space Shuttle orbiter accomplishes attitude control when in orbit through the use of 44 reaction control system (RCS<sup>†</sup>) thrusters. The 38 Primary RCS thrusters are arranged in 14 groups to provide both automatic rotational control and manual translation control. The six Vernier thrusters are arranged about the vehicle in orientations that allow three axis rotational control. Each of the 14 PRCS thruster groups and each of the six VRCS thrusters has an associated acceleration vector, called an angular acceleration increment, used to determine which thruster to select in the presence of a given command and to estimate the vehicle rate change in response to a thruster firing. These acceleration increments are calculated by the Shuttle computers using pre-flight determined models of the vehicle mass properties and orbiter RCS, including plume impingement components. The overall thruster arrangement is shown in Figure 1.

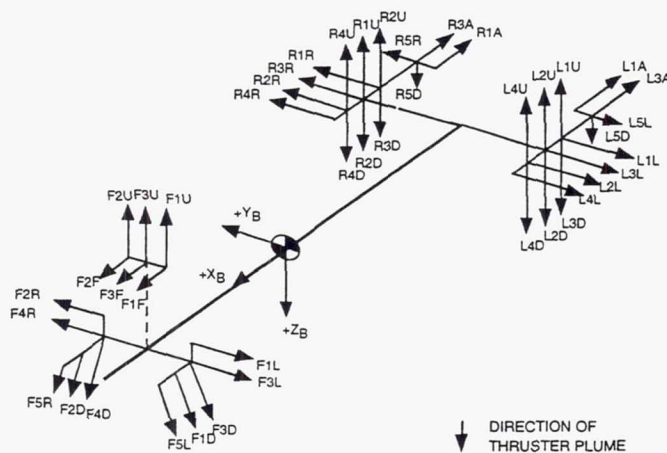


Figure 1 Shuttle Orbiter Thruster Locations and Plume Directions  
A 5 Indicates Vernier Thrusters, All Others are Primary Thrusters

<sup>†</sup> All acronyms used are defined in the accompanying notations section.

During the STS-71 mission, while the Orbiter was performing attitude control for the mated Orbiter/Mir stack, it was noted that the Orbiter Digital Autopilot (DAP<sup>7</sup>) was limit cycling at a rate higher than expected from pre-flight simulation results. This resulted in propellant expenditures roughly twice pre-flight predictions for some of the inertially held attitudes. Analysis of the DAP performance showed that the actual vehicle acceleration experienced for a minus Pitch command differed significantly from the DAP expected values. The DAP expected acceleration is calculated based upon transferring the torque about a reference CG to the predicted mission CG using the cross product of the jet forces and the difference between the reference and flight estimated CG positions. These predicted accelerations are then used in the feed-forward loop of the autopilot to estimate rate changes due to a thruster firing. When a difference between the predicted rate change (calculated) and the actual rate change (derived from IMU data) is seen, the DAP updates its estimate of undesired accelerations. These are then used to update the switching lines in the DAP phase plane controller. The STS-71 mated vehicle flight derived accelerations are compared to the DAP estimates and shown in Table 1, while Figures 2 and 3 display representations of the nonlinear Orbit DAP Pitch axis phase plane both from pre-flight expectation, and from in-flight experience.

**Table 1**  
**STS-71 MATED VEHICLE PREDICTED AND FLIGHT DERIVED ACCELERATIONS**

Axis	Positive		Negative	
	Actual (d/s <sup>2</sup> )	Predicted (d/s <sup>2</sup> )	Actual (d/s <sup>2</sup> )	Predicted (d/s <sup>2</sup> )
Roll	0.0025	0.0028	-0.0023	-0.0024
Pitch	0.0030	0.0029	-0.0019	-0.0026
Yaw	0.0118	0.0110	-0.0130	-0.0110

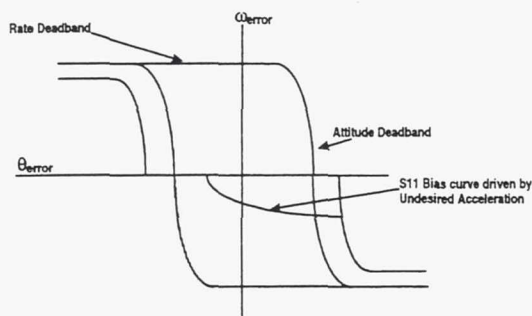


Figure 2 Typical Pitch Axis Phase Plane with Representative Switching Lines

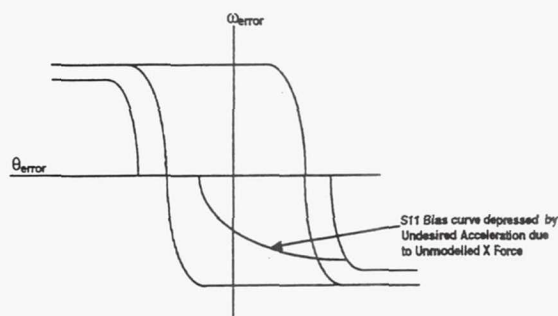


Figure 3 STS-71 Pitch Axis Phase Plane with Biased S11 Switching Line

Separate phase planes are maintained for each of the three rotational axes, with the switching lines defined from desired rate and attitude deadbands to determine when a control action is required. The autopilot maintains the vehicle state inside the bounds of these rate and attitude limits. The switching lines are derived based upon estimates of the available control and disturbance accelerations to provide propellant efficient operation, i.e. low rate one or two sided limit cycles. In the absence of substantial disturbances a two sided limit cycle is commanded, while in the presence of



disturbances, a single sided limit cycle is commanded. The efficiency of the limit cycles is therefore dependent upon the accuracy of the disturbance acceleration estimation.

As a result of the investigations conducted during the STS-71 mission, it was concluded that the errors in the DAP acceleration estimate were most probably due to an unmodelled force acting in the +X (Orbiter Body Axis) direction. This force was assumed to be primarily impingement forces from the aft downward firing vernier thrusters R5D and L5D acting upon the orbiter elevon and body flap. The VRCS plume model in use prior to STS-71 was derived from flight data after testing on STS-1 revealed that original (pre-STS-1) estimates for VRCS plume forces and moments significantly underestimated the effects of impingement on the Orbiter elevon and bodyflap<sup>1</sup>. This model was derived for orbiter surfaces at trail (0.0 degrees deflection) and, unlike the PRCS thrusters, does not have a modifier to correlate changes in orbiter self-impingement with aerosurface deflections. The STS-71 in-flight investigation, its progress, and its attendant conclusions are completely documented in various post-flight reports and papers<sup>2,3,4</sup>

Following the STS-71 mission, analysts from the NASA/JSC Engineering Directorate Applied Aeroscience and CFD Branch used a plume analysis tool to generate impingement forces and torques which, when used in off-line simulations, matched STS-71 mated flight signatures. None of these models were able to provide a satisfactory match to flight signatures for the mated configuration without unacceptably affecting the orbiter alone signatures. It was the opinion of the analysts that a full CFD analysis be funded or alternately, a flight derived model be pursued<sup>5</sup>. The decision was made to pursue derivation of a model based on flight data.

## APPROACH

To develop the new model, it was decided to capitalize on the sensitivity of two accelerometer payloads (SAMS and OARE) on the STS-73 microgravity mission to measure translational accelerations from VRCS thruster firings. A DTO was designed which required 19.6 second firings from both a single aft down-firing VRCS thruster, and 2 simultaneous down-firing aft thrusters<sup>6</sup>. These were done at a fixed (-7.5 degree) elevon position. The accelerations due to the thruster firings were analyzed post-flight to determine a flight-derived plume model. This model was compared against signatures from several shuttle flights. It was also compared against similar data from STS-78, a micro-gravity mission where the DTO was performed twice in an effort to quantify elevon position effects on VRCS plume impingement. The STS-78 results were used to verify the STS-73 derived model. Small changes in the STS-73 derived model resulted from analysis of the STS-78 data. The resulting model was compared against data from several missions and orbiter configurations (mated to the Mir, and Orbiter alone)

## DISCUSSION

STS-73 Shuttle Accelerometer Measurement System (SAMS) and Orbiter Accelerometer Research Experiment (OARE) data was downloaded from the NASA/Lewis Research Center Microgravity Services Lab via Internet FTP. This data was first evaluated using the data viewers made available through the FTP site. A sample of the SAMS viewer data from STS-73 is presented in Figure 4.

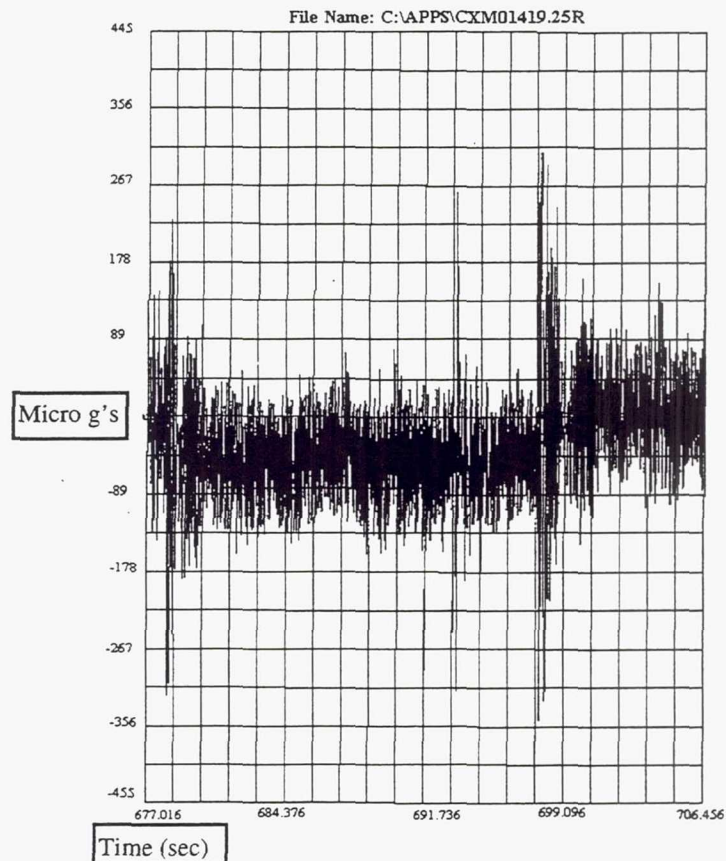


Figure 4 STS-73 SAMS Data from SAMS Viewer  
X-axis Acceleration, R5D+L5D

The desired thruster acceleration data was initially difficult to extract due to the frequency of the accelerometer data and the low level of acceleration from the VRCS thruster(s). To aid in data extraction, the accelerometer data was normalized to remove acceleration biases due to on-board activities and vehicle attitude, then filtered using a filter with a 0.2 Hz cutoff frequency to eliminate the high frequency content which made the plots difficult to read. Figure 5 presents the data from Figure 4 after processing through the MATLAB tools. After determination of the sensed acceleration, the accelerations were transformed into the Orbiter structural reference frame at the orbiter CG, rather than in the accelerometer frame at the accelerometer location. Preliminary force and moment models were then developed using the acceleration data derived from the accelerometer measurements.



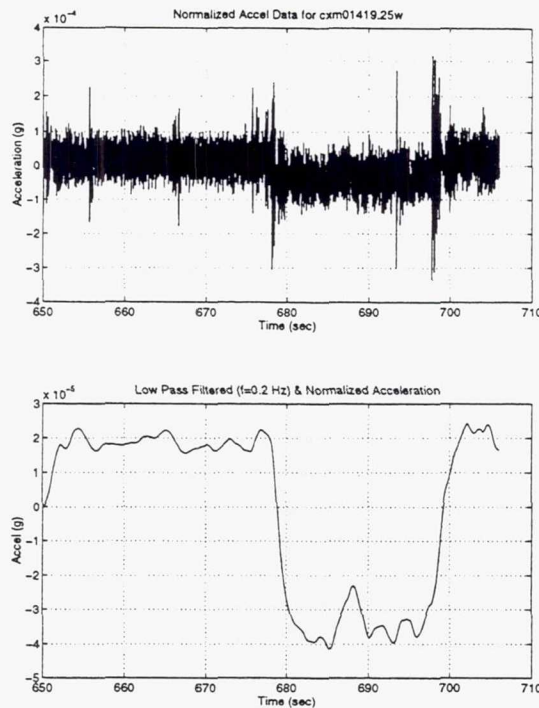


Figure 5- STS-73 SAMS Data, Normalized and Filtered  
X-axis Acceleration, R5D+L5D

To perform a check on the reasonableness of the accelerations determined via reading the plots from the flight data, a MATLAB tool was developed using the System Identification Toolbox. The tool attempts to simultaneously solve for both forces and moments through repetitive iterations, searching for a local minimum of a specified function using a Gauss-Newton minimization procedure, subject to some criteria. In this case, the specified criteria was a minimum error between the SAMS acceleration data and the tool results. Optimal solutions for the X force value, as determined by the MATLAB tool using STS-73 and STS-78 SAMS data, ranged from  $3.8lb_f$  to  $5.3lb_f$ . This bracketed the value of  $3.9lb_f$  determined from reading the plots. The large range in values is a result of two problems encountered with the System Identification toolbox.

The first problem encountered was that the MATLAB system Identification toolbox requires that the equations of motion be represented by a linear model, and this is not accurate due to Euler cross-axis coupling. Euler coupling has a significant effect on shuttle vehicle dynamics while in orbit when using vernier thrusters and may not be ignored in this case. The second problem was numerical precision related. Accelerations measured were in the  $1 \times 10^{-5}$  to  $4 \times 10^{-5}$  range and consequently were near the precision limits of the tools. Because of these problems the results from this tool were refined using a high fidelity six degree of freedom simulation with non-linear equations of motion.



The various candidate force and moment models were input to the high fidelity simulation as both environment and autopilot software values. Initial simulation runs were performed and compared against flight data from STS-73 and STS-71. The revised force and moment models all came closer to matching mated flight data than the original model but the match for orbiter alone cases was adversely affected. When using the models which contained the larger forces in the Orbiter X axis ( $F_x > 4$  lb), large under-predictions in rate change (rather than over-predictions seen with the old model) were seen for the mated flight data. The models with lower values of  $F_x$  all matched flight data closely, but universally the new models adversely affected results from single jet and two jet cases when compared to the orbiter alone results. A small trade study was performed which resulted in the determination that, for orbiter alone cases, the moment values for  $M_y$  and  $M_z$  had greater effect on system response than the forces  $F_x$  and  $F_y$ . The opposite was true for orbiter/Mir mated cases due to the large difference between the system reference and the actual vehicle center-of-gravity, where the moment generated by the revised plume forces is significantly large when compared to the generated control moment. This result led to the conclusion that the original model, created after STS-1, closely approximated the moments generated by the vernier thrusters, but did not accurately represent the forces generated. In creation of the final model, a decision was made to create a hybrid model consisting of new forces and the old moments, since the original model had matched orbiter alone cases well. The final impingement model, and the associated K-load jet model is shown in Tables 2 and 3, with the old model for comparison.

**Table 2**  
**IMPINGEMENT MODELS: NEW VS. OLD FORCES AND MOMENTS**

Thruster	New Model		Old Model	
	<u>R5D</u>	<u>L5D</u>	<u>R5D</u>	<u>L5D</u>
$F_{ix}$ (lb)	3.91	3.91	0.403	0.403
$F_{iy}$ (lb)	-4.35	4.35	-4.293	4.293
$F_{iz}$ (lb)	10.93	10.93	10.906	10.906
$M_{ix}$ (ft-lb)	92.6	-92.6	92.64	-92.64
$M_{iy}$ (ft-lb)	435.3	435.3	435.29	435.29
$M_{iz}$ (ft-lb)	170.4	-170.4	170.4	-170.4

**Table 3**  
**ONBOARD SOFTWARE MODEL- NEW VS. OLD FORCES AND MOMENTS**

Thruster	New Model		Old Model	
	<u>R5D</u>	<u>L5D</u>	<u>R5D</u>	<u>L5D</u>
$F_{ix}$ (lb)	3.91	3.91	0.403	0.403
$F_{iy}$ (lb)	-4.35	4.35	-4.293	4.293
$F_{iz}$ (lb)	-13.07	-13.07	-13.09	-13.09
$M_{ix}$ (ft-lb)	-143.3	143.3	-143.32	143.32
$M_{iy}$ (ft-lb)	-541.4	-541.4	-541.39	-541.39
$M_{iz}$ (ft-lb)	170.4	-170.4	170.4	-170.4

## RESULTS

The new model was evaluated against flight data from twelve cases spanning five shuttle missions. The evaluations included both orbiter alone and Orbiter/Mir configurations, and four different elevon positions. The new models were first used in an open loop jet selection program to determine raw vehicle rotational acceleration differences for cases where L5D, R5D, or both L5D and R5D were selected. The percentage differences in rotational accelerations between the old and the new models and flight data for the twelve cases are presented in Table 4.

**Table 4**  
**ROTATIONAL ACCELERATION DIFFERENCES: FLIGHT VS. OLD AND NEW MODELS**

Mission	Condition	Elevon		Absolute Difference- Flight vs. Open Loop (%)					
		Position (deg)	Thruster	Flight to Old Model			Flight to New Model		
				Roll	Pitch	Yaw	Roll	Pitch	Yaw
STS-71	Docked	0.0	L5D + R5D	96.83	21.84	103.5	97.37	0.073	102.7
STS-71	Docked	+21.6	L5D + R5D	97.16	31.22	93.43	97.64	7.61	94.88
STS-71	Docked	-7.5	L5D + R5D	31.61	18.07	124.7	42.28	1.46	119.6
STS-71	Orbiter	-7.5	L5D + R5D	75.47	5.44	66.20	74.67	2.56	113.3
STS-73	Orbiter	-7.5	L5D	0.098	7.89	14.10	4.06	0.91	12.15
STS-73	Orbiter	-7.5	L5D + R5D	88.94	12.31	101.4	87.74	3.94	101.7
STS-74	Docked	-7.5	L5D + R5D	6.91	22.16	19.27	14.79	3.10	16.14
STS-78	Orbiter	-7.5	L5D + R5D	116.91	15.19	99.91	119.7	7.18	102.4
STS-78	Orbiter	-7.5	R5D	0.13	18.50	30.08	4.04	10.80	31.73
STS-78	Orbiter	-25.3	L5D + R5D	115.74	16.17	99.82	127.0	8.34	48.97
STS-78	Orbiter	-25.3	R5D	4.69	16.11	19.15	0.73	7.96	18.21
STS-79	Orbiter	-7.5	L5D + R5D	41.65	42.4	99.98	66.67	2.16	99.89

From examination of the tabular data, it is apparent that the new model produces, on the whole, smaller differences between simulation and flight measured accelerations in the axis of interest. All the percentage errors in the table greater than 10% are due to small differences between very small numbers. For example, the Yaw axis 101% error for the STS-73 2 jet case results from the difference between an open loop predicted rotational acceleration of  $\sim 2.6\text{E-}06 \text{ deg/sec}^2$  and an actual acceleration of  $1.4\text{E-}04 \text{ deg/sec}^2$ . Figures 6 and 7 show the filtered STS-73 SAMS flight measured accelerations (in Orbiter Body Axis) cross plotted with the output of a closed loop simulation for the L5D+R5D -Pitch case. Evaluation of the open loop acceleration comparisons also showed that the plume force and moments vary with elevon position, as might be expected. Due to the sparseness of data points an accurate correlation between elevon position and plume force variation was not possible. Since the variations in rotational acceleration were within the autopilot feed-forward loop angular acceleration increment (angular acceleration over autopilot step time) design criteria of 10% it was determined that the VRCS plume model need not be elevon position dependent as the PRCS models are.



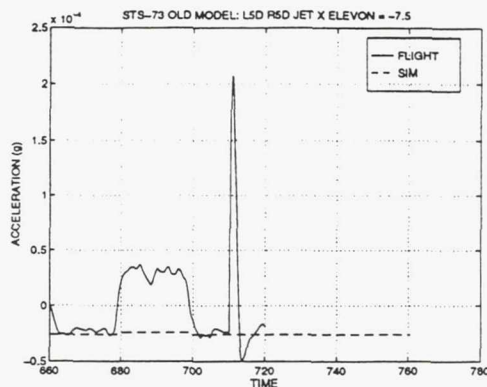


Figure 6 Old Model X Axis Accelerations v. Flight  
L5D+R5D -Pitch Firing,  $\delta_e = -7.5$  deg

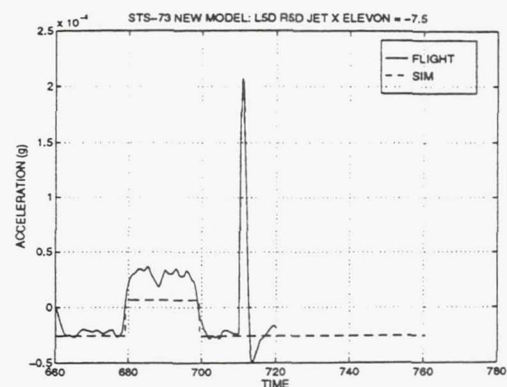


Figure 7 New Model X Axis Accelerations v. Flight  
L5D+R5D -Pitch Firing,  $\delta_e = -7.5$  deg

Following the open loop comparisons, closed loop cases were run using both the old and new models for comparison against flight data from five missions: STS-71, STS-73, STS-74, STS-78, and STS-79. Simulation results were plotted against orbiter downlisted flight data obtained from the shuttle downlist. Figure 6 shows the system comparison to STS-73 flight data using the old models, while Figure 7 shows the results using the new models. Both figures represent an L5D thruster firing for 19.6 seconds. Figures 10 and 11 display the results of a 19.6 second firing of L5D and R5D in response to a -Pitch command. As can be seen, there is little difference between the new and old models for an Orbiter alone case. Very small improvements in comparison to the STS-73 flight data for the single jet case were noted. No change was visible in the 2 jet cases shown in Figures 8 and 9. As an item of interest, it was noted that, in the orbiter alone cases examined for STS-71 and -73, both the new and the old models slightly overpredicted the vehicle rate change due to a thruster firing, while in the STS-78 cases the rate change was slightly underpredicted compared to flight. These differences were attributed to mass property variations between the missions.

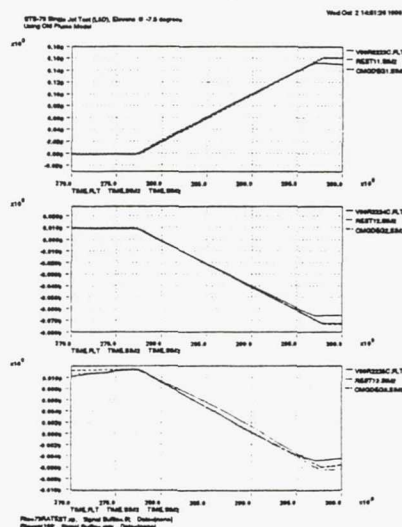


Figure 8 STS-73- Flight vs. Simulation, Old Plume Model,  
Roll, Pitch & Yaw Rate from L5D Firing,  $\delta_e = -7.5$  deg

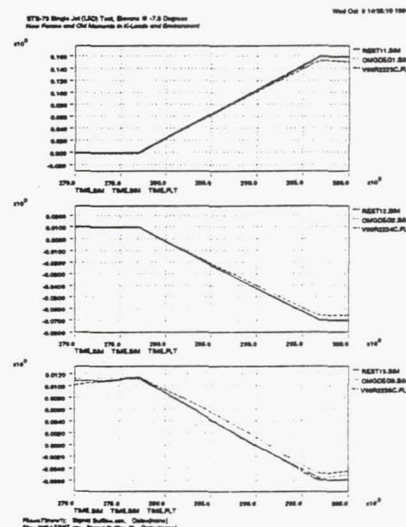


Figure 9 STS-73 Flight vs. Simulation, New Plume Model,  
Roll, Pitch & Yaw Rate from L5D Firing,  $\delta_e = -7.5$  deg



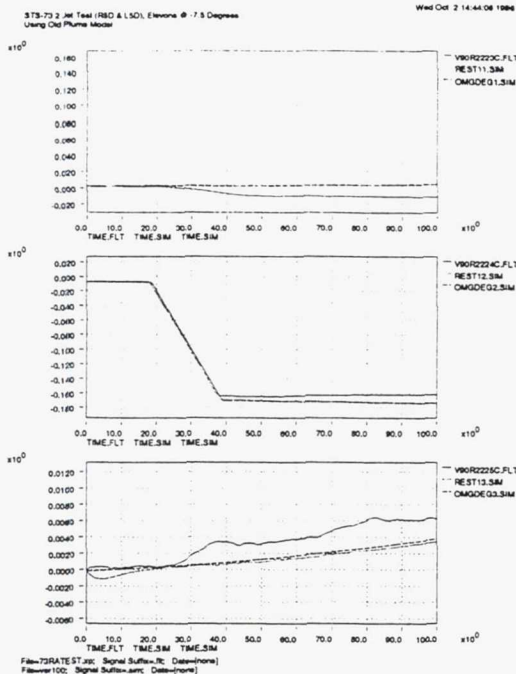


Figure 10 STS-73- Flight vs. Simulation, Old Plume Model, Vehicle Rates from -Pitch Firing (L5D+R5D),  $\delta_e = -7.5$  deg

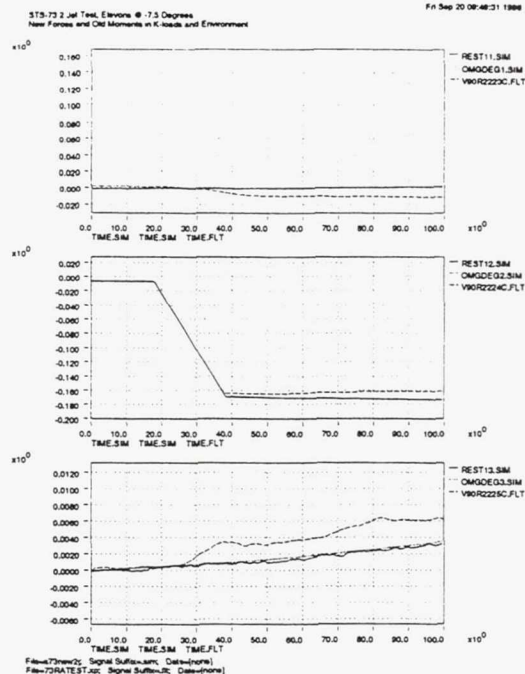


Figure 11 STS-73 Flight vs. Simulation, New Plume Model, Vehicle Rates from -Pitch Firing (L5D+R5D),  $\delta_e = -7.5$  deg

Although the differences between the orbiter alone configurations examined were minimal, in the orbiter/Mir mated cases, differences were much more evident. Simulations were run for STS-71, STS-74 and STS-79. Since STS-71 flight data was available for several elevon positions (0.0 degrees, +21.6 degrees, and -7.5 degrees) each was individually examined. A single case was performed for STS-74 since the elevons were fixed at -7.5 degrees, and two cases were examined for STS-79 since data was available for both L5D and R5D together, and R5D alone.

The STS-71 simulations were performed using the flight initialization load (I-load) software parameters with the DAP acceleration filter enabled. The STS-74 and STS-79 cases used the defined flight I-loads with the acceleration filter disabled during thruster firings. The acceleration filter was disabled for these missions to mask the plume impingement effects of each thruster firing from the orbiter autopilot, since the onboard software models had not been updated to account for the plume forces. Figures 12 and 13 illustrate the system response for the STS-71 mated case with the elevons at their full down position of +21.6 degrees. Discontinuities visible on the plots are due to data dropouts in the flight data. Figures 14 and 15 are comparisons between old and new plume models and STS-79 flight data, while Figure 16 compares the single jet system response using the new model to STS-79 flight data. As is apparent from examining Figures 12 through 16, the new model compares much more closely to flight results than the previous model.

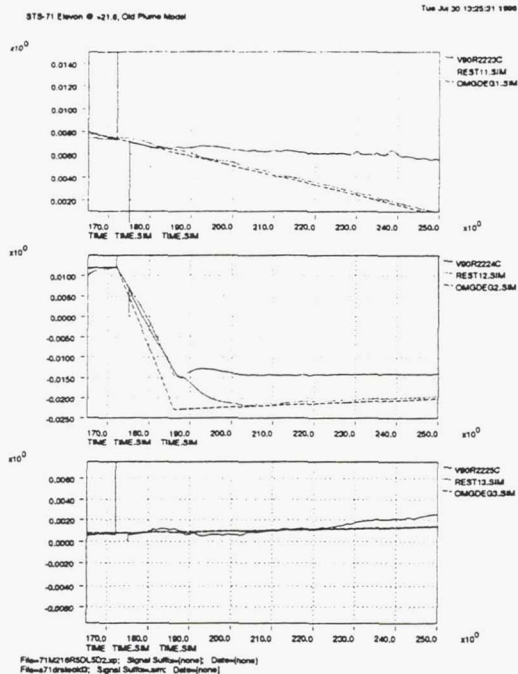


Figure 12 STS-71- Flight vs. Simulation, Old Plume Model, Vehicle Rates from -Pitch Firing ( $\delta_e = +21.6^\circ$ )

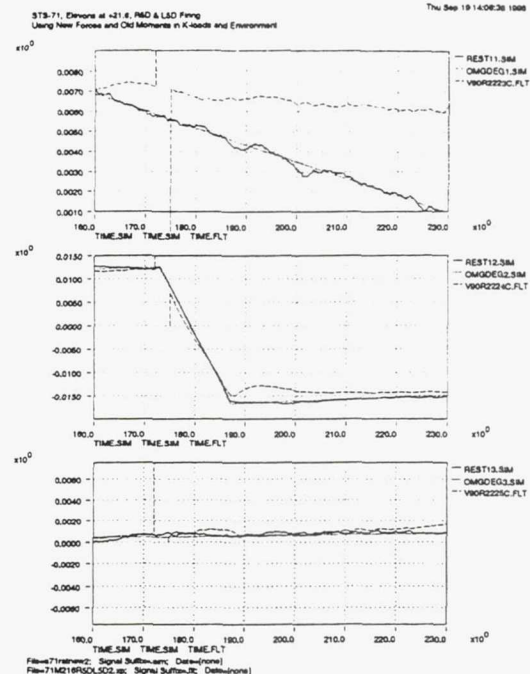


Figure 13 STS-71 Flight vs. Simulation, New Plume Model, Vehicle Rates from -Pitch Firing ( $\delta_e = +21.6^\circ$ )

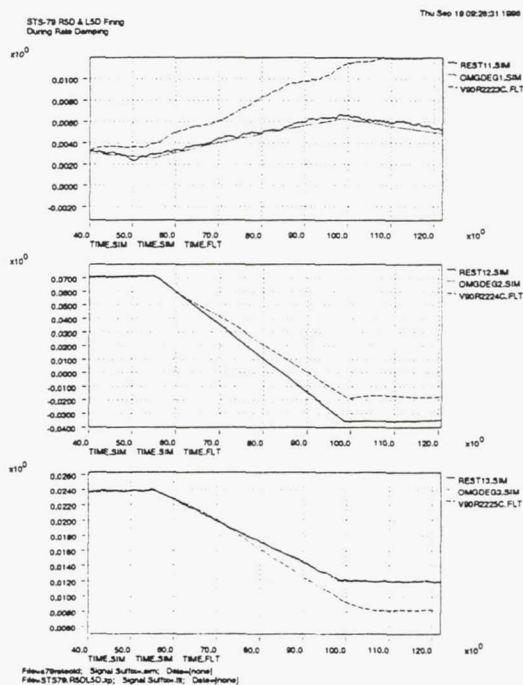


Figure 14 STS-79- Flight vs. Simulation, Old Plume Model, Vehicle Rates from -Pitch Firing (L5D+R5D),  $\delta_e = -7.5^\circ$

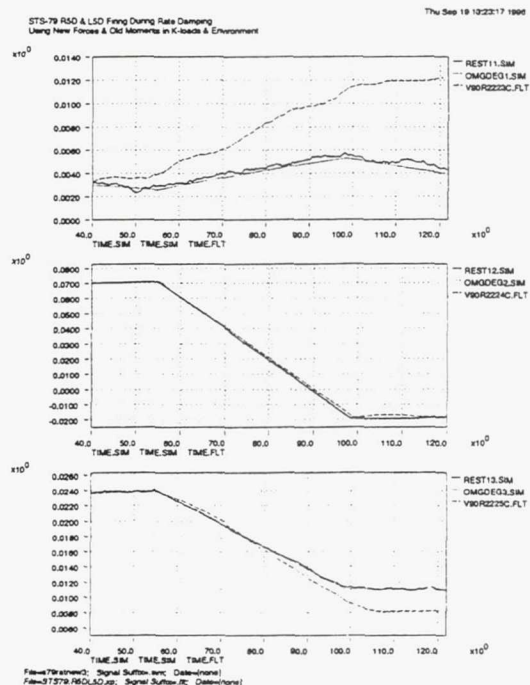


Figure 15 STS-79 Flight vs. Simulation, New Plume Model, Vehicle Rates from -Pitch Firing (L5D+R5D),  $\delta_e = -7.5^\circ$

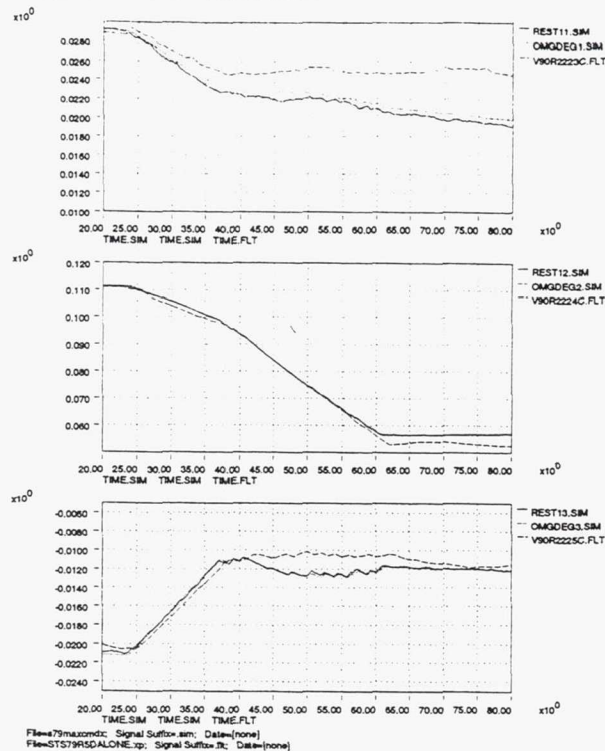


Figure 16 STS-79- Flight vs. Simulation, New Plume Model,  
Vehicle Rates from firing R5D, with some pulsing from LSD,  $\delta_e = -7.5$  deg

## CONCLUSIONS

It was apparent, from STS-71 flight data, that the vernier RCS plume model created after STS-1 did not represent the actual vehicle self-impingement forces accurately. An investigation to more accurately define plume impingement effects of the aft down-firing vernier thrusters was completed, resulting in a new model of VRCS self impingement forces. The new model has been verified against multiple Shuttle missions and on-orbit configurations. From comparison of the flight data with simulation results using the new plume model, it is evident that much closer matches between simulation and flight signatures may be obtained for both orbiter alone scenarios and scenarios with the Orbiter mated to a large structure. The new model is in use by analysts and mission planners on the shuttle program. Its incorporation into flight design and stability and control analyses results in more accurate estimation of propellant consumption and vehicle performance, both extremely important parameters in the pending Space Station assembly missions requiring Orbiter control of the mated Orbiter/ISS configuration.



## ACKNOWLEDGEMENTS

The author wishes to acknowledge the efforts and assistance of the following individuals who contributed to the efforts documented here and to the preparation of this paper; Tigran Poladian, Ashwani Chaudhary, Demetrious Zaferis, Doug Zimpfer, Joe Turnbull, Ray Barrington, and Steve Fitzgerald. The work documented here was completed by BNA under USA contract 1970483303, NAS9-20000 contract to the NASA.

## NOTATIONS

PRCS- Primary Reaction Control System, each thruster develops 870 lb<sub>f</sub> thrust  
VRCS- Vernier Reaction Control System, each thruster develops 25 lb<sub>f</sub> thrust  
DAP- Shuttle Digital Autopilot  
OARE- Orbital Acceleration Research Experiment  
SAMS- Shuttle Acceleration Measurement System  
CG- Center-of-Gravity  
DTO- Developmental Test Objective  
DOF- Degree-of-Freedom  
I-Load- Initialization Load, a shuttle software parameter that may change each flight  
K-load- Constant Load, a shuttle parameter that is hard coded into the software  
F<sub>x</sub>- Force acting in the Orbiter X axis  
M<sub>x</sub>- Moment about the Orbiter X axis  
CFD- Computational Fluid Dynamics  
 $\delta_e$ - Delta Elevon position, with - sign denoting upward deflection, and + denoting downward  
 $\omega_e$ - Attitude rate error, the differenced between desired and sensed vehicle rate  
 $\theta_e$ - Attitude error, the difference between desired and actual position

## REFERENCES

- [1] Kanipe, D. B., "Vernier RCS On-Orbit Plume Impingement Values", NASA Memorandum EX32/8202-24, February 10, 1982
- [2] Friend, R., "STS-71 Transition and On-Orbit Post-Flight Report", Rockwell International Letter, IL292-600-JO-95-078, September 9, 1995
- [3] Zimpfer, D., Kirchwey, K., Hanson, D., Jackson, M.,/Draper; Smith, N. NASA, "Shuttle Stability and Control of the STS-71 Shuttle/Mir Mated Configuration, American Astronautical Society Paper AAS 96-131, Shuttle/Mir session, AAS/AIAA Spaceflight Mechanics Conference, Austin Texas, 12-15 February, 1996
- [4] Zimpfer, D., "STS-71 Shuttle/Mir Mission Report", Charles Stark Draper Laboratory Report, CSDL-R-2699, July 31, 1995
- [5] "Predictions", e-mail from R. Hughes to D. Zimpfer, 20 November, 1995
- [6] Barrington, R. "STS-73 VRCS Hot Fire OARE Results", Charles Stark Draper Laboratory Memo #RDB-95-018, 1 December, 1995
- [7] STS83-0009-26, Space Shuttle Orbiter Operational Level C Functional Subsystem Software Requirements, Guidance, Navigation and Control, Part C, Flight Control, Orbit DAP, May 15, 1996

**Page intentionally left blank**

## ATTITUDE COMMANDS AVOIDING BRIGHT OBJECTS AND MAINTAINING COMMUNICATION WITH GROUND STATION

Hari B. Hablani<sup>†</sup>

Boeing North American, Downey, CA

The objective of the paper is to develop attitude commands for slewing a vehicle such that the angle of its boresight with the centroid of a bright object is not less than a minimum angle and its antennae do not lose communication with ground. These commands involve three angles: required pitch/yaw slew angle, bright object exclusion angle normal to the slew angle, and a roll angle for maintaining communication. The location of a bright object's centroid is formulated in terms of the first two angles. If the minimum-angle slew path enters the forbidden perimeter around a bright object, two alternative exclusion angles are determined, minimum and nonminimum, to pass the object tangentially from either of the two sides. Of the two angles, that exclusion angle is selected which steers the ground station trace toward the communication beam axis and not to the boundary and out of the beam. To develop time-varying command profiles, the pitch/yaw slew angle is varied as a time/fuel optimal profile and the exclusion angle is varied as a versine function of the slew angle joining the centroidal exclusion angle(s) with the initial and final directions of the boresight. If the versine profile enters the forbidden perimeter around a bright object, the intrusive segment of the profile is replaced with the perimeter. Communication link of the antennae along the three body axes is maintained by rolling the vehicle before, during or after slewing. The area forbidden to the ground station trace within the conical beam of -x antenna, for a 90 deg pitch/yaw motion, is identified. Finally, the three-axis attitude commands and rate commands are illustrated for a stressing scenario in which two bright objects are closeby and hence pose special circumstances for the algorithm to tackle.

### I. INTRODUCTION

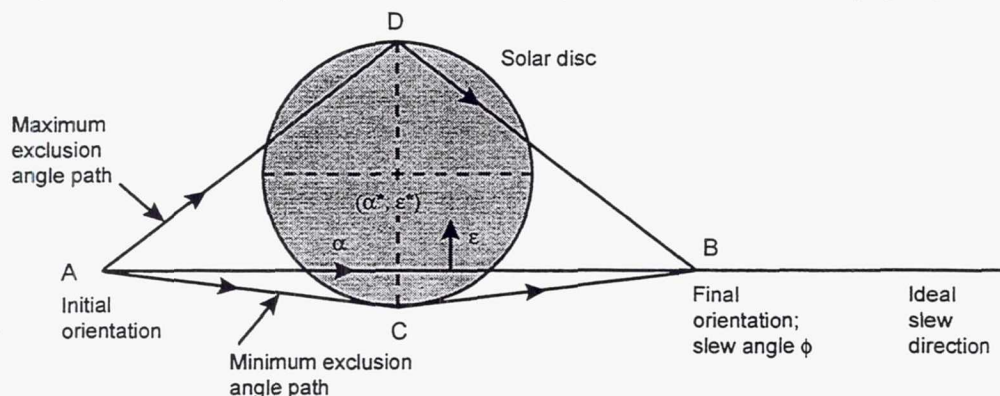
Spacecraft, whether earth-pointing, inertially-stabilized or interplanetary, are sometimes required to slew from one direction in space to other in such a way that, en route, the sensitive payloads not see bright objects such as Sun, Moon and Earth, and that antennae not lose communication with ground. This paper is concerned with devising attitude commands for these purposes. The subject of attitude maneuvers avoiding certain directions in space has been considered in the past and Ref. 1, an early version of this paper, cites these contributions. References 2-4 are pertinent here. Singh et al.<sup>2</sup> developed a constraint monitor algorithm to protect sensors of Cassini spacecraft from viewing the Sun. McCullough et al.<sup>3</sup> devised a velocity avoidance algorithm to protect Heavy Ion Large Telescope instrument boresight from hazardous debris in the neighborhood of spacecraft orbit. The algorithm maintains a minimum 90 degrees ram angle of the boresight with the spacecraft velocity vector. Rivera<sup>4</sup> conceived of a fixed axis of rotation located somewhere in a plane bisecting the ideal, minimum slew angle, the exact location dictated by the requirement that the boresight's new path (circular arc) avoid a bright disc

<sup>†</sup>Principal Engineering Specialist, Avionics Engineering, Flight Control Systems, Reusable Space Systems, Associate Fellow AIAA



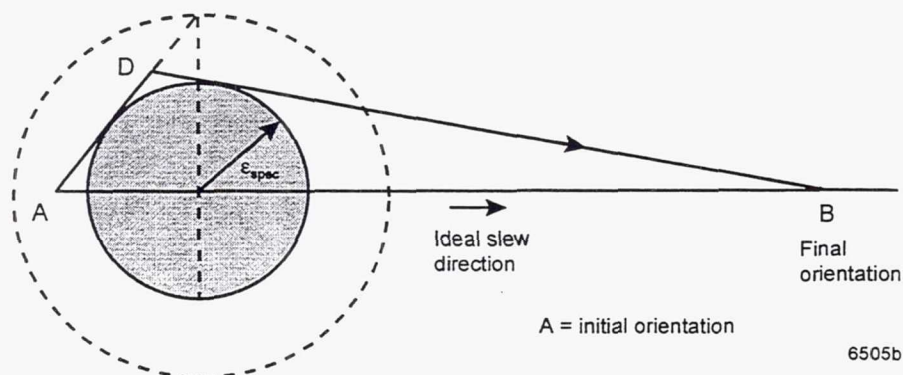
if the disc intersects the minimum-angle ideal path. Though well-thought-of, a shortcoming of this approach is that it results in maximum deviation of the boresight at half-slew angle regardless of the disc's location. In contrast, the approach devised in this paper has many general features that will be apparent subsequently.

Whereas the exclusion/communication algorithm developed here generates reference, time-varying attitude and angular rate commands, one may instead use step commands, for simplicity. For example, Figure 1a illustrates a minimum-angle slew path AB of a sensor starting from its initial orientation A to its final orientation B. En route, the sensor crosses Sun. To avoid this crossing, the sensor is step-commanded first to turn to the point C or to the opposite point D on the disc (the selection contingent upon the communication requirements). After arriving there, the sensor is step-commanded to the final orientation B. This approach is simple in that the attitude controller receives two sequential step commands and therefore the associated flight software is brief. However, the disadvantage of this approach is that, if the time/fuel optimal path ADB or ACB taken by the sensor enters the disc, depending on the location  $(\alpha^*, \epsilon^*)$  of the disc's centroid relative to the initial and final orientation of the sensor, this incursion will be neither detected nor averted by the flight controller. To redress this, the step commands may be devised more judiciously as shown in Figure 1b (the disc's centroid in Figure 1b lies on the ideal slew path AB,  $\epsilon^* = 0$ ). Now, the forbidden radius around the bright disc is enlarged so that, ignoring transients, the sensor will traverse the path ADB where AD and DB are tangential to the earlier forbidden area. The sensor is thus step-commanded to the orientation D and, after arriving there and stopping, it is step-commanded next to its final orientation B. The intermediate orientation D may be determined analytically or numerically. The actual path of the sensor in these two illustrations might differ significantly from the expected path ADB, depending on the flight controller and actuators (wheels, thrusters). For one thing, because of the step commands, the controller must stop and restart the sensor at D, which is wasteful. More importantly, since the slew



6505a

**Figure 1a Step Commands Producing Exclusion Paths That Cross Sun**



6505b

**Figure 1b Ideal Tangential Exclusion Path Avoiding Sun, Using Step Commands**

angle  $\alpha$  and the exclusion angle  $\varepsilon$  are about arbitrary axes in the pitch/yaw plane of the vehicle, this causes a coupled multi-axis motion. As a result, the actual path of the sensor may not be as well-behaved as what it will be if the flight controller receives reference  $\alpha$  and  $\varepsilon$  command profiles from A to B and three-axis body rate commands involving  $\dot{\alpha}$  and  $\dot{\varepsilon}$ . For this reason, the paper develops such reference commands.

This, then, brings us to the contents of the present paper. Section II formulates various aspects of attitude motion for a bright object avoidance. The parameters of a minimum-angle slew, namely, slew angle, slew axis, and its orientation relative to the initial vehicle frame and the final boresight direction are determined first. The coordinates  $\alpha^*$ ,  $\varepsilon^*$  of the centroid of a bright object relative to the ideal slew plane are determined next. Then follows the determination of the two opposite exclusion angles (Figure 1a) about an axis in the pitch/yaw plane, each enabling the telescope to pass the forbidden disc around a bright object tangentially at  $\alpha = \alpha^*$ . While the slew angle  $\alpha$  is varied as a time/fuel optimal profile, the exclusion angle  $\varepsilon$  varies as a versine function of  $\alpha$ , reaching the desired avoidance angle at the slew angle  $\alpha = \alpha^*$ . Should this  $\varepsilon(\alpha)$  profile intersect the disc for a certain range of  $\alpha$ , this versine segment is replaced by the corresponding arc of the forbidden circle around the bright object. The formulation for this replacement is developed in this section. Sections III and IV deal with the roll motions required for communication maintenance of antennae with a ground station. For the antennae with their communication cones along pitch and yaw axes, a roll motion restores the communication if the geometry of the vehicle and ground station locations and the communication cone size permit it at all. For  $-x$  antenna, a roll motion prior to the slew is formulated so as to keep the ground station within the cone of the antenna for a complete slew maneuver. This pre-roll motion, however, does not always maintain the communication, and the corresponding forbidden region of the ground station projection within the communication cone is identified. Regarding the two opposite exclusion angles determined in Sec. II, one turns the antenna away from the ground station while the other aligns it more with it. Thus, while one exclusion angle is desirable, the other is not, and the conditions to identify them are devised in Sec. V. The time-varying angular rate commands associated with slew, exclusion, and roll motion for communication maintenance are furnished in Sec. VI. Finally, in the context of an exoatmospheric vehicle, these attitude and rate commands are illustrated in Sec. VII and the paper is concluded in Sec. VIII.

## II. BRIGHT OBJECT AVOIDANCE: FORMULATION

### Ideal Slew

Figure 2 portrays the unit vector  $\underline{\ell}_0$  along the initial direction of the boresight, and  $\underline{\ell}_f$  along its final

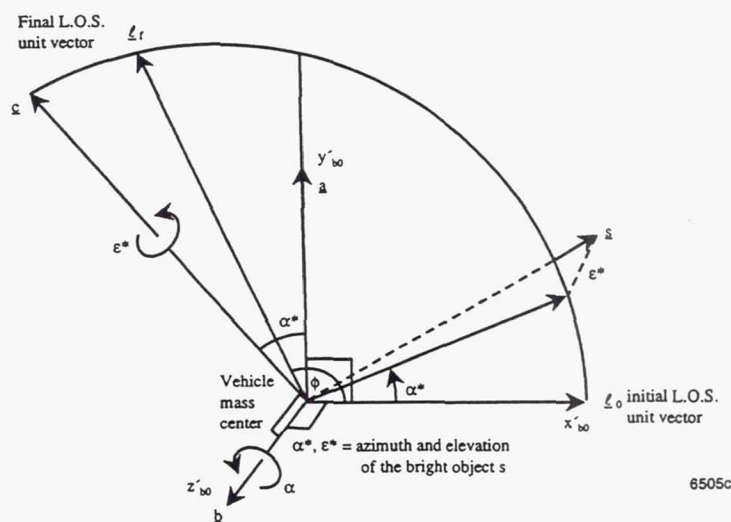


Figure 2 Location of a Celestial Object Relative to the Ideal Slew Plane of The Boresight



desired direction. It further depicts a bright object  $s$  to be avoided by the telescope. Clearly, the most natural axis of rotation to slew the telescope from  $\underline{\ell}_0$  to  $\underline{\ell}_f$  is normal to the plane containing these two noncollinear unit vectors. Denote the unit vector along this axis of rotation as  $\underline{b}$  (Figure 1) and the angle between  $\underline{\ell}_0$  and  $\underline{\ell}_f$  as  $\phi$ . Then

$$\sin \phi = | \underline{\ell}_0 \times \underline{\ell}_f |, \quad 0 < \phi < \pi \quad (1)$$

$$\underline{b} = (\underline{\ell}_0 \times \underline{\ell}_f) / \sin \phi \quad (2)$$

To complete the right-handed triad associated with the unit vectors  $\underline{\ell}_0$  and  $\underline{b}$ , define a unit vector  $\underline{a}$  in the plane  $\underline{\ell}_0 - \underline{\ell}_f$  such that  $\underline{a} = \underline{b} \times \underline{\ell}_0$ . The coordinate frame associated with the triad  $\underline{\ell}_0 \underline{a} \underline{b}$  (in this sequence) is denoted  $x'_{b0} y'_{b0} z'_{b0}$  where the subscript  $b$  denotes the spacecraft body, 0 denotes the initial orientation of the spacecraft, and the prime distinguishes it from the initial spacecraft frame  $x_{b0} y_{b0} z_{b0}$ :  $x_{b0} = x'_{b0}$ , and the axes  $y_{b0}, z_{b0}$  are related to  $y'_{b0}, z'_{b0}$  through a roll angle  $\gamma$  (Figure 3). Since the initial line-of-sight unit vector  $\underline{\ell}_0$  is along the boresight axis  $x_{b0}$ , the components of  $\underline{\ell}_0$  in the initial frame  $\mathcal{F}^{b0}$ :  $x_{b0} y_{b0} z_{b0}$  are  $\underline{\ell}_0 = [1 \ 0 \ 0]^T$ . Moreover, the unit vectors  $\underline{a} (y'_{b0})$  and  $\underline{b} (z'_{b0})$ , both being normal to  $\underline{\ell}_0$ , are in the pitch-yaw ( $yz$ ) plane, inclined at a roll angle  $\gamma$  with  $y_{b0}$  and  $z_{b0}$ , respectively. Therefore,

$$\tan \gamma = \underline{\ell}_f \cdot \underline{b}_{30} / \underline{\ell}_f \cdot \underline{b}_{20} \quad (3)$$

where the unit vector  $\underline{b}_{20}$  is along  $y_{b0}$ -axis and  $\underline{b}_{30}$  along  $z_{b0}$ . Since the components  $\underline{\ell}_f \cdot \underline{b}_{20}$  and  $\underline{\ell}_f \cdot \underline{b}_{30}$  are known, the angle  $\gamma$  can be calculated.

### Exclusion Angles

As shown earlier in Figure 1a, the center of a bright object  $s$  is specified by an angle (called azimuth here)  $\alpha^*$  in the slew plane  $\underline{\ell}_0 - \underline{\ell}_f$  (or  $x'_{b0} y'_{b0}$ ) about the axis  $\underline{b}$  and an elevation angle  $\epsilon^*$  about the once-displaced axis  $y'_{b0}$  (the unit vector  $\underline{c}$  in Figure 2). The unit vector  $\underline{s}$  pointing to the center of the celestial object  $s$  ( $s$  from the sun) can be expressed in the frame  $\underline{\ell}_0 \underline{a} \underline{b}$  thus

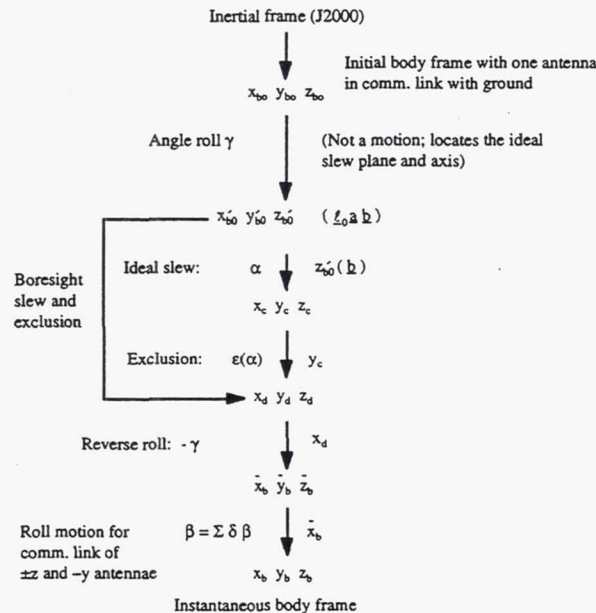


Figure 3 Coordinate Frames and Angular Motions for Boresight Slew ( $\alpha$ ), Bright Object Avoidance ( $\epsilon$ ), and Roll ( $\beta$ ) for Communication Maintenance of  $-y$  and  $\pm z$  Antennae



$$\underline{s} = \underline{s} \cdot \underline{\ell}_0 \underline{\ell}_0 + \underline{s} \cdot \underline{a} \underline{a} + \underline{s} \cdot \underline{b} \underline{b} \quad (4)$$

these three components being known because the unit vectors  $\underline{s}$ ,  $\underline{\ell}_0$ ,  $\underline{\ell}_f$  and therefore  $\underline{a}$  and  $\underline{b}$  are all known in an inertial frame, J2000 for example. Furthermore, using the angles  $\alpha^*$ ,  $\varepsilon^*$ ,  $\underline{s}$  is expressed in the frame  $\underline{\ell}_0 \underline{a} \underline{b}$  as (Figure 3)

$$\underline{s} = c\varepsilon^* c\alpha^* \underline{\ell}_0 + c\varepsilon^* s\alpha^* \underline{a} - s\varepsilon^* \underline{b} \quad (5)$$

where  $s(\cdot) = \sin(\cdot)$  and  $c(\cdot) = \cos(\cdot)$ . Comparing the three components in Eqs. (4) and (5) the angles  $\alpha^*$  and  $\varepsilon^*$  are found to be

$$\alpha^* = \tan^{-1} [ (\underline{s} \cdot \underline{a}), (\underline{s} \cdot \underline{\ell}_0) ], \quad -\pi \leq \alpha^* \leq \pi \quad (6)$$

$$\varepsilon^* = -\sin^{-1} (\underline{s} \cdot \underline{b}) - \pi/2 < \varepsilon^* < \pi/2 \quad (7)$$

provided  $-\pi/2 < \varepsilon^* < \pi/2$  so that  $c\varepsilon^* > 0$ .

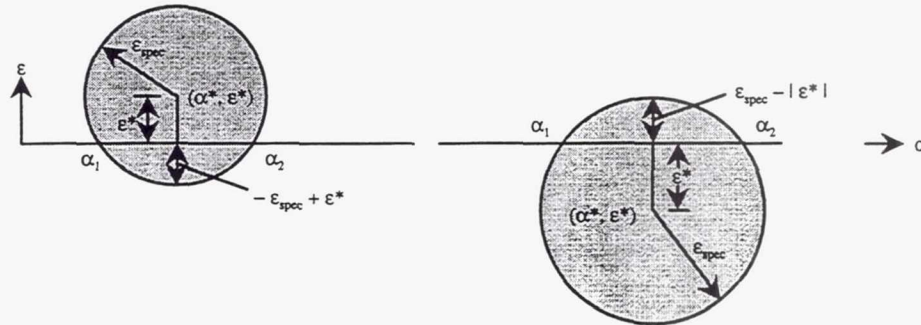
A bright object is considered for avoidance when, loosely speaking,  $0 \leq \alpha^* \leq \phi$ . This condition is not exact for the following reason. An infrared celestial object is to be avoided by a minimum specified angle denoted  $\varepsilon_{\text{spec}}$ , (Figure 1b), that is, there is a disc of radius  $\varepsilon_{\text{spec}}$  around the celestial object centered at  $(\alpha^*, \varepsilon^*)$  which the boresight must not enter. For  $\varepsilon^* = 0$ , the extreme azimuth angles of the disc boundary will then be  $\alpha^* \pm \varepsilon_{\text{spec}}$  and for the disc to be considered for avoidance the azimuth angle  $\alpha^*$  must satisfy the exact condition:  $-\varepsilon_{\text{spec}} \leq \alpha^* \leq \phi + \varepsilon_{\text{spec}}$ . But, usually, mission planning will ensure that the initial and final orientations of the sensor boresight are not within the  $\varepsilon_{\text{spec}}$  radius of a bright object. In any event, for simplicity, we will continue to use the loose condition stated earlier. For a bright object within  $0 \leq \alpha^* \leq \phi$ , the minimum deviation angle  $\varepsilon_{\text{min}}$  required for avoiding this object is determined as follows. Figure 4 illustrates two celestial objects, one with  $\varepsilon^* > 0$  and the other with  $\varepsilon^* < 0$ . It is apparent from the illustration that the ideal slew path of the boresight (the azimuth,  $\alpha$ , axis) about the axis  $\underline{b}$  will intersect the  $\varepsilon_{\text{spec}}$  disc if  $|\varepsilon^*| < \varepsilon_{\text{spec}}$  and then, for boresight to avoid entering the disc,  $\varepsilon_{\text{min}}$  at  $\alpha = \alpha^*$  must be

$$\varepsilon_{\text{min}} = \begin{cases} -\text{sign}(\varepsilon_{\text{spec}} - |\varepsilon^*|, \varepsilon^*) & \text{if } |\varepsilon^*| < \varepsilon_{\text{spec}} \\ 0 & \text{if } |\varepsilon^*| > \varepsilon_{\text{spec}} \end{cases} \quad (8a)$$

$$(8b)$$

In subsequent sections we will see that sometimes the sign of  $\varepsilon_{\text{min}}$  is such that the avoidance motion  $\varepsilon$  causes the antenna to turn away from the ground station and possibly break the communication link altogether. In that event,  $\varepsilon_{\text{min}}$  must be replaced by its maximum value

$$\varepsilon_{\text{max}} = \text{sign}(\varepsilon_{\text{spec}} + |\varepsilon^*|, \varepsilon^*) \quad \text{if } |\varepsilon^*| < \varepsilon_{\text{spec}} \quad (9)$$



6505d

Figure 4 Minimum Deviation Angle for Avoiding a Celestial Object Exclusion Angle: Versine Profile

to pass the disc tangentially from the opposite side. This will align the antenna more with the ground station. Furthermore, when two or more bright objects are close together or overlap (sunrise, sunset, moonrise, moonset, Sun and Moon in the neighborhood, etc.), the minimum or maximum deviation angles prescribed by Eqs. (8)-(9) may not be able to prevent the boresight from entering the disc of a neighboring celestial object. Ad hoc solutions for such special circumstances are presented in Ref. 1.

The discrete angles ( $\alpha^*$ ,  $\varepsilon_{\min}$  or  $\varepsilon_{\max}$ ) could be used to construct step commands discussed in Introduction. But, if one desires to input a reference command profile to the attitude controller, the slew angle  $\alpha$  must be expressed as a function of time and  $\varepsilon$  as a function of  $\alpha$ . For this purpose, an  $\varepsilon(\alpha)$  profile is composed, piecing together discrete exclusion angles for the centroids of different bright objects that cross the ideal slew path, and the initial and final exclusion angles at zero and final slew angles. Note that the initial and final exclusion angles are zero unless a bright object covers the initial or final direction of the sensor. Since a versine ( $1 - \cos \theta$  type) profile has zero slope at the beginning and at the end and can be shaped to be tangential to a disc at its centroidal angle  $\alpha^*$ , this profile is used here as an  $\varepsilon(\alpha)$ . One such profile and its slope, satisfying the boundary conditions  $\varepsilon = \varepsilon_i$  @  $\alpha = \alpha_i$ , and  $\varepsilon = \varepsilon_{i+1}$  @  $\alpha = \alpha_{i+1}$  is ( $\alpha_i$  and  $\alpha_{i+1}$  are the centroidal slew angles of the discs  $i$  and  $i + 1$ , respectively)

$$\varepsilon = \frac{1}{2} (\varepsilon_i + \varepsilon_{i+1}) - \frac{1}{2} (\varepsilon_{i+1} - \varepsilon_i) \cos \eta \quad (10)$$

$$\frac{d\varepsilon}{d\alpha} = \frac{\pi}{2} \frac{\varepsilon_{i+1} - \varepsilon_i}{\alpha_{i+1} - \alpha_i} \sin \eta \quad (11)$$

$$\eta = \frac{\alpha - \alpha_i}{\alpha_{i+1} - \alpha_i} \pi \quad (12)$$

These relations can be specialized for  $\varepsilon_i = 0$  at  $\alpha_i = 0$ , or  $\varepsilon_{i+1} = 0$  at  $\alpha_{i+1} =$  the final slew angle  $\phi$ , or for any other special circumstance. Also the rate  $\dot{\varepsilon}$  is calculated from  $\dot{\varepsilon} = (d\varepsilon/d\alpha) \dot{\alpha}$  where  $\dot{\alpha}$  = the instantaneous slew rate determined from a time/fuel optimal slew profile of  $\alpha$ .

### Forbidden Disc Entry

Depending on the location and size of the disc relative to the slew path, the  $\varepsilon$ -profile (10) may cause the sensor to enter a bright disc. In that instance, this  $\varepsilon(\alpha)$  is replaced by an  $\varepsilon(\alpha)$  that commands the sensor to slide along the disc perimeter. Reference 1 shows that the disc boundary is governed by:

$$c\varepsilon c\varepsilon^* c(\alpha - \alpha^*) + s\varepsilon s\varepsilon^* = c\varepsilon_{\text{spec}} \quad (13)$$

At the intersection slew angles  $\alpha_1$  and  $\alpha_2$  (Figure 4) the avoidance angles  $\varepsilon$  are zero, by definition. Hence, substituting  $\varepsilon = 0$  in Eq. (13), we arrive at

$$\varepsilon = 0: \quad c(\alpha_{1,2} - \alpha^*) = c\varepsilon_{\text{spec}} / c\varepsilon^* \quad (14)$$

which furnishes the angles  $\alpha_1 < \alpha^*$  and  $\alpha_2 > \alpha^*$ . The boresight's entry of the forbidden area is checked within the range  $\alpha_1 < \alpha < \alpha_2$  as follows.

For a given  $\alpha$ , whether the boresight at an angle  $\varepsilon$ , Eq. (10), will enter a disc or not is determined from Eq. (13). Specifically, if a point  $(\alpha, \varepsilon)$  of the versine profile is within a disc, the angle between  $(\alpha, \varepsilon)$  direction and  $(\alpha^*, \varepsilon^*)$  direction will be less than  $\varepsilon_{\text{spec}}$  and therefore

$$\text{boresight entered the disc} \Leftrightarrow c\varepsilon c\varepsilon^* c(\alpha - \alpha^*) + s\varepsilon s\varepsilon^* > c\varepsilon_{\text{spec}} \quad (15)$$

If this condition is not satisfied, the boresight is outside the disc. Thus, if the commanded orientation  $(\alpha, \varepsilon)$  of the next sample satisfies the above inequality, the boresight will be commanded to enter the disc unless this  $\varepsilon$  is replaced by a perimeter  $\varepsilon$  for the same slew angle. The perimeter  $\varepsilon$  may be obtained by solving the transcendental Eq. (13) for a given  $(\alpha - \alpha^*)$  angle using Newton-Raphson technique, by substituting  $\varepsilon = \varepsilon^* + \delta\varepsilon$  and expanding  $s\varepsilon$  and  $c\varepsilon$  up to the second-order of  $\delta\varepsilon$ . Alternatively, define a frame  $x_d^* y_d^* z_d^*$  analogous to the frame  $x_d y_d z_d$  (Figure 3) arrived at after the rotation  $\alpha = \alpha^*$  and  $\varepsilon = \varepsilon^*$ . Then, the disc perimeter may be expressed parametrically in terms of an angle  $\theta$   $(-\pi \leq \theta \leq \pi)$  measured from  $y_d^*$ -axis. The boresight  $x_b$  can be oriented in a direction  $(\alpha, \varepsilon)$  on the disc boundary by an angle of rotation  $\Delta\alpha$  about  $z_d^*$ -axis and  $\Delta\varepsilon$  about  $\Delta\alpha$ -displaced  $y_d^*$ -axis. Expressing then the boresight unit vector in the frame  $x_d^* y_d^* z_d^*$ , Ref. 1 shows that

$$\tan \Delta\alpha = c\theta \tan \varepsilon_{\text{spec}} \quad (16)$$

$$s\Delta\varepsilon = -s\varepsilon_{\text{spec}} s\theta \quad (17)$$

To determine the boundary angle  $\varepsilon$  corresponding to a slew angle  $\alpha$   $(\alpha_1 < \alpha < \alpha_2)$  we first note that, for  $|\varepsilon^*| \ll 1$  rad,  $\Delta\alpha \approx \alpha - \alpha^*$ ,  $\Delta\varepsilon \approx \varepsilon - \varepsilon^*$ . For a given  $\Delta\alpha$ , then, Eq. (16) yields

$$c\theta = \tan \Delta\alpha / \tan \varepsilon_{\text{spec}} \quad (18)$$

which presents two values of  $\theta$ , and therefore two values of the boundary angle  $\varepsilon$  for a given  $\alpha$ :  $\Delta\varepsilon > 0$  and  $\Delta\varepsilon < 0$ . Deducing  $\sin\theta$  from Eq. (18), Eq. (17) furnishes

$$s\Delta\varepsilon = \pm s\varepsilon_{\text{spec}} \left[ 1 - \frac{\tan^2 \Delta\alpha}{\tan^2 \varepsilon_{\text{spec}}} \right]^{1/2} \quad (19)$$

Between the two  $\Delta\varepsilon$ 's, that value is selected whose sign matches with the sign of the original  $\Delta\varepsilon$  that will have brought the boresight inside the disc. The new  $\varepsilon$  is finally calculated from  $\varepsilon = \varepsilon^* + \Delta\varepsilon$  and the boresight is commanded to slide along the disc until the  $\varepsilon$  of the versine profile does not bring the boresight inside the disc anymore. While sliding along the disc perimeter, the slope  $d\varepsilon/d\alpha$  is governed by

$$\frac{d\varepsilon}{d\alpha} = \frac{\cos \varepsilon^* \cos \varepsilon \sin(\alpha - \alpha^*)}{\sin \varepsilon^* \cos \varepsilon - \cos \varepsilon^* \sin \varepsilon \cos(\alpha - \alpha^*)} \quad (20)$$

### III. COMMUNICATION MAINTENANCE OF PITCH (Y) AND YAW (Z) ANTENNAE

Figure 5 illustrates communication cones of  $-y$  (pitch) and  $\pm z$  (yaw) antennae. If the vector from an antenna to the ground station is enveloped by the antenna's cone, the communication link is maintained, otherwise not. The axes of the antennae cones are along the pitch and yaw axes, so if the communication link is broken for any antenna, it is restored by a roll rotation  $\beta$  of the vehicle about the  $x$ -axis (Figure 3). The magnitude of this rotation must be such that while the communication link is regained for one antenna, it is not lost for the other since the  $y$  and  $z$  antennae are mounted on orthogonal axes and signal strength for one antenna is made stronger at the expense of the other. It therefore seems logical to incrementally roll the vehicle, as shown in Figure 3, about  $x$ -axis so as to maintain equal signal strengths for one of the  $z$  antennae and  $-y$  antenna while the boresight ( $x$ -axis) is commanded to slew. This roll motion is formulated below.

A time-varying vehicle body frame  $\bar{x}_b \bar{y}_b \bar{z}_b$ , shown in Figure 3, is arrived at after a rotation of  $(\alpha, \varepsilon)$  formulated in Sec. II. The antennae in this orientation of the vehicle may or may not have a communication link with the ground. Our objective now is to determine that roll angle  $\beta$  which not only links  $-y$  antenna and either  $+z$



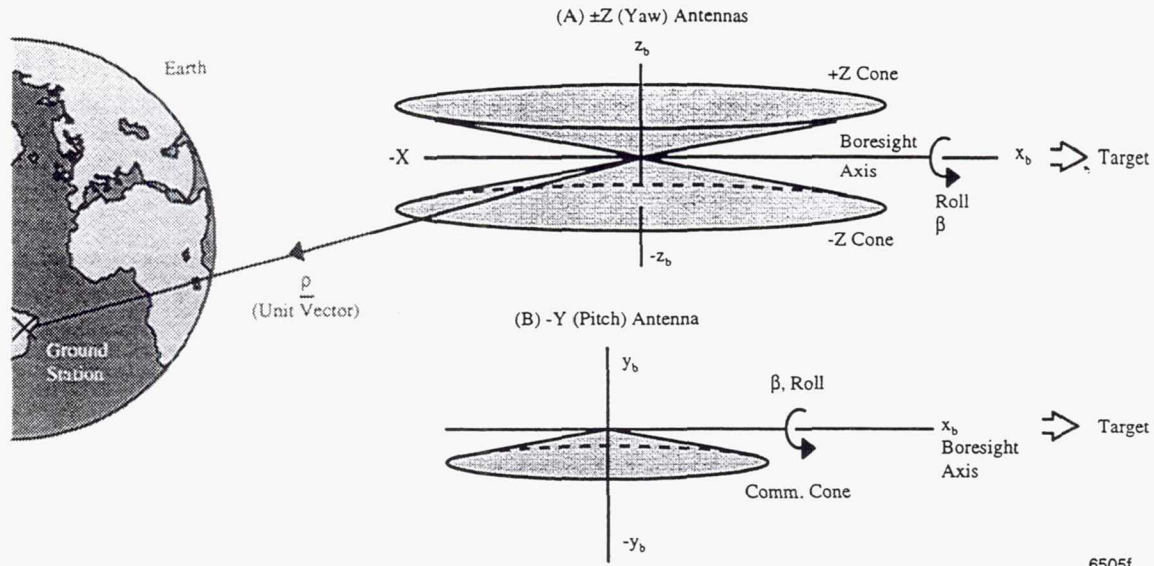


Fig 5 Communication Cones of Pitch and Yaw Antenna

or  $-z$  antenna with the ground, but equalizes as well the signal strengths of the two. Let  $\underline{\rho}$  be a unit vector from the vehicle to the ground station (Figure 5), with the components in the frame  $\mathcal{F}^b$ :  $\bar{x}_b \bar{y}_b \bar{z}_b$  as  $\underline{\rho}^{\mathcal{F}^b} = [\bar{x}_b \bar{y}_b \bar{z}_b]^T$  where the superscript T means transpose. When the vehicle is rolled by an angle  $\beta$  about the axis  $\bar{x}_b = x_b$ , equalizing the signal strengths, the body frame  $\mathcal{F}^b$ :  $x_b y_b z_b$  is arrived at. The components of  $\underline{\rho}$  in this frame are  $[x_b y_b z_b]^T$ . Let  $\phi_{+z}$ , or  $\phi_z$  for short, be the angle between  $+z$  antenna cone axis and  $\underline{\rho}$ ; likewise, let  $\phi_{-z}$  be the angle between  $-z$  antenna cone axis and  $\underline{\rho}$ , and  $\phi_{+y}$ , between  $-y$  axis and  $\underline{\rho}$ . Ref. 1 then shows that, for equal signal strengths for  $+z$  and  $-y$  antennae ( $\phi_z = \phi_{-y}$ ) the required roll rotation  $\beta$  in terms of the components of  $\underline{\rho}$  prior to  $\beta$  rotation is

$$+ \text{z antenna: } \tan \beta = \frac{\bar{y}_b + \bar{z}_b}{y_b - z_b} \quad (21)$$

and after rotation

$$\phi_{-y} = \phi_z = \cos^{-1} \frac{1}{\sqrt{2}} (1 - x_b^2)^{1/2} \quad (22)$$

One infers from Eq. (22) that for a given  $\underline{\rho}$  vector and therefore a given  $x_b$  which does not change by rotation, the angle  $\phi_{-y}$  ( $=\phi_{+z}$ ) achieved after the roll is predetermined by  $x_b = \bar{x}_b$  whether this establishes the communication link of the two antennae or not, that is, whether  $\phi_{-y} = \phi_z < \theta_{\text{cone}}$  or not. Consider now the antenna along  $-y$  axis and the antenna along  $-z$  axis. For  $\phi_{-y} = \phi_{-z}$ , the required roll angle  $\beta$  is (Ref. 1)

$$-z \text{ antenna: } \tan \beta = \frac{-\bar{y}_b + \bar{z}_b}{y_b + z_b} \quad (23)$$

and, after the rotation  $\beta$ ,  $y_b = z_b$ .

In actual implementation of the above algorithm, the angle  $\beta$  is not calculated for each sample relative to the frame  $\bar{x}_b \bar{y}_b \bar{z}_b$ . Instead, one calculates  $\delta\beta$  rotation with respect to the frame  $x_b y_b z_b$  of the previous sample and then increment the previous roll by  $\delta\beta$  as the azimuth and elevation angles  $\alpha$  and  $\epsilon$  evolve. This will maintain, throughout the slew, the same yaw antenna (either  $+z$  or  $-z$ ) in link with the ground which was in link before the slew initiated.

#### IV. COMMUNICATION MAINTENANCE OF -X ANTENNA

While the roll rotation  $\beta$  following the slew angle  $\alpha$  and exclusion motion  $\epsilon$  maintains communication for  $y$  and  $z$  antennae, such rotations do not help in the case of an  $x$ -antenna because, now, a post-roll rotation (about  $x$ ) cannot change the angle of the ground station vector  $\underline{\rho}$  with the cone axis- $x$ . However, because of the noncommutativity of large angles, a roll rotation  $\beta$  before the rotations  $\alpha$  and  $\epsilon$  will aid in maintaining communication of  $-x$  antenna. In actual flights, though, the rotations  $(\alpha, \epsilon)$  do not need to take place after the completion of the roll ( $\beta$ ) rotation; indeed, the three rotations  $(\beta, \alpha, \epsilon)$  can take place simultaneously as one equivalent rotation. But a separate consideration of the pre-roll  $\beta$  and the slew/exclusion motion  $(\alpha, \epsilon)$  facilitates the analysis and understanding. We will now determine the conditions under which a pre-roll rotation is required and its sense and magnitude.

Let  $\phi_{-x}$  be the angle between  $\underline{\rho}$  and the antenna beam axis  $-x_b$ . The requirement for communication, then, is:  $\phi_{-x} \leq \theta_{\text{cone}}$  where  $\theta_{\text{cone}}$  is the semicone angle of the  $-x$  antenna beam. Since  $\underline{\rho} \cdot (-\underline{b}_1) = \cos \phi_{-x}$  ( $\underline{b}_1$  is the unit vector along the  $x_b$  axis) the just-stated requirement is equivalent to

$$\cos \phi_{-x} \geq \cos \theta_{\text{cone}} \quad (24)$$

In terms of the components of  $\underline{\rho} = [x_b y_b z_b]^T$  the requirement (24) is the same as the following two requirements

$$-x_b \geq \cos \theta_{\text{cone}} \quad (25)$$

$$y_b^2 + z_b^2 \leq \sin^2 \theta_{\text{cone}} \quad (26)$$

Satisfaction of these constraints will now be examined in the context of a large angle maneuver.

##### Pitch or Yaw Rotation of $\pm \pi/2$

Suppose the mission planning requires any of the four possible  $\pm 90$  deg rotations about pitch and yaw axis of the vehicle. Of the four, that rotation is to be selected for which the ground station remains within the beamwidth of  $-x$  antenna throughout the rotation. Consider a pitch rotation of  $\phi$  about  $y_b$ -axis. Let  $[x_{b0} y_{b0} z_{b0}]^T$  be the unit vector to the ground station before rotation and  $[x_{bf} y_{bf} z_{bf}]^T$  after rotation. For  $\phi = \pi/2$ ,  $[x_{bf} y_{bf} z_{bf}] = [-z_{b0} y_{b0} x_{b0}]$ . Applying the requirement (25) to the initial and final  $x$ -components we obtain

$$\pi/2 \text{ pitch: } -x_{b0} \geq \cos \theta_{\text{cone}} \quad (27a)$$

$$z_{b0} \geq \cos \theta_{\text{cone}} \quad (27b)$$

If the initial ground vector satisfies these conditions, it will remain in communication before, during, and after a  $90$  deg pitch rotation. For  $\phi = -\pi/2$  rotation the requirement (25) leads to

$$-\pi/2 \text{ pitch: } z_{b0} \leq -\cos \theta_{\text{cone}} \quad (28)$$

From (27) and (28) we conclude that, if the ground is in link with the vehicle before rotation, a  $\pi/2$  y-rotation is to be chosen if  $z_{b0}$  satisfies the condition (27b), and a  $-\pi/2$  y-rotation if  $z_{b0}$  satisfies the condition (28). If neither condition is satisfied, a rotation about  $z_b$  axis, considered next, is then resorted to. Imposing the requirement (25) on  $x_b$  for  $\phi = 0$  and  $\pm \pi/2$  angle of rotation about  $z_b$ -axis, the following conditions emerge for maintaining communication before and after rotation

$$\text{initially: } -x_{b0} \geq \cos \theta_{\text{cone}} \quad (29)$$

$$\pi/2 \text{ yaw: } -y_{b0} \geq \cos \theta_{\text{cone}} \quad (30)$$

$$-\pi/2 \text{ yaw: } y_{b0} \geq \cos \theta_{\text{cone}} \quad (31)$$

We infer from (30) that if  $y_{b0}$  component of the initial ground unit vector meets this condition, then a  $\pi/2$  rotation about  $z_b$ -axis is to be commanded whereas if it satisfies the condition (31), a  $-\pi/2$  rotation about  $z_b$ -axis is to be commanded.

Figure 6 illustrates the four constraints (27b), (28), (30) and (31) on the initial location of the ground station projection in the communication cone of -x antenna. If the ground station is located such that either  $|y_{b0}| \geq c\theta_{\text{cone}}$  or  $|z_{b0}| \geq c\theta_{\text{cone}}$ , the communication will be preserved after a suitably chosen, as determined above,  $\pm 90$  deg rotation about  $y_b$  or  $z_b$ -axis of the vehicle. This is shown in Figure 6 by the four directions of travel of the ground station from its initial to final location within the cone. Also, these four constraints imply that if the initial ground unit vector is located such that  $|y_{b0}| < c\theta_{\text{cone}}$  and  $|z_{b0}| < c\theta_{\text{cone}}$  – the unshaded square concentric with the cone

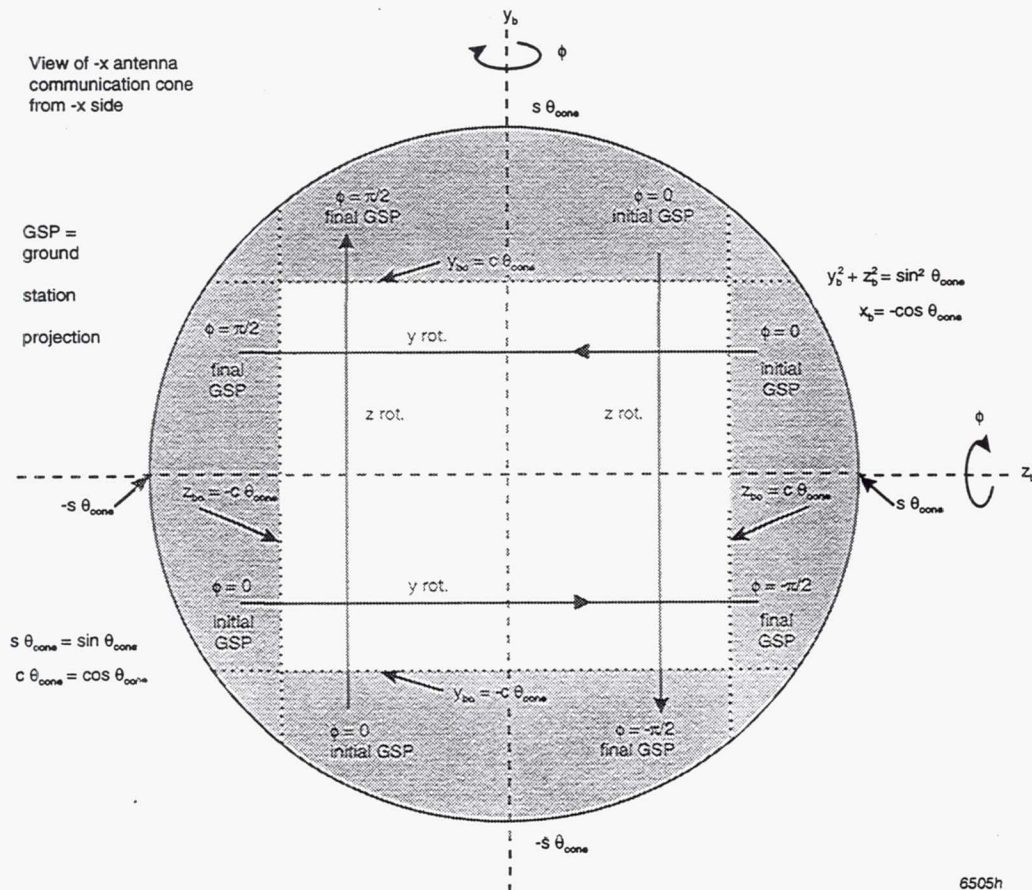


Figure 6 Regions of Ground Station Projection for Maintaining Communication With -x Antenna in a  $\pm 90$  Deg Pitch or Yaw Maneuver



circle, the communication *might* be broken after a pitch or yaw 90 deg maneuver. The word *might* is sharpened below.

### Forbidden Region of Ground Station Projection in the Communication Cone of -x Antenna

If the ground station is initially within the cone and if  $|y_{b0}| < c\theta_{\text{cone}}$  and  $|z_{b0}| < c\theta_{\text{cone}}$  (Figure 6), a 90 deg maneuver about pitch or yaw will drive it outside the cone. Communication may still be restorable by a roll motion *before* the pitch or yaw maneuver if the components  $y_{b0}$ ,  $z_{b0}$  are such that this preroll motion brings the ground station within any of the four segments  $|y_{b0}| > c\theta_{\text{cone}}$  and  $|z_{b0}| > c\theta_{\text{cone}}$ , that is, if  $(y_{b0}, z_{b0})$  point lies on a concentric circle of radius greater than  $c\theta_{\text{cone}}$ . Figure 7 identifies these regions in shade. To formulate them, note that the square region  $|y_{b0}| = c\theta_{\text{cone}}$  and  $|z_{b0}| = c\theta_{\text{cone}}$  in Figures 6 and 7 circumscribe a circle of radius  $c\theta_{\text{cone}}$  governed by  $y_b^2 + z_b^2 = c^2 \theta_{\text{cone}}$ , equivalent to  $x_b = -\sin \theta_{\text{cone}}$  ( $x_b < 0$  so that the ground station is within -x antenna). If the ground station is initially within this circle

$$y_{b0}^2 + z_{b0}^2 < c^2 \theta_{\text{cone}} \quad \text{or} \quad -x_{b0} > \sin \theta_{\text{cone}} \quad (\text{forbidden region}) \quad (32)$$

a roll motion can never bring the ground station to the region  $|y_b| > c\theta_{\text{cone}}$  or  $|z_b| > c\theta_{\text{cone}}$  and hence the communication will not be restorable. The ground station, therefore, must not be initially in this forbidden region. In terms of the angle  $\phi_{-x}$ , the forbidden circle (32) can be rewritten as

$$\cos \phi_{-x} > \sin \theta_{\text{cone}} \quad (\text{forbidden region}) \quad (33)$$

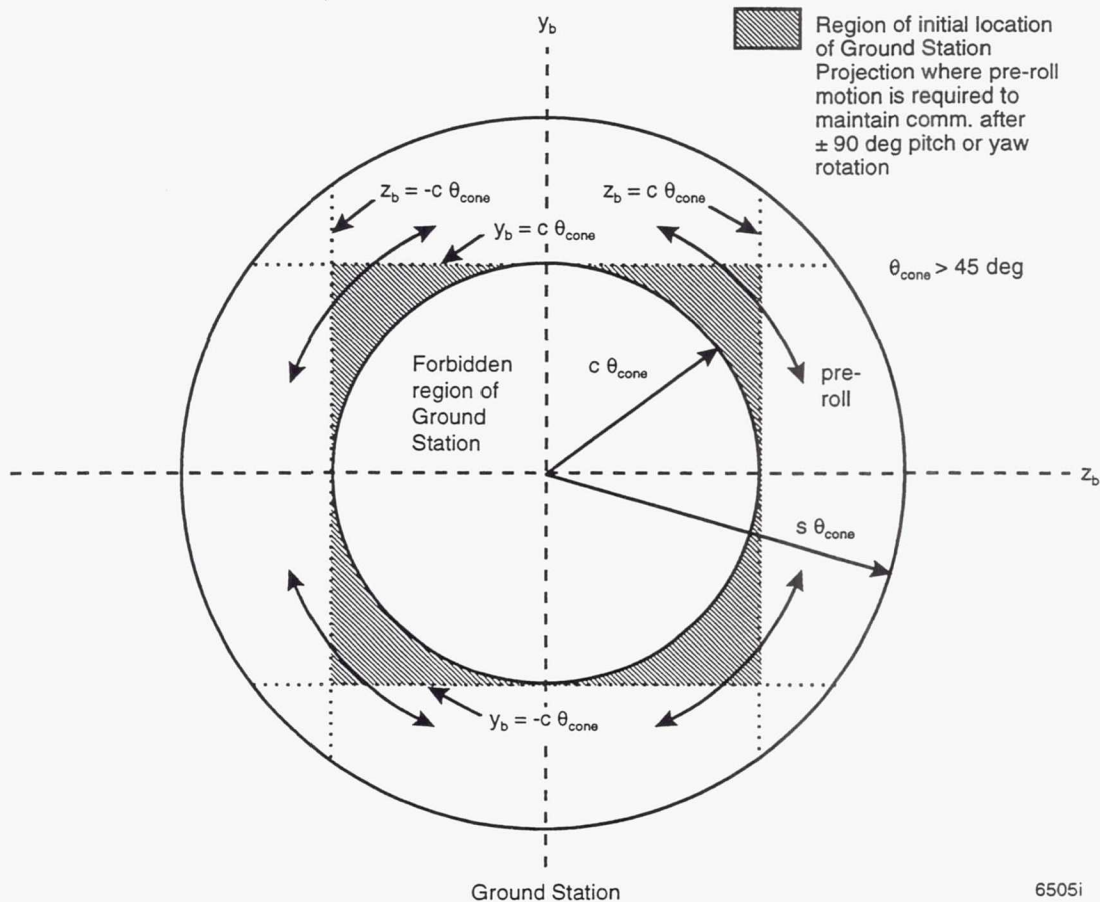


Figure 7 Forbidden Region of Ground Station and the Regions Where a Pre-Roll Motion Aids in Communication of -x Antenna After a  $\pm 90$  Deg Pitch or Yaw Rotation

For example, for  $\theta_{\text{cone}} = 60$  deg, the ground station at  $\phi_x < 30$  deg will be in the forbidden region for an imminent 90 deg maneuver. This result appears obviously correct since if  $\phi_x < 30$  deg, a 90 deg maneuver in the opposite direction of the initial  $\phi_x$  will lead to a final  $\phi_x > (90 - 30) = 60$  deg, outside the cone. We are thus led to the conclusion that if the ground station is initially within the shaded region of the cone shown in Figure 7, a pre-roll motion will maintain communication even after the pitch/yaw maneuver.

Regarding the magnitude and direction of this pre-roll angle, denoted  $\beta$ , we first require that its magnitude be minimum. To achieve this, intuition suggests that if  $|y_{b0}| < |z_{b0}|$ , then  $\beta$  rotation should decrease  $|y_{b0}|$  to zero. Likewise, if  $|z_{b0}| < |y_{b0}|$ , then  $\beta$  rotation should render  $|z_{b0}|$  to zero. This rule keeps  $|\beta| \leq 45$  deg. Following this rule, we arrive at

$$\begin{aligned} \text{if } |y_{b0}| < |z_{b0}|: \beta &= \tan^{-1}(-y_{b0}/z_{b0}) \Rightarrow y_b = 0 \\ \text{if } |z_{b0}| \leq |y_{b0}|: \beta &= \tan^{-1}(z_{b0}/y_{b0}) \Rightarrow z_b = 0 \end{aligned} \quad (34)$$

Thus, the vehicle is rolled by the angle (34) first and then it performs the multi-axis slew motion  $(\alpha, \epsilon)$ . One may, of course, use an equivalent single rotation instead just as well.

## V. COMPATIBILITY OF EXCLUSION MOTION WITH COMMUNICATION CONSTRAINT

Figure 8 illustrates a large rotation  $\alpha$  of the vehicle about  $z'_b$  axis inclined at an angle  $\gamma$  (Figure 3) from  $z_b$ -axis. Because of positive rotation, the ground station, which is on  $-x_b$  side so as to communicate with the  $-x$  antenna, moves relatively in a direction parallel to  $+y'_b$ -axis. On the other hand, the sensor axis  $x_b$  moves such that a bright object disc appears to move in the  $-y'_b$  direction. Then, if the disc parameters are such that  $\epsilon_{\text{spec}} > |\epsilon^*|$  (as in Figure 8), the sensor axis  $x_b$  crosses the disc while turning about  $z'_b$  axis. To avoid this crossing, the vehicle is rotated by  $\epsilon$  about the  $\alpha$ -displaced  $y'_b$ -axis. Since the sensor can pass the bright object tangentially from either side of the disc (points A and B in Figure 8 and as illustrated in Figures 1a-b), our objective now is to determine which of the two choices is consistent with the requirement of keeping the ground station within the comm. cone, because we observe in Figure 8 that the  $\epsilon$ -rotation moves the ground station either closer to the cone axis or away from it and possibly out of the cone, depending on the sign ( $\epsilon$ ).

From the sequence of transformations in Figure 3 (not considering the roll angle  $\beta$  for  $\pm z$  and  $y$  antenna) we obtain

$$x_b = x_{b0} \cos \alpha + y_{b0} (\cos \alpha \cos \gamma + \sin \alpha \sin \gamma) + z_{b0} (\cos \alpha \sin \gamma - \sin \alpha \cos \gamma) = -\cos \phi_x \quad (35)$$

where, as before,  $x_{b0}$ ,  $y_{b0}$ ,  $z_{b0}$  are the components of the initial ground unit vector. To determine  $\epsilon$  that decreases  $\phi_x$  ( $\partial \phi_x < 0$ ), so that the ground station moves towards the cone axis, differentiate Eq. (37) with respect to  $\epsilon$  and evaluate the derivative at  $\epsilon = 0$ . We then arrive at

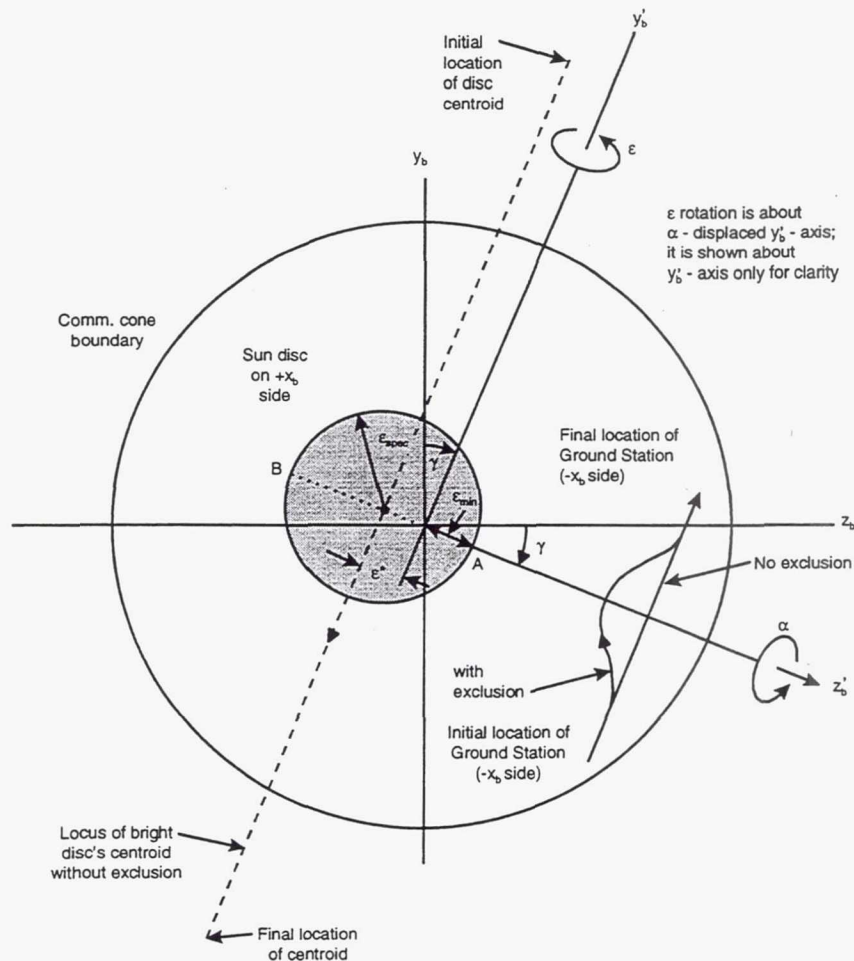
$$\left. \frac{\partial \phi_x}{\partial \epsilon} \right|_{\epsilon=0} = - \frac{z'_{b0}}{\sin \phi_{-x}} \quad (36)$$

where  $z'_{b0}$  is the component of the ground station unit vector along the axis of rotation  $z_{b0}$  before the rotation. The slope is evaluated at  $\epsilon = 0$  because we intend to decrease  $\phi_x$  relative to its ideal value corresponding to  $\epsilon = 0$  for complete range of  $\epsilon$  including its zero initial value. Initially, since  $0 \leq \phi_x \leq \theta_{\text{cone}} < \pi/2$ ,  $\sin \phi_x \geq 0$  and therefore the requirement  $\partial \phi_x < 0$  leads to the condition  $z'_{b0} \partial \epsilon > 0$ , which gives the following rule for selecting the sign of exclusion motion

$$\text{sign}(z'_{b0}) = \text{sign}(\epsilon) \quad (37)$$

Also note that if the exclusion motion is not required at all (that is,  $\epsilon = 0$  for complete range of maneuver  $\alpha$ ),  $z'_{b0}$  will not be changed by  $\alpha$  because  $\alpha$  is the angle of rotation about  $z'_{b0}$ . Finally, we note that the condition (37) is invoked just once to determine the sign of  $\epsilon$  for a given bright object provided  $|z'_{b0}|$  is greater than some small number, say, 0.1, below which the ground station is assumed to be already so close to the cone axis that  $\epsilon$  motion of either sign would not push it outside the cone.

As an illustration, apply the condition (37) to a situation depicted in Figure 8 where  $z'_{b0} > 0$ , implying that  $\epsilon > 0$ . Notice that according to the sign convention of counterclockwise positive,  $\epsilon^*$  is positive in Figure 8 and therefore the avoidance angle  $\epsilon$  for this bright disc must be  $\epsilon = \epsilon^* + \epsilon_{\text{spec}} > 0$ . If the comm. constraint were absent, the minimum avoidance angle  $\epsilon_{\text{min}} = -\epsilon_{\text{spec}} + \epsilon^* < 0$  would have sufficed. The influence of comm. constraint on the exclusion motion is thus apparent.



6505j

**Figure 8** Motion of Ground Station in the Communication Cone of -x Antenna and the Motion of a Bright Object Relative to the Sensor Along +x Side of the Vehicle



## VI. ANGULAR RATE COMMANDS FOR LARGE ANGLE MANEUVERS

When the vehicle is commanded to perform at once the ideal slew  $\alpha$ , the exclusion motion  $\epsilon$ , and the roll motion  $\beta$  for maintaining communication with  $\pm z$  and  $-y$  antennae, according to the transformations shown in Figure 3, the associated rate commands in the instantaneous, commanded body frame are found to be:

$$\omega_{c1} = -\dot{\alpha} \sin \epsilon + \dot{\beta} \quad (38a)$$

$$\omega_{c2} = \dot{\alpha} \cos \epsilon \sin (\beta - \gamma) + \dot{\epsilon} \cos (\beta - \gamma) \quad (38n)$$

$$\omega_{c3} = \dot{\alpha} \cos \epsilon \cos (\beta - \gamma) - \dot{\epsilon} \sin (\beta - \gamma) \quad (38c)$$

If the vehicle is commanded to pre-roll to maintain communication of  $-x$  antenna (without  $\alpha$  and  $\epsilon$  rotations), the commanded rate of rotations will then be:  $\omega_{c1} = \dot{\beta}$  and  $\omega_{c2} = 0 = \omega_{c3}$ .

## VII. ILLUSTRATIONS

While developing the preceding exclusion-communication algorithm, it was applied to innumerable scenarios, from simplest to most complex, including a Monte Carlo simulation in which the sun was located randomly in a celestial sphere, equivalent to specifying an arbitrary initial attitude of the vehicle. In the following, we present one of the worst-case stressing scenarios simulated. Consider a vehicle in a near-Earth ballistic trajectory (Figure 9). En route it performs five different large-angle maneuvers, avoiding Sun, Moon, and Earth and maintaining communication with the ground station. Figures 10a-h illustrate these maneuvers, the associated commands, avoidance of bright objects, and maintenance of communication. Sun and Moon locations are hypothetical. The moon's phases are ignored and it is considered to be full bright regardless of its location relative to the Sun. This assumption is not tenable but it allows us to illustrate the versatility of the algorithm. The centroids of Sun and Moon are placed at  $\alpha^* = 20$  deg,  $\epsilon^* = 5$  deg, and  $\alpha^* = 30$  deg,  $\epsilon^* = -10$  deg, respectively, relative to each slew plane. Forbidden angular radius  $\epsilon_{\text{spec}}$  around each bright object is taken to be 15 deg and therefore the minimum exclusion angle is -10 deg for Sun and 5 deg for Moon. Each large-angle maneuver is followed by a tracking or attitude hold phase for a short duration. The maneuvers are: (1) a 180 deg pitch, after separation from the launch vehicle, to point the sensor in the expected direction of a target; (2) a 90 deg yaw to align a particular thruster in the line-of-sight direction; (3) a 90 deg pitch/yaw to align the sensor with a star, Star-1, for gyro calibration; (4) a perpendicular 75 deg pitch/yaw to view another star, Star-2; and, finally, (5) a 45 deg pitch/yaw to point the boresight in a desired direction. Figure 10 illustrates the avoidance of Sun and Moon in  $\alpha$ - $\epsilon$  plane. Two special features of this example are: (1) the two bright discs overlap so much that they cover each other's  $\epsilon_{\text{min}}$  tangent point at respective  $\alpha^*$ ; and (2) the first object is so close to the initial orientation of the sensor ( $\alpha^* = 20$  deg whereas  $\epsilon_{\text{spec}} = 15$  deg) that the versine  $\epsilon$  profile enters this disc. As such, and also because of the communication requirements, the modified centroidal exclusion angles  $\epsilon$  in Figure 10 for both  $\alpha^* = 20$  and 30 deg, for every maneuver, are not equal to their minimum values. Furthermore, because the versine  $\epsilon$  profile for the maneuvers 2 and 5 enter the first bright disc for some range of  $\alpha < \alpha^*$ , the versine profile is replaced by the bright disc perimeter where necessary, so the sensor glides around the disc. The time-fuel optimal profiles of  $\alpha$ , and corresponding  $\epsilon(\alpha)$  profiles partly versine and partly along the disc perimeter, versus time are illustrated in Figure 11. The unnumbered 90 deg maneuver is a roll motion to select a particular thruster. The angle  $\phi$  in this figure is single-axis equivalent of  $(\alpha, \epsilon)$ . The slew rates  $\dot{\alpha}$  and  $\dot{\epsilon}$  are displayed in Figure 12,  $\dot{\alpha}$  as a time/fuel optimal profile and  $\dot{\epsilon} = \dot{\alpha} \, d\epsilon/d\alpha$ . The point where a versine profile enters the disc and the motion around the disc perimeter introduce rapid variation in  $d\epsilon/d\alpha$  and hence in  $\dot{\epsilon}$ . Figure 13 portrays communication maintenance of  $-x$  antenna. It shows a 60 deg circular boundary of the conical beam and a 30 deg boundary of the forbidden region of the ground station, as earlier in Figure 6. Prior to 180 deg pitch rotation,  $-z$  antenna is in link with the ground station and  $-x$  antenna is not. After the rotation, the communication of  $-x$  antenna is established and that of

-z antenna is relinquished. This is evident in Figure 13 by the ground station unit vector's entry of the -x antenna cone. From then on, the ground station trace remains within the conical beam during all maneuvers.

In the absence of exclusion motion, a pitch/yaw rotation causes the ground station trace in the yz plane of the vehicle to move in a straight line, and a roll motion produces a circular arc trace. With the perpendicular exclusion motion, the ground station trace becomes sinuous. This was implied in Figures 6 and 8 and now illustrated in Figure 13. The requirement of communication maintenance imposes  $\varepsilon < 0$  for acquiring the stars and  $\varepsilon > 0$  to point the boresight in the final desired direction. As a result, the corresponding straight traces have wriggled toward the beam center in Figure 13. On the other hand, the signs of  $\varepsilon$  for a 180 deg pitch and a 90 deg yaw (the maneuvers 1 and 2) are not influenced by this requirement because the corresponding traces start from  $y_b = 0$  and  $z_b = 0$ , respectively.

The commanded motions just illustrated are multi-axis, formulated in terms of three large angles: slew angle, exclusion angle, and roll angle for communication, giving rise to a time-varying commanded transformation matrix for the flight controller to follow. For this purpose, singularity-free quaternion commands are derived from the transformation matrix. These commands, relative to J2000 frame, not the vehicle frame immediately before a maneuver which would have enabled us to identify roll, pitch and yaw motions, are shown in Figure 14. The corresponding three angular rate commands in the commanded body frame are shown in Figure 15. To maneuver the vehicle, the quaternion and rate commands are inputted to a three-axis attitude controller such as one for Hubble Space Telescope<sup>5</sup> or interplanetary spacecraft Viking<sup>6</sup> using thrusters and phase plane control logic.

## VIII. CONCLUDING REMARKS

The exclusion-communication algorithm developed in the preceding is accompanied with the sun and moon ephemerides, time-varying inertial location of the ground station, trajectory of the vehicle and the desired direction of its boresight in J2000 frame, initial inertial attitude of the vehicle, etc. The resulting time-varying attitude commands are multi-axis, effecting a desired slew of a vehicle sensor from one direction to other, swerving the sensor away from a hot source if it is in the way, and rolling the vehicle to maintain communication of the antennae with the ground. Because of versatility of the algorithm, the flight software to generate the attitude and rate commands for all phases of flight is likely to be long. It can be shortened somewhat, though, by combining the pre-roll motion for communication maintenance of -x antenna with the ensuing slew and exclusion motion, effecting an equivalent rotation; by considering only one bright object (Sun) instead of Sun, Moon, and Earth; and by enlarging the forbidden perimeter of the bright disc and not insisting on sliding along the perimeter in case the boresight enters the outer annular region of the enlarged disc. Whereas this abridged version of the algorithm may be accommodated on a flight computer, the original version may be used for mission planning on ground.

## ACKNOWLEDGMENTS

Technical discussions with D. Pearson, M. Rivera, M. Nakano, and C. Robson, lending considerable insight into the exclusion-communication problem investigated here, are gratefully acknowledged. The step command approach sketched in Introduction is credited to B. Nguyen.



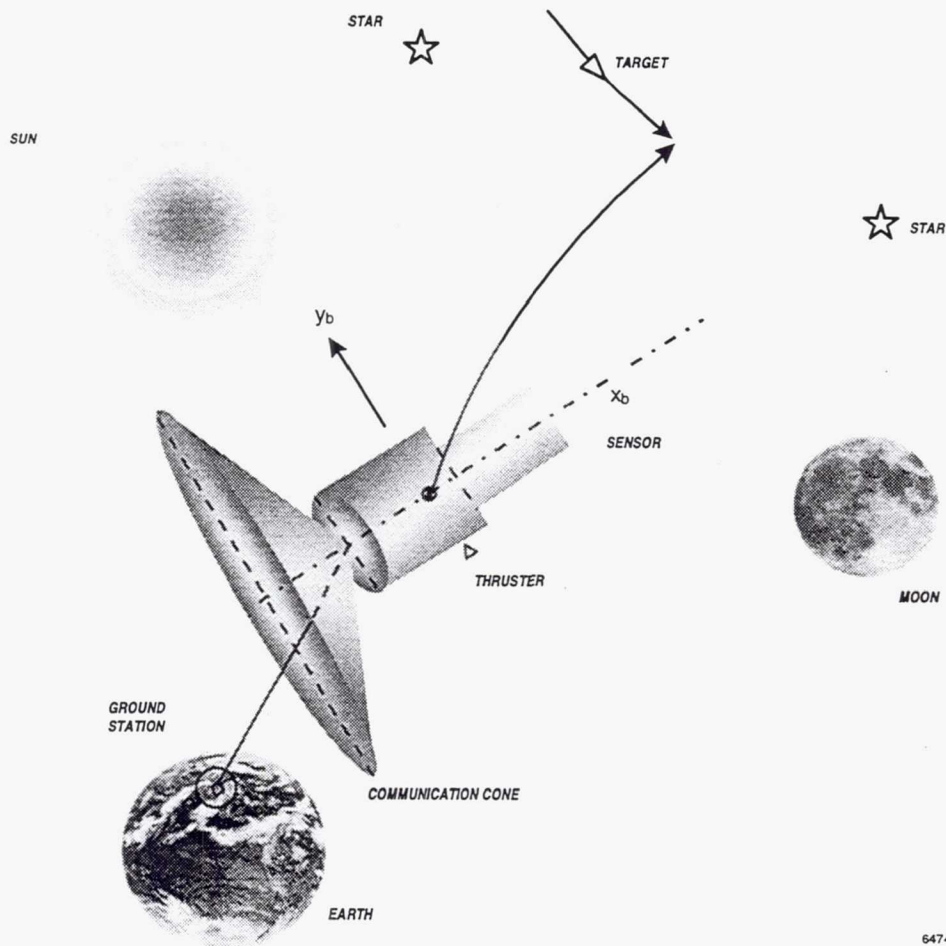


Figure 9 A Vehicle to Be Maneuvered, Avoiding Sun, Moon and Earth, Maintaining Communication With Ground Station

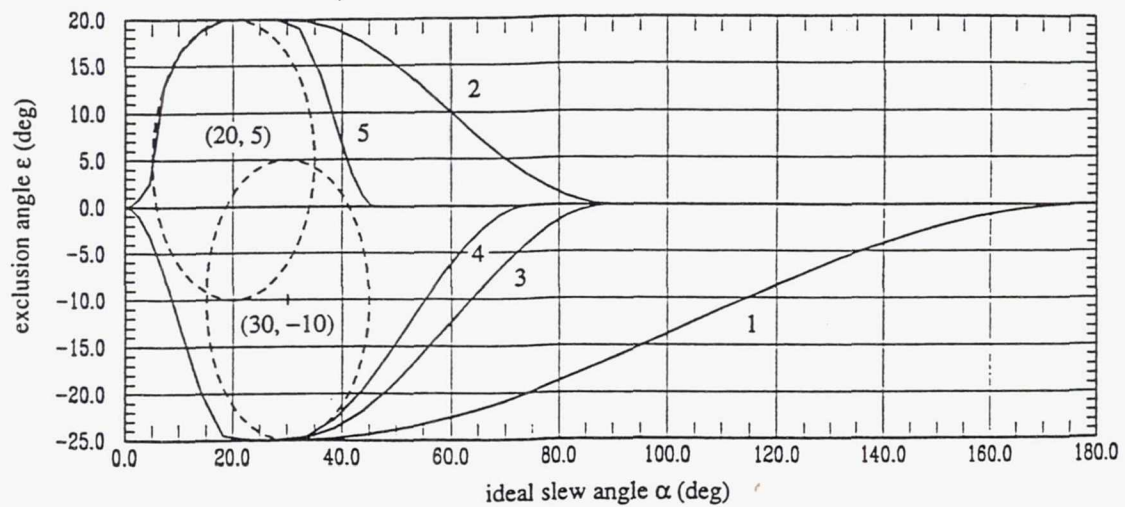


Figure 10 Avoidance of Overlapping Sun and Moon in a Multislew Scenario: Diverted Slew Paths



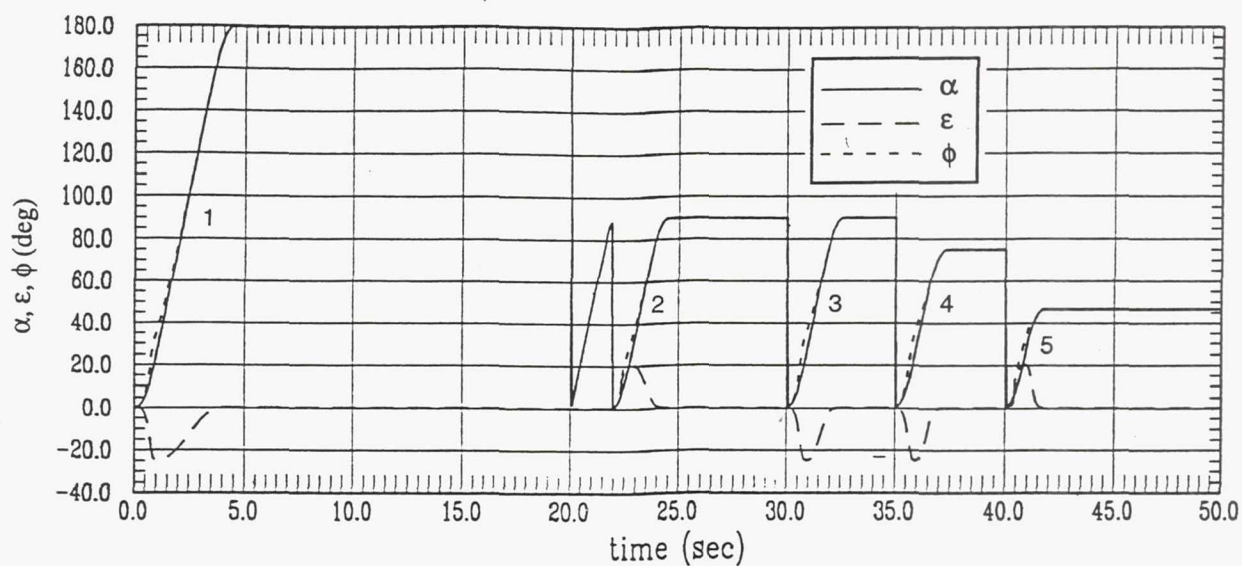


Figure 11 Ideal Slew Angle  $\alpha$ , Exclusion Angle  $\epsilon$ , and Equivalent Single-Axis Rotation Angle  $\phi$  vs. Time

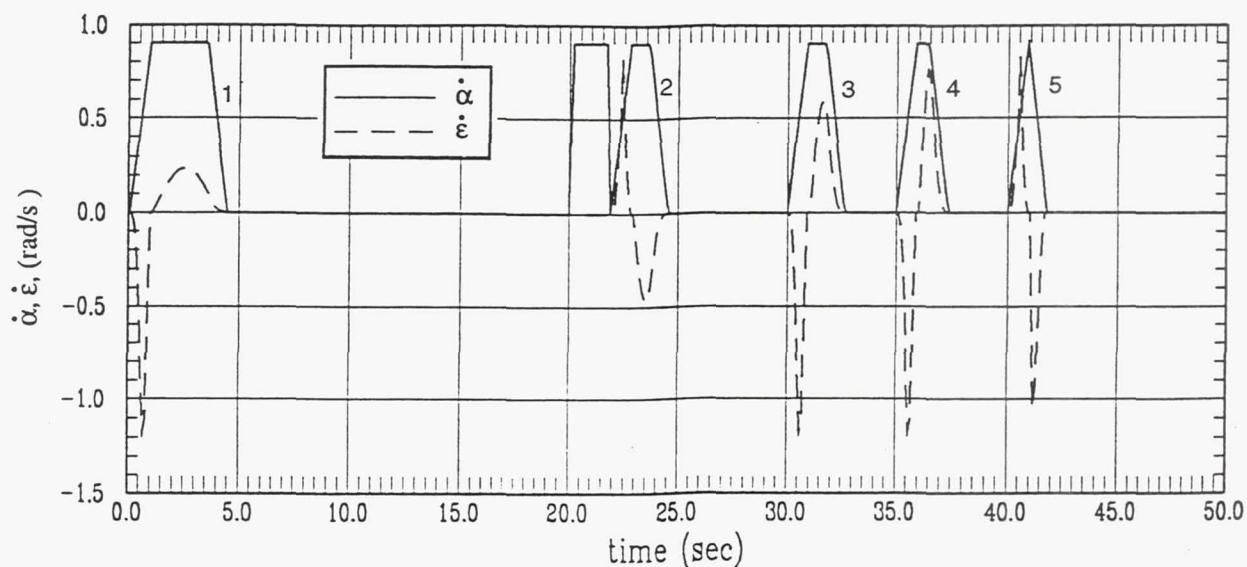


Figure 12 Ideal Slew Rate  $\dot{\alpha}$  and Exclusion Rate  $\dot{\epsilon}$  vs. Time

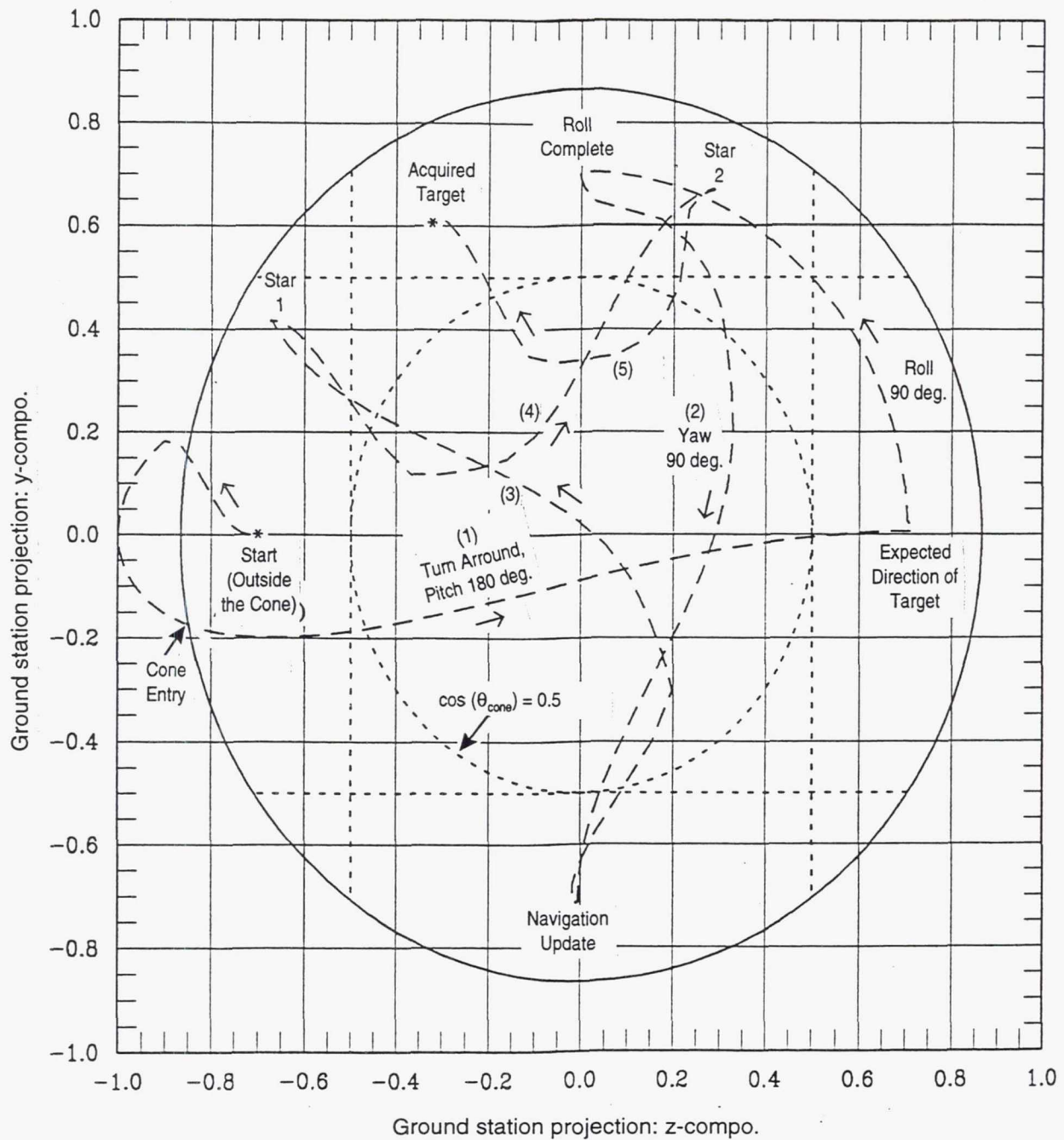


Figure 13 Motion of Ground Station Projection in the Communication Cone of -x Antenna During Large Angle Maneuvers and Small Angle Tracking: y-Compo. vs. z-Compo.

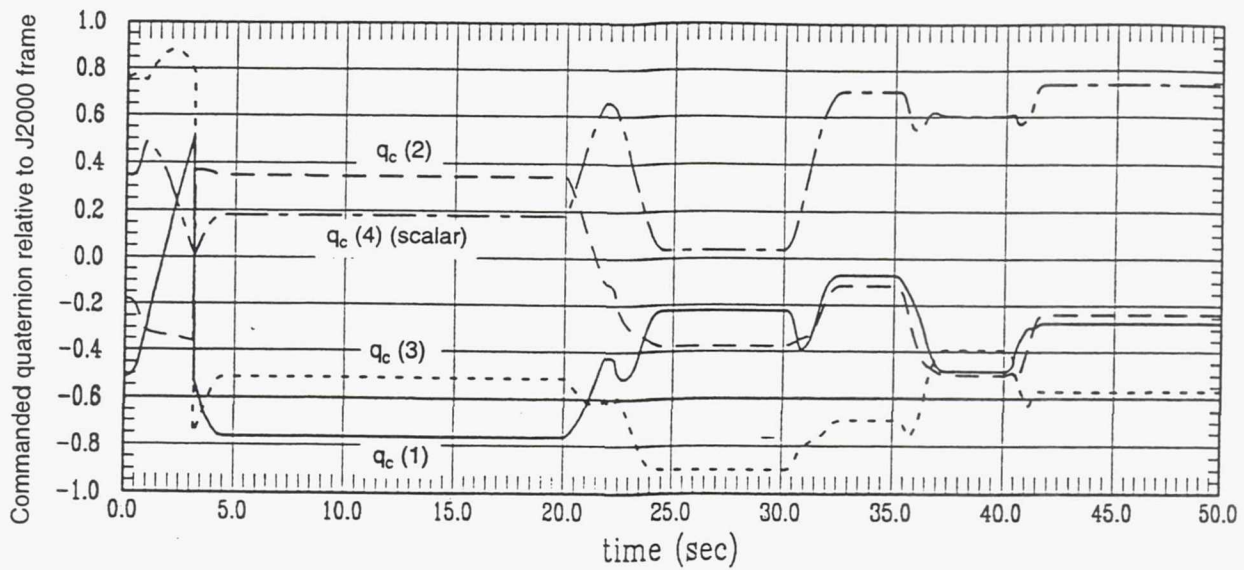


Figure 14 Commanded Quaternion Relative to J2000 Frame vs. Time

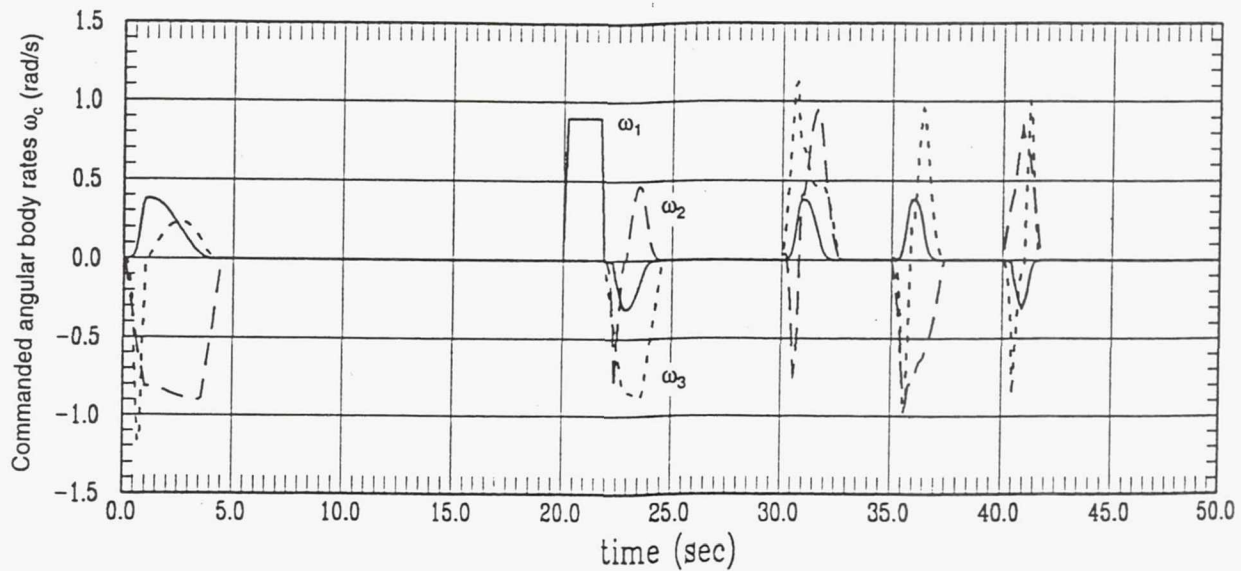


Figure 15 Commanded Angular Body Rate vs. Time



## REFERENCES

1. Hablani, H. B., "Spacecraft Slews Avoiding Celestial Objects and Maintaining Communication with Ground Station," NASA CP-3345, *Proceedings of Flight Mechanics Symposium*, May 1997, pp. 61-76.
2. Singh, G., Macala, G., Wong, E., and Rasmussen, R., "A Constraint Monitor Algorithm for the Cassini Spacecraft," *AIAA Guidance, Navigation, and Control Conference*, August 1997, New Orleans, LA.
3. Frakes, J. P., et al., "SAMPEX Science Pointing With Velocity Avoidance," *AAS Paper 92-182, AAS/AIAA Spaceflight Mechanics Meeting, Colorado Springs, CO*, February 1992.
4. Rivera, M., "Fixed Rotation Axis Slew Maneuvers With Attitude Avoidance," *AIAA Guidance, Navigation and Control Conference*, Boston, MA, August 1998, under review.
5. Glaese, J. R., et al., "Low-Cost Space Telescope Pointing Control System," *J. Spacecraft and Rockets*, Vol. 13, No. 7, July 1976, pp. 400-405.
6. Holmberg, N. A., Faust, R. P., and Holt, H. M., *Viking '75 Spacecraft Design and Summary, Vol. 1—Lander Design*, NASA Reference Publication 1027, 1980.

# MAGNETIC TORQUE ATTITUDE CONTROL OF AN EXPERIMENTAL MICROSATELLITE IN EQUATORIAL ORBIT

D. Vera<sup>1</sup>, V. Alexandrov<sup>2</sup>, A. Rangel<sup>3</sup>,  
A. Pedroza<sup>4</sup>, D. Mocencahua<sup>5</sup>, R. Fournier<sup>6</sup>

In this work a stabilization algorithm is presented for the mexican microsatellite SATEX-1 which will be placed in equatorial orbit. Passive control will be by means of a gravitational gradient boom; while active control will be accomplished with five magnetic torques of 4 Am<sup>2</sup>. Euler equations for small deviations with respect to the principal axes were used. Related to each of these axes, the magnetic torque produced by the interaction of the magnetic torques with the earth's magnetic field was computed. Whithin the framework of State Space Theory, a theorem is set forth, which allows a transformation of the sensor equations to analytical expressions that are not time-dependent, although it is required to expand the dynamical systems dimensions from 6 to 12 state variables. Under these conditions observability is verified, and controllers for microsatellite stabilization are proposed.

## INTRODUCTION

The SATEX-1 microsatellite has the followings general charecteristics: dimensions of 45x45x45 cm<sup>3</sup>, a 6.3m boom with a mass-top of 2.7 Kg, and a weight of 45 Kg. Its moments of inertia with an undeployed boom are:  $I_{xx}=1.22\text{Kg}\cdot\text{m}^2$ ,  $I_{xy}=0.204\text{Kg}\cdot\text{m}^2$ ,  $I_{xz}=0.224\text{Kg}\cdot\text{m}^2$ ,  $I_{yy}=1.22\text{Kg}\cdot\text{m}^2$ ,  $I_{yz}=2.20\text{Kg}\cdot\text{m}^2$  and  $I_{zz}=1.35\text{Kg}\cdot\text{m}^2$ . The moments of inertia with a deployed boom are:  $I_1=62.296\text{Kg}\cdot\text{m}^2$ ,  $I_2=62.736\text{Kg}\cdot\text{m}^2$ , and  $I_3=1.318\text{Kg}\cdot\text{m}^2$ . The boom deployment conditions require that the angular velocities for the pitch and yaw axes be less than 0.2 rpm.

In this study we considerer the microsatellite to be placed in an equatorial orbit at an altitude of 800km. When the boom is correctly deployed, the optical payload points towards earth, and boom oscillations have an amplitude of approximately 12°. The problem presented here is to reduce the angular oscillations to 3°, by means of active control by magnetic torques with an air core and a magnetic moment of approximately 2-4 Am<sup>2</sup>.

<sup>1</sup> Departamento de Microelectrónica, Posgrado de Matemáticas de la Facultad de Ciencias Físico Matemáticas, ICUAP, BUAP. 4 sur 104, centro 72000 Puebla, Pue. Tel 44-39-39, Fax 44-34-66.

<sup>2,5</sup> Posgrado de Matemáticas de la Facultad de Ciencias Físico Matemáticas, BUAP.

<sup>3</sup> Posgrado de la Facultad de Ciencias de la Computación, BUAP.

<sup>4,6</sup> Departamento de Microelectrónica, ICUAP, BUAP.

## EULER ATTITUDE EQUATIONS

Starting with Euler attitude equations that describe the attitude in a circular orbit considering the gravitational gradient <sup>1</sup>

$$\begin{cases} I_1 \ddot{\alpha}_1 + (I_3 + I_1 - I_2) \omega_c \dot{\alpha}_3 + (I_2 - I_3) \omega_c^2 \alpha_1 = g_{1m} \\ I_2 \ddot{\alpha}_2 = g_{2m} \\ I_3 \ddot{\alpha}_3 - (I_3 + I_1 - I_2) \omega_c \dot{\alpha}_1 + (I_2 - I_3) \omega_c^2 \alpha_3 = g_{3m} \end{cases}$$

where  $\alpha_1, \alpha_2, \alpha_3$  are the angular deviations respect to the principal axes  $P_1, P_2, P_3$  and  $\omega_c = 0.001^\circ/\text{seg}$ , is the orbital frequency of the microsatellite.

The magnetic torques which are generated by the interaction of the magnetic moment of the torques with earth's magnetic field is given by the following expressions:  $g_{1m} = -(1/\sqrt{2}) P_{p,X+Y} B_{ZG} + (1/\sqrt{2}) P_{Zm} B_{G+}$ ,  $g_{2m} = -(1/\sqrt{2}) P_{p,Y-X} B_{ZG} - (1/\sqrt{2}) P_{Zm} B_{G-}$ , and  $g_{3m} = (1/2) P_{p,Y-X} B_{G+} + (1/2) P_{p,X+Y} B_{G-}$ , where  $P_{p,X+Y}$  and  $P_{p,Y-X}$  are functions of the magnetic moments  $P_{Zm+}, P_{Ym+}, P_{Ym-}, P_{Xm+}, P_{Xm-}$ , generated by the five coils whose normal is in the  $Z_+, Y_+, Y_-, X_+, X_-$  directions respect to the center of mass reference frame. These magnetic moments have the following expressions:  $P_{p,X+Y} = P_{Ym+} - P_{Ym-} + P_{Xm+} - P_{Xm-}$ ,  $P_{p,Y-X} = P_{Ym+} - P_{Ym-} - P_{Xm+} + P_{Xm-}$ , with  $|P_{Xm+}| = |P_{Xm-}| = |P_{Ym+}| = |P_{Ym-}| = 2\text{Am}^2$  and  $|P_{Zm+}| = 4\text{Am}^2$ . Also,  $B_{G+}, B_{G-}$  are functions of the geomagnetic field components  $B_{XG}, B_{YG}, B_{ZG}$  corresponding to the IGRF<sup>2</sup> geomagnetic field model. Its expressions are:  $B_{G+} = B_{YG} - B_{XG} = (-1.4067 \sin \lambda - 4.00007 \cos \lambda + 21.11468) \times 10^{-6} \text{T}$ ,  $B_{G-} = B_{YG} + B_{XG} = (-1.4067 \sin \lambda - 4.00007 \cos \lambda - 21.11468) \times 10^{-6} \text{T}$ , and  $B_{ZG} = (-8.00014 \sin \lambda - 2.81351 \cos \lambda) \times 10^{-6} \text{T}$ , where  $\lambda = \omega_c t$  is the phase of the orbital motion. The torque produced by the magnetic moment of the coils is many times stronger than the environmental torque to which the satellite is subjected<sup>3</sup>.

## MAGNETIC SENSORS

The magnetic sensor equations were obtained from the magnetic field component expressions referenced to the principal axes, to which are applied an infinitesimal oscillation  $[\alpha_1, \alpha_2, \alpha_3]^T$ <sup>4</sup>. The expressions for the deviations of the magnetic sensors are:  $\Delta Z_1(\lambda) = (0.99473 \sin \lambda + 2.82848 \cos \lambda) \alpha_3 \times 10^{-6} \text{T} - (8.00014 \sin \lambda + 2.81351 \cos \lambda) \alpha_2 \times 10^{-6} \text{T}$ ,  $\Delta Z_2(\lambda) = -(0.99473 \sin \lambda + 2.82848 \cos \lambda) \alpha_3 \times 10^{-6} \text{T} + (8.00014 \sin \lambda + 2.81351 \cos \lambda) \alpha_1 \times 10^{-6} \text{T}$ ,  $\Delta Z_3(\lambda) = (0.99473 \sin \lambda + 2.82848 \cos \lambda) \alpha_2 \times 10^{-6} \text{T} - (0.99473 \sin \lambda + 2.82848 \cos \lambda) \alpha_1 \times 10^{-6} \text{T}$ .

## STABILIZATION

The dynamical system representing the microsatellite is given by the following set of differential equations

$$\begin{cases} \dot{X} = G_0 X + g \\ X_1(0) = X_3(0) = X_5(0) = 12^\circ \\ X_2(0) = X_4(0) = X_6(0) = 0.00461^\circ / \text{seg} \end{cases}$$



where

$$G_0 = \begin{pmatrix} 0 & 1 & 0 & 0 & 0 & 0 \\ -3.94362 & 0 & 0 & 0 & 0 & 14.094 \\ 0 & 0 & 0 & 1 & 0 & 0 \\ 0 & 0 & -2.91592 & 0 & 0 & 0 \\ 0 & 0 & 0 & 0 & 0 & 1 \\ 0 & -666.16085 & 0 & 0 & -0.33384 & 0 \end{pmatrix}$$

$X=[X_1, X_2, X_3, X_4, X_5, X_6]^T$ ,  $g=[0, T_{1m}u_1, 0, T_{2m}u_2, 0, T_{3m}u_3]^T$  and the magnetic torques for the case when coils are activated in the  $X_{m+}$ ,  $Y_{m+}$ ,  $Z_{m+}$  axes are:  $T_{1m} = 0.331299\sin\lambda + 0.0369362\cos\lambda + 0.4793306$ ,  $T_{2m} = 0.03171\sin\lambda + 0.0901699\cos\lambda + 0.475973$ ,  $T_{3m} = -2.13469\sin\lambda - 6.06991\cos\lambda - 32.04048$ . Control functions  $u_1, u_2, u_3$  will be proposed later. To eliminate the time-dependence in the sensor equations, we use the following theorem: So that the dynamical system  $(dy/dt=Ay+B(t)u, \Delta z=H(t)y)$ , may be transformed to the dynamical system  $(dz/dt=Gz+B_2(t)u, \Delta z=\Gamma y)$ , where  $G$  and  $\Gamma$  are matrices that are not time-dependent, it is necessary and sufficient that the  $H(t)$  matrix be expressed as a linear combination:  $H(t)=\Sigma H_j\alpha_j$ ,  $j=1,\dots,r$ , of constant matrices  $H_j$  and of continuous functions  $\alpha_j$  differentiable and linearly independent, which also are solutions of an ordinary differential equation with constant coefficients<sup>5</sup>.

Applying this last theorem, we obtain a dynamical system with expanded dimensions:

$$\dot{Z} = GZ + g_0, \quad \Delta Z = \Gamma Z$$

with

$$G = \begin{pmatrix} G_0 & -I_{66} \\ I_{66} & G_0 \end{pmatrix}$$

$$G_0 = [0, \cos\lambda T_{1m}u_1, 0, \cos\lambda T_{2m}u_2, 0, \cos\lambda T_{3m}u_3, 0, \sin\lambda T_{1m}u_1, 0, \sin\lambda T_{2m}u_2, 0, \sin\lambda T_{3m}u_3]$$

$$Z = [\cos\lambda X_1, \cos\lambda X_2, \cos\lambda X_3, \cos\lambda X_4, \cos\lambda X_5, \cos\lambda X_6, \sin\lambda X_1, \sin\lambda X_2, \sin\lambda X_3, \sin\lambda X_4, \sin\lambda X_5, \sin\lambda X_6]$$

$$\Gamma = [\Gamma_1, \Gamma_2, \Gamma_3]^T$$

$$\Gamma_1 = [0, 0, -2.81351, 0, 2.82284, 0, 0, 0, -8.00014, 0, 0.99473, 0]$$

$$\Gamma_2 = [2.81351, 0, 0, 0, -2.82848, 0, 8.00014, 0, 0, 0, -0.99473, 0]$$

$$\Gamma_3 = [-2.82848, 0, 2.82848, 0, 0, 0, -0.99473, 0, 0.99473, 0, 0, 0]$$

and  $I_{66}$  is the unitary matrix.

By using known theorems<sup>6</sup> we may verify the observability of the dynamical system calculating the rank of the  $(\Gamma, \Gamma G, \Gamma G^2, \Gamma G^3)$  matrix; with the aid of MATLAB<sup>R</sup> we

obtained a rank of 12. This allows us to construct a set of unbiased and consistent estimators for the dynamical system, and which have the following form:

$$\dot{E} = (G - K\Gamma)E + K\Delta Z + u.$$

The matrix  $(G - K\Gamma)$  has proper values with negative real part; this last is accomplished with an adequate selection of  $K$  using MATLAB<sup>R</sup>. An adequate control for stabilization is proposed as follows:  $u_1 = -\text{sign}(E_2 \cos \lambda T_{1m})$ ,  $u_2 = -\text{sign}(E_4 \cos \lambda T_{2m})$ ,  $u_3 = -\text{sign}(E_{12} \cos \lambda T_{3m})$ . With these estimators we may establish feedback and obtain asymptotic stabilization.

## REFERENCES

1. Hughes, P.C., Spacecraft Attitude Dynamics, John Wiley & Sons, 1986.
2. IGRF, International Geomagnetic Reference Field, 1965, IAGA, commission 2, Working Group 4, Analysis of the Geomagnetic Field, Journal of Geophysical Research, Vol. 74, No 17, August 1979.
3. Larson, W.J., Wertz J.R., Space Mission Analysis and Design, second Ed., Kluwer Academic Pub, 1992.
4. Goldstein, H., Classical Mechanics, Addison-Wesley Pub, 1969.
5. Vera, D., Problemas Matemáticos de Estabilización Magnética de un Satélite Ecuatorial, BUAP, Tesis, 1998.
6. Casti, J.L., Dynamical Systems and their Applications, Linear Theory, Academic Press, N.Y., 1977.

## MAP Stability, Design and Analysis

A. J. Ericsson-Jackson, S. F. Andrews, J. R. O'Donnell, Jr., F. L. Markley  
*NASA Goddard Space Flight Center, Code 570, Greenbelt, MD, 20771*

### Abstract

The Microwave Anisotropy Probe (MAP) is a follow-on to the Differential Microwave Radiometer (DMR) instrument on the Cosmic Background Explorer (COBE) spacecraft. The design and analysis of the MAP attitude control system (ACS) have been refined since work previously reported. The full spacecraft and instrument flexible model was developed in NASTRAN<sup>1</sup>, and the resulting flexible modes were plotted and reduced with the Modal Significance Analysis Package (MSAP).<sup>2</sup> The reduced-order model was used to perform the linear stability analysis for each control mode, the results of which are presented in this paper. Although MAP is going to a relatively disturbance-free Lissajous orbit around the Earth-Sun  $L_2$  Lagrange point, a detailed disturbance-torque analysis is required because there are only a small number of opportunities for momentum unloading each year. Environmental torques, including solar pressure at  $L_2$ , aerodynamic and gravity gradient during phasing-loop orbits, were calculated and simulated. Thruster plume impingement torques that could affect the performance of the thruster modes were estimated and simulated, and a simple model of fuel slosh was derived to model its effect on the motion of the spacecraft. In addition, a thruster mode linear impulse controller was developed to meet the accuracy requirements of the phasing loop burns. A dynamic attitude error limiter was added to improve the performance of the ACS during large attitude slews. The result of this analysis is a stable ACS subsystem that meets all of the mission's requirements.

### INTRODUCTION

The Microwave Anisotropy Probe (MAP), one of the first two Medium-Class Explorer (MIDEX) missions, will measure the anisotropy of the Cosmic Microwave Background (CMB), which is believed to be a remnant of the Big Bang, or Primordial Fireball, marking the birth of the universe.<sup>3</sup> This anisotropy was first measured by the Differential Microwave Radiometer (DMR) instrument on the Cosmic Background Explorer (COBE) satellite.<sup>4-6</sup> MAP has been designed to measure the spectrum and spatial distribution of the CMB with sensitivity 50 times that of the DMR and angular resolution 20 times finer, specifically  $0.3^\circ$  or 18 arc-minutes. These increases in sensitivity and resolution should enable MAP to determine the values of key cosmological parameters and to answer questions about the formation of structure in the early universe.

MAP is scheduled to launch in the Fall of 2000 on a Delta launch vehicle, and will be placed in a Lissajous orbit around the Sun-Earth  $L_2$  point using a lunar assist with phasing loops,



reaching its final orbit approximately 100 days after launch. The MAP radiometers cover two fields of view (FOVs)  $135^\circ$  apart on the celestial sphere. To obtain a highly interconnected set of measurements over a large area of the celestial sphere, the MAP observatory will execute a fast spin (0.464 rpm) and a slower precession ( $0.1^\circ/\text{sec}$ ) of its spin axis about the Sun line. The entire celestial sphere will be observed once every six months, or four times in the planned on-station mission life of two years.

There are six ACS operational modes: Inertial, Observing, Delta V, Delta H, Sun Acquisition, and Safehold. Inertial mode acts as a staging mode between the other operations of the spacecraft; it can either hold the spacecraft in an inertially-fixed orientation or slew the spacecraft between two different orientations. Observing mode is used for science operations. Delta V mode uses the REMs to adjust the orbit. Delta H mode uses the REMs to unload excess angular momentum. Sun Acquisition mode acquires and maintains a thermally-safe power-positive orientation of the spacecraft. Safehold mode puts the spacecraft in a -power and thermal-safe attitude.

The remainder of the paper will present various analyses of the MAP ACS. The effect of flexible modes, reaction wheel jitter, and fuel slosh on pointing stability a performance will be discussed. Estimates of thruster plume impingement torques and environmental torques in the phasing loops, lunar swingby, and final  $L_2$  orbit will be presented, along with contingency procedures for managing these torques. A linear impulse controller designed to improve the accuracy of MAP's thruster firings will also be discussed. Lastly, a dynamic attitude error limiter was added to improve the performance of the ACS during large attitude slews; this will be presented as well.

## STRUCTURAL MODEL

### Reduced Order Flexible Modes

Initially, NASTRAN<sup>1</sup> modeled large bodies like the antenna and thermal reflector as point masses. The newer NASTRAN model incorporated the physical dimensions of these large appendages and instruments. With these new inclusions the dominant flexible mode frequencies increased from 1.9 Hz to 5.7 Hz. From this model a reduced order flexible model has been created which reduced the system to include only 3-4 dominant modes for each Spacecraft Mode. By using the MSAP<sup>2</sup> software, the associated energy for each mode was compared through the formulation of various summary methods: Frequency, Modal Gain, Peak Amplitude and Gregory's Method which are listed below in Table 1. In addition, each mode's singular value plots for the rigid body, the flexible modes and a combination of the two were analyzed. The dominant mode frequencies are 5.744, 5.787, 27.73, 33.26, 36.2 and 44.93 Hz.

The structural system is fairly rigid; therefore, the flexible modes have less effect on the spacecraft system's stability. As a result, the majority of analysis was done for a plant derived as a combination of the rigid body modes and the chosen dominant flexible modes. The various structural plants analyzed were: 1) the rigid body modes, 2) the rigid body modes plus flexible body modes, and; 3) the rigid body plus the reduced flexible body modes (respectively, line 1, 2 and 3 in Figure 1). The system plant was modeled as the  $\text{Plant} = 1/(Is^2) + \text{Flexible modes}$ , where,  $I$  is the spacecraft inertia. Since the inertia values change by less than 1% (0.1 dB) from "Beginning of Life" to "End of Life" stability analysis will hold for all phases of the mission.

**Table 1**  
**DOMINANT FLEXIBLE MODES**

Modes	Freq. Hz	Modal Gain	Peak Ampl.	Gregory	Actuators	Sensors
<b>Inertial/Observing</b>						
11	5.744	6.537	98.33	100	Rotation Theta x,y,z	Rotation Theta x,y,z
12	5.787	6.749	100	100	Wheels 1,2,3	IRU
27	33.26	20.85	9.35	11.38		
34	44.93	100	24.58	20.08		
<b>Delta V/H</b>						
7	5.272	14.48	100	100	Translation	Rotation Theta x,y,z
11	5.744	37.95	45.29	46.62	Thrusters	IRU
27	33.26	41.59	3.27	2.764	1,2,3,4,5,6,7,8	
40	46.16	100	4.08	7.5		
<b>Safehold</b>						
11	5.744	14.75	97.49	100	Rotation Theta x,y,z	Rotation Theta x,y,z
22	27.73	50.29	14.26	8.35	Wheels 1,2,3	CSS 1,3,5
34	36.82	100	16.08	15.12		
<b>Sun Acquisition</b>						
11	5.744	14.75	97.49	100	Rotation Theta x,y,z	Rotation Theta x,y,z
(not used in analysis) 12	5.787	15.36	100	91.31	Wheels 1,2,3	CSS 1,3,5
22	27.73	50.29	14.26	8.34		IRU
34	36.82	100	16.08	15.101		

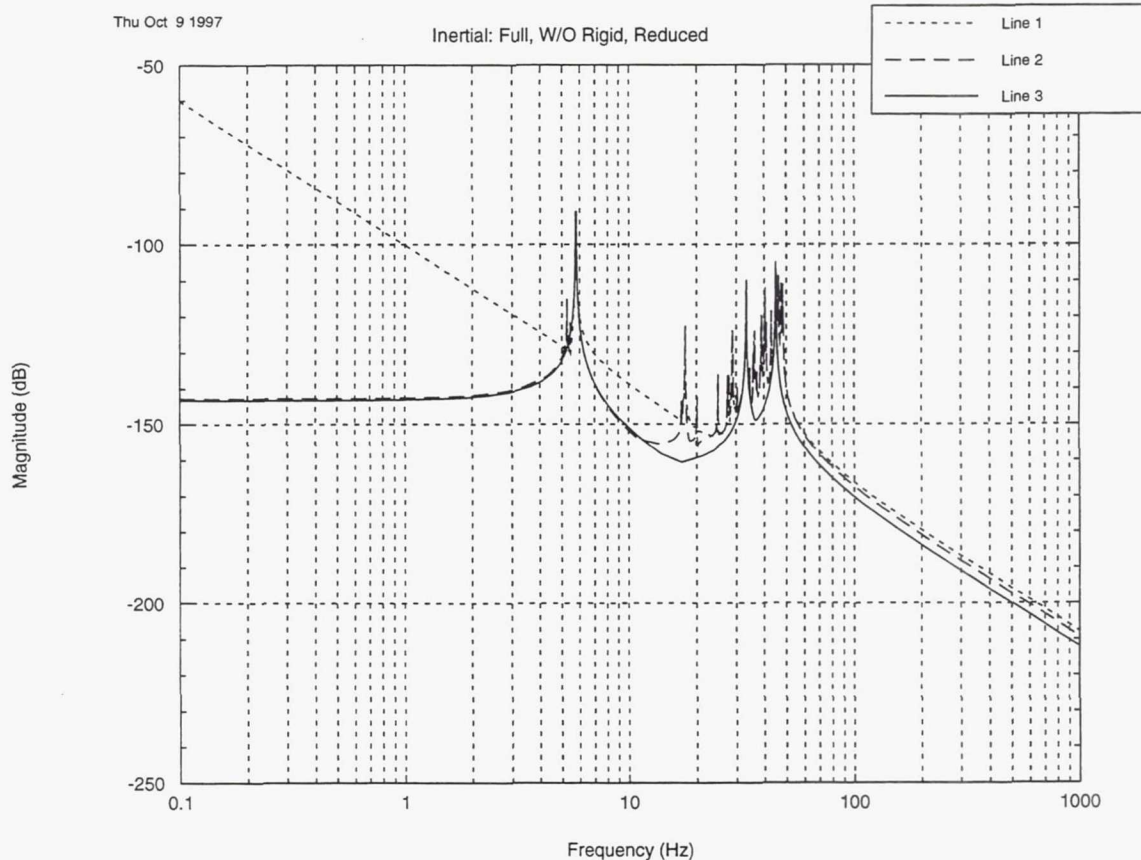


**Figure 1. Singular Value Plot of Flexible modes for MAP**

## Stability

Nichols stability charts were created for each spacecraft system mode in INCA<sup>7,8</sup>. The dynamic plant prescribed as a structural plant multiplied by the gyro dynamics (a simple second order system) was included in a closed loop feedback system with a proportional derivative (PD) controller. By implementing the Nichols and Bode techniques, the proportional and rate controller gains were used to calculate the stability margins for all the modes. All of the modes except one satisfied the Guidance Navigation and Control Center design criteria of at least 12 dB phase margin and 30° gain margin. Typically, the gain margin fell between 14-22 dB and the phase margin was between 36°-81°. Since the Safehold Mode Y-axis was unable to meet the required bounds, it was necessary to add a low pass structural filter in that axis. The addition of a structural filter to the dynamic plant produced the Nichols plot shown in Figure 2.

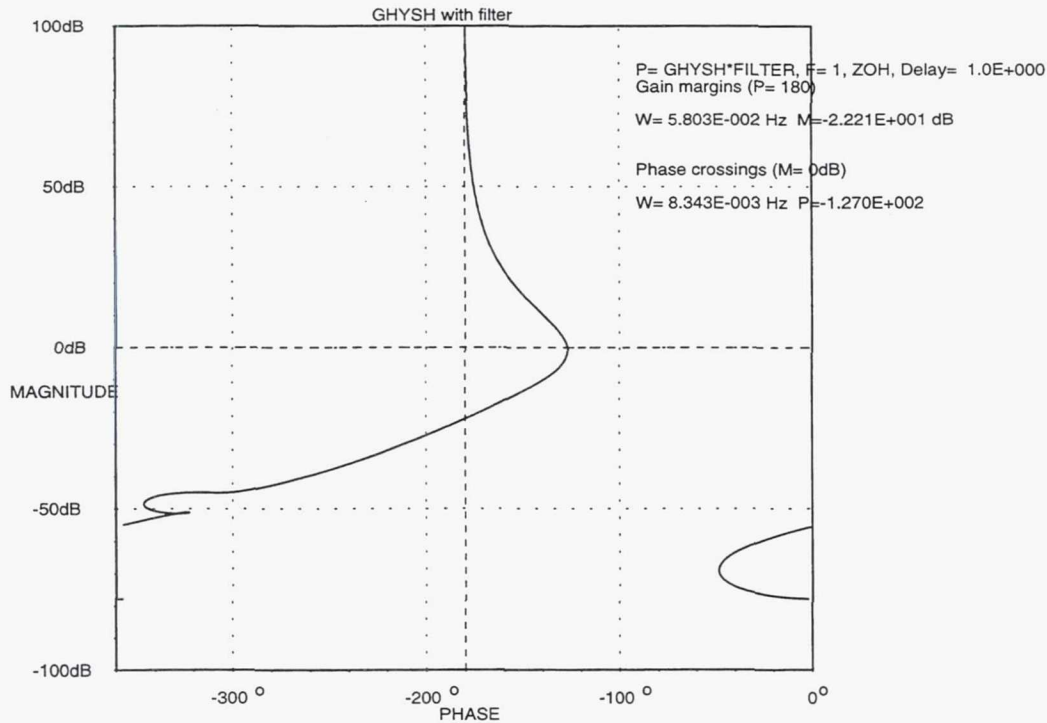


Figure 2. Nichols Stability Chart for Safehold Mode Y-axis

## WHEEL JITTER RESONANCE

Since Observing mode requirements are so stringent it was necessary to examine wheel jitter resonance. This wheel jitter resonance is due to the dominant flexible modes resonating with the wheel imbalance torques. The forces and torques due to structural resonance are described as:

$$\begin{aligned}
 F_x &= \Delta_{sr} * \omega_r^2; T_x = \Delta_{sr} * \omega_r^2 * L_{zr} + \Delta_{dr} * \omega_r^2 \\
 F_y &= \Delta_{sr} * \omega_r^2; T_y = \Delta_{sr} * \omega_r^2 * L_{zr} + \Delta_{dr} * \omega_r^2 \\
 F_z &= 0.0; T_z = \Delta_{sr} * \omega_r^2 * \sqrt{L_{xr}^2 + L_{yr}^2}
 \end{aligned} \tag{1}$$



where,  $\omega_r$  is the wheel's angular velocity,  $L$  is the length to the wheel from the gyroscope, and  $\Delta_{sr}$  and  $\Delta_{dr}$  are the static and dynamic imbalance of the wheels, respectively.

MAP's wheels have associated imbalance values of  $\Delta_{sr}=2.5E-5$  kg-m and  $\Delta_{dr}=2.5E-5$  kg-m<sup>2</sup>. Two angular velocities were considered: the first wheel frequency was near the flexible mode of 44.94 Hz and the second one is when the 3 wheels are running simultaneously at 25 Hz, near the (28.95 Hz flexible mode. The body rotation torques seen at the gyroscope due to wheel resonance were calculated to be between 22.7–36.1 arc-sec at 44.94 Hz and between 1.04-1.65 arc-sec at 25 Hz. This analysis showed that the wheel jitter in resonance with the flexible mode frequencies does not cause problems with MAP's Observing Mode pointing requirements.

## ENVIRONMENTAL TORQUES

The environmental disturbance torques that may act upon the spacecraft while it is orbiting the Earth are as follows: aerodynamic, gravity gradient, solar radiation and magnetic.<sup>9</sup> Since most of MAP's orbit is very high, torques due to the Earth's magnetic field are not significant.

### Orbit Phasing Loops

After MAP's injection into orbit about the Earth there are multiple three phasing loops. During these loops the thrusters will burn to increase the eccentricity and semimajor axis of the orbit, placing the vehicle in position for a lunar swingby. In this orbit, drag is the most important external torque at perigee because the density of the planet's atmosphere increases exponentially as the altitude decreases. Therefore, at the perigee altitude, a maximum aerodynamic force and torque were calculated. In addition, the gravity gradient torque and resultant momentum buildup were computed for both the Earth and the Moon.

**Aerodynamic Torques.** The drag torque and momentum build up is calculated for the portion of the Earth's orbit below 1000 km altitude. Initially, the sun-side surface areas are utilized to calculate the aerodynamic forces. These areas are primarily made up of the Solar panels, the Teflon webbing, and the middle spacecraft body hexagon. A three-dimensional model of MAP was created in SPAD<sup>10</sup>. All momentum values were calculated by multiplying the torque by the total elapsed time of 1 day. At the perigee altitude, the maximum aerodynamic force and torque are 0.0471 N and  $7.68 \times 10^{-4}$  N-m respectively. The orbital altitude is less than from 1000 km for approximately 7 minutes, which produces a momentum of 0.32 N-m-s. The sun-side SPAD results that were averaged during one rotation verified that the average torque is only  $3.367 \times 10^{-4}$  N-m and the momentum is 0.14 N-m-s. The density, velocity and aerodynamic torque were plotted as a function of altitude. The SPAD results for the x and y face exposure were put into SystemBuild<sup>11</sup> and simulated during the portion of the orbit when the altitude was 2250 km to 300 km to 2250 km. The simulation produced data very similar to the previous SPAD results. The maximum x and y face aerodynamic torque is 0.012 N-m and the momentum has a peak of 0.47 N-m-s and an average of 0.28 N-m-s.

**Gravity Gradient for Earth.** The calculation of the Earth gravity gradient torque on the spacecraft and the momentum buildup are calculated and simulated for the portion of the Earth orbit below the altitude of 1000 km. The Earth's gravity gradient momentum and an average torque were calculated to be 0.1744 N-m-s and  $2.0 \times 10^{-4}$  N-m in the x-direction, and 0.221 N-m-s and  $4.1 \times 10^{-5}$  N-m in the z-direction. Gravity gradient simulation results further verified values for torque and momentum buildup. The Earth gravity gradient simulations displayed a maximum torque of  $1.7 \times 10^{-4}$  N-m in the x and y-axes and  $1.0 \times 10^{-5}$  N-m in the z-axis and a maximum momentum of 0.15 N-m-s in the x and y axes, 0.07 N-m-s in the z-axis, and a maximum system momentum of 0.15 N-m-s.

### **Lunar Swingby**

As previously mentioned the phasing orbits insert the spacecraft into the proper trajectory for a lunar swingby. As a result, the gravity gradient torque and momentum associated with the Moon's environment were calculated. These values were computed for a 20 minute portion of the orbit during the closest approach to the Moon, which is approximately 1000 km.

**Gravity Gradient for Moon.** The torque and momentum values for the Lunar gravity gradient torque on the spacecraft are 0.0736 N-m-s and  $3.6 \times 10^{-5}$  N-m in the x-direction, and 0.064 N-m-s and  $5.0 \times 10^{-6}$  N-m in the z-direction. Gravity gradient simulation results further verified values for torque and momentum buildup. Lunar gravity gradient simulations displayed a maximum torque of  $3.5 \times 10^{-5}$  N-m in the x and y axes and  $2.5 \times 10^{-6}$  N-m in the z-axis and a maximum momentum of 0.04 N-m-s in the x and y axes, 0.026 N-m-s in the z-axis, and a maximum system momentum of 0.047 N-m-s.

### **Libration Point**

After MAP's lunar swingby, the spacecraft will be in orbit about the Earth-Sun L<sub>2</sub> point. The solar radiation pressure and a solar pinwheel torque associated with a solar array deployment misalignment have been calculated. For these computations, the primary surface areas exposed to the Sun are the solar array panels, the silver Teflon webbing, and a black and white painted hexagon. For the solar pinwheel torque, the hexagon area in the middle of the z-face was excluded because it will not experience an angular deflection due to deployment.

**Solar Radiation Pressure.** The calculated values of solar radiation result in an instantaneous Solar pressure torque ( $T_{\text{solar}}$ ) and average momentum buildup ( $\Delta H_{\text{solar}}$ ) of  $1.85 \times 10^{-6}$  N-m and 0.16 N-m-s per day. Under ideal conditions the  $T_{\text{solar}}$  and  $\Delta H_{\text{solar}}$  about spin and precession axes average out to zero. With a misalignment tolerance of  $\pm 0.25^\circ$  about the spin axes the  $T_{\text{solar}} = 1.07 \times 10^{-8}$  N-m and  $\Delta H_{\text{solar}} = 9.3 \times 10^{-4}$  N-m-s for a period of 1 day. For further verification these calculated values were compared to SPAD generated data. Results from SPAD produced an average solar torque and momentum buildup per day of  $1.88 \times 10^{-8}$  N-m and 0.00162 N-m-s. It was realized that calculations could be off by an order of magnitude because of different assumptions and the greater precision of the SPAD method.

**Pinwheel Torque.** The solar arrays may deploy improperly resulting in a canted surface area. A combination of their tilted surface and the solar pressure torque could cause a pinwheel torque, which is a torque about the spacecraft spin (z) axis. This disturbance effect has been calculated for a solar array canted angle of  $1^\circ$  and a spin axis misalignment of  $\pm 0.5^\circ$ .



The maximum instantaneous pinwheel torque and the accumulated momentum in the z-axis are  $1.46 \times 10^{-6}$  N-m and 0.126 N-m-s/°-day. The average momentum buildup per day in the x and y-axes (with a misalignment angle of  $0.5^\circ$  in the spin axis) are 0.0736 N-m-s and 0.0645 N-m-s, respectively. The SPAD pinwheel torque and momentum results have been produced for two cases. For the maximum case of the sun vector parallel to the normal vector they are  $5.82 \times 10^{-7}$  N-m and 0.0503 N-m-s, respectively. For a pitch sunline angle of  $22.5^\circ$  the torque and momentum are  $5.31 \times 10^{-7}$  N-m and 0.0459 N-m-s, respectively.

The SPAD data was curve-fit to produce the torque and momentum equations. After integrating the torque to get the momentum and using zero initial conditions for the momentum; a maximum system momentum magnitude of 1 Nms leads to a buildup time of 23.36 days. However, it was found that the SPAD model has errors due to:

- 1) Solar array and webbing areas are too small by 35%; these areas are 2/3 of the total bottom area. This leads to an error of 23%, and
- 2) The moment arms are off by 11.7% due to smaller solar array length than originally thought.

The total system momentum buildup for one day becomes 0.059 N-m-s and the total time for the momentum to buildup to 1.5 N-m-s is 25.5 days. The data presented could mean that a momentum dump has to be performed every 3-4 weeks. For each simulation that will run later the momentum vector in the body frame will be initialized to  $[0, \pm 1.5, \pm 1.5]/\sqrt{2}$ . The system's momentum tolerance is 1.5 N-m-s and the total time between unloading burns is 90 days; the maximum solar array deployment misalignment angle is  $0.228^\circ$ . See Table 2 for summary of environmental torques and momentum.

**Table 2**  
**Summary of Environmental Disturbances**

Calculated Disturbances	Torque (N-m)	Momentum (N-m-s)
Aerodynamic Phasing Burn	$7.68\text{E-}4$ (@300km)	0.32 @ $t=7\text{min}$ (1000 km)
Gravity Gradient Phasing Burn	$T_x=2\text{E-}4$ , $T_z=4.1\text{E-}5$	$H_x=.174$ , $H_z=0.221$ @1 orbit
Gravity Gradient Lunar Swingby	$T_x=3.6\text{E-}5$ , $T_z=5\text{E-}6$	$H_x=.073$ , $H_z=0.064$ @1 orbit
Solar Pressure (instantaneous)	$T_x=1.85\text{E-}6$	$H_x=0.16$ @ $t=1$ day
Solar Pressure (average)	$T_x=1.07\text{E-}8$	$H_x=9.3\text{E-}4$ @ $t=1$ day
Solar Pinwheel (instantaneous)	$T_{x,y,z}=1.23\text{E-}4, 1.32\text{E-}4, 1.46\text{E-}6$	$H_x=10.6, H_y=10.06, H_z=.126$ @1day
Solar Pinwheel (average)		$H_x=0.073$ & $H_y=0.064$ @1day
Simulated Disturbances	Torque (N-m)	Momentum (N-m-s)
Aerodynamic Phasing Burn SPAD z-face	$3.147\text{E-}4$ (@300km)	0.131 @ $t=7\text{min}$ (1000 km)
Aerodynamic Phasing Burn SPAD x&y-face	0.012 (2250km $\rightarrow$ 300km $\rightarrow$ 2250km)	0.47 (peak), 0.28 (avg)
Gravity Gradient Phasing Burn SB	$T_x=1.7\text{E-}4$ , $T_z=1.0\text{E-}5$	$H_x=0.15$ , $H_z=0.07$ @1 orbit
Gravity Gradient Lunar Swingby SB	$T_x=3.5\text{E-}5$ , $T_z=2.5\text{E-}6$	$H_x=0.04$ , $H_z=0.026$ @1 orbit
Solar Pressure (average) SPAD	$T_x=1.88\text{E-}8$	$H_x=1.62\text{E-}3$ @ $t=1$ day
Solar Pinwheel (average) SPAD	$T_x=5.31\text{E-}7$	$H_x=0.0459$ @ $t=1$ day
SPAD- Solar Pressure & Aerodynamic Drag		SB- System Build

#### **Solution for Handling Environmental Torques**

As a response to the concern about the pinwheel torque, a method was developed to unload excess system momentum while in Observing Mode, using a series of three "one shot" thruster firings. This algorithm is not currently baselined to be flown on MAP, but was



developed as a contingency procedure in the event that system momentum build-up on station is greater than expected. The algorithm was designed to meet the following constraints and design goals:

1. Unload momentum to less than 0.3 Nms while in Observing Mode.
2. Always keep the solar arrays normal within  $25^\circ$  of the sunline (violations of the  $22.5 \pm 0.25^\circ$  Observing Mode sunline angle constraint are permissible).
3. Perform the entire operation during one ground pass (37 minutes)

Using the MAP thruster pair 1 and 2 as an example, the steps in this process are as follows,:

- A. Wait until the momentum transverse to the z-axis is all in the +x axis. Fire thruster 2 to remove as much of this momentum as possible.
- B. After thruster firing A, wait until the sun is in the (-x,z) quadrant of the x-z plane. Fire thruster 1 or 2 (depending on the sign of the z-axis momentum) to add x momentum equal to the amount of momentum in the z-axis. By doing this, the system momentum vector is positioned such that half a precession cycle later it will be almost entirely in the +x-axis. This results in an intermediate system momentum state as much as  $\sqrt{2}$  higher than the initial value, but simulations show that this system momentum value does not pose an attitude control problem.
- C. After thruster firing B, wait approximately half of a precession cycle (30 minutes), and then wait until all of the system momentum is in the +x axis. Fire thruster 2 to remove as much of this momentum as possible.

The total procedure requires a maximum of 35.5 minutes and reduces system momentum to near zero. The algorithm could be adjusted to use only one of the two thrusters, or to use one of the other two thruster sets.

## THRUSTER PLUME IMPINGEMENT TORQUES

### Fuel Slosh

Propellant slosh is a mechanical effect of liquid propellants. At the moment the propellant mass impacts the wall of the fuel tank, it will transfer momentum to the spacecraft. If the tank is not at the center of mass of the vehicle, this will create an impulse moment that will affect the vehicle attitude. This disturbance can be significant and unacceptable, and must be limited through tank design. Fortunately, the MAP tank is close to the center of mass and the moment arm is small. In addition, a flexible membrane (diaphragm) has been placed in the tank to assure that the propellant remains in contact with the propellant port and to help damp out the sloshing effects.

The original analysis for the ACS Critical Design Review used a model for fuel slosh that was found in two reports.<sup>12, 13</sup> The TDRS slosh model from NASA CR 166745 report<sup>12</sup> is presented in Figure 3. According to that model, the slosh natural frequency,  $\omega_n$ , depends on the torsional spring constant, K, and the overall acceleration, a, of the tank:

$$\omega_n = \sqrt{\frac{K}{M_1 L^2} + \frac{a}{L}} \quad (2)$$

Figure 4 is the model used in a study for the CRAF/Cassini spherical tanks.

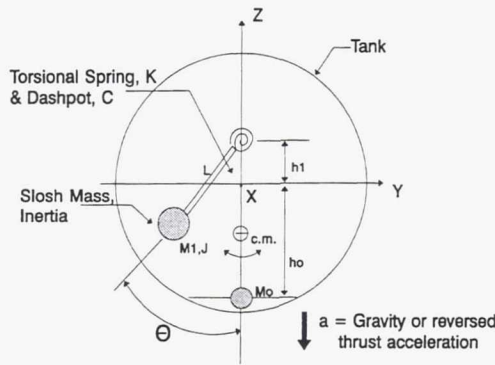


Figure 3. TDRS Fuel Slosh Model

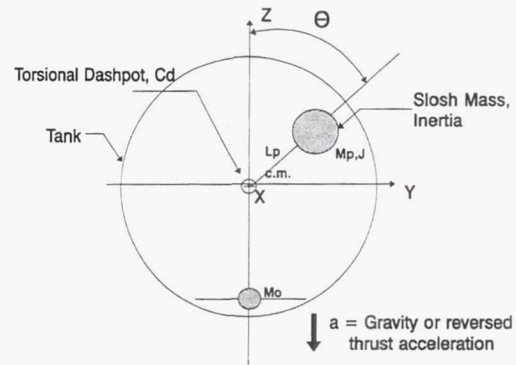


Figure 4. Cassini Fuel Slosh Model

The angular position,  $\theta$ , of the model pendulum is a representation of the position of the liquid bulk and the lateral offset,  $Z_{cg}$ , of the liquid center with respect to the direction of the settling acceleration can be calculated as (see Figure 4):

$$z_{cg} = \frac{M_p L_p \cos \theta}{M_p + M_o}. \quad (3)$$

Assume  $\theta = \frac{\pi}{4} \sin \omega_n t$ , where the natural frequency of the slosh material is defined as in the TDRS report already presented. Then the equations of motion for the system are defined as:

$$\text{linear torque, } T_{linear} = r \times F = r_{cm} \times M \omega^2 r = r_{cm} L M_1 \frac{\pi^2 \omega_n^2}{16} \cos^2 \omega_n t, \quad (4)$$

$$\text{angular torque, } T_{angular} = J \ddot{\theta} = -J \frac{\pi \omega_n^2}{4} \sin \omega_n t, \text{ and} \quad (5)$$

$$\text{angular momentum, } H_{angular} = J \dot{\theta} = -J \frac{\pi \omega_n}{4} \cos \omega_n t. \quad (6)$$

From the initial analysis, the calculated fuel slosh inertia,  $J$  is 0.007 % of the total system inertia and the derived natural frequency,  $\omega_n$  is several times larger than the system's bandwidth frequency, 0.02 Hz.

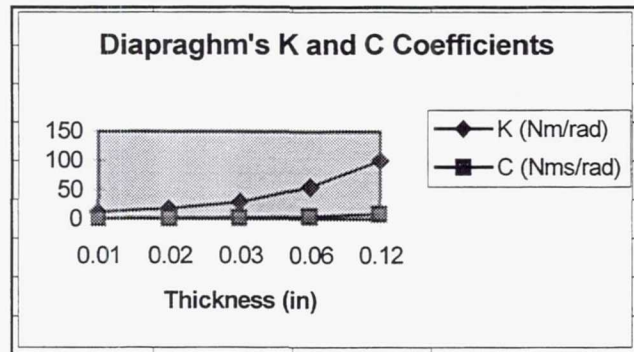
The previous reports had several questionable aspects. However, one of the models did not include a stiffness factor and the equation for the natural frequency was incorrect for the corresponding dynamic equation. Therefore, it was necessary to derive our own scenario for each aspect of the fuel slosh's movement. The five worst cases considered were:

- (1) Radial Thrust with a full tank of fuel;
- (2) Slew Maneuver with a full tank and a half full tank;
- (3) Linear Station Keeping Effects at  $L_2$  (half tank);
- (4) Angular Station Keeping Effects at  $L_2$  (half tank); and
- (5) Observing Mode Fast Spin, accelerating and constant rate (all ranges of fuel).

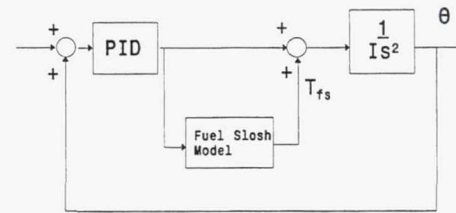
Simple models were drawn for each case to obtain dynamic equations describing the motion of the fluid. Further research was done to find a better value for the stiffness coefficient,  $K$  and the damping coefficient,  $C$ . Values for  $K$  and  $C$  could be associated with MAP's diaphragm thickness (0.12 in) and were extrapolated from References 14-15. The results are shown below in

Figure 5. Calculation of the torques and momentum buildup due to the fuel slosh were done for each case. In addition, an angular response due to the fuel slosh torque was calculated,

$\frac{\theta}{T_{fs}} = \frac{1}{Is^2}$ . The basic block diagram for the analytical system is shown in Figure 6.



**Figure 5. Extrapolation of MAP's K and C with Diaphragm Thickness**



**Figure 6. Block Diagram to Analyze Angular Effect due to Fuel Slosh**

All the results for the various cases are presented below.

Case 1- Radial Thrust with a full tank of fuel:

The angular frequency was 1.05 to 1.5 Hz, the linear torque was  $3.65 \times 10^{-5}$  to  $7.52 \times 10^{-5}$  N-m, the angular torque was 0.055 to 0.025 N-m, and the angular momentum was 0.004 to 0.001 N-m-s.

Case 2- Slew Maneuver with both a full and half full tank a fuel:

The angular frequency was 1.04 to 1.5 Hz, the linear torque ranged from 0.752-0.69 N-m, the angular torque ranged from 4.13-6.36 N-m and the angular momentum ranged from 0.55-1.24 N-m-s.

Case 3- Linear Station Keeping Effects at  $L_2$  (half a tank):

Radial Thrusting produces an angular frequency of 1.64 to 2.05 Hz, a linear torque of  $8.54 \times 10^{-5}$  to  $1.13 \times 10^{-4}$  N-m, an angular torque of 0.011 to 0.02 N-m and an angular momentum ranging from 0.0007 to 0.001 N-m-s.

Perpendicular Thrusting produces an angular frequency of 6.23 to 8.25 Hz, a linear torque of 11 N-m, an angular torque of 61 N-m and an angular momentum ranging from 1.5 to 2 N-m-s.

Case 4- Angular Station Keeping Effects at  $L_2$  (half a tank):

The angular frequency was 1.62 to 2.04 Hz, the linear torque was 0.69 N-m, the angular torque was between 3.76-4.19 N-m and the angular momentum ranged from 0.37-0.52 N-m-s.

Case 5- Observing Mode Fast Spin, accelerating and constant rate (for all ranges of fuel).

A constant angular rate applied to the spacecraft produced an angular frequency of 0.39 to 0.503 Hz, a linear torque between  $4.6 \times 10^{-6}$ - $1.3 \times 10^{-5}$  N-m, the angular torque was between 0.0014-0.002 N-m and the angular momentum ranged from  $1.33 \times 10^{-5}$ - $1.7 \times 10^{-5}$  N-m-s.

An angular acceleration applied to the spacecraft produced an angular frequency of 0.39 to 0.503 Hz, a linear torque between 0.01-0.017 N-m, the angular torque was between 0.00013-0.00017 N-m and the angular momentum ranged from  $6.4 \times 10^{-5}$ - $8.9 \times 10^{-5}$  N-m-s.



After this analysis, it was found that fuel slosh would not have a large affect on the spacecraft's attitude. Although some of the instantaneous torque and momentum values are large, their overall effect was small. The natural frequency of the slosh system is several orders of magnitude larger than the bandwidth of the control system. The angular displacement due to either the linear or angular torque is from  $10^{-9}$  to  $10^{-5}$  radians. This analysis determined that fuel slosh should not be a concern to the MAP mission.

## **CONTROLLERS**

### **Thruster Mode Linear Impulse Controller**

The Thruster Mode linear impulse controller was designed to improve the accuracy of MAP's z-axis Delta V's. There are some tradeoffs involved in usage of this impulse controller; with the impulse controller the spacecraft uses about 12% more fuel, without it, errors during Delta V are about 12% larger. Current implementation allows for burn accuracy of less than 1 sec but this could be improved to 0.04 sec if necessary. This excludes subsequent firings in the Delta H mode.

The operational plan is to enable the impulse controller right after MAP's lunar swingby during the mid-course correction (MCC) so it is available L<sub>2</sub>. At L<sub>2</sub>, the absolute duration of the burns is smaller so the percentage errors tend to be higher. Without the impulse controller the burn is corrected with a one-sided impulse controller in both x and z. Regardless of whether or not the impulse controller is enabled, the current design will ensure that the burn duration will be at least the desired amount of time. Figures 7 and 8 shows a sample L<sub>2</sub> burn with and without the impulse controller, respectively; the commanded thruster time for each run was 60 seconds in the x-axis and 30 seconds in the z-axis. Notice the error caused without the impulse controller and the extra thruster firings to correct the error with it.

### **Dynamic Attitude Error Limiter**

The dynamic rate limiter enables the spacecraft to meet the sunline requirement during a slew in Inertial Mode. When the limiter is not utilized, Inertial Mode slews that include high spin errors in the z-axis can cause the spacecraft to violate the 25° sun constraint, as shown in Figure 9. The dynamic rate limiter calculates an attitude error limit for each axis proportional to the error in that axis. This preserves the direction of the resulting Inertial Mode slew and prevents the spacecraft from violating the sun constraint as in Figure 10. Both Figures 9 and 10 show a series of 45° Inertial Mode slews across the sunline with spin angles from 0° to 180°; with the dynamic attitude error limiter, the spacecraft on these slews does not violate the sun constraint.

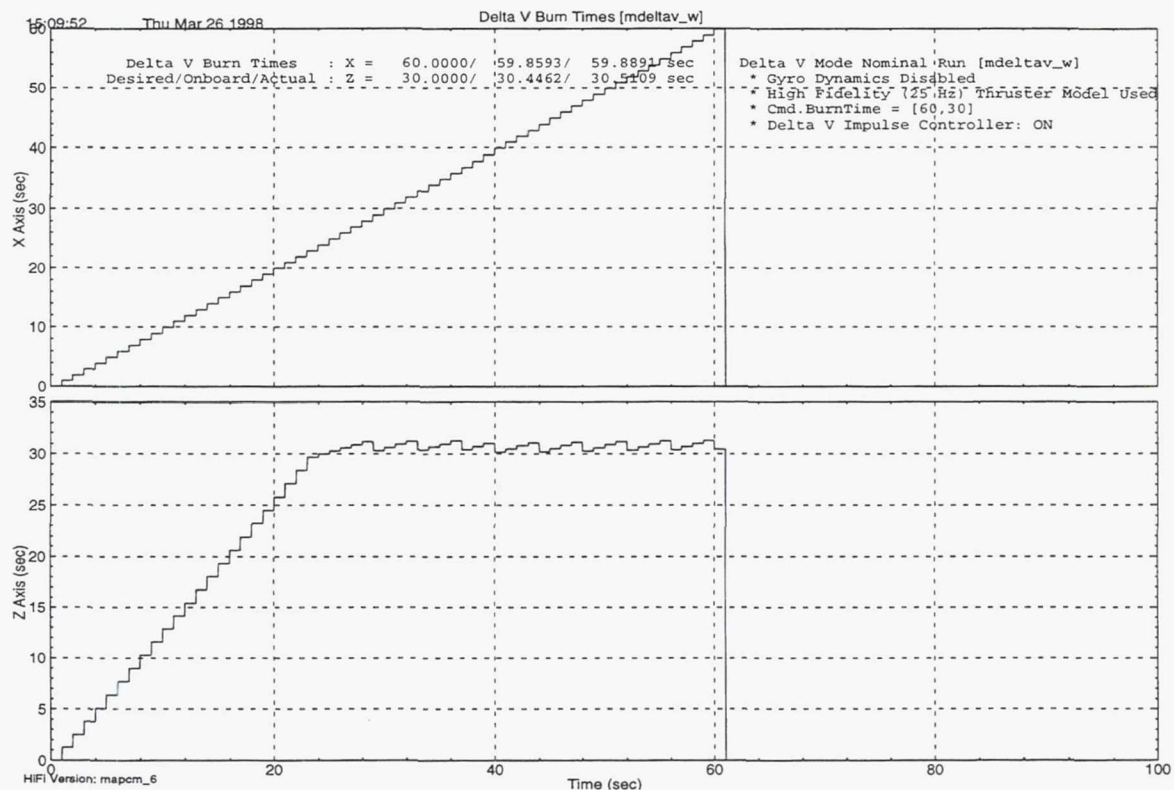


Figure 7. Delta V burntime in X & Z axis with impulse controller

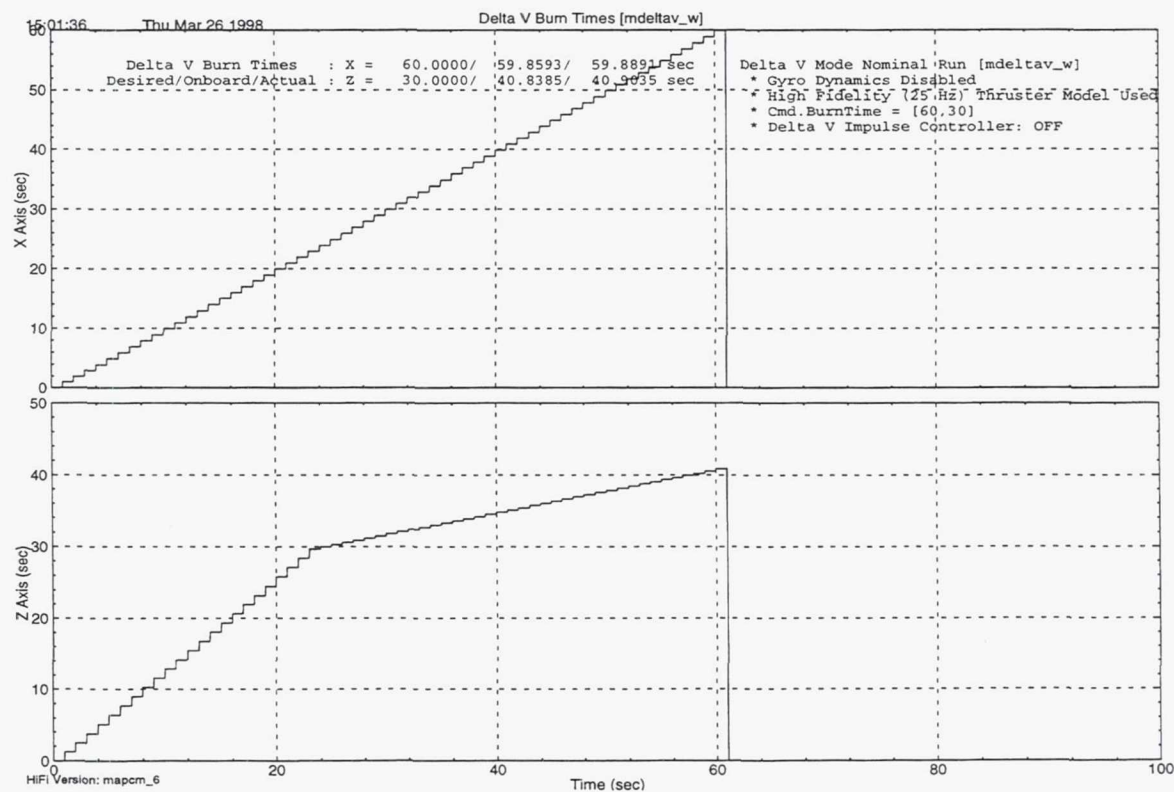


Figure 8. Delta V burntime in X & Z axis without impulse controller

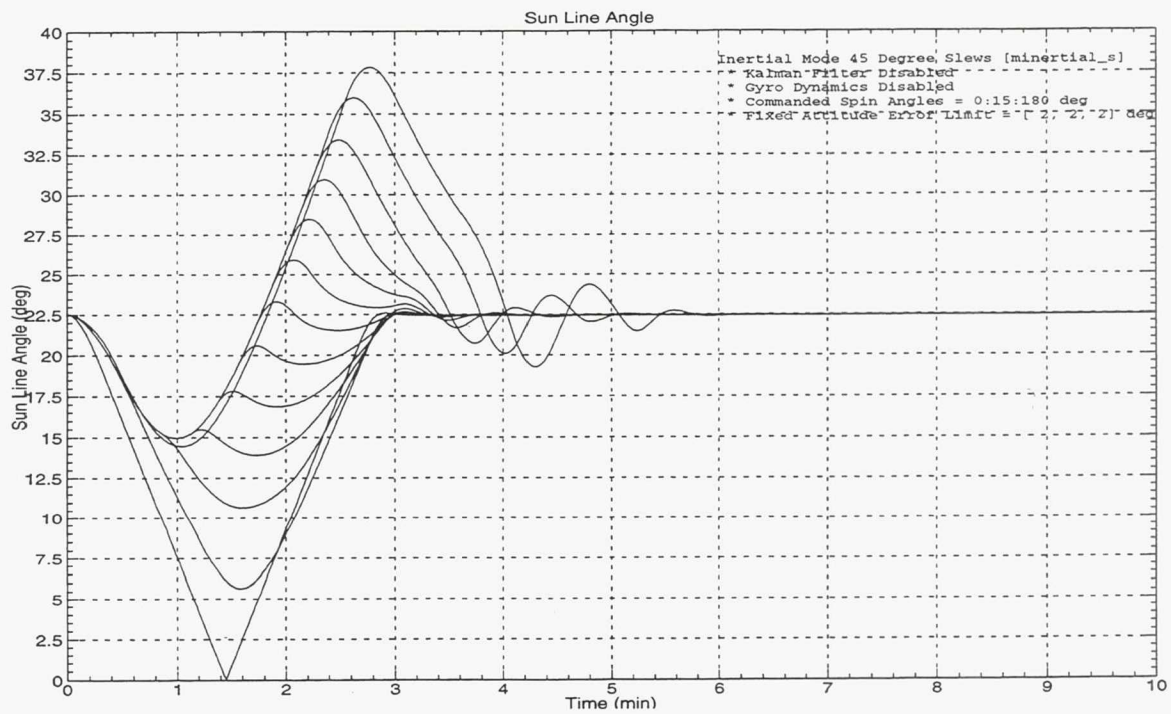


Figure 9. Inertial Mode slews with no dynamic attitude error limiter

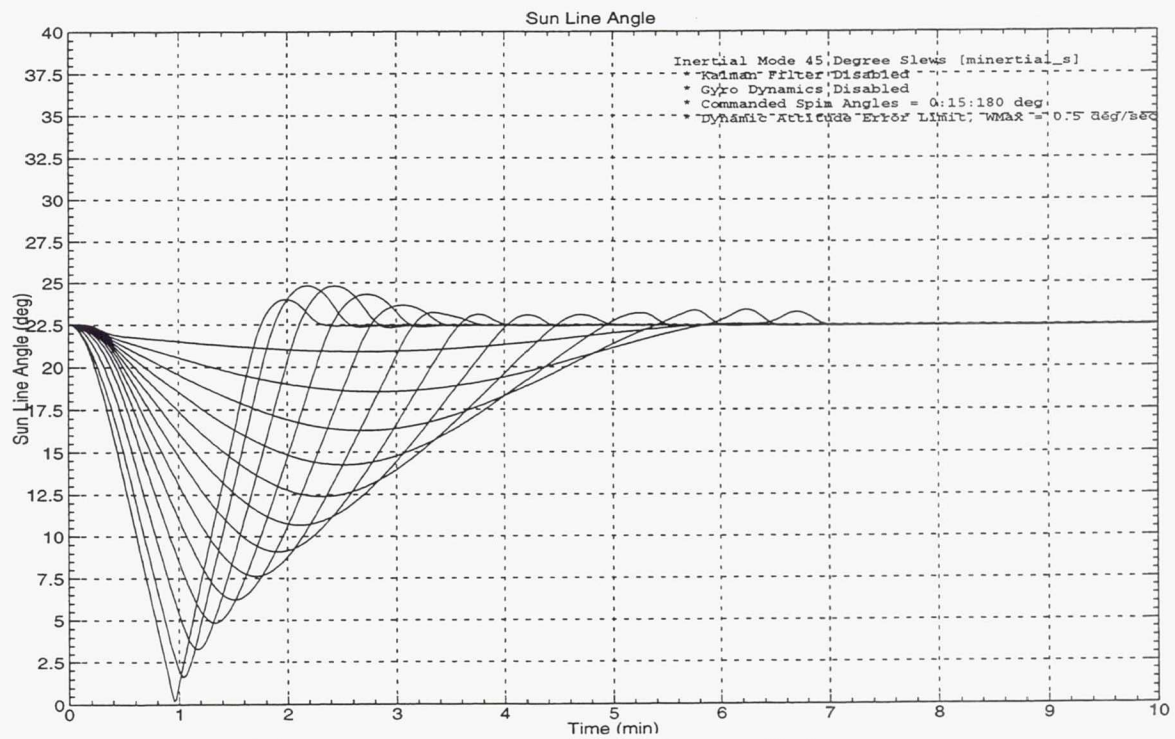


Figure 10. Inertial Mode slews with dynamic attitude error limiter



## CONCLUSIONS

The structural system is fairly rigid; therefore, the majority of analysis was done for a plant derived as a combination of the rigid body modes and the chosen dominant flexible modes. Analysis determined that the wheel jitter in resonance with the flexible mode frequencies does not cause problems with MAP's Observing Mode pointing requirements.

All of MAP's operational modes except one satisfied the Guidance Navigation and Control Center design criteria. Since the Safehold Mode Y-axis was unable to meet the required bounds, it was necessary to add a low pass structural filter.

The maximum x and y face aerodynamic torque is 0.012 N-m and the momentum has a peak of 0.47 N-m-s and an average of 0.28 N-m-s. The Earth's gravity gradient an average torque and momentum were calculated to be  $2.0 \times 10^{-4}$  N-m and 0.1744 N-m-s in the x-direction, and  $4.1 \times 10^{-5}$  N-m and 0.221 N-m-s in the z-direction. Gravity gradient simulation results further verified values for torque and momentum buildup. The Earth gravity gradient simulations displayed a maximum torque of  $1.7 \times 10^{-4}$  N-m in the x and y-axes and  $1.0 \times 10^{-5}$  N-m in the z-axis and a maximum momentum of 0.15 N-m-s in the x and y axes, 0.07 N-m-s in the z-axis, and a maximum system momentum of 0.15 N-m-s.

Under ideal conditions, the solar radiation torque about the spin and precession axes average out to zero. However, misalignment of the solar panels can give rise to a pinwheel torque that cause momentum buildup. This situation calls for a maximum allowable solar array deployment misalignment angle is  $0.228^\circ$ . Simulations show that a proposed solution of a three-shot momentum unloading in Observing Mode can be used if the misalignments exceed this limit.

The natural frequency of the slosh system is several orders of magnitude larger than the bandwidth of the system. Therefore, the angular displacement due to either the fuel slosh's linear or angular torque is small and fuel slosh should not be a concern to the MAP mission.

The end result of the analysis is a MAP controller that meets attitude control requirements with margin.

## REFERENCES

1. The NASTRAN Theoretical Manual", NASA SP-221-(06), COSMIC, University of Georgia, Athens, GA, January 1981.
2. Swales & Associates, Inc., "Modal Significance Analysis Package (MSAP): User's Manual", Technical report SAI-RPT-080, Ver.2, July 1995.
3. Andrews, S.F., Campbell, C.E., Ericsson-Jackson, A.J., Markley, F.L., and O'Donnell Jr., J.R., "MAP Attitude Control System Design and Analysis", NASA CP-3345, Flight Mechanics Symposium, Greenbelt, MD, 1997.
4. Bogges, N. W., *et al.*, *Astrophysical Journal*, vol. 397, p. 420 (1992).
5. Gulkis, S., Lubin, P. M., Meyer, S. S., and Silverberg, R. F., *Scientific American*, vol. 262, no. 1, p. 132 (1990).
6. Smoot, G. F., *et al.*, *Astrophysical Journal*, vol. 396, p. L1 (1992).

7. Bauer, F.H. and Downing, J., "Control System Design And Analysis Using The INteractive Controls Analysis (INCA) Program", Paper No. 87-2517, AIAA Guidance, Navigation And Control Conference, Monterey, Ca August 1987.
8. Bauer, F.H. and Downing, J., "INteractive Controls Analysis (INCA) Version 2.0", Program Number GSC-12988, COSMIC, University of Georgia, Athens, GA, 1985, updated to Version 3.13, 1989.
9. Wertz, J.R., Spacecraft Attitude Determination and Control, Kluwer Academic Publishers, Dordrecht, Netherlands, 1978.
10. Downing, J., and Surber, J. L., "Solar Pressure and Aerodynamic Drag (SPAD) Version 1.51", NASA in-house software pending publication with COSMIC, 1998.
11. Integrated Systems, Inc., "MatrixX & SystemBuild User's Guides", January 1996
12. "Study of Liquid Slosh in the Tracking and Data Relay Satellite Hydrazine Tanks", NASA CR 166745, November 1981;
13. Dodge, F.T., "Propellant Dynamics and PMD Design for the Near Earth Asteroid Rendezvous (NEAR) Spacecraft", Southwest Research Institute, SwR Project: 04-6297, Final Report, April 1994.
14. Sirlin, S.W., "Mars Pathfinder Launch Vehicle Nutation Analysis", Jet Propulsion Laboratory, interoffice memo: IOM 3546-96-032, July 19, 1996.
15. Stofan, A., "Experimental Damping of Liquid Oscillations of a Spherical Tank by Positive-Expulsion Bags and Diaphragms", NASA Technical Note D-1311, July 1962.

**Page intentionally left blank**



## TOPEX/POSEIDON ORBIT MAINTENANCE FOR THE FIRST FIVE YEARS\*

R. S. Bhat<sup>†</sup>, B. E. Shapiro<sup>†</sup>, R. B. Frauenholz<sup>†</sup>, and R. K. Leavitt<sup>\*\*</sup>

The TOPEX/Poseidon orbit maintenance strategy was changed following launch to include the effects of observed unmodeled, and hence anomalous, along-track accelerations. The anomalous force causes the semi-major axis,  $a$ , to either increase (called "boost") or decrease ("deboost" or "decay") depending on the satellite attitude and solar array pitch angle offset. Although this force is the most uncertain parameter in ground track prediction, it has been used as a passive technique for orbit maintenance, thereby reducing the number of propulsive maneuvers, enhancing maneuver spacing, and to place maneuvers at convenient times. This passive technique was first demonstrated in May 1993. The TOPEX/Poseidon orbit has been uniquely maintained using both passive (non-propulsive) and active (propulsive) maneuvers. Furthermore, the orbit has been maintained using only the passive technique since the ninth orbit maintenance maneuver on January 15, 1996.

Only nine orbit maintenance maneuvers have been required to maintain the ground track, including verification site over flights, since achieving the operational orbit on September 21, 1992 (mission requirement: 95% within  $\pm 1$  km). During this period,  $a$  has varied within  $7714,429 \pm 7$  m, while the inclination  $i$  periodically fluctuated in the range  $66.0408^\circ \pm 0.0040^\circ$ . The frozen orbit (required  $e < 0.001$  and  $\omega \approx 90^\circ$ ) has been maintained without any dedicated eccentricity maneuvers. The frozen eccentricity vector has completed two periodic cycles and it is currently tracing its third cycle (period  $\approx 26.7$  months).

### INTRODUCTION

Since its launch on August 10, 1992, TOPEX/Poseidon<sup>††</sup> has precisely mapped the topography of over 95% of the earth's ice-free seas. The wealth of scientific information provided by its very high quality ocean-altimetry data prompted NASA and CNES to further extend the TOPEX/Poseidon mission through 2001 to overlap with the successor Jason-1 mission. To facilitate high quality altimetry data acquisition, the satellite is maintained in a nearly-circular, frozen orbit ( $e \approx 0.000095$ ,  $\omega \approx 90^\circ$ ) at an altitude of  $\approx 1336$  km and an inclination of  $i = 66.04^\circ$  (Ref. 1). This orbit provides an exact repeat ground track every 127 orbits ( $\approx 10$  days) and over flies two verification sites: a NASA site off the coast of Point Conception and a CNES site near the islands of Lampione and Lampedusa in the Mediterranean Sea.

After launch, six orbit maintenance maneuvers (OMMs) were implemented to acquire the operational orbit from the injected orbit.<sup>2</sup> These maneuvers achieved the frozen orbit, removed inclination errors induced by the launch vehicle, and synchronized the ground track with the reference grid and two

\* The research described in this paper was carried out by the Jet Propulsion Laboratory, California Institute of Technology, under contract with the National Aeronautics and Space Administration. Address all correspondence to: R. S. Bhat, M/S 264/355, 4800 Oak Grove Dr., Pasadena, Ca, 91109. Electronic mail: ramachand.s.bhat@jpl.nasa.gov.

<sup>†</sup> Jet Propulsion Laboratory, California Institute of Technology, Pasadena, California.

<sup>\*\*</sup> Sterling Software, Pasadena, California.

<sup>††</sup> TOPEX/Poseidon is a joint mission of the US National Aeronautics and Space Administration (NASA) and the French Centre National d'Etudes Spatiales (CNES). The primary mission lifetime was 3 years and the extended mission an additional 2 years.

verification sites. The operational orbit was achieved on September 21, 1992 and altimeter data acquisition started on September 23, 1992.

The Jet Propulsion Laboratory (JPL) of the California Institute of Technology is responsible for conducting all mission operations including operational navigation. Operational orbit determination (OD) using radiometric data acquired via the NASA Tracking Data Relay Satellite System (TDRSS) is provided by the Flight Dynamics Facility (FDF) of NASA's Goddard Space Flight Center (GSFC).

Prior to launch, orbit maintenance maneuver (OMM) design<sup>1</sup> was expected to depend primarily on atmospheric drag and the uncertainty of its prediction. The consequent maneuver targeting strategy had to be changed following launch due to the observation of unexpected along-track accelerations<sup>3</sup> called "anomalous forces". These forces did not influence operational orbit acquisition; however, it became necessary to accurately model and predict the anomalous force for effective ground track control. OMM1 was delayed for one ground track repeat cycle to collect additional OD data so that a reasonable empirical model could be constructed, thereby causing the ground track to leave the control band for a few days. Thus OMM1 was implemented outside the eastern edge of control band.

An empirical model<sup>4</sup> based on observed MOE (Medium-accuracy Orbit Ephemeris) accelerations is used for the anomalous force prediction. The MOE is based on a combination of laser ranging and GPS (Global Positioning System) data. The anomalous force model is validated using thrust parameters provided by the FDF. The magnitude of the anomalous forces is equivalent to or greater than the effects of the atmospheric drag and either raises ("boosts") or lowers ("decays") the orbit depending on the satellite attitude and solar array orientation. Its uncertainty significantly influences ground track prediction accuracy, especially during low drag conditions ( $70 < F_{10.7} < 120$ )<sup>\*</sup>, when it is the largest uncertainty in orbit determination. The potential of using the anomalous force as a tool for ground track control was soon recognized and this passive technique<sup>4,5</sup> was demonstrated for the first time in May 1993 to avoid a propulsive maneuver near the western boundary of the control band, and later, in October 1995 to postpone OMM9 until Jan. 15, 1996. Since OMM9, the orbit has been maintained using *only* the passive technique, thereby greatly simplifying mission operations.

The TOPEX/Poseidon mission has been uniquely maintained utilizing a combination of both active (e.g., propulsive) and passive (e.g., non-propulsive) maneuvers. This paper describes the maneuver design and implementation strategies used for orbit maintenance in the presence of the anomalous force during the first five years of satellite operations. Maneuver performance characteristics and ground track maintenance statistics are provided. Use of the passive techniques in reducing the number of maneuvers and complexity of the mission operations are summarized.

## MISSION REQUIREMENTS AND OPERATIONAL CONSTRAINTS<sup>6</sup>

Science objectives require that 95% of all equatorial crossings be contained within a  $\pm 1$  km control band centered on a pre-defined earth-fixed reference ground track grid, and that 95% of all verification site over flights have a miss distance at closest approach of  $< 1$  km. The OMMs are constrained to occur over land at or near the boundary of the  $\approx 10$  day ground track repeat cycles ( $\pm 1$  orbit). Maneuver spacing must be as large as practical, with a minimum spacing of 30 days. Eccentricity must be maintained less than 0.001 throughout the mission; this requirement has been met by utilizing a frozen-orbit for the eccentricity vector ( $e, \omega$ ). Furthermore, maneuvers may not compromise satellite health and welfare; such requirements prevail over other mission requirements when conflicts arise. This leads to additional restrictions on the timing of maneuvers and the command sequence for maneuver implementation. The primary restrictions are due to satellite power, thermal, and star-tracker field-of-view constraints.

## REFERENCE ORBIT

Mean orbital parameters<sup>7</sup> of the TOPEX/Poseidon operational orbit are shown in Table 1. This operational orbit provides an exact repeat ground track every 127 orbits in 10 sidereal days and over flies both the NASA and CNES verification sites once per repeat cycle. The first orbit of the 127-orbit ground

<sup>\*</sup>  $F_{10.7}$  is the 10.7 cm solar flux reported by the Penticton Dominion Radio Observatory. Units are  $10^{-22}$  watts/(m<sup>2</sup>-Hz).



track repeat cycle has an ascending node at  $99.92^\circ$  E. longitude. The operational orbit is referred to as the *reference orbit* and the mean elements describing this orbit are called the *reference elements*. The ascending nodal crossing longitudes of the *reference orbit* define the sub-satellite earth fixed *reference grid*. The *reference orbit* was initially designed<sup>8</sup> using a  $17 \times 17$  truncation of the GEMT2 earth gravity field and was later refined using a  $20 \times 20$  truncation of GEMT3. This orbit was again refined using a  $20 \times 20$  truncated JGM2 (Joint Gravity Model-2)<sup>9</sup> during July 93. The JGM2 was derived by refining GEMT3 using TOPEX/Poseidon precision orbit determination (POD) results.

Table 1. TOPEX/POSEIDON REFERENCE ELEMENTS (EPOCH: JULY 1, 1993 00:00 UTC).

Semi-Major Axis ( $a$ )	7714.42942 km
Eccentricity ( $e$ )	0.000095
Inclination ( $i$ )	$66.040^\circ$
Right Ascension of Ascending Node ( $\Omega$ )	$139.552^\circ$
Argument of Perigee ( $\omega$ )	$270.000^\circ$
Mean Anomaly ( $M$ )	$0.000^\circ$

## SATELLITE CHARACTERISTICS

TOPEX/Poseidon is a three-axis stabilized satellite (Fig.1) and utilizes nearly continuous yaw steering and solar array pitching for optimal solar array sun pointing. A pitch bias  $\psi$  is applied to the solar array to control battery charging, and is changed based on solar-array degradation and observed battery performance. It has changed three times during the first five years of operation; currently  $\psi=50.5^\circ$ . There is a plan to set  $\psi=48.5^\circ$  in April 1998. The satellite nominally flies with the solar panel in a "Lead" position ( $\psi>0$ ). The solar panel is said to be in a "Lag" position when  $\psi<0$ .

To avoid excessive yaw rates, the satellite yaw angle is held fixed when  $-15^\circ < \beta' < 15^\circ$ , where  $\beta'$  is the angle between the orbital plane and earth-sun line. Two different fixed yaw angles  $Y$  are used:  $Y=0^\circ$  when  $0 < \beta' < 15^\circ$  (*flying forward*); and  $Y=180^\circ$  when  $\beta' < 0$  (*flying backward*). The satellite is "flipped" ( $\Delta Y=180^\circ$ ) near  $\beta'=0$ . This ensures that the sun is kept on the correct side of the solar array, avoids shadowing of the solar array by the high gain antenna, and prevents overheating of satellite subsystems. The satellite is continuously yaw steered for all other values of  $\beta'$ . When  $\beta' > 15^\circ$  this is referred to as *positive yaw steering*, and when  $\beta' < -15^\circ$  it is referred to as *negative yaw steering*.

The propulsion module is a mono-propellant hydrazine blow-down system consisting of twelve 1 N (0.2 lbf) and four 22 N (5 lbf) thrusters. The 22 N thrusters and four of the 1 N thrusters are used for orbit adjustment; the remaining 1 N thrusters are used for attitude control when required to dump excess

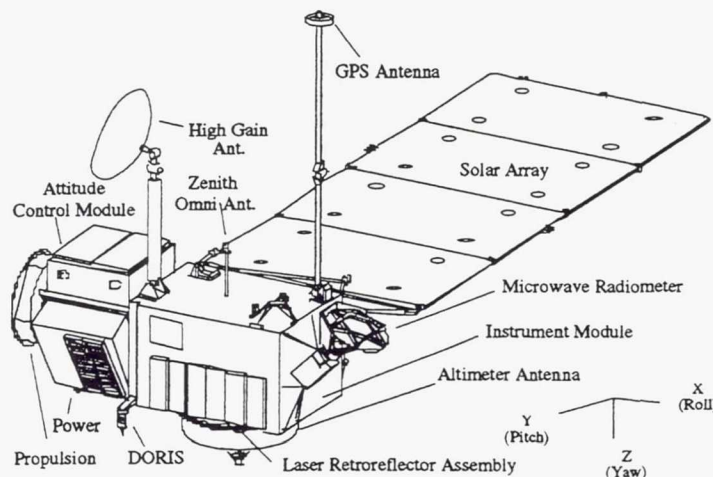


Figure 1. TOPEX/Poseidon satellite.

momentum. Nominal attitude control is maintained via reaction wheels which are unloaded with magnetic torquers. The 22 N thrusters were used for large maneuvers ( $> 400$  mm/s) during orbit acquisition.<sup>1</sup> The smaller maneuvers ( $< 400$  mm/s) of the orbit acquisition sequence and all orbit maintenance maneuvers, which are  $< 10$  mm/s, are performed using two 1 N thrusters. The same pair of thrusters has been used for all nine OMMs. The center of mass (CM) of the satellite does not coincide with the center of body coordinates due to one sided large solar panel. Each



of the orbit adjust thrusters is oriented axially along the body roll-axis and individually canted to be aligned through the CM prior to the launch when the propellant tanks are full. The propellant tank was fully loaded prior to the launch to provide a total  $\Delta V$  of  $\approx 172$  m/s. The orbit acquisition process used only  $\approx 11.55$  m/s and the nine OMMs have used  $\approx 40$  mm/s. Thus the satellite is still flying with nearly full propellant tanks after five years of operations.

To correctly orient the thrusters along with the velocity vector for propulsive maneuvers, yaw steering is temporarily suspended and the satellite is slewed to a fixed angle.<sup>1</sup> The yaw turn is accomplished using only reaction wheels. Attitude errors caused by the burn are removed with attitude thrusters. The turn or unwind duration varies depending on the yaw rate and angle. The total duration of a "turn-burn-turn" sequence varies from 20 to 90 min.

## ORBIT DETERMINATION

Operational orbit determination is routinely performed by the FDF, primarily using one-way TDRS Doppler data; a small amount of two-way Doppler data is also used.<sup>10</sup> The orbit determination accuracy required for the orbit maintenance and maneuver evaluation was established jointly by JPL and FDF.<sup>11</sup> Modeling consistency between the FDF orbit determination program GTDS (Goddard Trajectory Determination System)<sup>12</sup> and the JPL trajectory program DPTRAJ<sup>13</sup> (double precision trajectory program) was established prior to the launch.<sup>14</sup> The critical requirement on orbit determination is to determine semi-major axis better than 1 m ( $3\sigma$ ) throughout the mission.

The FDF supplies orbit determination results three times weekly (Monday, Wednesday, and Friday) and daily near maneuver and fixed yaw periods. The anomalous forces are estimated as an effective thrust  $T=1+\tau$   $\mu$ N as part of routine orbit determination. Onboard oscillator frequency bias and drift rate are also estimated during orbit determination.

Timing and polar motion data tables (UT1-UTC and polar coordinates) are provided by FDF approximately monthly. Variable Mean Area (VMA)<sup>2</sup> models used for atmospheric drag and solar radiation pressure are supplied by JPL to FDF. The VMA model is a function of the solar array pitch bias and is updated whenever the solar array pitch bias is changed. Furthermore, JPL supplies a fixed yaw plan to the FDF prior to any mode changes so that the appropriate models are used for OD. Current solar and geomagnetic activity data are obtained electronically from the National Oceanic and Atmospheric Administration (NOAA) Space Environment Center by both JPL and FDF. NOAA supplies observed and predicted data including a long-term outlook. Changes in other models (e.g., gravity, sun-moon ephemerides, etc.) are performed mutually as required.

OD results<sup>15-21</sup> have been consistently better than pre-launch requirements. The semi-major axis  $a$  has been determined to  $3\sigma_a \approx 45$  cm (required:  $3\sigma_a = 1$  m). Knowledge of  $a$  is a function of both OD accuracy and conversion errors in the osculating to mean value conversion process. The osculating to mean value conversion error for  $a$  consistently satisfies  $3\sigma_a < 40$  cm. Thus the total  $\sigma_a < 20$  cm for the mean semi-major axis. Knowledge of other orbital parameters is also much better than the specified pre-launch requirements. These improved OD results have contributed to a reduction in maneuver frequency and more precise ground track determination and control.

## ERROR MODEL USED FOR MANEUVER DESIGN

All major error sources are included in the maneuver design process to ensure that 95% of all equatorial crossings are contained in the control band. These include uncertainties of the anomalous force and drag predictions, orbit determination errors, and maneuver execution errors. Drag modeling error is dominated by uncertainties in predicted solar activity. Maneuver execution errors are categorized into fixed, proportional, and pointing errors. Orbit determination error is reflected primarily as an error in semi-major axis.

Solar activity data of previous cycles was used to construct error models for solar flux and geomagnetic index data prediction.<sup>22</sup> High- and low-density trajectories are constructed based on the observed statistical variations over the previous 3 months and the resulting differences in the ground track with the

error-free trajectory are used to calculate the drag error. The uncertainty in the anomalous force prediction is modeled from the observed statistical variations about the empirical model. Different uncertainty models are constructed for different yaw modes of the satellite. The ground track prediction error allocated to orbit determination is 225 m ( $3\sigma$ ) of equatorial longitude after 30 days, equivalent to an initial semi-major axis error of  $\approx 1$  m. Maneuver execution error budgets<sup>23</sup> are summarized in Table 2. These error budgets were used for all OMMs. The errors due to drag and anomalous force predictions, orbit determination, and maneuver execution are propagated, converted into ground track units, and then combined to predict a total root sum square (RSS) error envelope in the ground track.<sup>24</sup>

Table 2. MANEUVER ERROR MODEL.\*

$\Delta V$ (Proportional)	10% for CAL 5% for OMM 1 3% for Subsequent OMMs
$\Delta V$ (Fixed)	0.013 mm/s.
Pointing Error (Pitch)	2.0°
Pointing Error (Yaw)	2.0°

\*All values are  $3\sigma$ . CAL: Calibration maneuver. OMM=Orbit Maintenance Maneuver.

Table 3. OMM EVALUATION REQUIREMENTS.\*

$a$	< 1 m
$e$	< $5 \times 10^{-6}$
$i$	0.0001°
$\Delta a$	< 20 cm
$\Delta V$ Tangential	< 0.2 mm/s
Radial	< 10 mm/sec
Out of plane	< 10 mm/sec

\*All values are  $3\sigma$ . Elements are osculating.

## MANEUVER EVALUATION REQUIREMENT

Precise maneuver evaluation is required to calibrate the thrusters so as to reduce the effect of  $\Delta V$  errors on ground track predictions and to enhance maneuver spacing. The maneuver evaluation accuracy requirements were jointly determined by JPL and FDF, as summarized in Table 3.<sup>25</sup> To achieve the required accuracy in maneuver evaluation the FDF performs special ODs before and after a maneuver using a  $26 \times 26$  gravity field and a four day tracking arc.

## MANEUVER DESIGN AND IMPLEMENTATION

The NAVT\* continually monitors the ground track and provides a 30-day advance notice of all maneuvers to other mission operations teams, including geographic maneuver location and centroid time. The maneuver centroid time is chosen to allow time for a backup one repeat cycle ( $\approx 10$  days) later without violating the km control band. Furthermore, maneuvers are not scheduled near a fixed yaw period so that there is sufficient pre- and post-maneuver tracking data (at least 7 days) for orbit determination. This shortens maneuver spacing by one to two repeat cycles from the optimal value. The preliminary maneuver design is done using GTARG (which uses an analytical propagator) to determine maneuver magnitude ( $\Delta V$ ) and its direction.<sup>24</sup> Two maneuver design strategies were developed prior to launch:<sup>1</sup> (a) *longitude targeting*, which practically maximizes maneuver spacing, and (b) *time targeting*, which fixes the maneuver spacing. All maneuvers implemented so far were designed using the *longitude targeting* strategy. To ensure maneuver spacing as large as practical in the presence of various error sources, every maneuver was designed using a 95-percentile confidence envelope about the ground track.

Under low drag conditions ( $F_{10.7} < 120$ )\*\* the ground track prediction is very sensitive to small variations in  $\Delta V$ . The uncertainty of the anomalous force causes significant variations in the predicted ground track (and hence the maneuver spacing) under these conditions. To ensure verification site over flight requirements, as well as enhance maneuver spacing, a "shoot-short" strategy<sup>26</sup> is applied in maneuver design. In this strategy the targeted maneuver magnitude is updated based on a detailed sensitivity analysis conducted using both GTARG and DPTRAJ.

\* The TOPEX/Poseidon Navigation Team.

\*\* See the footnote on page 2.



The preliminary maneuver design is verified and updated (if needed) with DPTRAJ before generating and delivering the ideal maneuver parameters, consisting of maneuver centroid time and  $\Delta V$ , to SPAT.<sup>†</sup> SPAT generates the maneuver commands, which may result in a slightly different maneuver magnitude or centroid time due to thruster pulse quantization and on-board computer (OBC) constraints. These updated values are verified again using DPTRAJ before they are loaded into the satellite OBC. The maneuver is normally designed seven to ten days in advance to provide sufficient time for command preparation and TDRS scheduling. The maneuver magnitude is then "tweaked," whenever needed, 8-24 hours before execution using the latest OD.<sup>26</sup>

Only nine maneuvers have been required during the first five years of operations. These OMMs all occurred within one orbit of the transition between the  $\approx 10$  day ground track repeat cycles, and were implemented using a complex "turn-burn-turn" sequence. The geographic location of the maneuver has been selected to accommodate satellite star-tracker field-of-view constraints, thermal constraints, and available TDRS view periods. (Fig. 2). Two maneuvers (OMM6 and OMM9) were performed over water because of these constraints, in conflict with scientific requirements.

## MANEUVER PERFORMANCE

The frequency of maneuvers has been significantly lower than expected because of the use of the passive technique, the prevailing low drag, improved OD (compared to requirements) from FDF, better than predicted satellite performance, and precise maneuver evaluation. The maneuver magnitude for all maneuvers was in the range of 2-5 mm/s, except OMM1. The OMM1  $\Delta V$  was somewhat higher as it absorbed some of the residual ground track drift following operational orbit acquisition.

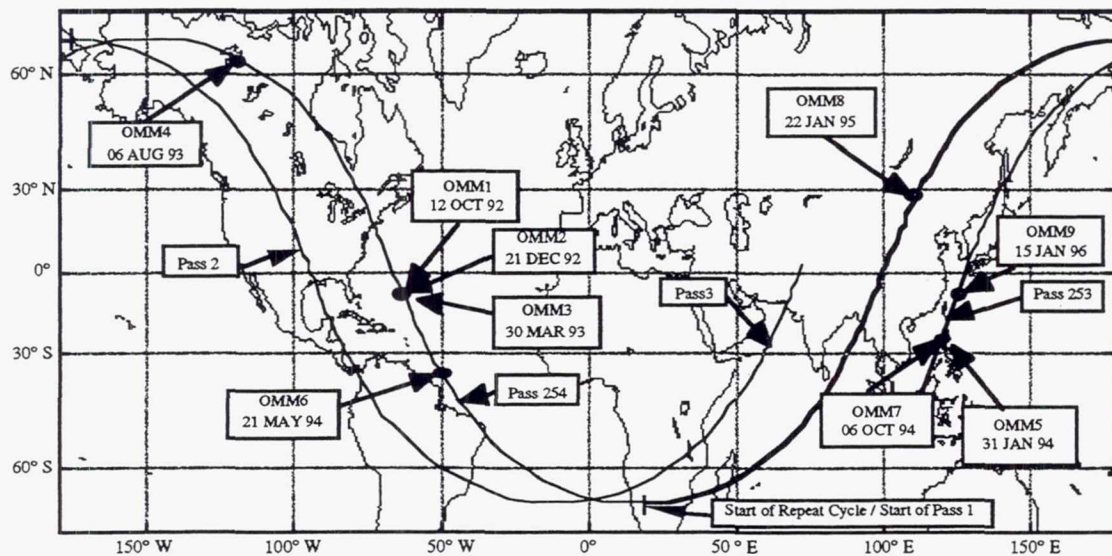


Figure 2. Geographic locations of orbit maintenance maneuvers.

Maneuver evaluation is based upon a comparison of pre- and post-maneuver OD. JPL and FDF each independently evaluate the magnitude of each maneuver using different techniques.<sup>2</sup> Both results have agreed to within 0.03 mm/s for all maneuvers<sup>27</sup> (Table 4). The close agreement between the JPL and FDF results provide greater confidence in maneuver evaluation. The accuracy of maneuver magnitude determination has been better than 0.05 mm/s for all maneuvers based on the analyses of post maneuver orbit determination and the resulting ground track behavior. The performance of all maneuvers except OMM9 was significantly better than the pre-launch expected performances. The performance of OMM1 was  $\approx 3.6\%$  and the thrusters were calibrated using this maneuver. Subsequent maneuvers (except for

<sup>†</sup> The TOPEX/Poseidon Satellite Performance and Analysis Team.



OMM9) showed better than 3% performance. The resultant  $\Delta V$  of OMM9 was 46% higher due to unexpected attitude thruster firings during the "unwind" turn (turn after burn) of the satellite.

The presence of the anomalous force significantly altered the orbit determination strategy for maneuver evaluation. Pre- and post-maneuver ODs utilize 4-day tracking arcs. Initially (through OMM5) the thrust parameter representing the anomalous force was estimated along with state parameters. Experience (corroborated by both the JPL and FDF techniques) indicated that a minimum duration 6-day tracking arc is needed to obtain sufficiently accurate estimates of the anomalous force; shorter arcs corrupt estimates of  $a$ . To obtain a more reliable  $\Delta V$  value, the anomalous force parameter is not estimated using short arcs (< 6-day), but instead use an *a priori* value based on the latest prediction model. This strategy has been used for subsequent pre- and post-maneuver orbit determinations, and a similar strategy is used for OD near fixed yaw periods. The maneuver evaluation accuracy improved further with this strategy. Pointing errors were all <1° in both pitch and yaw.<sup>27</sup>

Table 4. MANEUVER PERFORMANCE.

OMM #	Date	$\Delta V$ , mm/sec	$\Delta V$ achieved, mm/sec		Difference, % Achieved-Ideal
		Ideal	JPL	FDF	
1	Oct 12, 92	9.100	9.431	9.425	+3.64
2	Dec 21, 92	3.200	3.153	3.151	-1.47
3	Mar 30, 93	4.640	4.692	4.688	+1.12
4	Aug 6, 93	4.620	4.611	4.611	-0.20
5	Jan 31, 94	4.000	4.089	4.065	+2.25
6	May 20, 94	3.150	3.123	3.128	-0.78
7	Oct 6, 94	3.150	3.146	3.162	-0.13
8	May 22, 95	3.860	3.832	3.832	-0.73
9	Jan 15, 96	2.500	3.652	Not Requested	+46.08

## ANOMALOUS FORCE

Analysis of the OD results subsequent to launch indicated the existence of an unmodeled anomalous force.<sup>3</sup> The magnitude of this anomalous force is equivalent to that of a continuous thrust of a few micro-Newtons ( $\mu\text{N}$ ). This force is believed to arise from a combination of radiative forces (including reflected radiation), solar array curling, thermal imbalances, and outgassing. The direction and magnitude are a function of the satellite attitude, solar array pitch angle offset, and  $\beta'$ . An empirical model (Fig. 3) was developed based on observations of unmodeled along-track accelerations.

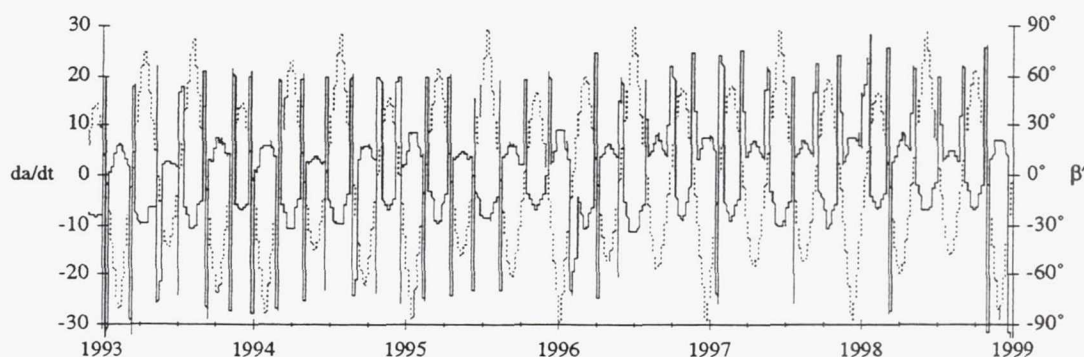


Figure 3. Change of  $a$  due to Anomalous Force. Solid line:  $da/dt$ , cm/day (left scale); Dotted Line:  $\beta'$  (right scale).

The anomalous force causes a decay during positive yaw steering and when *flying backward* at fixed 180° yaw mode, and causes a boost during negative yaw steering and when *flying forward* at fixed 0° yaw mode (Fig. 3). The anomalous force results in  $da/dt \approx 3$ -12 cm/day during yaw steering and  $\approx 18$ -30 cm/day

during fixed yaw. The magnitude of the acceleration varies with  $\psi$ ,  $\beta'$ , the earth to sun distance, and thermal variations of the solar panel and some parts of the satellite bus. The uncertainty in anomalous force prediction has been  $\sigma \approx 1$  to 3 cm/day during yaw steering and  $\sigma \approx 1$  to 4 cm/day during fixed yaw.<sup>4,5</sup> The relative prediction uncertainty  $|\sigma/(da/dt)|$  is consistently smaller in fixed yaw than in yaw steering.

## PASSIVE TECHNIQUES FOR ORBIT MAINTENANCE

Two passive techniques were developed utilizing the anomalous force during fixed yaw for orbit maintenance.

### Fixed Yaw Variation Strategy

Nominally, the length of *flying forward* or *flying backward* is around five days. The orbit may be raised or lowered by varying the nominal duration of fixed yaw periods. The fixed  $Y=0^\circ$  period is increased and the fixed  $Y=180^\circ$  yaw period is shortened to apply orbital boost and the opposite is done to apply decay. The maximum variation that is allowed is limited by satellite health and safety considerations to require a switch between fixed yaw and yaw steering (or *vice versa*). The current guideline (at  $\psi=50.5^\circ$ ) is that fixed yaw period can be as short as  $-13^\circ \leq \beta' \leq 13^\circ$  or as long as  $-26^\circ \leq \beta' \leq 27^\circ$ . The upper limit of a fixed yaw period varies with time of year and solar array degradation. The yaw flip ( $\Delta Y=180^\circ$ ) must be performed near  $\beta' = 0$  during all fixed yaw periods. Even with this constraint the orbit may be raised or lowered up to  $\approx 1.5$  m during a typical fixed yaw period. This strategy was been used to selectively adjust the ground track from OMM3 (March 1993) through October 1995. This strategy was also used to avoid a "micro-maneuver" (around June 17, 1993) near the west boundary of the control band.<sup>4</sup>

### Solar Array Lead/Lag Strategy

The second passive method makes use of the fact that there is a large decay while *flying backward* and a large boost *flying forward*. The satellite normally flies with solar array in Lead position (pitch bias is positive). A positive pitch bias ("Lead Angle,"  $\psi > 0$ ) indicates that the solar array normal is ahead of the sun direction. Utilization of negative pitch bias ("Lag,"  $\psi < 0$ ) reverses the direction of the force and the anomalous force causes boost when the satellite is *flying backward* and decay when *flying forward*. A continuous boost can be obtained by using a "Lag" when *flying backward* and "Lead" when *flying forward* (Fig. 4); or a continuous decay can be obtained by using a Lag angle when *flying forward* and a Lead angle when *flying backward*. This technique is summarized in Table 5. In addition, fixed yaw  $\beta'$  limits are varied to apply extra boost or decay. The orbit may be raised or lowered up to  $\approx 4$  m, equivalent to propulsive maneuvers of up to  $\approx 2$  mm/s, with this technique. This "Lead/Lag" strategy<sup>5</sup> was used for the first time during the October 1995 fixed yaw period to increase the semi-major axis and postpone OMM9 to January 15, 1996. Reversing the solar array orientation (Lead to Lag) for a smaller portion of  $180^\circ$  or  $0^\circ$  yaw part of a fixed yaw period is called a "partial Lead/Lag strategy." The partial Lead/Lag strategy has been used to apply a desired amount of either orbital boost or decay. A partial Lead/Lag strategy was first applied during the March/April 1996 fixed yaw period to increase the inter-maneuver spacing.

Table 5. TERMINOLOGY AND ORIENTATION OF ALONG-TRACK FORCE IN FIXED YAW.

Fixed Yaw Angle	Solar Array "Lead" ( $\psi > 0$ )	"Lag" ( $\psi < 0$ )
$0^\circ$ "Flying Forwards"	$da/dt > 0$ ("boost")	$da/dt < 0$ ("decay")
$180^\circ$ "Flying Backwards"	$da/dt < 0$ ("decay")	$da/dt > 0$ ("boost")

The very first experience during October 1995 demonstrated the power of the Lead/Lag strategy to effectively control ground track. In a fixed yaw variation strategy, the limits of fixed  $180^\circ$  and  $0^\circ$  yaw periods are varied within the maximum allowable  $\beta'$  limits to apply the desired additional orbital boost or decay. These limits need can not be finalized a few days before the beginning of a fixed yaw period because of uncertainties in the anomalous force, violating normal mission planning constraints which require 30 days advance notice. However, with the development of the partial Lead/Lag strategy this problem was eliminated, as the fixed yaw limits can be determined several months in advance. Ground track uncertainty is absorbed by changing the times of Lead to Lag and/or Lag to Lead switch, which can be accomplished by real time commands.



## APPLICATION OF PASSIVE MANEUVERS FOR ORBIT MAINTENANCE

The solar array Lead/Lag strategy<sup>5</sup> was used during the October 1995 fixed yaw period to postpone OMM9 until the middle of January 1996. The observed boost level during the Lag period (fixed 180° yaw) was only 75% of the expected boost. This unexplained discrepancy was used to recalibrate the model.

The satellite entered safehold\* on November 26, 1995, two days before a fixed yaw period was scheduled to begin. The recovery process took several days and the satellite remained in safehold mode throughout the period during which the fixed yaw angle is normally 0° and 10 hours into the period when the fixed yaw is 180°. The postponement of OMM9 to January 15, 1996 was accomplished by (1) reducing the solar array pitch bias† from 54° to 50.5°, (2) applying Lead/Lag strategy while flying backward during fixed 180° yaw period, and (3) extending the fixed 180° yaw period duration to the maximum allowable value.

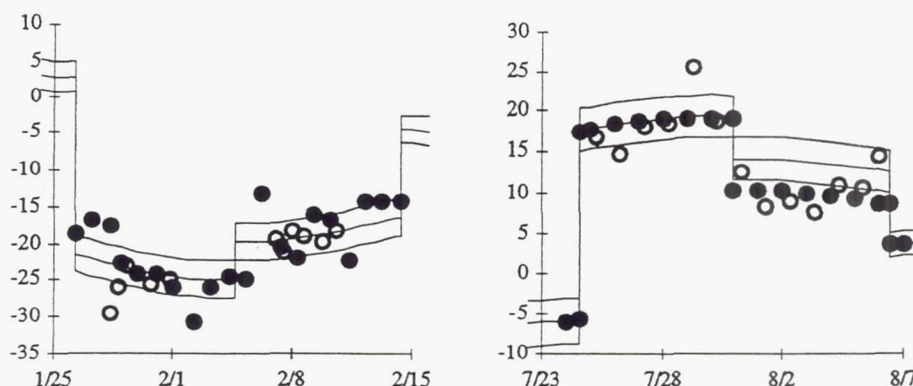


Figure 4. Variation of orbital lead/lag strategy to obtain optimal semi-major axis control. Abscissas give date in 1996; ordinates give  $da/dt$  due to the anomalous force in cm/day. Filled Circles: MOE Data; Hollow circles: FDF Data; Left: Orbit lowering when  $\beta' > 0$ . Right: Orbit raising when  $\beta' < 0$ . Solid lines: predicted  $da/dt \pm 95\%$ .

The resultant  $\Delta V$  of OMM9 was 46% higher (3.623 mm/s) due to unexpected attitude thruster firing during the "unwind." This resulted in a predicted ground trace<sup>6</sup> that would cross the western boundary of the control band during the last week of February 1996. This situation meant that a retrograde OMM would need to be implemented near the western boundary. This retrograde maneuver was avoided by lowering the orbit using lag during the January/February 1996 fixed yaw period.

As a demonstration for future missions, an autonomous maneuver experiment (TAME) was planned for the summer of 1996 using TOPEX/Poseidon. The NAVT was responsible for targeting the pre-maneuver orbit, including the ground track, so that TAME could occur on a specific date with a specified minimum  $\Delta V \geq 1.34$  mm/sec, yet still meet all established ground track requirements and operational constraints. It was decided to achieve the required pre-TAME conditions utilizing Lead/Lag strategies only. The objective was to avoid, if possible, the use of any propulsive maneuvers prior to TAME.<sup>6</sup> The maneuver was designed using the minimum  $\Delta V$  because of the prevailing low drag conditions. The TAME, originally scheduled for April 6, 1997, was postponed three times due to unexpected technical problems before finally being scheduled for December 19, 1997. However, during last week November 1997, the Project elected to postpone TAME indefinitely to avoid the possible loss of valuable altimeter data related to studying the El Niño conditions.

Currently, the satellite orbit/ground track is maintained using only passive techniques. The 81-day mean solar flux has been steadily increasing since November 1997 and currently the average flux varies

\* An autonomous on-board safing mode controlled by analog electronics and triggered by anomaly detection software in the OBC.

† This was done for power reasons; however, the magnitude of the boost in fixed yaw increases with decreasing yaw angle.



between 90 and 145.\* It is expected that uncertainties in solar flux prediction will become a significantly larger factor in the ground track prediction accuracy as the solar maximum is approached. Until then it is intended to maintain orbit control using only passive techniques as long as practically feasible. No propulsive maneuver is expected until mid-1999.

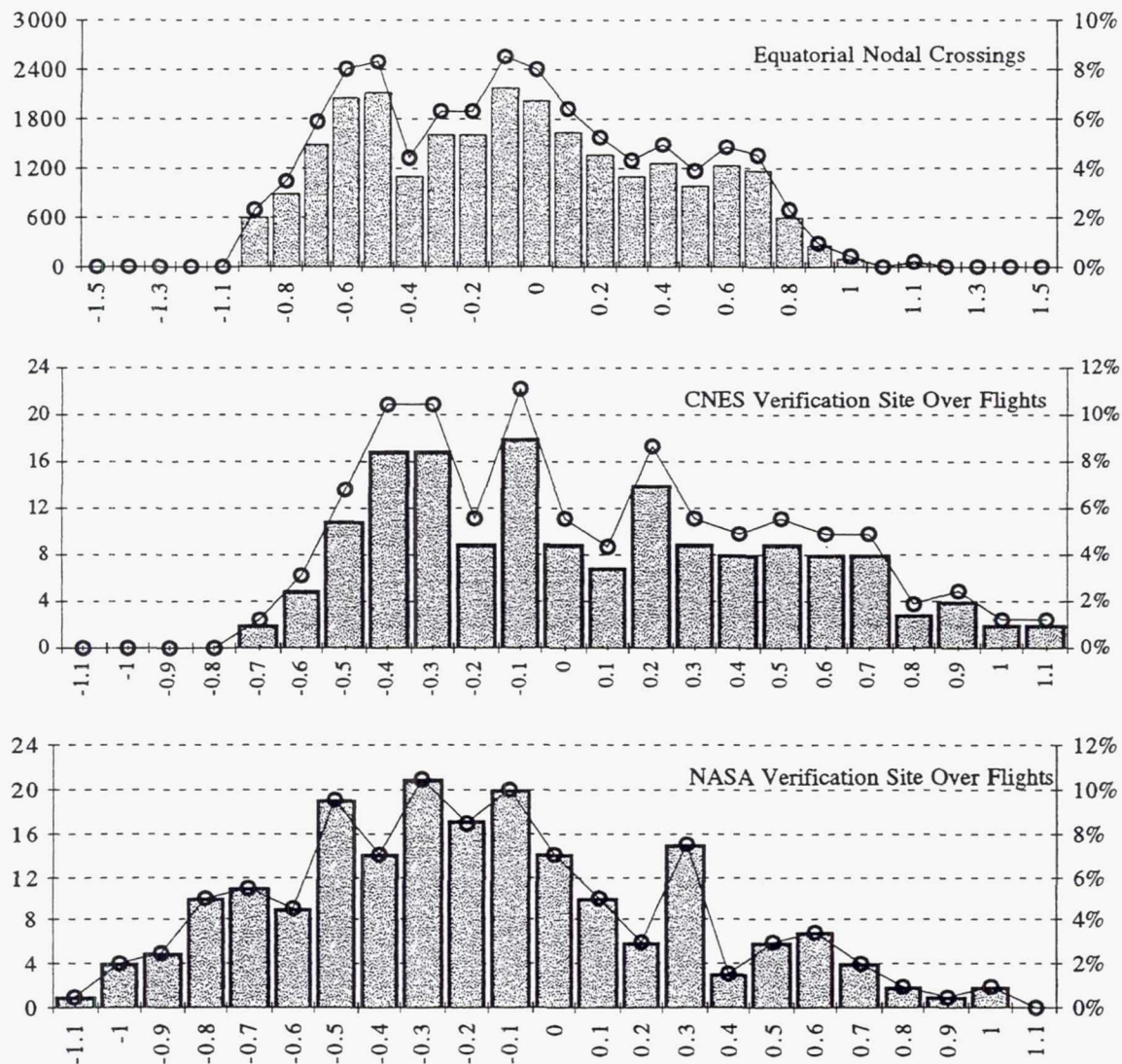


Figure 5. Ground track maintenance statistics. Left ordinates: absolute number of crossings or over flights (bars). Right Ordinate: percentages (lines). Abscissas: ground track in kilometers.

## GROUND TRACK MAINTENANCE STATISTICS

As of February 28, 1998 TOPEX/Poseidon had completed 200 ground track repeat cycles in the operational orbit. A total of 99.63% of all equatorial crossings (25,422 crossings) were within the control band of  $\pm 1$  km, comfortably meeting mission requirements (95% within the control band), even in presence of the anomalous force. Only 95 nodal crossings were outside the control band, and these all occurred at the very beginning of the operational mission. Cycle 1 was defined to begin at the end of the orbit acquisition process, three days before the ground track entered the control band, and the ground track was allowed to move outside the control band before implementing OMM1 to allow more time to develop

\* See the footnote on page 2.

an empirical model for the anomalous force. Nearly 70% of the nodal crossings were west of the reference track (Fig. 5).

Fig. 6 shows the ground track history of the satellite. Distinct and important features in the ground track behavior are the periodic variations near the western boundary of the control band. These periodic variations are due to lunar and solar gravity and its influence on the ground track is distinguishable when the semi-major axis is within  $\pm 2$  m of the reference value. However, the precise nature of the variation depends on a complex combination of lunar and solar gravity, anomalous forces, and atmospheric drag. The solar activity has been relatively low ( $70 < F_{10.7} < 120$ )<sup>\*</sup> during last five years. As a result, the influence of lunar and solar gravity has become more prominent.

#### VERIFICATION SITE OVER FLIGHTS

The original mission requirement was to maintain the NASA and CNES verification site over flights within  $\pm 1$  km during the first six months of operations only (the "Initial Verification Phase"), but not later. However, this requirement was extended to continue throughout the mission. The closeness of the ground track to the verification site depends on the nodal crossing longitude and the mean inclination, which varies ( $\pm 3.5$  mdeg) due to lunar and solar gravity. A 1 mdeg variation in mean inclination causes a 70 m ground track offset at either verification site. The verification site over flight control requirement has been taken into account in the design of all orbit maintenance maneuvers. Histograms of verification site over flights are shown in the bottom two plots of Fig. 5. The CNES site was closed on February 1, 1997 and its over flight requirement was discontinued at that time; the NASA site remains in use and its over flight requirement continues to be met.

The control requirements were met for all verification site over flights except five NASA and two CNES site over flights. One NASA over flight miss was voluntary, at the beginning of first ground track repeat cycle. Three involuntary over flight misses occurred during March/April 1996 and one during May 1996. These violations were due to unfavorable inclination variations when the ground track was near the western boundary (within 150 m). Two CNES site over flights were outside the control band: one in September 1996 and the other in January 1997. During this time the effect of lunar and solar gravity was unfavorable on the inclination and the ground track was near the eastern boundary (Fig. 6). However, the mission requirement to keep 95% of all verification site over flights within the control band has been comfortably met for both the NASA and CNES sites.

#### ORBITAL PARAMETERS

The ground track is maintained by controlling mean semi-major axis about the reference value (7714.429 km) through periodic maneuvers or controlling its variations by passive techniques. While maintaining the ground track and verification site over flights within the  $\pm 1$  km control band, the mean semi-major axis has been controlled within  $\pm 7$  m of the reference value through five years of operation<sup>15</sup> (Fig. 7). The mean semi-major axis variations are due to a combination of atmospheric drag and the anomalous force.

The semi-major axis is raised above the reference after each maneuver and slowly decreases due to drag. The semi-major axis decreases rapidly during positive yaw steering as both the anomalous force and drag contribute to decay, whereas the semi-major axis variation during negative yaw steering period is much slower and near zero at times as the anomalous force and drag oppose each other. The semi-major axis varies by a larger amount during fixed yaw than yaw steering, and is four to seven times the effect of atmospheric drag. The semi-major axis variation has been controlled utilizing the solar array Lead/Lag strategy since OMM9 (January 15, 1996) and has stayed within  $\pm 3$  m of the reference since then (Fig. 7).

The mission requirement to keep the eccentricity within 0.001 has been easily met without implementing dedicated eccentricity maneuvers since achieving the operational orbit. The selection of a frozen orbit assured that the mean eccentricity remained an order of magnitude smaller than the mission requirement. The eccentricity has varied within the range  $95 \pm 50$  PPM<sup>\*</sup> (Fig. 8) throughout the mission. The eccentricity vector subject to only gravitational perturbations would follow a closed loop with a period

---

<sup>\*</sup> Parts Per Million.



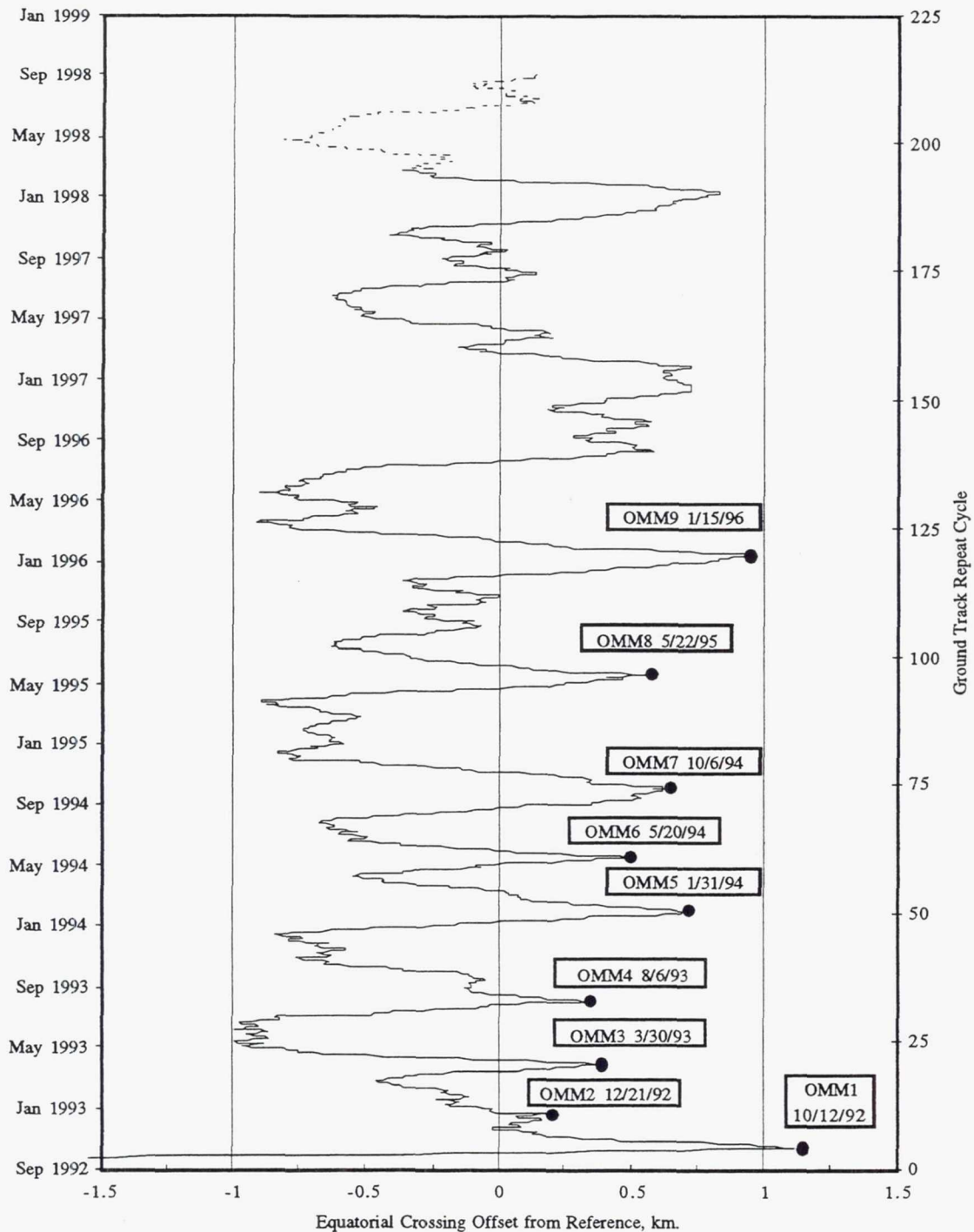


Figure 6. TOPEX/Poseidon ground track. A positive abscissa indicates an offset to the east; a negative abscissa an offset to the west. The dashed segment is the predicted continuation of the ground track at the time of publication.

of  $\approx 26.74$  months; it has completed two such loops during the mission and is currently tracing the third loop. The observed eccentricity vector varies from the loop because of (a) solar radiation pressure, drag, and anomalous forces; (b) discontinuous jumps due to propulsive maneuvers; and (c) the inherent uncertainty in the osculating to mean element conversion process and determination of the perigee for a nearly circular



orbit. The variation of argument of perigee ( $\omega$ ) has been relatively large, as expected, varying between 48 and 120°. The variation of  $\omega$  within a single ground track repeat cycle ( $\approx 10$  days) is as large as 15°.

The inclination remained within a  $\pm 4$  mdeg band (Fig. 9). No inclination maneuvers have been required. There are several periodic perturbations in  $i$ , mostly due to lunar and solar gravity, including one  $\approx 9.5$  year component. Inclination variations are strongly correlated with  $\beta'$ . The peak amplitude of the inclination variation synchronizes with the peak values of  $\beta'$  during periods of full sun. The ground track variation near the western boundary is also strongly correlated with the inclination variation.

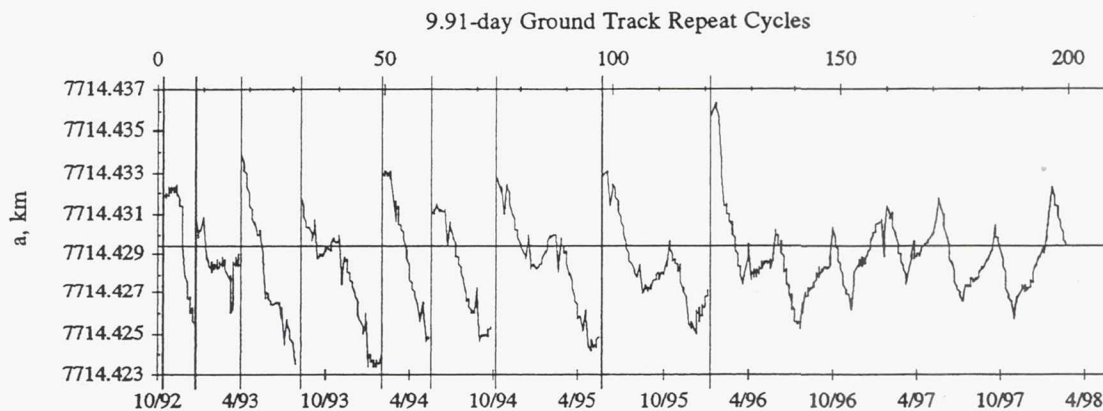


Figure 7. Mean semi-major axis,  $a$ . Vertical lines indicate maneuvers (see tab. 4). The horizontal line indicates the reference semi-major axis of 7714.42938 km.

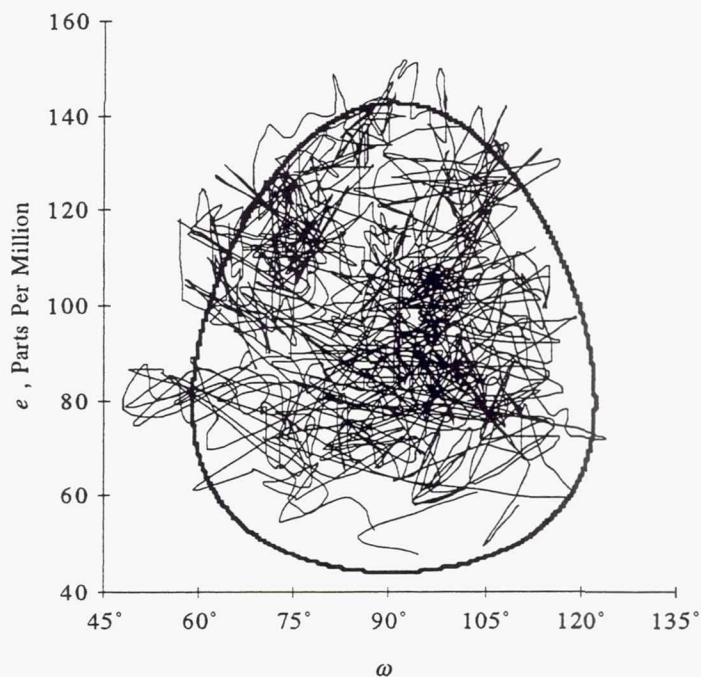


Figure 8. Observed eccentricity vector ( $e$ ,  $\omega$ ) (thin line) and gravity-only frozen orbit (heavy line).

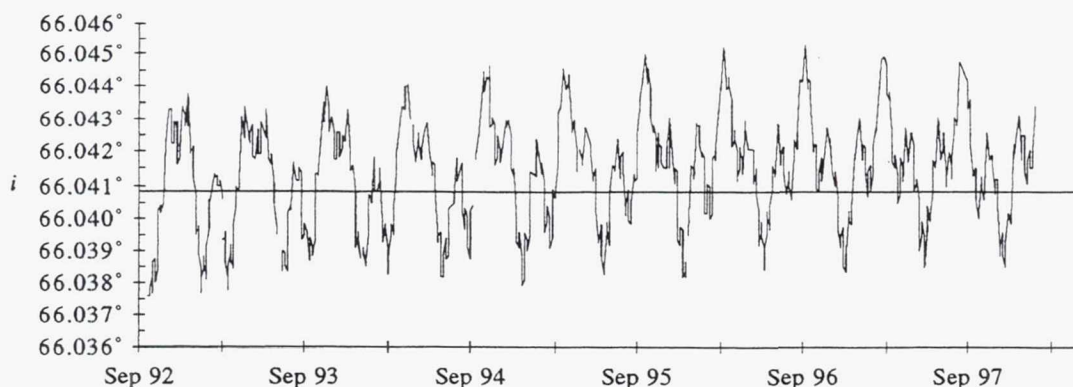


Fig. 9. Observed mean inclination. The indicated reference (horizontal line) is at  $i=66.0408^\circ$ .

## CONCLUSION

TOPEX/Poseidon orbit maintenance maneuver design, originally expected to depend primarily on effective predictions of atmospheric drag, also depends on reliable predictions of the anomalous force during the current period of low solar activity. These forces constitute the largest uncertainty to ground track prediction and maneuver design. Although the force is continuous, it causes significantly larger orbital boost or decay levels (18-30 cm/day) during fixed yaw periods. This property of the anomalous force has been used to develop a so-called "passive" maneuver technique (the "Lead/Lag" strategy) to effectively control the TOPEX/Poseidon orbit and ground track. This technique can be used to perform "passive" micro-maneuvers that raise or lower the orbit by up to 4 meters, equivalent to propulsive maneuvers of 1-2 mm/s. In fact, it was possible to avoid a retrograde maneuver near the western boundary of the control band during February 1996 using this strategy. It has also been demonstrated that the orbit can be maintained using *only* the passive techniques for a long time ( $> 2$  years) under low drag conditions. Thus these passive techniques have eliminated the need for several propulsive maneuvers for the TOPEX/Poseidon mission.

When propulsive maneuvers were required, their performances surpassed requirements in all areas, and all aspects of satellite performance during maneuvers was excellent. Only nine propulsive maneuvers (in the range of 2-5 mm/sec, except for OMM1) have been required during five years of mission operations because of our use of the passive technique, prevailing low drag, improvements in OD, and precise maneuver evaluation. The total fuel used by all OMMs is equivalent to 40 mm/s. The satellite is using significantly less fuel compared to that expected prior to the launch (40-60 mm/s/year) and fuel tanks remain nearly full.

The TOPEX/Poseidon orbit has been maintained using both passive and active maneuver techniques. All mission requirements have been comfortably met. The semi-major axis exhibits unique variations because of the anomalous force. It increases or decreases depending on satellite attitude. Inclination variations are highly correlated with  $\beta'$ . Selection of a frozen orbit has eliminated the need for dedicated eccentricity maneuvers to keep the eccentricity within 0.001. It is planned to use the passive techniques described above throughout the operational life of the satellite to minimize the number of propulsive maneuvers.

## ACKNOWLEDGMENT

The authors wish to thank the other teams with the TOPEX/Poseidon flight operations system for generous support and suggestions provided throughout the mission. Thanks are also due to the GSFC FDF for providing timely and accurate orbit determination results and other support whenever needed.

## REFERENCES

1. Bhat, R. S., Frauenholz, R. B., and Cannell, P. E., "TOPEX/Poseidon Orbit Maintenance Maneuver Design," *Adv. in the Astronautical Sciences*, Vol. 71, part 1, Univelt, Inc., San Diego, 1989, pp. 645-670.



2. Bhat, R. S., Shaporo, B. E., and Frauenholz, R. B., "TOPEX/Poseidon Orbit Acquisition Maneuver Sequence," AAS/AIAA Astrodynamics Specialists Conference, *Adv. in the Astronautical Sciences*, Vol. 85, part 1, Univelt, Inc., San Diego, 1993, pp. 103-112.
3. Frauenholz, R. B., Hamilton, T. W., Shapiro, B. E., and Bhat, R. S., "The Role of Anomalous Satellite-Fixed Accelerations in TOPEX/Poseidon Orbit Maintenance," *Adv. in the Astronautical Sciences*, Vol. 85, part 1, Univelt, Inc., San Diego, 1993, pp. 83-102.
4. Shapiro, B. E., Bhat, R. S. and Frauenholz, R. B. "Using Anomalous Along-Track Forces to Control the TOPEX/Poseidon Ground Track," *Adv. in the Astronautical Sciences*, Vol. 87, part2, Univelt, Inc., San Diego, 1994, pp. 799-812.
5. Bhat, R. S., Shapiro, B. E., and Leavitt, R. K., "Use of Solar Array Lead/Lag Strategy in TOPEX/Poseidon Ground Track Control," Jet Propulsion Laboratory IOM FOS 97 - 018, March 20, 1997(Internal Document).
6. TOPEX/Poseidon Project, "Mission and Systems Requirements," Jet Propulsion Laboratory, JPL D-5901, April 1989 (Internal Document).
7. Shapiro, B. E., "TOPEX/Poseidon Repeat Orbit and Reference Grid Definition using a JGM2 Gravity Field," Jet Propulsion Laboratory IOM FOS 93 - 028, August 5, 1993 (Internal Document).
8. Vincent, M. A., "TOPEX/Poseidon Orbit Characteristics," Jet Propulsion Laboratory, JPL D-7511, June 1990 (Internal Document).
9. Nerem, R. S., et al., "Gravity Model Development for TOPEX/Poseidon: Joint Gravity Models 1 and 2," *Journal of Geophysical Research*, 99(C12): 24,421-24,447, December 15, 1994.
10. Bolvin, D., "Flight Dynamics Facility Operational Orbit Determination for the Ocean Topography Experiment," GSFC Flight Mechanics and Estimation Theory Symposium, Greenbelt, MD, May 1991
11. Royer, D. A., "Support Instrumentation Requirements Document (SIRD)," Jet Propulsion Laboratory, D-8469, May 22, 1992 (Internal Document).
12. Long, A. C., et al., "Goddard Trajectory Determination System(GTDS): Mathematical Theory," Revision 1, FDD/552-89/001, Code 550, FDF/GSFC, NASA, July 1989.
13. Spier, G. W., "Design and Implementation of Models for the Double Precision Trajectory Program (DPTRAJ)," Jet Propulsion Laboratory, TM 33-451, April 15, 1971.
14. Salama, A., M. Nemesure, J. Guinn, D. Bolvin and R. Leavitt, "Compatibility of TOPEX/Poseidon Trajectory Propagation With JPL and GSFC/FDF Operational Software," GSFC Flight Mechanics and Estimation Theory Symposium, Greenbelt, MD, 1994.
15. Frauenholz, R. B., Bhat, R. S., Shapiro, B. E., and Leavitt, R. K., "An Analysis of the TOPEX/Poseidon Operational Orbit: Observed Variations and Why", *Journal of Spacecraft and Rockets*, Mar. - Apr. 1998.
16. Doll, C., G. Mistretta, R. Hart, D. Oza., C. Cox, M. Nemesure, D. Bolvin, and M. Samii, "Comparison of TOPEX/Poseidon Orbit Determination Solutions Obtained by the Goddard Space Flight Center Flight Dynamics Division and Precision Orbit Determination Teams," *Adv. in the Astronautical Sciences*, Vol. 84, Part 1, Univelt, Inc., San Diego, 1993, pp. 221-236.
17. Doll, C., G. Mistretta, R. Hart, D. Oza, C. Cox, M. Nemesure, and D. Bolvin, "Accuracy Assessment of TDRSS-Based TOPEX/Poseidon Orbit Determination Solutions," *Adv. in the Astronautical Sciences*, Vol. 85, Part 1, Univelt, Inc., San Diego, 1993, pp. 123-142.
18. Doll, C.E., G.D. Mistretta, R.C. Hart, D.H., Oza, D. T. Bolvin, C.M.Cox, M.Nemesure, D.J.Niklewski and M. V. Samii, "Improved Solution Accuracy for TDRSS-Based TOPEX/Poseidon Orbit Determination," GSFC Flight Mechanics and Estimation Theory Symposium, Greenbelt, MD, 1994.
19. Doll, C. E., D. H. Oza, J. M. Lorah and D. T. Bolvin, "Accurate Orbit Determination Strategies for TOPEX/Poseidon Using TDRSS," AIAA 95-3243, AIAA Guidance, Navigation, and Control Conference, Baltimore, MD, Aug. 1995.
20. Doll, C. E., D. H. Oza, D. T. Bolvin, and J. M. Lorah, "TOPEX/Poseidon Orbit Determination Using TDRSS," MS95/059, CNES International Symposium on Space Dynamics, Toulouse, France, June 1995.
21. Oza, D. H., D. T. Bolvin, C. M. Cox, M. V. Samii, and C. E. Doll, "Accuracy Assessment of TDRSS-Based TOPEX/Poseidon Orbit Determination," *Advances in Space Research*, 16(12): 85-88, 1995.
22. Frauenholz, R. B., and Shapiro, B. E., "The Role of Predicted Solar Activity in TOPEX/Poseidon Orbit Maintenance Maneuver Design," AAS 91-515, AAS/AIAA Astrodynamics Specialist Conference, Durango, Colorado, August 19-22, 1991.
23. Bhat, R. S. "Execution Error model for TOPEX/Poseidon Orbit Maintenance Maneuver Design," Jet Propulsion Laboratory, IOM FOS 92-034, October 2, 1992 (Internal Document).
24. Shapiro, B. E., and Bhat, R. S., "GTARG - The TOPEX/Poseidon Ground Track Maintenance Maneuver Targeting Program", AIAA 93 - 1129, AIAA/AHS/ASSEE Aerospace Design Conference, Irvine, CA, February 16-19, 1993.
25. "Ocean Topography experiment (TOPEX)/Poseidon Flight Dynamics Facility (FDF)/TOPEX ProjectInterface Control Document" NASA/GSFC 553-FDD-92/028R0UD0, August 1992.
26. Bhat, R. S., "Performance of TOPEX/Poseidon Orbit Maintenance Maneuver-6 (OMM6)," Jet Propulsion Laboratory, IOM FOS 94 - 064, July 8, 1994 (Internal Document).
27. Bhat, R. S., "TOPEX/Poseidon Orbit Maintenance Maneuvers Performance (OMM1-OMM5)," Jet Propulsion Laboratory, IOM FOS 94 -056, April 29, 1994 (Internal Document).



**Page intentionally left blank**

## BeppoSAX GROUND ATTITUDE DETERMINATION

Carlo De Libero<sup>(\*)</sup>, Giuseppe Gennaro<sup>(\*)</sup>  
 Carlos L. Pastor<sup>(\*)</sup>, Maurizio Stornelli<sup>(\*)</sup>

This paper describes the Attitude Determination techniques implemented in the BeppoSAX Attitude and Orbit Control Ground Support System (AOCGSS) developed by TELESPAZIO to support the Attitude and Orbit Control Subsystem (AOCS) operations. Two different attitude determination software's have been developed. The first based on a Star Matching Algorithm using collected Star Tracker's (STRs) mapping data. The second adopting a Kalman Filter method to produce the best satellite attitude estimation. The latter is used as a post facto attitude solution and used in the analysis of each scientific observation results.

### INTRODUCTION

The BeppoSAX (Beppo Occhialini X-ray Astronomy Satellite) project has been conceived, by the Italian Space Agency (ASI), to carry out systematic and comprehensive observations of celestial X-ray sources over the 0.1 to 300 keV energy range. To this end six instruments payload containing Narrow Field Instruments (NFI) and Wide Field Cameras (WFC) are used. The spacecraft is three-axis stabilised by using Reaction Wheels System (RWS) as actuators and Gyros (GYRs) and Star Trackers (STRs) as main sensors. Its objectives are to perform systematic and comprehensive observation of celestial X-ray sources over the 0.1 to 300 keV energy range. Aims of the SAX mission include spectral, spectroscopic and timing measurements of celestial X-ray sources, together with all-sky monitoring over the 2 to 30 keV energy range for investigation of long-time source variability and for localisation and study of transient sources. In order to meet the above mentioned objectives the following payload instruments are mounted on-board:

- Low Energy Concentrator Spectrometer (LECS) covering the 0.1 - 10 keV range with a field of view (FOV) of 40 arcmin;
- Medium Energy Concentrator Spectrometer (MECS) covering the 1.3 - 10 keV range having a FOV of 30 arcmin;
- High Pressure Concentrator Proportional Counter (HP-GSPC) covering the 3.5 - 120 keV range having a FOV of 1.1 degrees;
- Phoswich Detector System (PDS) covering the 15 - 300 keV range having a FOV of 1.5 degrees;
- Two Wide Field Cameras (WFC) covering the 2 - 30 keV range having a FOV of 20x20 degrees.

The LECS, MECS, HP-GSPC and PDS are briefly called Narrow Field Instruments (NFI), each of them having the boresight directed as the satellite Z axis. The WFCs are mounted along the +Y and -Y satellite axis.

---

\* Telespazio S.p.A., Via Tiburtina, 965 I-00156 ROME-ITALY - Phone: +39 6 40793764 -  
 FAX: +39 6 40796291 - EMAIL: aocs@napa.sdc.asi.it  
 ♦ Dataspazio S.p.A., ROME-ITALY

In addition to the scientific observations plan execution the major event of the BeppoSAX mission is the detection of the Gamma Ray Bursts (GRB). The AOCS provides the operational flexibility required to perform fast follow up pointing which bring the NFI instrument in the direction from which the GRB has been detected.

The BeppoSAX program is the result of a scientific cooperation between the Italian Space Agency and the Dutch Government. The satellite main contractor is the Italian company ALENIA Aerospazio (Turin) and the Netherlands was involved in the project with regard to the AOCS, provided by the FOKKER Space and Systems as ALENIA subcontractor, and the GFE (Government Furnished Equipments) LECS, MECS and WFC. In the framework of the Ground Support System (GSS), whose development was under TELESPIAZIO responsibility, the following subsystems have been manufactured: TT&C Ground Station, STation Computer (STC), Data Relay System (DRS), Operations Control Centre (OCC), Scientific Data Centre (SDC), SAX SIMulator (SAXSIM).

BeppoSAX (weight 1400 Kg) was launched the April 30th 1996 with an Atlas Centaur vehicle into a near circular equatorial orbit at 600 Km altitude and it is currently successfully operated by the TELESPIAZIO Operations Team. The latter performs also the Mission Planning and Timelining activities together with the Scientific Data Quick Look Analysis and Archiving.

The BeppoSAX Ground Station is placed to Malindi and connected via Intelsat Business Service (IBS) to OCC and SDC located in Rome. Ground/BeppoSAX contact covers a minimum of 10 each 103 minutes. The data collected during the non visibility period are stored on the on-board tape recorder and sent to the ground station during the generic passage at HBR (High Bit Rate) of 1.2 Mbit/s together with the real time telemetry.

The paper describes the attitude dynamics system developed to support the AOCS operations and in particular the two different attitude determination software's, one performing an accurate attitude calibration necessary before starting nominal scientific operations and the other producing an high precision post facto attitude reconstruction useful for X-ray sky positioning and image deblurring. For these some results are presented and discussed.

## **BEPPOSAX ATTITUDE AND ORBIT CONTROL SUBSYSTEM (AOCS)**

The AOCS is a modular subsystem consisting of a number of units which communicate with the Attitude Control Computer (ACC) via a redundant digital serial MACS-bus. The BeppoSAX attitude is constrained always to remain inside the Pointing Domains defined by the fact that the sun-vector shall be no more 30° away from the +X satellite axis, assuring the required power generation from the Solar Array Subsystem (SAS) for battery recharging during sunlight and to avoid sun impingement of the NFIs FOV. The AOCS is designed in order to autonomously obtain and keep a safe attitude and to support scientific observations. It contains safeguards, as that regarding the pointing domain, to ensure the detection of errors and its proper reconfiguration. It will be capable of pointing the Z-axis of SAX within an Absolute Pointing Error (APE) of 1.5 arcmin and the Y-axis within an APE of 16.5 arcmin with a rate limit of 40 arcsec/sec. With regard to the accuracy required for the post facto attitude solution, obtained on ground using data coming from GYR and STRs, it is defined by an Absolute Measurements Accuracy (AMA) of 0.5 arcmin.

### **AOCS UNITS<sup>1</sup>**

The AOCS consists of the following units:

- ACC, containing two identical computers (ACC A and ACC B) each one connected to a dedicated MACS-bus (no cross-strapping);
- Power Distribution Unit (PDU) (internal redundancy);



- Two Sun Acquisition Sensors (SAS1 and SAS2 each one composed of: 8 Sun Presence Indicators (SPIs) redunded along both the +X and -X axis direction; one Quadrant Sun Sensor (QSS) only present on +X side i.e. QSS+XA for SAS1 and QSS+XB for SAS2). This sensors are used as reference of the sun direction and to drive the satellite from a target attitude to an other one without the sun leaves the active pointing domain;
- Monitor and Reconfiguration Unit (MRU) containing the subsystem watchdog and two set of electronics to process the signals coming from the two SASs;
- Four Gyroscopes (GYRs) in an all-skewed configuration for three out of four hot redundancy; each one consists of rate integrating gyroscope for sensing the satellite rotation about its input axis; it can operate in two internal modes, coarse and fine, measuring angular change during the AOCS cycle (0.5 sec) respectively inside the ranges  $\pm 1.25^\circ/\text{sec}$  and  $\pm 0.36^\circ/\text{sec}$  for the two modes with scale factors of 0.4" and 0.1" and drift bias of  $0.044^\circ/\text{hr}$ . Two additional gyros were integrated on the satellite before launch taking into account the single unit life time. The lathers are located in the Z/ $\pm$ Y planes,  $30^\circ$  from the Z axis.
- Three STRs (-X, +Y, +Z); two out of three STRs provide accurate pointing capability. Availability of the STRs depends on their health and on the attitude relative to the Earth, Moon and some Bright Objects). The detector of the STR sensor is a CCD with  $384 \times 288$  pixels, each of them having 39.5 arcsec of dimension providing a total FOV of  $4^\circ \times 3^\circ$ . The STR is able to detect each star having visual magnitude,  $m_V$ , in the range [2,8] and to track five stars simultaneously. The Elementary Search Window (ESW), the maximum window that the STR can use for star search, has  $62 \times 46$  pixels dimension. The STR reachable accuracy are 5.7 arcsec in position (by means of the interpolation algorithm) and from 0.2 to 0.62  $m_V$  in magnitude depending on the star class. The STR electronics are microprocessor-based and contain the software responsible for sensor data processing, drive the STR operating modes executing the relevant tasks. The AOCS EAC-ASW uses the STR to track one star at a time. Moreover it uses the following STR modes: stand-by, search/track, mapping.
- Four Reaction Wheels (RWLs) in an all-skewed configuration for three out of four cold redundancy with two Reaction Wheels Electronic (RWEs) boxes each containing two channels to control the RWLs. Each RWL stores up to 20Nms of angular momentum and provides a torque up to 0.2 Nm in 63 torque steps;
- Three Magnetic Torquers (MTR) along the X, Y and Z axes each one containing two coils differently powered by the PDU. They will be used for momentum unloading and provide a magnetic moment of  $100 \pm 10 \text{ Am}^2$ .
- Two Magnetometers (MGM) used either in attitude acquisition after SAX-launcher separation or in order to provide the MTR with correct current polarity during the RWL unloading; it provides the measurement of the Earth Magnetic Field (EMF) vector along the spacecraft axis in the range of  $\pm 50 \mu\text{T}$  with a resolution of  $0.5 \mu\text{T}$ .

After launch four out of the six gyros failed: May '96, December '96, January '97, May '97. With the third failure it was decided to uplink a new safe mode developed by Alenia, Gyroless Safe Mode (GSM), and in the same period the implementation of the Extended Science Modes (ESM) using only one gyro, started and it was successfully commissioned in August '97 with the satellite maintained in GSM from June to August '97.

The operational scenario was contemporary modified by the implementation of the new AOCS Control Logic and the AOCGSS was required to be upgraded to fulfil the different constraints related to the slew strategy.

## AOCS ENVIRONMENT<sup>8</sup>

Although the BeppoSAX AOCS is designed to guarantee the on board autonomous control, an attitude dynamics system, AOCGSS, was properly developed in order to support its operation, e.g. for attitude manoeuvre computation, AOCS sensors and attitude calibration, STR sensors availability prediction, X-ray

source observation feasibility taking into account the attitude and sensor constraints. This system was integrated in the OCC and interfacing with the Spacecraft Control System (SCS), the Orbit Determination and Dynamics System (ODDS) and Scientific Operation Centre (SOC) it forms an unique working environment permitting Mission Planning and Monitor and Control operations.

A typical operational sequence involving the OLAV, VERIFY\_ESM and AOPSPS tools for pointing feasibility analysis, long/short term planning, attitude manoeuvres preparation and target acquisition can be summarised as follow:

1. OLAV (Off- Line Attitude Validation) represents an off line tool included at Mission Plan level performing a sort of feasibility analysis on the achievement of a scientific target. The observation feasibility period is an output of this tool. The inertial pointing direction defining the position of the X-ray source is given in input to the OLAV tool together with the specification of the prime direction (NFI or WFC), the year in which the analysis has to be performed, the minimum duration for the scientific target observation, the Euler manoeuvres sequence, the angular distance  $\Omega$  from the two nodes determined by the intersection between the two great circle of pole Polaris and the Target (in the following these will be called 'Polar and Target plane' respectively). The latter defines other two points on the Polar plane defining the possible starting attitudes of the slews sequence for the final scientific target acquisition. Two final attitudes can be computed starting from the two starting one. From these data OLAV analyses the feasibility of the target acquisition for both the possible solutions using the selected Euler manoeuvre sequence. The output will be a set of information, including the time range in which the observation can be started and the guide stars used for each of the elementary manoeuvre computed. The more suitable of the two proposed solutions will be selected by the mission planner and next used to edit the Long Term Interface File (LTIF). If a different scientific target has to be analysed an other execution of the OLAV tool shall be initiated.

3. LTIF together with Mission Plan File (MPF) represent the inputs for the Long Term Plan (LTP) sw for the preparation of the LTP file. The LTP sw includes the VERIFY\_ESM library working with the 'Long' option. In this context this module, repeats the same computation performed in OLAV, relevant to the slew path computation together with all other information for the Euler sequence selected by the mission planner after the OLAV execution. The Observation time interval will be fixed in the time range coming from OLAV taking into account the coherence with respect to other pointings fixed yet. In addition the percentage of full performance observability has to be taken into account to properly dimension the observation duration.

4. After the LTP file is ready the Short Term Plan (STP) sw can start using the VERIFY\_ESM library working with the 'Short' option. At this level the computation relevant to one target acquisition performed by OLAV and LTP are repeated using the satellite ephemeris data. The latter permits to correctly plan the attitude manoeuvres with respect the STR availability and avoid to start the manoeuvre during the visibility period.

Three files are produced by the STP: NPF (Nominal Pointing File), PTF (Polling Table File), NPP (Nominal Payload Plan). The first represents the attitude manoeuvre planning relevant to the next week of operations.

5. The Attitude Operations Plan Preparation tool (AOPSPS) uses the NPF and prepares for each elementary request linked to a scientific observation the set of AOPs in order to both reach the final target and come back from it before starting the next observation. Seven is the maximum number of the (Science Pointing Mode Attitude Operations Plan) SPM AOPs associated to each scientific target. The first one is relevant to the start attitude acquisition and corresponds to a simple rotation about the Z axis pointing Polaris. The AOP n.2 to n.4 are those relevant to the three Euler manoeuvres, the AOP n.5 to 7 are the reverse of the manoeuvre 2 to 4. The latter will be enabled at the end of the scientific observation before starting the next one.

6. The prepared AOP macrocommands will be collected in a dedicated file for next telecommand preparation by the AOP Load SCS tool.



In addition to the above indicated tasks an other one has been foreseen, whose involvement will be essential for the sudden (target of opportunity) TOO handling and for pointing execution outside of the automatic channel. This tool, called TOO\_HANDLING, includes VERIFY\_ESM working with the 'Short' option. To reach a sudden GRB direction occurred in the WFC the following alternatives can be analysed from an operational point of view:

- try to reach the TOO with the NFI starting from the current target directly using the TOO\_HANDLING tool and next the AOPSPS tool (starting attitude = current attitude; final attitude = too target with slave axis corresponding to minimum Sun Aspect Angle).
- using the TOO\_HANDLING anticipate the end of the current observation by updating the enable time for the reverse manoeuvres, try to plan the TOO starting the OLAV tool from the AOCGSS environment, activate the TOO\_HANDLING for the elementary slew computation and next the AOPSPS for the AOP preparation.
- command the DPM fallback, perform the fine attitude calibration, try to plan the TOO starting OLAV tool from the AOCGSS environment, activate the TOO\_HANDLING for the elementary slew computation and next the AOPSPS for the AOP preparation.

This task can be also used to re-enter in the nominal observation plan at the end of the TOO. Figure 1 provides a schematic of the aforementioned logic.

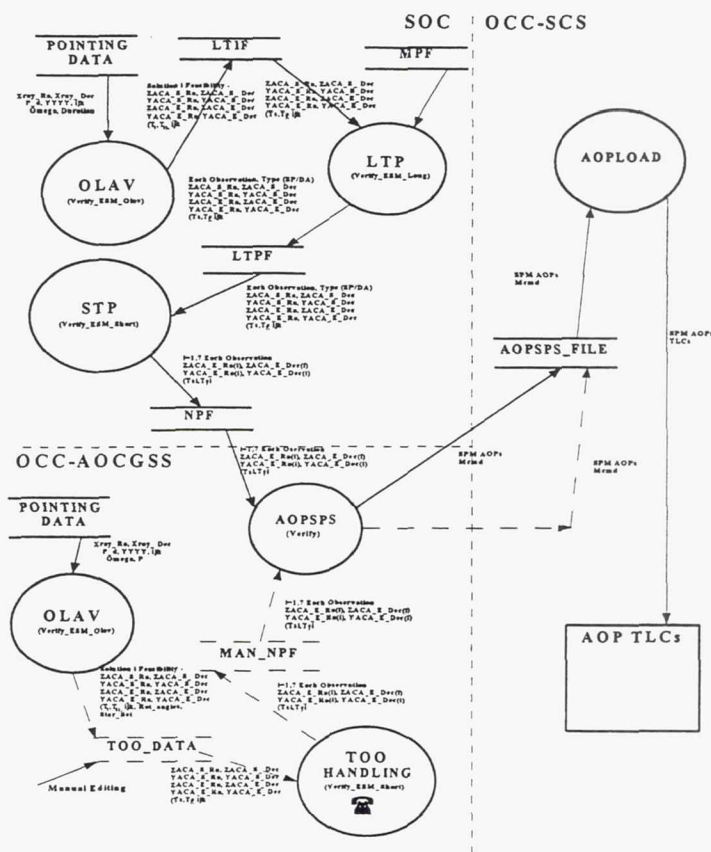


Figure 1 SAX ESM Rel 1. Operational Scenario  
BEPOSAX ATTITUDE AND ORBIT CONTROL GROUND SUPPORT SYSTEM

The AOCGSS is broken down by means of a menu whose structure is sketched in Figure 2.



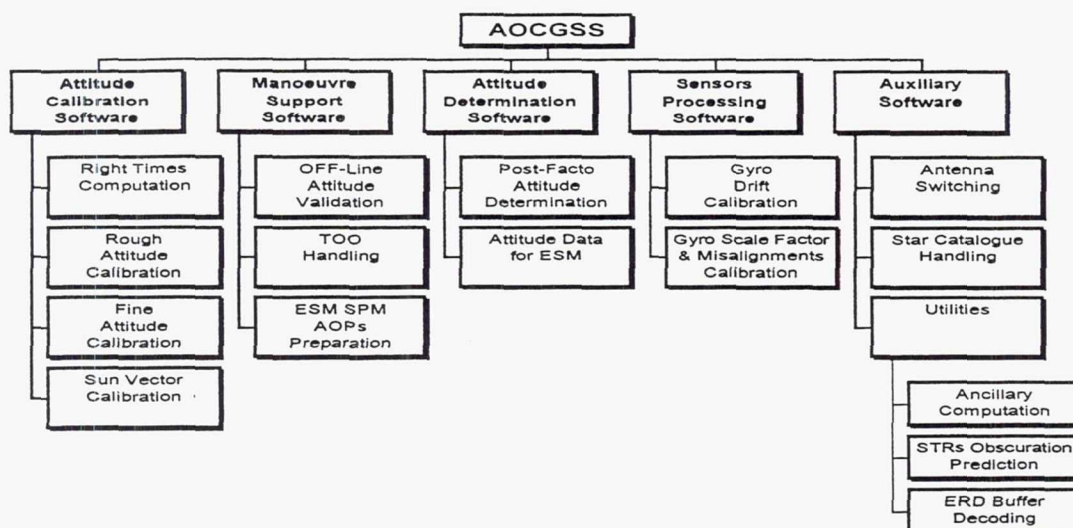


Figure 2 AOCSS SW Overall Overview

- **Attitude Calibration Software** Contains SW Tasks for the AOCSS Operations Procedure support in case of loss of Science Pointing Mode (SPM) control logic.

- **Manoeuvre Support Software** Contains SW Tasks for X-ray Source Pointing Feasibility in terms of Slew Path Existence and Pointing Maintainability.

Attitude Manoeuvre Computation and Attitude Operations Plan (AOP) Preparation relevant to a manual or an automatic weekly basis schedule.

Target of Opportunities Handling - useful in case of GRB for a fast computation and planning of the required attitude manoeuvres to reach the correct position for the Follow-Up execution.

- **Attitude Determination Software** Contains Two SW Tasks implementing different methods for Attitude Determination: Stochastic Approach using Kalman Filtering Technique (First Year of Operations). Data coming from this task have been used for Final Observation Tape (FOT) preparation and high precision X-ray source positioning. The latter permitted to perform a more accurate follow-up observation execution.

Deterministic approach based on STR Mapping Data. The latter are used to perform first a Star Constellation identification (three stars as minimum) and then Attitude Determination using two Star Vectors.

- **Sensor Processing Software** Contains SW Tasks devoted to Gyro Drift, Scale Factor & Misalignment Estimation and calibration command preparation.

STR Misalignment Estimation computing the guide star position correction to be applied before commanding the STR inside the AOP context.

- **Auxiliary Software** The main tasks are: TX/RX in coverage & Antenna switching time prediction for link acquisition and antenna switching procedure execution respectively taking into account the satellite attitude foreseen for each passage.

Star Catalogue Handling containing a set of tool for star catalogue operations performed at level of AOP preparation, Star Constellation identification. Master & Guide Star Catalogue checking-out tools.

Satellite and AOCSS performances permitted to reach the GRB position last 09-05-97 in 5 hour and 40 minutes from the event. Position refinement was possible on the first Follow-Up thanks to the Attitude Data provided on FOT that for the baseline attitude control logic was output of the on ground Post Facto Attitude Determination software.

The operations consisted of attitude manoeuvre computation and implementation. No payload operation plan modification was required. At epoch the Baseline Attitude Control Logic was running on-board using three gyroscopes for control.

The current ESM 1 AOCS performances based on one gyro only guarantees the same level of accuracy in pointing execution. The expected required time for an operations similar to that executed the May 9th 1997 remains less than the 15 hours baseline figure, taking also into account the additional constraints coming from the new attitude control modes. This expectation has been confirmed in occasion of the first GRB follow up handled with the ESM 1 logic running. The GRB direction was reached the December 15th 1997 in 6h 37m 17s from the event. The activity breakdown is described in Figure 3.

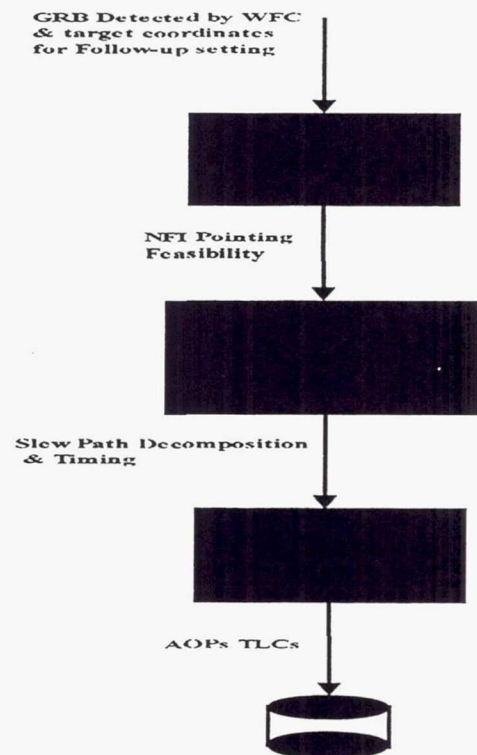


Figure 3 GRB Follow-Up Attitude Operations

## GROUND ATTITUDE DETERMINATION

As anticipated in the previous sections two different attitude determination software's have been developed, the first to give the proper support to the satellite operations and the second to provide a post facto attitude solution necessary for the correlation of the scientific result for each observation to the actual spacecraft attitude. The former is that specified in the Attitude Calibration software when performing the Fine Attitude Calibration, the latter is the Post Facto Attitude Determination.

The star data are extracted by a Master Star Catalogue at epoch 2000.0 containing star with visual magnitude contained in the  $M_v$  range [2,9] in combination with a Guide Star Catalogue being a subset of the previous one with stars in the magnitude range [2,8]. Both the catalogue has been provided by ASI and produced taking into account the BeppoSAX STR characteristics and performances.



## Fine Attitude Calibration<sup>5,6,7</sup>

A fine attitude calibration is performed each time the AOCS has to reach the science pointing mode starting from a lower level control state. This permits the accurate definition of the spacecraft attitude in inertial coordinates necessary to guarantee the acquisition of each X-ray source in the sky. An other operational scenario in which the attitude calibration is necessary is the case in which at the end of an attitude manoeuvre one of the commanded STR locks on an unknown star.

To produce its output, the calibration attitude quaternion, the Fine Attitude Calibration task needs mapping data coming from a STR properly commanded in a period in which they are not obscured by the Earth. From the STR mapping data a star pattern recognition is performed by means of a star constellation matching algorithm. Next from the measured star vectors and their inertial position the QUaternion ESTimation (QUEST) algorithm produces an accurate attitude solution. The computed quaternion defines the attitude calibration command which resets the current attitude quaternion to the right satellite attitude representation.

The computer application of the star constellation matching algorithm uses a subset of the Master Star Catalogue containing a circle of  $3^{\circ}/4^{\circ}$  degrees around of the boresight direction of the STR commanded in mapping. A few seconds processing are necessary to provide the required attitude estimation. The same program can also be used in case no rough attitude knowledge is available with an increased processing time.

This task had been successfully working during the flight operations conducted up to now in the recovery activity after autonomous fallbacks toward lower level attitude control mode.

## Post Facto Attitude Determination<sup>2,3,4</sup>

This task is the software module which computes the attitude for a time interval in which a scientific observation has been performed (AOCS in SPM) making use, for requirements on accuracy, of a Kalman filtering technique. The attitude solution calculated by this task has been used during the first year of operations, either to correctly place the observed sources in a well defined inertial reference or in general to correlate the scientific observation results with the accurate attitude data. As for the Kalman filter, it generally consists of a state dynamic model described by a set of non-linear differential equations and a set of non-linear measurement equations. Since for SAX the gyro measurements are available and provide information about the angular velocity present on-board the satellite, a model replacement approach is used; the measurements include alignment errors, drift biases and noise. The kinematic equations are represented in quaternion notation and the on-board computed attitude quaternion is used to initialise the algorithm. So the starting point of the generic algorithm is the integration of the kinematic equations which computes the predicted attitude quaternion  $q(k+1/k)$ . The quaternion error is expressed not as the difference between the true and the estimated quaternions, but as the quaternion composed by means of quaternion algebra with the estimated one in order to obtain the true one. From that an approximate representation of the state vector and covariance matrix is used. Being this incremental quaternion a small rotation, the fourth component is close to unity and the attitude information is contained in the three vector components. Therefore the state vector defined as a six component vector given by the three components of the error quaternion and the gyros drift biases provide a non redundant representation of the state error. Moreover the STR measurements are modelled to perform the correction of the predicted estimate. The algorithm can be summarised as follow:

Using quaternion notation:

$$q_1 = e_1 \cdot \sin(\vartheta/2) \quad q_2 = e_2 \cdot \sin(\vartheta/2) \quad q_3 = e_3 \cdot \sin(\vartheta/2) \quad q_4 = \cos(\vartheta/2) \quad (1)$$

where  $\underline{e}$  and  $\theta$  are respectively the rotation axis and angle, the kinematic equations can be written as:



$$\frac{d}{dt} \underline{q}(t) = \frac{1}{2} \Omega(\omega(t)) \underline{q}(t) \quad (2)$$

where:

$$\Omega(\omega(t)) = \begin{bmatrix} 0 & \omega_3 & -\omega_2 & \omega_1 \\ -\omega_3 & 0 & \omega_1 & \omega_2 \\ \omega_2 & -\omega_1 & 0 & \omega_3 \\ -\omega_1 & -\omega_2 & -\omega_3 & 0 \end{bmatrix} \quad (3)$$

Given the initial conditions:

$$\begin{aligned} \underline{\bar{q}}(k/k) &= \underline{\bar{q}}(k) \\ \underline{\bar{b}}(k/k) &= \underline{\bar{b}}(k) \\ \underline{\bar{x}}(k/k) &= [\underline{\bar{q}}(k), \underline{\bar{b}}(k)]^T \\ \underline{\bar{a}}(k/k) &= M(u(k) - \underline{\bar{b}}(k/k)) \end{aligned} \quad (4)$$

and taking into account that the spacecraft angular velocity  $\underline{\omega}$  is related to the gyro output 4 component vector  $\underline{u}$  according to:

$$\begin{aligned} \underline{u} &= (1+k)B\underline{\omega} + \underline{b} + \underline{n}_1 \\ \frac{d}{dt} \underline{b} &= \underline{n}_2 \end{aligned} \quad (5)$$

where  $k$  is the scale factor error,  $B$  is the 4x3 gyro input axis alignment matrix,  $\underline{b}$  is the gyro drift rate bias,  $\underline{n}_1$  and  $\underline{n}_2$  are noise components, typically represented by means of a Gaussian white noise processes mutually uncorrelated:

$$\begin{aligned} E[n_1(t)] &= 0 \quad E[n_1(t)n_1^T(t')] = Q_1(t)\delta(t-t') \quad E[n_2(t)] = 0 \\ E[n_2(t)n_2^T(t')] &= Q_2(t)\delta(t-t') \quad E[n_1(t)n_2^T(t')] = 0 \end{aligned} \quad (6)$$

we integrate the system:

$$\begin{aligned} d\underline{\bar{q}}/dt &= \frac{1}{2} \Omega(\underline{\bar{a}}) \underline{\bar{q}} \\ d\underline{\bar{b}}/dt &= 0 \end{aligned} \quad (7)$$

from which we obtain

$$\underline{\bar{x}}(k+1/k) = [\underline{\bar{q}}(k+1/k), \underline{\bar{b}}(k+1/k)]^T \quad (8)$$

we would like to compute

$$\underline{\bar{q}}(k+1/k+1) = \delta \underline{\bar{q}}(k+1/k+1) \otimes \underline{\bar{q}}(k+1/k) \quad (9)$$

where the fourth component can be considered equal to 1. Defining as the state vector

$$\underline{X} = (\delta \underline{q}, \underline{b}) \quad (10)$$

the differential equation describing the time variation of the error state vector can be written as follows:

$$d\Delta X / dt = F(t)\Delta X + Gv(t) \quad \text{with} \quad F = \begin{bmatrix} W & -1/2M \\ 0 & 0 \end{bmatrix} \quad G = \begin{bmatrix} -1/2M & 0 \\ 0 & I \end{bmatrix}$$

$$M = (B^T B)^{-1} B^T \quad (11)$$

$$W = \begin{bmatrix} 0 & \omega_3 & -\omega_2 \\ -\omega_3 & 0 & \omega_1 \\ \omega_2 & -\omega_1 & 0 \end{bmatrix} \quad v = (\eta_1, \eta_2)^T$$

with  $\eta_2$  is a Gaussian white noise process relevant to the drift bias time dependence. The integration of the previous equation can be written as

$\Delta X(t) = \Phi(t, t_0)\Delta X(t_0) + \int_{t_0}^t \Phi(t, t')G(t')v(t')dt'$  where  $\Phi(t, t_0)$  is then state transition matrix and satisfies

$$\partial \Phi(t, t_0) / \partial t = F(t)\Phi(t, t_0) \quad \Phi(t_0, t_0) = I. \quad \text{Writing} \quad \Phi(t, t_0) = \begin{bmatrix} \Theta & \Psi \\ 0 & I \end{bmatrix} \quad \Delta X \text{ is}$$

solution of the equation above if  $\Theta$  and  $\Psi$  fulfil the following  $\partial \Theta / \partial t = W\Theta$  and  $\partial \Psi / \partial t = W\Psi - 1/2M$  with the initial conditions  $\Theta(t_0, t_0) = I$   $\Psi(t_0, t_0) = 0$ .

Performing the integration of these equations we have:

$$\Theta(t, t_0) = \cos(\Delta\theta)I + \sin(\Delta\theta)W / \omega + [1 - \cos(\Delta\theta)][W / \omega^2 + I] \quad (12)$$

$$\Psi(t, t_0) = -1 / (2\omega) \{ \sin(\Delta\theta)I + [1 - \cos(\Delta\theta)]W / \omega + [\Delta\theta - \sin(\Delta\theta)][W / \omega^2 + I] \} M$$

Considering the state errors covariance matrix  $P(t) = E[\Delta X(t)\Delta X^T(t)]$  we have:

$$P(t) = \Phi(t, t_0)P(t_0)\Phi^T(t, t_0) + \int_{t_0}^t \Phi(t, t')G(t')Q(t')G^T(t')\Phi^T(t, t')dt' \quad (13)$$

where

$$E[v(t)v^T(t')] = Q(t) \quad E[\Delta X(t)v^T(t')] = 0 \quad \text{in this way we are in position to compute } P(k+1/k).$$

The next is to perform the filtering part of the algorithm, using the measurement coming from the STRs comparing them with those predicted on the basis of the predicted state. The comparing is performed applying the Kalman Filter gain Matrix  $K(k+1)$  given by the following expression:

$$K(k+1) = P(k+1/k)MP^T(k+1)[MP(k+1)P(k+1/k)MP^T(k+1) + R(k+1)]^{-1} \quad (14)$$

being  $MP(k+1)$  is defined as the partial derivative of the measurement with respect to the state vector component computed at  $q(k+1/k)$ . The matrix  $R$  defines the measurement noise. The state updating equation is:

$$\delta \vec{q}(k+1/k+1) = K(k+1)[z(k+1) - z(k+1/k)] \quad (15)$$

with  $z(k+1)$  are the measurements coming from the STRs and  $z(k+1/k)$  are the predicted ones. After that the  $q(k+1/k+1)$  representing the best state estimation can be computed as indicated in eq.(9). The propagation of the STRs measurement taking into account the predicted estimate is also performed using the actual STRs alignment computed during the commissioning phase by means of a dedicated procedure described in the following, combined with the seasonal aberration effect. The covariance matrix relevant to the state estimation after the filtering activity is:

$$P(k+1/k) = B(k+1)P(k+1/k)B^T(k+1) + K(k+1)R(k+1)K^T(k+1) \quad (16)$$

$$\text{with } B(k+1) = I - K(k+1)MP(k+1)$$

Figure 4 reports the post facto attitude reconstruction relevant to the GRB occurred the May 9th 1997.

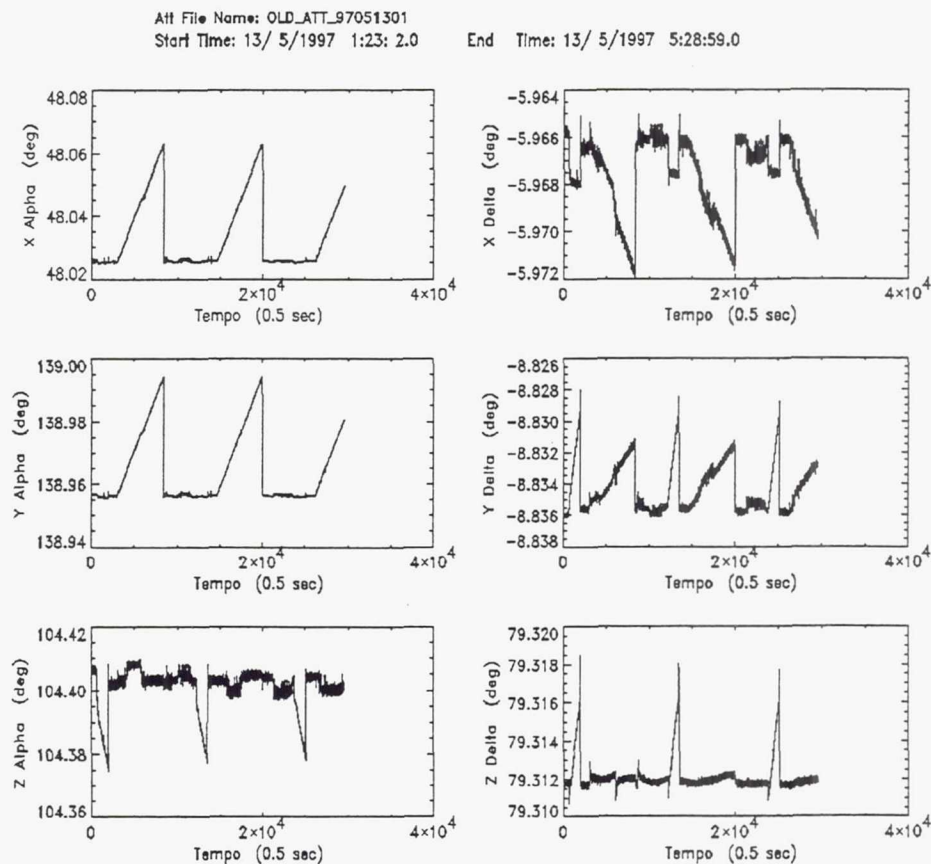


Figure 4 BeppoSAX Post Facto Attitude Reconstruction



## Star Tracker's Alignment Estimation Procedure

The scope of the flight operational procedure was to command an SPM AOP without STRs for a short time span in a part of the orbit in which the three STRs are not obscured by the Earth. At this point each STR was directly commanded in Search/Tracking mode on two guide stars via the MACS interface for the period in which it is not used by the AOP logic.

The command parameters useful for the STRs commanding came out from the utilities of the Attitude Dynamics System. The latter selected the stars for each STR on the basis of the input attitude quaternion, computed their position on the STR CCD and dimensions of the search windows to avoid overlap.

Data coming from the execution of the operational procedure above was cleaned of the aberration error and used as input in the STR Misalignment Estimation task whose output was for each STR the misalignment quaternion that composed with the ideal one produce the actual alignment quaternion.

The algorithm consists of the correlation of the observation of the known stars commanded on CCD of two STRs simultaneously. From this the concept is to estimate the systematic mutual misalignments of ZSTR to YSTR, YSTR to -XSTR and ZSTR to -XSTR. This corresponds to the determination of a set of six angles. From the definition of the satellite control axes with respect to the STRs orientation one angle defines the rotational error of the ZSTR, two angles define the two rotational errors relevant to the YSTR and three angles completely represent the orientation errors of -XSTR.

An accurate solution is guaranteed by the QUEST algorithm application for the estimation of each STR orientation with respect to the inertial reference frame. Considering each pair of STRs the solution is independent from the current attitude quaternion.

A fine attitude calibration is performed each time the AOCS has to reach the science pointing mode starting from a lower level control state. This permits the accurate definition of the spacecraft attitude in inertial coordinates necessary to guarantee the acquisition of each X-ray source in the sky. An other operational scenario in which the attitude calibration is necessary is the case in which at the end of an attitude manoeuvre one of the commanded STR locks on an unknown star.

To produce its output the Fine Attitude Calibration task needs either one or two STR mapping data properly commanded in a period in which they are not obscured by the Earth. From the STR mapping data a star pattern recognition is performed by means of a star constellation matching algorithm. Next from the measured star vectors and their inertial position the QUaternion ESTimation (QUEST) algorithm produces an accurate attitude solution. The computed quaternion defines the attitude calibration command which resets the current attitude quaternion to the right satellite attitude representation.

The computer application of the star constellation matching algorithm uses a subset of the Master Star Catalogue containing a circle of  $3^{\circ}/4^{\circ}$  degrees around of the boresight direction of the STR commanded in mapping. A few seconds processing are necessary to provide the required attitude estimation. The same program can also be used in case no rough attitude knowledge is available with an increased processing time.

This task had been successfully working during the flight operations conducted up to now in the recovery activity after autonomous control mode fallbacks.

## CONCLUSION

The AOCGSS SW represents one of the most important element in the satellite operations and scientific observation execution. Due to scientific nature of the mission the accuracy required by the Attitude Dynamics Software is high and in particular for the attitude determination task this is required to 0.5 arcminutes. The attitude determination tasks fulfil this requirement and the high performance in the AOCS and in the ground provided software and operations are responsible for the success of the mission worldwide acknowledged as formalised by the AAS Rossi Prize assigned to the SAX team.

## REFERENCES

- <sup>1</sup>SAX AOCS Users' Manual for Flight Operations; Document: SX-MA-AI-019 Vol.3.
- <sup>2</sup>E.J. Lafferts, F.L. Markley, M.D. Shuster; Kalman Filtering for Spacecraft Attitude Estimation. *Journal of Guidance, Navigation and Control*, Vol.5, NO 5, Sept.-Oct. 82, pp.417-429.
- <sup>3</sup>M. Bollner & G. Schneiders; Attitude Determination & Control for the X-Ray Satellite Rosat. *39<sup>th</sup> Congress of the International Astronautical Federation*, Bangalore, India, 08-15 Oct.88.
- <sup>4</sup>T. Rupp, G. Schneiders; High Precision Post Facto Attitude Determination of the X-Ray Satellite Rosat. *2<sup>nd</sup> International Symposium on Spacecraft Flight Dynamics*, Germany, 20-23 Oct.86.
- <sup>5</sup>A. Batten; ISO Ground Attitude Determination during Operations *3rd International Symposium on Spacecraft Flight Dynamics*, Germany, 30 Sept.-04 Oct. 91.
- <sup>6</sup>D. Baldini, M. Barni et al.; A New Star-Constellation Matching Algorithm for Satellite Attitude Determination. *ESA Journal 1993, Vol. 3*.
- <sup>7</sup>M.D. Shuster and S.D. Oh; Three-Axis Attitude Determination from Vector Observations. *Journal of Guidance, Navigation and Control*, Vol.4, NO 1, AIAA81-4003, Jan-Feb 1981, pp 70-77.
- <sup>8</sup>C. De Libero, G. Mauceri; On-Ground AOCS Support Software for the SAX Satellite"; *'First International Symposium On Spacecraft Ground Control and Flight Dynamics'*, Sao José dos Campos (Brasil), February 1994.

**Page intentionally left blank**



## ATTITUDE DETERMINATION AND CONTROL IN INTERBALL PROJECT

Nathan A. Eismont<sup>1</sup>, Vladimir V. Khrapchenkov<sup>1</sup>,  
Pavel Triska<sup>2</sup>, Vladimir Truhlik<sup>2</sup>, Jaroslav Chum<sup>2</sup>

After two years of operations in framework of INTERBALL project the large volume of data has been received and some new expertise in attitude control of the spacecraft (s/c) has been developed. Three s/c are in flight now on high elliptic orbit; each one is spin stabilized with spin axis following the Sun. To control the attitude motion of the s/c cold gas jets are used. For one of the s/c solar radiation pressure is used to keep the s/c axis directed to the Sun.

The paper describes the method of attitude determination based on the simplest approximation of the motion law and presents the estimation of the accuracy of this method based on real telemetry data of attitude sensors received during the mission. Also theory of prediction of attitude parameters evolution under influence of solar radiation pressure and gravity gradient torques is compared with the measurements.

New approaches for attitude parameters determination based on the only Sun sensors measurements are described. Methods of attitude control using solar radiation pressure are presented.

Algorithm of optimal attitude control without use of direct spin rate measurements is demonstrated. As optimisation criteria the propellant consumption is supposed.

The principal idea of this algorithm is applying of the control torques in such a way which allows to damp nutation simultaneously with angular momentum vector demanded rotation.

### 1. MISSION DESIGN AND ATTITUDE MOTION PROBLEM.

The goal of the INTERBALL project is to explore phenomena in the Earth magnetosphere and in the solar wind. It was planned to measure parameters of plasma simultaneously onboard four s/c; two of them were due to fulfil these studies in distant

---

<sup>1</sup> Space Research Institute, Russian Academy of Sciences. Profsoyuznaya Str. 84/32, 117810 Moscow, Russia.  
Phone: +7 095 333 10 78, fax: +7 095 310 70 23, E-mail: neismont@iki.rssi.ru, vkhr@mx.iki.rssi.ru.

<sup>2</sup> Institute of Atmospheric Physics, Academy of Sciences of Czech Republic. Bochni II, No.1401-14131 Prague 4, Czech Republic.  
Phone: + 420 2 71762548, fax: +420 2 71752528, E-mail: ptr@ufa.cas.cz, vtr@ufa.cas.cz, jvo@ufa.cas.cz.

parts of the magnetospheric tail (Tail Probe), the other two ones were planned to investigate the phenomena in Auroral Region (Auroral Probe) (Ref. 1). Unfortunately one s/c from the last pair survived only one day because of operation error. In spite of the different mass and sizes of the s/c in each pair (main satellites with the mass 1250 kg for Tail Probe and 1370 kg for Auroral Probe; subsatellite about 60 kg) the common approach has been applied during development of the s/c.

All s/c are spin stabilized with spin axis to be directed toward the Sun inside some tolerable limits. Nominal value for the spin period was planned to be 120 sec., but the possibilities to alter the spin period have been provided in wide margins: the main satellite could be spin up to the 40 sec. period during the procedure of the subsatellite separation; subsatellite spin rate is planned to be slow down for reaching of solar radiation stabilization conditions.

Spin stabilization has been chosen for two reasons: to diminish the cost of attitude control systems and operations, and to satisfy the demands of experiments onboard s/c which included the necessity to monitor the plasma environment in different directions by the same instrument in the close enough instants.

Following the demand to decrease the cost of mission the minimum set of attitude sensors have been installed onboard main s/c: solar sensor and three component spin rate sensors, which allows to target the spin axis into Sun direction, but generally does not permit to target it into any desirable point in the sky sphere and to determine the full set of attitude parameters. So to bypass this difficulty the scientific instruments such as magnetometer was planned to be used. Still the problem could be solved by use of the magnetometer data only for low enough altitudes (less than 30 000 km) where magnetic field model is applicable. For the Tail Probe the initial apogee height is about 190 000 km and it means that other approaches for attitude determination are necessary.

It should be also mentioned that scientific instruments installed onboard main satellites are to be controlled by the signal generated by onboard attitude determination system. This signal is to be sent to the instruments at the beginning of each spin of s/c (when one of the s/c axis, orthogonal to the spin axis, goes through the ecliptic plane). It led to the necessity of development simple enough algorithm including of attitude motion model which could be applied to all INTERBALL project s/c in spite of differences in their orbits and characteristics influencing their dynamics. This model was applied also for the purposes of attitude control of subsatellite (MAGION-4) (Ref. 2) which was not equipped by spin rate sensors.

## **2. MODEL OF ATTITUDE MOTION.**

It is obvious that the simplest model for attitude determination is local model because it does not demand neither kinematic nor dynamic approach for orientation calculations. For our case it would be applied if magnetometer and solar sensor measurements are fulfilled for the same moment and height of s/c orbit allows to use magnetic field model. So the



Auroral Probe could be included in that case but the obstacle here are oscillations of the magnetic field and its time dependent deviation from the model. For the other INTERBALL s/c the difficulties have been described above.

To balance between complexity and accuracy some approximation of motion law has been chosen (Ref. 3) for short term parts of flight. This model is based on Euler - Poinsoit solid body free motion (Ref. 4).

Let us introduce the system of coordinates connected with the satellite. The  $X$  axis is directed along the satellite structural axis which nominally coincides with the spin axis and is close to the principal axis of the maximum moment of inertia  $I_X$ . The  $Y$  axis is the structural axis close to the intermediate moment of inertia  $I_Y$ ; the  $Z$  axis corresponds to the minimum inertia moment. Balancing of the satellite is performed to reach the maximum coincidence of structural and principal inertia axes.

INTERBALL s/c have been manufactured as modification of the earlier launched PROGNOZ series s/c. For these s/c the deviation of the inertia axes from structural axes usually lied in  $1.5^\circ$  limits.

In the same limits were the deviations of angular momentum vector from the principal axis  $X_P$ , i.e. the motion is very close to rotation around constant axis. It allows to simplify expressions for description of Euler-Poinsoit case and to use instead elliptical functions more convenient for calculations trigonometric functions.

Supposing that for taken time interval the Sun vector  $\vec{S}$  does not move in inertial space and its position is determined by  $\alpha$  and  $\beta$  angles between  $X$  axis and projection of  $\vec{S}$  onto  $XY$  and  $XZ$  planes, the following expressions are valid (Ref. 2, 5):

$$\alpha = A_1 + A_2 \sin(\omega_1 t + \xi_1) + A_3 \sin(\omega_2 t + \eta_1),$$

$$\beta = B_1 + B_2 \sin(\omega_1 t + \xi_2) + B_3 \sin(\omega_2 t + \eta_2).$$

Here  $A_1, B_1$  are the angles between  $X$  axis and the projection of the principal axis  $X_P$  onto  $XY$  and  $XZ$  planes;  $A_2=B_2$  is the angle between Sun vector and angular momentum vector  $\vec{L}$ ;  $A_3, B_3$  are nutation amplitude in  $XY$  and  $XZ$  planes. Geometrically it means that the Sun vector moves along cone surface with the semiangle  $A_2=B_2$  and its axis moves along elliptical cone with maximum and minimum semiangles  $A_3, B_3$ . The relation between these values is the following:

$$B_3 = \sqrt{\frac{I_Z(I_X - I_Y)}{I_Y(I_X - I_Z)}} \cdot A_3.$$

The phase velocities  $\omega_1, \omega_2$  of Sun and angular momentum vectors are connected by expression:

$$\omega_2 = \sqrt{\frac{(I_X - I_Y)(I_X - I_Z)}{I_Y I_X}} \cdot \omega_1.$$



It should be mentioned that for determination of the constants of motion model one needs only solar sensors measurements presented as  $\alpha$ ,  $\beta$  angles. Using method of least squares it is possible to reduce the problem to the linear equations system solution for calculation of  $A_i$ ,  $B_i$ ,  $\xi_i$ ,  $\eta_i$  constants.

So the iteration procedure includes the calculation  $\omega_1$ , and  $\omega_2$  only. After first more precise definition of relation between them in further calculations only one parameter is used in iterations minimizing standard deviation.

The interval duration of data processing for this model was determined by comparing of the accuracy of model and sensor accuracy. For the main s/c their errors is about 3 angular minutes ( $3\sigma$ ) and for MAGION it is two times higher. For the Tail Probe s/c the interval duration is limited by the Sun direction rotation due to orbital motion of the Earth. So  $\sim 1.5$  hours was accepted as tolerable limits for this interval. In case of Auroral Probe the angular momentum vector changes its direction with a rate up to 1 degree per 20 minutes in perigee region, so the interval was restricted by 15 minutes. For long term intervals the external torques are to be taken into account in motion model which is usually considered as evolution of parameters.

### 3. ATTITUDE PARAMETERS EVOLUTION MODELS.

To develop of algorithm for the description of motion evolution standard approach has been applied: fast parameters have been averaged and differential equations of motion for the slow changing parameters have been used.

MAGION-4 s/c has been designed supposing the solar radiation pressure use to control its spin axis keeping it in acceptable limits of angles with Sun direction. So the solar panels and the booms were mounted in such a way which provided some shift of centre of solar radiation pressure from centre of mass. To estimate the expected torques, the model of forces generated by light pressure influence on s/c surfaces has been developed. The s/c (Figure 1) has been presented for this purpose as a set of flat surfaces with different coefficients of specular reflection, diffuse reflection and absorption.

For example for solar panels it was supposed 10% of incoming radiation to be specularly reflected and 90% to be absorbed. It was supposed that the secondary s/c radiation does not produce torques as a whole. For the supposed centre of mass the data base of torque in reference coordinates system of s/c  $\vec{M}(\varphi, \lambda)$  as function of Sun direction  $\vec{S}$  has been built (example of torque dependence from angle between X axis and Sun direction for fixed "longitude" is presented by Figure 2a). Then the averaged through spin ("longitude"  $\lambda=0^\circ \rightarrow 360^\circ$ ) torque  $M(\varphi)$  has been calculated (Figure 2b).

As it could be seen from this figure the function is rather close to the sine, what means that the integrated influence of light pressure on s/c is very similar to the case when s/c has sphere form fully absorbing radiation and having some bias between centre of mass

and centre of radiation pressure. Supposing that angular momentum unit vector  $\vec{L}$  goes along construction axis  $X$  the vector equation could be written (Ref. 6):

$$\frac{d\vec{L}}{dt} = k(\varphi)[\vec{L}, \vec{S}],$$

where

$$k(\varphi) = \frac{M(\varphi)}{\sin \varphi} \cdot \frac{1}{L}.$$

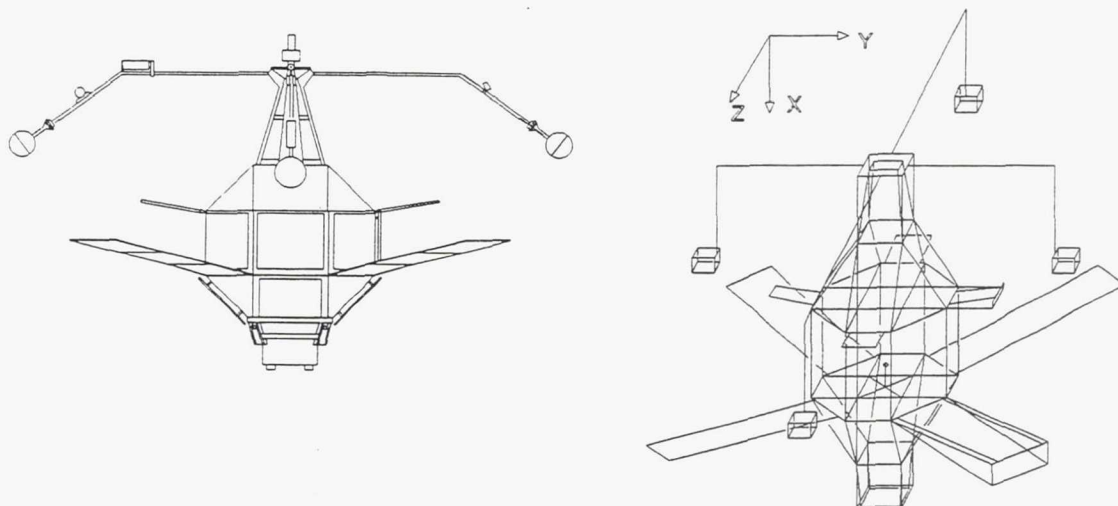


Figure 1. View of MAGION-4 s/c and its presentation as a set of surfaces.

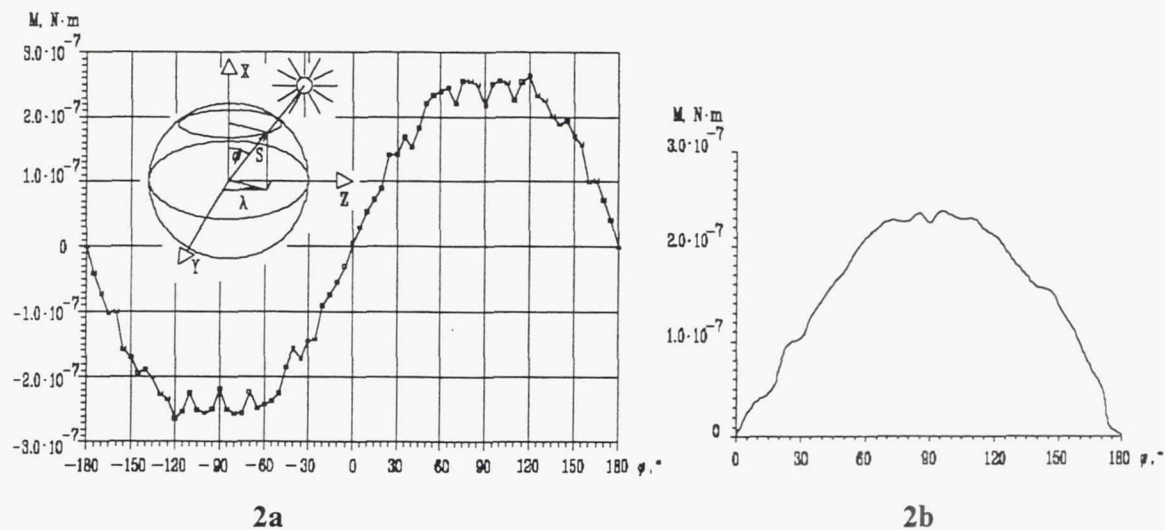


Figure 2.

For the case when  $M(\varphi)$  is approximated by  $\sin \varphi$  function  $k(\varphi)=k$  is constant and the equation for  $\vec{L}$  can be integrated, so the solution given in projections of  $\vec{L}$  vector onto ecliptic coordinate system ( $X, Y$  axes lie in ecliptic plane)  $L_X, L_Y, L_Z$  is the next (Ref. 6):

$$\begin{aligned}
L_x &= k \left[ \frac{c}{\omega} \cos(\omega t) - \frac{a}{2} \left[ \frac{1}{\Omega - \omega} \sin(\Omega - \omega)t - \frac{1}{\Omega + \omega} \sin(\Omega + \omega)t \right] + \right. \\
&\quad \left. + \frac{b}{2} \left[ \frac{1}{\Omega + \omega} \cos(\Omega + \omega)t + \frac{1}{\omega - \Omega} \cos(\omega - \Omega)t \right] \right]; \\
L_y &= k \left[ \frac{c}{\omega} \sin(\omega t) - \frac{a}{2} \left[ \frac{1}{\Omega - \omega} \cos(\Omega + \omega)t - \frac{1}{\Omega - \omega} \cos(\Omega - \omega)t \right] + \right. \\
&\quad \left. + \frac{b}{2} \left[ \frac{1}{\Omega - \omega} \sin(\Omega - \omega)t + \frac{1}{\Omega + \omega} \sin(\Omega + \omega)t \right] \right]; \\
L_z &= c + a \cdot \sin(\Omega t) + b \cdot \cos(\Omega t).
\end{aligned}$$

Here  $\omega$  is angular velocity of the Earth orbital motion;  $a, b, c$  are the constants determined by the initial parameters of motion. The value of  $\Omega$  is determined by the expression:

$$\Omega^2 = k^2 + \omega^2.$$

Parameter  $\Omega$  is the phase velocity of angular momentum vector moving along cone surface.

The axis projection of this cone onto ecliptic plane  $XY$  constantly coincides with the Sun direction vector and has the constant angle  $\psi$  with ecliptic  $\psi = \arccos(c)$ .

This angle corresponds equilibrium (or stationary) case of angular momentum evolution, i.e. if initial direction of angular momentum coincides with this axis then in further motion this coincidence is kept.

It is easy to receive:

$$\tan \psi = \frac{\omega}{k}.$$

If  $I_x = 5.9 \text{ kg}\cdot\text{m}^2$ , spin period equal 415 sec. (one of the MAGION-4 flight regime) and given above (Figure 2) solar radiation torque (approximating it as  $M = k_1 \sin \phi$  with  $k_1 = 3 \cdot 10^{-7} \text{ N}\cdot\text{m}$ ) then according to this formula  $\psi = 3.4^\circ$ . For the same parameters  $\Omega = 0.291 \text{ day}^{-1}$  what corresponds to period  $P_L$  of angular momentum rotation equal 21.57 days.

Figure 3 gives the dependence of the angle between angular momentum vector and Sun direction for MAGION-4 during experiment with solar radiation pressure stabilization during flight 49 days interval beginning February 11, 1997. The spin period during this interval was changed from 390 to 455 seconds. As it could be seen from this Figure  $\psi$  angle (half of amplitude of function oscillations here) is about 2.1 degrees, and mean period  $P_L \approx 15$  days. According to the expression given above this period corresponds  $\psi = 2.36^\circ$ , instead  $2.1^\circ$  observed and  $k_1 = 4.24 \text{ N}\cdot\text{m}$  instead estimated from Figure 2  $k_1 = 3 \text{ N}\cdot\text{m}$ . In addition Figure 3 is demonstration of the influence of the Earth reflected light on attitude. These parts of the plot with strong Earth light influence are marked by arrows and correspond to the perigee regions of the orbit.



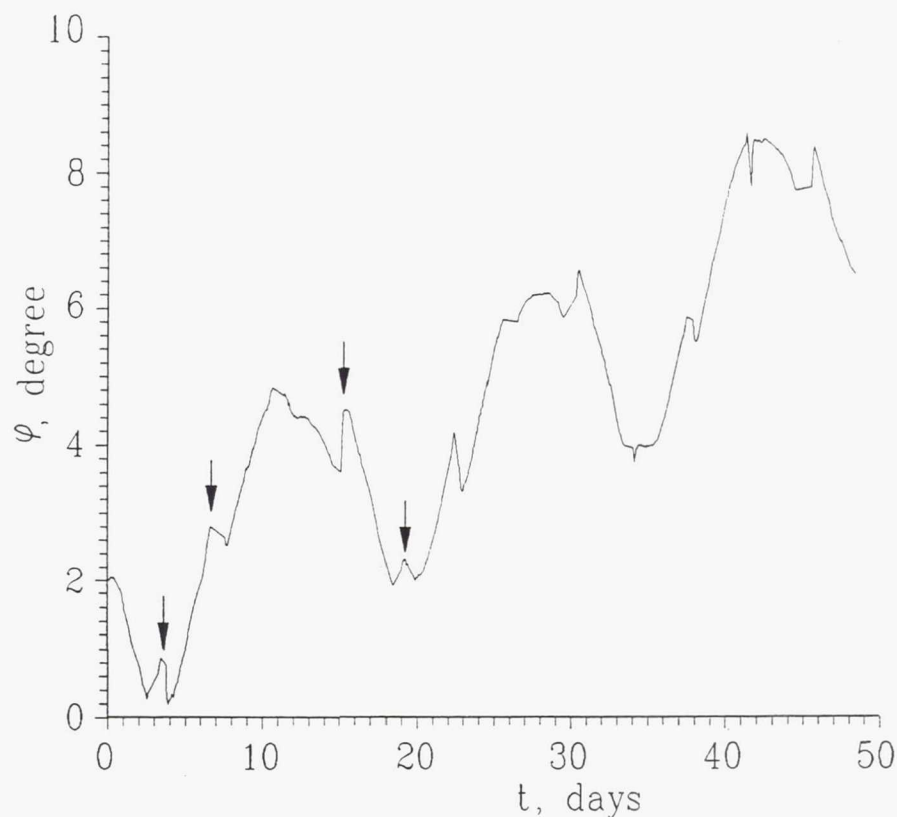


Figure 3.

Resulting impact is slow raise of mean deviation of angular momentum from the Sun direction.

Evolution of attitude parameters under influence of gravity gradient torques was calculated according to Ref. 7. For the axially symmetric s/c with null nutation gravitational torque is:

$$\bar{M} = 3 \frac{\mu}{r^3} (I_x - I_y) [\bar{r}^0, \bar{L}^0] (\bar{r}^0, \bar{L}^0),$$

or

$$\bar{M} = \frac{3}{2} (I_x - I_y) \frac{\mu}{r^3} \sin(2(\bar{r}^0, \bar{L}^0)) \bar{M}^0 = M \bar{M}^0,$$

where

$$\bar{M}^0 = \frac{[\bar{r}^0, \bar{L}^0]}{[\bar{r}^0, \bar{L}^0]},$$

$\mu$  - Earth gravitational parameter,

$r$  - distance of s/c from the Earth centre,

$\bar{r}^0$  - unit vector of direction from the Earth centre towards s/c,

$\bar{M}^0$  - unit vector of gravitational torque,

$\bar{L}^0$  - unit vector of angular momentum.

Presenting angular momentum vector  $\vec{L}$  as

$$\vec{L} = L\vec{L}^0 = I_x \omega_1 \vec{L}^0,$$

where  $\omega_1$  is spin rate of s/c, we receive

$$\frac{d\vec{L}^0}{dt} = \frac{3}{2} \frac{1}{\omega_1} \left(1 - \frac{I_y}{I_x}\right) \frac{\mu}{r^3} \sin(2(\vec{r}^0, \vec{L}^0)) \vec{M}^0.$$

This equation was integrated together with the integration of equations for the s/c centre of mass motion.

#### 4. ATTITUDE DETERMINATION AND CONTROL IN SITUATION OF SENSORS DATA DEFICIT.

For each s/c of INTERBALL project there were some specific difficulties connected with attitude determination and control. Auroral probe during initial phase of its flight demonstrated unexpected rise of the nutation - up to the critical limits (40°).

The nature of this phenomenon was supposed to be the energy pumping to the s/c body through the flexible booms in the conditions of gravity gradient torque. Its influence has been simulated for the solid body model according to the equations given in the previous paragraph.

Example of the mentioned simulation is presented by Figure 4 for the one day of flight April the 4<sup>th</sup> 1997 as the dependence of  $\varphi$  angle between angular momentum vector and Sun direction. It was supposed that in initial instant angular momentum was directed towards the Sun. Bold line gives the modelling results, stars present the values received by solar sensor processing. Thin line is for geocentric distance of s/c. The discrepancy of the presented functions is explained by the fact that in initial instant the angular momentum was not exactly directed towards the Sun (error is ~0.25°). Further one can see slightly more fast rise of the simulated angle as compared with the measured one. It is due to fact that for the simulation it was taken the nominal ratio of inertia moments ( $r=I_y/I_x=0.566$ ), at the same time from the ratio of spin rates of s/c and its angular momentum it follows that  $r=0.5737$ . Displacement marked by arrow is caused by operations of nutation damping, executed each 12 hours (Figure 5). During this operations the angular momentum is not changed nominally in inertial space, still some minor deviations are possible.

As it could be seen on Figure 5 nutation is raising for some of subintervals from 0.15° to 0.80° during 10 hours. This phenomena look quite opposite to what could be expected for solid body nutation with some internal dissipative torques and the external torques of the level observed in Auroral Probe case. And it is opposite to what observed for the other INTERBALL s/c: Tail Probe and MAGION-4. The examples of nutation amplitude decreasing for these s/c are given by Figure 6 (Tail Probe) and Figure 7 (MAGION-4).

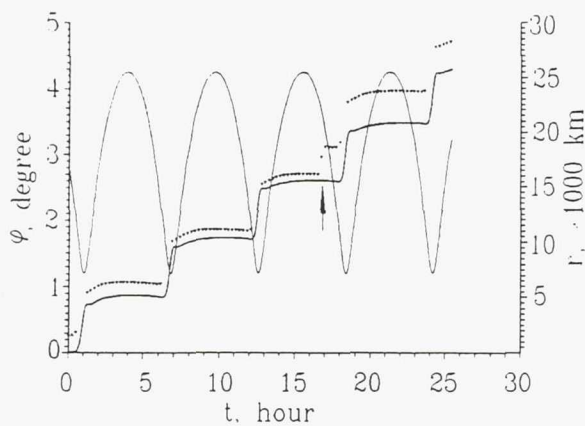


Figure 4.

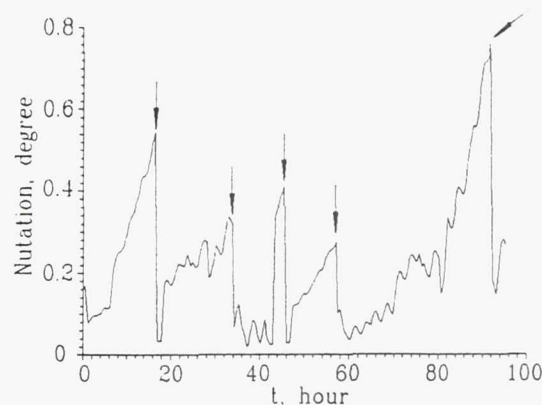


Figure 5.

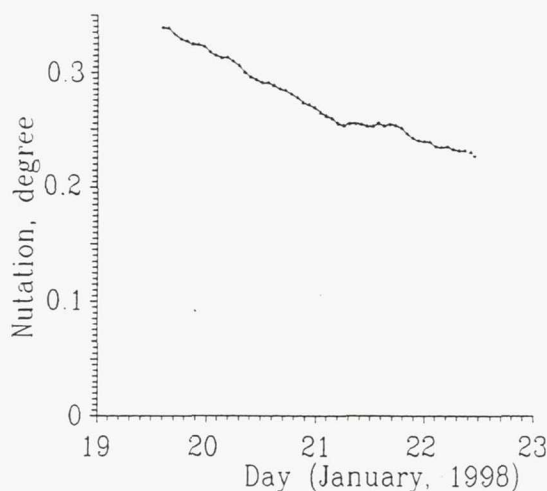


Figure 6.

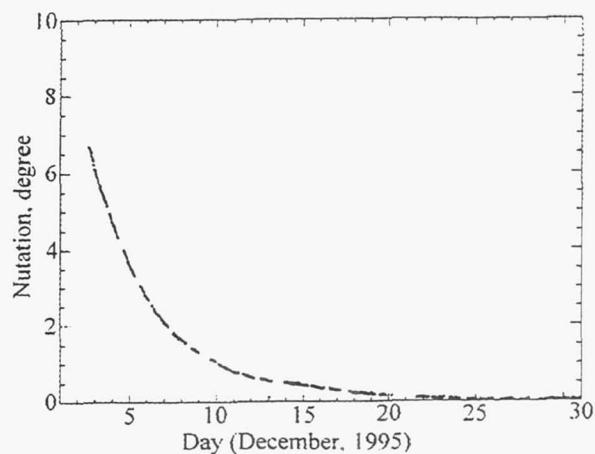


Figure 7.

So as it was mentioned above to prevent uncontrolled raise of nutation the additional operations have been introduced in procedure of attitude control: damping of nutation each 12 hours. It caused excessive consumption of propellant and consecutive reduction of expected lifetime of s/c.

The task of attitude control system for INTERBALL s/c is to keep spin axis directed towards Sun in some limits. It means that during the year this system should rotate angular momentum by  $360^\circ$  if it is not necessary to compensate the influence of external torques. For the Tail Probe these torques are low enough to cause visible rise of propellant consumption. For Auroral Probe with its perigee height 870 km and apogee 20 000 km the influence of gravity torques and necessity to prevent the nutation increasing the consumption of the propellant was almost 4 times higher. So to cut the propellant consumption the next procedure has been developed. It was decided to allow more broad limits for the spin axis deviation from the Sun: up to  $30^\circ$ .



Because the main reason of the additional propellant expenditure is compensation of angular momentum  $\vec{L}$  rotation due to gravity torque, it was proposed to put  $\vec{L}$  in direction either orthogonal to the orbit plane either in orbit plane. In this case mean evolution of the  $\vec{L}$  is equal zero. When the angle of  $\vec{L}$  with Sun reaches  $30^\circ$  then  $\vec{L}$  is rotated in intermediate direction, so that under natural evolution this angle would not rise. The idea of this approach is illustrated by Figure 8.

Initially Sun direction  $\vec{S}_0$  and  $\vec{L}_0$  almost coincide, then after Sun comes into position  $\vec{S}_1$  vector  $\vec{L}$  is moving into  $\vec{L}_1$  position in order to keep angle between them in tolerable limits after this manoeuvre till reaching them the position  $\vec{S}_2$  and  $\vec{L}_2$  (according Ref. 7  $\vec{L}$  moves along cone with the axis perpendicular to the orbit plane). After that  $\vec{L}$  is rotated into orbit plane. In described approach the sum of  $\vec{L}$  rotations angles is close to the angle of Sun rotation what allows to cut significantly the propellant expenditure.

Attitude control system was not planned to be used for targeting s/c spin axis into any prescribed point besides Sun. So for this purpose before such operation angular momentum vector was determined with the use of magnetometer and solar sensors measurements and then its direction was forecasted in inertial space to the instant when attitude control manoeuvre planned to be done. It allowed to know full set of attitude parameters for solving the task of attitude control.

The principal peculiarity of MAGION s/c attitude control was the open loop off line procedure applicable without any direct measurements of spin components. The operations have been separated on four phases. During the first phase (lasted about 20-30 minutes) the telemetry data of solar sensor and infrared Earth sensors are collected and processed. The result of this phase was full set of attitude parameters including angular momentum vector in the inertial space and what is more important - in s/c reference system. Then the forecast for ~30 minute of attitude parameters has been done using simple attitude motion model described in paragraph 1 in order to calculate the instants when the control torque vector (fixed in s/c coordinate system) goes in direction of necessary angular momentum alteration. Normally it is principal axis vector (coinciding at the moment with angular momentum  $\vec{L}$ ) to Sun vector direction.

The main idea of this approach was to rotate  $\vec{L}$  by half of the needed angle (Ref. 3) at the second phase of procedure. After applying the needed impulse the resulted attitude parameters are determined again (third phase) and the instants for the final control impulse are calculated. These instants are to satisfy two conditions: Sun vector  $\vec{S}$  goes along principal axis and direction from  $\vec{L}$  to  $\vec{S}$  coincides with control torque vector. At the fourth phase of operations this impulse is applied. With this approach no additional propellant consumption is needed for the nutation damping.

For the Tail Probe only solar sensor measurements are used for determination of full set of attitude parameters. The next procedure has been applied.

Let us introduce the coordinate system with ecliptic longitude  $\lambda$  along abscissa axis and ecliptic latitude  $\delta$  along ordinate axis. Zero longitude corresponds initial longitude of angular momentum vector  $\vec{L}$ . Initial ecliptic latitude of  $\vec{L}$  is  $\delta$ , initial longitude of Sun is  $\lambda$ , angular velocity of Sun direction rotation is  $\omega$ , angle between Sun and  $\vec{L}$  is  $\varphi$  and time is  $t$ , then

$$\varphi^2 = \delta^2 + (\lambda + \omega t)^2.$$

Defining:

$$y_i = \frac{\varphi_i^2}{\omega^2}, \quad A = \frac{\delta^2}{\omega^2}, \quad B = \frac{\lambda}{\omega},$$

and supposing that  $\vec{L}^0$  is constant (what is Tail Probe case) it is possible to calculate  $A, B$  by minimizing the sum of square of residuals:

$$S = \sum (A + (B + x_i)^2 - y_i)^2.$$

It should be mentioned that for the case when assumption about constant direction of  $\vec{L}^0$  is not valid, the same approach could be used, but instead constant  $A, B$  their initial values are to be taken. But for constant  $A, B$  the solution in closed form is easy to receive:

$$B = \frac{\sum_i t_i y_i + \frac{1}{n} \sum_i t_i \sum_i t_i^2 - \sum_i t_i^3 - \frac{1}{n} \sum_i t_i \sum_i y_i}{2 \cdot (\sum_i t_i^2 - \frac{1}{n} \sum_i t_i \sum_i t_i)},$$

$$A = \frac{1}{n} (\sum_i y_i - 2B \sum_i t_i - \sum_i t_i^2) - B^2,$$

where  $n$  is number of measurements.

Thus using these expressions it is possible to calculate angular momentum direction but without knowledge of its latitude  $\delta$  sign. As additional information to determine sign of  $\delta$  the spin rate function of time  $\omega_i(t)$  of Sun vector with respect to s/c could be used.

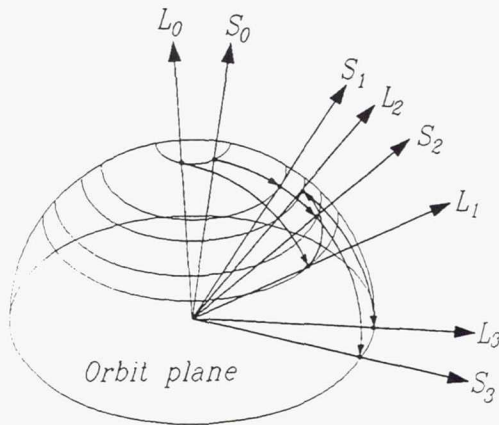


Figure 8.

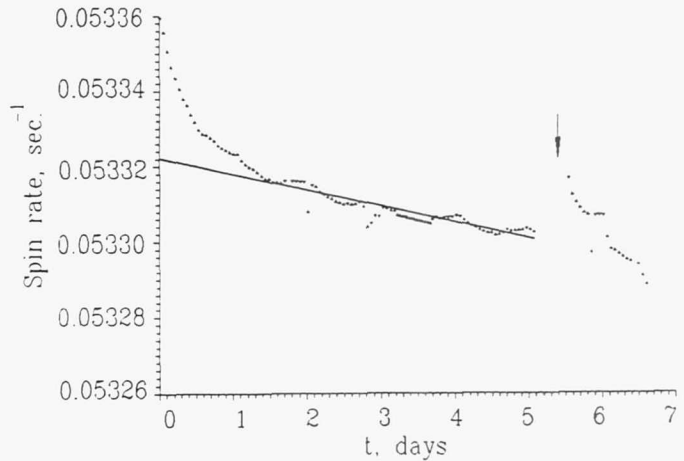


Figure 9.



Figure 9 presents the example of this function from the time interval beginning at November the 20<sup>th</sup> 1996, immediately after session of reorientation of the spin axis (construction axis  $X$ ) towards the Sun. Usually for the Tail Probe the error of angular momentum targeting to the Sun was in  $0.6^\circ$  limit. With the preceding notation the additional spin rate of Sun vector with respect to the s/c due to Earth orbital motion is:

$$\Delta\omega_1 = -\frac{\delta}{\varphi^2} \omega.$$

Supposing that the error in  $L$  targeting goes fully along ecliptic latitude  $\delta$ , i.e.  $\varphi=\delta=0.6^\circ$  we receive

$$\Delta\omega = -1.9 \cdot 10^{-5} \text{ sec.}^{-1}.$$

As it could be seen from figure 9  $\Delta\omega > 0$ , so for this case  $\delta < 0$ . Also from this Figure 9 one can observe the decreasing of spin rate with the rate  $\frac{d\omega}{dt} = -5.4 \cdot 10^{-8} \text{ sec.}^{-1}$ . This value is almost constant during the flight and is explained by propeller effect of solar radiation pressure due to asymmetric mounting of solar panels and booms. Interesting peculiarity of  $\omega_1(t)$  function is sine oscillations with a period equal one day.

Actually there is no these actual oscillations and what one observes is the result of onboard clock rate nearly sinusoid variations caused by diurnal variations of temperature inside s/c. The thermal regime in pressurized s/c body is kept by heaters turned on and switched off once per day so that temperature changes inside  $\pm 5^\circ\text{C}$  limits around mean value about  $25^\circ\text{C}$ . At the part of this curve marked by arrow the big rise of spin rate is seen, but really this visible increasing is caused by deep decreasing of temperature due to durable (about 5 hours) eclipse of s/c when it crossed the Earth shadow. According to thermal sensors measurements the temperature dropped during this event by more then  $15^\circ\text{C}$  with respect to its mean value.

As it could be seen from Figure 9 the amplitude of spin rate oscillation is about  $1.5 \cdot 10^{-6} \text{ sec.}^{-1}$ , i.e.  $2.8 \cdot 10^{-5} \omega_1$ . It means that onboard clock lags behind maximum 0.29 sec. during 0.5 day and then advances beyond next 0.5 day. For the correct clock it leads to the error in spin phase (nominal spin rate is 3 degree/sec.) up to 0.87 degrees. But if clock rate for the scientific instruments using attitude is the same as the one used for spin rate determination the error will be compensated (besides the small enough part connected with the error in position of centre of mass knowledge and relevant error in modelled magnetic field calculation).

Described above method of angular momentum vector determination in inertial space can be applied without significant loss of accuracy only for the data in vicinity of reorientation (1-1.5 days). If these data are not available the other approach works. It is obvious that ~5 days since reorientation the error in spin phase does not exceed  $6^\circ$  if for calculation it is supposed that angular momentum lies in ecliptic plane.



So extrapolating the spin rate of s/c back to the instant of reorientation and using the spin phase taken for the instant several days after reorientation one can calculate the spin phase for any instant. This extrapolation of spin rate is shown on Figure 9 by bold straight line.

## CONCLUSIONS

More than two years experience of attitude determination and control of INTERBALL Project s/c has confirmed the approach based on simple trigonometric approximation of attitude law is effective enough to fulfil all necessary flight dynamics operations. The regimes of solar radiation pressure stabilization have been successfully executed, and attitude manoeuvre have been done without use of spin rate components measurements. Also it has been proven that full set of attitude parameters can be determined with the use only solar sensor measurements.

## REFERENCES

1. Galeev A.A. et al. The INTERBALL Project to Study Solar Terrestrial Physics. Cosmic Research, Vol. 34, No. 4, pp. 339-362.
2. Eismont N., Klas J., Simunek J. Onboard Algorithm for Attitude Determination of Spin Stabilized Spacecraft of INTERBALL Project Based on Optical Sensors and Magnetometer Measurements. Interball Mission and Payload. CNES-IKI-RSA, 1995.
3. Ryazanova E., Eismont N., Chum J. et al. Attitude Control of MAGION Spacecraft. Interball Mission and Payload. CNES-IKI-RSA, 1995.
4. Buchgoltz N. N., Basic Course of Theoretical Mechanics, Part II (in Russian) "Nauka" Publishing House, Moscow, 1967.
5. Eismont N., Khrapchenkov V., et al. Flight Dynamic Operations in INTERBALL Project. Proceedings of the 12<sup>th</sup> International Symposium on "Space Flight Dynamic", ESOC, Darmstadt, Germany, 2-6 June 1997 (SP-403, August 1997), pp. 457-462.
6. Eismont N., Khrapchenkov V., et al. Attitude Determination and Control of MAGION around Centre of Mass of a Satellite and Subsatellite in the INTERBALL Project. Cosmic Research, Vol.34, No. 4, pp. 391-399.
7. Beletsky V.V. Motion of the Earth Artificial Satellite around Center of Mass (in Russian). "Nauka" Publishing House, Moscow, 1965.

**Page intentionally left blank**

## FLIGHT DYNAMICS LEOP AND ROUTINE OPERATIONS FOR SCD2, THE INPE'S SECOND ENVIRONMENTAL DATA COLLECTING SATELLITE

Valcir Orlando\*  
Hélio Koiti Kuga  
Ulisses Thadeu Vieira Guedes

The launch of the second INPE's environmental data collecting satellite, SCD2, is preliminary scheduled for May 1998, by the American Pegasus launcher. This satellite is similar to the SCD2-A, whose launch, in November 2, 1997, by the Brazilian VLS launcher unfortunately, failed. When compared with the SCD1, the SCD2 presents important differences related mainly to attitude stabilization and control. This paper presents an analysis of the main differences between both satellites and discusses their impacts on the flight dynamics system and related operations. For instance, the restriction on spin-axis attitude is, for the SCD2, more stringent than the ones imposed on the SCD1, requiring the application of a Quarter-Orbit Magnetic Attitude Control procedure (QOMAC). The spin-axis attitude control of SCD2 is detailed and its performance is analyzed with the help of available simulation results. Finally, the planning of the flight dynamics operations for the LEOP and routine phase of the SCD2 is described.

### INTRODUCTION

The SCD1, the first environmental INPE's data relay satellite<sup>1</sup>, completed five years in orbit on February 9<sup>th</sup>, 1998, still presenting an overwhelming overall performance. During the SCD1 mission exploitation, the Data Collecting Platform (DCP) network, spread over the Brazilian territory, presented a significant boost, not only in quantity, but also in application diversity. During the first year after the SCD1 launch, the network consisted of about 20 platforms<sup>2</sup>. Nowadays there are 204 DCPs operating, other 167 ones in acceptance phase, and more 106 in acquisition process. As these figures show, the number of operating DCPs, which currently surpasses ten times the initial ones, will soon be doubled. The existing DCPs comprise a wide number of applications, mainly in the fields of Meteorology, Hydrology, Agricultural Planning, Geomagnetism, Atmospheric Chemistry, Tide Monitoring and Tropical Forest Regeneration studies.

---

\* INPE, CP 515, São José dos Campos, SP, Brazil, CEP 12201-970. †Phone: ++55-12-3456374, Fax: ++55-12-3411873



In order to assure the continuity of the environmental data-collecting mission, the second data collecting satellite, the SCD2, has been scheduled by INPE to be lofted in orbit around May 1998, by the North-American Pegasus launcher, which had successfully launched the SCD1<sup>3-4</sup> in February 1993. In spite of the existing similarities between SCD2 and SCD1, there are some fundamental differences that impose important changes on the ground attitude control system. The main differences and the consequences on the flight dynamics operations activities are exposed and discussed in next sections. A further section is dedicated to the presentation of the modified version<sup>5</sup> of a QOMAC<sup>6</sup> (Quarter Orbit Magnetic Attitude Control) algorithm for the spin-axis attitude control which will be used for the SCD2. The expected algorithm performance is discussed based upon simulation results. Finally, the main aspects of the flight dynamics operations for LEOP and routine phase planned for the SCD2 are presented. To close the paper a last section is dedicated to the presentation of the concluding remarks.

## THE SCD2 SATELLITE

The SCD2 satellite has been developed in order to assure continuity of Brazilian Environmental Data Collecting Mission, which is currently being performed using solely the SCD1 satellite. Likewise the SCD1, it will be spin stabilized and will be injected into a low altitude ( $\approx 750$  km) orbit with  $25^\circ$  inclination. It will not have any orbit control. In order to minimize the possibility of having simultaneous passes of both satellites over a ground station visibility region, the right ascension of ascending node of SCD1 and SCD2 shall be separated by about 180 degrees. The attitude control subsystem is composed of a partially fluid filled nutation damper, a three-axis flux-gate type magnetometer, two redundant  $180^\circ$  field of view digital sun sensors, two redundant spin plane coil with magnetic moment of  $4 \text{ Am}^2$  each, and one axis torque coil of  $12 \text{ Am}^2$ . The spin plane coil is automatically activated by an autonomous control system whenever the spin rate reaches the lower limit of its allowable variation range:  $34 \pm 2$  rpm. The attitude sensors outputs will be sampled at a rate of 2 samples per second. Regarding the axis coil, it will be activated by real-time or time-tagged telecommands in order to perform spin-axis attitude maneuvers. Time-tagged telecommands will be needed due to the use of the before mentioned QOMAC algorithm for spin-axis attitude control.

The SCD2 launch will be the INPE' second trial to put a new in-house manufactured environmental data collecting satellite into orbit since the launch of SCD1. The first try was the launch of SCD2-A in the beginning of November 1997, from the Alcântara launching facility, in the northeast of Brazil. It has been the first shot of the Brazilian launcher VLS, which unfortunately failed due to a problem occurred in one of the first stage four boosters.

When compared to SCD1, the SCD2 presents some improvements, mainly related to attitude stabilization and control. The main differences between the satellites and their impacts on the flight dynamics ground operations are discussed in further sections of the paper.

## SPIN-AXIS ATTITUDE

The SCD2 has the same shape as SCD1: octagonal prism with 0.7m height whose base fits within a circle of 1m diameter. The SCD1, however, has the whole lateral faces and the upper one covered by solar cells. The remaining bottom face is used as a heat sink by the passive thermal control subsystem. In this way, sunlight incidence on this face shall not occur, in order to avoid thermal problems with on-board equipment. As the spin-axis is the satellite longitudinal one, this restriction is equivalent to having  $\theta \leq 90^\circ$  where  $\theta$  is the sun aspect angle. In the case of the SCD2, only the lateral panels are covered by solar cells. However, the passive thermal subsystem of this satellite has been designed so as to allow direct sunlight incidence on the top and bottom panels, with maximum angle incidence of up to  $10^\circ$ . In other words, for the SCD2, the sun aspect angle excursion is limited to the range:  $80^\circ \leq \theta \leq 100^\circ$ . Besides, in order to increase the time interval (decrease periodicity) between the execution of successive spin-axis maneuvers, it has been decided to maintain the angle  $\phi$ , between the axis normal to the ecliptic plan and the spin-axis, to less than  $10^\circ$ . It shall be noted that this condition necessarily implies in having  $80^\circ \leq \theta \leq 100^\circ$ . If spin-axis is aligned with the normal to ecliptic plan then the translation motion of the Earth around the Sun does not contribute for the sun aspect angle variation, resulting in a overall lower precession rate. As a consequence, the time needed by the angle  $\phi$  to reach the limit value ( $10^\circ$ ) becomes longer, reducing the need of frequent spin axis attitude maneuvers. In this way, the target of the spin-axis attitude control for the SCD2 will be to maintain  $\phi \leq 10^\circ$ . Whenever the angle  $\phi$  attains ten degrees a maneuver shall be executed in order to decrease this angle to a value less than one degree.

The operational range for spin-axis attitude excursion is narrower for the SCD2 than the one corresponding to SCD1. As a consequence, higher rate of maneuver executions will be required for the spin-axis attitude control of SCD2. Besides this, a more complex attitude control procedure will be needed, in order to comply with the SCD2 spin-axis pointing requirement to be fitted after maneuver execution ( $\phi \leq 1^\circ$ ). As mentioned earlier, a modified version of the QOMAC algorithm has been implemented for this purpose.

## SPIN-AXIS ATTITUDE CONTROL

Nominally, the ideal attitude for the SCD2 spin-axis is the direction orthogonal to the ecliptic plan. In the real case, however, it is allowed a variation of up to  $10^\circ$  of the alignment error angle,  $\phi$ , between the satellite spin-axis and the ecliptic plan normal direction. In order to comply with this requirement, the strategy to be adopted will consist of monitoring the time evolution of  $\phi$  with help of the attitude determination and prediction processes. When the attitude prediction indicates that  $\phi$ , in about two days, will surpass its maximum allowable limit, then a decision to compute a spin-axis maneuver shall be taken. The goal of the attitude control procedure is to reduce the angular alignment error  $\phi$  to near-zero neighborhood. Actually, the final results of a spin-axis



maneuver will be acceptable when the angular error is decreased to a value less than one degree.

In what follows boldfaced characters will represent vector variables and the non-boldfaced characters will represent scalar magnitudes. The  $x$ ,  $y$  and  $z$  axes unit vectors of the satellite body-fixed coordinate system will be denoted, respectively, by  $\mathbf{i}$ ,  $\mathbf{j}$  and  $\mathbf{k}$ .

It is assumed that the satellite nutation motion is maintained close to zero by the action of the satellite partially fluid-filled nutation damper (cone angle less than  $0.25^\circ$ ). As a consequence one can assume that the spin-axis is in the same direction of the satellite angular momentum,  $\mathbf{L}$ , that is:  $\mathbf{s} = \mathbf{k} \equiv \mathbf{L}/L$ , where  $\mathbf{s}$  is the spin-axis unit vector. Calling  $\mathbf{n}$  the unit vector of the direction orthogonal to the ecliptic plan, the vector misalignment error between the spin-axis and  $\mathbf{n}$  can be written as:

$$\mathbf{e} = \mathbf{n} - \mathbf{L}/L \quad (1)$$

Hence,

$$e^2 = (\mathbf{n} - \mathbf{L}/L) \cdot (\mathbf{n} - \mathbf{L}/L) = 2(1 - \mathbf{n} \cdot \mathbf{L}/L). \quad (2)$$

In order to analyze the variation of the quadratic error as a function of the control torque, the derivative of Equation 2 has been, at first, computed:

$$de^2/dt = -2\mathbf{n} \cdot [(1/L)d\mathbf{L}/dt - \mathbf{L}/L^2)dL/dt] \quad (3)$$

The total torque which arises from the interaction between the geomagnetic field,  $\mathbf{B} = B_x\mathbf{i} + B_y\mathbf{j} + B_z\mathbf{k}$ , with the magnetic moment generated by the axis-coil,  $M_{ac}$ , plus the  $z$ -axis component of the residual magnetic moment of the satellite,  $M_{re}$ , is given by:

$$\mathbf{T} = u \mathbf{M} \mathbf{k} \times \mathbf{B} \quad (4)$$

with  $\mathbf{M} = M_{ac} + M_{re}$ , and  $u$  is the discrete control variable defined as:

- $u = -1$  if the axis-coil has been activated inversely ( $M_{ac}$  in the  $-\mathbf{k}$  direction),
- $u = 1$  if the axis-coil has been activated directly ( $M_{ac}$  in the  $\mathbf{k}$  direction) and,
- $u = 0$  if the axis-coil is off ( $M_{ac} = 0$ ).

Because  $M_{re} \ll M_{ac}$  when the axis-coil is activated,  $\mathbf{M}$  will have the same direction of  $M_{ac}$ . From Equation 3 one can see that the torque  $\mathbf{T}$  is always in the  $xy$  plane of the satellite reference frame and hence, orthogonal to the spin-axis direction. For this reason it will cause changes only in the spin-axis direction, having no effect on the spin-axis magnitude. As the magnitude variation of the satellite angular momentum due to the effect of only environmental disturbing torque (mainly caused by eddy currents) is very slow then,



during execution of spin-axis maneuver, one can assume that  $dL/dt \equiv 0$ . Considering this assumption and recalling that  $T = dL/dt$ , Equation 3 can be put in the following form:

$$de^2/dt = -(2/L)n \cdot dL/dt = -(2/L)n \cdot T. \quad (5)$$

Applying the Equation 4 in the equation above one finally arrives to:

$$de^2/dt = -u(2M/L)v. \quad (6)$$

where  $v = n \cdot k \times B$ . Analyzing Equation 6, one can conclude that the scalar  $v$  can be treated as a switching function. If  $v=0$  then, in order to generate a control torque  $uMk \times B$  which causes a reduction of the alignment error ( $de/dt < 0$ ), one shall impose  $u=1$ . As seen above this means that the axis-coil polarity shall be commuted to the positive one (direct). In the same way, Equation 6, indicates that one shall impose the negative polarity to coil ( $u=-1$ ) if  $v=-1$ , and deactivate the coil in the case of having  $v=0$ . This kind of spin-axis attitude control algorithm takes advantage of the fact that the local geomagnetic field acting on a satellite into an inclined orbit oscillates with a frequency of about double of the orbital one. Hence, in order to generate the control torque in only one sense during the entire orbital period, the torque coil polarity shall be switched four times per orbit. Due to this characteristic, this kind of algorithm is called QOMAC. The switching function,  $v$ , defines the adequate torque coil polarities and switching times needed to reduce the alignment error to the zero neighborhood.

In the routine phase of the SCD2 lifetime, the need of spin-axis maneuvers will be predicted by monitoring the alignment error angle with help of the attitude determination and prediction processes. If in a time span of two days the error angle exceeds the maximum allowable limit of operation ( $10^\circ$ ), then a new spin-axis maneuver shall be scheduled. The output of the maneuver calculation procedure consists of the control sequence  $[(t_1, u_1), (t_2, u_2), \dots, (t_m, u_m)]$  to be applied to the satellite in order to decrease the error near to zero ( $\phi < 1^\circ$ , as stated before). The computed control sequence will be transmitted to the satellite in the form of time-tagged telecommands, which are automatically handled by the on-board computer in order to be executed in the proper time instants,  $t_i$ .

Some results, which have been obtained from realistic computer simulations of spin-axis maneuver executions for SCD2, covering a sixty-day time span, are presented in Figures 1 and 2. Nominal parameter values were considered. The numerical attitude integration step has been set to 5 minutes. The Figure 1 shows the curve, which has been obtained for the alignment angle error,  $\phi$ , as a function of time. One can observe from this figure that three spin-axis maneuvers has been needed, during the whole simulation period, in order to maintain the alignment error inside the allowed variation range. Also observed is that about one maneuver every thirteen days was necessary, showing that, in nominal situation, no maneuver execution will be needed during LEOP.

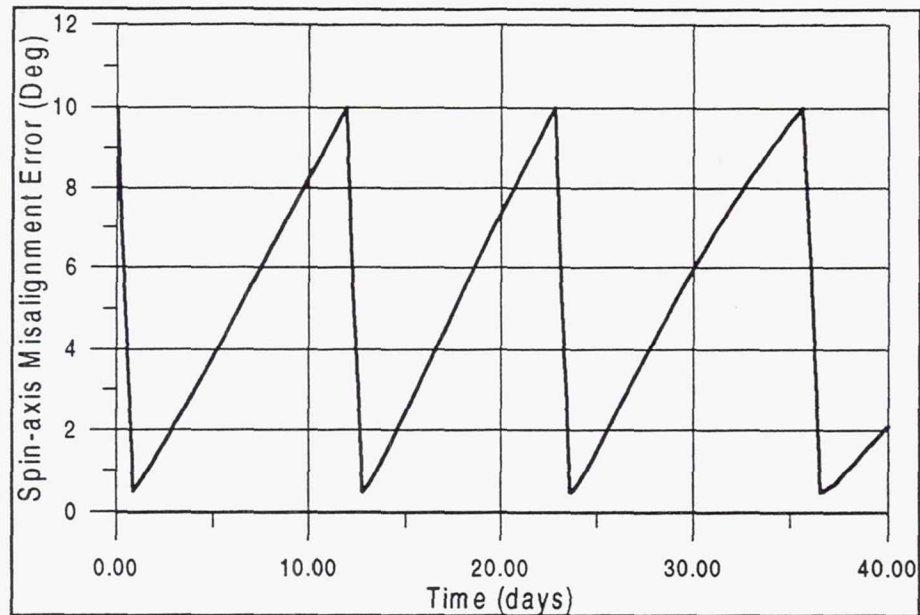


Figure 1. Spin-axis Angle Alignment Error Time Evolution

The Figure 2 shows the time evolution curve of the discrete control variable,  $u$ , during the first maneuver execution time.

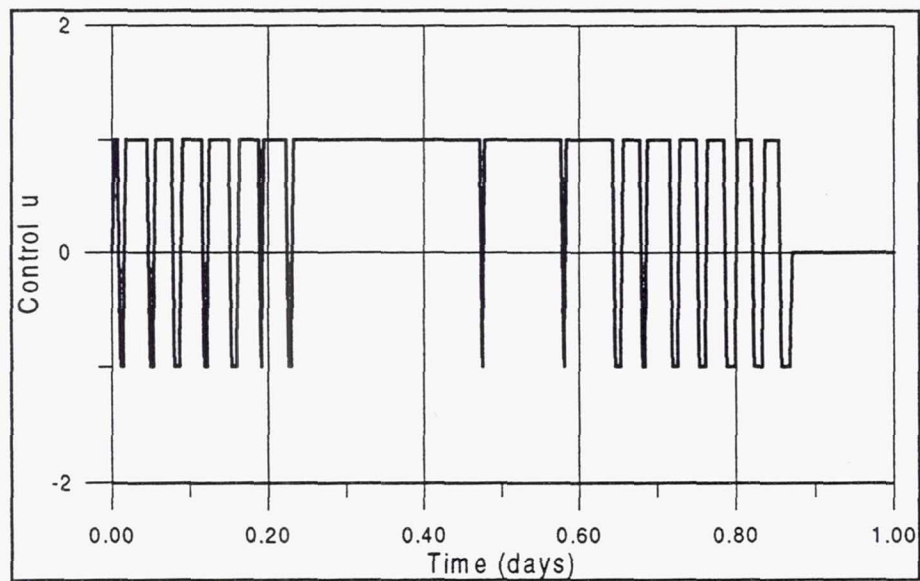


Figure 2. Coil Polarity During Maneuver Execution

## SPIN RATE CONTROL

The flying SCD1 satellite has no spin rate control. It was launched with spin rate of 120 rpm, which decayed to current values of about 50 rpm. In order to reduce the time required for execution of spin-axis maneuver, the spin rate has been reduced for SCD2 to

the range between 32 to 36 rpm. Every time the spin rate decreases to the lower limit an autonomous control system driven by magnetometer outputs automatically activates the spin plane torque coils, in order to increase again the spin rate up to the maximum value (36 rpm). If, on one hand, having a lower spin rate will reduce the time needed to perform spin-axis attitude maneuvers, on the other hand it will increase the periodicity between two successive maneuvers, since the spin axis precession motion will also be faster due to decreased gyroscopic stiffness.

Calling  $B_{xy}$  the orthogonal projection of the geomagnetic field in the satellite frame  $xy$ -plane and  $M_{pc}$  the magnetic moment of a magnetic coil fixed along the  $x$ -direction, the torque generated by the interaction between  $M_{pc}$  and the geomagnetic field,  $T_{pc}$ , is then given by:

$$T_{pc} = u_{pc} M_{pc} \times B_{xy} = u_{pc} M_{pc} B_{xy} \sin \beta k. \quad (7)$$

In this equation:  $u_{pc}$  is the discrete spin rate control variable which defines the plane coil state: deactivated ( $u_{pc} = 0$ ), activated in the direct sense ( $u_{pc} = 1$ ) or in the inverse sense ( $u_{pc} = -1$ ) and  $\beta$  is the phase angle between the plane coil axis and  $B_{xy}$ . As the coil is aligned with the  $x$ -axis of the satellite frame one can write:

$$B_{xy} \sin \beta = B_y \quad (8)$$

Hence, the Equation 7 becomes:

$$T_{pc} = u_p M_{pc} B_y k \quad (9)$$

This equation shows that the control variable  $u_p$  shall have the same or opposite sign of  $B_y$ , in order to, respectively, increase or decrease the satellite spin. In this way, as  $B_y$  has a sinusoidal time variation owing to the satellite rotational frequency, the plane coil polarity shall be commuted every half rotation, in order to control the spin rate. In the case of SCD2 this is accomplished automatically with help of the  $y$ -axis output signal of the satellite three-axis magnetometer. During actuating periods of the spin rate control system, the plane coil polarity is automatically commuted every time the magnetometer output voltage changes its signal. As mentioned above, the control system will be automatically activated every time the satellite rotation decreases to 32 rpm. When, under its action the spin rate is increased to 36 rpm the system actuation stops. The spin rate, then, begins to decrease again under the main influence of the  $z$ -axis component of the eddy current disturbing torque. Calling  $\omega$  the satellite angular velocity magnitude and  $p$  to the eddy-current parameter, which depends on the satellite geometry and material conductivity, this torque is given by:

$$T_{ed} = -p\omega (B_x^2 + B_y^2) k \quad (10)$$



Is important to mention that, as a redundant safeguard, the spin-axis control system can also be activated from ground telecommands.

The SCD2 will be inserted into orbit with a spin rate of about 50rpm. Although this rate is higher than the nominal upper limit value (36 rpm), the activation from the ground of the spin rate control system, in order to reduce the rotation, is not intended to be performed. The spin rate control shall act automatically the first time only when the spin rotation naturally reaches its lower limit of the operation range (32 rpm). During the satellite in-orbit acceptance tests, however, the system performance will be analyzed.

## **DIFFERENT ANTENNA POLARIZATION AND CONSEQUENCES**

The former SCD1 satellite has TM/TC and payload antennas on both top and bottom panels. All satellite antennas work in LHC (Left-Hand Circular) polarization. The SCD2 has also TM/TC antennas on both panels but it has only one payload antenna located on the lower panel. Another important difference between the satellites concerning the antennas is related to the antenna polarization. In the SCD2 satellite the antennas of the top and bottom panel work with opposite polarization.

It has been observed in the SCD1 that the use of equal polarization for both the upper and bottom panel antennas caused a small satellite to ground communications silent periods, when the angle between the ground station to satellite and spin-axis directions (aspect angle) is near  $90^\circ$ . Actually, these silent periods (communication gaps) were of very weak magnitude being not enough to cause the loss of the down and uplink signals. During such occurrences the down link signal becomes a little noisy, returning however to the normal state after few seconds. The silent periods are predicted with help of the attitude determination and prediction processes and inserted in the pass prediction reports, which are periodically sent to the ground stations. The actions of sending telecommands or performing ranging sections are avoided near and within the time intervals when silent zones are predicted to happen. In the case of SCD2, the occurrence of satellite to ground silent periods are expected to be eliminated with the use of opposite polarization between the top and bottom panel antennas. The existence of such periods will, however, be replaced by the need of commutation of the ground station antenna polarization each time the aspect angle crosses  $90^\circ$ . With this purpose the ground stations antenna control software has been modified in order to read from the pass prediction file, the information about the instant when the aspect angle crosses  $90^\circ$  during a given pass, and automatically to commute, in real time, the antenna polarization. This feature makes invisible to ground station operators the occurrence of ground antenna polarization commutations, as regarding the downlink signal. The TM reception is not interrupted when such commutations occur. Unfortunately, that is not the case with the uplink signal. The uplink is always lost when the satellite antenna which is receiving the ground station signal, is replaced by the other one located at the opposite panel, due to the evolution of the satellite to ground station relative attitude. One estimates that about 30 seconds is needed to reestablish the uplink, each time it is lost. This is a major drawback of adopting different polarization between the top and bottom panel antennas.

## LEOP AND ROUTINE PLANNING OF FLIGHT DYNAMICS OPERATIONS

The Figure 3 shows the first nominal orbit ground tracks of the SCD2, and the visibility regions of the Alcântara and Cuiabá Brazilian ground station antennas. It is to be noted that the two initial orbits are visible only from Alcântara. Follows a sequence of eight consecutive orbits, which are visible from Cuiabá, beginning from the third one after orbit injection.

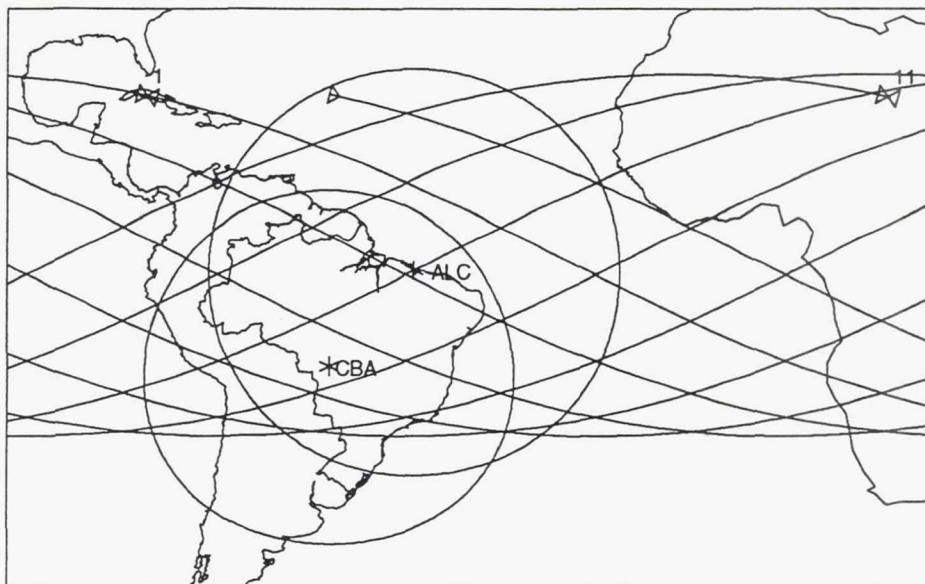


Figure 3. First Orbit Ground Tracks

The needed information about the injection time and related orbit and attitude state, are expected to be handed over to INPE's control center by the Launcher Control Center within 10 minutes after in-orbit injection. The received data set will be analyzed and compared with the nominal one. At first it will be validated, in order to verify if it does not present inconsistently large errors, which could be caused by problems occurred in any phase of the data acquisition and transmission process. In case the validation shows there have been a problem with the data, and if a new set of valid data can not be made available before the next pass over Alcântara then, the next pass will be predicted from the nominal orbit and attitude state at injection point. In the reverse case, the ground station pass prediction data will be computed using the just received information as initial conditions. Redundant pass prediction sets, computed from nominal parameters, will be employed as backup, if the use of the previous set does not yield a prompt satellite signal acquisition from the ground station antenna.

From here it will be described the planned flight dynamics operations during the considered nominal situation. Independently of which initial information set has been used in the generation of the first pass prediction data, it is assumed that, in the future passes, the satellite signal is acquired with no problem by both ground stations.



After the second satellite pass over Alcântara the first orbit determination is planned to be performed. The obtained results will be used in the generation of the pass prediction data set for tracking the third orbit. Redundant set of pass prediction will also be computed from the initial conditions used to track the previous pass.

In the third orbit, as seen before, the satellite begins a sequence of eight consecutive passes over Cuiabá. One quick look orbit determination after each pass is planned to be performed until the end of the first cycle of visible passes over Cuiabá. Each orbit determination will be generated from the entire set of ranging data available until the corresponding current time. At the end of the first cycle of consecutive passes over Cuiabá, the (hopely) convergent orbit determination results should, nominally, be accurate enough in order to allow the generation of one-day pass prediction data set. Therefore, after the eighth orbit only one orbit determination will be performed daily. After the first week since orbit injection, a weekly routine will be adopted. At this time, in the nominal situation, the accuracy of the pass predictions should be good enough to allow the satellite tracking during the next three weeks, with no satellite signal acquisition problem. From this time on a weekly routine will then be adopted for orbit determination operations.

The SCD2 attitude determination process is similar to the SCD1 one<sup>7</sup>. It is needed not only to monitor and control the spin-axis attitude. For this satellite also needed is to compute, and include in the pass predictions, the information concerning the instant when the aspect angle will cross 90°, during each predicted pass. When this occurs, as explained in a previous section, the ground station antenna polarization shall be automatically commuted. In the initial orbits, one **preliminary attitude determination** is expected to be performed after each satellite pass over the ground stations. The preliminary attitude determination process, consists of the estimation of the satellite angular velocity vector,  $\omega$ , from the entire amount of the telemetry data which has been collected during one single satellite pass. In other words, after each pass the attitude TM data, which has been just gathered in the finished pass, is used to compute an updated estimation of  $\omega$  through the execution of the preliminary attitude determination process. This estimate will be used, together with the orbit determination results, in the computation of the next pass prediction set to be sent to the ground stations. The first **fine attitude determination** will be performed only one week after the injection. This process consists of the computation of an improved estimate of  $\omega$  and the estimates of the dynamical parameters  $M_{re}$  (residual magnetic moment) and  $p$  (eddy current parameter) by using as observations the pre-estimates of the satellite angular velocity computed by the previous preliminary attitude determination. The estimates of  $M_{re}$  and  $p$  are used in the attitude propagation process in order to improve the long term prediction accuracy. After the execution of the first fine attitude determination, this process and the preliminary one will follow a weekly execution routine.

Once the Pegasus launcher has maneuver capability, which allows the insertion of the satellite in the required attitude then, in the nominal case, no spin-axis maneuver execution will be needed during LEOP. The first spin-axis attitude maneuver is, as mentioned before,



to be executed only when the error limit of the alignment angle,  $\phi$ , is attained the first time, during the routine phase.

## CONCLUSIONS

The SCD2 satellite shows some important differences when compared with SCD1 satellite. These differences imposed more stringent restrictions to the satellite attitude control. With the aim of satisfying the new spin-axis attitude alignment accuracy, a new software was developed, which implements a rather sophisticated attitude control algorithm. Besides, the significant reduction of the spin-axis attitude variation range imposed the need of having a higher rate of maneuver executions for the SCD2. In order to reduce the gyroscopic stiffness of the spin-axis to attitude changes, therefore reducing the maneuver duration, a lower nominal spin-rate value of about  $34 \pm 2$  rpm has been adopted. In addition, to avoid that the spin rate decreases to excessively small values, which can imply losing the satellite attitude stabilization, an autonomous spin-rate control system has been added to the satellite hardware.

Hence, it is foreseen that the SCD2 operation will add to INPE's flight dynamics crew an extra gain of skillness towards an economical and functional magnetic attitude control of spin stabilized satellites.

## REFERENCES

1. V. Orlando, R. V. F. Lopes, H. K. Kuga, "INPE's Flight Dynamics Team Experience Throughout Four Years of SCD1 In-Orbit Operations: Main Issues, Improvements and Trends", 12<sup>th</sup> International Symposium on Space Flight Dynamics, ESOC, Darmstadt, Germany, June 1997, p. 433-437.
2. W. Yamaguti, E. A. Ribeiro, J. C. Becceneri, and S. N. Itami, "Collection and Treatment of the Environmental Data with the Brazilian Satellite SCD1", Revista Brasileira de Ciências Mecânicas, vol. XVI, special issue, February 1994, p. 205-211.
3. P. Rozenfeld, V. Orlando, E. M. Schneider, "Overview of the INPE's Satellite Tracking and Control Center and Main Aspects of its Debut in Satellite Operations", Revista Brasileira de Ciências Mecânicas, Vol. XVI, Special issue, February 1994, p. 421-425.
4. P. Rozenfeld, V. Orlando, R. R. B. Miguez, "SCD1 Three Years In-Orbit Operations", SPACEOPS-96: Fourth International Symposium on Space Mission Operations and Ground Data Systems, ESOC, Darmstadt, Germany, September 1996.
5. L. D. D. Ferreira, J. J. Cruz, "Attitude and Spin Rate Control of a Spinning Satellite Using Geomagnetic Field", Journal of Guidance, Control, and Dynamics, Vol. 14, no. 1, January-February 1991, p. 216-218.
6. M. Shigehara, "Geomagnetic Attitude Control of an Axisymmetric Spinning Satellite, Journal of Spacecraft and Rockets, vol. 9, n. 6, June 1972, p. 391-398.
7. R. V. F. Lopes, V. Orlando, H. K. Kuga, U. T. V. Guedes; R. R. Kondapalli, "Attitude Determination of the Brazilian Satellite SCD1", Revista Brasileira de Ciências Mecânicas, Vol. XVI, Special issue, February 1994, p. 11-18.

**Page intentionally left blank**

## **ANALYSIS OF DOCKING OPERATIONS EXPERIENCE OF THE PROGRESS VEHICLES AND THE MIR STATION USING TELEOPERATOR CONTROL MODE**

**T. V. Matveeva**

**Rocket Space Corporation ENERGIA**

**Lenin St., 4a, Korlev, Moscow Region, 141070, Russia**

**Tel: 007(095)513-8133, fax: 007(095)513-6138**

**E-mail: [sandy@mcc.rsa.ru](mailto:sandy@mcc.rsa.ru)**

### **ABSTRACT**

Teleoperator control mode (Russian acronym is TORU) was developed to enhance reliability of docking operations of the Progress transport cargo and the Mir orbital complex. In the cases of automatic mode failure while docking an operator can take up the motion control function and finish the docking manually. This operator may be either a member of the orbital station crew or a ground controller. Pros and cons of TORU mode are considered in this paper. Its advantages over other methods of docking reliability increasing are discussed.

The final result of TORU mode usage mostly depends on correct planning of the docking operation. To take into account all the specific conditions, limitations and requirements is very important. This paper presents the basic principles of consideration TORU features during mission planning, which can be recommended for transport operations in the International Space Station (ISS) program.

For the first time TORU mode was tested in 1993 while Progress M-15 and Progress M-16 missions. Since then this method was repeatedly checked in flight and was adopted as alternate nominal mode. The experience of docking operations of the Progress vehicles in the Mir station program is analyzed in this paper. The real facts from the Progress vehicles planning practice are given.

TORU mode has attracted considerable attention on the 25<sup>th</sup> of June 1997 when the collision between Progress vehicle and the Mir orbital complex occurred. This paper presents short analysis of that off-nominal situation together with the demonstration of computer animation of mutual vehicle and station motion.



**Page intentionally left blank**

## MARS GLOBAL SURVEYOR NAVIGATION AND AEROBRAKING AT MARS

**P. Esposito, V. Alwar, S. Demcak, E. Graat, M. Johnston and R. Mase**  
**Jet Propulsion Laboratory, California Institute of Technology**  
**4800 Oak Grove Drive**  
**Pasadena, California 91109, USA**  
**E-mail: Pasquale.B.Esposito@jpl.nasa.gov**  
**Phone: (818) 393-1264; Fax: (818) 393-3147**

The Mars Global Surveyor (MGS) spacecraft was successfully inserted into an elliptical orbit around Mars on 9/12/97, 01:53:49 UTC. This orbit was near polar (inclination=93.26 deg) with an orbital period of 44.993 hours and apoapsis and periapsis altitudes of 54,025.9 km and 262.9 km respectively. After a short aerobraking (AB) initiation interval (9/12/97 to 10/2/97), the main phase of AB or orbit period reduction was established. However shortly thereafter, a significant problem with the minus-Y axis solar array developed which necessitated a temporary suspension of AB. Ultimately, this forced the Project to abandon the original plan to complete AB on 1/18/98 and establish the mapping orbit on 3/15/98.

The revised plan called for a reduced level of AB, thus subjecting the solar array and yoke assembly to less aerodynamic stress. After 201 orbits and 196 days after MOI, the first phase of AB has ended; the orbital period was 11.64 hours with apoapsis and periapsis altitudes of 17,870.3 and 170.7 km respectively. At present, MGS is in a science phasing orbit (SPO) and shall acquire science data from 3/28/98 to 9/11/98. Thereafter the second phase of AB shall begin and is expected to end during Feb 1999 when the orbital period shall be 1.9 hours and the orbit's descending node shall be at the 2:00 am (local mean solar time) orientation.

## MARS ORBIT INSERTION AND CAPTURE ORBIT ACCURACY

The Mars Global Surveyor (MGS) spacecraft was successfully inserted into an elliptical orbit around Mars on 9/12/97, 01:53:49 UTC. This was accomplished by accurate orbit determination establishing the Mars approach trajectory and precise control of the spacecraft during the main-engine, Mars orbit insertion (MOI) burn. The velocity-change specified by the Navigation Team was accomplished as a "pitch-over" maneuver. Thus, the thrust vector was directed along the spacecraft's anti-velocity vector throughout the burn. A pitch-rate of 1.21 deg/min was specified for the burn duration resulting in a 27.5 deg burn, angular arc centered on periapsis. This procedure was adopted in order to improve the efficiency of this maneuver. It saved the equivalent of 20 m/s in propellant as compared to an inertially-fixed attitude. The implementation of the MOI burn involved a 20 sec ullage burn using a series of eight small thrusters, with an effective thrust of 31.1 N, followed by

a 1339.7 sec firing of the main engine, with an effective thrust of 655.3 N. The braking velocity-change was 973.0 m/sec. Both targeted and achieved capture orbital elements are specified in Table 1. This paper provides a continuation of the state of navigation activities; interplanetary phase results were presented in Ref. 1.

**Table 1**  
**MGS MARS ORBIT INSERTION RESULTS**

<u>Orbit Element</u>	<u>Target Value</u>	<u>Achieved Value</u>
Period, hours	45.0	44.993
Periapsis altitude, km	250.0	262.9
Inclination, deg	93.3	93.258

## AEROBRAKING INITIALIZATION

With the capture orbit established, we now initialized aerobraking by gently stepping into the atmosphere, by lowering the periapsis altitude, by a series of small propulsive maneuvers executed at apoapsis. Our orbit numbering procedure identified the first periapsis which occurred during the MOI maneuver as P1. Thus, orbit one started at P1, goes through the first apoapsis, A1, and ends at the second periapsis, P2. A series of six AB initialization maneuvers occurred as shown in Table 2. Given are the velocity-change magnitude for each maneuver, the resulting periapsis altitude and an estimate of the atmospheric density and dynamic pressure at the altitude shown. The densities were derived from an analysis of approximately one orbit of two-way, coherent doppler data. This completed the initialization or walk-in phase; the next AB phase, called the main phase, was defined by a dynamic pressure corridor with upper and lower limits being 0.68 N/m<sup>2</sup> and 0.58 N/m<sup>2</sup> respectively. The upper limit provided for adequate orbit period reduction and safety against aerodynamic heating of critical spacecraft components. The lower limit insured a minimum level of orbit period reduction. Ref. 2 provides the basis for the AB design and planning implemented during flight operations.

Two basic requirements were levied on navigation to insure that MGS was in the correct attitude throughout the drag pass and to guard against unexpected, intrinsic density variation from periapsis to periapsis. These were a) predict the time of periapsis-passage (Tp) to within 225 seconds and b) predict the altitude at periapsis-passage (hp) to within 1.5 km.

**Table 2**  
**INITIALIZATION OF AEROBRAKING: THE WALK-IN PHASE**

<u>Apoapsis and Walk-in Maneuver</u>	<u>Velocity-Change Magnitude (m/sec)</u>	<u>Resultant Periapsis Altitude (km)</u>	<u>Atmospheric Density and Dynamic Pressure at Periapsis ( kg/km<sup>3</sup>; N/m<sup>2</sup> )</u>
3 AB-1	4.4	149.3	0.36; 0.00 at P4
4 AB-2	0.8	128.4	5.61; 0.06 at P5
5 AB-3	0.3	121.4	10.7; 0.12 at P6
7 AB-4	0.2	116.1	20.1; 0.23 at P8
10 AB-5	0.2	111.2	42.2; 0.49 at P11
11 AB-6	0.05	110.5	45.7; 0.53 at P12



## MAIN PHASE AEROBRAKING AND TEMPORARY SUSPENSION

The main phase of AB began with P12 on 10/2/97. During P12 through P15, the orbital period decreased on average by 75.1 min per pass or from 40.4 hours to 36.4 hours due to AB. However, during these periapses, a problem was detected with one of the solar arrays; the minus-Y axis, solar array was deflecting more than was expected as MGS was going through periapsis-passage. During this time, the plus-Y axis, solar array behaved normally. In order to proceed prudently, the Project decided to reduce the AB induced pressure on the solar array and thus the periapsis altitude was increased by 11.0' km with a maneuver at A15. During P16 through P18, the solar array problem persisted and a decision was made to raise the periapsis altitude out of the atmosphere. On A18, this maneuver was performed which increased the altitude to 171.7 km at the following periapsis. MGS remained in this "hiatus orbit" for seventeen orbits (P19 through P36). Mean atmospheric densities were determined for each of these using doppler data and analysis to be described in the next section. After considerable analysis and review of engineering and science data and solar panel ground tests (Ref. 3), AB was resumed with maneuver ABM-3 on 11/7/97. However, the intensity of AB was reduced to a safer level; the new dynamic pressure corridor was 0.15 to 0.25 N/m<sup>2</sup>.

**Table 3**  
**ABMs EXECUTED TO ESTABLISH THE "HIATUS ORBIT"**

Apoapsis and ABM	Velocity- Change Magnitude (m/sec)	Resultant Periapsis Altitude (km)	Atmospheric Density and Dynamic Pressure at Periapsis (kg/km <sup>3</sup> ; N/m <sup>2</sup> )
15 ABM-1	0.5	121.0	17.8; 0.20 at P16
18 ABM-2	2.3	171.7	0.04; 0.00 at P19

## WALK-IN AND RE-ESTABLISH THE MAIN PHASE OF AEROBRAKING

A second walk-in strategy was executed similarly to the first walk-in procedure; that is, by slowly reducing the altitude at periapsis by ABMs and assessing the atmospheric density. Once the safety of the spacecraft was assured, another ABM was executed decreasing the periapsis altitude. This continued until a steady level of period reduction (or the dynamic pressure was within the new corridor) was achieved while maintaining safety margins for any stress exerted on the solar array and yoke assembly.

### Orbit Analysis Strategy

From MOI until the end of phase 1 AB, orbit determination was performed every orbit by analysis primarily of two-way, coherent doppler and on occasion using one-way doppler (spacecraft to station doppler-shift using the ultra-stable oscillator on the spacecraft as the frequency reference). This was done to a) determine the atmospheric density at periapsis, b) establish a density database for trending and prediction, c) provide the spacecraft team with orbital predictions within the previously stated requirements, d) provide the science teams reconstructed and predicted orbital information for planning and analysis and e) provide the DSN with tracking station angular and doppler-shift predictions. The data acquisition strategy was to acquire a little over one orbit of doppler measurements extending 2-5 hours past periapsis-passage. Because of the spacecraft's

attitude during the drag pass and the geocentric occultation, no tracking data were acquired within approximately one hour centered on periapsis-passage. Range data were acquired occasionally but for Mars ephemeris refinement rather than for orbit determination.

A fiftieth order and degree Mars gravity field model was used as the baseline model in this analysis and is described in Ref. 4. Initial estimates of Mars atmospheric density were determined from the Mars-GRAM (MG) program (Ref. 5). This density information was converted to a static, exponential density model with three input parameters: the base density at the base altitude and the density scale height. Note that other perturbations occurred throughout periapsis-passage, notably spacecraft thrusting in order to maintain spacecraft attitude. Thrusting usually started 5-7 minutes after periapsis and lasted intermittently for about 5 minutes. This effect was modeled initially in our software from telemetry information provided by the spacecraft team. The effective velocity perturbation due to thrusting, usually 1-10 mm/sec, was small compared to that due to the integrated drag effect, approximately 1 m/sec (excluding the hiatus orbits).

In a representative analysis, doppler data were sampled at sixty second intervals. Post-fit doppler residuals generally have a standard deviation of 2.9 mHz (X-band) or 0.051 mm/sec in range-rate.

### Atmospheric Density Determination and Orbit Period Reduction

The acceleration due to atmospheric drag was modeled in the navigation software as

$$\ddot{\mathbf{r}} = -\frac{1}{2}\rho v_r^2 \frac{C_d A}{m} \hat{\mathbf{v}}_r \quad (1)$$

with an exponential density model

$$\rho = \rho_0 e^{-(h-h_0)/H} \quad (2)$$

In these equations,  $C_d$  is the drag coefficient (= 1.89 initially and 1.99 after P13),  $A$  the effective, cross-sectional area of the spacecraft (= 17.02 m<sup>2</sup>),  $m$  the mass (= 767.8 kg after MOI to 760.4 kg after A201),  $\rho(h)$  is the density at altitude  $h$  and  $\mathbf{v}_r$  is the spacecraft's velocity relative to the atmosphere (with the circumflex denoting a unit vector). The base density and base altitude are given by  $\rho_0$  and  $h_0$  with  $H$  being the density scale height. Note that the dynamic pressure is defined as  $\rho v_r^2/2$  as in Eq. 1. An estimate of the orbit period change per periapsis passage is given by (Ref. 6)

$$\Delta P = -6\pi \left(\frac{\pi}{2}\right)^{\frac{1}{2}} \frac{C_d A}{m} \rho_p H^{\frac{1}{2}} \frac{a^2}{\mu} \left[ \frac{(1+e)^3}{e(1-e)} \right]^{\frac{1}{2}} \quad (3)$$

where  $\rho_p$  is the density at periapsis,  $a$  and  $e$  are the orbit's semi-major axis and eccentricity and  $\mu$  is Mars' gravitational constant (= 42,828.3 km<sup>3</sup>/sec<sup>2</sup>). It is clear from Eq. 3 that the periapsis density and scale height will be highly correlated if one attempts to solve for both parameters from a single orbit of data under the data acquisition condition mentioned previously. Also note that for the same density, significantly larger period reduction shall occur early in AB because of the dependence on the square of the semi-major axis.



For every orbit, the base density was estimated, holding the scale height constant, along with other relevant parameters. Based upon the Viking mission results (Ref. 7) and a cooperative collaboration with the MGS accelerometer experiment team (Ref. 8), we used an average scale height of 6.0-7.0 km throughout much of our analysis. This was the basis for the determination of the densities and dynamic pressures given in Tables 2-5 and Figures 1 and 2. The single density near 150 km was evaluated during the initial walk-in and the smaller densities were determined during the hiatus orbits and several orbits in the SPO phase. A mean scale height of 9.0 km was deduced over the altitude range given in Figure 2.

The orbit period reduction due to AB is summarized in Figure 3. Clearly shown is the initial steep rate of period reduction, the suspension of AB and the re-initialization of AB at a reduced level. Figure 4 shows the period change per orbit. The largest period change per orbit, -93.9 min, occurred during P15 when the density was  $78.3 \text{ kg/km}^3$  corresponding to a dynamic pressure of  $0.90 \text{ N/m}^2$ . Note that this figure was truncated at minus 30 min period change in order to clearly resolve smaller changes. From P8 to P15, seven orbits had period reductions greater than 30 minutes.

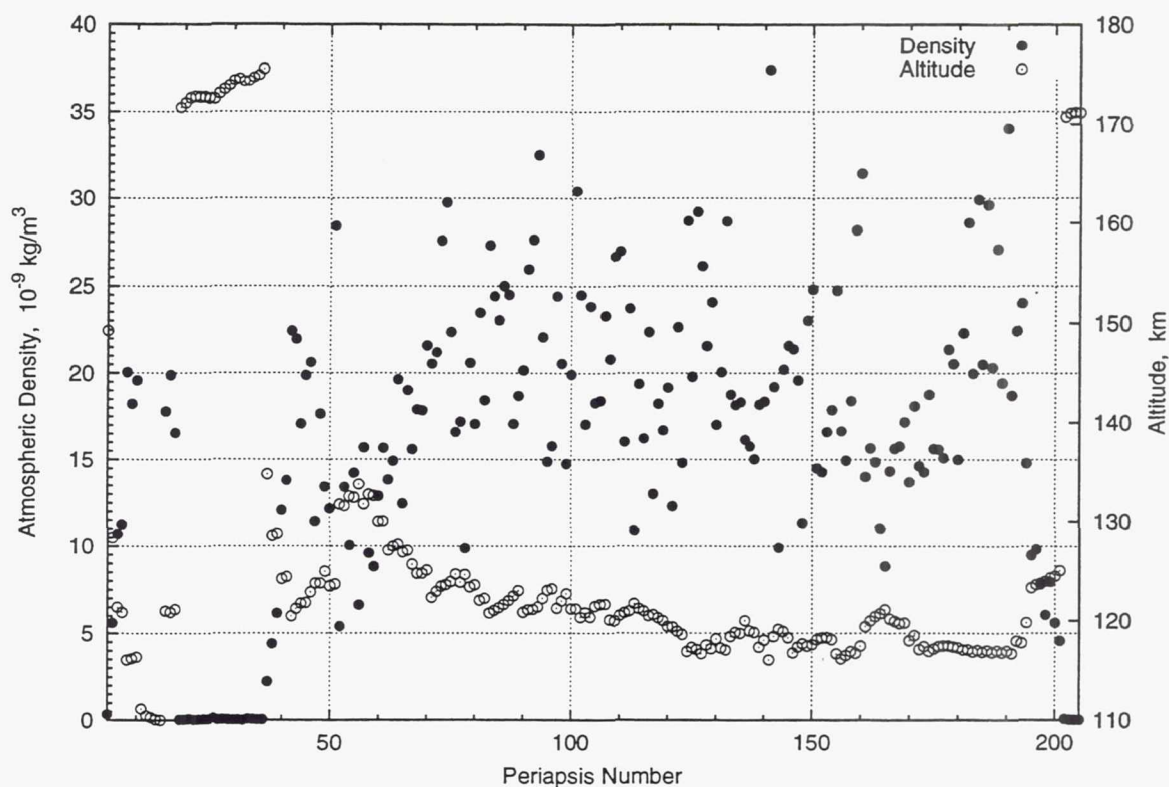


Figure 1 Atmospheric Density At Periapsis Evaluated At The Altitudes Shown Throughout AB Phase 1.



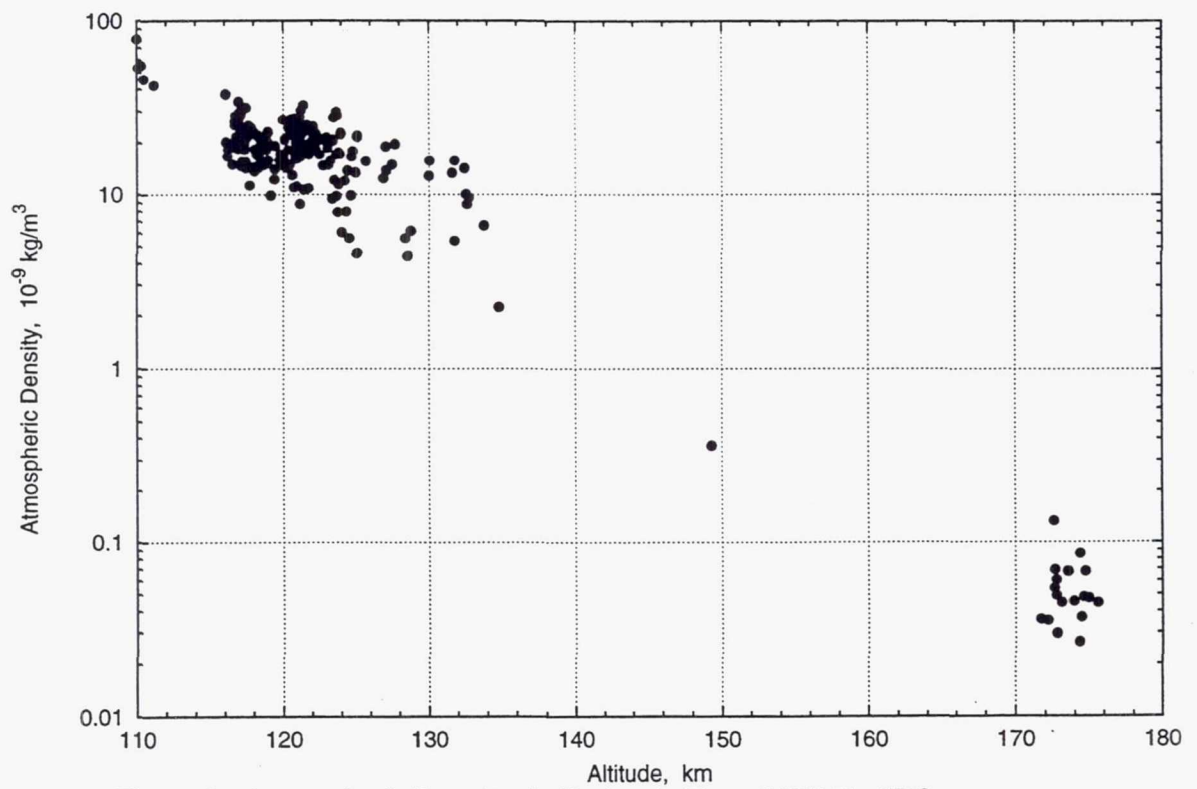


Figure 2 Atmospheric Density At Periapsis From MOI To SPO.

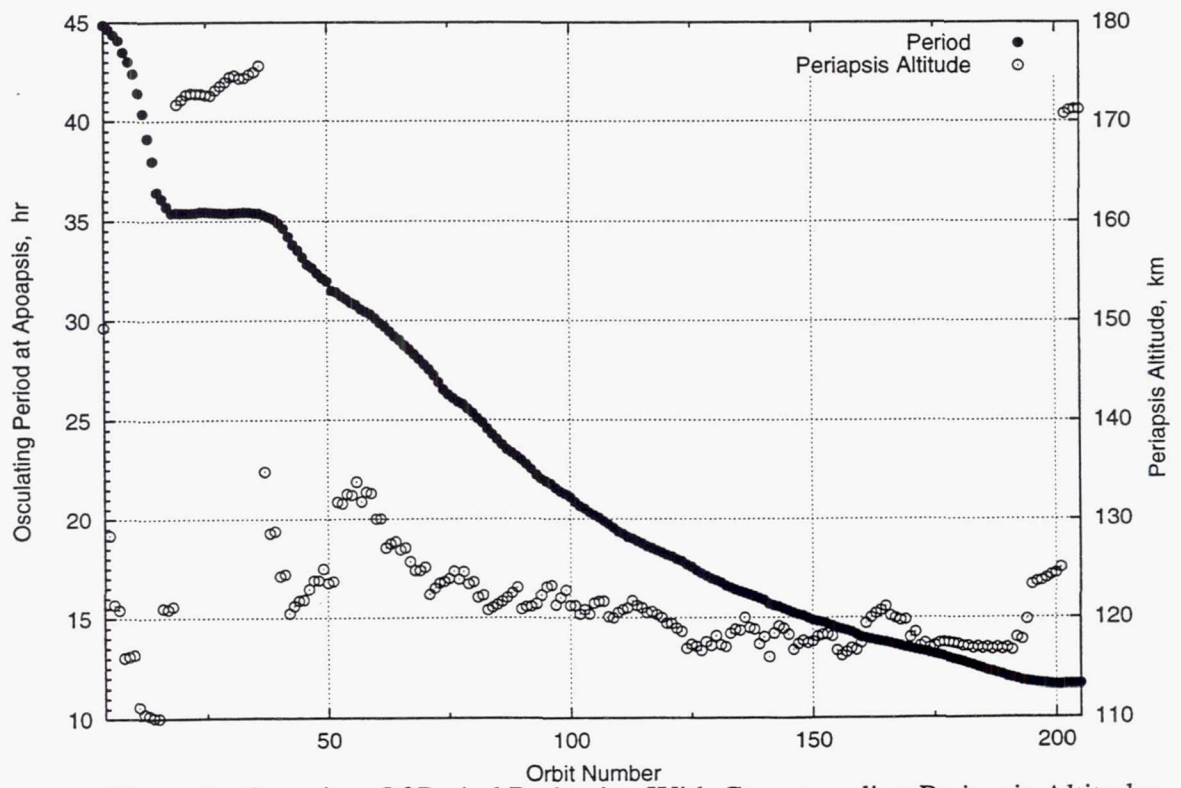


Figure 3 Overview Of Period Reduction With Corresponding Periapsis Altitudes.

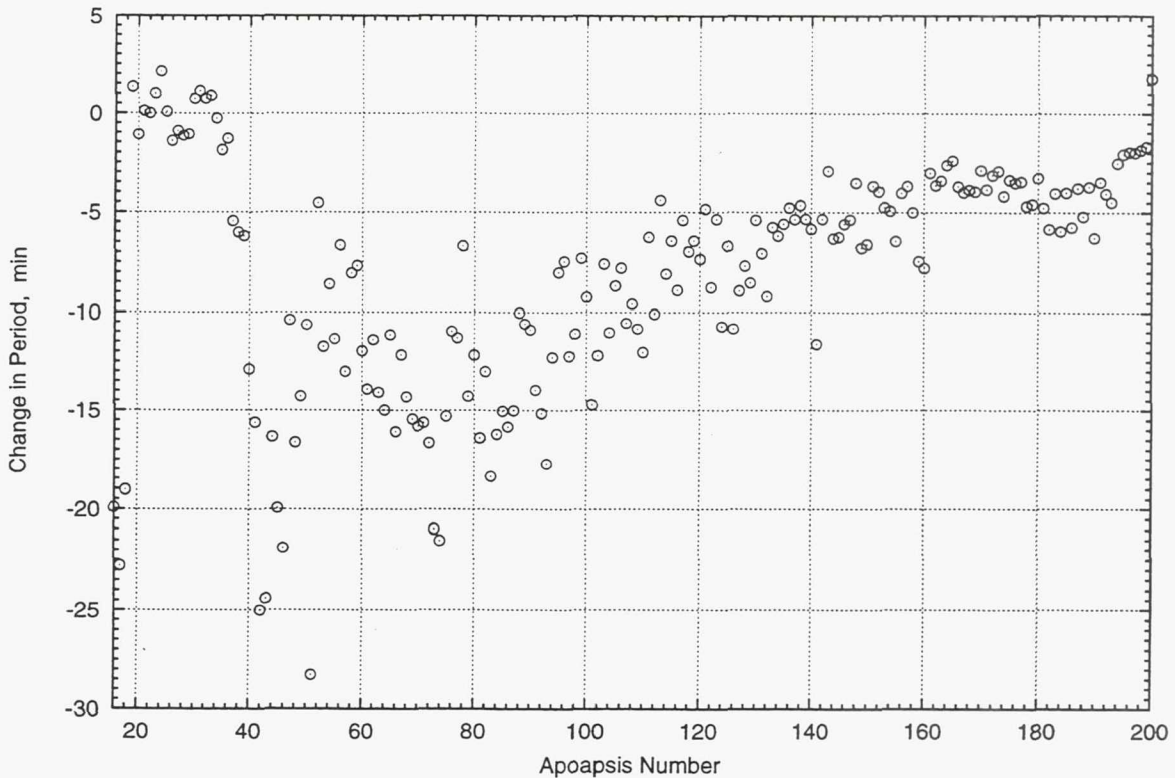


Figure 4 Period Changes Per Orbit During AB.

### ABMs - Adjusting the Altitude At Periapsis-Passage For Corridor Control

During the main phase of the revised AB plan, the near term objective was to achieve an 11.64 hour orbit period by 3/22/98 but no later than 4/22/98 near the start of the solar conjunction phase of the mission. While this provided substantial time margin for achieving the objective, an early termination of AB was desirable. This would allow more science data acquisition in the SPO prior to solar conjunction which shall occur on 5/13/98.

In principle, the plan was straightforward. Stay within the dynamic pressure corridor, achieve the expected level of orbit period reduction and terminate AB as scheduled. In practice, difficulties arose because of the uncertainty in predicting the atmospheric density throughout the drag pass even one orbit into the future.

Assembled in Table 4 are all of the AB propulsive maneuvers (ABMs) necessary for MGS to remain within the dynamic pressure (or density or periapsis altitude) corridor established in the overall plan. For the most part, third body perturbations due to the Sun and Mars' gravity field tended to increase hp. As the density decreased, period reduction would be reduced beyond the lower limit necessary to keep AB on schedule. Thus, a "down" ABM would be executed. Some ABMs were executed to increase hp (an "up" ABM) either as a response to a) the Noachis regional dust storm (centered approximately at 0 deg longitude and 40 deg south latitude) on A51 and b) approaching or exceeding the upper limit of the corridor thereby threatening the already weakened solar array assembly. In this table, "up" ABMs are indicated with an asterisk and "+" signs mean the ABM was executed several hours after apoapsis

**Table 4**  
**ABMs FOR WALK-IN AND MAIN PHASE AEROBRAKING**

Apoapsis and ABM	Velocity- Change Magnitude (m/sec)	Resultant Periapsis Altitude (km)	Atmospheric Density and Dynamic Pressure at Periapsis (kg/km <sup>3</sup> ; N/m <sup>2</sup> )
36 ABM-3	1.9	134.8	2.25; 0.03 at P37
37 ABM-4	0.3	128.6	4.41; 0.05 at P38
39 ABM-5	0.2	124.2	---
39 ABM-6+	0.2	120.2	---
39 ABM-7+	0.5 *	124.2	12.1; 0.14 at P40
41 ABM-8	0.2	120.5	22.4; 0.26 at P42
49 ABM-9	0.1	123.5	12.2; 0.14 at P50
51 ABM-10	0.1 *	---	---
51 ABM-11+	0.25 *	131.7	5.40; 0.06 at P52
56 ABM-12	0.1	131.8	15.7; 0.18 at P57
59 ABM-13	0.2	130.0	12.9; 0.15 at P60
61 ABM-14	0.2	127.1	13.8; 0.16 at P62
64 ABM-15	0.1	126.9	12.5; 0.14 at P65
66 ABM-16	0.1	125.7	15.6; 0.18 at P67
67 ABM-17	0.1	124.8	17.9; 0.20 at P68
70 ABM-18	0.2	122.4	20.6; 0.23 at P71
76 ABM-19	0.1	123.9	17.2; 0.19 at P77
78 ABM-20	0.1	123.4	20.6; 0.23 at P79
80 ABM-21	0.1	122.1	23.5; 0.26 at P81
82 ABM-22	0.1	120.8	27.3; 0.31 at P83
89 ABM-23	0.17	120.9	20.2; 0.23 at P90
96 ABM-24	0.11	121.3	24.4; 0.27 at P97
99 ABM-25	0.11	121.2	19.9; 0.22 at P100
101 ABM-26	0.12	120.4	24.5; 0.27 at P102
106 ABM-27	0.18	121.7	23.3; 0.26 at P107
107 ABM-28	0.18	120.1	20.8; 0.23 at P108
114 ABM-29	0.12	121.0	16.2; 0.18 at P115
116 ABM-30	0.06	120.6	13.0; 0.14 at P117
118 ABM-31	0.13	120.0	16.7; 0.18 at P119
120 ABM-32	0.07	119.4	12.3; 0.14 at P121
122 ABM-33	0.13	118.6	14.8; 0.16 at P123
123 ABM-34	0.13	116.9	28.7; 0.32 at P124
130 ABM-35	0.13	117.3	20.1; 0.22 at P131
136 ABM-36	0.13	119.0	15.8; 0.17 at P137
138 ABM-37	0.23	117.4	18.2; 0.20 at P139
140 ABM-38	0.15	116.1	37.4; 0.41 at P141
141 ABM-39	0.15 *	118.4	19.2; 0.21 at P142
145 ABM-40	0.15	116.8	21.4; 0.23 at P146
154 ABM-41	0.15	116.7	24.8; 0.27 at P155
155 ABM-42	0.08	116.2	16.7; 0.18 at P156
159 ABM-43	0.09 *	117.5	31.4; 0.34 at P160
160 ABM-44	0.17 *	119.4	14.0; 0.15 at P161
165 ABM-45	0.09	120.2	14.3; 0.15 at P166
169 ABM-46	0.17	118.0	13.7; 0.15 at P170
171 ABM-47	0.17	117.1	14.6; 0.16 at P172
173 ABM-48	0.09	117.0	18.8; 0.20 at P174



## Atmospheric Density Prediction Using the Mars-GRAM Model

The Navigation Team used the exponential model as the basis for the estimation of the base density from doppler data analysis. Since the base altitude was always chosen to be close to the actual periapsis altitude, this density was essentially a periapsis density. However for predicting densities for future periapsis-passages, we used the Mars-GRAM (MG) model. One significant correction was made to Mars-GRAM based predictions. Based on our estimate of density for past orbits, we trended the density and the following ratio was calculated:

$$f = \text{Navigation determined density} / \text{MG predicted density.} \quad (4)$$

From successive orbits, a three orbit, running mean, f-ratio was calculated. Thus the density used in the numerical integration of the drag equations of motion (Eq. 1) was adjusted as follows:

$$\text{density(updated)} = f * \text{density(MG)} \quad (5)$$

thus providing a more accurate density for future predictions. Initially, the MG model was under-estimating the density (the average value for f was 1.21 for P78 to P103). After P104, the MG input climate factors were updated to account for actual observations made over the previous orbits. Initially, the density predictions were reasonably accurate. However, thereafter the average f-value was 0.73 from P111 to P178 indicating that the model was over-estimating the atmospheric density. Figure 5 summarizes these results.

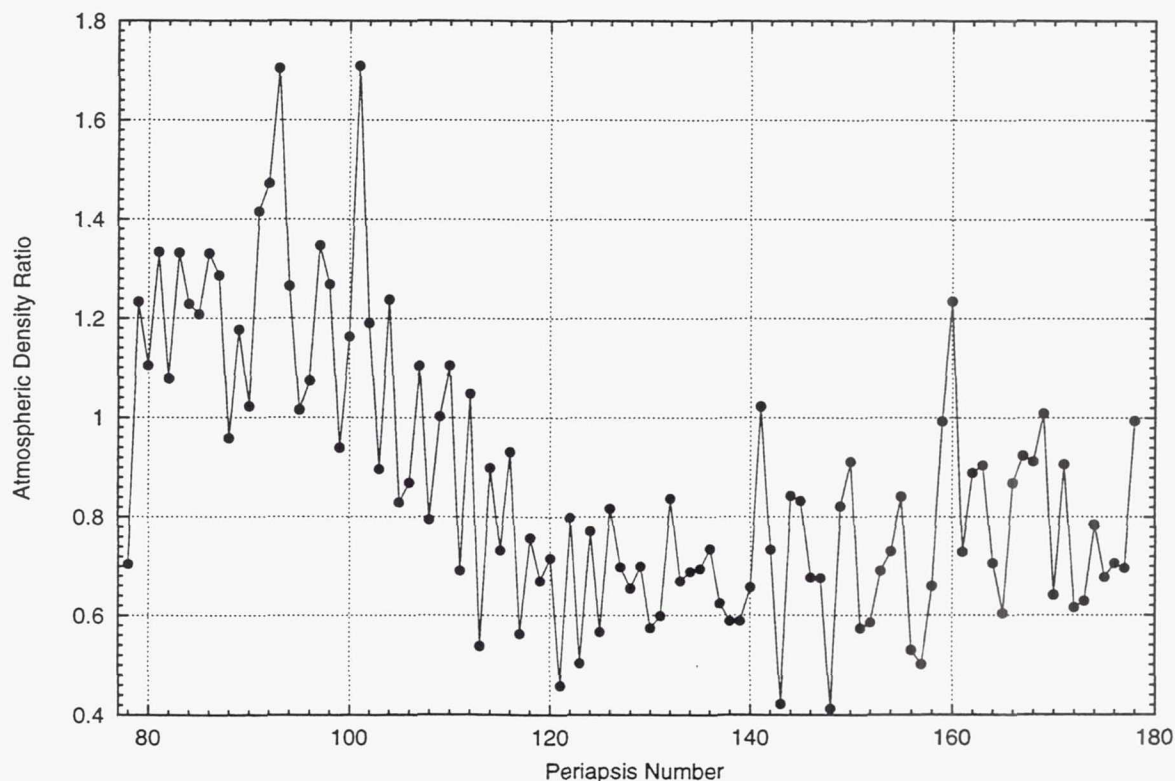


Figure 5 Atmospheric Density Ratio Used To Evaluate MG Model Predictions, Trend The Density And Generate A Three-Orbit Running Mean f-Ratio.

When this density ratio was plotted against the east longitude of the periapsis-passage location, a periodic trend was evident and unexpected. As shown in Figure 6, peaks occurred near 90 deg and 270 deg east longitude. We believe these are partially associated with the gross topography of Mars which also exhibits highs near these longitudes. This longitude dependence became an important tool for predicting densities, thus providing more accurate predictions over several orbits.

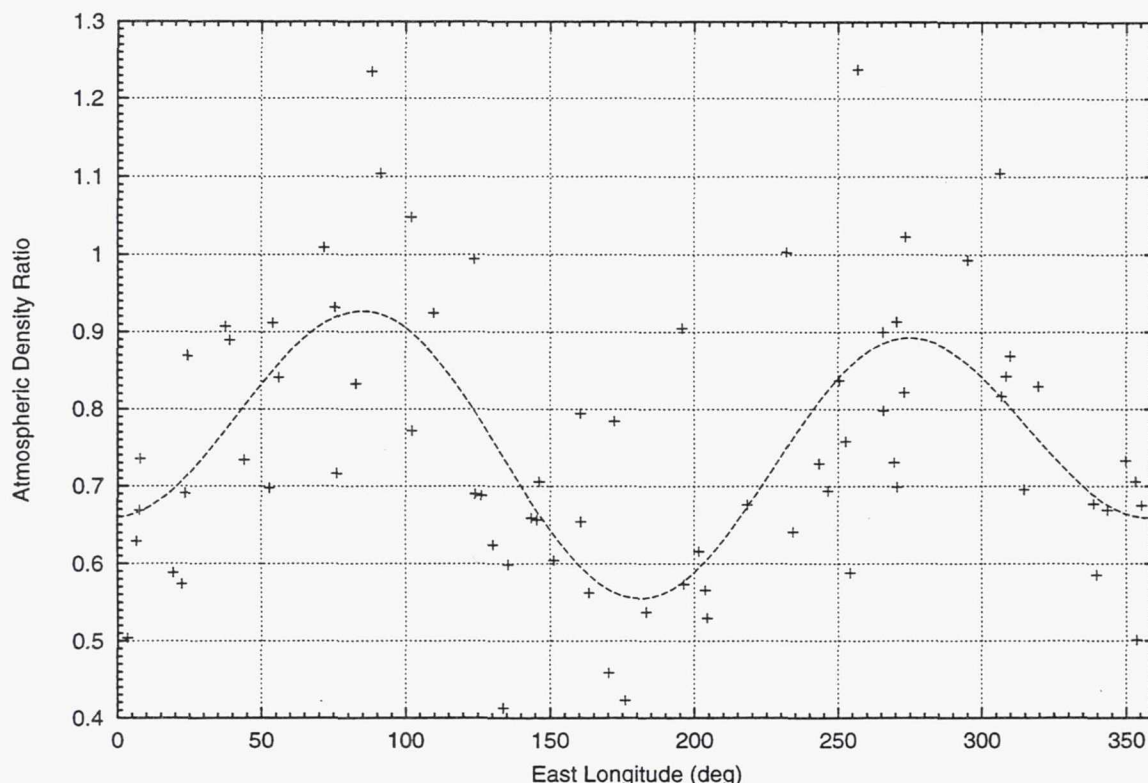


Figure 6 Periodic Trend Evident In The Density Ratio When Plotted As A Function Of The Longitude Of The Periapsis-Passage Location.

## TERMINATION OF PHASE 1 AEROBRAKING

The objective of the exit ABM was to establish the SPO with a) an orbital period of 11 hr 38 min 30 sec (= 11.642 hours, osculating period at apoapsis) with a tolerance of 1 min 30 sec and b) a periapsis altitude of 170.0 km with a tolerance of 3.0 km. This maneuver was nominally targeted for A199 and once designed could not be updated. This period was selected in order to avoid ground track repeat patterns at nearby periods of 11.664 hours and 11.588 hours. Criteria for the selection of the periapsis altitude included a) consensus input by the scientists for optimal observations, b) be outside the atmosphere to avoid or minimize drag perturbations, and c) minimize the propellant required to reach this altitude. Due to fluctuations in the atmospheric density from periapsis to periapsis and the necessity of executing the final maneuver at a precise orbital period, a "walk-out" of the atmosphere was executed as shown in Table 5. This resulted in the exit ABM being executed at A201 instead of A199. In addition to increasing hp, this maneuver also increased the orbit period by 1.9 min as shown in Figure 4. Targeted and achieved SPO elements are given in Table 6.



**Table 5**  
**WALK-OUT ABMs EXECUTED TO END AEROBRAKING**

Apoapsis and ABM	Velocity- Change Magnitude (m/sec)	Resultant Periapsis Altitude (km)	Atmospheric Density and Dynamic Pressure at Periapsis (kg/km <sup>3</sup> ; N/m <sup>2</sup> )
191 ABM-49	0.09	118.0	22.4; 0.24 at P192
193 ABM-50 +	0.17	119.8	14.8; 0.16 at P194
194 ABM-51	0.33	123.4	9.5; 0.10 at P195
201 ABM-52	4.43	170.7	0.08; 0.00 at P202

**Table 6**  
**SCIENCE PHASING ORBIT TARGETING RESULTS**

Orbit Element	Target Value For A199 ABM	Target Value For A201 ABM	Achieved Value
Period, hr:min:sec	11:38:30	11:38:24	11:38:38
Periapsis altitude, km	170.0	170.58	170.7

## NAVIGATION CAPABILITY COMPARED TO REQUIREMENTS

Navigation easily satisfied the two major requirements (predict  $T_p \leq 225$  sec and predict  $h_p \leq 1.5$  km) for all orbits from MOI to the end of AB. This was monitored by accurately determining or reconstructing the  $T_p$  (accuracy  $\leq 0.1$  sec) for each of the 201 orbits by the doppler analysis strategy previously mentioned. For each analysis, at least five predicted orbits were generated. Differences, such as  $T_p$ (reconstructed for orbit n) minus  $T_p$ (reconstructed for orbit n-1 but predicted one orbit ahead to orbit n), were plotted as shown in Figure 7. Almost all these differences are less than 2 sec with a few as high as 4-6 sec. As the period reduction became smaller, the predicted  $T_p$  accuracy correspondingly improved. A similar analysis was made for  $h_p$  with the results given in Figure 8. All of the single orbit predictions are within 0.1 km of the known or reconstructed altitudes at periapsis-passage. For two orbit predictions, the  $T_p$  accuracy was within  $\pm 500$  seconds (except for five predictions) for orbits 1 through 100 and within  $\pm 200$  seconds (except for three predictions) for orbits after 100. The  $h_p$  accuracy was within  $\pm 0.1$  km for all two-orbit predictions. Note that over this time interval, the latitude of periapsis-passage varied from 32.1 deg to 61.0 deg North and the orbit period was reduced from 45.0 to 11.64 hours.



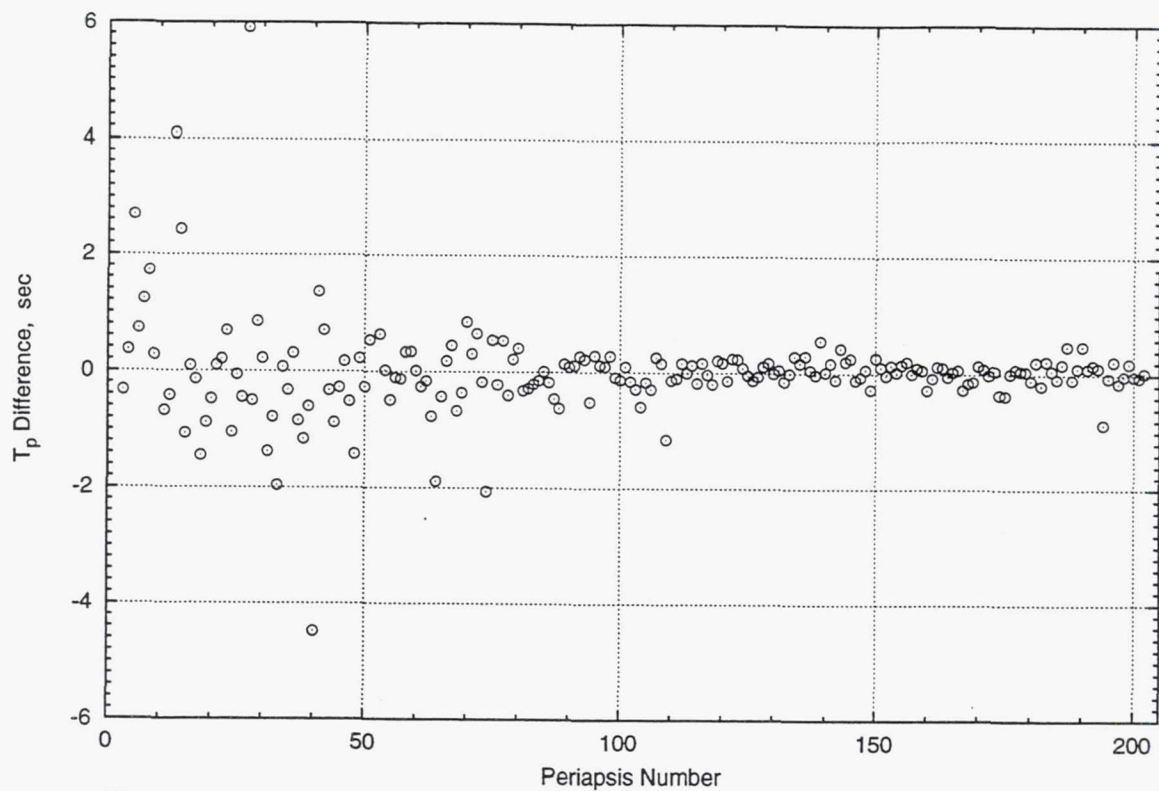


Figure 7 Accuracy Of  $T_p$  Predictions When Predicting One Orbit Ahead.

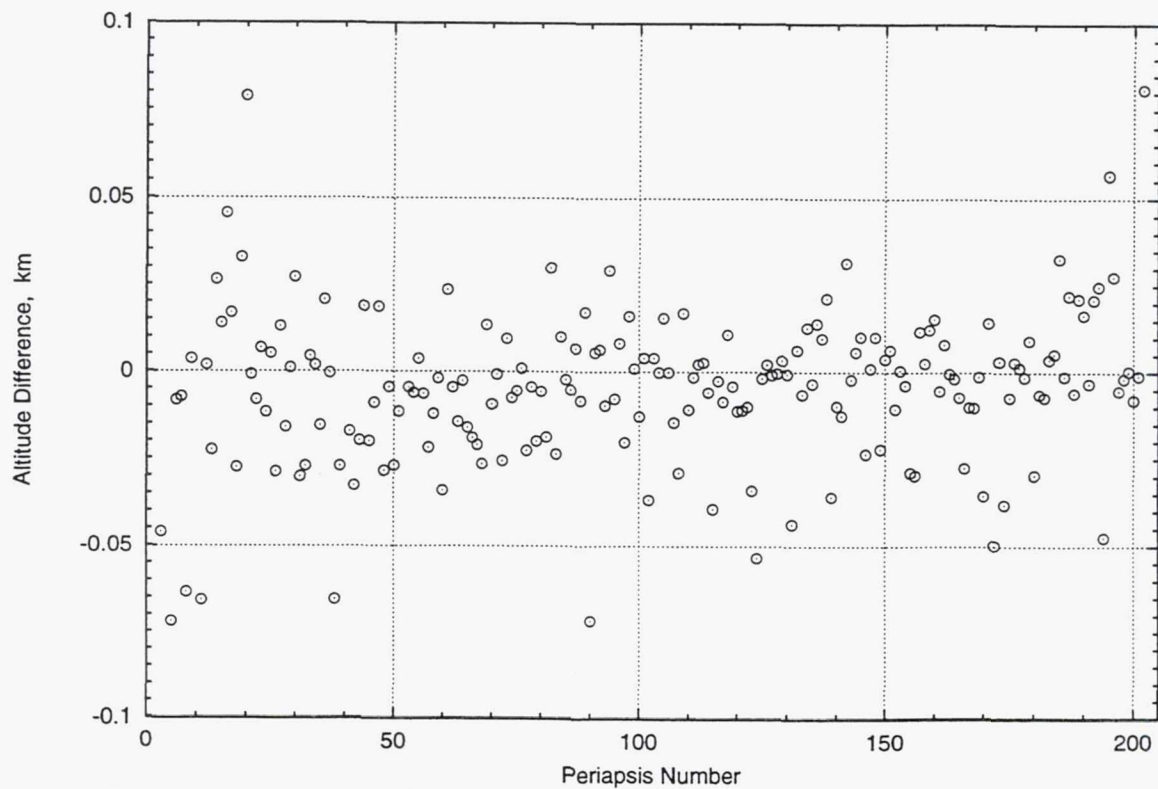


Figure 8 Accuracy Of The Periapsis Altitude,  $h_p$ , Predictions When Predicting One Orbit Ahead.

## ACKNOWLEDGMENT

The work described in this paper was performed at the Jet Propulsion Laboratory, California Institute of Technology, under contract with the National Aeronautics and Space Administration.

The Navigation Team gratefully acknowledges the support and interaction with many members of the MSOP flight team, both at JPL and the Lockheed Martin Astronautics facility at Denver, CO.

## REFERENCES

1. P. Esposito et al, "Navigation and the Mars Global Surveyor Mission," Proceedings of the 12th International Symposium on Space Flight Dynamics, ESOC, Darmstadt, Germany, 2-6 June 1997.
2. M. D. Johnston et al, "Mars Global Surveyor Aerobraking at Mars," AAS/AIAA Space Flight Mechanics Meeting, Paper AAS 98-112, Monterey, CA, 9-11 Feb 1998.
3. M. Dornheim, "Crooked Solar Wing Forces MGS Aerobraking Changes," Aviation Week and Space Technology, p. 26, 15 Sept 1997 and B. Smith, "Solar Panel Problem Triggers Major MGS Assessment," Aviation Week and Space Technology, pp. 25-27, 20 Oct 1997.
4. A. Konopliv and W. Sjogren, The JPL Mars Gravity Field, Mars 50c, Based Upon Viking and Mariner 9 Doppler Tracking Data," JPL Publication 95-5, Feb 1995.
5. C. G. Justus et al, "A Revised Thermosphere for the Mars Global Reference Atmospheric Model (Mars-GRAM Version 3.4)," NASA Technical Memorandum 108513, Marshall Space Flight Center, July, 1996.
6. T. Sterne, *An Introduction to Celestial Mechanics*, Interscience Publishers Inc., New York, 1960, pp. 158-160.
7. A. Seiff and D. Kirk, "Structure of the Atmosphere of Mars in Summer at Mid-Latitudes," J. Geophysical Research, Vol 2, No 28, pp. 4364-4378, 1977.
8. G. Keating et al, "The Structure of the Upper Atmosphere of Mars: In Situ Accelerometer Measurements from Mars Global Surveyor," Science, Vol 279, pp. 1672-1676, 13 March 1998.

**Page intentionally left blank**



## MARTIAN ELLIPTIC BALANCED SATELLITE ORBITS

Viktor W. Kudielka\*

Highly inclined and highly elliptic orbits around an oblate planet are subject to third body perturbations, and especially the eccentricity may vary dramatically, owing to resonances of apsidal and nodal motion. There exist only a few special orbits, where the perturbations due to the oblateness of the central body and the perturbations by the third body cancel out. For these "balanced" orbits, five Kepler elements (longitude of node, argument of periapsis, inclination, semi-major axis and eccentricity) remain constant in the long term, only small fluctuations occur with double the period of the disturbing body.

A first feasibility study for a Mars mission in a "balanced" orbit is presented. Compatibility with mission objectives and spacecraft configuration is discussed. A major problem is to find a transfer strategy and date, where the propulsion requirements are near the theoretical minimum.

## INTRODUCTION

Preliminary plans for a first planetary mission have been made by the radio amateur satellite community (Ref. 6). In order not to interfere with the ongoing research on the planetary surface, the target orbit around Mars should be selected with the goal of avoiding an entry in the atmosphere or an impact on the planet or on the moons for a long time (decades, centuries). Due to the restricted propellant mass, only a highly elliptic orbit can be considered.

Taking into account the second zonal harmonic of the planetary gravitational field and the major third body perturbation (in the case of Mars it is the Sun only), we find for planets with moderate inclinations of the plane of the third body versus the equator plane – like Earth or Mars – in two planes elliptic orbits which are in an equilibrium. For the plane orthogonal to the direction of equinox, the solutions are somewhat hidden in results obtained by direct integration of the perturbation equations (Ref. 5). The other plane is aligned with the direction of equinox and has also a high inclination, which depends on the inclination of the third body only. These solutions have been found by an analytical perturbation model proposed by G.E. Cook (Ref. 1) and finished by the author (Ref. 3,4). The orbits have been named "balanced", since it was not a priori obvious, that they are stable. They originate at the borders of stability of circular orbits (Ref. 7).

---

\*Retired from IBM Vienna Software Development Laboratory. Member of AMSAT-NA/DL/UK.  
E-mail: oelvwk@oelxtu.ampr.org

This paper describes the potential target orbits in some detail and discusses possibilities of reaching these orbits.

## BALANCED ELLIPTIC ORBITS AROUND AN OBLATE PLANET WITH THIRD BODY PERTURBATIONS

We define the ratio of oblateness and third body perturbations as follows:

$$\begin{aligned}\gamma &= c_2/c_3 \\ &= 2 J_2 (n n_0/n_d^2)(n/n_0)^{7/3} \\ &= 2 J_2 (m_c/m_d)(R/a)^5(r_d/R)^3\end{aligned}$$

where

$c_2$	factor of oblateness perturbation
$c_3$	factor of third body perturbation
$J_2$	$2^{nd}$ zonal harmonic of central body
$R$	equatorial radius of central body
$a$	semi-major axis of satellite orbit
$n$	angular mean motion of satellite
$n_0$	angular mean motion for $a = R$
$n_d$	angular mean motion of third body
$m_c$	mass of central body
$m_d$	mass of third body
$r_d$	distance of third body from central body.

For  $\gamma = 4$ , which is a significant value as we will see later, the period of a satellite around Mars is 52.12 hours, compared to 19.68 hours around the Earth. This is due to the greater  $J_2$  of Mars, the greater distance from the Sun, and the absence of a massive moon, despite the smaller mass of the planet. Here we have neglected the influences of Phobos and Déimos altogether.

### Balanced Elliptic Orbits in the Plane Orthogonal to the Direction of Equinox

In the plane orthogonal to the direction of equinox, the equilibria for elliptic orbits ( $\dot{\Omega} = \dot{\omega} = \dot{i} = \dot{e} = 0$ ) are at  $\omega = i_d$  and  $\omega = \pi + i_d$ , with  $e = \sqrt{1 - (\gamma/4)^{2/5}}$ .  $i_d$  denotes the inclination of the disturbing third body, that is the inclination of the orbital plane,  $i_d = 25.19^\circ$  for Mars. The line of apsides lies in the orbital plane. The four possible cases are as follows:

$\Omega$	$i$	$\omega$
$90^\circ$	$90^\circ$	$25.19^\circ, 205.19^\circ$
$270^\circ$	$90^\circ$	$334.81^\circ, 154.81^\circ$

The following table presents a few examples for these balanced orbits, with height of periareon, semi-major axis, eccentricity, orbital period, and the corresponding value of  $\gamma$ .

$h_{pa}$ km	sma km	ecc	period hrs	$\gamma$
0250	157300	.976812	526.14	0.001799
0500	147452	.973568	477.51	0.002486
1000	131157	.966472	400.59	0.004465
2000	107765	.949915	298.35	0.011923
4000	080358	.907945	192.11	0.051712
8000	055454	.794472	110.13	0.330431

The fairly high periods of 100 to 500 hours are the penalty for achieving such "balanced" orbits around Mars. Mission goals have to be evaluated for a match with such orbits.

A minor problem in the selection of an elliptic orbit around Mars is, to avoid collision with Phobos and Déimos in the long run.

### Balanced Elliptic Orbits in Planes aligned with the Direction of Equinox

In planes aligned with the the direction of equinox we find for elliptic orbits equilibria at certain inclinations  $i = i_b$ , which can be defined only implicitly (Ref. 3) by

$$(5 \cos^2 i_b - 1) \sin 2(i_d - i_b) + 3 \sin 2i_b + 2 \cos i_b \sin(i_b - 2i_d) = 0.$$

The corresponding eccentricity evaluates to

$$e = \sqrt{1 - (\gamma \sin 2i_b / \sin 2(i_d - i_b))^{2/5}}.$$

The inclination for Mars balanced orbits evaluates to  $i_b = 94.88^\circ$ . The line of apsides lies in the direction of equinox. The four possible cases are here as follows:

$\Omega$	$i$	$\omega$
$0^\circ$	$94.88^\circ$	$0^\circ, 180^\circ$
$180^\circ$	$85.12^\circ$	$0^\circ, 180^\circ$

The following table presents some examples of these orbits, with very similar eccentricities and orbital periods as for orbits in the plane orthogonal to the direction of equinox.

$h_{pa}$ km	sma km	ecc	period hrs	$\gamma$
0250	159820	.977178	538.84	0.001662
0500	149811	.973985	489.02	0.002296
1000	133248	.966998	410.21	0.004125
2000	109468	.950694	305.45	0.011023
4000	081601	.909347	196.59	0.047892
8000	056261	.797419	112.54	0.307410



## TRANSFER STRATEGIES

In order to arrive at Mars in or very near to one of the two special planes, we are looking for transfer orbits which arrive in the direction of Martian equinox or orthogonal to it. The direction of Martian equinox is approximately at  $102^\circ$  with respect to the direction of vernal equinox for the Earth.

### Direct Ballistic Transfer

During the first quarter of the next century, there will be eight launch windows for a direct ballistic transfer to Mars requiring minimum energy. Analysing these opportunities, we find that for only one of them (20 March 2016) the arrival direction will be differing 15 degrees from the wanted direction. All others will deviate between 30 to 40 degrees. Therefore a direct transfer does not seem feasible.

### Other Strategies

For Mars missions, gravity assists by Venus have been proposed. The drawbacks of this approach are longer flight times and in most cases much higher energy requirements for orbit insertion around Mars.

Another interesting strategy is that one planned for the Japanese PLANET-B mission (Ref. 2). Two lunar swing-bys and a gravity assist by Earth could reduce the total energy requirements substantially. Also the frequency of possible launch windows seems to be much higher than for the other approaches.

## CONSIDERATIONS FOR THE AMSAT P5-A MISSION

### Earth Departure

As for all of the AMSAT Phase 3 missions (highly inclined, highly elliptic Earth orbits), the P5-A spacecraft is intended to be a secondary payload on a commercial flight and will be released in a GTO (geostationary transfer orbit) at an inclination of about  $7^\circ$ . In order to reach the orbital plane of Mars for a direct ballistic transfer, an initial inclination change of at least  $15^\circ$  (worst case  $32^\circ$ ) would be necessary.

In case of a lunar swing-by, there might be a chance to use the swing-by also for the inclination change, but the necessary initial conditions for reaching the Moon from a specific GTO might reduce the number of potential start windows substantially.

### Spacecraft Configuration

The current plans for the propulsion system (based on P3-D) are as follows:

- One 400 N bipropellant system ( $MMH$  and  $N_2H_4$ ), specific impulse 308 s
- Two 115 mN, 750 W arc-jet thrusters ( $NH_3$ ), specific impulse 475 s (or 1.5 kW arc-jets, yet to be qualified)
- 12 resistojets ( $NH_3$ ) for attitude control.

Depending upon size and position of the solar panels, battery capacity, and power budget, constraints on the operation of the arc-jets have to be taken into account.

With the high-gain antenna and the main thrusters on opposite sides of the hexagonal structure, only an omni-directional antenna will be available for (low speed, 5 to 10 bps) communications and groundstation tracking during orbital manoeuvres. Autonomous operation is asked for.

## SUMMARY

If we consider balanced elliptical orbits around a planet, the match with mission objectives is crucial. For orbits in the plane aligned with the direction of equinox, the periapsis remains over the equator, while for orbits in the plane orthogonal to the direction of equinox, the periapsis lies in the orbital plane. Specifically, the peri-areon occurs over latitudes in the range of  $\pm 25^\circ$  only. This could restrict, for example, plans for remote sensing or imaging.

One major problem, as yet unresolved, is to find a proper transfer strategy from a GTO to one of the two highly-inclined planes at Mars, with propulsion requirements near minimum.

## REFERENCES

1. G.E. Cook: "Luni-Solar Perturbations of the Orbit of an Earth Satellite", *Geophys.J. R.Astr.Soc.* **6**, 1962, pp. 271-291.
2. J. Kawaguchi et al.: "On Making Use of Lunar and Solar Gravity Assists in LUNAR-A, PLANET-B missions", *Acta Astronautica* **35**, No. 9-11, 1995, pp. 633-642.
3. V. Kudielka: "Balanced Earth Satellite Orbits", *Celest. Mech.* **60**, 1994, pp. 455-470.
4. V. Kudielka: "Equilibria Bifurcations of Satellite Orbits", in R. Dvorak and J. Henrard (eds.): "The Dynamical Behaviour of our Planetary System" (Proc. 4<sup>th</sup> A. v. Humboldt Colloquium), 1997, pp. 243-255.
5. M.L. Lidov and M.V. Yarskaya: "Integrable cases in the problem of the evolution of a satellite orbit under the joint effect of an outside body and of the noncentrality of the planetary field", *Kosm. Issled.* **12**, No. 2, 1974, pp. 155-170.
6. K. Meinzer (ed.): "AMSAT P5-A to Mars", *Proc. Kick-Off Mtg, Darmstadt*, July 1996.
7. M.A. Vashkovyak: "The stability of circular satellite orbits for combined action of perturbations from an external body and from the noncentrality of the planetary gravitational field", *Kosm. Issled.* **12**, No. 6, 1974, pp. 834-847.

**Page intentionally left blank**



# 'SOLAR PHOTONIC ASSIST' TRAJECTORY DESIGN FOR SOLAR SAIL MISSIONS TO THE OUTER SOLAR SYSTEM AND BEYOND

M. Leipold\* and O. Wagner\*\*

Innovative scenarios are described where solar sails are utilized to carry a micro-sciencecraft outwards in our solar system to a flyby of Pluto and targets beyond. Advanced micro-sciencecraft design, i.e. high-performance light-weight subsystems, and passive low-thrust propulsion using solar sail technology would be combined to completely change mission planning for high-priority science missions to the outer solar system. The paper describes how solar sails, not consuming any propellant for primary propulsion, as a potential low-cost interplanetary delivery system, could enhance these scenarios by employing a 'solar photonic assist' trajectory: A navigation approach for the sail was derived and simulated numerically where the sailcraft first builds up orbital energy in a trajectory about the Sun and, subsequently, performs a 'swing-by' at the Sun to generate the necessary  $\Delta v$  to enter a hyperbolic orbit for fast transfers to targets in the outer region of our solar system. This low-thrust mission opportunity, first described by C. Sauer from JPL, was analyzed and extended to several variations, including 'dual solar photonic assist' trajectories. Utilizing high-performance solar sails in combination with such a trajectory design and a close solar fly-by can also lead to high-velocity solar system escape missions with a travel speed of more than 30 AU/year.

## INTRODUCTION

NASA's 'Ice and Fire' preproject currently under investigation consists of three missions designed to explore the coldest and hottest regions of our solar system. Two missions to 'cold destinations' are under consideration: One will probe Jupiter's moon Europa to search for evidence of liquid water beneath its icy surface, and the other mission will explore Pluto and its moon Charon, and continue to explore objects in the Kuiper belt (Ref. 1). In the baseline scenario, formerly known as the 'Pluto Express' mission, the sciencecraft heading for Pluto would utilize either a 12.2 year VVVJGA-trajectory or a 8.5 to 10 year transfer using SEP (Ref. 2,3). After a fly-by of the Pluto-Charon system the sciencecraft is expected to continue its journey to explore the small planetesimals in the Kuiper Belt. On the other side, within the 'Ice and Fire' scenario, the mission to the solar corona, referred to as 'Solar Probe', involves a high energy launch and a Jupiter gravity assist for a 3.6 year trajectory to reach a perihelion of 0.02AU (Ref. 4).

Solar sails would completely change this scenario: Bound for Pluto, a sailcraft would employ a single swingby at the Sun at about 0.45AU, referred to as 'solar photonic assist' (Ref. 5,6). Thereby it can generate enough thrust to enter a hyperbolic trajectory out to Pluto. A sailcraft with a more moderate performance concerning maximum acceleration could be utilized employing a 'dual solar photonic assist', performing two solar approaches before proceeding out to Pluto. Typical trip times for a  $C_3$  of zero are between 10.4 and 13 years, without performing an

\* Space Systems Engineer, German Aersospace Center (DLR), Institute of Planetary Exploration, Mission Architecture and Advanced Technologies Section, Linder Hoehe, D-51147 Cologne

\*\* Professor, Technical University of Munich, Department of Flight Mechanics and Flight Control, D-80290 Munich

intermediate Jupiter gravity assist. This advanced propulsion technology could also enable or at least enhance challenging high energy missions for robotic solar system exploration which require a high  $\Delta v$  such as a Mercury orbiter mission, missions out of the ecliptic plane to e.g. orbit the Sun in a close polar orbit, and comet or main belt asteroid rendezvous including sample return (Ref. 5,6,7,8).

## SOLAR SAIL PROPULSION AND NAVIGATION

At 1 AU solar distance the light pressure exerted on 1 m<sup>2</sup> of surface area is only 9.1mN for a perfect reflector. However, the acceleration of a sailcraft due to momentum transfer of photons accumulates over time as the thrust is continuously available. The acceleration due to solar pressure  $a_{SP}$ , assumed to be always directed along the unit vector perpendicular to the sail surface and defining the sail attitude around two axes, can be expressed by

$$a_{SP} = 2\eta \frac{S_o}{c} \cdot \left(\frac{1}{r}\right)^2 \frac{A}{m_{sc}} \cdot \cos^2 \beta \cdot e_n \quad (1)$$

The parameter  $\eta$ , the sail efficiency, includes non-perfect reflection on the sail,  $S_o$  is the solar constant (1,368W/m<sup>2</sup>), the solar distance  $r$  is expressed in [AU], and  $c$  is the speed of light ( $c=2.9979 \cdot 10^8$  m/s). The angle  $\beta$  is the Sun incidence angle between the sunlight direction and the sail normal  $e_n$ ,  $A$  is the sail area, and  $m_{sc}$  is the total spacecraft mass. The performance of a solar sail is generally expressed by the characteristic acceleration  $a_c$ , which is the maximum acceleration a sailcraft can experience at 1 AU solar distance. Values between 0.7mm/s<sup>2</sup> and 1.0mm/s<sup>2</sup> are used in this analysis since this range represents the performance level required in order to realize reasonable trip times. In addition, for high-speed transfers leaving the solar system high-performance sails of up to 3.0mm/s<sup>2</sup> are considered.

The ratio of the total spacecraft mass  $m_{sc}$  to the sail area  $A$  is furthermore defined as sail loading  $\sigma_{sc}$

$$\sigma_{sc} = \frac{m_{sc}}{A} \quad (2)$$

and is usually expressed in terms of grams per square meter [g/m<sup>2</sup>]. In addition, in order to specify the level of light-weight technology available for the sail material and support structure, the sail assembly loading  $\sigma_{sail}$  is introduced

$$\sigma_{sail} = \frac{m_{sail}}{A} \quad (3)$$

Trajectories are generated numerically using a variable order variable step-size Adams-Bashford-Moulton method including interpolation for the output. The equations of motion of the sailcraft are expressed in a system of six first order differential equations:

$$\frac{dr}{dt} = v \quad (4)$$

$$\frac{dv}{dt} = -\mu \frac{r}{r^3} + a_{SP} + \sum_{i=1}^n \mu_i \cdot \left( \frac{\Delta_i}{\Delta_i^3} - \frac{\rho_i}{\rho_i^3} \right) \quad (5)$$

Here,  $\mu$  is the gravitational parameter of the Sun,  $r$  and  $v$  are the heliocentric radius and velocity vector, respectively,  $a_{SP}$  is the acceleration vector due to solar sail propulsion. Third body perturbations are included where  $\Delta_i$  and  $\rho_i$  are the vectors from the spacecraft and the central body,



respectively, to the perturbing body with index  $i$  and gravitational parameter  $\mu_i$ . The trajectories are computed in a heliocentric, ecliptic cartesian coordinate system where the x-axis points to the vernal equinox of 1950. For the numerical simulation of interplanetary solar sail trajectories a program has been developed to enhance a local thrust vector control strategy with a parameter optimization method to solve two-point boundary value problems (Ref. 5). A 'local' thrust vector control strategy based on Lagrange's planetary equations for the perturbed orbital elements is used to generate approximate solutions and associated control estimates for the sail attitude angles over the estimated flight time. These control estimates are used to generate a reference trajectory and corresponding trajectory variations, monitored by the program STROM (Sequential TRajjectory Optimization Method) (Ref. 9). This allows to generate the input for the non-linear programming method SLSQP (Sequential Least Squares Programming) (Ref. 10), which is able to solve general nonlinear optimization problems. The code iteratively updates the control history to satisfy the terminal constraints within a certain accuracy, i.e. matching the state vector of the target body, which can be the heliocentric position and velocity. This allows to generate rendezvous trajectories to e.g. Mercury or main belt asteroids. At the same time the performance index can be expressed as the transfer time allowing for optimization for minimum flight time.

### Inward and Outward Heliocentric Spiral Transfers

In principal, any target in the solar system can be reached by either spiraling inward or outward once the sailcraft has left the gravitational sphere of influence of the Earth as shown in Figure 1.

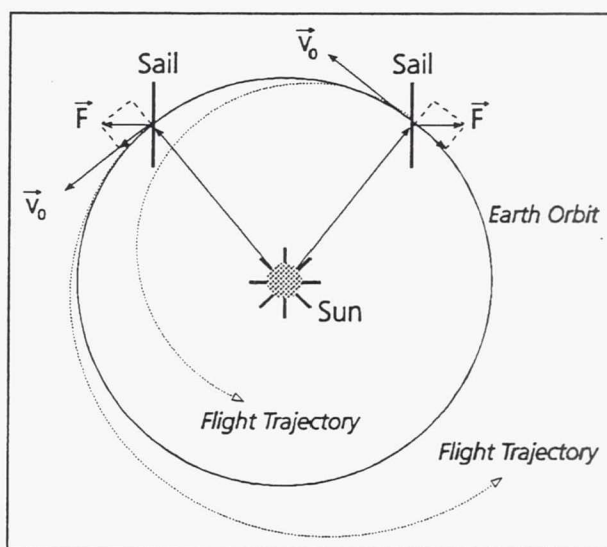


Figure 1: Spiraling Inward and Outward in the Solar System

The force resulting from the solar radiation pressure onto the sail, which for perfect reflection is perpendicular to the sail area, can be utilized to generate a force component in direction of the heliocentric velocity vector which then results in an outward spiral when e.g. heading for Mars or main belt asteroids. On the other side, the sail can be used to generate a 'breaking' force component in the anti-velocity direction in order to perform a descent spiral when e.g. heading for Mercury. By turning the sail to generate an out-of-plane thrust component the heliocentric inclination can be changed.



## 'Solar Photonic Assist' Trajectories

The outer planets are so distant from the Sun that solar sailing is not very effective in this region. Since the solar radiation pressure is reduced with a  $1/r^2$  relation as going away from the Sun, the propulsive capabilities of a solar sail are more and more limited as proceeding into the outer regions of the solar system. Consequently, continuous outward spiraling to reach the outer planets is not adequate. However, a sailcraft may gain an enormous amount of orbital energy when first approaching the Sun before proceeding to the outer planets. By performing such a 'Solar Photonic Assist' the transfer orbit about the Sun can turn hyperbolic, allowing reasonable trip times to the outer planets without applying gravity assists. Such 'indirect' trajectories generally have the advantage of relatively short trip times, however, the hyperbolic approach velocities at the target body are high. This type of trajectory was first discovered by C.G. Sauer and described in (Ref. 11,12). Arrival speeds are directly related to the trip times to the outer planets: Short trip times will result in high arrival speeds which has to be considered if e.g. atmospheric probes to the outer planets are delivered.

The 'indirect' trajectories imply that missions to the outer planets will almost exclusively be one-way missions, except for a Jupiter mission: Here the sailcraft could deploy a payload and utilize a Jupiter gravity assist to return to the inner solar system. Figure 2 shows the orbital parameters for a typical 'solar photonic assist' trajectory for a sail with  $a_c=1 \text{ mm/s}^2$  and with  $C_3=0$ . The size of the initial heliocentric orbit in this case is  $1.77 \times 0.45 \text{ AU}$ . As can be seen in Figure 2, the trajectory turns hyperbolic after perihelion passage. Beyond about 1.5 AU the curve of the eccentricity levels off, indicating the decreasing efficiency of solar sail propulsion.

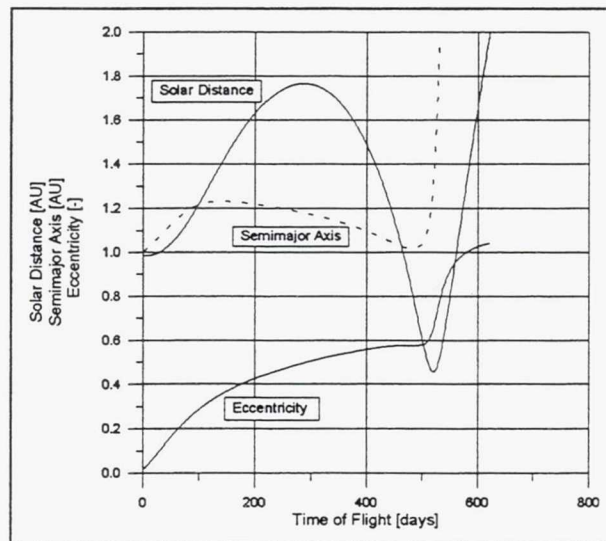


Figure 2: Orbital Parameters for Typical "Solar Photonic Assist" Transfer  
( $C_3 = 0$ ,  $a_c = 1.0 \text{ mm/s}^2$ )

## TO PLUTO WITH SOLAR SAILS

Pluto, the only planet not yet visited by any spacecraft, is believed to be the largest of a class of primordial bodies at the edge of our solar system which have comet-like properties and have not been processed by solar heating, remaining relatively unmodified. With its large moon Charon, this

double body system may have important clues to the origin of comets and the evolution of our solar system (Ref. 2).

For transfers to Pluto with solar sails, only 'solar photonic assist' trajectories will allow reasonable trip times. The advantage of this kind of trajectory is that an intermediate planetary flyby to gain orbital energy, i.e. a Jupiter gravity assist, is not necessarily required. This allows high flexibility with respect to launch window planning. Also, a launch at essentially zero  $C_3$  can be baselined. Figure 4 shows an example of an Earth - Pluto transfer with a single 'solar photonic assist' where a direct method to solve the two-point boundary value problem was used to match Pluto's out-of-ecliptic position for the flyby. The trajectory reaches hyperbolic energy after an initial 'solar flyby' orbit of  $1.56 \text{ AU} \times 0.49 \text{ AU}$ . The transfer time is 4,805 days (13.2 years), and the relative flyby velocity at Pluto is 10.3 km/s. Figure 3a and 3b show the ecliptic projection and the view from within the ecliptic, respectively.

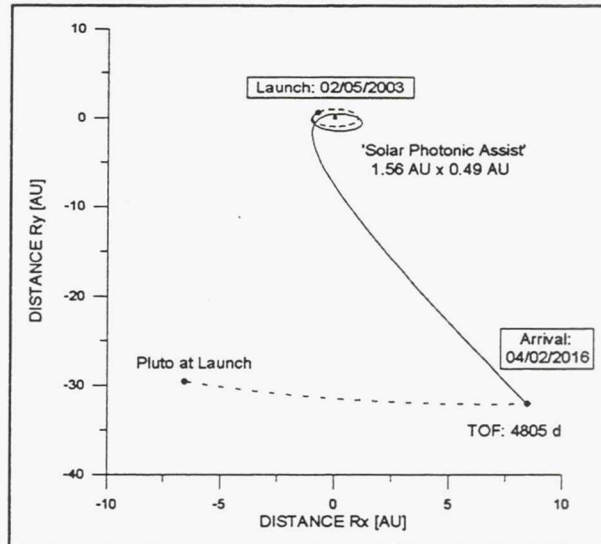


Figure 3a: 'Solar Photonic Assist' Transfer to Pluto ( $C_3=0$ ,  $a_c = 1.0 \text{ mm/s}^2$ ), Ecliptic Projection

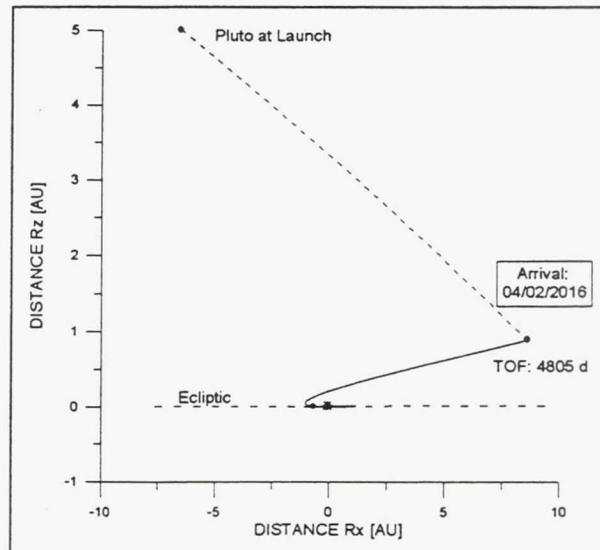


Figure 3b: 'Solar Photonic Assist' Transfer to Pluto, View from within the Ecliptic

Using this approach, the trajectory in Figure 3b shows how the ‘solar photonic assist’ is utilized to propel the sailcraft out of the ecliptic plane. Whereas the initial sail attitude control law based on maximizing the rate of change in eccentricity results in a trajectory which remains within the ecliptic plane, the direct optimization method applied modifies the sail attitude profile to match Pluto’s position in three-dimensional space.

Extending the basic concept of ‘solar photonic assist’ trajectories, transfer options were investigated that apply two consecutive solar approaches. This analysis is carried out in order to derive scenarios with solar sails of lower characteristic acceleration. This allows the application of smaller sail sizes and reduces the requirement for the sail technology  $\sigma_{\text{sail}}$  expressed in terms of  $\text{g/m}^2$ . Figure 4a shows the ecliptic projection of a transfer to Pluto using a sailcraft with a characteristic acceleration of  $0.7\text{mm/s}^2$  and a double swing-by at the Sun.

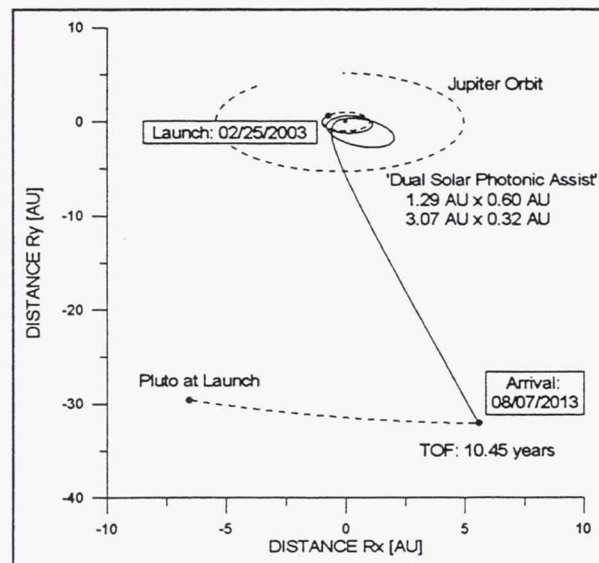


Figure 4a: ‘Dual Solar Photonic Assist’ Transfer to Pluto ( $C_3=0$ ,  $a_c = 0.7 \text{ mm/s}^2$ ), Ecliptic Projection

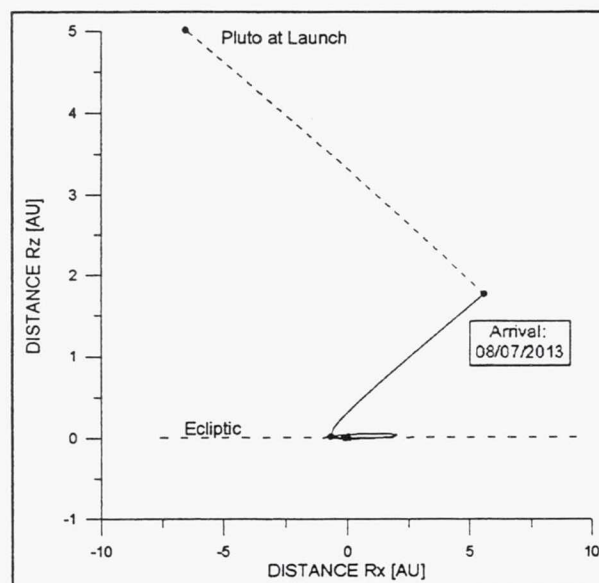


Figure 4b: ‘Dual Solar Photonic Assist’ Transfer to Pluto, View from within the Ecliptic



Table 1 shows a comparison to the recent baseline for 'Pluto Express' (Ref. 2) using chemical propulsion, as well as an advanced micro-spacecraft mass example with a net mass of 20kg. Here a sail efficiency  $\eta$  of 0.9 is assumed which takes into account non-perfect reflection of the sail, and for the solar sail subsystem a 30% contingency on mass is added. It is interesting to note that considering a net spacecraft of 115kg and given the assumptions for the sail assembly loading  $\sigma_{\text{sail}}$  of 5.2g/m<sup>2</sup> and 7.7g/m<sup>2</sup>, respectively, the flight system mass (launch mass) could be reduced compared to the chemical propulsion baseline of 'Pluto Express'. However, the sail sizes are still relatively large.

**Table 1:**  
**PROPULSION COMPARISON FOR PLUTO FLYBY MISSION**

	'Pluto Express' (Chemical)	Solar Sail Options		
Sciencecraft Net Mass	100 kg	100 kg		20kg
Russian <i>DROP ZOND</i>	15 kg	15 kg		--
Propulsion Module / Sail	392 kg (incl. Propellant)	154 + 46 kg $\sigma_{\text{sail}} : 5.2\text{g/m}^2$ $a_c = 1.0\text{ mm/s}^2$	175 + 53 kg $\sigma_{\text{sail}} : 7.7\text{g/m}^2$ $a_c = 0.7\text{ mm/s}^2$	31 + 9 kg $\sigma_{\text{sail}} : 7.7\text{g/m}^2$ $a_c = 0.7\text{ mm/s}^2$
Sail Size	--	196m x 196m	171m x 171m	72m x 72m
Flight System Mass (incl. 30% Sail Conting.)	574 kg --	315 kg (46 kg)	238 kg (53 kg)	60 kg (9 kg)
Trajectory	EVVVJP <sup>1</sup>	ESP <sup>2</sup>	ESSP <sup>3</sup>	ESSP <sup>3</sup>
Transfer Time	11.8 years	13.2 years	10.4	10.4
Potential Launch Vehicles	MOLNIYA	TAURUS / MED LITE		Pegasus XL, ARIANE5 'Piggy-Back'

The numbers for the sail assembly loading assumed in this analysis were chosen to reflect sail technologies of 4 g/m<sup>2</sup> and 6 g/m<sup>2</sup>, respectively, increased by a contingency of about 30%. Considering furthermore the recent advances in spacecraft miniaturization it seems feasible to build highly capable micro-spacecraft with a total mass on the order of a few 10 kg. Utilizing such technologies a 20 kg net spacecraft could be carried by a 72m x 72m solar sail with a characteristic acceleration of 0.7 mm/s<sup>2</sup> on a 'Dual Solar Photonic Assist' trajectory to Pluto (ESSP transfer) in 10.4 years, comprising a launch mass of about 60kg (see Table 1). As the  $C_3$  is still essentially zero in this scenario, such a sailcraft comes in the throw mass capability of a *PEGASUS XL* launch vehicle (103 kg for  $C_3=0$ ). Alternatively, a 'piggy-back' launch with ARIANE 5 together with a small chemical kick stage to insert the sailcraft into an Earth escape trajectory, or a dedicated launch with a TAURUS/STAR37 or Russian ROCKOT vehicle at relatively low cost could be considered. If the payload volume constraints can be met, a highly interesting mission to Pluto could be performed on a low-cost launch vehicle, avoiding also the radiation hazards of a Jupiter gravity assist.

<sup>1</sup> EVVVJP: Earth-Venus-Venus-Venus-Jupiter-Pluto Transfer

<sup>2</sup> ESP: Earth-Sun (single photonic assist)-Pluto Transfer

<sup>3</sup> ESSP: Earth-Sun-Sun (dual solar photonic assist)-Pluto Transfer

## HIGH-VELOCITY SOLAR SYSTEM ESCAPE TRAJECTORIES

Solar sail missions designed to go beyond Pluto's orbit such as scenarios to reach solar distances of 500 to 1,000 AU or even beyond have been investigated by several authors. All-metallic sails have been proposed for missions to the heliopause (Ref. 13) which follow heliocentric trajectories characterized by orbital angular momentum reversal and a perihelion of about 0.2 to 0.3 AU. This requires solar sails with characteristic acceleration on the order of 2.5 to 5 mm/s<sup>2</sup> and involves an in-orbit removal of the plastic film after sail deployment (Ref. 13). Such an advanced solar sail design has also been described in (Ref. 14) where degradation of a UV-sensitive plastic film substrate as well as sail film perforation are proposed to finally realize ultra-light, all-metallic sails. Going beyond the utilization of solar radiation pressure, laser pushed lightsails have been proposed to achieve high speeds to leave our solar system (Ref. 15). In this scenario a one-way interstellar flyby probe would use a 1,000 kg lightsail 3.6 km in diameter and a space-based 65 GW laser system to achieve 11% of the speed of light (0.11 c). Thus,  $\alpha$  Centauri could be reached within about 40 years from launch. Another mission concept calls for a mission to reach 550 AU solar distance to utilize the gravitational lens effect of the Sun to get a largely magnified picture of the galactic center (Ref. 16).

Coming back to the principle of single or multiple 'Solar Photonic Assist' trajectories with solar sails, some examples are shown here which outline the performance of advanced solar sails to achieve high speeds to leave our solar system. Based on this mission concept the technological challenges of all-metallic sails or high-power laser systems could possibly be avoided. When assuming '2<sup>nd</sup> generation' solar sails with high characteristic acceleration  $a_c$  on the order of 1 mm/s<sup>2</sup> to 3 mm/s<sup>2</sup> and ultra-light sail structures of 1 g/m<sup>2</sup> to 5 g/m<sup>2</sup>, very high speeds could be obtained with 'solar photonic assist' trajectories. Allowing furthermore close solar approaches to 0.1 AU or less, using special sail coatings and high performance materials capable to handle high temperatures, escape velocities of 50 km/s to 100 km/s or even higher could be achieved. The minimum solar distance a sail can operate depends on the thermal and structural load capacity of the sailcraft design. Ordinary sail designs with a high backside emissivity are estimated to be operational down to 0.2 AU (Ref. 5,12), while specialized sails might withstand reaching 0.06 AU (about 8 million km, or 15 solar radii from the surface) (Ref. 12).

Figure 5 shows an example of such a high-speed heliocentric escape trajectory for a solar sail with a characteristic acceleration of 1.5 mm/s<sup>2</sup>. Here the sailcraft is launched with a hyperbolic excess velocity of 5 km/s ( $C_3=25 \text{ km}^2/\text{s}^2$ ) from Earth. The sail then increases its heliocentric distance to about 9.9 AU still building up orbital energy, before 'falling back' towards the Sun to perform the 'Solar Photonic Assist'. The perihelion radius for this case is about 0.1 AU. After this close solar fly-by, assuming the sailcraft is capable to survive the severe thermal environment, the sailcraft has accelerated to an escape velocity of 86.7 km/s. This corresponds to a travel speed of 18.3 AU/year, or 0.0289% of the speed of light. This transfer option has not yet been optimized for the initial heliocentric orbit concerning overall minimum flight time. A lower initial aphelion distance may as well be suitable to achieve similar solar system escape velocities. Based on this solar system escape velocity it would take 3.8 years to reach 70 AU, which has taken the Voyager 1 spacecraft about 20.5 years to reach (Ref. 17). Voyager 1 currently travels at a speed of 17.4 km/s and has passed Pioneer 10 in terms of solar distance on February 17, 1998, thus now being the most distant human made object from Earth.



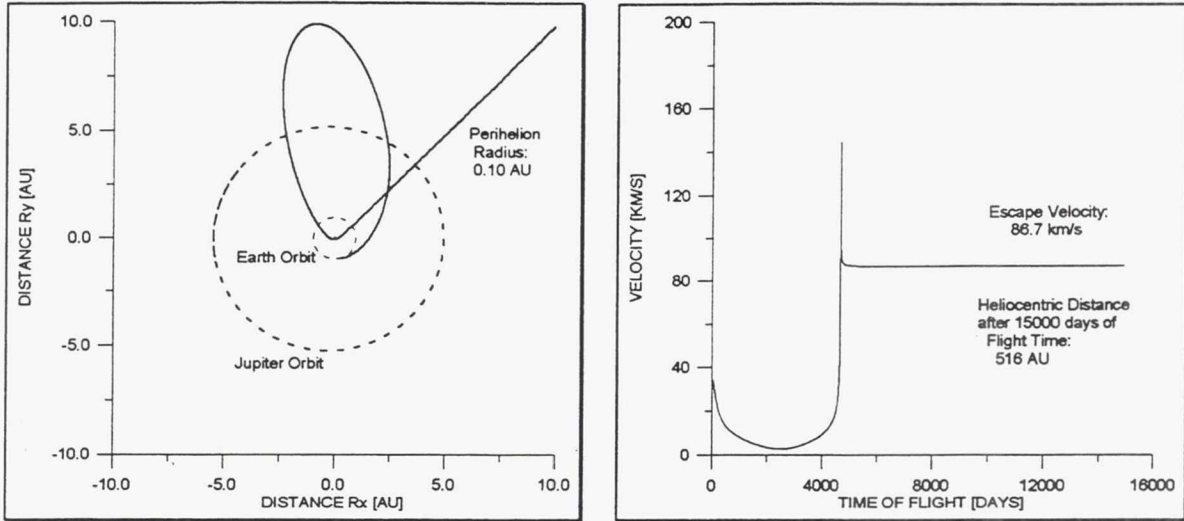


**Figure 5: 'Solar Photonic Assist' Heliocentric Escape Trajectory ( $C_3=25 \text{ km}^2/\text{s}^2$ ,  $a_c = 1.5 \text{ mm/s}^2$ ),**  
**a) Ecliptic Projection** **b) Heliocentric Velocity vs Flight Time**

An even more capable sailcraft with a characteristic acceleration of  $3.0 \text{ mm/s}^2$  was considered in order to assess the feasibility of ultra-high solar system escape velocities. Figure 6 shows an example for a launch with a hyperbolic excess velocity of  $5 \text{ km/s}$  ( $C_3=25 \text{ km}^2/\text{s}^2$ ) from Earth. Here the sailcraft goes out slightly beyond the orbit of Jupiter before performing a solar flyby at about  $0.05 \text{ AU}$ . This initial heliocentric phasing prior to the solar swing-by takes about 6.2 years. The close solar approach together with the extreme acceleration capability of the sailcraft allows to reach an escape velocity of  $159.35 \text{ km/s}$ , or  $33.6 \text{ AU/year}$ . This corresponds to roughly  $0.05\%$  of the speed of light. This result might be academic, but it shows the potential of ultra-high performance sails to leave our solar system with high travel speeds.

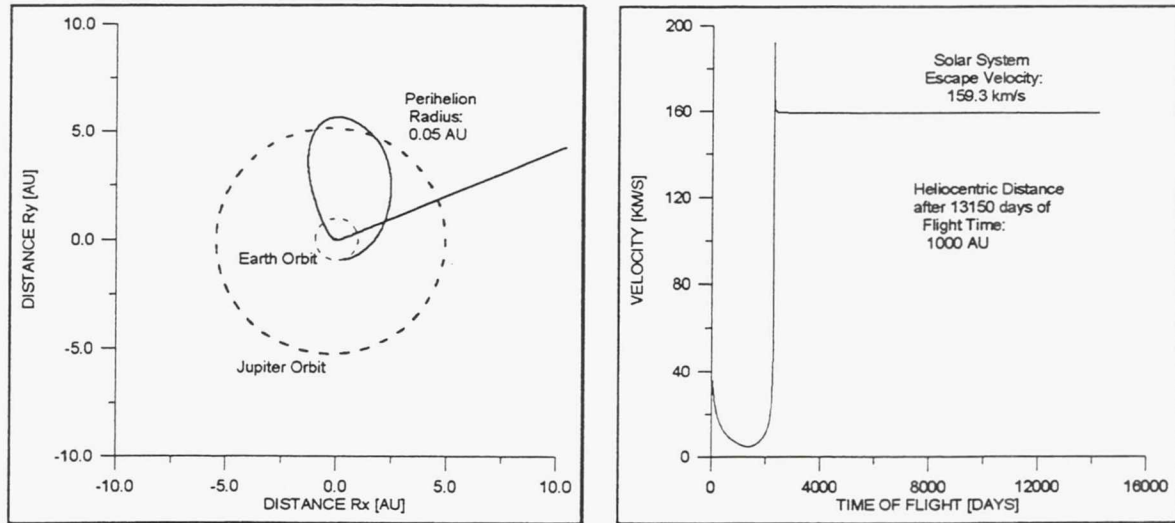


**Figure 6: 'Solar Photonic Assist' Heliocentric Escape Trajectory ( $C_3=25 \text{ km}^2/\text{s}^2$ ,  $a_c = 3.0 \text{ mm/s}^2$ ),**  
**a) Ecliptic Projection** **b) Heliocentric Velocity vs Flight Time**

The travel time starting from the 'solar photonic assist' to reach  $40 \text{ AU}$ , a distance similar to Pluto's semimajor axis, is only 469 days. Compared to Voyager 1, this travel speed is higher by a factor of about 9.1. A solar distance of  $1,000 \text{ AU}$  could thus be reached within 36.14 years from



launch. At this point it should be noted, however, that the purpose of this paper is to show that high-speed flights into interstellar space utilizing high-performance solar sails are not forbidden by the laws of physics. Whether it can be engineered and is financially or politically feasible has to be left for the new millennium to be determined.

The trajectory design outlined here shows that close solar approaches with solar sails could enable very high hyperbolic excess velocities to leave our solar system. The 'solar photonic assist' provides a method to apply a high  $\Delta v$  close to the Sun. In analogy, it was shown in another analysis baselining conventional, chemical propulsion that a 2-impulse trajectory leaving Earth to descend to the Sun to about 0.2 AU and applying a second impulse there can result in much higher solar system escape velocities than applying the same total amount of  $\Delta v$  for a direct escape trajectory (Ref. 18). This principle is referred to as the 'Hohmann Paradoxon' and is also described briefly in (Ref. 19).

## SAILCRAFT CONFIGURATION OPTION

The basic sailcraft configuration for a mission to Pluto or beyond could be based on the recent solar sail concept feasibility study conducted cooperatively between DLR and NASA/JPL (Ref. 20). The studies led to the baseline concept shown in Figure 7. The sail structure is composed of three major elements: a central deployment module, light-weight Carbon Fiber Reinforced Plastics (CFRP) booms, and the sail film. The spacecraft is attached to the sail structure via a control mast and a 2-degree-of-freedom gimbal to allow an offset of the center-of-mass to the center-of-pressure for passive attitude control using solar radiation pressure.

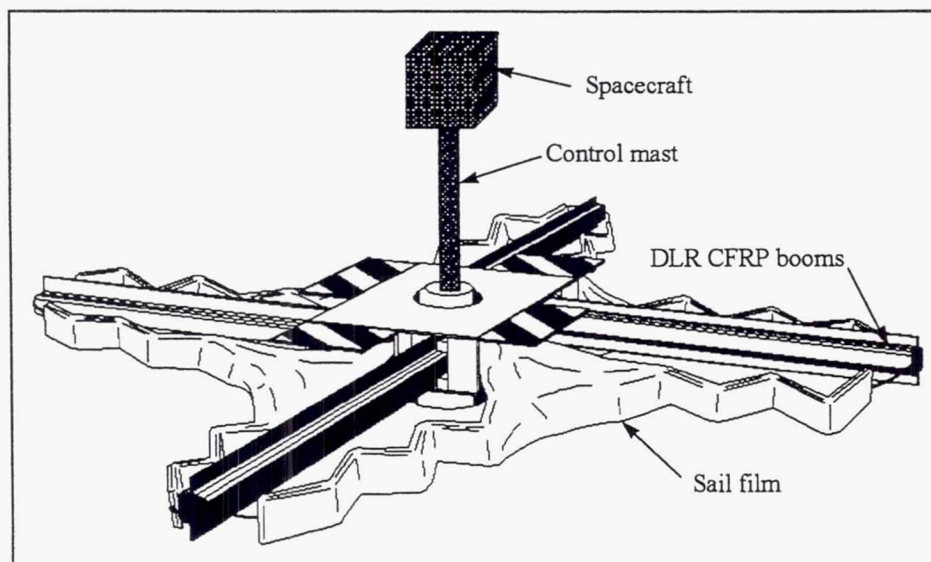


Figure 7: Sailcraft Baseline Concept - Partially Deployed

Figure 7 shows a partially unfolded sail. After completion of the deployment sequence the booms support four triangular sail film segments in the diagonals of the square sail. For the proposed solar sail demonstration mission in Earth orbit ODISSEE (Ref. 20) a Kapton film with  $7.5 \mu\text{m}$  thickness and CFRP booms with a specific mass of about  $60 \text{ g/m}$  are considered. Consequently, a sail loading of about  $20 \text{ g/m}^2$  seems feasible for a  $40\text{m} \times 40\text{m}$  sail. In order to realize a sail loading of  $10 \text{ g/m}^2$  or less as required for the missions to Pluto and beyond, i.e. thinner film

materials of 1 to 3  $\mu\text{m}$  thickness are required. This indicates the technological challenge to construct ultra-light weight sails. The solutions to these challenges must be demonstrated in space before solar sail propulsion is considered viable for any advanced deep-space mission.

## CONCLUSIONS

Single or multiple 'Solar Photonic Assist' trajectories provide a method for high-speed missions to the outer solar system and beyond utilizing solar sail propulsion. In this trajectory design a solar sail would first build up orbital energy and subsequently perform a close solar flyby to gain orbital energy and reach hyperbolic heliocentric velocities. Considering advanced micro-spacecraft technologies as currently being developed within several programs, it might be assumed that the net spacecraft mass can be reduced to several 10s of kg. Together with advanced materials and ultra-light weight components for the sail assembly resulting in a mass-to-area ratio of the sail of less than  $10\text{g/m}^2$ , relatively small sail sizes could be realized. Such a micro-sailcraft could utilize a single or dual 'solar photonic assist' trajectory to reach Pluto within 10.4 to 13 years from launch. In addition, for missions designed to go beyond the orbit of Pluto some examples were shown which outline the performance of advanced solar sails to achieve very high speeds to leave our solar system. Involving '2<sup>nd</sup> generation' solar sails and close solar approaches of 0.05AU to 0.1 AU, assuming the sailcraft can survive the extreme thermal environment, solar system escape velocities of 80 km/s to 160 km/s could be obtained. Compared to Voyager 1, this travel speed is higher by a factor of about 9.1. A solar distance of 1,000 AU could thus be reached within 36.14 years from launch. It should be noted, however, that one aspect of this paper is to show that high-speed flights to the outer solar system to perform a flyby at Pluto or objects in the Kuiper belt or going beyond into interstellar space utilizing high-performance solar sails are not forbidden by the laws of physics. Whether it can be engineered and is financially or politically feasible has to be left for the new millennium to be determined. In any case, a low-cost orbital demonstration mission to validate the basic principles of solar sail packaging, deployment, and in-orbit control is a necessary first step towards considering this advanced propulsion technology viable for any future deep-space mission.

## ACKNOWLEDGEMENTS

The research described here was partly performed at the Jet Propulsion Laboratory, California Institute of Technology, by the first author being supported by a DAAD fellowship (HSP II) financed by the German Federal Ministry of Education, Science, Research and Technology. The author would like to thank the DAAD, DLR and NASA/JPL for making this research visit possible. Furthermore, special thanks to D. Stetson, R. Staehle, S. Williams, C. Sauer, T. Sweetser, T. Spilker, J. Beckman, J. Randolph and R. Wallace, all at JPL, for providing helpful information and suggestions.



## REFERENCES

1. N.N., „Ice and Fire Preprojects“, Internet Information <http://www.jpl.nasa.gov/pluto/icefire.htm>
2. Price, H.W., Carraway, J.B., Matousek, S.E., Staehle, R.L., Terrile, R.J., Wyatt, E.J., „Pluto Express Sciencecraft System Design“, 2<sup>nd</sup> IAA Int. Conference on Low-Cost Planetary Missions, Laurel, Maryland, April 1996
3. Pagel, G., „Pluto Express - Jupiter-Io Encounter Trajectories for Io Probe Spacecraft“, ISU Individual Project, ISU Strasbourg, May 1996
4. Randolph, J., „Solar Probe - Mission and System Design Concepts“, Jet Propulsion Laboratory, 1994
5. Leipold, M., *Solar Sail Trajectory Analysis and Mission Design*, Dissertation in prep., 1998
6. Leipold, M., „Solar Sail Mission Applications“, NASA/JPL Workshop on Solar Sail Propulsion, Jet Propulsion Laboratory, Pasadena, February 13, 1997
7. Leipold, M., Seboldt, W., Lingner, S., Borg, E., Herrmann, A., Pabsch, A., Wagner, O., Brückner, J., „Mercury Orbiter with a Solar Sail Spacecraft“, *Acta Astronautica*, Vol.39, No. 1-4, pp. 143-151, 1996
8. McFarland, C., Leipold, M., „Mainbelt Asteroid Rendezvous Missions using Solar Electric and Solar Sail Propulsion“, *Spaceflight Mechanics 1996*, Vol. 93, Part II, pp. 1169-1183, Proceedings of the AAS/AIAA Spaceflight Mechanics Conference held February 12-15, 1996, Austin, Texas, (AAS 96-168)
9. Daum, A., „STROM 2.0 - Sequential Trajectory Optimization Method“, DLR, Cologne, March 1993
10. Kraft, D., Schnepfer, K., „SLSQP - A Nonlinear Programming Method with Quadratic Programming Subproblems“, Revised Version, DLR Oberpfaffenhofen, Feb. 1989
11. Wright, J., Warmke, J., „Solar Sail Mission Applications“, AIAA/AAS Astrodynamics Conference, San Diego, August 18-20, 1976
12. Wright, J.L., *Space Sailing*, Gordon and Breach Science Publishers, Philadelphia, 1992
13. Vulpetti, G., „3D High-Speed Heliocentric Trajectories by All-Metallic-Sail Low-Mass Sailcraft“, *Acta Astronautica*, Vol. 39, No. 1-4, 1996, pp. 161-170
14. McInnes, C., „Advanced Orbits and Mission Applications“, NASA/JPL Workshop on Solar Sail Propulsion, Jet Propulsion Laboratory, Pasadena, February 13, 1997
15. Forward, R.L., „Roundtrip Interstellar Travel Using Laser-Pushed Lightsails“, *Journal of Spacecraft and Rockets*, Vol. 21, No. 2, March-April 1984, pp. 187-195
16. Maccone, C., „Solar Foci Missions“, 2<sup>nd</sup> IAA Int. Conference on Low-Cost Planetary Missions, Laurel, Maryland, April 16-19, 1996
17. Savage, D., Hardin, M., „Voyager 1 Now Most Distant Human-Made Object in Space“, NASA News Release, 98-30, February 13, 1998
18. Jochim, E.F., „Paradoxa in der Raumfahrt“, GSOC, DLR Oberpfaffenhofen, IB 94-13, July 1994, pp. 135-143
19. Stanek, B., *Raumfahrt Lexikon*, Hallwag, Bern, 1983, pp. 116-117
20. Leipold, M., Garner, C., et al., „ODISSEE - A Proposal for Demonstration of a Solar Sail in Earth Orbit“, 3<sup>rd</sup> IAA Int. Conference on Low-Cost Planetary Missions, Pasadena, April 27- Mai 01, 1998



## ACCURACY OF ORBIT DETERMINATION FOR LOW THRUST TRAJECTORY TO THE MARS

Efraim L. Akim, Victor A. Stepaniants, Andrey G. Tuchin\*

Spacecraft with low-thrust-engine (LTE) allows to research of Solar system more effective. The specific thrust of such engine in some times exceeds the specific thrust of liquid-propellant one. So it is possible to reduce the cost of space mission by use more light spacecraft. The project of spacecraft with LTE for Mars mission is considered in Russia now. The mission profile includes the insertion of spacecraft into the parking LEO and transfer on trajectory to the Mars by ordinary liquid-propellant engine. Further increase of energy is realized by the electric LTE on trajectory Earth-Mars. Acceleration due to LTE generates considerable problems for navigation and mission control:

- The actual acceleration created by LTE differs from nominal value, due to attitude and thrust value errors. As a result an accuracy of reconstructed trajectory and spacecraft's predicted motion decreases.
- It is not possible to use the ordinary impulse scheme to control. It is necessary to consider the continuous control of thrust attitude and value.

The paper studies an accuracy of reconstructed trajectory and predicted one. The paper contains some results of expected accuracy of the predicted trajectory for different measurement sets.

### INTRODUCTION

Errors of measurements, as well as errors of thrust value and attitude are taken into account for estimation of orbit accuracy. Two approaches are considered: an error estimation based on the recursive filter of Kalman, and a global processing of sequence measurements. In the first case the continuous model of LTE error is used. The Kalman's filter technique is suitable for an estimation of a noise part of error with given correlation function. In the second case a difference of the actual acceleration and nominal one is represented as piecewise constant function with given limitation. The developed in KIAM technique of simultaneous determination of orbit parameters and time-extended maneuvers are used.

---

\* Keldysh Institute of Applied Mathematics RAS, Russia  
phone: (095) 333-80-67, e-mail: stepan@kiam1.rssi.ru

A scheme presented in the figure 1 illustrates the implemented tools for estimation of the orbital errors.

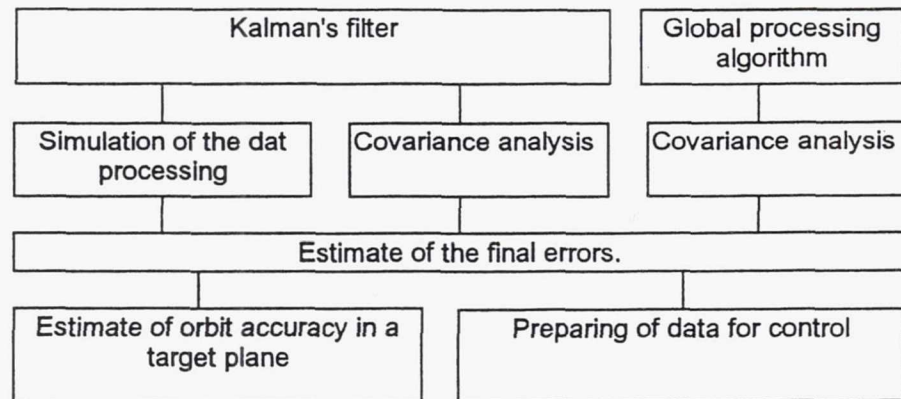


Figure 1 The stages of the orbital errors estimate

## TRAJECTORY OF SPACECRAFT WITH LTE

The trajectory of a spacecraft with LTE is described in the Earth-centered coordinate system J2000 by equations including gravity terms, solar pressure and jet acceleration. The additional spacecraft acceleration  $\bar{w}(t)$  created by LTE is described in the J2000 coordinate system as a time function corresponding to a nominal trajectory. Function  $\bar{w}(t)$  is presented in the tabular form. For intermediate points acceleration is calculated by interpolation. Deviation of thrust from the nominal value is considered as a noise.

## ERRORS OF THE THRUST VECTOR

The acceleration  $\bar{w}$  and ellipsoid of errors are presented at the Figure 2. The

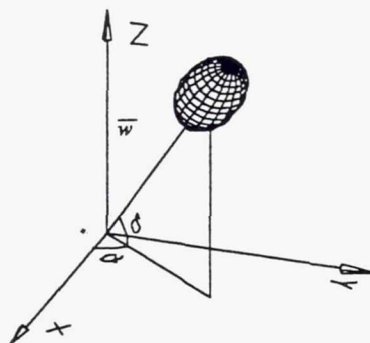


Figure 2 The ellipsoid of the acceleration error

direction of thrust vector is defined by the angles  $\alpha$  and  $\delta$ . Error of actual acceleration module  $\sigma_w$  is expected to be 5%. Expected error of the orientation angles  $\sigma_\alpha$  and  $\sigma_\delta$  is 5 angular minutes. The components of  $\bar{w}$  are written as

$$\begin{aligned} w_x &= w \cos \alpha \cos \delta, \\ w_y &= w \sin \alpha \cos \delta, \\ w_z &= w \sin \delta. \end{aligned} \quad (1)$$

Let us introduce a vector  $\bar{p} = \{w, \alpha, \delta\}$  and assume that  $\sigma_w$ ,  $\sigma_\alpha$  and  $\sigma_\delta$  are independent and have the standard distribution. Then we obtain the covariance matrix of  $\bar{p}$

$$K_{\bar{p}} = \begin{pmatrix} \sigma_w^2 & 0 & 0 \\ 0 & \sigma_\alpha^2 & 0 \\ 0 & 0 & \sigma_\delta^2 \end{pmatrix}. \quad (2)$$

The required covariance matrix  $K_{\bar{w}}$  can be calculated as

$$K_{\bar{w}} = \frac{\partial \bar{w}}{\partial \bar{p}} K_{\bar{p}} \left( \frac{\partial \bar{w}}{\partial \bar{p}} \right)^T. \quad (3)$$

The matrices of partial derivatives  $\frac{\partial \bar{w}}{\partial \bar{p}}$  are calculated by differentiation of equations (1):

$$\begin{aligned} \frac{\partial w_x}{\partial w} &= \cos \alpha \cos \delta, & \frac{\partial w_x}{\partial \alpha} &= -w \sin \alpha \cos \delta, & \frac{\partial w_x}{\partial \delta} &= -w \cos \alpha \sin \delta, \\ \frac{\partial w_y}{\partial w} &= \sin \alpha \cos \delta, & \frac{\partial w_y}{\partial \alpha} &= w \cos \alpha \cos \delta, & \frac{\partial w_y}{\partial \delta} &= -w \sin \alpha \sin \delta, \\ \frac{\partial w_z}{\partial w} &= \sin \delta, & \frac{\partial w_z}{\partial \alpha} &= 0, & \frac{\partial w_z}{\partial \delta} &= w \cos \delta. \end{aligned} \quad (4)$$

According to (1) we have

$$\begin{aligned} \sin \alpha &= \frac{w_y}{\sqrt{w_x^2 + w_y^2}}, & \cos \alpha &= \frac{w_x}{\sqrt{w_x^2 + w_y^2}}, \\ \sin \delta &= \frac{w_z}{w}, & \cos \delta &= \frac{\sqrt{w_x^2 + w_y^2}}{w} \end{aligned} \quad (5)$$

and thus

$$\frac{\partial \bar{w}}{\partial \bar{p}} = \begin{pmatrix} \frac{w_x}{w} & -w_y & -\frac{w_x w_z}{\sqrt{w_x^2 + w_y^2}} \\ \frac{w_y}{w} & w_x & \frac{w_y w_z}{\sqrt{w_x^2 + w_y^2}} \\ \frac{w_z}{w} & 0 & \frac{\sqrt{w_x^2 + w_y^2}}{w} \end{pmatrix}. \quad (6)$$



# ORBIT DETERMINATION BY THE METHOD OF DYNAMIC FILTRATION

## Linearization of the dynamic model

Let us introduce the following notations:

$\bar{x}_{nom}(t) = \{\bar{r}_{nom}(t), \bar{v}_{nom}(t)\}$  is a state vector of spacecraft, corresponding to the nominal trajectory,

$\bar{x}_r(t) = \{\bar{r}_r(t), \bar{v}_r(t)\}$  is an actual state vector of spacecraft,

$\bar{x}(t) = \bar{x}_r(t) - \bar{x}_{nom}(t)$  is a deviation of an actual state vector from nominal one.

The equations of spacecraft motion can be written in the form

$$\begin{aligned}\dot{\bar{x}}_{nom} &= \bar{f}_{nom}(\bar{x}_{nom}, t), \\ \bar{x}_{nom}(t_0) &= \bar{x}_0.\end{aligned}\tag{7}$$

Deviation  $\bar{x}(t)$  satisfies to equation

$$\dot{\bar{x}} = \bar{f}_r(\bar{x}_{nom} + \bar{x}, t) - \bar{f}_{nom}(\bar{x}_{nom}, t).\tag{8}$$

A measured function depends on spacecraft state vector

$$\psi = \psi(\bar{x}).\tag{9}$$

In the linearized form the equations (8) and (9) are written as

$$\begin{aligned}\dot{\bar{x}} &= A(t)\bar{x}(t) + B(t)\Delta\bar{w}(t), \\ \psi &= \psi(\bar{x}_{nom}) + H(t)\bar{x},\end{aligned}\tag{10}$$

where

$$A(t) = \frac{\partial \bar{f}_r}{\partial \bar{x}_r}, \quad B(t) = \frac{\partial \bar{w}}{\partial \bar{p}}, \quad H(t) = \frac{\partial \psi(\bar{x}_{nom})}{\partial \bar{x}_{nom}}\tag{11}$$

and  $\Delta\bar{w}$  is a deviation of the actual LTE acceleration from the nominal one.

## The algorithm

Continuous processing of measurements is performed by the Kalman's filter. The estimation  $\hat{x}(t_i)$  of state vector at a time  $t_i$  is made after obtaining of the current measurement. The algorithm is defined by

$$\begin{aligned}
\hat{x}(t_i) &= \Phi(t_i, t_{i-1})\hat{x}(t_{i-1}) + P_i H_i^T R_i^{-1} [\psi_i^m - H_i \Phi(t_i, t_{i-1})\hat{x}(t_{i-1})], \\
P_i &= P_{i/i-1} - P_{i/i-1} H_i^T [H_i P_{i/i-1} H_i^T + R_i]^{-1} H_i P_{i/i-1}, \\
P_{i/i-1} &= \Phi(t_i, t_{i-1}) P_i \Phi^T(t_i, t_{i-1}) + Q_i, \\
\hat{x}_0 &= \bar{x}_0,
\end{aligned} \tag{12}$$

where

$$\Phi(t, \tau) = \frac{\partial \bar{x}_{nom}(t)}{\partial \bar{x}_{nom}(\tau)},$$

$P_i$  is a covariance of the vector  $\hat{x}(t_i)$ ,

$P_{i/i-1}$  is a covariance of the vector  $\hat{x}(t_{i-1})$ , mapped at the moment  $t_i$ ,

$H_i = \frac{\partial \psi(\bar{x}_{nom}(t_i))}{\partial \bar{x}_{nom}(t_i)}$  is a matrix of partial derivatives of measured function with respect

to the state vector,

$\psi_i^m$  is  $i$ -th measurement,

$Q_i = \int_{t_{i-1}}^{t_i} \Phi(t_i, \tau) K_w(\tau) \Phi^T(t_i, \tau) d\tau$  is a covariance of spacecraft state vector caused by

LTE errors at  $[t_{i-1}, t_i]$ .

## ORBIT DETERMINATION BY GLOBAL PROCESSING OF MEASUREMENTS

Now the actual acceleration of LTE is presented as a sum

$$\bar{w}(t) = \bar{w}_{nom}(t) + \Delta \bar{w}(t), \tag{13}$$

where

$\bar{w}_{nom}(t)$  is a nominal acceleration,

$\Delta \bar{w}$  is a deviation of acceleration.

We consider the deviation of actual acceleration to be a piecewise constant function

$$\Delta \bar{w}(t) = \begin{cases} \Delta \bar{w}_1 & \text{at } [t_1, t_2], \\ \dots\dots\dots \\ \Delta \bar{w}_n & \text{at } [t_{n-1}, t_n], \end{cases} \tag{14}$$

where  $n$  is number of steps.

At a time  $t$  within  $[t_{i-1}, t_i]$  the actual state vector of the spacecraft  $\bar{X}\{\bar{r}(t), \bar{v}(t)\}$  is expressed by recursive relations:

$$\begin{aligned}
\Delta \bar{r}(t_i) &= \Delta \bar{r}(t_{i-1}) + \frac{1}{2}(t_i - t_{i-1})^2 \Delta \bar{w}_{i-1}, \\
\Delta \bar{v}(t_i) &= \Delta \bar{v}(t_{i-1}) + (t_i - t_{i-1}) \Delta \bar{w}_{i-1}, \\
\bar{r}(t) &= \bar{r}_0(t) + \Delta \bar{r}(t_i) + \frac{1}{2}(t - t_i)^2 \Delta \bar{w}_i, \\
\bar{v}(t) &= \bar{v}_0(t) + \Delta \bar{v}(t_i) + (t - t_i) \Delta \bar{w}_i.
\end{aligned} \tag{15}$$

Vectors  $\Delta \bar{w}_i$  are included in the set of estimated parameters. Their mathematical expectations are equal to zero. Deviation of  $\Delta \bar{w}_i$  depends on LTE performance and is described by the covariance  $K_{w_i}$  according to (3).

Parameters of orbit are determined by minimization of the functional

$$J(\bar{q}) = \sum_{i=1}^N \frac{1}{\sigma_i^2} \left( \psi_i^m - \psi_i^c(\bar{x}(\bar{q}, t)) \right)^2 + \sum_{j=1}^n \Delta \bar{w}_j K_{w_j} \Delta \bar{w}_j^T, \tag{16}$$

where

- $\bar{q}$  is a vector of estimated parameters,
- $K_{w_j}$  is a covariance of  $\Delta \bar{w}_j$ ,
- $\psi_i^m$  is an  $i$ -th measurement,
- $\psi_i^c$  is a calculated value,
- $\sigma_i$  is a error of  $i$ -th measurement,
- $N$  is a number of measurements.

We use the technique similar to [2] and [3] to minimize (16) and obtain the covariance matrix  $K_{\bar{q}}$ .

## ESTIMATION OF ORBIT ACCURACY

We consider trajectory Earth-Mars with launch on June, 12, 2003, and the Mars flyby in May, 8, 2004. The final estimate of orbit errors is constructed by the comparative analysis of covariant dependencies of Kalman's filter and global processing of measurements. However, both algorithms assume that measurements are independent and have the standard distribution. This assumption is not true always. So to increase the reliability of the estimate we simulate of Kalman's filter operation on the disturbed LTE acceleration and trajectory measurements. For the simulation of LTE errors we used the testing results of similar engines and some random functions with slow variation on time.

We suppose to use the measurement system "Quant-D" in the C-band. The errors do not exceed 50 m for range and 1 mm/s for range rate. We consider the following configuration of tracking stations.

1. There are three tracking stations in Eupatoria, Ussuriysk and Medveji lakes (Moscow district). All tracking stations measure range and range rate.
2. There are three tracking stations. Stations in Eupatoria and Ussuriysk measure range and range rate, while the station in Medveji lakes measures only the range rate.



3. Present configuration: measurements of range and range rate are performed by two tracking stations in Evpatoria and Ussuriisk.
4. The configuration of item 2 and 3-way dopler. In the case the reemitted by spacecraft signal is received by two tracking stations simultaneously. Then the joint data processing is performed.

For each configuration we obtain covariance matrices by the Kalman's filter technique and by the global processing of measurements. We introduce errors of LTE acceleration and errors of tracking data to simulate dynamic filtration process. The following sets of perturbations, due to thrust vector errors were considered:

1. Perturbations of thrust module are same as in LTE tests. Orientation errors are 5 angular minutes.
2. The same kind of perturbations but without orientation errors.
3. There are no errors of thrust vector module. The orientation errors are simulated by random function and do not exceed 5 angular minutes.
4. As in item 3 but there are errors of thrust vector module within 5%.

The results for position and velocity errors (in the worst case) are summarized in the Table 1. Arc 1 corresponds to duration of tracking interval up to 3 months after the launch; arcs 2,3,4 — up to 3,2,1 months before encounter. The errors correspond to the end of tracking interval.

**Table 1**  
**MAXIMAL ERRORS OF POSITION AND VELOCITY**

Case	Variant of		Position errors (km)				Velocity errors (m/s)			
	mea- sure- ment set	per- turba- tion	Arc 1	Arc 2	Arc 3	Arc 4	Arc 1	Arc 2	Arc 3	Arc 4
1	1	1	500	5000	3500	2500	1	0.9	0.9	1
2	1	2	200	700	200	250	0.6	0.2	0.4	0.1
3	1	3	100	500	300	150	0.5	0.5	0.5	0.5
4	1	4	1000	5000	2500	3000	2	2.4	2.0	3.0
5	2	1	500	12000	8000	2500	1.0	2.0	1.0	1.0
6	3	1	1000	27000	10000	2500	1.0	8.0	2.0	1.5
7	4	1	400	4500	1500	1500	0.8	1.1	0.6	1.1

Cases 1,2,3,4 show that the accuracy depends on the structure of perturbations, due to errors of thrust module and orientation. The variants 1 and 4 are similar. The reason is that the errors, obtained in LTE tests are about 5% of the thrust module. In

future the accuracy can be increased by estimating the LTE performance from the tracking data. For this purpose it is possible to use the model of perturbations, proposed in [1].

Cases 5,6,7 show that an accuracy depends on a set of measurements. Compare cases 1 and 6 we can see that for orbit determination it is necessary to have three tracking stations. Unfortunately case 1 is not possible, because the tracking station in Medveji lakes has not measurement of range. As a result an accuracy of estimation decreases (see case 5). By the 3-way dopler we can obtain a high accuracy (case 7).

## ESTIMATION OF ORBIT ACCURACY IN A TARGET PLANE

The trajectory of spacecraft is predicted by the model described above. As encounter parameters we consider coordinates  $\bar{p}\{\xi, \zeta\}$  in the target plane. The plane is orthogonal to spacecraft velocity in the pericenter of the Mars centered trajectory. Axes of the coordinate system in the target plane are defined as:

$$\bar{e}_1 = \frac{\bar{e}_2 \times \bar{v}_{sc}}{|\bar{e}_2 \times \bar{v}_{sc}|}, \quad \bar{e}_2 = \frac{\bar{l} \times \bar{v}_{sc}}{|\bar{l} \times \bar{v}_{sc}|}. \quad (17)$$

Here  $\bar{v}_{sc}$  is the spacecraft velocity in the Mars-centered coordinate system and  $\bar{l}$  is a unit vector, directed from the Mars mass to the Sun. Spacecraft coordinates in the target plane are

$$\xi = (\bar{e}_1, \bar{r}_{sc}), \quad \zeta = (\bar{e}_2, \bar{r}_{sc}), \quad (18)$$

where  $\bar{r}_{sc}$  is Mars-centered radius-vector of a spacecraft.

For the error estimation we choose the most probable configuration of tracking stations — variant 4. The covariance matrices  $K_{\bar{q}}$  are obtained by global processing of measurements. In this case we have best agreement with simulation results.

The covariance matrix  $K_{\bar{p}}$  in the target plane is

$$K_{\bar{p}} = \left( \frac{\partial \bar{p}}{\partial \bar{q}} \right) K_{\bar{q}} \left( \frac{\partial \bar{p}}{\partial \bar{q}} \right)^T. \quad (19)$$

Figure 3 illustrates one sigma uncertainty ellipses for different tracking arcs. Date shows a time of measurement end. We can see how errors of orbit decrease when measurement base increases and the prediction interval decreases.

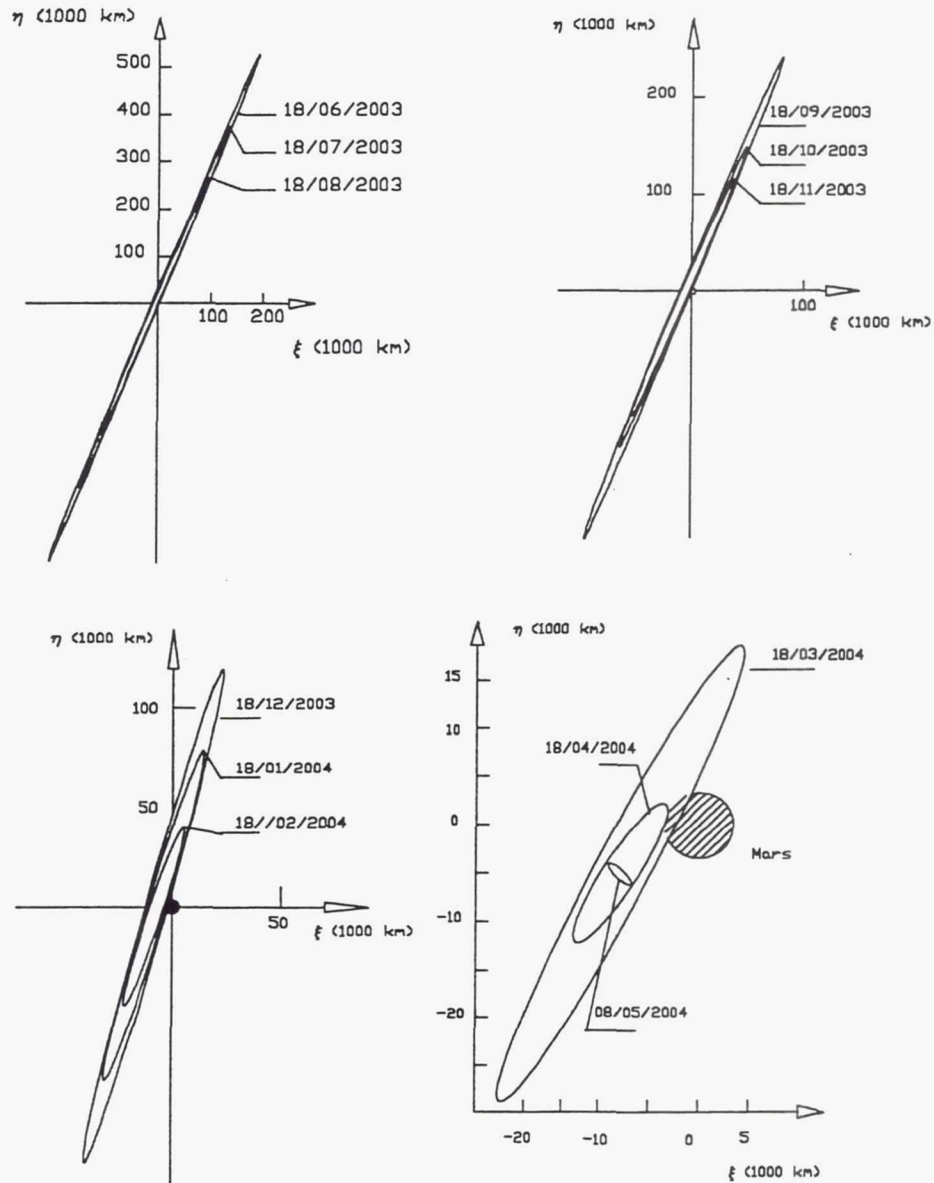


Figure 3 ellipses of error in the target plane

## DATA FOR ESTIMATION OF REQUIRED ENERGY

The spacecraft control must provide an encounter with the minimal energy. The estimation of the trajectory accuracy is important for choice of the control strategy. Let us suppose that at a time  $t$  we determine a state vector of the spacecraft  $\bar{X}(t)$  and its covariance matrix  $K_x(t)$  by processing of previous measurements. We can use the result for real-time control only after the time  $t + \tau$ . Here  $\tau$  is a minimal required time for



technological operations, such as orbit determination, calculation of control parameters, sending data onboard, checking of the onboard system and so on. At the time  $t+\tau$  errors of the state vector  $\bar{X}(t+\tau)$  are described by a covariance matrix  $K_x(t+\tau)$ . They are produced by errors of orbit determination before  $t$  and LTE errors during the time interval  $\{t, t+\tau\}$ . Delay  $\tau$  may be from a day to several weeks. A change of accuracy within  $\tau$  should be taken into account at the control strategy, in particular, for estimation of energy expenditure. To solve the problem we prepared required data as following.

A duration of mission is divided into intervals  $\{t_0, t_1\}, \dots, \{t_{n-1}, t_n\}$  (as a rule 1 month, but shorter near the Earth and at encounter). For each time  $t_k$  we compute the covariance matrix  $K_x(t_k, t_k)$  of  $\bar{X}(t_k)$  by use results of previous measurements. For a given time interval the covariances

$$K_x(t_k, t_{k+1}), \dots, K_x(t_k, t_n)$$

are computed also for all subsequent times till the Mars flyby. Constructing these matrices we take into account the errors of orbit determination till  $t_k$  and LTE errors within  $\{t_k, t_l\}$ .

The collected covariance form a triangle matrix. Its columns correspond to increasing of prediction interval and its rows correspond to increasing of tracking arc. Each matrix is written in a separate file along with the terminal date of tracking arc and the date of prediction interval end. File names are collected in the table 2.

**Table 2**  
**A SET OF COVARIANCE MATRIXES**

End of tracking arc	Prediction interval														
	2003							2004							
	06/16	06/23	07/21	08/25	/09/22	10/20	11/24	12/22	01/19	02/23	03/22	04/05	04/26	05/03	
2003/06/16	a001001	a001002	a001006	a001011	a001015	a001019	a001024	a001028	a001032	a001037	a001041	a001043	a001046	a001047	
2003/06/23		a002002	a002006	a002011	a002015	a002019	a002024	a002028	a002032	a002037	a002041	a002043	a002046	a002047	
2003/07/21			a006006	a006011	a006015	a006019	a006024	a006028	a006032	a003037	a006041	a006043	a006046	a006047	
2003/08/25				a011011	a011015	a011019	a011024	a011028	a011032	a011037	a011041	a011043	a011046	a011047	
2003/09/22					a015015	a015019	a015024	a015028	a015032	a015037	a015041	a015043	a015046	a015047	
2003/10/20						a019019	a019024	a019028	a019032	a019037	a019041	a019043	a019046	a019047	
2003/11/24							a024024	a024028	a024032	a024037	a024041	a024043	a024046	a024047	
2003/12/22								a028028	a028032	a028037	a028041	a028043	a028046	a028047	
2004/01/19									a032032	a032037	a032041	a032043	a032046	a032047	
2004/02/23										a037037	a037041	a037043	a037046	a037047	
2004/03/22											a041041	a041043	a041046	a041047	
2004/04/05												a043043	a043046	a043047	
2004/04/26													a046046	a046047	
2004/05/03														a047047	

Figures 4 and 5 illustrate a dependence of position

$$\sigma_r = \sqrt{\sigma_x^2 + \sigma_y^2 + \sigma_z^2}$$

and velocity

$$\sigma_v = \sqrt{\sigma_{v_x}^2 + \sigma_{v_y}^2 + \sigma_{v_z}^2}$$

errors on the value of tracking arc and prediction interval. Here  $\sigma_x^2, \sigma_y^2, \sigma_z^2, \sigma_{v_x}^2, \sigma_{v_y}^2, \sigma_{v_z}^2$  are diagonal elements of a covariance matrix.

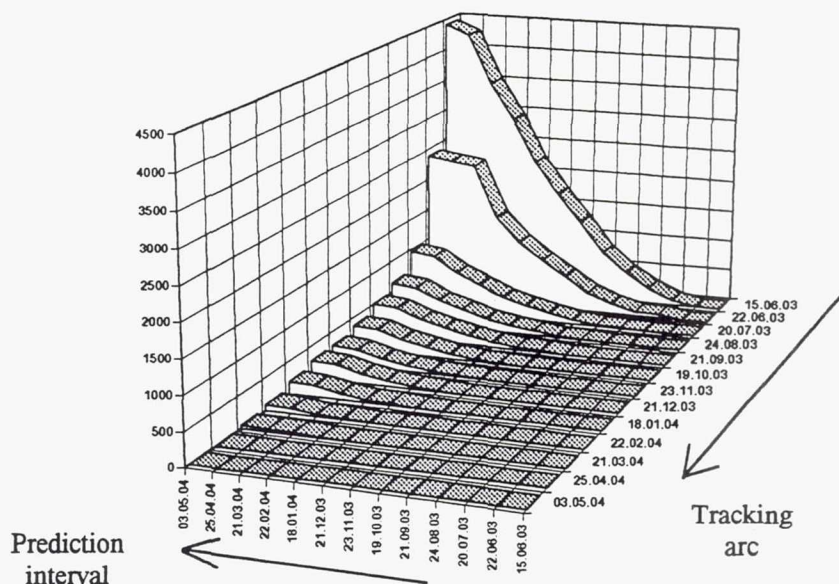


Figure 4 Dependence of position errors (1000 km) on tracking arc and prediction interval

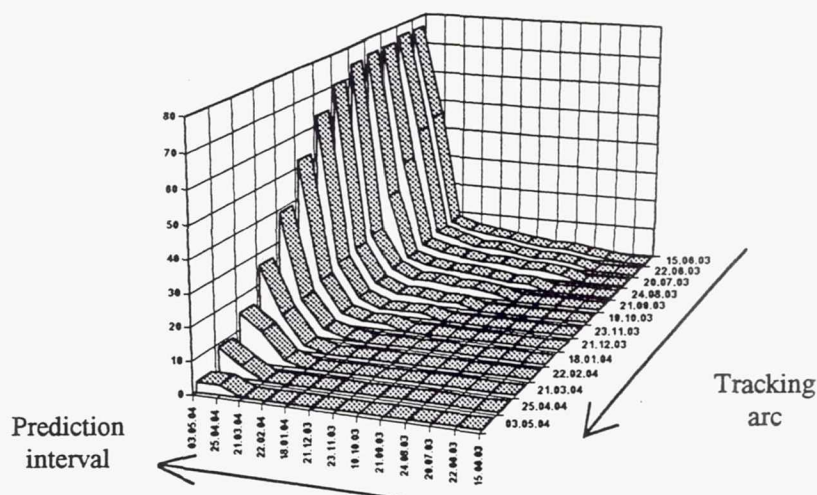


Figure 5 Dependence of velocity errors (m/s) on tracking arc and prediction interval

#### REFERENCES:

- P. Yu. Gnizdor, L. A. Latishev, A. V. Maligin, N. A. Maslennikov, K. A. Pavlov, S. A. Hartov, "Application of optimal filtration methods for identification of electric LTE parameters" //Russian Journal "Aviation technique", (1997), to be published (in Russian).
- Akim E.L., Eneev T.M. Determining spacecraft motion parameters from trajectory measurements. //Russian Journal "Cosmic Research", 1963, vol. 1, No.5 pp5-50
- Akim E.L., Vlasova Z.P. Stepaniants V.A. Tuchin A.G. Orbit determination for a radar mapping satellite of Venus "Earth, Moon, and Planets" 50/51: 559-578, 1990.

**Page intentionally left blank**



# THE COMPARATIVE ANALYSIS OF THE OPTIMAL INTERPLANETARY TRANSFERS WITH LARGE AND LOW -THRUSTS AT USING THE MIDDLE-CLASS LAUNCH VEHICLES

Yu.F.Kolyuka, G.V.Zyuzin

*Mission Control Center, 141070, Korolev, Moscow region, Russia*  
*Phone: (095) 586-8464; Fax: (095) 274-0025; E-mail: yfk@mcc.rsa.ru*

## ABSTRACT

It is considered the problem of finding the optimal trajectories of flight to the planets of the Solar system of space vehicles of two types:

- a) equipped by the traditional thrusters;
- b) equipped by the low-thrust engines.

It is supposed, that in both cases the spacecrafts are inserted into a near-Earth parking orbit by the average class launch vehicles like "Molnia-L" or "Soyuz"- "Fregat".

As a test of optimality were considered both minimum time of flight, and maximum of a payload, delivered to a target planet.

The schemes of flights to the Mars, Venus, Mercury and outer planets were analyzed.

It was assumed, that on the way to the target planet the spacecraft can make active - gravitational manoeuvres in the gravity sphere of the intermediate planets, including the multiple manoeuvres.

The terminal conditions of interplanetary missions were:

- a) flyby the target planet;
- b) landing to its surface;
- c) injection into an orbit of a planet's artificial satellite.

For the decision of a variational problem on optimization of low-thrust flight scheme the maximum principle was used. In this case an optimal control of thrust and the appropriate optimum trajectory were found by simultaneous integration of the equations of a spacecraft motion and a conjugate system of the differential equations. The motion of a spacecraft was described in a classical Cartesian coordinate system, and the action of all main perturbing factors was taken into account. The integration of a joint system was executed with the help of an original effective numerical method.

It is offered the original way of choice of starting approximation for the solution of an appropriate boundary-value problem, giving good results of convergence of iterative process, including the difficult cases.

The results of the solution of a problem at the choice of the optimal flight schemes in both variants are given, and their comparative characteristics are analyzed.

**Page intentionally left blank**

## CLOSE APPROACH TO SUN USING GRAVITY ASSISTS OF THE INNER PLANETS

A.A. Sukhanov\*

Earth, Mars, and Venus gravity assists used for the close approach to the Sun (down to 15 - 30 solar radii) are considered. A few spacecraft trajectories for launch in 2002 are suggested. Launch delta-V in LEO is 3.6 - 4.1 km/s and flight duration to the closest approach is 4.5 - 13.3 years for the trajectories. The advantages of this way of performing the solar mission are its low cost relatively to the Jupiter gravity assist and the possibility of frequent approaches to the Sun. Multiple Mercury flyby is also possible. Some merits of the electric propulsion use for the mission are considered: it can perform the correction maneuvers, shorten the flight duration, lower the perihelion, turn the orbit plane.

### INTRODUCTION

A few missions to the Sun were considered for last few years [1, 2]. The missions concepts usually implied Jupiter gravity assist (JGA) and approach to the Sun down to 4 - 15 solar radii ( $R_S$ ). Since the poles of the Sun are of most interest near polar orbits usually were considered, i.e. after the Jupiter swingby the spacecraft orbit has high inclination to ecliptic. Total flight duration is about 3.5 to 4 years.

However this way of approaching the Sun has the following serious disadvantages:

- Launch delta-V is very high. For instance in order to approach to the Sun to 15 - 30  $R_S$  for the launch in 2002 the delta-V in LEO must be more than 7 km/s (without turning the orbit plane) what corresponds to the launch  $C_3 \approx 100 \text{ km}^2/\text{s}^2$ . The polar orbit needs the launch delta-V in 0.6 km/s higher.
- Flight to Jupiter puts additional requirements to the spacecraft thermal and power supply systems (RTG is needed).
- Period of the final spacecraft orbit is longer than 4 years. This means that actually just a single approach to the Sun is possible.

The launch delta-V can be lowered by means of VEGA maneuver (which is not always possible) or  $\Delta$ VEGA one. However these maneuvers make the mission longer in 1 - 3 years and even after them the total delta-V is still high; for instance the  $\Delta$ VEGA 3<sup>+</sup> maneuver saves just about 1 km/s of the delta-V.

---

\* Senior scientist of Space Research Institute (IKI) of the Russian Academy of Sciences, 84/32 Profsoyuznaya St., 117810 Moscow, Russia. Phone: +7 (095) 333-2433, FAX: +7 (095) 913-3040, e-mail: sukhanov@iki.rssi.ru.



The gravity assists of the inner planets are an alternative to the JGA for the close approach to the Sun. The alternative provides much lower launch delta-V and a smaller and cheaper launch vehicle can be used for the mission. Also the spacecraft distance from the Sun is always within 200 - 260 million kilometers in this case (depending on the mission option) and no RTG is needed. All this makes the mission cost rather low. Another advantage of the alternative is the short period of the final spacecraft orbit what means that many approaches to the Sun are possible.

However the considered alternative to the JGA has some disadvantages: the flight duration is longer and the polar orbit is practically impossible in this case. Nevertheless the advantages of the solar mission using the inner planets gravity assists make it quite attractive. Below a few spacecraft trajectories approaching the Sun down to 15 - 30  $R_S$  after Earth, Mars, and Venus swingbys are offered. Also use of the electric propulsion for the correction maneuvers, shortening the mission duration, lowering the perihelion, or turning the final orbit plane is considered.

### PRELIMINARY ANALYSIS

To approach to the Sun closely after an inner planet swingby the spacecraft should have high excess velocity near the planet. Fig.1 shows the excess velocity necessary to approach to the given distance from the Sun for Earth and Venus.

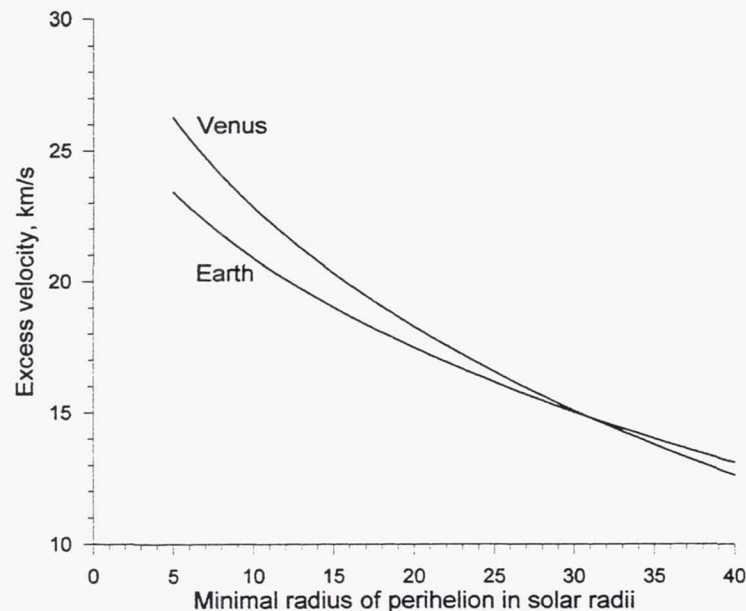


**Figure 1. Excess velocity necessary for providing the given perihelion**

Close approach to the Sun can be done in the following two steps:

Step 1: the spacecraft performs a few swingbys of the inner planets in order to get necessary excess velocity near the last swingbyed planet.

Step 2: the spacecraft performs a few swingbys of the last planet of the step 1 in order to turn the excess velocity vector to the direction opposite to the planet velocity vector and thus to provide closest approach to the Sun.

Earth and Venus are the only inner planets having the gravity field powerful enough to do the second step for a reasonable time. As it is seen on Fig.1 the difference between the necessary excess velocities for the planets is rather small; however if Earth is used for the second step of the considered maneuver the duration of the step is much longer than in case of Venus. Therefore below only Venus will be considered for the second step.

## THE MISSION OPTIONS

The mission options for the launch in 2002 will be considered in this section. Let the E, V, and M letters denote the Earth, Venus, and Mars swingbys respectively; E also means launch from the Earth. First consider EVEVEV option for the step 1 of the multiple gravity assist maneuver. This option provides excess velocity value 19.9 km/s during the last Venus swingby; Fig.1 shows that this value allows approaching the Sun down to  $16 R_S$  after the second step of the maneuver. There are many different options for the second step; table 1 gives the parameters of the maneuver including the EVEVEV option and one of the options for the second step. Fig.2 shows the corresponding spacecraft trajectory.

**Table 1**  
**APPROACH TO  $16 R_S$  USING EVEVEV OPTION**

	Planet	Date (d/m/y)	$\Delta V$ (km/s)	Flyby altitude ( $10^3$ km)	No.of complete revolutions s/c	S/major axis Venus ( $10^6$ km)	Radius of perihelion ( $10^6$ km)	( $R_S$ )
1	Earth	9/8/2002	3.58	0.2	-	-	128.3	104.8
2	Venus	7/12/2002	0	12.3	0	-	148.2	107.6
3	Earth	8/9/2004	0	4.6	1	-	111.4	66.3
4	Venus	19/1/2005	0	0.5	0	-	164.0	86.8
5	Earth	15/12/2005	0	0.4	1	-	115.5	53.3
6	Venus	13/1/2006	0	1.4	0	-	94.0	40.0
7	Venus	25/9/2007	0	3.4	3	2	82.6	31.1
8	Venus	17/12/2008	0	4.0	3	2	74.9	24.6
				(0.3)			(71.7)	(21.8)
9	Venus	20/11/2010	0	1.9	5	3	68.2	18.6
				(0.3)			(67.0)	(17.5)
10	Venus	2/7/2011	0	1.7	2	1	63.6	14.6
				(0.3)			(63.0)	(14.0)
11	Venus	6/12/2013	0	2.2	8	3	61.0	12.3
12	Venus	17/10/2015	0	0.3	7	3	59.7	11.2

As it is seen in the table 1 the launch delta-V is 3.58 km/s and all the swingbys are free. 11 swingbys are needed and total flight duration is more than 13 years. Note that if such close approach to the Sun is not needed and approach to 20, 25, or 30  $R_S$  is required then the sequence of swingbys can be interrupted earlier; corresponding values of the trajectory parameters are given in the table 1 in brackets. The orbital periods of the spacecraft and Venus are not commensurable in this cases and further lowering the perihelion for a reasonable time is not possible anymore.

Table 2 describes the multiple gravity assist maneuver using EVMEV option as the first step, Fig.3 shows the spacecraft trajectory. This option provides excess velocity near Venus equal to 19.3 km/s; according to Fig.1 this gives minimal perihelion distance of about 17  $R_S$ . The flight duration is in 5 years shorter in this case than in the previous one, however the launch delta-V is larger in 460 m/s (the gravity loss is not taken into account).

**Table 2**  
**APPROACH TO 17  $R_S$  USING EVMEV OPTION**

	Planet	Date (d/m/y)	$\Delta V$ (km/s)	Flyby altitude (km)	No.of complete revolutions s/c	Venus	S/major axis ( $10^6$ km)	Radius of perihelion ( $10^6$ km)	( $R_S$ )
1	Earth	6/8/2002	4.04	0.2	-	-	129.4	107.0	153
2	Venus	19/12/2002	0	0.7	0	-	180.4	106.9	153
3	Mars	10/5/2003	0	1.7	0	-	167.4	91.9	131
4	Earth	2/5/2004	0	0.7	0	-	116.8	55.4	79
5	Venus	7/12/2004	0	1.3	0	-	92.0	39.9	57
6	Venus	10/9/2005	0	5.5	1	1	79.3	29.5	42
7	Venus	3/12/2006	0	1.6	3	2	72.9	23.7	34
				(0.3)			(71.6)	(22.5)	(32)
8	Venus	21/6/2007	0	5.1	1	0	68.2	19.4	28
				(0.3)			(65.7)	(17.1)	(25)
9	Venus	1/2/2008	0	7.6	2	1	65.2	16.7	24
				(0.3)			(63.0)	(14.7)	(21)
10	Venus	26/9/2008	0	0.3	2	1	61.5	13.3	19
11	Venus	1/8/2010	0	0.3	7	3	60.2	12.1	17

The values in the brackets in the table 2 as well as in the table 1 correspond to the cases when longer distance from the Sun is required.

A small increment in launch delta-V in the EVMEV option makes the final excess velocity exceeding 20 km/s and allows approaching the Sun down to 15.5  $R_S$ ; however this leads to the longer flight duration. The values of the maneuver parameters are given in table 3.



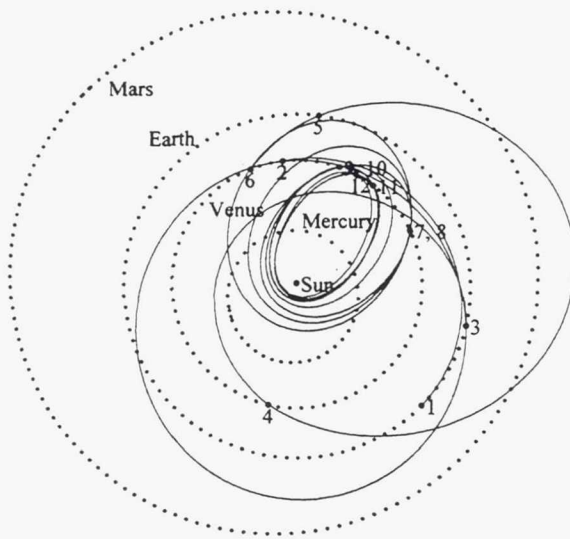


Figure 2. Approach to  $16 R_S$  (EVEVEV)

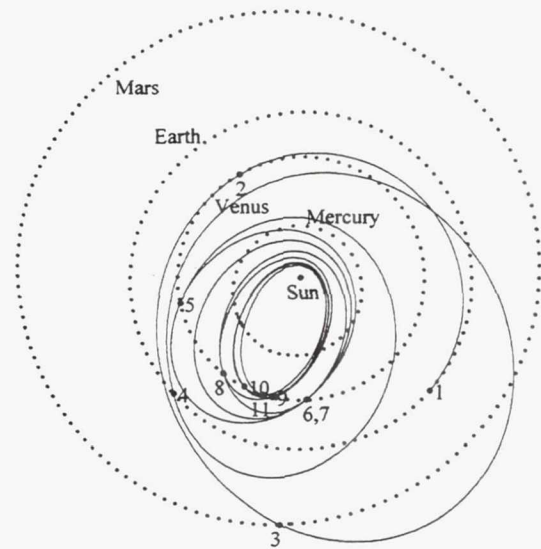


Figure 3. Approach to  $17 R_S$  (EVMEV)

**Table 3**  
**APPROACH TO  $15 R_S$  USING EVMEV OPTION**

	Planet	Date (d/m/y)	$\Delta V$ (km/s)	Flyby altitude (km)	No.of complete revolutions s/c	S/major axis Venus (10 <sup>6</sup> km)	Radius of perihelion (10 <sup>6</sup> km)	(R <sub>S</sub> )	
1	Earth	12/8/2002	4.10	0.2	-	-	129.6	107.3	153
2	Venus	22/12/2002	0	0.3	0	-	184.0	107.2	153
3	Mars	7/5/2003	0	0.6	0	-	167.6	89.0	127
4	Earth	3/5/2004	0	0.4	0	-	116.7	53.3	76
5	Venus	9/12/2004	0	0.8	0	-	91.5	37.8	54
6	Venus	10/9/2005	0	5.7	1	1	82.6	30.9	44
7	Venus	4/12/2006	0	1.8	3	2	73.3	23.0	33
				(0.3)			(71.8)	(21.6)	(31)
8	Venus	20/6/2007	0	0.8	1	0	66.4	16.8	24
				(0.3)			(65.7)	(16.5)	(24)
9	Venus	27/9/2008	0	0.7	4	2	62.2	13.1	19
10	Venus	25/7/2010	0	11.3	6	2	61.0	12.1	17
				(0.3)			(59.9)	(11.2)	(16)
11	Venus	4/6/2012	0	0.3	7	3	59.6	10.9	15.5

It is seen in the table 3 that almost two years are needed to lower the spacecraft orbit perihelion from  $16$  to  $15.5 R_S$ .

If the mission goal is approaching the Sun to  $30 R_S$  then option EVEV can be used for the first step of the maneuver. Parameters of the maneuver are given in table 4, the spacecraft trajectory is shown on Fig. 4.

**Table 4**  
**APPROACH TO 30  $R_S$  USING EVEV OPTION**

	Planet	Date	$\Delta V$	Flyby altitude,	No.of complete	S/major		Perihelion	
		(d/m/y)	(km/s)	(km)	revolutions	axis		( $10^6$ km)	( $R_S$ )
					s/c	Venus	( $10^6$ km)	( $10^6$ km)	( $R_S$ )
1	Earth	3/8/2002	3.58	0.2	-	-	128.3	104.8	150
2	Venus	7/12/2002	0	24.3	0	-	148.8	107.3	153
3	Earth	20/9/2004	0	2.6	1	-	108.9	63.1	90
4	Venus	30/1/2005	0	0.4	0	-	82.6	40.7	58
5	Venus	24/4/2006	0	12.6	3	2	77.0	34.8	50
6	Venus	27/2/2008	0	0.5	5	3	68.2	25.0	36
7	Venus	9/10/2008	0	0.3	2	1	64.8	21.2	30

An increment in launch delta-V in the EVEV option allows to approach to the Sun down to 27  $R_S$  for approximately the same time. The corresponding values of the parameters of the multiple gravity assist maneuver are given in table 5, the spacecraft trajectory is shown on Fig.5.

**Table 5**  
**APPROACH TO 27  $R_S$  USING EVEV OPTION**

	Planet	Date	$\Delta V$	Flyby altitude	No.of complete revolutions		S/major axis	Perihelion	
		(d/m/y)	(km/s)	(km)	s/c	Venus	( $10^6$ km)	( $10^6$ km)	( $R_S$ )
1	Earth	24/7/2002	3.73	0.2	-	-	129.1	106.0	151
2	Venus	10/12/2002	0	24.3	0	-	149.8	105.9	151
3	Earth	9/10/2004	0.02	2.6	1	-	105.4	58.0	83
4	Venus	16/2/2005	0	0.6	0	-	82.6	38.8	55
5	Venus	12/5/2006	0	32.4	3	2	79.7	35.9	51
6	Venus	8/9/2007	0	2.5	3	2	71.1	26.8	38
7	Venus	30/3/2008	0	3.5 (0.3)	1	0	66.4 (65.1)	21.8 (20.5)	31 (29)
8	Venus	21/11/2008	0	0.3	2	1	63.6	18.8	27

Times of the flight to the given distance from the Sun and periods of the final spacecraft orbits for the considered options are given in the table 6. The values in brackets for the EVMEV-2 option correspond to the shortened flight down to the distance 16  $R_S$  from the Sun (see also table 3). As the table 6 shows the spacecraft returns to the Sun every 3 - 4 months. Note that Mercury flybys are possible during the flight in the final orbit.

The perihelion distance versus time of flight for the considered mission options is also shown on Fig.6.

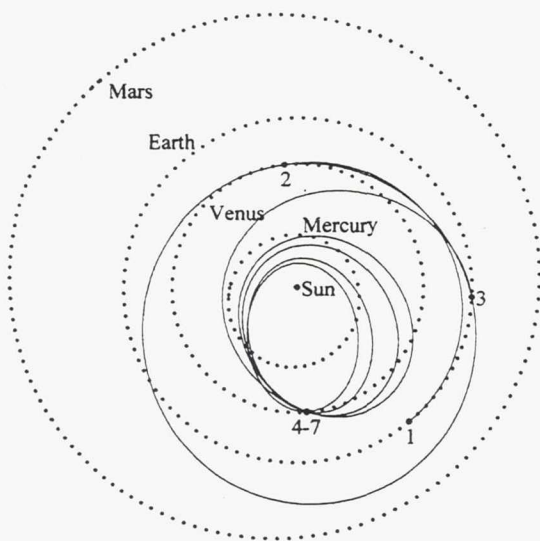


Figure 4. Approach to 30  $R_S$  (EVEV)

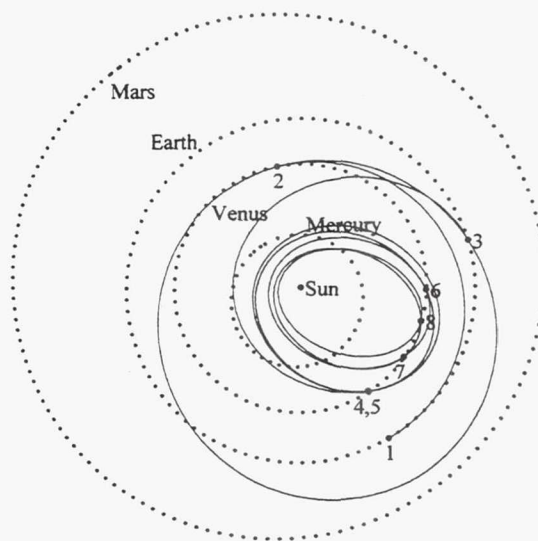


Figure 5. Approach to 27  $R_S$  (EVEV)

**Table 6**  
**FLIGHT TIMES AND PERIODS OF THE FINAL ORBIT**

Mission option	Minimal distance from the Sun ( $R_S$ )							
	15 - 17	19 - 21	24 - 27	29 - 32	15 - 17	19 - 21	24 - 27	29 - 32
	Time of flight (years)				Period of the final orbit (days)			
EVEVEV	13.3	9.0	8.4	6.5	92	100	110	121
EVMEV-1	8.1	7.6	5.0	4.5	93	100	106	121
EVMEV-2	9.9 (8.1)	6.3	5.0	4.5	92 (93)	98	106	121
EVEV-1	-	-	-	6.4	-	-	-	104
EVEV-2	-	-	6.5	5.8	-	-	101	105

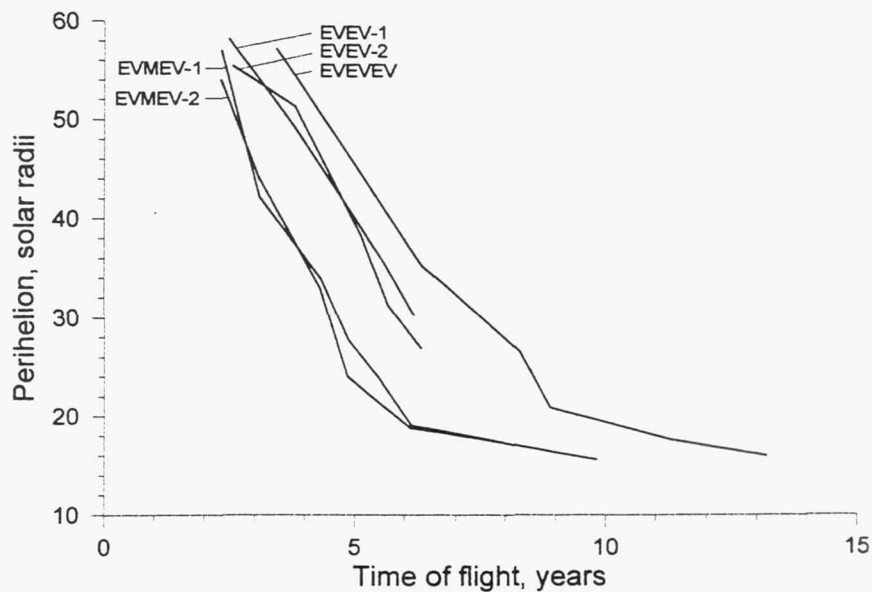


Figure 6. Perihelion distance versus time of flight



## LAUNCH VEHICLE AND SPACECRAFT MASS

Thus the launch delta-V in LEO varies from 3.6 to 4.1 km/s for the considered mission options. This means that a low-cost launch vehicle such as Russian Rockot (SS 19 missile) can be used for the mission. This launch vehicle can deliver about 1900 kilos to LEO. Assuming that a solid motor rocket is used as a kick-stage for Rockot one can obtain that the spacecraft wet mass can be about 370 kilos for the EVEVEV and EVEV options and about 270 kilos for the EVMEV ones. Table 7 contains more detailed information about the spacecraft initial mass for all considered mission options and for three Russian launch vehicles.

**Table 7**  
**THE SPACECRAFT WET MASS\***

Option	Launch vehicle		
	Rockot	Molniya	Soyuz 2/Fregat
EVEVEV	370	1190	1450
EVMEV-1	280	-	1120
EVMEV-2	270	-	1090
EVEV-1	370	1190	1450
EVEV-2	340	1120	1340

## SOLAR ELECTRIC PROPULSION

As one can see on the figures 2 - 5 the spacecraft spends most of the flight time within the Earth orbit. This makes reasonable using the solar electric propulsion (SEP) for active spacecraft maneuvers. Assume the following SEP characteristics:

Power = 4 W per 1 kilo of the spacecraft mass near Earth

Specific impulse = 2000 s

Efficiency = 0.6

Below some active maneuvers which can be performed by means of SEP are described. All assessments below are approximate, degradation of the solar arrays with time is ignored. In the reality strong Sun radiation can cause the degradation, however it is assumed that the solar panels are somehow protected.

### Correction Maneuvers

Cost of the correction maneuvers varies from 20 to 50 m/s for each swingby; total cost of the maneuvers for the mission options considered above is about 300 - 400 m/s. To provide such delta-V by means of the SEP the propellant consumption must be of about 2 percent of the spacecraft mass.

---

\* Launch from Baikonur is supposed.

## Shortening the Flight Duration and Lowering Perihelion

The flight duration can be shortened using SEP in two ways:

- using the active maneuvers between the swingbys; this can shorten the time intervals between the swingbys and possibly diminish amount of them;
- interrupting the multiple gravity assist maneuver earlier during its second step and lowering perihelion of the final orbit by means of SEP.

The second way will be considered here. As it is seen on Fig.6 lowering perihelion below  $20 R_S$  using the multiple gravity assist maneuver takes a long time. It can be done much faster using SEP. Consider the EVEVEV option and assume that the swingbys are terminated on 17/12/2008 (see table 1) and further lowering of the perihelion is performed by means of SEP. Also assume that the SEP runs only in the short arc of about 40 degrees near the aphelion in order to diminish the gravity loss. The perihelion distance versus time of flight is shown in Fig.7; the solid and dashed lines correspond to the maneuvers using Venus gravity assists and the SEP respectively. Change of the spacecraft mass due to the propellant consumption is also shown on Fig.7.

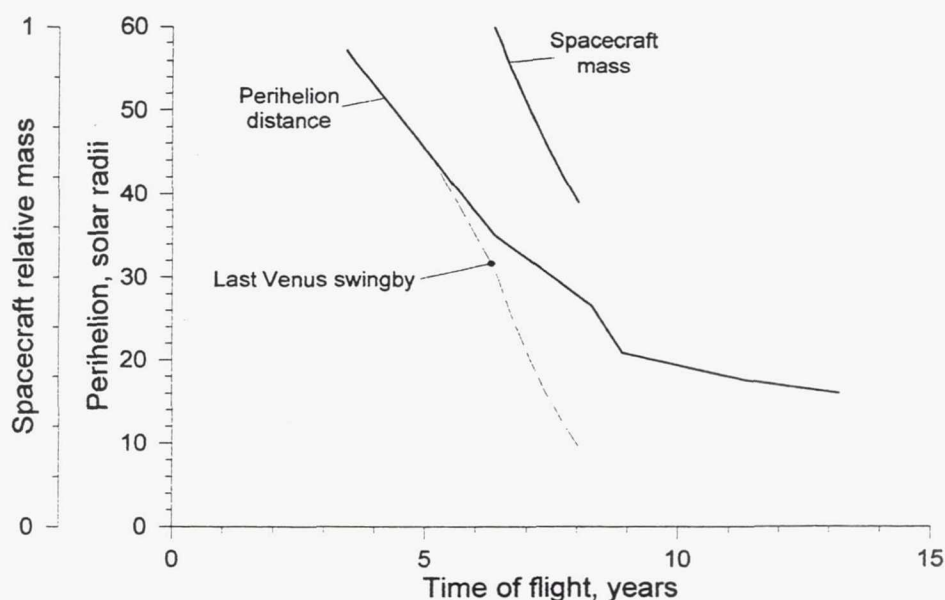


Figure 7. Perihelion distance and spacecraft relative mass versus time

As one can see on Fig.7 the perihelion distance  $16 R_S$  can be reached for 7.4 years using SEP, i.e. almost in 6 years faster than in case of the Venus swingbys only; this operation will take the propellant amount of about 23 percent of the spacecraft mass. Then the perihelion can be lowered down to  $10 R_S$  during next 8 months (two revolutions of the spacecraft around the Sun). Total propellant consumption will be of about 35 percent of the spacecraft mass.

## Turning the Orbit Plane

Assume that the orbit with perihelion distance  $16 R_S$  and semi-major axis 59.7 mil. km is somehow reached (this corresponds to the final orbit for the option EVEVEV or

EVMEV-2, see tables 1, 3). Then the orbit plane can be turned by means of SEP. Assume that the SEP runs only within the 30 degree arc near aphelion (this corresponds to the 40 days of continued SEP run). Values of the orbit inclination to the ecliptic\* and the spacecraft relative mass versus time are shown on Fig.8.

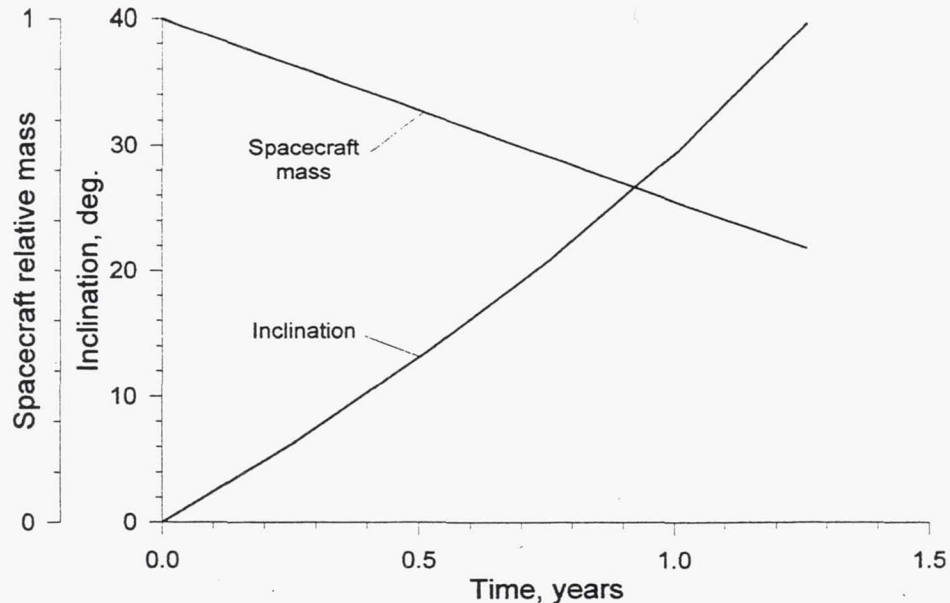


**Figure 8. Spacecraft orbit inclination and relative mass versus time**

It is seen on Fig.8 that the inclination of about 40 degrees can be reached for about 15 months (5 spacecraft revolutions).

### General Remarks

Note that if both the lowering perihelion and turning the orbit plane are needed it is better to do the maneuvers simultaneously using an optimal low thrust direction. This will save time and propellant.

All the maneuvers described above can be performed faster if the SEP will run in a longer arc of the orbit; however this will lead to an increased propellant consumption. The SEP also can be used for the phasing orbit in order to encounter Mercury and for other spacecraft maneuvers.

### REFERENCES

1. A.A. Galeev, O.L. Vaisberg et al., Project Ziolkovsky - Solar Probe Mission Concept, *Adv. Space Research*, V. 17, No. 3, 1995, pp. (3)13 - (3)20.
2. B.T. Tsurutani and O.L. Vaisberg, The Solar Probe Mission and Comments on Plasma Wave Observations, in *Robotic Exploration Close to the Sun*, editor Shadia Rifai Habbal, AIP Press, New York, 1996, p. 255.

\* To be correct the inclination to the initial spacecraft orbit plane (i.e. to the Venus one) is shown on Fig.8.



# REPORT DOCUMENTATION PAGE

Form Approved  
OMB No. 0704-0188

Public reporting burden for this collection of information is estimated to average 1 hour per response, including the time for reviewing instructions, searching existing data sources, gathering and maintaining the data needed, and completing and reviewing the collection of information. Send comments regarding this burden estimate or any other aspect of this collection of information, including suggestions for reducing this burden, to Washington Headquarters Services, Directorate for Information Operations and Reports, 1215 Jefferson Davis Highway, Suite 1204, Arlington, VA 22202-4302, and to the Office of Management and Budget, Paperwork Reduction Project (0704-0188), Washington, DC 20503.

1. AGENCY USE ONLY (Leave blank)		2. REPORT DATE May 1998	3. REPORT TYPE AND DATES COVERED Conference Publication	
4. TITLE AND SUBTITLE Preprint—AAS/GSFC 13th International Symposium on Space Flight Dynamics, Volume 2			5. FUNDING NUMBERS 572	
6. AUTHOR(S) Tom Stengle, Editor				
7. PERFORMING ORGANIZATION NAME(S) AND ADDRESS (ES) Guidance, Navigation and Control Center Flight Dynamics Analysis Branch Goddard Space Flight Center Greenbelt, Maryland 20771			8. PERFORMING ORGANIZATION REPORT NUMBER 98B00041	
9. SPONSORING / MONITORING AGENCY NAME(S) AND ADDRESS (ES) National Aeronautics and Space Administration Washington, DC 20546-0001			10. SPONSORING / MONITORING AGENCY REPORT NUMBER CP-1998-206858	
11. SUPPLEMENTARY NOTES				
12a. DISTRIBUTION / AVAILABILITY STATEMENT Unclassified-Unlimited Subject Category: 13 Distribution: Nonstandard Availability: NASA CASI (301) 621-0390.			12b. DISTRIBUTION CODE	
13. ABSTRACT (Maximum 200 words) This conference proceedings preprint includes papers and abstracts presented at the 13th International Symposium on Space Flight Dynamics, May 11-15, 1998. Cosponsored by American Astronautical Society and the Guidance, Navigation and Control Center of the Goddard Space Flight Center, this symposium featured technical papers on a wide range of issues related to orbit-attitude prediction, determination, and control; attitude sensor calibration; attitude dynamics; and mission design.				
14. SUBJECT TERMS American Astronautical Society, spaceflight dynamics.			15. NUMBER OF PAGES 531	
			16. PRICE CODE	
17. SECURITY CLASSIFICATION OF REPORT Unclassified	18. SECURITY CLASSIFICATION OF THIS PAGE Unclassified	19. SECURITY CLASSIFICATION OF ABSTRACT Unclassified	20. LIMITATION OF ABSTRACT UL	